

University of Windsor

Scholarship at UWindor

Electronic Theses and Dissertations

Theses, Dissertations, and Major Papers

2017

Solid-state NMR of Complex Nano- and Microcrystalline Materials

David Hirsh

University of Windsor

Follow this and additional works at: <https://scholar.uwindsor.ca/etd>

Recommended Citation

Hirsh, David, "Solid-state NMR of Complex Nano- and Microcrystalline Materials" (2017). *Electronic Theses and Dissertations*. 7361.

<https://scholar.uwindsor.ca/etd/7361>

This online database contains the full-text of PhD dissertations and Masters' theses of University of Windsor students from 1954 forward. These documents are made available for personal study and research purposes only, in accordance with the Canadian Copyright Act and the Creative Commons license—CC BY-NC-ND (Attribution, Non-Commercial, No Derivative Works). Under this license, works must always be attributed to the copyright holder (original author), cannot be used for any commercial purposes, and may not be altered. Any other use would require the permission of the copyright holder. Students may inquire about withdrawing their dissertation and/or thesis from this database. For additional inquiries, please contact the repository administrator via email (scholarship@uwindsor.ca) or by telephone at 519-253-3000ext. 3208.

Solid-state NMR of Complex Nano- and Microcrystalline Materials

By

David A. Hirsh

A Dissertation
Submitted to the Faculty of Graduate Studies
through the Department of Chemistry and Biochemistry
in Partial Fulfillment of the Requirements for
the Degree of Doctor of Philosophy
at the University of Windsor

Windsor, Ontario, Canada

2017

© 2017 David A. Hirsh

Solid-state NMR of Complex Nano- and Microcrystalline Materials

by

David Hirsh

APPROVED BY:

E. Munson, External Examiner
University of Kentucky

C. Weisener
Great Lakes Institute for Environmental Research

C. Macdonald
Department of Chemistry and Biochemistry

H. Eichhorn
Department of Chemistry and Biochemistry

R. Schurko, Advisor
Department of Chemistry and Biochemistry

December 11, 2017

DECLARATION OF CO-AUTHORSHIP / PREVIOUS PUBLICATION

I am the primary author of all of the publications resulting from, and the text of this thesis. I performed all of the primary characterization experiments and interpretation of data described herein. However, each project was conducted in collaboration with researchers at other Universities and/or in Industry. Their contributions were the synthesis of the materials studied, acquisition of supporting characterization data (*e.g.*, TEM, XRD, and ICP-MS results), and assistance in proof-reading. I also acknowledge the significant contributions of my supervisor, Professor R.W. Schurko, who aided in the analysis of spectroscopic data, planning of experiments, and writing.

I am aware of the University of Windsor Senate Policy on Authorship and I certify that I have properly acknowledged the contribution of other researchers to my thesis, and have obtained written permission from each of the co-author(s) to include the above material(s) in my thesis. I certify that, with the above qualification, this thesis, and the research to which it refers, is the product of my own work.

Two of the chapters in this thesis have been previously published in peer-reviewed journals:

Chapter 2: Hirsh, D. A.; Johnson, N. J. J.; Van Veggel, F. C. J. M.; Schurko, R. W. *Chem. Mater.* **2015**, 27, 6495.

Chapter 5: Hirsh, D. A.; Rossini, A. J.; Emsley, L.; Schurko, R. W. *Phys. Chem. Chem. Phys.* **2016**, 18, 25893.

I certify that I have obtained written permission from the copyright owners to include the above published materials in my thesis. I certify that the above material describes work completed during my registration as a graduate student at the University of Windsor.

Two of the chapters in this thesis will be submitted for publication in December 2017/January 2018:

Chapter 3: Hirsh, D.A.; Zhang, X.; van Veggel, F.C.J.M.; Schurko, R.W.; Structural Characterization of NaYF₄ Nanocrystals Containing Paramagnetic Ln³⁺ Dopants.

Chapter 6: Hirsh, D.A.; Su, Y.; Stueber, D.; Schurko, R.W.; Quantifying Disproportionation in Pharmaceutical Formulations with ³⁵Cl Solid-State NMR.

Chapters 4 and 7 are also being prepared for publication, and will be submitted in January/February 2018.

I declare that, to the best of my knowledge, my thesis does not infringe upon anyone's copyright nor violate any proprietary rights and that any ideas, techniques, quotations, or any other material from the work of other people included in my thesis, published or otherwise, are fully acknowledged in accordance with the standard referencing practices. Furthermore, to the extent that I have included copyrighted material that surpasses the bounds of fair dealing within the meaning of the Canada Copyright Act, I certify that I have obtained a written permission from the copyright owner(s) to include such material(s) in my thesis.

I declare that this is a true copy of my thesis, including any final revisions, as approved by my thesis committee and the Graduate Studies office, and that this thesis has not been submitted for a higher degree to any other University or Institution.

ABSTRACT

The work in this thesis demonstrates the utility and broad applicability of solid-state nuclear magnetic resonance (SSNMR) spectroscopy to the study of complex materials containing mixtures of multiple structures and/or disparate local environments. Multinuclear SSNMR is particularly well-suited to the characterization of such systems, and can provide a wealth of information that cannot be obtained with other instrumental methods. Studies involving two classes of materials are detailed herein, namely rare-earth nanoparticles and active pharmaceutical ingredients.

The first three projects described involve the study of inorganic rare-earth (RE, RE = Y, Sc, La-Lu) nanoparticles (NP), which have unique optical and magnetic properties that are desirable for a diverse range of applications. Many of the properties of these materials are related to the incorporation of dopants into the host structures. The chemical reactions necessary to prepare these materials are complex and challenging to optimize; however, careful structural analysis of these materials is imperative to inform and to improve their rational design. Herein, we first use multinuclear (*i.e.*, ^{19}F , ^{23}Na , ^{89}Y , ^1H , ^{13}C , ^{45}Sc) SSNMR to establish the molecular-level structure of a widely used undoped host material, $\beta\text{-NaYF}_4$, resolving a longstanding debate regarding the crystal structure. Similar experiments are used to probe the structures of NaYF_4 nanomaterials formed with advanced core/shell structures containing multiple RE-materials and having oleates bound to their surfaces. Expanding on this foundation, the structural effects of the incorporation of paramagnetic dopant ions in NaYF_4 NPs is described in a second study. Through the use of ultra-fast magic angle spinning (UFMAS) SSNMR experiments, we have obtained spectra with valuable details regarding the distributions of the dopant ions and their mean distances from other atoms in the

NP cores and surfaces. The final project in this area pertains to a distinct class of zeolitic RE-doped nanomaterials, where the structural effects of different dopants are compared using numerous characterization techniques, including multinuclear SSNMR spectroscopy, powder X-ray diffraction (PXRD), transmission electron microscopy (TEM), and electron paramagnetic resonance (EPR) spectroscopy.

The second half of this thesis concerns a prominent class of materials found in everyday life, active pharmaceutical ingredients (APIs). The identification of solid forms of APIs plays an important role in drug development, both in the discovery of new forms and quality assurance in manufacturing. Herein, three important areas of pharmaceutical research are addressed using multinuclear SSNMR methods, with a primary focus on the application of ultra-wideline ^{35}Cl SSNMR. (^{35}Cl is a spin-3/2 quadrupolar nucleus). First, methods to improve the lower detection limit of Cl in low wt-% dosage formulations through the use of dynamic nuclear polarization (DNP) enhanced ultra-wideline ^{35}Cl SSNMR spectra are presented. Next, a new method using ^{35}Cl SSNMR for the quantification of APIs in dosage formulations with a high level of accuracy is detailed. In this proof-of-concept study, it is also shown how quantification methods can be used to measure the amount of disproportionation (*i.e.*, conversion of cationic APIs to neutral free-base forms with distinct structures and properties) that occurs in a model dosage formulation. Finally, a case study of a variable hydrate HCl salt API is presented. Such materials form stable structures over a continuous range of non-stoichiometric hydration levels. This work demonstrates how ^{35}Cl SSNMR is well-suited to characterize such materials, given the ability of this technique to probe the sites of hydration and detect changes in the hydrated Cl^- anion environments as the material is dehydrated or rehydrated. For each of these projects, ^{35}Cl SSNMR data are supported by additional multinuclear experiments (*e.g.*, ^1H , ^2H , ^{13}C , ^{19}F , ^{23}Na) and other characterization methods (*e.g.*, XRD and thermal analysis).

DEDICATION

In memory of
William A. Hass, and Albert “Red” Hirsh
May 8, 1986
זיכרונם לברכה

ACKNOWLEDGEMENTS

I would like to thank the many people who have made one of the many contributions to the production of this thesis. To those of you whom I have unintentionally omitted from the following, my negligence is inexcusable, yet certain, and for that I apologize.

I must begin by thanking my supervisor, Professor R.W. Schurko (or is it spelled Shurko, Sharko, or Roob?). Rob has helped me become an independent spectroscopist, encouraging me to pursue projects I was passionate about and helping me find new areas to explore. Though he rarely sets foot in the lab anymore, Rob's supervising style still manages to be extremely hands-on. His care and attention to daily research developments made me feel like what I was doing mattered, and encouraged me to press on even when I got stuck. I have enjoyed the casual, yet productive work environment Rob fosters, and I think it helped alleviate much of the stress that would have otherwise permeated my graduate career.

Next, I would like to thank those individuals who were instrumental in my early experiences with NMR, and ultimately caused me to pursue it as a career. First, Professor Sophia Hayes, for taking me on as an undergraduate and exposing me to SSNMR, thereby sealing my fate as a spectroscopist forever. She was also the one to give me a list of suggestions for graduate schools to checkout, which included Windsor; it was truly the best place for me. Dr. Sarah Mattler for the many lunches at Qdoba, and for letting me bug her in the lab incessantly even though I had no idea what was going on. Marcel Hildebrand, who was extremely friendly and welcoming when I visited the UWindsor campus; he was instrumental in convincing me to come to Windsor. Furthermore, his thesis (as well as that of

Andrew Namespetra, to whom I am also indebted) laid a lot of the groundwork for my pharmaceutical studies.

Thank you to those who trained me on the spectrometer and in the theory of NMR. Dr. Bryan Lucier, who was the graduate student in charge of making sure I didn't break stuff. Thank you for teaching me to be efficient, careful, and to not be paralyzed by a fear of breaking stuff. Now, in the late stages of my PhD, I can appreciate the time you took during yours; I know I must have been a nuisance when all you wanted to do was finish up. To Professor Karen Johnston, thank you for helping me to become an independent spectroscopist; I vividly remember your telling me to acquire a ^{23}Na nutation curve by myself and when I continued to ask you questions you ultimately told me that "you're going to have to learn how to do this by yourself at some point, might as well be today." Also, thank you for your companionship and constant support; sorry I asked so many questions, especially about my "team-written" CSC poster.

Thank you to Chris O'Keefe, for being my eye-rolling partner and colleague. I've benefitted greatly from our chats about NMR, especially in the analysis of some particularly challenging samples. Thank you for your contributions to the ^2H NMR results detailed in this thesis, and innumerable proof readings of things I've written over the years. Thank you to Mike Jaroszewicz, who is one of the most brilliant and humble spectroscopists I have ever met. You have inspired me tremendously. Dr. Stanislav Veinberg, thank you for your constant willingness to help, often to your own detriment. My sincerest appreciation also goes to Dr. Sean Holmes and Austin Peach for their edits to chapters in this thesis. Finally, to the many other coworkers I've had in the Schurko group, thank you for being a lively bunch who were always willing to chat about random things, and sometimes NMR.

I am severely indebted to the many collaborators involved in the production of materials studied in this thesis, including students, faculty supervisors and industrial contacts. Their expertise has made this thesis possible and allowed me to learn about and study exotic materials I never would have been able to otherwise. Furthermore, thank you to Dr. Victor Terskikh for help acquiring high field data at the National Ultrahigh-field NMR Facility in Ottawa.

There are numerous members of the staff at the University of Windsor who have helped me extensively over the years. Matt Revington for support with the 500 MHz instrument, Joe Lichaa for technical support (especially with the PXRD equipment), Sinisia Jezdic for electronics repairs to probes and the VT stack. Finally the department secretaries, Marlene Bezaire (for going above-and-beyond her duties to help me, especially when I first moved to Windsor), Cathy Wilson (for her incredibly supportive and sincere concern for my well-being), and Beth Kickham (for her incredible schedule skills, and tolerance for bureaucracy).

Also, thank you to my committee members, for reading this thesis and challenging me to improve my understanding of my own work, and the field of chemistry as a whole.

I would also like to thank my family for their constant love and support (even when we are separated across different countries and continents). To Steph, thank you for taking this journey with me and accepting me despite/in spite of my faults. Your perseverance in the face of adversity has galvanized me to address my own burdens, which seem surmountable by comparison. There is no-one I would rather share in this accomplishment with.

Finally, to peer reviewer #2: typos are not major revisions, but thank you for pointing them out nonetheless.

TABLE OF CONTENTS

DECLARATION OF CO-AUTHORSHIP / PREVIOUS PUBLICATION	iii
ABSTRACT	v
DEDICATION	vii
ACKNOWLEDGEMENTS	viii
LIST OF TABLES	xvi
LIST OF FIGURES	xix
LIST OF ABBREVIATIONS	xxvii
LIST OF SYMBOLS	xxxii
Chapter 1 : Introduction, Background, and Context	1
1.1 Nuclear Magnetic Resonance Spectroscopy (NMR)	1
1.1.1 Thence Spin	2
1.2 NMR Interactions	4
1.2.1 Quadrupolar Interaction (\hat{H}_Q)	5
1.2.2 Chemical Shielding Interaction (\hat{H}_{CS})	10
1.2.3 Dipolar Interaction (\hat{H}_D)	13
1.2.4 Paramagnetic Interaction (\hat{H}_{ue})	14
1.3 NMR Methods	16
1.3.1 Single-Resonance Pulse Sequences	16
1.3.2 Ultra-wideline NMR Techniques	19
1.3.3 Double-Resonance Pulse Sequences	21
1.3.4 Dynamic Nuclear Polarization (DNP)	23
1.3.5 Additional Methods	27
1.4 “Real-World” Materials	28
1.4.1 Nanomaterials	29
1.4.2 Active Pharmaceutical Ingredients	33
1.5 References	39
Chapter 2 : The Local Structure of Rare-Earth Fluorides in Bulk and Core/Shell Nanocrystalline Materials	47
2.1 Introduction	47

2.2 Methods.....	51
2.2.1 Chemicals	51
2.2.2 Synthesis of sacrificial nanocrystals (SNCs).....	51
2.2.3 Synthesis of core–shell nanocrystals.....	52
2.2.4 Synthesis of bulk NaYF ₄ and NaLuF ₄ powders	53
2.2.5 Transmission Electron Microscopy	54
2.2.6 Powder X-ray Diffraction.....	54
2.2.7 Solid-State NMR	54
2.3 Results and Discussion.....	56
2.3.1 Transmission Electron Microscopy	56
2.3.2 Powder X-ray Diffraction.....	57
2.3.3 ²³ Na MAS NMR	59
2.3.4 ²³ Na MQMAS NMR.....	62
2.3.5 ¹⁹ F- ⁸⁹ Y CP/MAS NMR.....	63
2.3.6 ¹⁹ F MAS NMR.....	65
2.3.7 ¹⁹ F UFMAS NMR.....	67
2.3.8 ¹ H- ²³ Na and ¹⁹ F- ²³ Na CP/MAS NMR	72
2.4 Conclusions	76
2.5 References	77
Chapter 3 : Structural Characterization of NaYF₄ Nanocrystals Containing Paramagnetic Ln³⁺ Dopants.....	80
3.1 Introduction	80
3.2 Experimental Methods	82
3.2.1 Chemicals	82
3.2.2 Synthesis of NCs	83
3.2.3 Synthesis of Bulk Materials.....	83
3.2.4 Transmission Electron Microscopy (TEM).....	84
3.2.5 Powder X-ray Diffraction (PXRD).....	84
3.2.6 Inductively Coupled Plasma Mass Spectrometry (ICP-MS).....	84
3.2.7 SSNMR Characterization	85
3.3 Results and Discussion.....	86
3.3.1 Transmission Electron Microscopy (TEM).....	86
3.3.2 Powder X-ray Diffraction (PXRD).....	87
3.3.3 Inductively Coupled Plasma Mass Spectrometry (ICP-MS).....	87

3.3.4 Solid-State NMR	88
3.3.5 Effects of NC Dopant Level and Identity	88
3.3.6 NC Surfaces	98
3.3.7 Particle Size effects	103
3.4 Conclusions	107
3.5 References	109
Chapter 4 : Multinuclear Solid-State NMR as a Probe of the Molecular-Level Structure in Rare Earth-Doped Yttrium Fluoride Nanoparticles	112
4.1 Introduction	112
4.2 Methods	116
4.2.1 Chemicals	116
4.2.2 Synthesis of the Yttrium Fluoride Nanoparticles (YF NPs)	116
4.2.3 Purification of the Yttrium Fluoride Nanoparticles	117
4.2.4 Transmission Electron Microscopy (TEM) Experiments	117
4.2.5 Solid-State NMR (SSNMR) Experiments	118
4.2.6 Powder X-ray Diffraction (PXRD) Experiments	120
4.2.7 Electron Paramagnetic Resonance (EPR) Experiments	120
4.3 Results and Discussion	120
4.3.1 Undoped NP Material, YF	120
4.3.2 Preparation of Samples with Other RE Elements	125
4.3.3 Sc-Containing NPs	126
4.3.4 Er-Containing Samples	135
4.3.5 Eu-Containing Samples	146
4.3.6 General Structural Discussion (All Dopants)	153
4.4 Conclusions	155
4.5 References	157
Chapter 5 : ³⁵Cl Dynamic Nuclear Polarization Solid-State NMR of Active Pharmaceutical Ingredients	160
5.1 Introduction	160
5.2 Methods	164
5.2.1 Sample Preparation	164
5.2.2 VT PXRD	165
5.2.3 NMR	165
5.2.4 Software	167

5.3 Results and Discussion.....	167
5.3.1 Histidine HCl.....	167
5.3.2 Ambroxol HCl.....	171
5.3.3 Isoxsuprine HCl.....	173
5.3.4 Diphenhydramine HCl.....	177
5.3.5 Cetirizine HCl.....	180
5.4 Conclusions.....	182
5.5 References.....	185
Chapter 6 : Quantifying Disproportionation in Pharmaceutical Formulations with ³⁵Cl Solid-State NMR.....	190
6.1 Introduction.....	190
6.2 Experimental Methods.....	195
6.2.1 Chemicals.....	195
6.2.2 Sample Preparation.....	196
6.2.3 Solid-State NMR (SSNMR) Experiments.....	198
6.2.4 Powder X-ray Diffraction (PXRD) Experiments.....	199
6.3 Results and Discussion.....	199
6.3.1 Pioglitazone HCl.....	199
6.3.2 PiogHCl:NaSt mixture.....	200
6.3.3 PiogHCl:MgSt Mixture.....	204
6.3.4 Quantification of ³⁵ Cl SSNMR Spectra.....	207
6.3.5 Quantification of Disproportionation.....	211
6.4 Conclusions.....	213
6.5 References.....	216
Chapter 7 : <i>In Situ</i> Characterization of Water in a Channel Hydrate API using ³⁵Cl SSNMR.....	219
7.1 Introduction.....	219
7.2 Methods.....	223
7.2.1 Chemicals.....	223
7.2.2 Sample Preparation.....	223
7.2.3 Solid-State NMR Experiments.....	224
7.2.4 NMR Tensor Calculations.....	225
7.3 Results and Discussion.....	226
7.3.1 Crystal Structure of GNE-A.....	226

7.3.2 Thermogravimetric Analysis (TGA)	228
7.3.3 ³⁵ Cl SSNMR of GNE-A.....	228
7.3.4 DFT-Calculations using CASTEP	231
7.3.5 Variable-Temperature ³⁵ Cl NMR of GNE-A	233
7.3.6 Characterization of Samples with Different Hydration Levels	235
7.3.7 ³⁵ Cl SSNMR of a Partially Deuterated sample	238
7.3.8 Multinuclear NMR	239
7.3.9 ¹³ C SSNMR.....	239
7.3.10 ¹ H SSNMR.....	241
7.3.11 ² H SSNMR.....	243
7.4 Conclusions	247
7.5 References	250
Chapter 8 : Conclusions and Future Outlook	253
8.1 General Overview	253
8.2 Nanoparticles.....	254
8.2.1 Future work - Nanomaterials.....	255
8.3 Active pharmaceutical ingredients	257
8.3.1 Future Work - APIs	258
8.4 Final Thoughts	260
8.5 References	262
Appendix A : Supporting Tables and Figures for Chapter 2	263
Appendix B : Supporting Tables and Figures for Chapter 3	276
Appendix C : Supporting Tables and Figures for Chapter 4	289
Appendix D : Supporting Tables and Figures for Chapter 5	303
Appendix E : Supporting Tables and Figures for Chapter 6	316
Appendix F : Supporting Tables and Figures for Chapter 7.....	329
Vita Auctoris.....	345

LIST OF TABLES

Table 2.1. Experimental ^{23}Na EFG Tensor Parameters corresponding to Site 2. ^a 60	60
Table 2.2. Summary of Experimental ^{19}F MAS NMR Parameters ($\nu_{\text{rot}} = 25$ kHz, $B_0 = 9.4$ T).....	68
Table 2.3. Summary of Experimental ^{19}F UFMAS NMR Parameters ($\nu_{\text{rot}} = 65$ kHz, $B_0 = 11.7$ T).....	68
Table 3.1. Particle sizes of the NC NaYF_4 samples obtained from TEM measurements.....	87
Table 3.2. Er and Tm content of the doped samples obtained from ICP-MS measurements. ^a	88
Table 3.3. Experimental values of the span of the DS tensor (Δ_{aniso}) and corresponding calculated nuclear- Ln^{3+} distances obtained from fits of the SSNMR data.	92
Table 4.1. Ionic radii of different RE ions with various coordination numbers as reported by Shannon <i>et al.</i> ⁶³	112
Table 4.2. Particle sizes measured using TEM (Figure C1).	118
Table 4.3. List of observed ^{19}F , ^{89}Y , and ^1H NMR chemical shifts and peak assignments for the undoped YF NP sample, as discussed in the text.	122
Table 4.4. List of observed ^{45}Sc , ^{19}F , ^{89}Y , and ^1H NMR chemical shifts and peak assignments for the Sc-containing samples, as discussed in the text.....	133
Table 4.5. List of observed ^{19}F , ^{89}Y , and ^1H NMR chemical shifts and peak assignments for the Eu-containing samples, as discussed in the text.	139
Table 4.6. Experimental values of the span of the DSA tensor (Δ_{aniso}) and corresponding calculated nuclear- Ln^{3+} distances obtained from fits of the ^{19}F and ^1H SSNMR data.	140
Table 6.1. Sample masses used to prepare materials for quantification with ^{35}Cl SSNMR.	197
Table 6.2. Experimental and calculated amounts of PiogHCl in the standard samples.....	210
Table 6.3. Experimental and calculated amounts of PiogHCl in the stearate mixture samples.	212
Table 7.1. Close H \cdots Cl contacts (< 2.2 Å) for the two crystallographically distinct Cl sites in GNE-A.	228
Table 7.2. Experimental and calculated ^{35}Cl NMR tensor parameters of GNE-A. ^a	230

Table 7.3. Experimental $T_2^{\text{eff}}(^{35}\text{Cl})$ constants obtained from the WURST-CPMG spectra of GNE-A acquired at different temperatures before and after heating in the magnet. ^a	235
Table 7.4. Experimental ^2H EFG tensor parameters from the spectrum of Rehydrate-D₂O acquired at $-125\text{ }^\circ\text{C}$. ^{a,b}	244
Table 2.1. Experimental ^{23}Na EFG Tensor Parameters corresponding to Site 2. ^a 60	
Table 2.2. Summary of Experimental ^{19}F MAS NMR Parameters ($v_{\text{rot}} = 25\text{ kHz}$, $B_0 = 9.4\text{ T}$).	68
Table 2.3. Summary of Experimental ^{19}F UFMAS NMR Parameters ($v_{\text{rot}} = 65\text{ kHz}$, $B_0 = 11.7\text{ T}$).	68
Table 3.1. Particle sizes of the NC NaYF ₄ samples obtained from TEM measurements.	87
Table 3.2. Er and Tm content of the doped samples obtained from ICP-MS measurements. ^a	88
Table 3.3. Experimental values of the span of the DS tensor (Δ_{aniso}) and corresponding calculated nuclear-Ln ³⁺ distances obtained from fits of the SSNMR data.	92
Table 4.1. Ionic radii of different RE ions with various coordination numbers as reported by Shannon <i>et al.</i> ⁶³	112
Table 4.2. Particle sizes measured using TEM (Figure C1).	118
Table 4.3. List of observed ^{19}F , ^{89}Y , and ^1H NMR chemical shifts and peak assignments for the undoped YF NP sample, as discussed in the text.	122
Table 4.4. List of observed ^{45}Sc , ^{19}F , ^{89}Y , and ^1H NMR chemical shifts and peak assignments for the Sc-containing samples, as discussed in the text.	133
Table 4.5. List of observed ^{19}F , ^{89}Y , and ^1H NMR chemical shifts and peak assignments for the Eu-containing samples, as discussed in the text.	139
Table 4.6. Experimental values of the span of the DSA tensor (Δ_{aniso}) and corresponding calculated nuclear-Ln ³⁺ distances obtained from fits of the ^{19}F and ^1H SSNMR data.	140
Table 6.1. Sample masses used to prepare materials for quantification with ^{35}Cl SSNMR.	197
Table 6.2. Experimental and calculated amounts of PiogHCl in the standard samples.	210
Table 6.3. Experimental and calculated amounts of PiogHCl in the stearate mixture samples.	212
Table 7.1. Close H \cdots Cl contacts ($< 2.2\text{ \AA}$) for the two crystallographically distinct Cl sites in GNE-A.	228

Table 7.2. Experimental and calculated ^{35}Cl NMR tensor parameters of GNE-A. ^a	230
Table 7.3. Experimental $T_2^{\text{eff}}(^{35}\text{Cl})$ constants obtained from the WURST-CPMG spectra of GNE-A acquired at different temperatures before and after heating in the magnet. ^a	235
Table 7.4. Experimental ^2H EFG tensor parameters from the spectrum of Rehydrate-D₂O acquired at $-125\text{ }^\circ\text{C}$. ^{a,b}	244

LIST OF FIGURES

- Figure 1.1** The effects of increasing external magnetic field strength (\mathbf{B}_0) on the spin energy levels of a spin-3/2 nucleus. Allowed transitions between the non-degenerate spin states are labeled as satellite transitions (ST) and the central transition (CT), which have equal transition energies ($\Delta E = \hbar\gamma B_0$).3
- Figure 1.2** Representations of nuclei with spherical ($Q = 0$), and non-spherical (oblate, $Q < 0$ or prolate, $Q > 0$) distributions of positive charge.6
- Figure 1.3** The effects of the a) Zeeman interaction, b) FOQI, and c) SOQI on the energy levels of an isolated spin-3/2 quadrupolar nucleus in an external magnetic field, where ω_0 is the Larmor frequency and $\omega_Q = (3C_Q)/[4I(I - 1)]$ is the quadrupolar frequency. The relative magnitudes of the interaction are not to scale.7
- Figure 1.4** Analytical simulations of ^{35}Cl central transition ($+1/2 \leftrightarrow -1/2$) NMR spectra under static sample conditions at $B_0 = 9.4$ T. a) $\eta_Q = 0.4$, C_Q ranges from 8 to 2 MHz; b) $C_Q = 6$ MHz, η_Q ranges from 1.0 to 0.2. These spectra represent typical ranges of the quadrupolar parameters for the Cl^- anions described herein.9
- Figure 1.5** Calculated quadrupole coupling constants, C_Q , of different sodium-oxygen coordination environments having different symmetry and coordination numbers. Created by the author based on the adaptation of a figure from Koller, H. *J. Phys. Chem.* **1994**, 98, 1544.10
- Figure 1.6** Different conventions used to describe the CS tensor. Top (green) the frequency-ordered principal shift convention,²⁹ middle (red) the Herzfeld-Berger convention,³⁰ and the Haeberlen-Mehring-Spiess convention.³¹⁻³³ Unlike the quadrupolar interaction, this tensor is non-traceless, and the average of the three PAS components produces the isotropic chemical shift, $\delta_{\text{iso}} = (\delta_{11} + \delta_{22} + \delta_{33})/3$. The isotropic chemical shift is the primary NMR observable in the spectra of solutions. In solids, however, the CSA provides additional information on the orientation of the constituent atoms with respect to the magnetic field.....12
- Figure 1.7** NMR pulse sequences used in this work. See text for details.18
- Figure 1.8** The a) phase profile, b) amplitude profile, and c) effective linear transmitter sweep that occurs over the course of a 50 μs WURST pulse.20

Figure 1.9 Schematic three-spin energy level diagrams detailing the key steps in the cross effect DNP mechanism a) at thermal equilibrium (<i>e.g.</i> , without DNP), b) after saturation of one of the electron EPR transitions, and c) the result of DNP-enhancement. The energy levels are labeled with the spin states (+ or -) of the dipolar-coupled electrons (red, s_1 , or green, s_2) and proton (blue, I), respectively. The areas of the purple circles indicate the relative populations of the energy levels. Red dashed lines correspond to EPR transitions that are saturated during the experiment (<i>i.e.</i> , $\Delta E = \omega_0, S1$, the Larmor frequency of one of the electrons), and blue arrows indicate the NMR transitions that are enhanced as a result of the process.....	24
Figure 1.10 Schematic depictions of different solid forms of APIs (shown in different colors). Different shapes correspond to distinct types of molecules in the solid-state structures.....	34
Figure 2.1. TEM images of the a) 27 nm NC b) 37 nm NC samples used to measure the particle sizes.....	57
Figure 2.2. PXRD diffraction patterns of a) bulk NaYF ₄ , b) bulk NaLuF ₄ , c) 27 nm NC, and d) 37 nm NC. The red and orange dashed lines indicate features in the JCPDS reference patterns of hexagonal phase β -NaYF ₄ (JCPDS: 16-0334) and β -NaLuF ₄ (JCPDS: 27-0726), respectively. Asterisks denote impurities, see text for details.	58
Figure 2.3. ²³ Na{ ¹⁹ F} MAS NMR spectra of a) bulk NaYF ₄ , b) bulk NaLuF ₄ , c) 27 nm NC, and d) 37 nm NC ($\nu_{\text{rot}}=12$ kHz). The inset shows the low frequency regions of the spectra.	61
Figure 2.4. ²³ Na MQMAS NMR spectrum of bulk NaYF ₄ ($\nu_{\text{rot}} = 12$ kHz). The two ²³ Na powder patterns indicate the presence of two magnetically distinct Na sites. Asterisks denote spinning sidebands from Site 1.	63
Figure 2.5. ¹⁹ F- ⁸⁹ Y CP static NMR spectra of a) bulk NaYF ₄ , b) 27 nm NC, and c) 37 nm NC.....	64
Figure 2.6. ¹⁹ F- ⁸⁹ Y CP/MAS NMR spectra of a) bulk NaYF ₄ , b) 27 nm NC, and c) 37 nm NC ($\nu_{\text{rot}} = 6$ kHz).....	65
Figure 2.7. ¹⁹ F MAS NMR spectra of a) bulk NaYF ₄ , b) bulk NaLuF ₄ , c) 27 nm NC, and d) 37 nm NC ($\nu_{\text{rot}} = 25$ kHz).....	66
Figure 2.8. ¹⁹ F UFMAS NMR spectrum of the 27 nm NC ($\nu_{\text{rot}} = 65$ kHz, $B_0 = 11.7$ T).....	69
Figure 2.9. A supercell (1×1×3) of Structure II, ³⁶ showing a possible arrangement of the fractional site occupancies in the disordered structure. Yellow = Na, Green = F, Blue = Y. The six-coordinate Na sites are along the cell-edges (in yellow).	71
Figure 2.10. ²³ Na MAS NMR spectra of the 27 nm NC ($\nu_{\text{rot}} = 6$ kHz), under the conditions of a) direct excitation, b) CP from ¹⁹ F, and c) CP from ¹ H.....	73

- Figure 3.1.** ^{19}F UFMAS ($v_{\text{rot}} = 60$ kHz) NMR spectra of a) undoped NaYF_4 NCs, b)-d) Er-doped NaYF_4 NCs and e)-g) Tm-doped NaYF_4 NCs. Percentages indicate the at.% Ln^{3+} dopant present in each sample. Arrows indicate the isotropic peaks; all other features in the spectra are spinning sidebands. The insets highlight the isotropic features of the spectra. 89
- Figure 3.2.** $^{23}\text{Na}\{^{19}\text{F}\}$ MAS ($v_{\text{rot}} = 12$ kHz) NMR spectra of a) undoped NaYF_4 NCs, b)-d) Er-doped NaYF_4 NCs and e)-g) Tm-doped NaYF_4 NCs. The insets highlight the isotropic features of the spectra. 96
- Figure 3.3.** ^{19}F - ^{89}Y CP/MAS ($v_{\text{rot}} = 5$ kHz) NMR spectra of a) undoped NaYF_4 NCs, b)-d) Er-doped NaYF_4 NCs and e)-g) Tm-doped NaYF_4 NCs. Percentages indicate the at.% Ln^{3+} dopant present in each sample. Asterisks denote spinning sidebands. 98
- Figure 3.4.** ^1H UFMAS ($v_{\text{rot}} = 60$ kHz) NMR spectra of a) undoped 19 nm NaYF_4 NCs, b)-d) Er-doped NaYF_4 NCs and e)-g) Tm-doped NaYF_4 NCs. Percentages indicate the at.% Ln^{3+} dopant present in each sample. Arrows indicate the isotropic peaks; all other features in the spectra are spinning sidebands. The insets highlight the isotropic features of the spectra. 99
- Figure 3.5.** $^{13}\text{C}\{^1\text{H}\}$ MAS ($v_{\text{rot}} = 12$ kHz) NMR spectra of a) 19 nm and b) 33 nm undoped NaYF_4 NCs, c)-e) Er-doped NaYF_4 NCs and f)-h) Tm-doped NaYF_4 NCs. Percentages indicate the at.% Ln^{3+} dopant present in each sample. Asterisks denote spinning sidebands. Daggers indicate signal from an impurity of trifluoroacetate, as discussed in the text. The insets on the right highlight the difference in relative intensity of the SSBs, and are scaled such that the intensities of the isotropic peaks are the same. The inset on the left contains an expansion of the alkene region of the spectra of the Er-doped samples. 101
- Figure 3.6.** ^1H - ^{89}Y CP/MAS ($v_{\text{rot}} = 5$ kHz) NMR spectra (green, top row) of NC samples and ^{19}F - ^{89}Y CP/MAS ($v_{\text{rot}} = 5$ kHz) NMR spectra of bulk samples (red, middle row) and NC samples (blue, bottom row). Each column contains spectra of samples with the same amount of dopant: a) undoped samples, b) with 2 at.% Er^{3+} dopant, c) with 2 at.% Tm^{3+} dopant. Dashed lines indicate features that are present in the spectra of the NC samples. 102
- Figure 3.7.** ^{19}F UFMAS ($v_{\text{rot}} = 60$ kHz) NMR spectra of the undoped NaYF_4 samples with different particle sizes: a) bulk samples (> 2 μm), b) NC (33 nm), c) NC (19 nm). Single and double daggers denote peaks from minor NaF and NH_4F impurities, respectively. Asterisks denote spinning sidebands. The insets highlight the isotropic features of the spectra. 104

- Figure 4.1.** Crystal structure of **YF** shown from two views (rotated 90° from one another, as indicated by the crystallographic axes). This representation highlights the void spaces produced by the pores (yellow spheres) in the dual channel structure. The void spaces are connected by H₃O⁺ ions, shown as red spheres. The [Y₆F₃₂]¹⁴⁻ UOA octahedral-like building units are represented by green polyhedra..... 115
- Figure 4.2.** Multinuclear SSNMR spectra of the undoped **YF** NPs: a) ¹⁹F UFMAS (ν_{rot} = 60 kHz) (inset shows an expansion of the isotropic peaks), b) ¹⁹F-⁸⁹Y CP/MAS (ν_{rot} = 5 kHz) (inset shows the peaks with increased vertical scaling), and c) ¹H UFMAS (ν_{rot} = 60 kHz). These spectra are reproduced in the subsequent figures for comparison with those of the other samples..... 121
- Figure 4.3.** ⁴⁵Sc{¹⁹F} UFMAS (ν_{rot} = 60 kHz) NMR spectra of the Sc-containing samples. The inset shows the full spectral window and low intensity spinning sidebands..... 127
- Figure 4.4.** ¹⁹F UFMAS (ν_{rot} = 60 kHz) NMR spectra of the Sc-containing samples. The inset shows an expansion of the isotropic peaks. Dashed lines indicate distinct features that are not present in the spectrum of **YF**. The dagger symbol denotes a F⁻ impurity. All of the other features are spinning sidebands..... 129
- Figure 4.5.** ¹⁹F-⁸⁹Y CP/MAS (ν_{rot} = 5 kHz) NMR spectra of the Sc-containing samples and **YF**. The inset shows an expansion of the same spectra with the spectra scaled to have same maximum intensity. The corresponding scaling factors are listed in the inset..... 131
- Figure 4.6.** ¹H UFMAS (ν_{rot} = 60 kHz) NMR spectra of the Sc-containing samples and **YF**. 135
- Figure 4.7.** ¹⁹F UFMAS (ν_{rot} = 60 kHz) NMR spectra of the Er-containing samples and **YF**. The inset shows an expanded view of the isotropic peaks. The dagger and double dagger symbols denote a F⁻ impurity and background signal from the probe, respectively (see **Figure C11**). All of the other features are spinning sidebands..... 136
- Figure 4.8.** ¹⁹F-⁸⁹Y CP/MAS (ν_{rot} = 5 kHz) NMR spectra of the Er-containing samples and **YF**. The inset shows the spectra scaled to the same maximum intensity. Asterisks denote spinning sidebands..... 142
- Figure 4.9.** ¹H UFMAS (ν_{rot} = 60 kHz) NMR spectra of the Er-containing samples and **YF**. The insets show expansions of the isotropic peaks. All other features are spinning sidebands. 143
- Figure 4.10.** ¹⁹F UFMAS (ν_{rot} = 60 kHz) NMR spectra of the Eu-containing samples and **YF**. The inset shows an expanded view of the isotropic peaks, dashed lines indicate the locations of signals from YF₃. The dagger symbol denotes a F⁻ impurity. All of the other features are spinning sidebands..... 147

- Figure 4.11.** ^{19}F - ^{89}Y CP/MAS ($v_{\text{rot}} = 5$ kHz) NMR spectra of the Eu-containing samples (solid lines) and **YF** (dashed line). The latter is shown in the outset with *ca.* 0.25 vertical scaling, so that the lower intensity features from impurities in the Eu-containing samples can be seen. The right inset shows an expanded view of the most intense features in the spectra vertically scaled to have the same maximum intensity. The left inset shows the full spectrum of **YF:Eu50** with increased vertical scaling. 149
- Figure 4.12.** ^1H UFMAS ($v_{\text{rot}} = 60$ kHz) NMR spectra of the Eu-containing samples and **YF**. The inset shows the full spectrum of **YF:Eu50** with increased vertical scaling. 152
- Figure 5.1.** Molecular structures of APIs. 164
- Figure 5.2.** ^{13}C and ^{35}Cl SSNMR spectra of finely ground **hist** impregnated with a 15 mM TEKPol/TCE solution acquired at 100 K and $B_0 = 9.4$ T. a) ^1H - ^{13}C CP/MAS spectra acquired with and without microwaves. The top inset shows the two ^{13}C spectra scaled to the same maximum intensity. Asterisks denote spinning sidebands. b) ^1H - ^{35}Cl CP-CPMG spectra acquired with microwaves and rotation during part of the recycle delay period (SOSO conditions, red), with microwaves and a stationary sample (blue), and a stationary sample without microwaves (black). The inset shows a vertical expansion of the ^{35}Cl SSNMR spectra. 168
- Figure 5.3.** a) DNP-enhanced ^{35}Cl SSNMR spectra of finely ground **hist** impregnated with a 15 mM TEKPol/TCE solution acquired with the CP-Echo pulse sequence under continuous slow MAS ($v_{\text{rot}} = 250$ Hz) (red) and with the sample stationary at all times (blue). b) 2D ^{13}C - ^{35}Cl D-HMQC- R_3 correlation spectrum of **hist** acquired under MAS ($v_{\text{rot}} = 8$ kHz) with a projection of the 2D data along the direct dimension axis and the ^{35}Cl CPMAS-echo spectrum shown along the indirect dimension axis. 169
- Figure 5.4.** ^{13}C and ^{35}Cl SSNMR spectra of finely ground **ambr** impregnated with 15 mM TEKPol/TCE solution acquired at 100 K and $B_0 = 9.4$ T. a) ^1H - ^{13}C CP/MAS spectra acquired with and without microwaves to drive DNP. The top inset shows the two ^{13}C spectra scaled to the same maximum intensity. The asterisks denote spinning sidebands. b) ^1H - ^{35}Cl BCP spectra acquired with microwaves and slow MAS rotation during most of recycle delay period (SOSO condition, red), with microwaves and with the sample stationary at all times (blue), and with the sample stationary without microwaves (black)... 172
- Figure 5.5.** SSNMR spectra of the bulk and dosage forms of **isox** impregnated with a 15 mM TEKPol/TCE solution acquired at 100 K and $B_0 = 9.4$ T. The left column has ^1H - ^{13}C CP/MAS spectra of a) the bulk API and b) the dosage samples acquired with microwaves on and off. The bottom inset shows the full spectra of the dosage form without vertical clipping. The right column has ^1H - ^{35}Cl BCP spectra of c) the bulk API with and without microwaves and d) the bulk API and dosage samples with DNP enhancement. The lineshapes in c) are lopsided to the high frequency side because only one sweep direction of the BCP contact pulse was used (see **Figure D10** for more details). 174

Figure 5.6. ^{13}C and ^{35}Cl SSNMR spectra of the bulk and dosage forms of diph impregnated with a 15 mM TEKPol/1,3-dibromobutane solution acquired at 100 K and $B_0 = 9.4$ T. The left column has ^1H - ^{13}C CP/MAS spectra of a) the bulk API and b) the dosage samples acquired with microwaves on and off. Asterisks denote spinning sidebands. The right column has ^1H - ^{35}Cl BCP spectra of c) the bulk API with and without microwaves and d) the bulk API and dosage samples with DNP enhancement. The lineshape in c) is lopsided to the high frequency side because only one sweep direction of the BCP contact pulse was used (see Figure D11 for more details).....	178
Figure 5.7. ^{13}C and ^{35}Cl SSNMR spectra of the bulk and dosage forms of ceti impregnated with 15 mM TEKPol/1,3-dibromobutane solution acquired at 100 K and $B_0 = 9.4$ T. The left column has ^1H - ^{13}C CP/MAS spectra of a) the bulk API and b) the dosage samples acquired with and without microwaves. Asterisks denote spinning sidebands. The right column shows the ^1H - ^{35}Cl BCP spectra of c) the bulk API with and without microwaves and d) the bulk API and dosage samples with DNP enhancement.	180
Figure 6.1. Proposed disproportionation reactions of PiogHCl with a) MgSt and b) NaSt.....	195
Figure 6.2. Experimental $^{35}\text{Cl}\{^1\text{H}\}$ WURST-CPMG NMR spectra of pure PiogHCl under static sample conditions, a) and b), and the corresponding analytical simulation, c). Experimental data were processed by a) applying a Fourier transform (FT) to the entire echo train (blue), or b) coadding the echoes together before performing a FT (red), see details in the text.....	200
Figure 6.3. $^{35}\text{Cl}\{^1\text{H}\}$ WURST-CPMG NMR spectra of PiogHCl samples mixed with NaSt (9:1 wt/wt), a) is the spectrum of the untreated control sample, and b) is the spectrum of the sample treated at 40 °C/75% RH for 5 days. The difference between the spectra (control – treated) is shown in c) and d). When calculating the latter, the intensity of the spectrum of the control (a) was decreased to produce only positive signal (see text for details).....	201
Figure 6.4. $^{23}\text{Na}\{^1\text{H}\}$ MAS ($v_{\text{rot}} = 12$ kHz) NMR spectra of a) NaSt_C , b) NaSt_X , and c) pure NaSt. The inset shows the NaSt region of the spectrum of NaSt_X with increased intensity.	204
Figure 6.5. $^{35}\text{Cl}\{^1\text{H}\}$ WURST-CPMG NMR spectra of PiogHCl samples mixed with MgSt (9:1 wt/wt), a) the untreated control sample, b) the sample treated at 40 °C/75% RH for 5 days, and c) the treated sample immediately after being rehydrated at 20 °C/75% RH for 4 hours. The difference between the spectra (control – treated) is shown in d) and e). When calculating the latter, the intensity of the spectrum of the control (a) was decreased to produce only positive signal.	205
Figure 6.6. $^{35}\text{Cl}\{^1\text{H}\}$ WURST-CPMG NMR spectra of the PiogHCl/PiogFB mixtures. The data are shown after processing by either (i) applying a FT to the entire echo train (“spikelet spectrum”) or (ii) combining the echoes together before performing the FT.....	208

Figure 6.7. Plots of PiogHCl wt-% measured experimentally using ^{35}Cl SSNMR (y -axis) and the wt-% determined from the salt : free base mass ratio of the sample (x -axis). Data were obtained from spikelets in the spectra by measuring a) the peak intensity or b) the integrated intensity of each spikelet. The plotted values are the average measurement obtained from the spikelets in a given spectrum between 39 and -84 kHz, and the error bars represent the root mean square deviation (RMSD). Standard deviations, σ , in the measured values (not shown) are smaller than the point markers. (See Table 6.2 for definitions of these two statistical values).	211
Figure 7.1. Molecular structure of GNE-A.	222
Figure 7.2. Crystal structure of GNE-A shown in two perpendicular orientations, as indicated by the orientation of the crystallographic b -axis. Shading highlights features of the structure that are discussed in the text. The crystal structure of GNE-A was solved by A. DiPasquale at Genentech. A full accounting of the solution of this structure will be released with the submission of a manuscript on this topic.	227
Figure 7.3. a) Experimental $^{35}\text{Cl}\{^1\text{H}\}$ WURST-CPMG NMR spectrum of GNE-A acquired under static sample conditions at 22 °C and b) the corresponding two-site analytical simulation. A deconvolution of the simulated spectrum is shown in c).	229
Figure 7.4. Experimental $^{35}\text{Cl}\{^1\text{H}\}$ WURST-CPMG NMR spectra of GNE-A acquired at various temperatures. Spectra were acquired on the same sample in the order shown from left to right. The spectra have been vertically scaled to account for the Boltzmann enhancement of the spin energy level populations due to temperature (<i>i.e.</i> , scaling factor = $T \times (295.15 \text{ K})^{-1}$).	234
Figure 7.5. $^{35}\text{Cl}\{^1\text{H}\}$ WURST-CPMG NMR spectra of the GNE-A samples prepared with different hydration levels acquired at -40 °C (see text for details of the sample preparations). The left and right columns show spectra acquired before and after heating in the magnet, respectively. Overlaid on top of the experimental spectra are simulated spectra generated with three distinct ^{35}Cl NMR tensor parameters. The subspectra are shown as solid shapes (Site I = purple, Site II = green, Site III = orange).	236
Figure 7.6. ^1H - ^{13}C CP/MAS ($\nu_{\text{rot}} = 12$ kHz) NMR spectra of the GNE-A samples prepared with different levels of hydration. See text for details of the sample preparations.	240
Figure 7.7. ^1H MAS ($\nu_{\text{rot}} = 12$ kHz) NMR spectra of the GNE-A samples prepared with different levels of hydration. See text for details of the sample preparations. The arrow indicates the position of a distinct feature in the spectrum of Rehydrate Long that is discussed in the text.	242

Figure 7.8. ^2H quadrupolar-echo spectra of the **Rehydrate-D₂O** sample acquired under static sample conditions at various temperatures. In a) experimental spectra acquired at different temperatures, as indicated. In b) four of the same experimental spectra overlaid with simulated spectra generated using a three-site simulation with dynamical motion. The rates of motion of **Site DI** are listed in parentheses (see text for details). Previously-published⁵⁴ rates of motion for ice were used to simulate **Site DIII**.245

LIST OF ABBREVIATIONS

ABMS	Anisotropic bulk magnetic susceptibility
AOT	Aerosol OT (Docusate sodium)
API	Active pharmaceutical ingredient
BRAIN-CP	BRoadband Adiabatic INversion Cross-Polarization
BRAIN-CP/WURST-CPMG	BRoadband Adiabatic INversion Cross-Polarization with WURST-CPMG
CASTEP	Cambridge serial total energy package
CP	Cross-polarization
CP/MAS	Cross-polarization magic-angle spinning
CPMG	Carr-Purcell Meiboom-Gill
CS	Chemical shielding
C/S	Core/shell
CSA	Chemical shift anisotropy
CT	Central transition
D-HMQC	Dipolar heteronuclear multiple-quantum coherence
DS	Dipolar shift
DSA	Dipolar shift anisotropy
DBB	1,3,-dibromobutane
DFT	Density functional theory
DNP	Dynamic nuclear polarization
DSC	Differential scanning calorimetry
EFG	Electric field gradient

EPR	Electron paramagnetic resonance
FID	Free induction decay
FOQI	First-order quadrupolar interaction
FT	Fourier transform
GGA	Generalized gradient approximation
GIPAW	Gradient-including projector augmented wave algorithm
HE	Hahn-echo
ICP-MS	Inductively-coupled mass spectrometry
JCPDS	Joint Committee on Powder Diffraction Standards
MAS	Magic-angle spinning
MQMAS	Multiple-quantum magic-angle spinning
NC	Nanocrystal
NMR	Nuclear magnetic resonance
NMS	Nuclear magnetic shielding
NP	Nanoparticle
NQM	Nuclear quadrupole moment
o.d.	Outer diameter
PA	Polarizing agent
PAS	Principal axis system
ppm	Parts per million
PXRD	Powder X-ray diffraction
QI	Quadrupolar interaction

QY	Quantum yield
RE	Rare-earth
rf	Radiofrequency
rPBE	Revised Perdew, Burke, and Ernzerhof
S/N	Signal-to-noise ratio
SOLA	Solid Lineshape Analysis
SOQI	Second-order quadrupolar interaction
SOSO	Spinning-on spinning-off
SSB	Spinning sideband
SSNMR	Solid-state nuclear magnetic resonance
ST	Satellite Transition
sw-TPPM	Swept-field two-pulse-phase-modulated
TCE	1,1,2,2-tetrachloroethane
TEM	Transmission electron microscopy
TGA	Thermogravimetric analysis
TMS	Tetramethylsilane
TPPM	Two-pulse-phase-modulated
UC	Upconversion
UFMAS	Ultra-fast magic-angle spinning
UW	Ultra-wideline
UWNMR	Ultra-wideline Nuclear Magnetic Resonance
VACP	Variable-amplitude cross polarization

VOCS	Variable Offset Cumulative Spectra
VT	Variable temperature
WURST	Wideband Uniform Rate Smooth Truncation
XRD	X-ray diffraction
YF	$(\text{H}_3\text{O})\text{Y}_3\text{F}_{10} \cdot x\text{H}_2\text{O}$

LIST OF SYMBOLS

a, b, c	Crystal lattice parameters
B_0	Static external magnetic field
B_1	Applied oscillating magnetic field
C_Q	Quadrupolar coupling constant
σ	Chemical/magnetic shielding
δ_{iso}	Isotropic chemical shift
Δ_{aniso}	Span of the DSA tensor
$\sigma_{11}, \sigma_{22}, \sigma_{33}$	Principal axis components of the MS tensor
$\delta_{11}, \delta_{22}, \delta_{33}$	Principal axis components of the CS tensor
δ_{iso}	Isotropic chemical shift
ε	DNP enhancement
σ_{iso}	Isotropic chemical shielding
γ	Gyromagnetic ratio
e	Elementary charge
g	Isotropic electron g -factor
g_J	Isotropic lanthanide g -factor
h	Plank's constant
\hbar	Plank's constant in radians
I	Nuclear spin
J	Total electron angular momentum quantum number
k_B	Boltzmann constant
κ	Skew
L	Electron orbital angular momentum quantum number
mol-%	Mole percent
m_I	Nuclear spin state
Ω	Span
pK_a	Acid dissociation constant

Q	Nuclear quadrupole moment
R_{DD}	Dipolar coupling constant
r	Internuclear distance
S	Electron spin quantum number
s_i	Electron spin i
T	Temperature
T_1	Longitudinal relaxation time constant
T_2	Transverse relaxation time constant
T_2^*	Transverse relaxation time constant, including effects from B_0 inhomogeneity
T_2^{eff}	Effective transverse relaxation time constant
μ	Nuclear spin magnetic moment
μ_0	Vacuum permeability constant
μ_B	Bohr magneton
ν_0	Larmor frequency (in MHz)
ν_Q	Quadrupolar frequency
ν_{rot}	Sample spinning rate (in Hz)
\mathbf{V}	Electric Field Gradient tensor (EFG)
V_{11}, V_{22}, V_{33}	Principal axis components of the EFG tensor
ω_0	Larmor frequency (in rad s^{-1})
wt-%	Weight percent
η	Asymmetry parameter

*When I heard the learn'd astronomer,
When the proofs, the figures, were ranged in columns before me,
When I was shown the charts and diagrams, to add, divide,
and measure them,
When I sitting heard the astronomer where he lectured with
much applause in the lecture-room,
How soon unaccountable I became tired and sick,
Till rising and gliding out I wander'd off by myself,
In the mystical moist night-air, and from time to time,
Look'd up in perfect silence at the stars.*

Walt Whitman, 1865.

Chapter 1: Introduction, Background, and Context

1.1 Nuclear Magnetic Resonance Spectroscopy (NMR)

Nuclear magnetic resonance (NMR) spectroscopy has become one of the premier methods for routine structural characterization in all branches of chemistry.¹ NMR spectra are exquisitely sensitive to subtle differences in chemical structure, bonding, and dynamical motion (NMR is the only technique capable of detecting motions on the time scale ranging from *ca.* 10^{-2} to 10^{10} Hz). NMR signals are inherently quantitative, and provide direct information on the relative amounts of nuclei in chemically or magnetically non-equivalent environments in a sample. Such experiments are non-destructive, and usually do not require extensive sample preparation. Finally, NMR spectroscopy can be used to study almost any type or phases of matter; while the specifics of the experimental design, hardware, and sample preparation may differ, the fundamental principles are the same.

Most of the substances we encounter in daily life are solids, which have bulk material properties that depend on the molecular-level solid-state structures, interactions, and dynamics of atoms or molecules. These properties are diverse and include: chemical properties (*e.g.*, reactivity, solubility, and melting point), mechanical properties (*e.g.*, flexibility, hardness, and tensile strength), optical properties (*e.g.*, fluorescence intensity, transmittance, and wavelength), magnetic properties (*e.g.*, diamagnetism, permeability, and hysteresis), and electrical properties (*e.g.*, capacitance, resistance, and permittivity). Careful consideration of the structural factors that produce these bulk properties is key to rationally designing advanced materials with novel and desirable properties. Given its sensitivity to local molecular structure and geometry, solid-state NMR (SSNMR)

spectroscopy is a particularly useful method to study materials, and is the primary characterization technique used in this work.

Nearly every element of the periodic table has at least one NMR-active nuclide, which could enable the study of a wide range of compounds and materials containing these elements. In practice, many nuclides are *unreceptive* to the NMR experiment due to (i) low natural abundances or dilutions, (ii) broad spectral widths, (iii) unfavorable relaxation properties, (iv) low gyromagnetic ratios, or (v) a combination of these factors; such nuclides require specialized techniques, hardware, and/or sample preparation to obtain their NMR spectra (*vide infra*). In the following sections, a brief discussion of the theory of NMR is presented, with a particular focus on areas that are relevant to the projects in this thesis. Due to the breadth of the field, no text on NMR can be comprehensive; fortunately, there are numerous excellent summaries of different aspects of NMR that have been published elsewhere.²⁻⁵

1.1.1 Thence Spin

NMR relies on an intrinsic property of elementary particles called *spin*.⁶ Spin is a form of angular momentum (*e.g.*, spin angular momentum of an electron, denoted S , or nuclear spin angular momentum, denoted I) that behaves analogously to the rotational angular momentum of a spinning object. However, spin is an *intrinsic property* that does *not* result from the spinning or rotational motions of the elementary particles. In a nucleus, contributions from the spins of both neutrons and protons produce a ground-state nuclear spin that varies depending on the isotope (*e.g.*, $I(^{14}\text{N}) = 1$, $I(^{15}\text{N}) = 1/2$).⁷ Nuclear spins have $2I+1$ spin states (described by the quantum number m_I , where $m_I = I, I-1, \dots, -I$) that are degenerate in the absence of a magnetic field.

The nuclear spin is proportional to the nuclear magnetic moment, $\boldsymbol{\mu}$, according to:

$$\boldsymbol{\mu} = \gamma \hbar \mathbf{I} \quad (1.1)$$

where γ is the gyromagnetic ratio in $\text{rad T}^{-1} \text{s}^{-1}$ (*N.B.* variables in boldface type correspond to vector quantities in this work). In the presence of an external magnetic field, \mathbf{B}_0 , the interaction of the nuclear magnetic moment and the magnetic field breaks the degeneracy of the nuclear spin states, such that each has an energy described by

$$E = -\boldsymbol{\mu} \cdot \mathbf{B}_0 = \gamma \hbar I_z B_0 = \hbar \omega_0 I_z \quad (1.2)$$

where I_z is the z -component of the spin angular momentum vector, and ω_0 is the *Larmor frequency* (in rad s^{-1}), $\omega_0 = -\gamma B_0$. The lifting of this degeneracy (called the *Zeeman splitting*) produces non-degenerate energy levels (**Figure 1.1**). Transitions between these energy levels are allowed for $\Delta m_l = \pm 1$, and it is these transitions that create the signals that are observed with NMR spectroscopy.

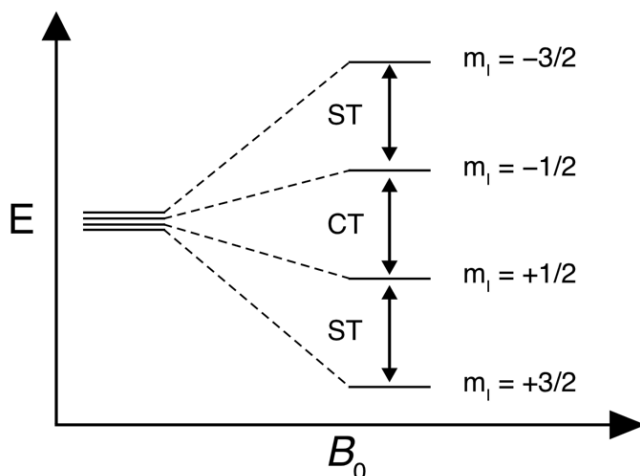


Figure 1.1 The effects of increasing external magnetic field strength (\mathbf{B}_0) on the spin energy levels of a spin-3/2 nucleus. Allowed transitions between the non-degenerate spin states are labeled as satellite transitions (ST) and the central transition (CT), which have equal transition energies ($\Delta E = \hbar \gamma B_0$).

1.2 NMR Interactions

NMR-active nuclides also interact with their surroundings: that is, NMR spectra are sensitive to several NMR interactions that change the relative energies of the spin energy levels and are the source of the rich structural information encoded in NMR spectra. There are numerous interactions that affect appearance of SSNMR spectra, each of which has different physical origins, distinct magnitudes, and an array of secular and non-secular effects on the spectra. It is these interactions that give rise to a large class of observable and measurable NMR parameters that can be correlated to structure and dynamics. The total Hamiltonian describing the interaction between an NMR-active nucleus with its surroundings can be represented using a sum of the energies calculated from each of the individual Hamiltonians:

$$\hat{\mathbf{H}}_{\text{total}} = \hat{\mathbf{H}}_{\text{Z}} + \hat{\mathbf{H}}_{\text{rf}} + \hat{\mathbf{H}}_{\text{Q}} + \hat{\mathbf{H}}_{\text{CS}} + \hat{\mathbf{H}}_{\text{D}} + \hat{\mathbf{H}}_{\text{UE}} + \hat{\mathbf{H}}_{\text{J}} + \dots \quad (1.3)$$

These terms correspond to interactions of nuclei with external factors (magnetic fields, $\hat{\mathbf{H}}_{\text{Z}}$, and oscillating radiofrequency (rf) fields, $\hat{\mathbf{H}}_{\text{rf}}$), single spin interactions that are internal to the sample (the quadrupolar, $\hat{\mathbf{H}}_{\text{Q}}$, and chemical shielding, $\hat{\mathbf{H}}_{\text{CS}}$ interactions), and two-spin interactions that are internal to the sample (direct dipolar, $\hat{\mathbf{H}}_{\text{D}}$, unpaired electron $\hat{\mathbf{H}}_{\text{UE}}$, and indirect spin-spin, $\hat{\mathbf{H}}_{\text{J}}$, coupling interactions). The exact forms of these Hamiltonians are described well elsewhere, and are not further discussed herein.^{2,11-14}

The interactions that are important for a particular sample and the manner in which they manifest in their NMR spectra varies depending on the nucleus of interest, the composition of the material, as well as experimental conditions (*e.g.*, the strength of the external magnetic field, temperature, *etc.*). It is important to note that even in cases where a particular interaction does not manifest as changes in an NMR spectrum (*e.g.*, the

quadrupolar interaction in solution NMR experiments), such interactions are still important as they can be major sources of nuclear relaxation mechanisms.^{3,15} In general, the Zeeman interaction (\hat{H}_Z) that breaks the degeneracy of the spin energy levels is significantly stronger than the other NMR interactions. As such, each interaction can be treated as a perturbation of the Zeeman states. The NMR interactions necessary for the understanding of this work are discussed in more detail in the following subsections.

1.2.1 Quadrupolar Interaction (\hat{H}_Q)

One of the most pertinent NMR interactions for the materials studied in this thesis is the quadrupolar interaction (QI), which results from the interaction of the nuclear electric quadrupole moment with surrounding electric field gradients (EFG) with their origins at the nuclear site. The former is an intrinsic property of each quadrupolar nuclide, whereas the latter is dependent upon the atomic/molecular level structure. The former is described by the product eQ , where e is the elementary charge and Q is the nuclear quadrupole moment (NQM) arising from the distribution of nuclear charge. For nuclides with nuclear spin $I = 1/2$, this distribution is spherically symmetric ($Q = 0$). For those with $I > 1/2$ (so-called quadrupolar nuclei), the charge distribution is asymmetric, and can be visualized as either prolate or oblate in shape (**Figure 1.2**). EFGs measure the changes in the electric field as a function of position, and therefore are highly dependent upon the arrangements of proximate atoms (and the associated nuclei and electrons). In molecular systems, the EFGs at a nuclear origin are dependent upon the surrounding distribution of the ground state electron density; as such, accurate measurement of the QI provides direct information on the local ground state electron distribution (in contrast to

the chemical shielding interaction, which is more complicated in its origins and interpretation, *vide infra*).^{16,17}

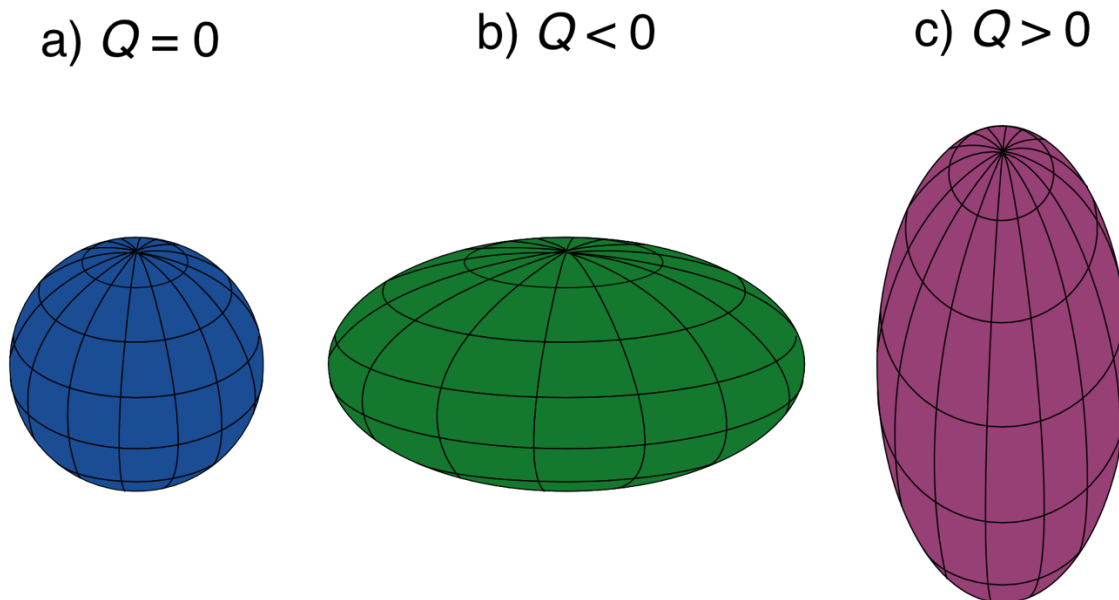


Figure 1.2 Representations of nuclei with spherical ($Q = 0$), and non-spherical (oblate, $Q < 0$ or prolate, $Q > 0$) distributions of positive charge.

The QI can be very large compared to most other NMR interactions, and is often the dominant NMR interaction in many materials containing quadrupolar nuclei. In fact, as is the case for several nuclides studied in this work, its effects on SSNMR spectra must be modeled with consideration of both first- and second-order perturbations of the Zeeman energy levels (*i.e.*, the first-order quadrupolar interaction (FOQI) and second-order quadrupolar interaction (SOQI), respectively). The effects of these perturbations for a spin-3/2 quadrupolar nucleus are shown in **Figure 1.3**. To second order, the QI affects both the central transition (CT, $+1/2 \leftrightarrow -1/2$ transition) and the satellite transitions (STs, $+3/2 \leftrightarrow +1/2$ and $-1/2 \leftrightarrow -3/2$). The former is most commonly studied in quadrupolar NMR experiments, as it produces narrower patterns that are easier to acquire (*vide infra*).

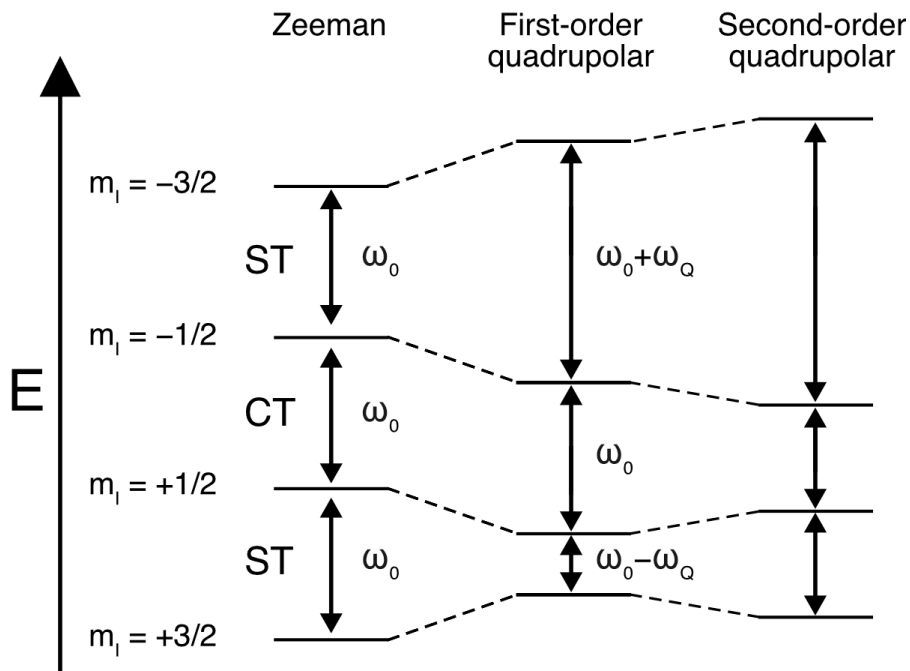


Figure 1.3 The effects of the a) Zeeman interaction, b) FOQI, and c) SOQI on the energy levels of an isolated spin-3/2 quadrupolar nucleus in an external magnetic field, where ω_0 is the Larmor frequency and $\omega_Q = (3C_Q)/[4I(2I - 1)]$ is the quadrupolar frequency. The relative magnitudes of the interaction are not to scale.

Like most NMR interactions, the QI is anisotropic, and can be described by the EFG tensor within the molecular frame as:

$$\ddot{V} = \begin{bmatrix} V_{xx} & V_{xy} & V_{xz} \\ V_{yx} & V_{yy} & V_{yz} \\ V_{zx} & V_{zy} & V_{zz} \end{bmatrix} \quad (1.4)$$

Typically, it is more convenient to diagonalize the matrix and express it with its own principal axis system (PAS) as:

$$\ddot{V}_{PAS} = \begin{bmatrix} V_{11} & 0 & 0 \\ 0 & V_{22} & 0 \\ 0 & 0 & V_{33} \end{bmatrix} \quad (1.5)$$

where the principal components are defined as $|V_{33}| \geq |V_{22}| \geq |V_{11}|$. The EFG tensor is traceless (*i.e.*, $V_{11} + V_{22} + V_{33} = 0$) and symmetric ($V_{ij} = V_{ji}$).

The quadrupolar interaction is often reported using two parameters: the quadrupolar coupling constant (C_Q) and the asymmetry parameter (η_Q). The $C_Q = V_{33}eQ/h$, and is usually reported in MHz or kHz, and $\eta_Q = (V_{11} - V_{22})/V_{33}$ is dimensionless. The former is typically used as a measure of the local spherical symmetry of the ground state, with small values indicating high spherical symmetry (*vide infra*); the latter is simply a measure of the axial symmetry of the EFG tensor, which often reflects the axial symmetry of certain bonding environments (*e.g.*, an atom involved in a bond along an axis of C_3 symmetry or higher will have an EFG tensor at its nuclear origin with $\eta_Q = 0$).¹⁸ Values of C_Q can range from zero to tens or hundreds of MHz depending on the nucleus and sample. Values of η_Q range from zero (perfect axial asymmetry) to one (perfect axial symmetry).

The effects of a large quadrupolar interaction on SSNMR spectra can be very dramatic. In many cases, SSNMR spectra of quadrupolar nuclei feature broad patterns that can be tens of kHz to tens of MHz in breadth, depending on the magnitude of the nuclear quadrupolar frequency, $\nu_Q = 3C_Q/(2I(2I-1))$, which is dependent upon I ; in general, CT powder patterns become more narrow as the value of I increases.^{14,19-21} These patterns have characteristic lineshapes that can be fit with analytical or numerical simulations from which the quadrupolar parameters can be determined; in turn, these parameters can be correlated to the local structural environment of the quadrupolar nuclei (**Figure 1.4**).

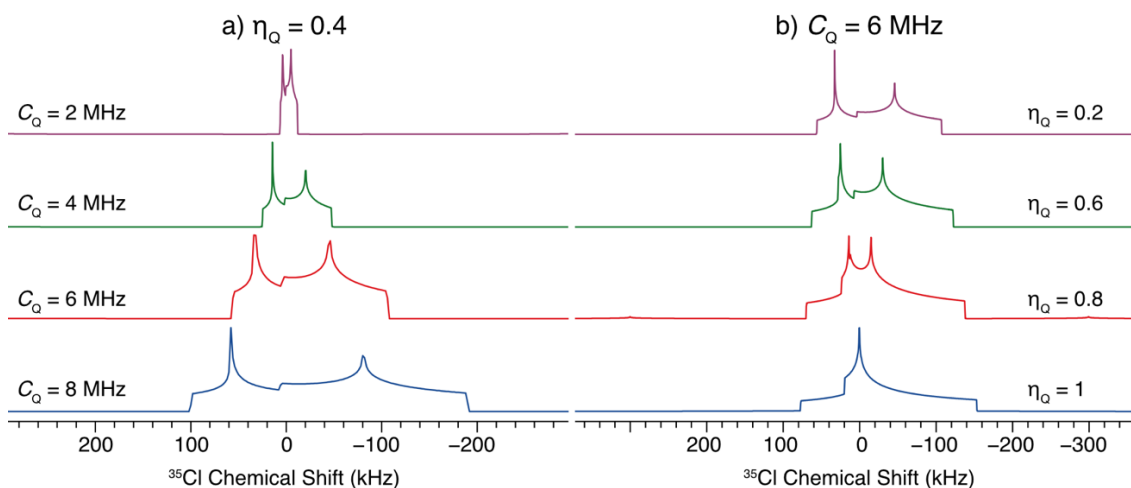


Figure 1.4 Analytical simulations of ^{35}Cl central transition ($+1/2 \leftrightarrow -1/2$) NMR spectra under static sample conditions at $B_0 = 9.4$ T. a) $\eta_Q = 0.4$, C_Q ranges from 8 to 2 MHz; b) $C_Q = 6$ MHz, η_Q ranges from 1.0 to 0.2. These spectra represent typical ranges of the quadrupolar parameters for the Cl^- anions described herein.

For certain molecular geometries, the magnitude of the EFG at the nucleus is small (≈ 0), meaning that the quadrupolar interaction is either very small or absent. However, for other geometries, the EFG can be quite large. This relationship between the EFG magnitude and local symmetry about the quadrupolar nucleus has been discussed in several publications,^{22,23,18} including a particularly elegant demonstration in a work by Koller *et al.* using ^{23}Na NMR of sodium oxides with different coordination numbers and geometries (**Figure 1.5**).^{18,24} Such relationships between local molecular structure and the effects of the quadrupolar interaction observed in SSNMR spectra are critical to many of the projects described in this thesis (*cf.* **Chapters 2, 4, and 7**).

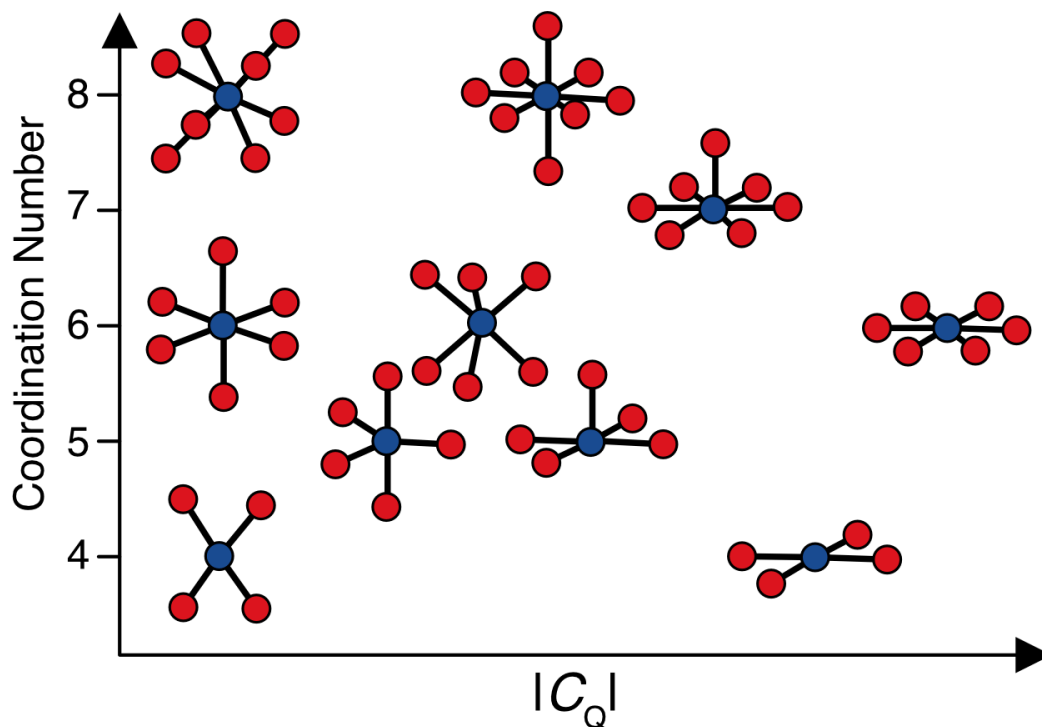


Figure 1.5 Calculated quadrupole coupling constants, C_Q , of different sodium-oxygen coordination environments having different symmetry and coordination numbers. Created by the author based on the adaptation of a figure from Koller, *H. J. Phys. Chem.* **1994**, 98, 1544.

1.2.2 Chemical Shielding Interaction (\hat{H}_{CS})

The discovery of the chemical shielding interaction (CS) is what made NMR particularly useful for chemists,¹ as CS produces clear distinctions between chemically and magnetically non-equivalent sites in a sample. The origins of the CS interaction were extensively developed by Ramsey and Pople in the 1950s.^{25–27} In brief, the presence of an external magnetic field induces circulation of electrons in the atomic/molecular orbitals, which in turn produce magnetic fields at the nuclei that are aligned anti-parallel or parallel with respect to the external magnetic field. Unlike the quadrupolar interaction (which is only affected by the ground-state wavefunction), CS involves contributions from both the ground and excited states; in particular, magnetic-field induced mixing of the ground- and excited-states is the main source of the enormous variations in chemical

shift and associated richness of structural information derived therefrom. The local fields that are either parallel or anti-parallel to B_0 effectively increase (*i.e.*, deshielding) or decrease (*i.e.*, shielding) the external field experienced by the nucleus, causing positive or negative frequency shifts, respectively. Chemical shielding is almost always reported in parts per million relative to the external magnetic field, which means that pure chemical shifts are the same in spectra acquired using magnets of different field strengths.

The term *chemical shielding* is often used interchangeably with the term *chemical shift*. Strictly speaking, the chemical shielding describes the amount of shielding relative to a bare nucleus (*i.e.*, one without surrounding electron density). Given the impracticality of conducting experiments on a bare nucleus, the chemical shift values are measured experimentally, and correspond to the frequency produced by a given site relative to that of some reference compound. The chemical shielding and shift are related by

$$\delta \equiv \frac{\sigma_{ref} - \sigma}{1 - \sigma_{ref}} \quad (1.6)$$

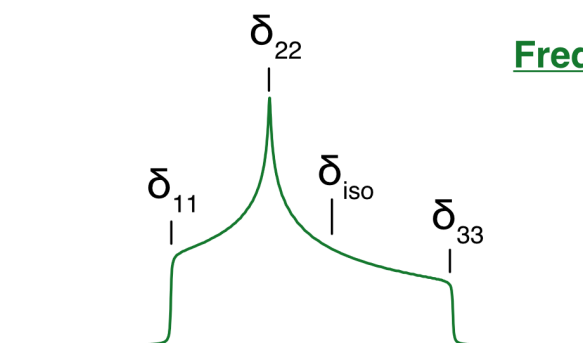
where σ_{ref} and σ are the nuclear magnetic shieldings of a reference standard and the sample of interest, respectively. If the shifts are not too far apart, **Eq. 1.6** can be written as $\delta \approx \sigma_{ref} - \sigma$.

The chemical shielding/shift interaction is anisotropic, and, like the QI, can be described by a second-rank tensor in its own PAS:

$$\ddot{\delta}_{PAS} = \begin{bmatrix} \delta_{11} & 0 & 0 \\ 0 & \delta_{22} & 0 \\ 0 & 0 & \delta_{33} \end{bmatrix} \quad (1.7)$$

where the principal components are defined in order of decreasing shift: $\delta_{11} \geq \delta_{22} \geq \delta_{33}$

(i.e., using the frequency-ordered principal shift values convention, **Figure 1.6**).²⁸

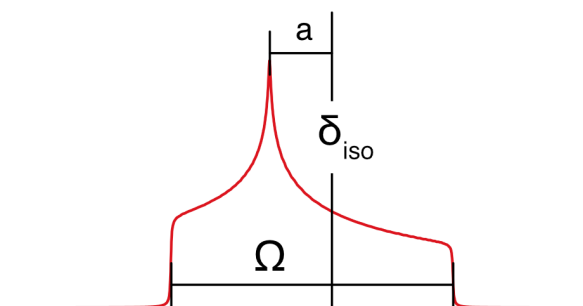


Frequency-Ordered Principal Shift

$$\delta_{11} \geq \delta_{22} \geq \delta_{33}$$

Isotropic Shift:

$$\delta_{\text{iso}} = (\delta_{11} + \delta_{22} + \delta_{33})/3$$



Herzfeld-Berger Convention

$$\delta_{11} \geq \delta_{22} \geq \delta_{33}$$

Isotropic Shift:

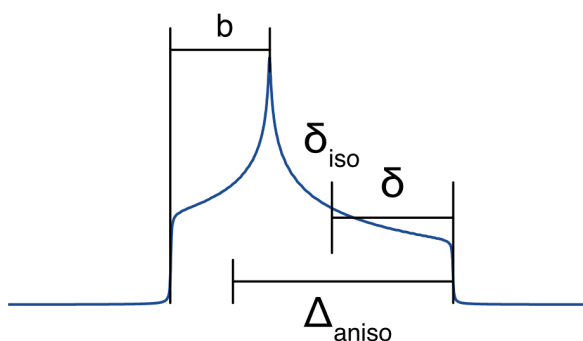
$$\delta_{\text{iso}} = (\delta_{11} + \delta_{22} + \delta_{33})/3$$

Span (Ω):

$$\Omega \approx \delta_{11} - \delta_{33}$$

Skew (κ):

$$\kappa = 3a/\Omega = 3(\delta_{22} - \delta_{\text{iso}})/\Omega$$



Haeberlen Convention

$$|\delta_{zz} - \delta_{\text{iso}}| \geq |\delta_{xx} - \delta_{\text{iso}}| \geq |\delta_{yy} - \delta_{\text{iso}}|$$

Isotropic Shift:

$$\delta_{\text{iso}} = (\delta_{11} + \delta_{22} + \delta_{33})/3$$

Asymmetry (η):

$$\eta = (\delta_{yy} - \delta_{xx})/\delta$$

Anisotropy (Δ_{aniso}):

$$\Delta_{\text{aniso}} = 3\delta/2 = \delta_{zz} - (\delta_{xx} + \delta_{yy})/2$$

Figure 1.6 Different conventions used to describe the CS tensor. Top (green) the frequency-ordered principal shift convention,²⁹ middle (red) the Herzfeld-Berger convention,³⁰ and the Haeberlen-Mehring-Spiess convention.^{31–33} Unlike the quadrupolar interaction, this tensor is non-traceless, and the average of the three PAS components produces the isotropic chemical shift, $\delta_{\text{iso}} = (\delta_{11} + \delta_{22} + \delta_{33})/3$. The isotropic chemical shift is the primary NMR observable in the spectra of solutions. In solids, however, the CSA provides additional information on the orientation of the constituent atoms with respect to the magnetic field.

Chemical shift anisotropy (CSA) can be described using combinations of the components of the CS tensor.^{29,34,35} Two conventions for expressing CSA are used in this work, as demonstrated in **Figure 1.6**. Like the QI, CSA produces broadening of the experimental NMR patterns, and characteristic lineshapes that depend on the magnitudes of the principal components of the CS tensor, as well as the tensor orientation.³⁶

1.2.3 Dipolar Interaction (\hat{H}_D)

The nuclear magnetic moments of nuclear spins interact with each other in a mutual, through-space interaction known as direct dipolar coupling. The strength of this interaction is expressed by the dipolar coupling constant

$$R_{jk}^{DD} = \frac{\mu_0 \gamma_j \gamma_k \hbar}{4\pi \langle r_{jk}^3 \rangle} \quad (1.8)$$

which is related to the gyromagnetic ratios, γ , of two spins, j and k , separated by an internuclear distance, r .

Both homonuclear and heteronuclear dipolar couplings can be major sources of broadening in SSNMR spectra. The former interaction can be particularly problematic for acquiring NMR spectra of high-gamma nuclides (*e.g.*, ^1H , ^{19}F), especially in samples featuring high concentrations of these nuclides in close proximity. For example, in common solid organic molecules, homonuclear dipolar couplings with magnitudes on the order of tens of kHz are typical. Fortunately, the influence of dipolar couplings can be reduced or eliminated in many cases by the use of carefully designed decoupling schemes and/or MAS (*vide infra*).

Despite the inconveniences of dipolar coupling in terms of producing broad power patterns and limiting spectral resolution, it is essential in a variety of NMR experiments. For example, it can be exploited for signal enhancement using techniques

like cross polarization (*vide infra*), or for correlating signals from distant nuclei through space, without the mediation of bonds, and measuring their bond lengths (*e.g.*, the REDOR family of pulses sequences).^{37,38} Even in systems where the dipolar coupling does not affect the appearance of the spectra (*e.g.*, in the majority of solution NMR spectra), it is still important, as dipolar coupling is most often the dominant mechanism of nuclear relaxation, without which many NMR experiments would not be possible.

1.2.4 Paramagnetic Interaction (\hat{H}_{ue})

Materials that contain unpaired electron spins (*i.e.*, those with paramagnetic centers) have strong magnetic properties that can influence the appearance of NMR spectra. Such materials include organic radicals, transition-metal ions, and lanthanides (the latter of which are important for the current work). As with nuclei (see **Section 1.1**), unpaired electrons have magnetic moments ($S = \frac{1}{2}$ particles), which interact with those of nuclei through the unpaired electron (UE) interaction (or often simply the "paramagnetic" interaction). The magnitudes of such interactions can be extremely large, and can reach over large nuclear-electron distances because the electron magnetic moment is *ca.* 650 times larger than that of a nucleus (recall that magnetic spin dipole-dipole interactions scale as r^{-3}).

Two factors contribute to the interactions between nuclear and electronic spins: (i) the *Fermi contact* interaction and (ii) the *dipolar shift* or *pseudocontact* interaction. The former results from unpaired electron density located near the nucleus (*i.e.*, largely in the atomic *s*-orbitals). Unpaired electron density from a paramagnetic center can influence the polarization of surrounding electron spins either through direct delocalization onto neighboring atoms or through intermediary bonds. As such, the Fermi contact interaction

can affect multiple nuclei in the sample, not merely that of the paramagnetic center that is the source of the unpaired spin density. The second contribution to the paramagnetic interaction is the through-space dipolar interaction between the nuclear spins and unpaired electron spin density. The pseudocontact interaction is often modeled using the point-dipole approximation (where the unpaired spin density is envisioned to be localized at the paramagnetic center). With this approximation, the interaction can be treated as a dipole-dipole interaction between a nucleus and the surrounding unpaired electrons (analogous to the dipolar interaction of two nuclei). For more details on the specifics of these interactions, the reader is directed to the excellent work of Bertini *et al.*, as well as several recent review articles.^{39–41}

Both mechanisms of the paramagnetic interaction are anisotropic, and can be described by tensors. For some samples, these tensors are non-traceless and can produce large paramagnetically induced shifts (on the order of 10s or 100s of ppm). The anisotropies of these interactions are also manifest in SSNMR spectra, and produce similar effects to the CSA, though they have different physical origins (see **Chapters 3 and 4** for a detailed description of these interactions).

The paramagnetic interaction can provide a relaxation mechanism that dominates the rate of longitudinal relaxation (T_1). In turn, rapid relaxation resulting from paramagnetic interactions can make the acquisition of NMR spectra challenging, as the signals arising from strongly paramagnetic species can disappear before they are detected. Additionally, rapid transverse relaxation (*i.e.*, small transverse relaxation constants, T_2) in paramagnetic species produces extensive line broadening in the NMR spectra that can make resolution of individual chemical environments difficult or

impossible.^{42,43} In some cases, such broadening can be eliminated or reduced with the use of modern magic-angle spinning (MAS) hardware that is capable of spinning at speeds of over 100 kHz.⁴⁴⁻⁴⁷ Rapid relaxation can be beneficial for the acquisition of some NMR spectra, as it can shorten the longitudinal relaxation time constant, decrease the recycle delay, and increase the number of scans that can be acquired in a given time frame. Such relaxation enhancements are commonly used in solution studies, where a small amount of a paramagnetic material can be added to a sample with slow longitudinal relaxation (*i.e.*, one with a large T_1 relaxation constant).⁴⁸⁻⁵⁰ The effects of paramagnetic rare-earth ions on NMR spectra of nanomaterials are discussed in **Chapters 3 and 4**.

1.3 NMR Methods

NMR experiments are conducted using a series of rf pulses, collectively known as a pulse sequence, that manipulate the nuclear spins in a sample. With modern NMR hardware, the frequency, amplitude, phase, and timing of these pulses can all be manipulated according to the needs of the experiment. The choice of pulse sequence depends on the available nuclei, properties of the sample being studied, and the structural information that is desired. As such, many different sequences have been used for the current work, as summarized in **Figure 1.7**.

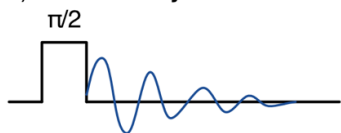
1.3.1 Single-Resonance Pulse Sequences

Some NMR experiments are single-resonance (*i.e.*, where pulses are applied on a single channel to excite the spins of a single type of nucleus). The simplest, known as the Bloch decay (**Figure 1.7a**), consists of a single pulse followed by acquisition of the NMR signal.^{51,52} This experiment is not always viable, as hardware limitations (*e.g.*, acoustic ringing, receiver delays) and rapid relaxation of nuclei can cause the signal to disappear

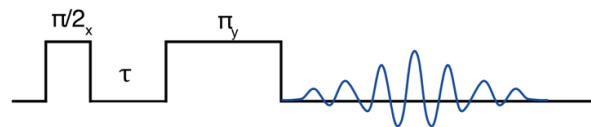
before it can be detected. Bloch decays are particularly ineffective for acquiring the spectra of broad patterns (like those present in many of the spectra in this work); some of these patterns are associated with nuclides with inherently fast nuclear relaxation, while others feature FIDs that decay rapidly due to inhomogeneous broadening. The Hahn echo (also known as a spin-echo) sequence (**Figure 1.7b**) is an improvement to the basic Bloch decay sequence, as it can refocus some of the signal that would otherwise be lost to decay or relaxation, and provides additional time for the NMR probe electronics to prepare for acquisition of the signal.⁵³ While they are not discussed further here, practical details of these (and numerous other) NMR pulse sequences are discussed in several excellent books.^{2,4,54}

A common extension of the Hahn echo sequence is the Carr-Purcell-Meiboom-Gill (CPMG) sequence (**Figure 1.7c**), which consists of a chain of repeated π pulses that continually refocus the NMR signal to produce a series of echoes known as an echo train.^{55,56} Originally designed for measuring T_2 constants, CPMG can also be used for signal enhancement in numerous SSNMR experiments on samples that have inhomogeneously broadened powder patterns, including both spin-1/2 and quadrupolar nuclides. Of relevance to the experiments reported herein is the frequent necessity to apply high-power ^1H decoupling (*vide infra*), in order to reduce contributions to T_2 relaxation from strong heteronuclear dipolar couplings. When decoupling is applied, the length of the echo train depends upon the effective T_2 , T_2^{eff} , in which the contributions of the heteronuclear dipolar relaxation mechanism are reduced or eliminated. Under such conditions, the T_2^{eff} is invariably larger than the T_2 , resulting in the acquisition of more echoes and an increase in net signal enhancement.

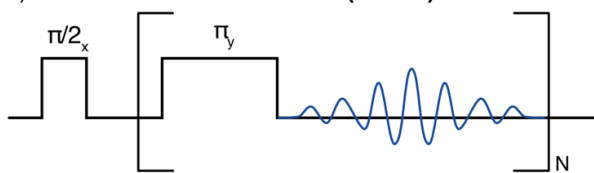
a) Bloch Decay



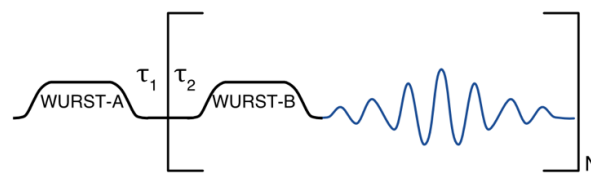
b) Hahn Echo



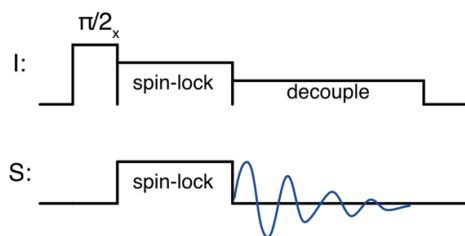
c) Carr-Purcell-Meiboom-Gill (CPMG)



d) WURST-CPMG



e) Cross Polarization



f) BRAIN-CP/WURST-CPMG

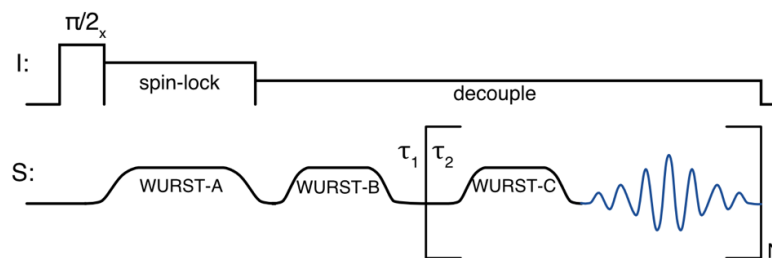


Figure 1.7 NMR pulse sequences used in this work. See text for details.

1.3.2 Ultra-wideline NMR Techniques

The acquisition of broad patterns (such as those produced by strong quadrupolar interactions or CSA) is challenging with conventional rectangular pulses (so-called due to the rectangular shapes of their amplitude profiles). Even with high pulse powers and very short pulse widths, such pulses are often not capable of uniformly exciting the broad bandwidths necessary in spectra ranging from 250 kHz to several MHz in breadth (so-called ultra-wideline NMR (UWNMR) spectra).^{21,57} One solution to this problem is to acquire multiple spectra at different transmitter frequencies, and then combine them to obtain the overall pattern (a method known as frequency stepping, or variable-offset cumulative spectroscopy, VOCS).^{58,59} Spectra can be combined by co-addition or skyline projection of the individual frequency domain sub-spectra. However, this method can be extremely time-consuming in cases where numerous spectra must be acquired to obtain the full pattern.

Our group has developed pulse sequences for broadband excitation of UWNMR patterns. These sequences involve the use of amplitude- and phase-modulated pulses called wideband uniform-rate smooth truncation (WURST) pulses (**Figure 1.8**) that were originally developed for broadband decoupling and excitation in solution NMR experiments.^{60,61} WURST pulses produce an effective sweep of the transmitter across the pattern to excite broad spectral ranges (on the order of hundreds of kHz) in a single experiment (the excitation bandwidths are often only limited by the probe electronics, in particular, the Q of the probe).⁶² WURST pulses can be incorporated into a CPMG-type sequence (known as WURST-CPMG, **Figure 1.7d**)⁶³⁻⁶⁵ that combines the benefits of broadband excitation with the S/N improvement from CPMG. WURST-CPMG also can

be used with frequency-stepped acquisitions (VOCS) to acquire patterns that are extremely broad (> 1 MHz),⁶² and has also found use in broadband cross polarization techniques (*vide infra*). UWNMR spectra are typically acquired under static sample conditions, because the spinning sidebands produced by MAS can overlap with the broad patterns and produce spectra that are difficult to accurately simulate.

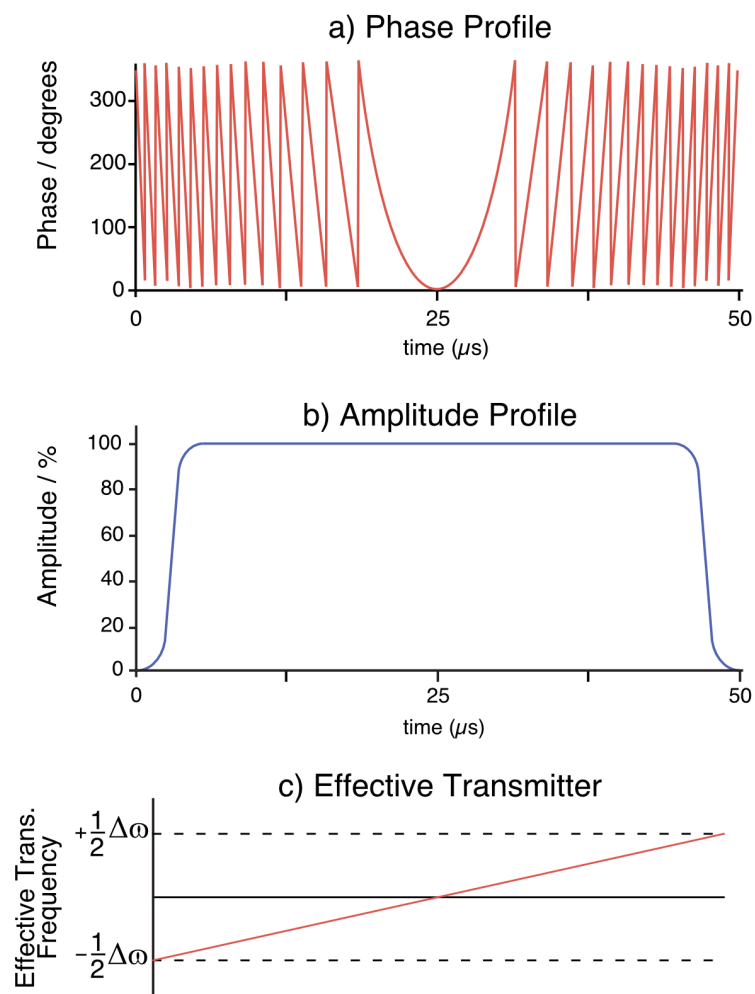


Figure 1.8 The a) phase profile, b) amplitude profile, and c) effective linear transmitter sweep that occurs over the course of a 50 μ s WURST pulse.

1.3.3 Double-Resonance Pulse Sequences

Most materials have multiple types of NMR-active nuclides. As discussed above for the cases of decoupling and internuclear distance measurements, double-resonance SSNMR experiments can exploit the spin-spin coupling (usually dipolar) interactions between different nuclides to increase spectral resolution, produce signal enhancements, and probe the nature of the internuclear interactions. Due to the importance of these interactions, most NMR probes have at least two channels that tune to two separate frequency ranges (triple-resonance probes are also relatively common, especially for applications in biological NMR, where experiments often feature correlations between ^1H , ^{13}C , and ^{15}N nuclides).

One of the most common double-resonance techniques in SSNMR is cross-polarization, (CP, **Figure 1.7e**), which involves the transfer of polarization from receptive spins, I (*e.g.*, ^1H , ^{19}F) to those of lower receptivity, S (*e.g.*, ^{13}C , ^{89}Y).⁶⁶⁻⁶⁹ CP produces a maximum theoretical signal enhancement that is proportional to the ratio of the nuclear gyromagnetic ratios of the two spins (*i.e.*, γ_I/γ_S). In a typical ^1H - ^{13}C CP experiment, CP can produce a theoretical 4-fold signal gain (corresponding to a 16-fold increase in S/N), since the reduction in time is proportional to the square of the signal enhancement). CP transfer occurs between dipolar-coupled spins, and therefore, requires that the spins be proximate (*e.g.*, within *ca.* 10 Å of each other for a ^1H - ^{13}C spin pair of each other).⁶⁹ As such, CP can also be used to selectively excite spins that are proximate to one another. Finally, CP is frequently combined with MAS, resulting in the CP/MAS method, which is among the most widely used techniques in SSNMR.⁷⁰

Conventional CP experiments use rectangular pulses to transfer polarization during the time period known as the contact time; however, the shape and long pulse width (*e.g.*, on the order of 1 to 50 ms) result in polarization transfer over a narrow spectral range. For the purposes of acquiring UWNMR spectra under CP conditions, this scheme is not adequate. Our group developed a modified version of CP that includes WURST pulses for broadband excitation. In this pulse sequence, a rectangular pulse is applied on the ^1H channel along with a simultaneous WURST pulse on the X channel. The WURST pulse serves to sweep a broad region in the X spectrum, while spin locking the polarization that is transferred from ^1H to X nuclides. The resulting polarization is positioned along the $-z$ axis of the rotating frame, and subsequently converted for observation in the xy plane by another WURST pulse. This sequence is known as the broadband adiabatic inversion cross polarization (BRAIN-CP) sequence (**Figure 1.7f**).⁷¹ This sequence is used extensively in **Chapter 5**.

Finally, high-power heteronuclear decoupling sequences are critical additions to many SSNMR experiments. These sequences reduce the effects of internuclear coupling in the spectrum of an observed nucleus by applying pulses on a second channel at or near the frequency of the coupled spins. Such methods can also eliminate the effects of heteronuclear dipolar relaxation on T_2 constants, which affect CPMG experiments (*vide supra*). For many of the samples in this work, the removal of dipolar couplings involving high- γ nuclides like ^1H is critical for the acquisition of spectra with high resolution and high S/N. Various decoupling schemes have been developed for use under different sample conditions. Herein, continuous wave (CW), small phase incremental alternation (SPINAL),⁷² or two-pulse phase-modulated (TPPM)⁷³⁻⁷⁵ decoupling sequences are

utilized under different experimental conditions. For instance, CW decoupling seems to work best for static experiments, whereas SPINAL/TPPM schemes are superior under MAS conditions.

1.3.4 Dynamic Nuclear Polarization (DNP)

One of the most revolutionary developments in NMR is the use of dynamic nuclear polarization (DNP) for signal enhancement. At a fundamental level, DNP relies on a concept similar to that of CP (*i.e.*, exploiting the abundant polarization of a receptive spin to enhance that of a less abundant one); but in the case of DNP, polarization is transferred from electron spins to nuclear spins (most commonly to ^1H spins). The theory of DNP has been reviewed in several excellent publications and books.^{76–78} In this section, the key aspects of DNP that are relevant to the work in this thesis (**Chapter 5**) are discussed.

The idea of enhancing NMR signals via the transfer of electron spin polarization is almost as old as NMR spectroscopy itself; it was first proposed by Overhauser in 1953⁷⁹ and demonstrated experimentally by Carver and Slichter in that same year.⁸⁰ However, the methods demonstrated in this early work were not feasible at higher magnetic fields (*i.e.*, 5 T and above, which are necessary for many modern NMR experiments). With more recent hardware advances (*e.g.*, the availability of high-frequency microwave sources), due in large part to the work of Griffin *et al.*,⁸¹ the production of commercial instrumentation,⁸² and the increased number of stable radicals (as sources of electron spin polarization)^{83–87} high-field DNP NMR has become an indispensable tool for the characterization of many different classes of materials.

There are several mechanisms by which DNP can enhance nuclear polarization. The most commonly used is the *cross effect*, which is efficient at moderate magnetic field strengths (e.g., 9.4 T), since its effects are inversely related to the strength of the applied field. The cross effect relies on the presence of two strongly dipolar-coupled unpaired electrons in a stable biradical in close proximity to the nuclear spins of interest (again, these are usually protons). The corresponding energy level diagram for this three-spin system is shown in **Figure 1.9a**.

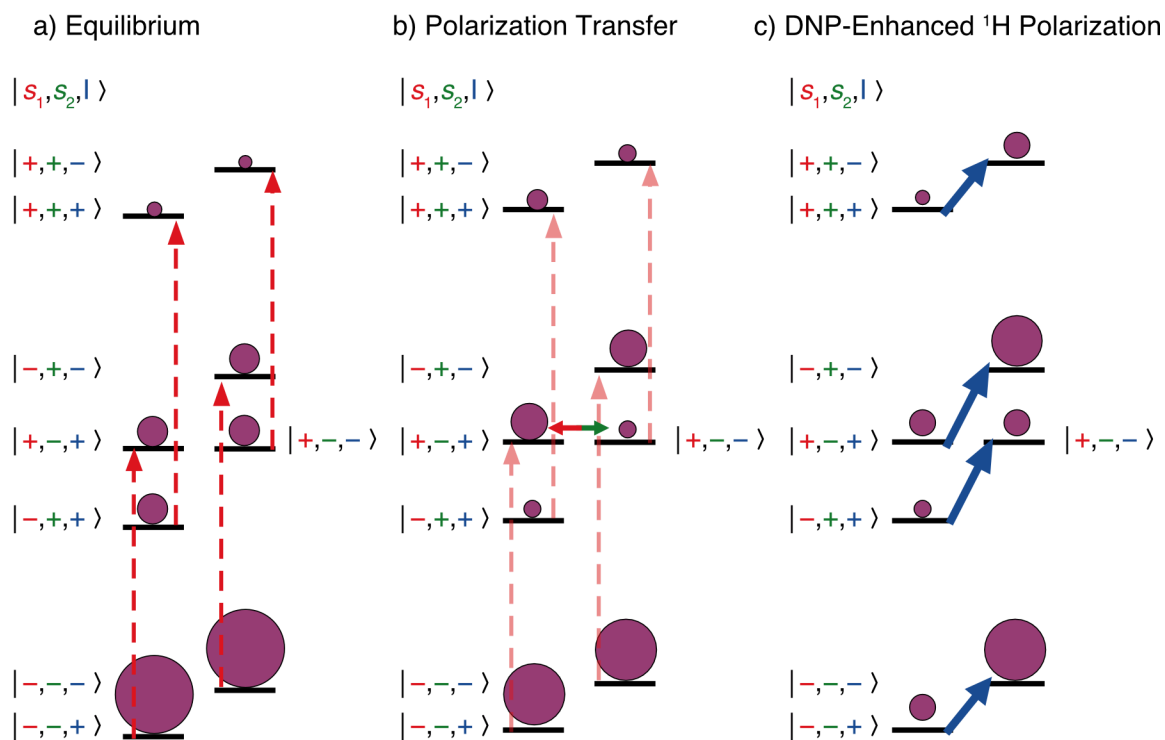


Figure 1.9 Schematic three-spin energy level diagrams detailing the key steps in the cross effect DNP mechanism a) at thermal equilibrium (e.g., without DNP), b) after saturation of one of the electron EPR transitions, and c) the result of DNP-enhancement. The energy levels are labeled with the spin states (+ or -) of the dipolar-coupled electrons (red, s_1 , or green, s_2) and proton (blue, I), respectively. The areas of the purple circles indicate the relative populations of the energy levels. Red dashed lines correspond to EPR transitions that are saturated during the experiment (i.e., $\Delta E = \omega_{0,s_1}$, the Larmor frequency of one of the electrons), and blue arrows indicate the NMR transitions that are enhanced as a result of the process.

At thermal equilibrium, **Figure 1.9a**, the difference in the populations of the nuclear spin states is small relative to those of the electrons. As the EPR transition of one of the electrons is saturated (by irradiating the system with microwaves at $\omega_{0,s1}$) polarization is transferred between the electron energy states. When the matching condition shown in **Eq. 1.9** is fulfilled, the central spin states (labeled $| - + + \rangle$ and $| + + - \rangle$), respectively in **Figure 1.9**) are degenerate and can exchange polarization, resulting in a change in the proton spin state (**Figure 1.9b**).

$$|\omega_{0,s1} - \omega_{0,s2}| = \omega_{0,I} \quad (1.9)$$

where $\omega_{0,s1}$ and $\omega_{0,s2}$ are the electronic Larmor frequencies of the two dipolar-coupled spins, and $\omega_{0,I}$ is the nuclear Larmor frequency. With continued saturation of the electron spin, the polarization of the nucleus (*e.g.*, ^1H) is enhanced (**Figure 1.9c**).

As demonstrated in **Figure 1.9**, saturation of the EPR transitions with microwaves leads to enhancement of the population differences between the ^1H spin energy levels.

This enhancement, ε_{CE} , is described by

$$\varepsilon_{CE} \propto \frac{\gamma_e}{\gamma_n} \left(\frac{B_{1e}^2}{B_0} \right) \frac{N_e^2}{\delta^2} T_{1n} \quad (1.10)$$

where γ_e and γ_n are the electronic and nuclear gyromagnetic ratios, respectively, B_{1e} is the microwave power, B_0 is the external magnetic field, N_e is the concentration of electrons in the sample, δ is the inhomogeneous EPR linewidth, and T_{1n} is the nuclear longitudinal relaxation time constant. For DNP enhancement of proton signals, the maximum theoretical signal enhancement in the NMR spectrum is on the order of 650, which corresponds to a reduction in experimental time of over 422,000 times.

Modern DNP experiments employing the cross effect require the use of specialized hardware, in addition to a conventional NMR spectrometer and magnet. The

first is a gyrotron, which produces high-power microwaves at the frequencies necessary to saturate the electrons (> 200 GHz).^{82,88,89} Second, a waveguide must transmit the microwaves such that the sample is uniformly irradiated (in the techniques used herein, the sample is in the NMR probe when irradiated). Third, since the DNP process is most efficient at lower temperatures (*e.g.*, 100 K or less), additional temperature control and probe hardware⁹⁰ is required. Currently, most DNP experiments that exploit the cross effect are acquired at *ca.* 100 K, though experiments at higher temperatures are a major focus of research in this area.^{91,92}

Finally, a biradical must be introduced into the system. One of the best ways to do so for many organic and inorganic materials is a simple impregnation procedure,⁹³ where the sample is wetted with a small amount of biradical dissolved in a compatible solvent (*i.e.*, one that does not dissolve the solid sample of interest, and is able to form a *spin glass* at 100 K). This liquid, called a *polarizing agent* (PA) solution, coats the surface of the solid particles or occupies inter-particle void spaces.^{93,86} The choice of radical plays a major role in the efficiency of the DNP process, and radicals with specific EPR properties are necessary for both a given target nucleus and magnetic field strength. Extensive work has focused on developing biradicals for this purpose, with the current state-of-the-art ¹H DNP NMR experiments involving the use of molecules like TEKPol,⁸⁶ TOTAPOL,⁸³ AMUPol,⁹⁴ and TEMTriPol.⁹⁵

The choice of solvent can also have a large impact on the DNP efficiency. Ideal solvents usually contain at least some protons (which improve the transfer of polarization from the radical to the sample of interest), but they must be of low concentration (< 30 M), as too many protons can decrease the amount of polarization transferred to the

protons in the sample of interest. Currently, some of the most common solvents used are 1,1,2,2-tetrachloroethane (TCE), and 1,3-dibromobutane (DBB).⁹⁶ It has also been shown that deuteration of the solvent can improve DNP enhancements in some cases.^{97,98}

DNP enhancement is particularly important for the study of the surfaces of various materials. Such features have historically been challenging to study with NMR due to the inherently low S/N that arises from the small energy differences between spin states and the concomitant small Boltzmann population differences. Nuclei located on or near surfaces are closest to the radical, and are therefore the most easily polarized (*i.e.*, signal enhancement occurs predominantly at the surface sites). DNP-enhanced ¹H polarization can also be transferred into the interior of the particles by spin diffusion,^{97,98} or to heteronuclei (*e.g.*, ¹³C, ¹⁵N) using cross-polarization or other techniques (see **Chapter 5**).

1.3.5 Additional Methods

Two additional hardware methods are used in this thesis to obtain high resolution spectra: ultra-fast magic-angle spinning (UFMAS) and high magnetic fields (*i.e.*, $B_0 = 21.1$ T). UFMAS has become a very popular method of averaging the effects of strong hetero- and homonuclear dipolar interactions in SSNMR spectra. However, in order for the anisotropic effects of NMR interactions (like the dipolar interaction) to be averaged, the sample must be spun at a rate roughly a factor of three to four times larger than the anisotropy of the interaction (in Hz).² High magnetic fields are another source of signal enhancement, as they increase the Zeeman splitting of the energy levels, which increases the population difference between the levels, and serves to increase signal by a factor proportional to B_0^2 . High fields are especially useful for studying quadrupolar nuclei, as

the spectral broadening arising from the SOQI are proportional to $1/B_0$.⁹⁹ On the other hand, the broadening effects of CSA increase proportional to B_0 , which can be problematic in SSNMR spectra of broad patterns arising from large CSAs. However, the two proportionalities turn out to be very useful for the acquisition of NMR spectra of half-integer quadrupolar nuclides affected by CSA, since spectra acquired at two fields can help refine the NMR parameters associated with a given site, and aid in accurately determining the CS and EFG tensor parameters, as well as the Euler angles that describe their relative orientations.¹⁰⁰

1.4 “Real-World” Materials

As discussed above, NMR interactions are highly sensitive to the local environments of nuclei; therefore, NMR spectra are rich with details that can be used to study molecular structure and dynamics in numerous materials. To date, much of the work involving unresponsive nuclei has focused on ideal systems containing pure bulk samples. Such studies are important for developing new methods to acquire spectra of unresponsive nuclides (*vide supra*), and to establish correlations between the appearance of the NMR spectra of well-known materials and their underlying molecular-level details under optimal conditions (by extraction of the NMR tensor parameters through simulations of the experimental spectra). However, the focus herein is the study of *complex* materials found in two types of "real-world" samples: nanomaterials and pharmaceuticals. Unlike pure bulk materials, these samples often contain complicated mixtures of multiple phases with distinct structures and/or disparate local environments. In some cases, these complications result from impurities and by-products; however, they can also result from distinct domains or regions within the material itself, for example: (i)

atomic environments near the surface of the particles that are different from those in the core, (ii) unique structures resulting from modifications of the material like the incorporation of dopants, (iii) physical mixtures of multiple compounds, and (iv) systems with multiple domains with distinct structures (*e.g.*, excipients, core/shell, amorphous solid dispersions). With the foundation established by the extensive fundamental work on SSNMR of unreactive nuclides over the past decade, we are now able to study samples of increasing complexity, and identify the molecular-level solid-state structures, interactions, and dynamics of atoms or molecules that determine the bulk properties of materials.

1.4.1 Nanomaterials

Materials that have particle sizes with at least one external dimension of < 100 nm are known as *nanomaterials*. Such materials can form with a variety of different structures depending on the number of nano-sized dimensions, including: nano sheets and thin films (two-dimensions > 100 nm), nanorods or tubes (one-dimension > 100 nm), or nanoparticles (zero dimensions > 100 nm).^{101–104} The latter are of particular interest in this thesis.

Nanoparticles (NPs, or sometimes nanocrystals, NCs) have bulk properties that are distinct from their microcrystalline analogues, including novel optical (*e.g.*, quantum confinement, luminescence), magnetic (*e.g.*, superparamagnetism), and physical (*e.g.*, extremely high surface area/volume ratios) properties. As such, these materials are of interest in numerous research areas for applications in bioimaging,^{105–108} lasers,^{109–111} phosphors,^{106,112–114} magnets^{115–117} and fuel cells,^{118–120} as well as surface chemistry and catalysis.^{121,122}

Many of the synthetic methods by which NPs are produced are not well understood, and their outcomes are frequently determined by slight variations in reaction conditions or components. Often, these syntheses can seem capricious; reproducibility and scalability of such syntheses can require brute-force empirical optimizations that are only loosely rationalized with experimental data. As such, methods of characterizing these materials on a *molecular level* are vital for improving their syntheses and for developing reliable means of obtaining desirable materials with high yield, high purity, and with bulk physical properties that can be directly tuned from rational synthetic methods.

NPs and their associated bulk phases are typically characterized using electron microscopy methods (to describe particle size and morphology) and UV-Vis spectroscopy (to compare optical properties and measure luminescence wavelengths or intensities). Sometimes, powder X-ray diffraction (PXRD) can also be used to analyze crystalline samples (to determine the space group and unit cell parameters, as well as for the identification of major impurity phases). Unfortunately, in many cases, NPs with interesting bulk properties are not characterized in terms of their molecular-level structures – this lack of additional study strongly impedes any sort of understanding of elemental composition, molecular-level structure, and perhaps even dynamical components, all of which may be important for ultimately improving the syntheses and tuning the bulk properties of NPs. Furthermore, many of these reactions produce physical mixtures of multiple structures including impurities and by-products, many of which are not easily discriminated by any of the aforementioned techniques. For example: (i) isomorphous crystals with different molecular structures can appear identical in TEM

images, (ii) luminescence may be quenched by the presence of impurities and remain undetected by UV-Vis experiments, and (iii) amorphous structures, which are common by-products of many NP syntheses, do not diffract in XRD experiments. Therefore, the use of many characterization methods in tandem, as well as the development and application of additional characterization methodologies, are of the utmost importance.

SSNMR is an excellent complementary technique to those mentioned above, but can also act as a standalone method of characterization when these other methods are inadequate. Among many classes of nanomaterials, SSNMR has been used to characterize inorganic NPs with various compositions, including mesoporous silica,^{123–127} metals,^{128–135} and metal oxides.^{136–143} These spectra can act as exquisite probes of the cores, shells, and surfaces of NPs, revealing critical information about composition, short- and long-range order, homogeneity of doping, the nature of surfactant molecules, and the local coordination environments of atoms or ions within the structure. More recently, much attention has been focused on the development of NPs containing rare-earth elements (RE = Y, Sc, La-Lu). As discussed in **Chapters 2-4**, these materials have unique magnetic and luminescent properties due to the presence of the RE elements.

The work on nanomaterials in this thesis consists of three studies of inorganic NPs containing rare-earth elements.¹⁴⁴ **Chapter 2** details a systematic study of NaYF₄, a widely-used host material for doping with other rare-earth elements, whose structure has been a source of debate for over 50 years. Using a combination of PXRD and multinuclear (⁸⁹Y, ²³Na, ¹⁹F) SSNMR, we provide conclusive evidence of the structure of NaYF₄. This work also includes comparisons of bulk (*i.e.*, microcrystalline) NaYF₄ material with RE-containing core/shell NCs, formed by the epitaxial growth of one RE-

NC around another. Such structures separate the optically-active core from both stabilizing ligands at the surface of the particles and the surrounding environment, which can cause reduced luminescence intensities due to quenching.

Expanding on this foundational work on undoped materials, **Chapter 3** focuses on the characterization of NaYF₄ materials that have been doped with paramagnetic lanthanide dopants (*i.e.*, Er³⁺ and Tm³⁺). These dopants strongly affect the appearance of the SSNMR spectra due to the paramagnetic interaction. With the use of UFMAS NMR experiments, useful data can be acquired, which provide valuable detail about the distributions of the dopant ions and their mean distances from other atoms in the NP cores and on the NP surfaces. Such information is critical for understanding the molecular origins of the luminescent properties of these materials. In a second part of this study, samples with different particle size (either nano- or microcrystalline) are compared to assess the effects of particle size on the distribution of dopant ions in the materials.

Finally, **Chapter 4** describes a study of a distinct class of RE-doped nanomaterials, where the structural effects of different dopants are compared using numerous characterization techniques (*i.e.*, multinuclear SSNMR, PXRD, TEM, and electron paramagnetic resonance, EPR). This work is an extension of previous reports from our research group,¹⁴⁵ which revealed that a reverse micelle synthesis combining YCl₃ and F⁻ ions produces NPs with an unexpected zeolitic NP structure. The work documented in this thesis involves materials prepared with other RE materials (RE = Sc, Er, Eu). Through the use of multinuclear (¹⁹F, ⁸⁹Y, ¹H, ⁴⁵Sc) SSNMR, PXRD, TEM, and EPR methods, the structures of these new samples are probed, distinct RE³⁺ ion environments are detected, and reaction by-products and impurities are identified. These

results demonstrate the complexity inherent in many NP syntheses, and highlight the great utility of SSNMR for characterizing NPs.

1.4.2 Active Pharmaceutical Ingredients

Active pharmaceutical ingredients (APIs) are the biologically active component of pharmaceutical drugs. APIs are ubiquitous in our daily lives, and of enormous importance to society in general. The study of APIs has massive implications in the pharmaceutical and chemical industries, but more importantly, has great impact on numerous public health considerations and related socioeconomic factors.¹⁴⁶ Careful investigations of the chemistry of APIs and their dosage forms (*i.e.*, pills, capsules, colloidal suspensions, liquids *etc.*) are necessary for ensuring that drugs are delivered reliably and safely to the public. As such, the development of novel and effective characterization methods is a critical subject of pharmaceutical materials science research.

The vast majority (*ca.* 90%) of APIs are produced, manufactured, and administered as solid materials.¹⁴⁷ Such materials are typically favored in pharmaceutical development because they tend to have better stability than APIs in solution and are more convenient for delivery and storage. However, the molecular structures of APIs have a significant effect on their bulk physical properties, including bioavailability, stability, dissolution rate, tensile strength, and compactibility.^{148–150} These properties can ultimately determine the viability of a drug compound, and can also influence the nature of the dosage form used for their delivery.

APIs can exist in a number of different solid forms, as summarized in **Figure 1.10**. These forms include distinct arrangements of the API molecules (*e.g.*, crystalline or

amorphous phases and polymorphs), as well as more complex multi-component materials containing combinations of the API with ions (*i.e.*, salts), water or solvent molecules (*i.e.*, hydrates and solvates), as well as other small molecules (*i.e.*, cocrystals).^{151–160}

Additionally, APIs may form structures that fit into combinations of these classes. Phase changes between these forms are common, and can occur unintentionally while in storage, or as a result of the dosage form manufacturing process.^{161–163}

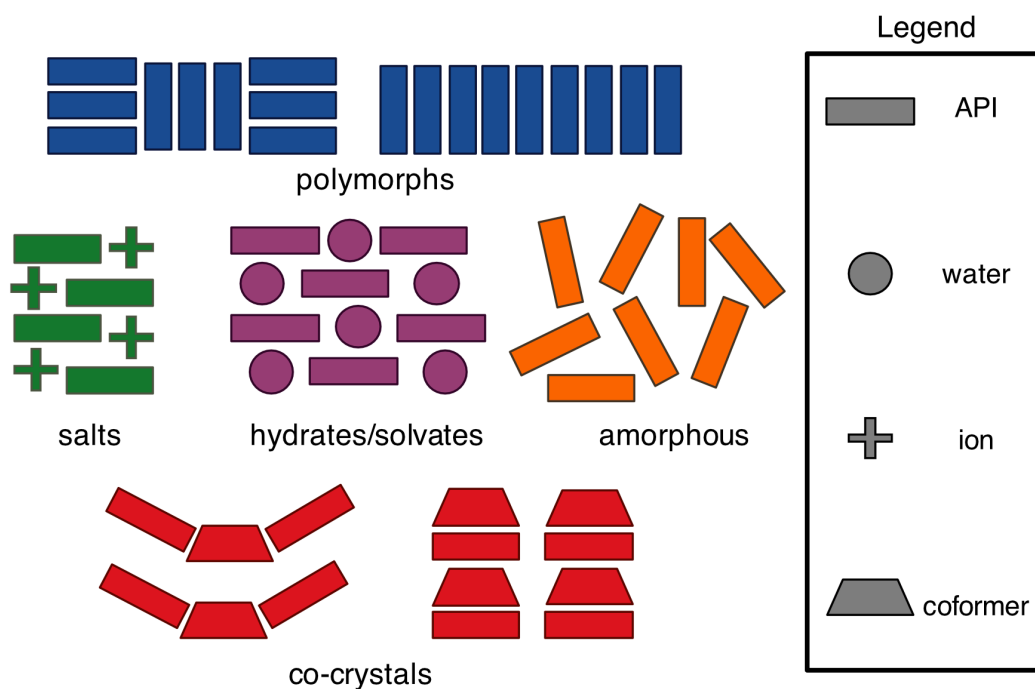


Figure 1.10 Schematic depictions of different solid forms of APIs (shown in different colors). Different shapes correspond to distinct types of molecules in the solid-state structures.

During dosage form manufacturing, a variety of additional ingredients (known as excipients) may be added to the API. These materials, which include binders, fillers, and lubricants, are necessary to ensure that the API is delivered reliably (*e.g.*, to stabilize the API), has the desired physical properties (*e.g.*, to create advanced delivery mechanisms like time-release tablets), and can be manufactured consistently (*e.g.*, to reduce sample

loss or damage during manufacturing). As such, most dosage formulations are complex heterogeneous solids with API domains dispersed within other ingredients. Ideally, the added ingredients are inert; however, in some cases, they can interact with the API and negatively affect both the manufacturing and performance of the drug (see **Chapter 6**).

Characterization of the API is critical throughout the manufacturing process of a dosage form. APIs must be studied both for the development of the formulation (*e.g.*, to identify alternative API forms that may have different physical properties), and for continued quality assurance and impurity screening, even after the drug is brought to market.^{148,164,165} APIs are routinely characterized using a variety of standard materials characterization techniques. Thermal analysis (*e.g.*, differential scanning calorimetry, DSC, and thermogravimetric analysis, TGA) is useful for identifying phase changes between different solid forms of an API as well as the uptake or loss of water (it is often one of the first indicators of unexpected changes in these materials, see **Chapter 7**). Vibrational spectroscopy (*e.g.*, Raman and infrared) can be used to provide chemical information on specific functional groups and provide structural fingerprints of many APIs. X-ray diffraction methods (XRD) are most commonly used to determine the structure of crystalline forms. However, these methods are not well suited to study some API systems. For example, an emerging class of API formulations, amorphous solid dispersions (ASDs), contain an amorphous phase of the API (which can have enhanced solubility relative to crystalline analogues); such materials cannot be detected with diffraction methods, and there is limited molecular structural information provided by the other techniques.¹⁶⁶

As with other areas in materials chemistry, SSNMR has become an essential technique for the study of pharmaceuticals.^{167–171} In particular, ¹³C SSNMR studies are now an established means of differentiating minor structural differences between polymorphs, and for the identification of APIs in both crystalline and amorphous materials.^{172–175} NMR can be used for quantitative analysis (an increasingly important area for quality assurance, see **Chapter 6**).^{176–180} ¹H NMR relaxation measurements (or relaxation measurements on other nuclides) can be used to determine domain sizes in dosage forms, and reveal interactions between the APIs and surrounding excipients.^{147,181} More recently, comparisons of experimental NMR observables (*e.g.*, chemical shift and quadrupolar parameters) to those calculated from model structures have been used in crystal structure prediction methods,^{182–185} which can determine full crystal structures with accuracies rivaling those of neutron diffraction. This burgeoning field is known as *NMR crystallography*.^{186,187} Similar methods can also be used to validate and refine structures obtained from XRD data via *NMR-assisted crystallography*.^{188–190} However, the aforementioned SSNMR methods are not always applicable to the study of a given API. In particular, it can be challenging to study dosage formulations with ¹H or ¹³C NMR experiments, since most excipient molecules and the APIs themselves contain numerous distinct environments that can obscure signals of interest (such interference is particularly problematic when the wt-% of the API in the dosage form is low).¹⁹¹ Clearly, new and innovative methods are desirable for characterizing APIs, both in the bulk phase (*i.e.*, the pure form), but particularly in solid dosage formulations.

Previous work by our group and others^{20,191–194} has demonstrated that ³⁵Cl SSNMR is particularly well-suited to characterizing the bulk *and* dosage forms of APIs

that have been synthesized as HCl salts (more than 60% of solid APIs are current manufactured as HCl salts).¹⁹⁵ The NMR spectra of the Cl⁻ anions in these materials are influenced by both CSA and the QI. The latter is particularly sensitive to small structural differences in the local Cl⁻ anion environments produced by variations in local hydrogen bonding.^{20,196–198} As a result, each solid phase of an API produces a distinct ³⁵Cl SSNMR spectral fingerprint. Furthermore, since Cl⁻ anions are not present in the excipient molecules, ³⁵Cl SSNMR is an attractive approach for characterizing the APIs in dosage formulations without interfering signals from the excipient. *N.B.* there are some excipients that contain covalently bound Cl atoms; however, the ³⁵Cl SSNMR signals produced by such environments are so broad that they do not obscure the spectra of anionic sites.^{20,199,200}

Three chapters of this thesis focus on the development and application of ³⁵Cl SSNMR to the study of pharmaceuticals in bulk and dosage forms. **Chapter 5** addresses the need for signal enhancement in ³⁵Cl SSNMR spectra through the use of DNP NMR. This work is the first demonstration of DNP-enhanced ³⁵Cl NMR spectroscopy, and also details a novel hybrid spinning/static sample method for enhancing the DNP efficiency in spectra of any nucleus collected under static sample conditions. The techniques developed here produce signal enhancements of as much as 110 (equivalent to more than a 12,000-fold improvement in S/N). With these methods, a high-quality ³⁵Cl NMR spectrum can be acquired in 2 minutes. Finally, this chapter shows how useful these methods can be for real-world samples, and the benefits of the signal enhancement from DNP are applied to the study of APIs in dosage formulations with low wt-% Cl (*i.e.*, < 0.5 wt-%).

Another important aspect of pharmaceutical characterization is the quantification of the API in dosage formulations. **Chapter 6** details a novel method for quantifying the amount of an API HCl salt in model formulations with excipients. As a proof-of-concept, this method is used to study a common deleterious reaction in which an API salt converts to its neutral "free base" form through a process known as *disproportionation*. The techniques developed in this chapter are applied to quantitatively determine the amount of disproportionation that occurs in model formulations with a high degree of accuracy.

Finally, **Chapter 7** is a case study of an API that forms a particularly interesting solid phase known as a *variable hydrate*, which has stable structures over a continuous range of non-stoichiometric hydration levels. ^{35}Cl SSNMR is particularly well-suited to the study of such materials, given that the Cl^- anions are the most prevalent binding sites for water molecules. As demonstrated in this chapter, ^{35}Cl SSNMR can determine the *in situ* hydration state of nuclei within the material and thus is a valuable method for characterizing the local structure of water molecules.

1.5 References

- (1) Jonas, J.; Gutowsky, H. S. *Annu. Rev. Phys. Chem.* **1980**, *31*, 1–28.
- (2) Duer, M. J. *Introduction to Solid-State NMR Spectroscopy*; Blackwell: Oxford, UK, **2004**.
- (3) Levitt, M. H. *Spin Dynamics: Basics of Nuclear Magnetic Resonance*; John Wiley & Sons, **2001**.
- (4) Keeler, J. *Understanding NMR Spectroscopy*, 2nd ed.; John Wiley & Sons, Ltd.: Chichester, UK, **2010**.
- (5) Fukushima, E.; Roeder, S. B. W. *Experimental Pulse NMR: a Nuts and Bolts Approach*; Addison-Wesley Reading, MA, **1981**.
- (6) Zumbulyadis, N. *Concepts Magn. Reson.* **1991**, *3*, 89–107.
- (7) Bass, S. D. *Science* **2007**, *315*, 1672–1673.
- (8) Andrew, E. R.; Bradbury, A.; Eades, R. G. *Nature*. **1958**, 1659.
- (9) Lowe, I. J. *Phys. Rev. Lett.* **1959**, *2*, 285–287.
- (10) Hennel J.W., Klinowski J. In *New Techniques in Solid-State NMR. Topics in Current Chemistry*; Klinowski J., Ed.; Springer: Berlin, Heidelberg, **2006**; Vol. 246, pp 1-14.
- (11) Schmidt-Rohr, K.; Spiess, H. W. *Multidimensional Solid-State NMR and Polymers*; Academic Press Ltd.: London, UK, **1994**.
- (12) *The Multinuclear Approach to NMR Spectroscopy*; Lambert, J. B., Riddell, F. G., Eds.; Springer Netherlands: Dordrecht, **1983**.
- (13) Mehring, M. *High-Resolution NMR in Solids*, 2nd ed.; Springer: Berlin, Germany, **1982**.
- (14) *NMR of Quadrupolar Nuclei in Solid Materials*, 1st ed.; Wasylishen, R. E., Ashbrook, S. E., Wimperis, S., Eds.; John Wiley & Sons, Ltd: Chichester, UK, **2012**.
- (15) Bakhmutov, V. I. *Practical NMR Relaxation for Chemists*; John Wiley & Sons, Ltd: Chichester, UK, **2004**.
- (16) Zwanziger, J. W. In *eMagRes*; John Wiley & Sons, Ltd: Chichester, UK, **1996**.
- (17) Autschbach, J.; Zheng, S.; Schurko, R. W. *Concepts Magn. Reson. Part A* **2010**, *36A*, 84–126.
- (18) Kentgens, A. P. M. *Geoderma* **1997**, *80*, 271–306.
- (19) Vega, A. J. In *Encyclopedia of NMR*; Grant, D. M., Harris, R. K., Eds.; Wiley: Chichester, **1996**; Vol. 4, pp 3869–3888.
- (20) Widdifield, C. M.; Chapman, R. P.; Bryce, D. L. In *Annual Reports on NMR Spectroscopy*; Elsevier Ltd., **2009**; Vol. 66, pp 195–326.
- (21) Schurko, R. W. *Acc. Chem. Res.* **2013**, *46*, 1985–1995.
- (22) Akitt, J. W.; McDonald, W. S. *J. Magn. Reson.* **1984**, *58*, 401–412.
- (23) Knop, O.; Palmer, E. M.; Robinson, R. W. *Acta Crystallogr. Sect. A Cryst. Physics, Diffraction, Theor. Gen. Crystallogr.* **1975**, *31*, 704–704.
- (24) Koller, H.; Engelhardt, G.; Kentgens, A. P. M.; Sauer, J. *J. Phys. Chem.* **1994**, *98*, 1544–1551.
- (25) Ramsey, N. F. *Phys. Rev.* **1950**, *78*, 699–703.
- (26) Pople, J. A. *Proc. R. Soc. A Math. Phys. Eng. Sci.* **1957**, *239*, 541–549.
- (27) Pople, J. A. *Proc. R. Soc. A Math. Phys. Eng. Sci.* **1957**, *239*, 550–556.

- (28) Grant, D. M. In *Encyclopedia of Magnetic Resonance*; John Wiley & Sons, Ltd: Chichester, UK, **2007**; pp 1–25.
- (29) Mason, J. *Solid State Nucl. Magn. Reson.* **1993**, *2*, 285–288.
- (30) Herzfeld, J.; Berger, A. E. *J. Chem. Phys.* **1980**, *73*, 6021–6030.
- (31) Spiess, H. W. Springer-Verlag 1978.
- (32) Mehring, M. *Principles of high resolution NMR in solids*; Springer Science & Business Media, **2012**.
- (33) Haeberlen, U.; Waugh, J. S. *Phys. Rev.* **1968**, *175*, 453–467.
- (34) Harris, R. K.; Becker, E. D.; Cabral de Menezes, S. M.; Granger, P.; Hoffman, R. E.; Zilm, K. W. *Pure Appl. Chem.* **2008**, *80*, 59–84.
- (35) Jameson, C. J. *Solid State Nucl. Magn. Reson.* **1998**, *11*, 265–268.
- (36) Widdifield, C. M.; Schurko, R. W. *Concepts Magn. Reson. Part A* **2009**, *34A*, 91–123.
- (37) Gullion, T. *Concepts Magn. Reson.* **1998**, *10*, 277–289.
- (38) Gullion, T.; Vega, A. *Prog. Nucl. Magn. Reson. Spectrosc.* **2005**, *47*, 123–136.
- (39) Bertini, Ivano; Luchinat, Claudio; Parigi, Giacomo; Ravera, E. *NMR of Paramagnetic Molecules. Applications to Metalloproteins and Models.*; **2016**.
- (40) Pintacuda, G.; Kervern, G. In *Modern NMR Methodology*; Heise, H., Matthews, S., Eds.; Springer Berlin Heidelberg: Berlin, Heidelberg, **2013**; pp 157–200.
- (41) Bertmer, M. *Solid State Nucl. Magn. Reson.* **2017**, *81*, 1–7.
- (42) Brough, A. R.; Grey, C. P.; Dobson, C. M. *J. Chem. Soc. Chem. Commun.* **1992**, 742–743.
- (43) Nayeem, A.; Yesinowski, J. P. *J. Chem. Phys.* **1988**, *89*, 4600–4608.
- (44) Kervern, G.; Pintacuda, G.; Zhang, Y.; Oldfield, E.; Roukoss, C.; Kuntz, E.; Herdtweck, E.; Basset, J.-M.; Cadars, S.; Lesage, A.; Copéret, C.; Emsley, L. *J. Am. Chem. Soc.* **2006**, *128*, 13545–13552.
- (45) Kervern, G.; Steuernagel, S.; Engelke, F.; Pintacuda, G.; Emsley, L. *J. Am. Chem. Soc.* **2007**, *129*, 14118–14119.
- (46) Wickramasinghe, N. P.; Shaibat, M.; Ishii, Y. *J. Am. Chem. Soc.* **2005**, *127*, 5796–5797.
- (47) Wickramasinghe, N. P.; Shaibat, M. A.; Jones, C. R.; Casabianca, L. B.; de Dios, A. C.; Harwood, J. S.; Ishii, Y. *J. Chem. Phys.* **2008**, *128*, 052210.
- (48) Peters, J. a.; Huskens, J.; Raber, D. J. *Prog. Nucl. Magn. Reson. Spectrosc.* **1996**, *28*, 283–350.
- (49) Parthasarathy, S.; Nishiyama, Y.; Ishii, Y. *Acc. Chem. Res.* **2013**, *46*, 2127–2135.
- (50) Wickramasinghe, N. P.; Ishii, Y. *J. Magn. Reson.* **2006**, *181*, 233–243.
- (51) Bloch, F. *Phys. Rev.* **1946**, *70*, 460–474.
- (52) Bloch, F.; Hansen, W. W.; Packard, M. *Phys. Rev.* **1946**, *70*, 474–485.
- (53) Hahn, E. L. *Phys. Rev.* **1950**, *80*, 580–594.
- (54) Berger, S.; Braun, S. *200 and More NMR Experiments: A Practical Course*; Wiley-VCH, **2004**.
- (55) Carr, H. Y.; Purcell, E. M. *Phys. Rev.* **1954**, *94*, 630–638.
- (56) Meiboom, S.; Gill, D. *Rev. Sci. Instrum.* **1958**, *29*, 688–691.
- (57) Schurko, R. W. In *Encyclopedia of Magnetic Resonance*; John Wiley & Sons, Ltd: Chichester, UK, **2011**, pp 77–93.
- (58) Clark, W. G.; Hanson, M. E.; Lefloch, F.; Ségransan, P. *Rev. Sci. Instrum.* **1995**,

- 66, 2453–2464.
- (59) Massiot, D.; Farnan, I.; Gautier, N.; Trumeau, D.; Trokiner, A.; Coutures, J. P. *Solid State Nucl. Magn. Reson.* **1995**, *4*, 241–248.
- (60) Kupce, E.; Freeman, R. J. *J. Magn. Reson.* **1995**, *115*, 273–276.
- (61) Bhattacharyya, R.; Frydman, L. *J. Chem. Phys.* **2007**, *127*, 194503.
- (62) O’Dell, L. A. *Solid State Nucl. Magn. Reson.* **2013**, *55–56*, 28–41.
- (63) O’Dell, L. A.; Schurko, R. W. *Chem. Phys. Lett.* **2008**, *464*, 97–102.
- (64) O’Dell, L. A.; Rossini, A. J.; Schurko, R. W. *Chem. Phys. Lett.* **2009**, *468*, 330–335.
- (65) Hung, I.; Gan, Z. *J. Magn. Reson.* **2010**, *204*, 256–265.
- (66) Pines, A.; Gibby, M. G.; Waugh, J. S. *Chem. Phys. Lett.* **1972**, *15*, 373–376.
- (67) Pines, A.; Gibby, M. G.; Waugh, J. S. *J. Chem. Phys.* **1972**, *56*, 1776–1777.
- (68) Gibby, M. G.; Griffin, R. G.; Pines, A.; Waugh, J. S. *Chem. Phys. Lett.* **1972**, *17*, 80–81.
- (69) Hartmann, S. R.; Hahn, E. L. *Phys. Rev.* **1962**, *128*, 2042–2053.
- (70) Schaefer, J.; Stejskal, E. O. *J. Am. Chem. Soc.* **1976**, *98*, 1031–1032.
- (71) Harris, K. J.; Lupulescu, A.; Lucier, B. E. G.; Frydman, L.; Schurko, R. W. *J. Magn. Reson.* **2012**, *224*, 38–47.
- (72) Fung, B. M.; Khitrin, A. K.; Ermolaev, K. *J. Magn. Reson.* **2000**, *142*, 97–101.
- (73) Bennett, A. E.; Rienstra, C. M.; Auger, M.; Lakshmi, K. V.; Griffin, R. G. *J. Chem. Phys.* **1995**, *103*, 6951–6958.
- (74) Bräuniger, T.; Wormald, P.; Hodgkinson, P. *Monatshefte für Chemie / Chem. Mon.* **2002**, *133*, 1549–1554.
- (75) Thakur, R. S.; Kurur, N. D.; Madhu, P. K. *J. Magn. Reson.* **2008**, *193*, 77–88.
- (76) Barnes, A. B.; De Paëpe, G.; van der Wel, P. C. A.; Hu, K.-N.; Joo, C.-G.; Bajaj, V. S.; Mak-Jurkauskas, M. L.; Sirigiri, J. R.; Herzfeld, J.; Temkin, R. J.; Griffin, R. G. *Appl. Magn. Reson.* **2008**, *34*, 237–263.
- (77) Ni, Q. Z.; Daviso, E.; Can, T. V.; Markhasin, E.; Jawla, S. K.; Swager, T. M.; Temkin, R. J.; Herzfeld, J.; Griffin, R. G. *Acc. Chem. Res.* **2013**, *46*, 1933–1941.
- (78) Kuhn, L. T. *Hyperpolarization Methods in NMR Spectroscopy*; Kuhn, L. T., Ed.; Topics in Current Chemistry; Springer: Berlin, Heidelberg, **2013**; Vol. 338.
- (79) Overhauser, A. W. *Phys. Rev.* **1953**, *92*, 411–415.
- (80) Carver, T. R.; Slichter, C. P. *Phys. Rev.* **1953**, *92*, 212–213.
- (81) Becerra, L. R.; Gerfen, G. J.; Temkin, R. J.; Singel, D. J.; Griffin, R. G. *Phys. Rev. Lett.* **1993**, *71*, 3561–3564.
- (82) Rosay, M.; Tometich, L.; Pawsey, S.; Bader, R.; Schauwecker, R.; Blank, M.; Borchard, P. M.; Cauffman, S. R.; Felch, K. L.; Weber, R. T.; Temkin, R. J.; Griffin, R. G.; Maas, W. E. *Phys. Chem. Chem. Phys.* **2010**, *12*, 5850–5860.
- (83) Song, C.; Hu, K.-N.; Joo, C.-G.; Swager, T. M.; Griffin, R. G. *J. Am. Chem. Soc.* **2006**, *128*, 11385–11390.
- (84) Sauvée, C.; Rosay, M.; Casano, G.; Aussenac, F.; Weber, R. T.; Ouari, O.; Tordo, P. *Angew. Chemie Int. Ed.* **2013**, *52*, 10858–10861.
- (85) Hu, K.-N.; Yu, H.; Swager, T. M.; Griffin, R. G. *J. Am. Chem. Soc.* **2004**, *126*, 10844–10845.
- (86) Zagdoun, A.; Casano, G.; Ouari, O.; Schwarzwälder, M.; Rossini, A. J.; Aussenac, F.; Yulikov, M.; Jeschke, G.; Copéret, C.; Lesage, A.; Tordo, P.; Emsley, L. *J. Am.*

- Chem. Soc.* **2013**, *135*, 12790–12797.
- (87) Kubicki, D. J.; Casano, G.; Schwarzwälder, M.; Abel, S.; Sauvée, C.; Ganesan, K.; Yulikov, M.; Rossini, A. J.; Jeschke, G.; Copéret, C.; Lesage, A.; Tordo, P.; Ouari, O.; Emsley, L. *Chem. Sci.* **2016**, *7*, 550–558.
- (88) Maly, T.; Debelouchina, G. T.; Bajaj, V. S.; Hu, K.-N.; Joo, C.-G.; Mak-Jurkauskas, M. L.; Sirigiri, J. R.; van der Wel, P. C. a; Herzfeld, J.; Temkin, R. J.; Griffin, R. G. *J. Chem. Phys.* **2008**, *128*, 52211.
- (89) Becerra, L. R.; Gerfen, G. J.; Bellew, B. F.; Bryant, J. A.; Hall, D. A.; Inati, S. J.; Weber, R. T.; Un, S.; Prisner, T. F.; McDermott, A. E.; Fishbein, K. W.; Kreischer, K. E.; Temkin, R. J.; Singel, D. J.; Griffin, R. G. *J. Magn. Reson.* **1995**, *117*, 28–40.
- (90) Hall, D. A.; Maus, D. C.; Gerfen, G. J.; Inati, S. J.; Becerra, L. R.; Dahlquist, F. W.; Griffin, R. G. *Science* **1997**, *276*, 930–932.
- (91) Lelli, M.; Chaudhari, S. R.; Gajan, D.; Casano, G.; Rossini, A. J.; Ouari, O.; Tordo, P.; Lesage, A.; Emsley, L. *J. Am. Chem. Soc.* **2015**, *137*, 14558–14561.
- (92) Geiger, M.-A.; Orwick-Rydmark, M.; Märker, K.; Franks, W. T.; Akhmetzyanov, D.; Stöppler, D.; Zinke, M.; Specker, E.; Nazaré, M.; Diehl, A.; van Rossum, B.-J.; Aussenac, F.; Prisner, T.; Akbey, Ü.; Oschkinat, H. *Phys. Chem. Chem. Phys.* **2016**, *18*, 30696–30704.
- (93) Lesage, A.; Lelli, M.; Gajan, D.; Caporini, M. A.; Vitzthum, V.; Miéville, P.; Alauzun, J. G.; Roussey, A.; Thieuleux, C.; Mehdi, A.; Bodenhausen, G.; Coperet, C.; Emsley, L. *J. Am. Chem. Soc.* **2010**, *132*, 15459–15461.
- (94) Sauvée, C.; Rosay, M.; Casano, G.; Aussenac, F.; Weber, R. T.; Ouari, O.; Tordo, P. *Angew. Chemie* **2013**, *125*, 11058–11061.
- (95) Mathies, G.; Caporini, M. A.; Michaelis, V. K.; Liu, Y.; Hu, K.-N.; Mance, D.; Zweier, J. L.; Rosay, M.; Baldus, M.; Griffin, R. G. *Angew. Chemie Int. Ed.* **2015**, *54*, 11770–11774.
- (96) Zagdoun, A.; Rossini, A. J.; Gajan, D.; Bourdolle, A.; Ouari, O.; Rosay, M.; Maas, W. E.; Tordo, P.; Lelli, M.; Emsley, L.; Lesage, A.; Coperet, C. *Chem. Commun.* **2012**, *48*, 654–656.
- (97) van der Wel, P. C. A.; Hu, K.-N.; Lewandowski, J.; Griffin, R. G. *J. Am. Chem. Soc.* **2006**, *128*, 10840–10846.
- (98) Rossini, A. J.; Zagdoun, A.; Hegner, F.; Schwarzwälder, M.; Gajan, D.; Copéret, C.; Lesage, A.; Emsley, L. *J. Am. Chem. Soc.* **2012**, *134*, 16899–16908.
- (99) Amoureux, J. P.; Fernandez, C.; Granger, P. In *Multinuclear Magnetic Resonance in Liquids and Solids — Chemical Applications*; Springer Netherlands: Dordrecht, **1990**, pp 409–424.
- (100) Dye, J. L.; Ellabundy, A. S.; Kim, J. In *Modern NMR Techniques and Their Application in Chemistry*; Marcel Dekker: New York, NY, **1991**, pp 217–322.
- (101) Ozin, G. A.; Arsenault, A. C.; Cademartiri, L. *Nanochemistry: A Chemical Approach to Nanomaterials*; Royal Society of Chemistry, **2009**.
- (102) Rao, C. N. R.; Müller, A.; Cheetham, A. K. *Nanomaterials Chemistry: Recent Developments and New Directions*; John Wiley & Sons, **2007**.
- (103) Vollath, D. *Nanomaterials*; Wiley-Vch, **2013**.
- (104) Wolf, E. L. *Nanophysics and Nanotechnology: An Introduction to Modern Concepts in Nanoscience*; John Wiley & Sons, **2015**.

- (105) Vetrone, F.; Capobianco, J. A. *Int. J. Nanotechnol.* **2008**, *5*, 1306.
- (106) Gai, S.; Li, C.; Yang, P.; Lin, J. *Chem. Rev.* **2014**, *114*, 2343–2389.
- (107) Chen, G.; Qiu, H.; Prasad, P. N.; Chen, X. *Chem. Rev.* **2014**, *114*, 5161–5214.
- (108) Chen, D.; Wang, Y. *Nanoscale* **2013**, *5*, 4621.
- (109) Klimov, V. I.; Mikhailovsky, A. A.; Xu, S.; Malko, A.; Hollingsworth, J. A.; Leatherdale, C. A.; Eisler, H.; Bawendi, M. G. *Science* **2000**, *290*, 314–317.
- (110) Wang, R.; Calvignanello, O.; Ratcliffe, C. I.; Wu, X.; Leek, D. M.; Zaman, M. B.; Kingston, D.; Ripmeester, J. a.; Yu, K. *J. Phys. Chem. C* **2009**, *113*, 3402–3408.
- (111) Zheng, H.; Zhang, J.; Yang, B.; Du, X.; Yan, Y. *Phys. Chem. Chem. Phys.* **2015**, *17*, 16341–16350.
- (112) Huang, X.; Han, S.; Huang, W.; Liu, X. *Chem. Soc. Rev.* **2013**, *42*, 173–201.
- (113) Bünzli, J.-C. G. *Coord. Chem. Rev.* **2015**, *293–294*, 19–47.
- (114) Wang, X.; Liu, Q.; Bu, Y.; Liu, C.-S.; Liu, T.; Yan, X. *RSC Adv.* **2015**, *5*, 86219–86236.
- (115) Sorace, L.; Benelli, C.; Gatteschi, D. *Chem. Soc. Rev.* **2011**, *40*, 3092–3104.
- (116) Gutfleisch, O.; Willard, M. A.; Brück, E.; Chen, C. H.; Sankar, S. G.; Liu, J. P. *Adv. Mater.* **2011**, *23*, 821–842.
- (117) Herbst, J. F. *Rev. Mod. Phys.* **1991**, *63*, 819–898.
- (118) Ormerod, R. M. *Chem. Soc. Rev.* **2003**, *32*, 17–28.
- (119) Antolini, E.; Perez, J. *Int. J. Hydrogen Energy* **2011**, *36*, 15752–15765.
- (120) Wang, F.; Deng, R.; Wang, J.; Wang, Q.; Han, Y.; Zhu, H.; Chen, X.; Liu, X. *Nat. Mater.* **2011**, *10*, 968–973.
- (121) Arnold, P. L.; McMullon, M. W.; Rieb, J.; Kühn, F. E. *Angew. Chemie Int. Ed.* **2015**, *54*, 82–100.
- (122) McFarland, E. W.; Metiu, H. *Chem. Rev.* **2013**, *113*, 4391–4427.
- (123) Atkins, T. M.; Cassidy, M. C.; Lee, M.; Ganguly, S.; Marcus, C. M.; Kauzlarich, S. M. *ACS Nano* **2013**, *7*, 1609–1617.
- (124) Mayeri, D.; Phillips, B. L.; Augustine, M. P.; Kauzlarich, S. M. *Chem. Mater.* **2001**, *13*, 765–770.
- (125) Carter, R. S.; Harley, S. J.; Power, P. P.; Augustine, M. P. *Chem. Mater.* **2005**, *17*, 2932–2939.
- (126) Akbey, Ü.; Altin, B.; Linden, A.; Özçelik, S.; Gradzielski, M.; Oschkinat, H. *Phys. Chem. Chem. Phys.* **2013**, *15*, 20706–20716.
- (127) Trébosc, J.; Wiench, J. W.; Huh, S.; Lin, V. S.-Y.; Pruski, M. *J. Am. Chem. Soc.* **2005**, *127*, 3057–3068.
- (128) Zhou, H.; Du, F.; Li, X.; Zhang, B.; Li, W.; Yan, B. *J. Phys. Chem. C* **2008**, *112*, 19360–19366.
- (129) Badia, A.; Demers, L.; Dickinson, L.; Morin, F. G.; Lennox, R. B.; Reven, L. *J. Am. Chem. Soc.* **1997**, *119*, 11104–11105.
- (130) Badia, A.; Gao, W.; Singh, S.; Demers, L.; Cuccia, L.; Reven, L. *Langmuir* **1996**, *12*, 1262–1269.
- (131) Li, Y.; Silverton, L. C.; Haasch, R.; Tong, Y. Y. *Langmuir* **2008**, *24*, 7048–7053.
- (132) Bower, P. V.; Louie, E. a.; Long, J. R.; Stayton, P. S.; Drobny, G. P. *Langmuir* **2005**, *21*, 3002–3007.
- (133) Fiurasek, P.; Reven, L. *Langmuir* **2007**, *23*, 2857–2866.
- (134) Schmitt, H.; Badia, A.; Dickinson, L.; Reven, L.; Lennox, R. B. *Adv. Mater.* **1998**,

- 10, 475–480.
- (135) Abraham, A.; Mihaliuk, E.; Kumar, B.; Legleiter, J.; Gullion, T. *J. Phys. Chem. C* **2010**, *114*, 18109–18114.
- (136) Pawsey, S.; Yach, K.; Reven, L. *Langmuir* **2002**, *18*, 5205–5212.
- (137) Gao, W.; Dickinson, L.; Grozinger, C.; Morin, F. G.; Reven, L. *Langmuir* **1997**, *13*, 115–118.
- (138) Luo, B.; Rossini, J. E.; Gladfelter, W. L. *Langmuir* **2009**, *25*, 13133–13141.
- (139) Bouvy, C.; Marine, W.; Sporcken, R.; Su, B. L. *Chem. Phys. Lett.* **2006**, *428*, 312–316.
- (140) Avadhut, Y. S.; Weber, J.; Hammarberg, E.; Feldmann, C.; Schellenberg, I.; Pöttgen, R.; Schmedt auf der Günne, J. *Chem. Mater.* **2011**, *23*, 1526–1538.
- (141) Holland, G. P.; Sharma, R.; Agola, J. O.; Amin, S.; Solomon, V. C.; Singh, P.; Buttry, D. A.; Yarger, J. L. *Chem. Mater.* **2007**, *19*, 2519–2526.
- (142) Coppel, Y.; Spataro, G.; Pagès, C.; Chaudret, B.; Maisonnat, A.; Kahn, M. L. *Chem. Eur. J.* **2012**, *18*, 5384–5393.
- (143) Wang, L.-Q.; Zhou, X.-D.; Exarhos, G. J.; Pederson, L. R.; Wang, C.; Windisch, C. F.; Yao, C. *Appl. Phys. Lett.* **2007**, *91*, 173107.
- (144) Hirsh, D. A.; Johnson, N. J. J.; Van Veggel, F. C. J. M.; Schurko, R. W. *Chem. Mater.* **2015**, *27*, 6495–6507.
- (145) Lucier, B. E. G.; Johnston, K. E.; Arnold, D. C.; Lemyre, J.; Beaupré, A.; Blanchette, M.; Ritcey, A. M.; Schurko, R. W. *J. Phys. Chem. C* **2014**, *118*, 1213–1228.
- (146) Snodin, D. J.; McCrossen, S. D. *Regul. Toxicol. Pharmacol.* **2012**, *63*, 298–312.
- (147) Geppi, M.; Mollica, G.; Borsacchi, S.; Veracini, C. A. *Appl. Spectrosc. Rev.* **2008**, *43*, 202–302.
- (148) Aaltonen, J.; Alleso, M.; Mirza, S.; Koradia, V.; Gordon, K.; Rantanen, J. *Eur. J. Pharm. Biopharm.* **2009**, *71*, 23–37.
- (149) Haleblian, J. K.; McCrone, W. *J. Pharm. Sci.* **1969**, *58*, 911–929.
- (150) Threlfall, T. L. *Analyst* **1995**, *120*, 2435–2460.
- (151) Borika, L.; Haleblian, J. K. *Acta Pharm. Jugoslavia* **1990**, *40*, 71–94.
- (152) Vishweshwar, P.; McMahon, J. A.; Bis, J. A.; Zaworotko, M. J. *J. Pharm. Sci.* **2006**, *95*, 499–516.
- (153) Yu, L. *Adv. Drug Deliv. Rev.* **2001**, *48*, 27–42.
- (154) Serajuddin, A. T. M. *Adv. Drug Deliv. Rev.* **2007**, *59*, 603–616.
- (155) Schultheiss, N.; Newman, A. *Cryst. Growth Des.* **2009**, *9*, 2950–2967.
- (156) Kumar, A.; Sahoo, S. *Pharm. Glob.* **2011**, *2*, 1–7.
- (157) Singhal, D.; Curatolo, W. *Adv. Drug Deliv. Rev.* **2004**, *56*, 335–347.
- (158) Vippagunta, S. R.; Brittain, H. G.; Grant, D. J. W. *Adv. Drug Deliv. Rev.* **2001**, *48*, 3–26.
- (159) Griesser, U. J. In *Polymorphism*; Wiley-VCH Verlag GmbH & Co. KGaA: Weinheim, FRG, **2006**; pp 211–233.
- (160) Caira, M. R. *Des. Org. Solids* **1998**, *198*, 163–208.
- (161) Morris, K. R.; Griesser, U. J.; Eckhardt, C. J.; Stowell, J. G. *Adv. Drug Deliv. Rev.* **2001**, *48*, 91–114.
- (162) Byrn, S. R.; Pfeiffer, R. R.; Stephenson, G.; Grant, D. J. W.; Gleason, W. B. *Chem. Mater.* **1994**, *6*, 1148–1158.

- (163) Datta, S.; Grant, D. J. W. *Nat. Rev. Drug Discov.* **2004**, *3*, 42–57.
- (164) Newman, A.; Knipp, G.; Zografis, G. *J. Pharm. Sci.* **2012**, *101*, 1355–1377.
- (165) Kesisoglou, F.; Panmai, S.; Wu, Y. *Adv. Drug Deliv. Rev.* **2007**, *59*, 631–644.
- (166) Trask, A. V.; Motherwell, W. D. S.; Jones, W. *Cryst. Growth Des.* **2005**, *5*, 1013–1021.
- (167) Vogt, F. G. *eMagRes* **2015**, *4*, 255–268.
- (168) Vogt, F. G. In *New Applications of NMR in Drug Discovery and Development*; **2013**; pp 43–100.
- (169) Harris, R. K. *J. Pharm. Pharmacol.* **2007**, *59*, 225–239.
- (170) Harris, R. K. *Analyst* **2006**, *131*, 351–373.
- (171) Pindelska, E.; Sokal, A.; Kolodziejcki, W. *Adv. Drug Deliv. Rev.* **2017**, *117*, 111–146.
- (172) Tishmack, P. A.; Bugay, D. E.; Byrn, S. R. *J. Pharm. Sci.* **2003**, *92*, 441–474.
- (173) Harris, R. K.; Olivieri, A. C. *ChemInform* **2003**, *34*, 1–10.
- (174) Ouyang, J.; Ratcliffe, C. I.; Kingston, D.; Wilkinson, B.; Kuijper, J.; Wu, X.; Ripmeester, J. A.; Yu, K. *J. Phys. Chem. C* **2008**, *112*, 4908–4919.
- (175) Brittain, H. G.; Morris, K. R.; Bugay, D. E.; Thakur, A. B.; Serajuddin, A. T. M. *J. Pharm. Biomed. Anal.* **1993**, *11*, 1063–1069.
- (176) Holzgrabe, U.; Deubner, R.; Schollmayer, C.; Waibel, B. *J. Pharm. Biomed. Anal.* **2005**, *38*, 806–812.
- (177) Offerdahl, T. J.; Salsbury, J. S.; Dong, Z.; Grant, D. J. W.; Schroeder, S. A.; Prakash, I.; Gorman, E. M.; Barich, D. H.; Munson, E. J. *J. Pharm. Sci.* **2005**, *94*, 2591–2605.
- (178) Stephenson, G. A.; Forbes, R. A.; Reutzel-Edens, S. M. *Adv. Drug Deliv. Rev.* **2001**, *48*, 67–90.
- (179) Liu, J.; Nagapudi, K.; Kiang, Y.-H.; Martinez, E.; Jona, J. *Drug Dev. Ind. Pharm.* **2009**, *35*, 969–975.
- (180) Stueber, D.; Jehle, S. *J. Pharm. Sci.* **2017**, *106*, 1828–1838.
- (181) Lubach, J. W.; Xu, D.; Segmuller, B. E.; Munson, E. J. *J. Pharm. Sci.* **2007**, *96*, 777–787.
- (182) Salager, E.; Day, G. M.; Stein, R. S.; Pickard, C. J.; Elena, B.; Emsley, L. *J. Am. Chem. Soc.* **2010**, *132*, 2564–2566.
- (183) Day, G. M. *Crystallogr. Rev.* **2011**, *17*, 3–52.
- (184) Pickard, C. J.; Needs, R. J. *J. Phys. Condens. Matter* **2011**, *23*, 53201.
- (185) Zilka, M.; Dudenko, D. V.; Hughes, C. E.; Williams, P. A.; Sturniolo, S.; Franks, W. T.; Pickard, C. J.; Yates, J. R.; Harris, K. D. M.; Brown, S. P. *Phys. Chem. Chem. Phys.* **2017**, *19*, 25949–25960.
- (186) Martineau, C.; Senker, J.; Taulelle, F. In *Annual Reports on NMR Spectroscopy*; **2014**; Vol. 82, pp 1–57.
- (187) Harris, R. K. *Solid State Sci.* **2004**, *6*, 1025–1037.
- (188) Widdifield, C. M.; Robson, H.; Hodgkinson, P. *Chem. Commun.* **2016**, *52*, 6685–6688.
- (189) Harper, J. K.; Iuliucci, R. J.; Gruber, M.; Kalakewich, K. *CrystEngComm* **2013**, *15*, 8693–8704.
- (190) Hofstetter, A.; Emsley, L. *J. Am. Chem. Soc.* **2017**, *139*, 2573–2576.
- (191) Namespetra, A. M.; Hirsh, D. A.; Hildebrand, M. P.; Sandre, A. R.; Hamaed, H.;

- Rawson, J. M.; Schurko, R. W. *CrystEngComm* **2016**, *18*, 6213–6232.
- (192) Hamaed, H.; Pawlowski, J. M.; Cooper, B. F. T.; Fu, R.; Eichhorn, S. H.; Schurko, R. W. *J. Am. Chem. Soc.* **2008**, *130*, 11056–11065.
- (193) Hildebrand, M.; Hamaed, H.; Namespetra, A. M.; Donohue, J. M.; Fu, R.; Hung, I.; Gan, Z.; Schurko, R. W. *CrystEngComm* **2014**, *16*, 7334.
- (194) Vogt, F. G.; Williams, G. R.; Strohmeier, M.; Johnson, M. N.; Copley, R. C. B. *J. Phys. Chem. B* **2014**, *118*, 10266–10284.
- (195) Paulekuhn, G. S.; Dressman, J. B.; Saal, C. *J. Med. Chem.* **2007**, *50*, 6665–6672.
- (196) Bryce, D. L.; Sward, G. D. *Magn. Reson. Chem.* **2006**, *44*, 409–450.
- (197) Bryce, D. L.; Sward, G. D. *J. Phys. Chem. B* **2006**, *110*, 26461–26470.
- (198) Chapman, R. P.; Widdifield, C. M.; Bryce, D. L. *Prog. Nucl. Magn. Reson. Spectrosc.* **2009**, *55*, 215–237.
- (199) Johnston, K. E.; O’Keefe, C. A.; Gauvin, R. M.; Trébosc, J.; Delevoye, L.; Amoureux, J.-P.; Popoff, N.; Taoufik, M.; Oudatchin, K.; Schurko, R. W. *Chem. Eur. J.* **2013**, *19*, 12396–12414.
- (200) O’Keefe, C. A.; Johnston, K. E.; Sutter, K.; Autschbach, J.; Delevoye, L.; Popo, N.; Taou, M.; Oudatchin, K.; Schurko, R. W. *Inorg. Chem.* **2014**, *53*, 9581–9597.

Chapter 2: The Local Structure of Rare-Earth Fluorides in Bulk and Core/Shell Nanocrystalline Materials

2.1 Introduction

Rare-earth (RE) inorganic nanocrystals (NCs) containing lanthanide(III)-dopants have desirable optical properties that make them ideal for use in solar cells,^{1,2} zero-threshold lasers,³ and fluorescent biolabels.⁴⁻⁸ Given the diversity and importance of their potential applications, these materials have been the subject of a variety of studies, several of which have been cited hundreds of times in the past decade.⁹⁻¹² Radiative emissions from RE NCs result from parity forbidden $f-f$ transitions, which have low absorption coefficients and long luminescence lifetimes (*i.e.*, slow emission rates).¹³ Lanthanide dopants are of particular interest due to their unique ability to down-shift, downconvert and upconvert light. The downshifting of light is a process in which a lower-energy photon is emitted for each single higher-energy photon that has been absorbed. Downconversion and upconversion are nonlinear processes in which a material absorbs higher energy light to yield two or more lower-energy photons, or absorbs two or more low-energy photons to yield one photon of higher energy, respectively. There is currently an emphasis on the design of optically-active upconverting NCs, which are the focus of this study, and discussed in more detail below.

One of the most efficient means of upconversion begins when a sensitizer (RE^{3+}) is excited by low energy radiation (*e.g.*, in the NIR range). This excited sensitizer then transfers energy to a proximate activator (Ln^{3+} dopant) via a non-radiative energy transfer. After a second excited sensitizer transfers energy to the excited activator, the activator can return to the ground state, emitting a higher energy photon (*e.g.*, visible

light).^{14,15} The wavelength of the emitted light can be controlled by changing the dopant and different Ln³⁺ ions can produce upconverting particles that emit throughout the visible (*e.g.*, Eu³⁺, Pr³⁺, Sm³⁺, Tb³⁺, and Er³⁺) and NIR (*e.g.*, Nd³⁺ and Yb³⁺) ranges.¹³ The study of upconverting materials has focused on improving synthetic procedures to make nanostructures with the highest possible quantum yields (QYs).^{16,17}

Ln³⁺-doped NCs of controlled size are routinely synthesized in high-boiling solvents using oleic acid and octadecene as coordinating and non-coordinating solvents, respectively.^{18–22} Oleate ligands coordinate on the surface of the NC to help to prevent aggregation, as well as increase the NC dispersibility in different organic environments.²³ However, the high energy vibrations of these surface ligands, along with imperfections in the particle and its surface, can quench the luminescence process and decrease the QY.

One promising solution to these problems is the creation of core/shell (C/S) NCs, which are formed by the epitaxial growth of one RE-NC around another. In such structures, the shell separates the optically-active core from the surface ligands and solvent environment, thus protecting the upconversion process from quenching.^{4,23–25} The added thickness of the shell can also be used to tailor the overall particle size for use in size-dependent applications like metal-enhanced luminescence and photoswitches.^{26–28} Despite these considerable synthetic efforts, the QYs of bulk materials are still much greater than that of their NC counterparts. As this optical property depends on the local inorganic structure and positioning of the dopant ions, there may be fundamental structural differences between the structures of the bulk materials and NCs. Such discrepancies are to be expected given the vastly different synthetic conditions under which the bulk materials (annealed at high temperature) and NCs (synthesized at much

lower temperature) are made. Clearly, characterization of the bulk and NC materials on a molecular-level is vital to improve their rational design and preparation, and to fine-tune their optical properties.

NCs, and their associated bulk (*i.e.*, microcrystalline) phases, are commonly characterized using electron microscopy (to describe the particle size and morphology) and UV-Vis spectroscopy (to compare optical properties). Powder X-ray diffraction (PXRD) can also be used to analyze crystalline samples (to determine the space group and unit cell parameters). Unfortunately, in many cases, NCs with interesting bulk observable properties are not further characterized in terms of their molecular-level structures.

Solid-state nuclear magnetic resonance (SSNMR) is a valuable, yet often overlooked, characterization technique that is capable of providing information on local structure and dynamics in NCs. As such, SSNMR spectra can act as exquisite probes of the cores and surfaces within the NC, revealing critical information about NC composition, short- and long-range order, and interactions at interfaces (*e.g.*, core/shell, surface/ligand).²⁹⁻³¹

One of the most common hosts for Ln³⁺-dopants is NaYF₄. Bulk NaYF₄ crystallizes in two distinct phases. The cubic form, α -NaYF₄, has been well characterized using TEM, PXRD, and SSNMR.³²⁻³⁴ Despite many attempts to study the hexagonal phase, β -NaYF₄, over the past 50 years, there is still a significant debate regarding its structure. Three crystal structures of β -NaYF₄ have been proposed, each having a different space group. Sobolev *et al.*,³⁵ and later Krämer *et al.*,³⁶ proposed structures that are analogous to the mineral gargarinite, which has a P6₃/m space group. Later, Burns *et*

*al.*³⁷ identified a $P\bar{6}$ structure. Roy and Roy³² suggested a third structure with the $P\bar{6}2m$ space group; this structure was later posited by Grzechnik *et al.*³⁸ for β -NaYF₄ under high-pressure conditions. Unfortunately, the experimental PXRD diffraction pattern of bulk NaYF₄ matches the simulated diffraction patterns of all three proposed structures (see **Figure A1**), and all of these structures continue to be cited for this compound.^{39–43} A recent computational study of β -NaYF₄ using Carr-Parrinello molecular dynamics⁴⁴ concluded that the models built using the $P\bar{6}$ and $P\bar{6}2m$ space groups are the same, and that this structure is better described by $P\bar{6}2m$. As such, we will refer to these two proposed structures collectively as Structure **I**. The $P6_3/m$ model is distinct from Structure **I**, and will be denoted as Structure **II**.

Structures **I** and **II** have the same F positions, but these structures differ in the location, coordination, and fractional occupancy of the heavier Na⁺ and Y³⁺ ions. Structure **I** contains only 9-coordinate sites: one is solely occupied by Y, while the other is fractionally occupied by Na and Y (in a 3:1 ratio). Structure **II** has one 6-coordinate Na site and one 9-coordinate site occupied by either Na or Y (with slightly more than 50% Na occupancy). Further structural details (lattice parameters, site occupancies etc.) are summarized in **Appendix A** (see **Table A1** and **Table A2**).

Luminescent NaYF₄ NCs have been crystalized in both the α - and β -phases.^{45–47} The latter structure is desirable because it has a much higher upconversion quantum yield (UC-QY) than the α -form.³⁶ In fact, the presence of α -phase impurities can severely limit the QY of a NC sample;⁴⁸ therefore, proper identification of the synthesized phase is imperative. Since the syntheses of the bulk and NC materials are unrelated (*i.e.*, the NCs described in this study are not made directly from the bulk compounds, see Experimental

section), *a priori* knowledge of the NC structure is unavailable, and the final product must be characterized.

With the two possible structures (**I** and **II**) in mind, we present a comprehensive characterization of bulk β -NaYF₄, which leads us to propose an unambiguous crystal structure for this material when prepared by the methods described herein. By comparing the NMR parameters and XRD powder patterns of the bulk materials, we obtain structural information on β -NaLuF₄, as well as the structural phase present in the NaYF₄/NaLuF₄ core/shell NCs. Our NMR results also demonstrate the presence of surface ligands attached to the NCs, and reveal the distinct nuclear environments near the surface of the particles.

2.2 Methods

2.2.1 Chemicals

Yttrium(III) acetate hydrate (99.9%), lutetium(III) oxide (99.9%), yttrium(III) oxide (99.9%), sodium trifluoroacetate (98%), ammonium fluoride (99.99+%), technical grade oleic acid (90%), technical grade 1-octadecene (90%), and hexanes were purchased from Sigma-Aldrich. Oleylamine (97%) from Acros, anhydrous ethanol from commercial Alcohols and methanol from Caledon were used. All chemicals were used as received.

2.2.2 Synthesis of sacrificial nanocrystals (SNCs)

Cubic NaREF₄ SNCs were synthesized based on a previously reported procedure with slight modifications.¹² In a typical synthesis, Lu₂O₃ (1 mmol) was mixed with 25 mL of 50 % aqueous trifluoroacetic acid and refluxed at 90 °C overnight or until a clear solution was obtained. The trifluoroacetate precursor, Lu(CF₃COO)₃, was obtained after removing excess trifluoroacetic acid and water by evaporation at 65 °C. Sodium

trifluoroacetate (2 mmol) was added to the precursor along with oleic acid (6 mL), oleylamine (6 mL), and 1-octadecene (12 mL) and heated to 120 °C under vacuum for 45 min to remove residual water and oxygen. The obtained transparent solution was subsequently heated to 290-295 °C (~20 °C/min) under argon and vigorously stirred until the reaction mixture turned turbid. Once turbid, the reaction was left for another 5 min and then cooled to room temperature. The NCs were precipitated by adding ethanol (25 mL), collected by centrifugation (1800 g), washed with ethanol (30 mL), centrifuged again (1800 g), and finally dispersed in hexane (10 mL). For the shell growth, calculated amount of SNCs were injected. Before injection, the synthesized SNCs dispersed in hexane were taken and a measured volume of the dispersion (200 µl) was transferred to a pre-weighed vial and hexane was removed by bubbling with argon. The SNCs in the vial were dried overnight at 70 °C under vacuum, and the vial was then weighed to determine the total organic and inorganic content (ligand + SNCs). The percentage of organic ligands was then determined by Thermogravimetric Analysis (TGA) under air and subtracted to obtain the total inorganic content in a given volume and the crystal yield. The SNCs were then aliquoted into vials such that each contained 0.5 mmol of inorganic content.

2.2.3 Synthesis of core-shell nanocrystals

The synthesis of core NCs was adapted from a reported procedure, with slight modifications.⁴⁹ The NaLuF₄ shell was chosen because it can be grown epitaxially and conformally, thereby allowing for the fine tuning of distances between the Ln³⁺-doped core and the outer shell. Y(CH₃CO₂)₃·xH₂O (1.0 mmol) was added to a 100 mL flask containing oleic acid (6 mL) and 1-octadecene (15 mL) and heated to 125 °C under

vacuum for 45 min and cooled to room temperature. To this solution at room temperature, a methanol solution (10 mL) of ammonium fluoride (4 mmol) and sodium hydroxide (2.5 mmol) was added dropwise and stirred for 30 min. The reaction mixture was then heated to 70 °C to remove methanol and subsequently heated to 300 °C (~10 °C/min) under argon and maintained for 60 min to obtain the core NCs. The synthesis of epitaxial shell on the core NCs was adapted from a previously reported procedure based on self-focusing by Ostwald ripening.^{50,51} After 60 min at 300 °C when the core NCs have formed, about 1 mL of the reaction mixture was retrieved (core) and immediately a calculated amount (0.5 mmol) of sacrificial NCs (SNCs) (α -NaLuF₄) in 1 mL octadecene was injected (for injection, the aliquoted 0.5 mmol of hexane dispersion of SNCs was taken and mixed with 1 mL of octadecene followed by bubbling argon to remove the hexanes) and ripened for 10 min, followed by two more SNC injections (0.5 mmol each) and ripening cycle of 10 min each to yield core-shell NCs. After the third injection and ripening cycle (total SNCs deposited 1.5 mmol) the reaction mixture was then cooled down to room temperature and the core-shell NCs were precipitated by adding ethanol (20 mL), collected by centrifugation (1800 g), washed with ethanol (30 mL), and centrifuged again (1800 g) before being dispersed in hexane (10 mL). Extensive characterization of the core/shell nature of these particles via techniques including TEM and high-angle annular dark-field microscopy has previously been reported.^{50,51}

2.2.4 Synthesis of bulk NaYF₄ and NaLuF₄ powders

Bulk powders were synthesized based on a previously reported procedure.¹⁶ In a typical synthesis, Lu₂O₃ or Y₂O₃ (1 mmol) was mixed with 25 mL of 50 % aqueous trifluoroacetic acid and refluxed at 90 °C overnight or until a clear solution was obtained.

The trifluoroacetate precursor ($\text{Lu}(\text{CF}_3\text{COO})_3$) or ($\text{Y}(\text{CF}_3\text{COO})_3$) was obtained after removing excess trifluoroacetic acid and water by evaporation at 65 °C. Sodium trifluoroacetate (2 mmol) was added to the trifluoroacetate precursor and the powders were ground together and dried in an oven overnight at 110 °C. The dried powder was then taken in a crucible and heated to 400 °C at the rate of 10 °C/min under air in a tube furnace and maintained at this temperature for 4 h and cooled to room temperature. The final bulk powder was then ground to a fine powder with a mortar and pestle.

2.2.5 Transmission Electron Microscopy

Transmission electron microscopy (TEM) images were obtained from a JEOL JEM-1400 microscope operating at 80 kV. Hexane dispersions of the NCs were drop cast on a formvar carbon-coated grid (300 mesh Cu) and air-dried before imaging.

2.2.6 Powder X-ray Diffraction

Powder X-ray diffraction (PXRD) patterns with a resolution of 0.05° (2 θ) and a scan speed of 1°/min, were collected using a Rigaku Miniflex diffractometer with a Cr source ($K\alpha$ radiation, $\lambda=2.2890$ Å) operating at 30 kV and 15 mA. Simulated diffraction patterns were obtained using the CrystalDiffract software package.

2.2.7 Solid-State NMR

Solid-state NMR spectra were collected on a Varian Infinity Plus NMR spectrometer with an Oxford 9.4 T wide-bore magnet ($\nu_0(^1\text{H}) = 399.73$ MHz, $\nu_0(^{23}\text{Na}) = 105.73$ MHz, $\nu_0(^{89}\text{Y}) = 19.69$ MHz, $\nu_0(^{19}\text{F}) = 376.73$ MHz, and $\nu_0(^{13}\text{C}) = 100.52$ MHz). All ^1H , ^{23}Na , and ^{13}C experiments were conducted on a Varian/Chemagnetics 4 mm HX probe. All ^{89}Y experiments were conducted using a Varian/Chemagnetics 4 mm HXY probe with a Chemagnetics low- γ tuning box and preamplifier on the X channel. ^{19}F

magic-angle spinning (MAS) experiments ($\nu_{\text{rot}} = 25$ kHz) were performed using a Varian/Chemagnetics 2.5 mm HX probe. Ultra-fast MAS (UFMAS) ($\nu_{\text{rot}} = 65$ kHz) ^{19}F experiments were conducted on a Bruker Avance III console equipped with a 11.7 T narrow-bore magnet ($\nu_0(^1\text{H}) = 500.13$ MHz, $\nu_0(^{19}\text{F}) = 470.59$ MHz) and a Bruker 1.3 mm HX probe. All samples were packed into 1.3 mm, 2.5 mm, or 4 mm o.d. zirconia rotors.

^{23}Na chemical shifts were referenced with respect to a 1.0 M NaCl (aq) solution ($\delta_{\text{iso}} = 0.0$ ppm). ^{89}Y chemical shifts were referenced to a 1.0 M YCl_3 (aq) solution ($\delta_{\text{iso}} = 0.0$ ppm) using $\text{Y}(\text{NO}_3)_3 \cdot 6\text{H}_2\text{O}$ ($\delta_{\text{iso}} = -53$ ppm) as a secondary reference.⁵² ^{19}F chemical shifts were referenced with respect to neat CFCl_3 (l) ($\delta_{\text{iso}} = 0.0$ ppm) using neat fluorobenzene (l) ($\text{C}_6\text{H}_5\text{F}$, $\delta_{\text{iso}} = -113.15$ ppm) as a secondary reference. ^1H and ^{13}C chemical shifts were referenced to tetramethylsilane (TMS, $\delta_{\text{iso}} = 0.0$ ppm) using adamantane ($\delta_{\text{iso}} = 1.85$ ppm and 38.57 ppm, respectively) as a secondary reference.

For complete details of the experimental parameters used for the NMR experiments, see **Table A3-Table A9**. Direct-excitation ^{23}Na MAS spectra ($\nu_{\text{rot}} = 12$ kHz) were acquired using a rotor-synchronized Hahn echo with two-pulse phase-modulation (TPPM) ^{19}F decoupling.⁵³ These experiments used a $1.25 \mu\text{s}$ ^{23}Na $\pi/2$ pulse that was selective for the central transition ($+1/2 \leftrightarrow -1/2$) of the ^{23}Na nuclei. Two-dimensional triple-quantum MAS (MQMAS) ^{23}Na spectra were acquired using a phase-modulated split- t_1 pulse sequence.⁵⁴ ^{19}F MAS and UFMAS NMR spectra ($\nu_{\text{rot}} = 25$ kHz and 64 kHz, respectively) were acquired using a rotor-synchronized Hahn echo pulse sequence, of the form $(\pi/2)_x - \tau_1 - (\pi)_y - \tau_2 - \text{acq}$. ^1H MAS NMR experiments ($\nu_{\text{rot}} = 11$ kHz) were conducted using a Bloch decay pulse sequence. ^{19}F - ^{89}Y , ^{19}F - ^{23}Na , ^1H - ^{13}C , and ^1H - ^{23}Na cross-polarization (CP)^{55,56} experiments were conducted using the variable-

amplitude CP (VACP) pulse sequence^{57,58} with TPPM decoupling. For CP experiments involving ²³Na, low power Hartmann-Hahn matching fields (*ca.* 30 kHz and 20 kHz for the ¹⁹F/¹H and ²³Na channels, respectively) were used to ensure efficient CP transfer to sites with a larger quadrupolar interaction. See text for details. Additional ¹H-²³Na and ¹⁹F-²³Na CP/MAS experiments using a high spin-locking power were conducted using *ca.* 55 kHz and 80 kHz matching fields for the ¹⁹F/¹H and ²³Na channels, respectively.

Simulations of all static solid-state NMR spectra were performed using the WSOLIDS software package.⁵⁹ In all cases, uncertainties in the extracted NMR tensor parameters were estimated using bidirectional variation of each parameter. Processing of 1D and 2D spectra was performed using the NUTS software package from Acorn NMR and GSIM software package, respectively. Line fitting and integration of spectra was performed using the Origin Lab Pro version 9.0 software package.

2.3 Results and Discussion

2.3.1 Transmission Electron Microscopy

The synthesis of the NC samples was based on a previously reported protocol from the van Veggel group, with full details given in the experimental section.^{51,60} Two samples of core/shell NaYF₄/NaLuF₄ NCs of different diameters were produced, as confirmed by transmission electron microscopy (TEM; 27±1 nm and 37±1 nm, respectively, see **Figure 2.1**). The TEM also confirms that the NCs are highly monodisperse.

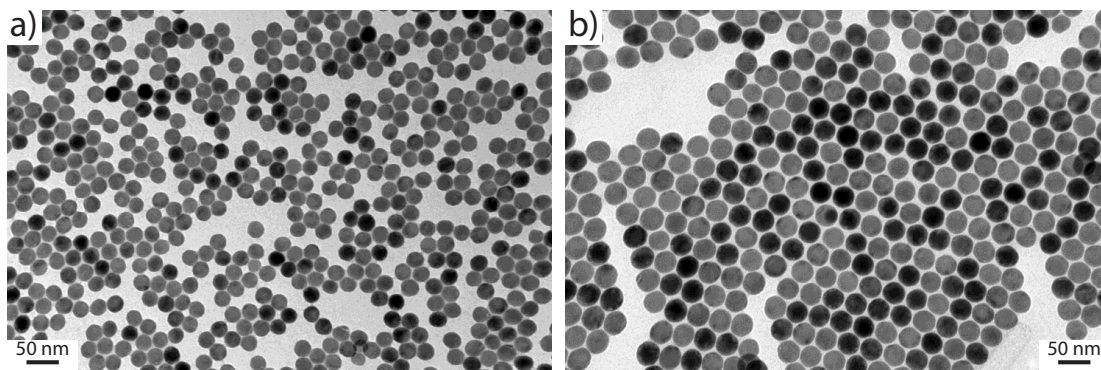


Figure 2.1. TEM images of the a) 27 nm NC b) 37 nm NC samples used to measure the particle sizes.

2.3.2 Powder X-ray Diffraction

The experimental powder X-ray diffraction (PXRD) patterns of the two bulk compounds (**Figure 2.2**) are consistent with the reference patterns of hexagonal NaYF_4 and NaLuF_4 , respectively.^{35,61} Based on the FWHM values obtained from fitting Gaussian profiles to the PXRD patterns with the Jade software package version 8, the grain (*i.e.*, crystallite) sizes are 96 and 130 nm for NaYF_4 and NaLuF_4 , respectively. We believe that these samples are representative of the bulk materials, as they were produced using the same synthetic method as what was reported in a previous paper by Boyer and van Veggel.¹⁶ This prior work focussed on the very low UC-QY of Er,Yb-doped NaYF_4 NCs, as compared to bulk materials. As a reference datum, it also contains the reproduction of the highest reported UC-QY for bulk Er,Yb-doped NaYF_4 upon excitation at 980 nm, as a way to verify our methods.

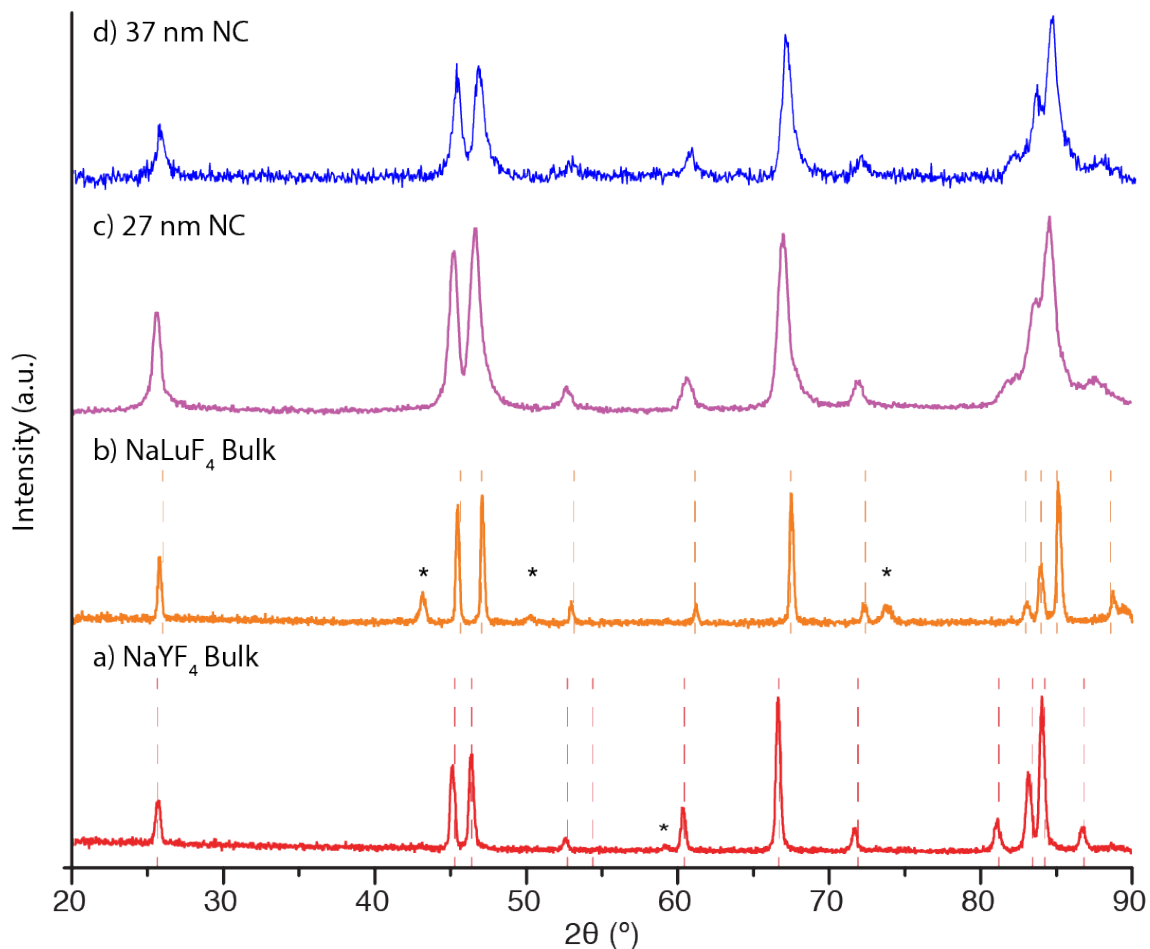


Figure 2.2. PXRD diffraction patterns of a) bulk NaYF₄, b) bulk NaLuF₄, c) 27 nm NC, and d) 37 nm NC. The red and orange dashed lines indicate features in the JCPDS reference patterns of hexagonal phase β-NaYF₄ (JCPDS: 16-0334) and β-NaLuF₄ (JCPDS: 27-0726), respectively. Asterisks denote impurities, see text for details.

The XRD pattern of NaYF₄ (**Figure 2.2a**) has an additional reflection at $2\theta = 59^\circ$, which corresponds to a small NaF impurity, (**Figure A2d**),⁶² whereas that of NaLuF₄ indicates that this sample contains some α-NaLuF₄ (**Figure A2b**). The diffraction pattern of the 27 nm NC sample (**Figure 2.2c**) is similar to the bulk compounds in that it has the same reflections and intensities; however, the peaks are much broader than those in the patterns of the bulk samples. This broadening results from the small grain size of the NCs and so-called *surface effects*, which are commonly observed in the PXRD patterns of nano-sized particles. Environments in the center of a NC are representative of the bulk

sample; however, closer to the particle surface there is a distribution of environments. Notably, the atoms that are closest to the NC surface exist in environments that are distinct from those in the center. Since NCs have higher surface area/volume ratios in comparison to microcrystals of the bulk material, these surface sites can constitute a large portion of the total sample; hence, the noticeably broader linewidths in the NC patterns are indicative of a distribution of slightly different atomic environments. For the three cases presented in **Figure 2.2**, the similarities between the PXRD patterns of the bulk and NC samples suggest that the NCs contain two distinct phases with similar structures to their corresponding bulk counterparts; however, these patterns do not provide a definitive picture of the NC structure on a sub-nanometer scale, as PXRD provides information on the long-range order of the structure/compound. Thus, we have used SSNMR to further characterize these samples.

2.3.3 ^{23}Na MAS NMR

The $^{23}\text{Na}\{^{19}\text{F}\}$ MAS ($\nu_{\text{rot}} = 12$ kHz) spectra of the four samples are pictured in **Figure 2.3**. We begin our discussion with the spectrum of NaYF_4 (**Figure 2.3a**), which has three distinct powder patterns: the first two are narrow and centered at 7.2(2) ppm and $-10.8(2)$ ppm, respectively, and the last is a broad pattern typical of a second order quadrupolar (SOQI) pattern, which has been partially averaged by MAS. The high frequency (leftmost) peak results from a NaF impurity, as discussed above. The sharp feature at $-10.8(2)$ ppm indicates a ^{23}Na environment of high spherical symmetry, which can be assigned to the nine-coordinate site in either of the proposed NaYF_4 crystal structures. The final pattern is broader, and simulations yield a quadrupolar coupling constant of $C_Q = 3.5(5)$ MHz, an asymmetry parameter of $\eta_Q = 0.15(5)$, and an isotropic

shift of $\delta_{\text{iso}} = -12(2)$ ppm (the spectral simulation is shown in **Figure A3**, definitions of quadrupolar and chemical shift parameters are given in **Table 2.1**).

Table 2.1. Experimental ^{23}Na EFG Tensor Parameters corresponding to Site 2.^a

Sample	C_Q^b (MHz)	η_Q^c	δ_{iso} (ppm)
NaYF ₄	3.5(5)	0.15(5)	-12(2)
NaLuF ₄	3.5(5)	0.15(5)	-10(2)
27 nm NC	3.5(5)	0.15(5)	-12(2)
	3.5(5)	0.15(5)	-10(2)
37 nm NC	3.5(5)	0.15(5)	-12(2)
	3.5(5)	0.15(5)	-10(2)

^aThe narrow feature corresponding to Site 1 can be simulated with a C_Q of < 1 MHz. The EFG tensor is described by three principal components ordered such that $|V_{11}| \leq |V_{22}| \leq |V_{33}|$ ^b $C_Q = eQV_{33}/h$.

^c $\eta_Q = (V_{11} - V_{22})/V_{33}$.

This pattern corresponds to a Na nucleus in a lower symmetry site, such as the six-coordinate position identified in crystal structure **II**. Furthermore, the intensity ratio of these two peaks, roughly 1:1, agrees with the 1:1 ratio predicted by structure **II** (note, the integrated areas underneath these patterns can be regarded as quantitative, since recycle delays were calibrated to allow for the recovery of maximum signal). The presence of a lower symmetry Na site in the SSNMR spectra is inconsistent with structure **I**, which has only higher spherical symmetry, nine-coordinate Na sites. The ^{23}Na spectrum of NaLuF₄ (**Figure 2.3b**) is similar to that of NaYF₄, and can be assigned in a similar fashion (a peak at *ca.* 7.2(2) ppm corresponding to the NaF impurity, a sharp feature at -8.0(2) ppm, and a broad pattern at -10(2) ppm). The NaLuF₄ chemical shifts are 2 ppm greater than the NaYF₄ sample (*i.e.*, the ^{23}Na nuclei in NaLuF₄ are deshielded slightly). For both samples, we denote the assignments of the nine-coordinate and six-coordinate Na sites as 1 and 2, respectively.

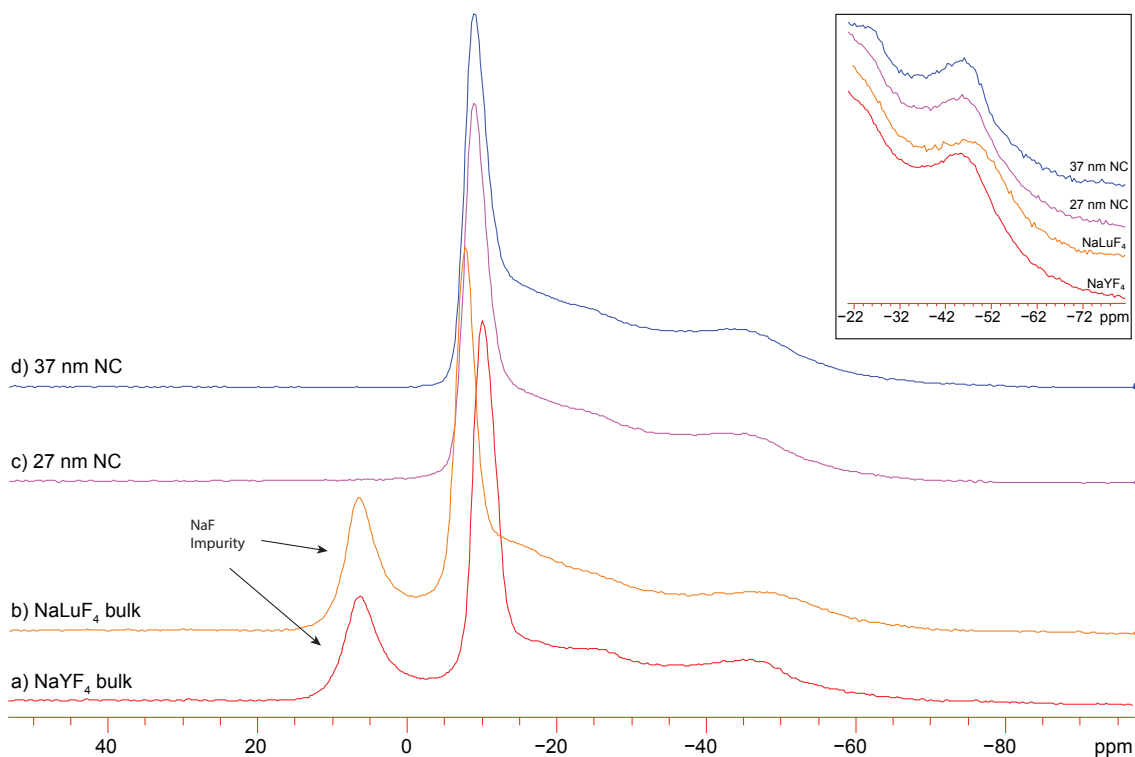


Figure 2.3. $^{23}\text{Na}\{^{19}\text{F}\}$ MAS NMR spectra of a) bulk NaYF_4 , b) bulk NaLuF_4 , c) 27 nm NC, and d) 37 nm NC ($\nu_{\text{rot}}=12$ kHz). The inset shows the low frequency regions of the spectra.

The spectra of the two NCs (**Figure 2.3c** and **Figure 2.3d**) are similar not only to each other, but also to the spectra of the bulk samples. The narrow resonance (at *ca.* -9 ppm, $\Delta\nu_{1/2} = 440(50)$ Hz) is broader than those in the spectra of the bulk samples ($\Delta\nu_{1/2} = 250(50)$ Hz), and likely arises from a distribution of chemical shifts that encompasses the frequency ranges observed in the spectra of the bulk NaYF_4 and NaLuF_4 samples (the quadrupolar interaction for this site is small, and has a negligible effect on this pattern). The broad second-order pattern also appears to result from an overlap of the two patterns corresponding to NaYF_4 and NaLuF_4 phases, as well as some degree of broadening from a distribution of chemical shifts and/or quadrupolar interactions. The spectra of the NCs lack peaks at *ca.* 7.2 ppm, suggesting that these samples do not contain a significant amount of the NaF impurity. This analysis is consistent with the PXRD spectra, and also

consistent with the distinct preparation of these NCs, which do not commence with bulk NaYF₄ and NaLuF₄ as the starting materials.

Though the PXRD data (**Figure 2.2b**) indicate the presence of the cubic, α -NaLuF₄ phase, we do not see evidence for it in the ²³Na SSNMR data. The lack of distinct α -NaLuF₄ peaks could be due to overlapping patterns for the hexagonal and cubic forms, the former of which is in much greater abundance. While ²³Na SSNMR spectra have not been measured for α -NaLuF₄, the broad chemical shift range of the β -NaYF₄ spectrum (*ca.* -5 to -70 ppm) spans a region that includes the shifts of α -NaYF₄ measured by Arnold *et al.* (*ca.* -10 to -40 ppm).³⁴ Therefore, distinguishing between the α - and β - forms of NaLuF₄ using ²³Na SSNMR may not be possible.

2.3.4 ²³Na MQMAS NMR

To ensure that the one-dimensional patterns pictured in **Figure 2.3** are assigned correctly, ²³Na MQMAS NMR experiments were conducted on all of the samples. The ²³Na MQMAS spectrum of bulk NaYF₄ is shown in **Figure 2.4**, with the direct and indirect dimensions displayed on the horizontal and vertical axes, respectively. The narrow Site 1 resonance and its spinning sidebands (denoted by asterisks) are clearly separated from the much broader Site 2 pattern. The spectrum projected on the indirect axis indicates two unique chemical shifts of -10.0(2) and -12.4(2) ppm, which are close to the values obtained from the corresponding one-dimensional spectrum. The projection on the direct axis is also consistent with the spectrum observed using one-dimensional MAS NMR techniques. The spinning sidebands associated with Site 1 may arise from a small sodium chemical shift anisotropy. Other ²³Na MQMAS NMR spectra are presented in the **Appendix A (Figures A4-A6)**. The peak corresponding to Site 1 in the MQMAS

spectrum of NaLuF₄ (**Figure A4**) is broader than the corresponding peak in the spectrum of NaYF₄ in both the direct and indirect dimensions. This added breadth might result from the presence of the α -NaLuF₄ phase. While all of the MQMAS spectra contain distinct patterns associated with the nine- and six-coordinate Na environments, respectively, the patterns corresponding to features from the core and shell are not resolved in the spectra of the NCs (**Figures A5 and A6**).

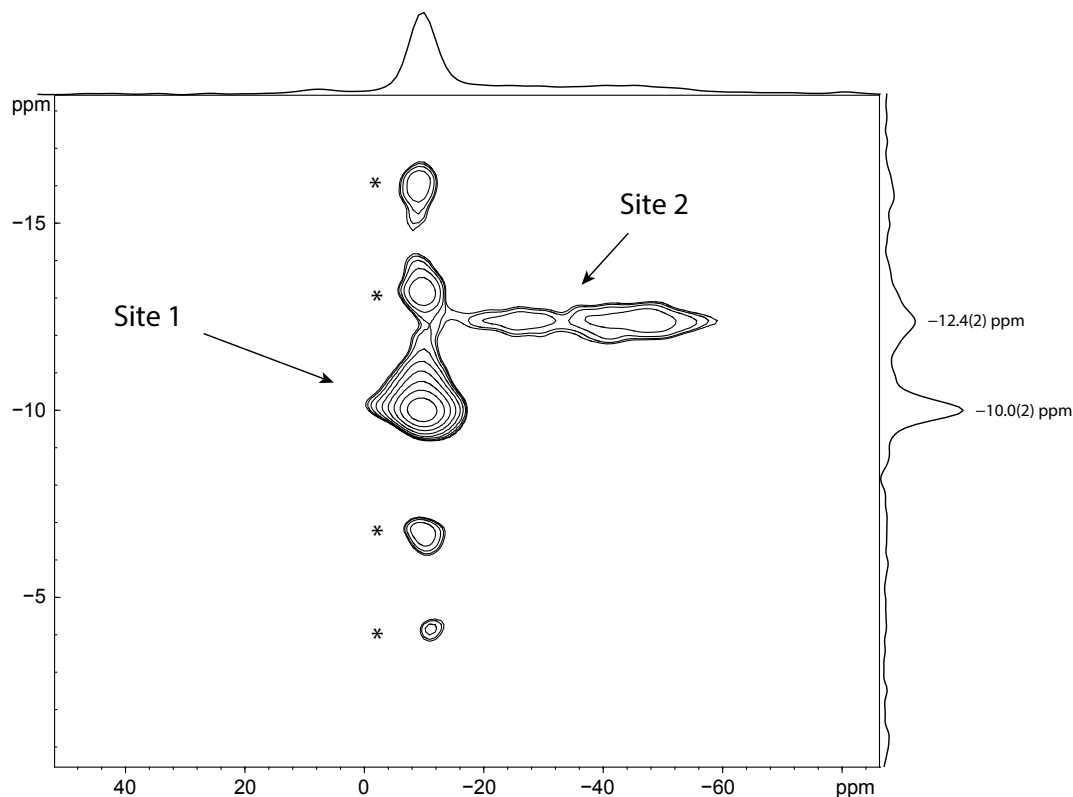


Figure 2.4. ²³Na MQMAS NMR spectrum of bulk NaYF₄ ($\nu_{\text{rot}} = 12$ kHz). The two ²³Na powder patterns indicate the presence of two magnetically distinct Na sites. Asterisks denote spinning sidebands from Site 1.

2.3.5 ¹⁹F-⁸⁹Y CP/MAS NMR

Despite the high natural abundance of the spin-1/2 ⁸⁹Y nucleus (100%), direct excitation (DE) ⁸⁹Y SSNMR experiments on inorganic samples are often hindered by a low gyromagnetic ratio (-1.3163×10^7 rad s⁻¹ T⁻¹) and very large longitudinal relaxation

time constants, $T_1(^{89}\text{Y})$. Preliminary tests on our bulk samples revealed that DE experiments are simply too inefficient, and such experiments were not pursued further. Cross polarization (CP) from proximate ^{19}F nuclei, however, affords shorter acquisition times due to the substantially shorter $T_1(^{19}\text{F})$ values, which allow for faster recycling and more scans, as well as the increased signal resulting from efficient CP.

We have used ^{19}F - ^{89}Y CP experiments to probe the Y environments in the bulk NaYF_4 and NC samples. The static ^{19}F - ^{89}Y CP spectra (**Figure 2.5**) of these three samples all feature rounded, Gaussian patterns with centers of gravity at $-75(1)$ ppm, and breadths ($\Delta\nu_{1/2}$) of *ca.* 4200 Hz. Under conditions of MAS at 6 kHz, the heteronuclear ^{19}F - ^{89}Y dipolar coupling is partially averaged, resulting in narrower linewidths (*ca.* 1500 Hz) in the ^{19}F - ^{89}Y CP/MAS spectra (**Figure 2.6**). Unfortunately, even at this low MAS rate, the CP efficiency is greatly reduced, resulting in CP/MAS spectra of very low S/N.

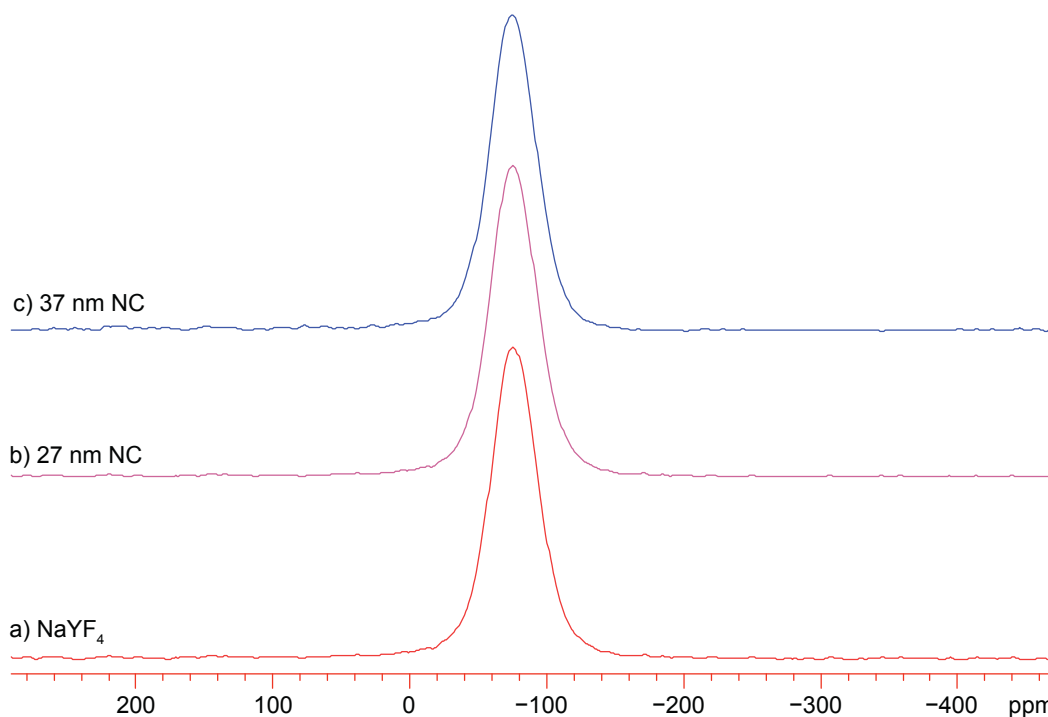


Figure 2.5. ^{19}F - ^{89}Y CP static NMR spectra of a) bulk NaYF_4 , b) 27 nm NC, and c) 37 nm NC.

Nonetheless, the ^{89}Y resonances are clearly observed, and the chemical shifts for all three samples are consistent with a 9-coordinate yttrium fluoride environment.⁶³ These spectra also confirm that only $\beta\text{-NaYF}_4$ is present in the bulk and NC samples, as $\alpha\text{-NaYF}_4$ has a distinct ^{89}Y isotropic chemical shift of -44 ppm,⁶³ which is not observed. The presence of only one center of gravity/isotropic peak per spectrum suggests that the structures of both the bulk NaYF_4 and the NC core (comprised solely of NaYF_4) have only one type of yttrium environment, as observed for structure **II**. Structure **I** has two crystallographically distinct yttrium sites, and is therefore inconsistent with our ^{89}Y NMR data.

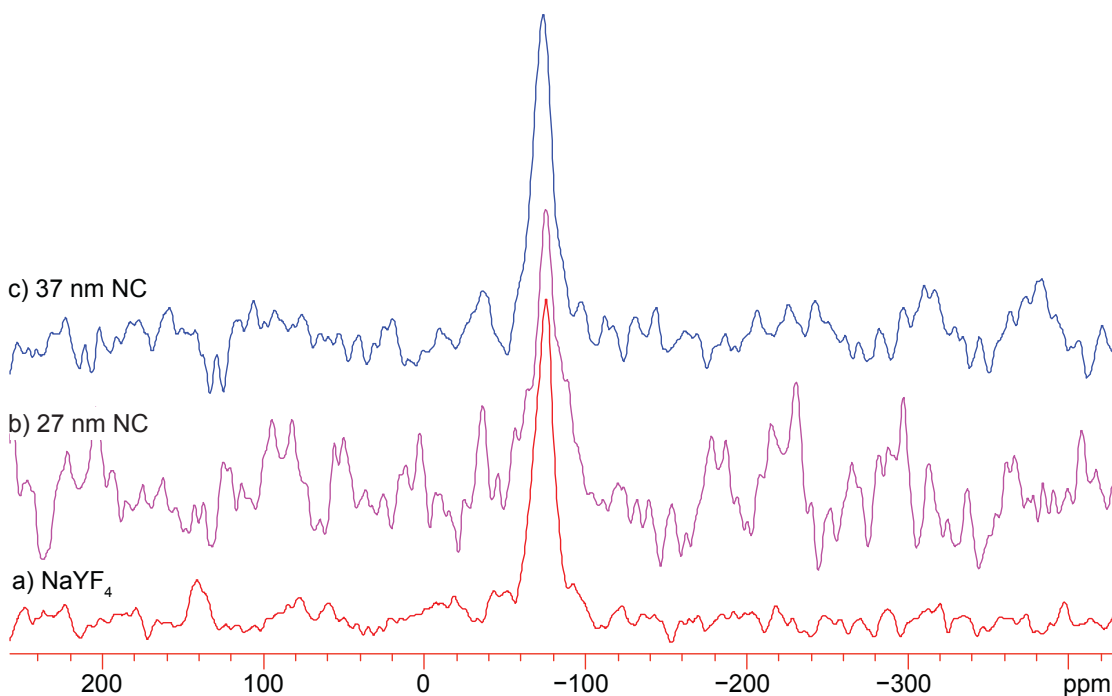


Figure 2.6. ^{19}F - ^{89}Y CP/MAS NMR spectra of a) bulk NaYF_4 , b) 27 nm NC, and c) 37 nm NC ($\nu_{\text{rot}} = 6$ kHz).

2.3.6 ^{19}F MAS NMR

The ^{19}F MAS ($\nu_{\text{rot}} = 25$ kHz) NMR spectra of the four samples are shown in **Figure 2.7**. The spectrum of NaYF_4 (**Figure 2.7a**) has a high intensity feature at $\delta_{\text{iso}} = -94(1)$ ppm with a shoulder centered at $\delta_{\text{iso}} = -85(1)$ ppm. A deconvolution of this

spectrum (**Figure A7**) reveals two peaks with breadths of approximately 4200(100) Hz each and an integrated intensity ratio of 2.6:1 (see **Table 2.2** for a full list of experimental NMR parameters). Clearly, these peaks result from two chemically similar, yet magnetically distinct, fluorine environments in NaYF₄. The spectrum of NaLuF₄ (**Figure 2.7b**) is similar to that of NaYF₄, but the positions of the two peaks are shifted by roughly 15 ppm to lower frequency (to the right) relative to those in the NaYF₄ spectrum, and the ratio of the peak intensities is 1.5:1. There is also a lower intensity feature at -227(1) ppm in the spectra of both bulk compounds, which we attribute to NaF.

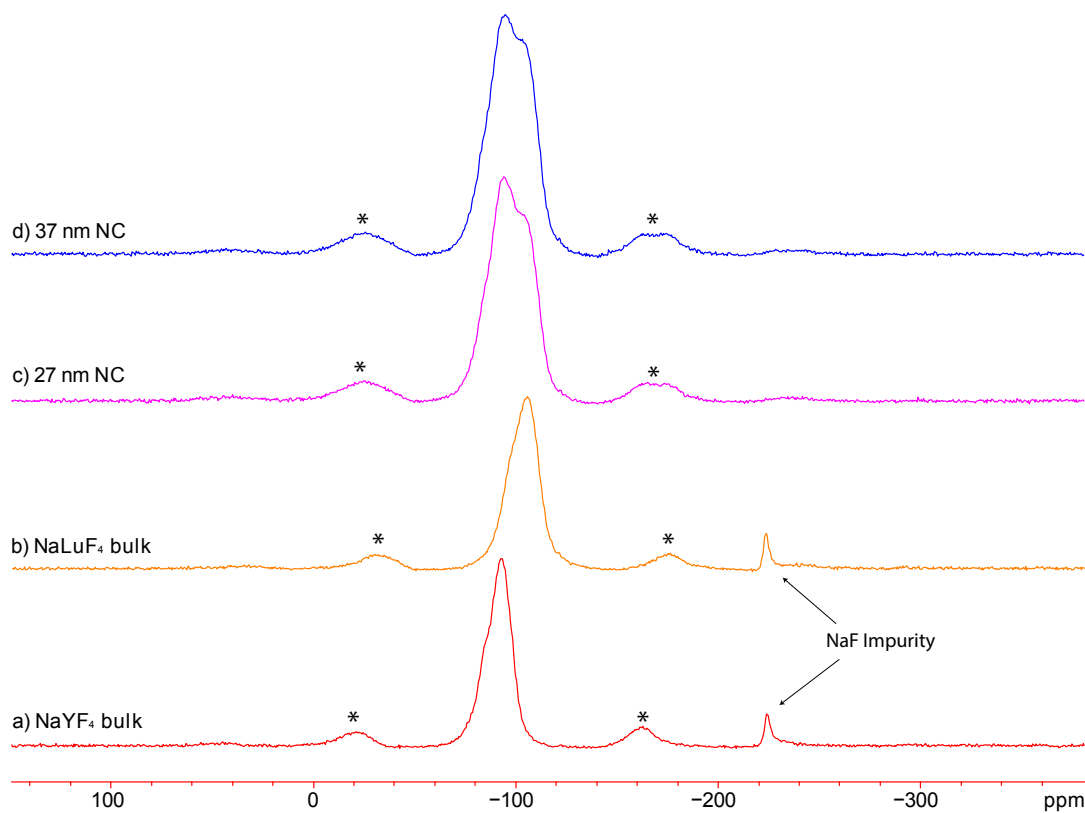


Figure 2.7. ¹⁹F MAS NMR spectra of a) bulk NaYF₄, b) bulk NaLuF₄, c) 27 nm NC, and d) 37 nm NC ($\nu_{\text{rot}} = 25$ kHz).

As previously discussed, our PXRD results suggest that the bulk NaLuF₄ sample contains a slight impurity of cubic phase α -NaLuF₄. Given that the chemical shift of α -NaYF₄ (-77 ppm)³⁴ is *ca.* 7 ppm greater than the features in our β -NaYF₄ spectrum, a

peak corresponding to α -NaLuF₄ should appear at a slightly higher shift than that of β -NaLuF₄, since these α - and β -NaLuF₄ phases are isostructural with those of NaYF₄. A low intensity α -NaLuF₄ peak could be obscured within the shoulder of the β -NaLuF₄ spectrum (at around -91 ppm in **Figure 2.7b**). Such a peak would explain the poor resolution of this shoulder, as well as the difference in peak intensity ratios between the NaLuF₄ (1.5:1) and NaYF₄ (2.6:1) spectra.

The chemical shift ranges observed in both of the ¹⁹F NMR spectra of the NCs (**Figure 2.7c** and **Figure 2.7d**) span the same ranges of shifts observed in the spectra of the bulk samples. As with the ²³Na spectra, the breadths of these patterns arise from a combination of overlapping peaks corresponding to the NaYF₄ and NaLuF₄ phases. Deconvolution of either NC spectrum reveals four peaks (**Figure A9** and **Figure A10**), each with a breadth of $\Delta\nu_{1/2} \approx 4000(100)$ Hz and shifts that are consistent with the peaks in the two bulk compounds (**Figure A7** and **Figure A8**). If the primary source of line broadening is strong homonuclear ¹⁹F-¹⁹F dipolar coupling, then SSNMR experiments featuring very fast spinning speeds might be useful in differentiating features in the spectra of the NCs.

2.3.7 ¹⁹F UFMAS NMR

¹⁹F ultra-fast (UF) MAS ($\nu_{\text{rot}} = 65$ kHz) NMR at $B_0 = 11.7$ T was used to improve the resolution in the spectra of the NCs. The ¹⁹F UFMAS NMR spectrum of the 27 nm NC is shown in **Figure 2.8**. At first sight, this spectrum appears to have three distinct peaks, which have centers of gravity of -85(1), -95(1), and -107(1) ppm, respectively. Deconvolution of this spectrum (**Figure A11**) reveals a fourth peak, at *ca.* -98(2) ppm (see **Table 2.3** for a full list of experimental NMR parameters).

Table 2.2. Summary of Experimental ^{19}F MAS NMR Parameters ($\nu_{\text{rot}} = 25$ kHz, $B_0 = 9.4$ T).

	NaYF ₄		NaLuF ₄		27 nm NC				37 nm NC			
δ_{iso} (ppm)	-85(1)	-94(1)	-93(1)	-107(1)	-85(1)	-92(2)	-98(2)	-107(1)	-84(1)	-93(2)	-99(2)	-107(1)
$\nu_{1/2}$ (Hz)	4200(100)	4100(100)	5300(200)	4600(100)	4800(400)	3500(800)	3700(800)	4200(200)	4800(400)	4000(800)	4000(1000)	4500(400)
Rel. Int.	1	2.6	1	1.5	1	1.5	1.3	1.8	1	1.8	1	2.1

Table 2.3. Summary of Experimental ^{19}F UFMAS NMR Parameters ($\nu_{\text{rot}} = 65$ kHz, $B_0 = 11.7$ T).

	27 nm NC			
δ_{iso} (ppm)	-85(1)	-95(1)	-98(2)	-107(1)
$\nu_{1/2}$ (Hz)	4700(200)	4700(400)	4700(400)	4500(200)
Rel. Int.	1	1.9	1.4	2.2

In comparison to the ^{19}F MAS spectrum acquired at $\nu_{\text{rot}} = 25$ kHz, the high frequency peak at -85 ppm is better resolved and the peaks at -95 and -107 ppm are more clearly separated.

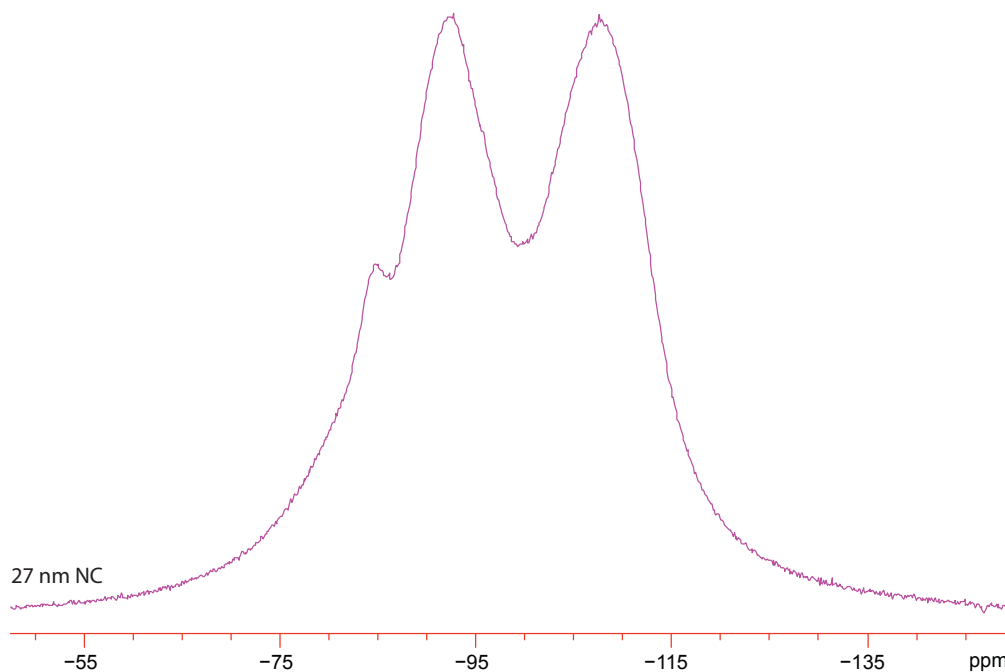


Figure 2.8. ^{19}F UFMAS NMR spectrum of the 27 nm NC ($\nu_{\text{rot}} = 65$ kHz, $B_0 = 11.7$ T).

The linewidths of the peaks in the UFMAS spectrum ($\Delta\nu_{1/2} \approx 4500$ Hz) are roughly the same as those in the 25 kHz MAS spectrum acquired at $B_0 = 9.4$ T. The linewidths (in Hz) of these spectra result from a combination of competing influences. Even with fast spinning, MAS may not completely average the strong ^{19}F - ^{19}F homonuclear dipolar coupling present in this sample, and some broadening may result from the residual coupling that is not averaged. However, this broadening cannot be separated from the effects of field-dependent interactions. First, the field is less homogeneous at 11.7 T than at 9.4 T, which produces inhomogeneous broadening. Second, the higher field causes chemical shift dispersion, which produces peaks with the

same linewidths in ppm, but broader linewidths in Hz. The effects of chemical shift dispersion are more pronounced when the sample contains a distribution of nuclear environments. A distribution of ^{19}F chemical shifts is likely in this sample, given that the reported NaYF_4 crystal structures predict a significant amount of positional disorder in the neighboring Na and Y atoms (*vide infra*). Such a distribution cannot be averaged by MAS, and thus produces a larger broadening effect (in Hz) at the higher field.

NaYF_4 structure **I** has two crystallographically distinct F sites, which are consistent with the two resonances seen in the ^{19}F NMR spectra. However, the ratio of F atoms in these sites (1:1) does not match the observed signal intensity ratios (*ca.* 2:1 for Sites 1 and 2, respectively). Crystal structure **II** has only *one* crystallographic F site (at the $6h$ position). The presence of a second F site cannot be rationalized using a single unit cell of NaYF_4 , as this cell represents an average structure of the disordered crystal. SSNMR, however, is sensitive to local environments throughout the sample, and thus a larger representation of the crystal structure must be considered. **Figure 2.9** depicts a small ($1 \times 1 \times 3$) supercell of structure **II** that more accurately approximates the positional disorder present in the larger crystal. The site occupancy of the $2b$ Na site (along the unit cell edges parallel to the c -axis) is particularly low (*ca.* 0.43); therefore, some F atoms have neighboring absences and do not interact with any Na^+ ions along the unit cell edge (**Figure 2.9**). These F sites are chemically distinct from those represented in a single unit cell, and likely result in the high frequency peaks in the corresponding ^{19}F NMR spectra. The other peak (which has higher intensity) results from the remaining F atoms that are bound to $2b$ Na sites. The ratio of these two F sites is 2:1, which agrees with the observed

intensity ratio in the ^{19}F MAS SSNMR spectra. Therefore, structure **II** is consistent with our ^{19}F results.

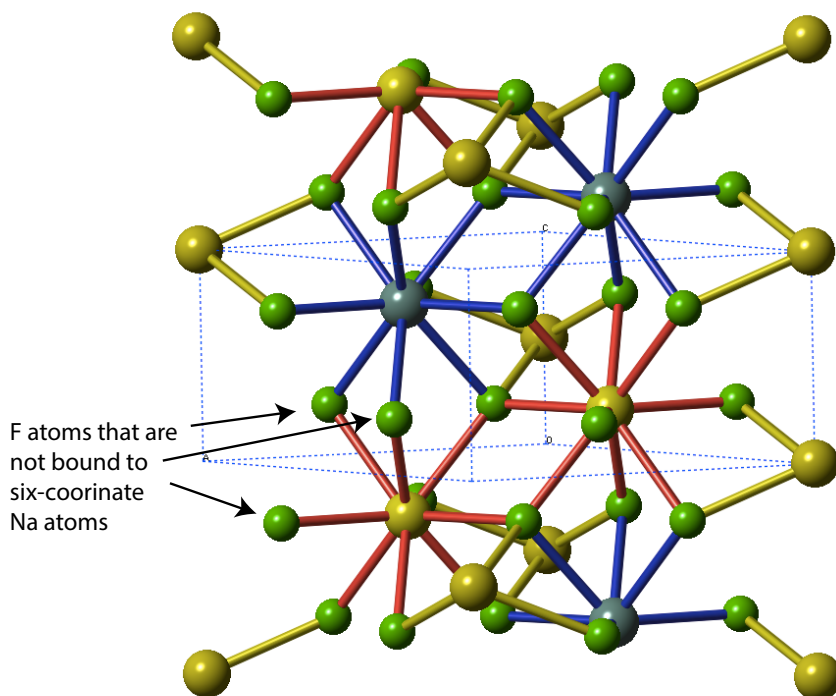


Figure 2.9. A supercell ($1\times 1\times 3$) of Structure II,³⁶ showing a possible arrangement of the fractional site occupancies in the disordered structure. Yellow = Na, Green = F, Blue = Y. The six-coordinate Na sites are along the cell-edges (in yellow).

All of our multinuclear SSNMR data support the $P6_3/m$ structure of bulk β - NaYF_4 (structure **II**), which was first proposed by Sobolev *et al.*³⁵ and later by Krämer *et al.*³⁶ The number of crystallographically distinct Na, Y, and F sites, as well as the coordination of these sites, predicted by this structure are consistent with our ^{23}Na , ^{89}Y , and ^{19}F SSNMR results. In contrast, the structure proposed by Roy and Roy³² (structure **I**) is also consistent with our ^{19}F NMR results, this model is directly contradicted by our ^{23}Na , ^{89}Y , and ^{19}F SSNMR experiments. Therefore, the $P6_3/m$ structure is the best representation of bulk β - NaYF_4 . The SSNMR spectra of the core/shell NC samples are similar to the spectra of bulk β - NaYF_4 , and β - NaLuF_4 , including the number of features,

chemical shifts, and linewidths. Such a close similarity would not be observed if the NCs contained (i) α -NaYF₄ and α -NaLuF₄ or (ii) a homogeneous mixture of the core and shell materials (e.g., interstitial/substitutional versions of the original phases), as any of these structures would produce distinct quadrupolar and chemical shift parameters arising from distinct ²³Na, ¹⁹F and/or ⁸⁹Y sites. As such, our results suggest that both NaYF₄ and NaLuF₄ are present in distinct domains within the NCs and that the core and shell contain β -forms of the bulk materials, with the same P6₃/m structure.

2.3.8 ¹H-²³Na and ¹⁹F-²³Na CP/MAS NMR

¹H and ¹³C SSNMR spectra (**Figure A12** and **Figure A13**, respectively) confirm the presence of oleic acid (OA) in the NC samples. If these hydrocarbon chains are bound to the NC, the proximity of protons in OA to the surface of the NC should enable ¹H CP to ²³Na nuclei at or near the surface. The ¹H-²³Na CP/MAS spectrum ($v_{\text{rot}} = 6$ kHz) of the 27 nm NC (**Figure 2.10c**) has one broad pattern, which is lopsided to low frequency, with a center of gravity around $-11(2)$ ppm, and a breadth ($\Delta v_{1/2}$) of roughly 2500(200) Hz. This spectrum is very broad compared to that of pure sodium oleate (**Figure A14**), which has a much narrower pattern ($\Delta v_{1/2} \approx 480(50)$ Hz) with a higher center of gravity ($-7.2(5)$ ppm). The reason for this broadening is that the sodium sites on the NC surface are associated with a range of slightly varying chemical environments, which lead to distributions of quadrupolar interactions and chemical shifts (the former, which have much larger frequency spreads for ²³Na, dominate the spectrum).

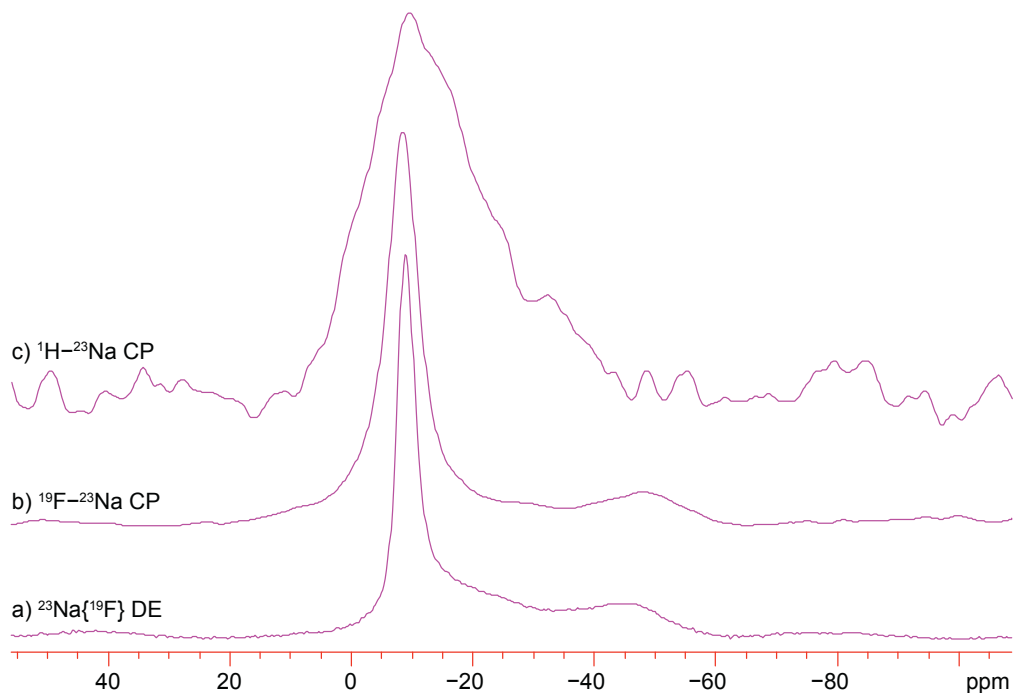


Figure 2.10. ^{23}Na MAS NMR spectra of the 27 nm NC ($\nu_{\text{rot}} = 6$ kHz), under the conditions of a) direct excitation, b) CP from ^{19}F , and c) CP from ^1H .

The ^{13}C SSNMR results (**Figure A13** and **Figure A15**) also support the presence of surface-bound oleic acid in the NC samples, as the peaks corresponding to the carbonyl carbon and attached methylene carbons (at roughly 180-185 ppm in **Figure A15**) are much broader in the spectra of the NC than in that of pure oleic acid. This result is consistent with the broadening reported in the spectra of oleic acid bound to the surface of other nanomaterials.^{64,65} While there might be a very small amount of Na^+ -oleate complex in the NC sample as an impurity (*i.e.*, represented by a pattern of very low intensity buried beneath the broad feature in **Figure 2.10**), it is not clearly detected in our NMR spectra. We also note that the synthetic procedures described herein involve a purification step in which the majority of excess “free” sodium oleate is removed (*vide supra*).

For comparison, ^{19}F - ^{23}Na CP/MAS and $^{23}\text{Na}\{^{19}\text{F}\}$ DE spectra were also acquired at the same spinning speed. The ^{19}F - ^{23}Na CP spectrum (**Figure 2.10b**) is similar to the ^{23}Na DE spectrum (**Figure 2.10a**), and contains a narrow peak from Site 1 centered at roughly $-8.5(5)$ ppm as well as the broad SOQI pattern from Site 2 at lower frequency. The S/N ratio of the ^1H - ^{23}Na CP spectrum is far lower than the ^{19}F - ^{23}Na CP spectrum, even after a significantly longer experimental time (*ca.* 5 times longer). This reduced signal is expected in the ^1H - ^{23}Na CP spectrum due to the relatively low number of Na sites near enough to surface protons to undergo CP (versus those in the bulk of the NC). Note that CP is dependent upon dipolar couplings between ^1H and ^{23}Na , which scale as the inverse cube of the internuclear distance. Such surface Na sites yield a distribution of chemical shifts (seen as a broad peak in **Figure 2.10c**) due to surface effects (see above). Since ^{19}F nuclei are present throughout the NC (*i.e.*, in both the shell *and* core), the ^{19}F - ^{23}Na CP spectrum (**Figure 2.10b**) represents Na sites from across the entire sample and has much higher S/N. The ^{23}Na DE spectrum (**Figure 2.10a**) also represents ^{23}Na environments throughout the particle, and has high S/N. The sharp resonances at $-8.5(5)$ ppm in the ^{19}F - ^{23}Na CP and ^{23}Na DE spectra are much narrower than the corresponding feature in the ^1H - ^{23}Na CP spectrum ($\Delta\nu_{1/2} = 700$ Hz, 700 Hz, and 2500 Hz, respectively). The inhomogeneous broadening that results from surface effects is most pronounced in the spectra of ^{23}Na sites that are closest to the surface. These effects are not as strong for sites nearer to the center of the particle, however, and the corresponding spectra contain a narrower distribution of chemical shifts. Most of the signal in the ^{19}F - ^{23}Na CP and DE spectra results from the non-surface sites (seen as a narrow peak in **Figure 2.10a** and

Figure 2.10b), and the signal intensity from sites affected by surface effects is too small to see.

The broad second-order pattern associated with the six-coordinate Site 2 Na is clearly present in both the ^{23}Na DE and ^{19}F - ^{23}Na CP NMR spectra (**Figure 2.10a** and **Figure 2.10b**), but absent in the ^1H - ^{23}Na NMR spectrum (**Figure 2.10c**). Observation of the Site 2 pattern is difficult given the low S/N ratio of the ^1H - ^{23}Na spectrum, but the fact that the pattern is slightly lopsided or biased to the low frequency direction could indicate that there is some underlying intensity from the broad pattern. The CP spectra shown in **Figure 2.10** were acquired with low power during the CP contact pulse. As seen in **Figure A16**, using a higher power matching condition can increase the signal intensity of Site 1; however, at higher powers the CP efficiency to ^{23}Na nuclei with larger quadrupolar interactions drops dramatically.⁶⁶⁻⁶⁸ As such, signal from the second Na site can only be observed under low power matching conditions.

These CP experiments on the NC samples confirm that oleic acid is in close proximity to the surface of the NC. This result is consistent with the notion that the oleates are bound to the NC surface, acting to compensate for the excess positive charge arising from Na^+ and Lu^{3+} cations in the material relative to the negative charge (from the F^- anions). The low S/N of the ^1H - ^{23}Na spectrum suggests that the oleic acid is only present at the NC surface (*i.e.*, it is not incorporated into the NC core). The inclusion of other NMR-active nuclides that are more receptive to CP NMR experiments (*e.g.*, ^{89}Y , ^{45}Sc , etc.) may aid in further studying the surface chemistry of these NCs.

2.4 Conclusions

Through a combination of PXRD and multinuclear SSNMR, we have resolved the long-standing debate about the structure of bulk β -NaYF₄, and shown that it crystallizes in the P6₃/m space group, as first proposed by Sobolev *et al.*³⁵ and later suggested by Krämer *et al.*³⁶ We have demonstrated that β -NaLuF₄ contains similar F and Na environments to β -NaYF₄, and therefore these compounds are isostructural. Comparison of the SSNMR spectra of the bulk compounds with those of the core/shell NCs reveals striking similarities in their spectral features (*i.e.*, chemical shifts and quadrupolar patterns). These results suggest that the NCs contain both NaYF₄ and NaLuF₄, as expected from the synthesis, in the same crystal structure as the bulk. Our results also show that the NCs contain only the β -phase of these compounds, which makes them ideal candidates for the synthesis of luminescent Ln³⁺-doped particles. Finally, the presence of stabilizing surface ligands (*i.e.*, oleates) is confirmed via CP experiments, which exploit the close proximity of NMR-active nuclides for efficient polarization transfer. SSNMR experiments, such as those described herein, will be applied to further study core/shell Ln³⁺-doped NCs with disparate core/shell arrangements and sizes, different paramagnetic dopants, and a selection of surface ligands. Molecular-level information obtained from SSNMR spectroscopy will aid in the future study of NCs containing dopant ions, where we expect SSNMR will be a valuable tool for monitoring structural changes, and aid in determining how the relatively low quantum yields from these NPs might be improved to levels comparable to those of the bulk materials. Such structural insight will facilitate the rational synthesis and preparation of NCs with controllable luminescent properties and improved quantum yields.

2.5 References

- (1) Shalav, A.; Richards, B. S.; Trupke, T.; Krämer, K. W.; Güdel, H. U. *Appl. Phys. Lett.* **2005**, *86*, 13505-1-013505-3.
- (2) Huang, X.; Han, S.; Huang, W.; Liu, X. *Chem. Soc. Rev.* **2013**, *42*, 173–201.
- (3) Klimov, V. I.; Mikhailovsky, A. A.; Xu, S.; Malko, A.; Hollingsworth, J. A.; Leatherdale, C. A.; Eisler, H.; Bawendi, M. G. *Science* **2000**, *290*, 314–317.
- (4) Vetrone, F.; Capobianco, J. A. *Int. J. Nanotechnol.* **2008**, *5*, 1306.
- (5) Gai, S.; Li, C.; Yang, P.; Lin, J. *Chem. Rev.* **2014**, *114*, 2343–2389.
- (6) Chen, G.; Qiu, H.; Prasad, P. N.; Chen, X. *Chem. Rev.* **2014**, *114*, 5161–5214.
- (7) Chen, G.; Yang, C.; Prasad, P. N. *Acc. Chem. Res.* **2013**, *46*, 1474–1486.
- (8) Zhou, J.; Liu, Z.; Li, F. *Chem. Soc. Rev.* **2012**, *41*, 1323–1349.
- (9) Wang, F.; Liu, X. *Chem. Soc. Rev.* **2009**, *38*, 976–989.
- (10) Haase, M.; Schäfer, H. *Angew. Chemie Int. Ed.* **2011**, *50*, 5808–5829.
- (11) Wang, X.; Zhuang, J.; Peng, Q.; Li, Y. *Nature* **2005**, *437*, 121–124.
- (12) Mai, H.-X.; Zhang, Y.-W.; Si, R.; Yan, Z.-G.; Sun, L.; You, L.-P.; Yan, C.-H. *J. Am. Chem. Soc.* **2006**, *128*, 6426–6436.
- (13) Maas, H.; Currao, A.; Calzaferri, G. *Angew. Chemie Int. Ed.* **2002**, *41*, 2495–2497.
- (14) Gamelin, D. R.; Güdel, H. U. *Acc. Chem. Res.* **2000**, *33*, 235–242.
- (15) Auzel, F. *Chem. Rev.* **2004**, *104*, 139–173.
- (16) Boyer, J.-C.; van Veggel, F. C. J. M. *Nanoscale* **2010**, *2*, 1417–1419.
- (17) Han, S.; Deng, R.; Xie, X.; Liu, X. *Angew. Chemie Int. Ed.* **2014**, *53*, 11702–11715.
- (18) Eastoe, J.; Hollamby, M. J.; Hudson, L. *Adv. Colloid Interface Sci.* **2006**, *128*, 5–15.
- (19) Qi, L. In *Encyclopedia of Surface and Colloid Science*; Somasundaran, P., Ed.; CRC Press, **2006**; pp 6183–6207.
- (20) Lee, M.-H.; Oh, S.-G.; Yi, S.-C. *J. Colloid Interface Sci.* **2000**, *226*, 65–70.
- (21) Zhou, L.; Shi, J.; Gong, M. *Mater. Lett.* **2005**, *59*, 2079–2084.
- (22) Lemyre, J.-L.; Lamarre, S.; Beaupré, A.; Ritcey, A. M. *Langmuir* **2011**, *27*, 11824–11834.
- (23) Stouwdam, J. W.; van Veggel, F. C. J. M. *Langmuir* **2004**, *20*, 11763–11771.
- (24) Schäfer, H.; Ptacek, P.; Zerzouf, O.; Haase, M. *Adv. Funct. Mater.* **2008**, *18*, 2913–2918.
- (25) Yi, G.; Chow, G. *Chem. Mater.* **2007**, *19*, 341–343.
- (26) Schietinger, S.; Aichele, T.; Wang, H.-Q.; Nann, T.; Benson, O. *Nano Lett.* **2010**, *10*, 134–138.
- (27) Carling, C.-J.; Nourmohammadian, F.; Boyer, J.-C.; Branda, N. R. *Angew. Chemie Int. Ed.* **2010**, *49*, 3782–3785.
- (28) Wang, M.; Hou, W.; Mi, C.-C.; Wang, W.-X.; Xu, Z.-R.; Teng, H.-H.; Mao, C.-B.; Xu, S.-K. *Anal. Chem.* **2009**, *81*, 8783–8789.
- (29) Lo, A. Y. H.; Sudarsan, V.; Sivakumar, S.; van Veggel, F.; Schurko, R. W. *J. Am. Chem. Soc.* **2007**, *129*, 4687–4700.
- (30) Lucier, B. E. G.; Johnston, K. E.; Arnold, D. C.; Lemyre, J.; Beaupré, A.; Blanchette, M.; Ritcey, A. M.; Schurko, R. W. *J. Phys. Chem. C* **2014**, *118*, 1213–1228.

- (31) Ratcliffe, C. I.; Yu, K.; Ripmeester, J. A.; Badruz Zaman, M.; Badarau, C.; Singh, S. *Phys. Chem. Chem. Phys.* **2006**, *8*, 3510.
- (32) Roy, D. M.; Roy, R. *J. Electrochem. Soc.* **1964**, *111*, 421–429.
- (33) Mathews, M. D.; Ambekar, B. R.; Tyagi, a. K.; Köhler, J. *J. Alloys Compd.* **2004**, *377*, 162–166.
- (34) Arnold, A. A.; Terskikh, V.; Li, Q. Y.; Naccache, R.; Marcotte, I.; Capobianco, J. A. *J. Phys. Chem. C* **2013**, *117*, 25733–25741.
- (35) Sobolev, B. P.; Mineev, D. A.; Pashutin, V. P. *Dokl. Akad. Nauk SSR* **1963**, *150*, 791–794.
- (36) Krämer, K. W.; Biner, D.; Frei, G.; Güdel, H. U.; Hehlen, M. P.; Lüthi, S. R. *Chem. Mater.* **2004**, *16*, 1244–1251.
- (37) Burns, J. H. *Inorg. Chem.* **1965**, *4*, 881–886.
- (38) Grzechnik, A.; Bouvier, P.; Mezouar, M.; Mathews, M. D.; Tyagi, A. K.; Köhler, J. *J. Solid State Chem.* **2002**, *165*, 159–164.
- (39) Wang, F.; Deng, R.; Wang, J.; Wang, Q.; Han, Y.; Zhu, H.; Chen, X.; Liu, X. *Nat. Mater.* **2011**, *10*, 968–973.
- (40) Stepuk, A.; Casola, G.; Schumacher, C. M.; Krämer, K. W.; Stark, W. J. *Chem. Mater.* **2014**, *26*, 2015–2020.
- (41) Tu, D.; Liu, Y.; Zhu, H.; Li, R.; Liu, L.; Chen, X. *Angew. Chemie Int. Ed.* **2013**, *52*, 1128–1133.
- (42) Fischer, S.; Fröhlich, B.; Krämer, K. W.; Goldschmidt, J. C. *J. Phys. Chem. C* **2014**, *118*, 30106–30114.
- (43) Sarakovskis, A.; Kriekė, G.; Doke, G.; Grube, J.; Grinberga, L.; Springis, M. *Opt. Mater. (Amst)*. **2015**, *39*, 90–96.
- (44) Szeftczyk, B.; Roszak, R.; Roszak, S. *RSC Adv.* **2014**, *4*, 22526–22535.
- (45) Boyer, J.; Cuccia, L. A.; Capobianco, J. A. *Nano Lett.* **2007**, *7*, 847–852.
- (46) Wang, F.; Han, Y.; Lim, C. S.; Lu, Y.; Wang, J.; Xu, J.; Chen, H.; Zhang, C.; Hong, M.; Liu, X. *Nature* **2010**, *463*, 1061–1065.
- (47) Zeng, J.-H.; Su, J.; Li, Z.-H.; Yan, R.-X.; Li, Y.-D. *Adv. Mater.* **2005**, *17*, 2119–2123.
- (48) Heer, S.; Lehmann, O.; Haase, M.; Güdel, H. U. *Angew. Chemie Int. Ed.* **2003**, *42*, 3179–3182.
- (49) Li, Z.; Zhang, Y.; Jiang, S. *Adv. Mater.* **2008**, *20*, 4765–4769.
- (50) Johnson, N. J. J.; Korinek, A.; Dong, C.; van Veggel, F. C. J. M. *J. Am. Chem. Soc.* **2012**, *134*, 11068–11071.
- (51) Johnson, N. J. J.; van Veggel, F. C. J. M. *ACS Nano* **2014**, *8*, 10517–10527.
- (52) Merwin, L. H.; Sebald, A. *J. Magn. Reson.* **1990**, *88*, 167–171.
- (53) Bennett, A. E.; Rienstra, C. M.; Auger, M.; Lakshmi, K. V.; Griffin, R. G. *J. Chem. Phys.* **1995**, *103*, 6951–6958.
- (54) Brown, S. P.; Wimperis, S. *J. Magn. Reson.* **1997**, *124*, 279–285.
- (55) Schaefer, J.; Stejskal, E. O. *J. Am. Chem. Soc.* **1976**, *98*, 1031–1032.
- (56) Pines, A. *J. Chem. Phys.* **1973**, *59*, 569–590.
- (57) Peersen, O.; Wu, X.; Smith, S. *J. Magn. Reson.* **1994**, *106*, 127–131.
- (58) Peersen, O. B.; Wu, X. L.; Kustanovich, I.; Smith, S. O. *J. Magn. Reson.* **1993**, *104*, 334–339.
- (59) Eichele, K.; Wasylishen, R. E. University of Tübingen: Tübingen, Germany **2001**.

- (60) van Veggel, F. C. J. M.; Dong, C.; Johnson, N. J. J.; Pichaandi, J. *Nanoscale* **2012**, *4*, 7309–7321.
- (61) Brunton, G. D.; Insley, H.; McVay, T. N.; Thoma, R. E. *Oak Ridge Natl. Lab. Rep. No. ORNL-3761* **1965**.
- (62) Shirako, Y.; Shi, Y. G.; Aimi, A.; Mori, D.; Kojitani, H.; Yamaura, K.; Inaguma, Y.; Akaogi, M. *J. Solid State Chem.* **2012**, *191*, 167–174.
- (63) Bessada, C.; Rakhmatullin, A.; Rollet, A.; Zanghi, D. *J. Fluor. Chem.* **2009**, *130*, 45–52.
- (64) Ramos-González, R.; García-Cerda, L. A.; Quevedo-López, M. A. *Appl. Surf. Sci.* **2012**, *258*, 6034–6039.
- (65) Pawsey, S.; Yach, K.; Halla, J.; Reven, L. *Langmuir* **2000**, *16*, 3294–3303.
- (66) Vega, A. J. *J. Magn. Reson.* **1992**, *96*, 50–68.
- (67) Ashbrook, S. E.; Wimperis, S. *J. Chem. Phys.* **2009**, *131*, 194509-1–15.
- (68) *NMR of Quadrupolar Nuclei in Solid Materials*, 1st ed.; Wasylishen, R. E., Ashbrook, S. E., Wimperis, S., Eds.; John Wiley & Sons, Ltd: Chichester, UK, **2012**.

Chapter 3: Structural Characterization of NaYF₄ Nanocrystals Containing Paramagnetic Ln³⁺ Dopants

3.1 Introduction

Upconverting micro- and nanocrystalline (NC) materials are desirable due to their unusual anti-Stokes emissions and large wavelength shift (*e.g.*, these materials can absorb low energy infrared radiation and emit higher energy visible light).^{1,2} Deliberate modifications of the material structure and particle size are necessary to develop structures that are appropriate for a wide range of potential applications in bioimaging, LEDs (light emitting diodes), and fiber optics.³⁻⁶ To date, the most successful class of compounds in this area is NaYF₄ doped with lanthanide ions (Ln³⁺, Ln = Er, Yb, Nd, Tm, *etc.*).^{2,7} The bulk optical properties of the material are largely dependent on the identity and local structural environments of the paramagnetic dopant ions, as well as the structure of the host material.^{8,9} Structural characterization on the molecular level is necessary to improve the rational synthesis of these materials.¹⁰

Recent works by our group¹¹ and others¹² have shown that solid-state nuclear magnetic resonance (SSNMR) spectroscopy is a valuable tool for the characterization of NaYF₄ NCs and their bulk (microcrystalline) analogues. These studies have confirmed the structures of the two polymorphs of bulk NaYF₄, the cubic (α) form and the hexagonal (β) form, the latter of which is known to produce samples with more efficient upconversion.^{7,13} However, the use of similar SSNMR techniques to study upconverting materials (*i.e.*, those containing lanthanide dopants) is complicated by the fact that many Ln³⁺ ions are paramagnetic.

Unpaired electrons affect NMR spectra through two electron-nuclear interactions: (i) the *Fermi contact* interaction, which is due to unpaired electron density at the nucleus (*i.e.*, in the atomic *s*-orbital), and (ii) the through-space dipolar or *pseudocontact* interaction. The paramagnetic effects on NMR spectra have been extensively reviewed elsewhere,^{14–17} in short, spin-spin coupling between an atomic nucleus and the unpaired electron density can cause faster nuclear relaxation (both longitudinal relaxation, T_1 , and transverse relaxation, T_2), and can produce substantially shifted and/or broadened peaks in the NMR spectra. Broadening can be particularly problematic for the acquisition of high-resolution spectra, as the peaks are often so broad that they cannot be distinguished from the baseline, and the overlap of multiple features can make spectral assignment difficult. Fortunately, the effects of the anisotropic paramagnetic interaction in solids can be partially averaged with magic-angle spinning (MAS) to produce narrower peaks, provided that the spinning speed is on the order of the strength of the interaction (which can range from tens to hundreds of kHz). As such, a key development for the study of paramagnetic materials has been the development of advanced MAS hardware capable of spinning samples at speeds of 45–110+ kHz (*i.e.*, so-called *ultra-fast MAS*, UFMAS).^{18,19}

The acquisition of solid-state NMR (SSNMR) spectra of paramagnetic materials can be challenging; however, when these spectra are acquired, they can provide valuable structural information. Early seminal works in this area include those by Bryant,²⁰ Yesinowski,²¹ and Grey.^{22,23} In the years since, the study of paramagnetic compounds with SSNMR has been extremely valuable for a variety of inorganic and organic materials.^{15,24–29}

In this report, we expand upon our previous work on undoped NaYF₄ nanomaterials¹¹ to characterize samples containing various amounts of paramagnetic Er³⁺ and Tm³⁺ dopants up to 10 at.% of the total RE³⁺ content. Together with transmission electron microscopy (TEM) and powder X-ray diffraction (PXRD) data, we present multinuclear (¹⁹F, ²³Na, ⁸⁹Y, ¹H, and ¹³C) SSNMR spectra that reveal the effects of dopants on the local structures of the materials. These spectra provide detailed information on the average distance between the observed nucleus and the closest lanthanide, dopant homogeneity, and surface structures. Finally, we compare the results from the NC samples (*ca.* 18 nm diameter) with their corresponding bulk phases (microcrystals with an average diameter greater than 2 μm) to examine the effects of particle size on the structures of the doped and undoped materials.

3.2 Experimental Methods

3.2.1 Chemicals

All of the raw materials were used as received without further purifications. Yttrium chloride hexahydrate (99.99%), yttrium nitrate tetrahydrate (99.99%), erbium chloride hexahydrate (>99.99%), erbium nitrate pentahydrate (>99.9%), thulium chloride hexahydrate (99.99%), thulium nitrate pentahydrate (>99.9%), oleic acid (technical grad, 90%), 1-octadecene (technical grad, 90%), ammonium fluoride (>99.99%), citric acid (99%), sodium fluoride (99%), hexane (ACS reagent, ≥98.5%) were purchased from Sigma Aldrich. Sodium hydroxide (pellets, ACS reagent) was purchased from ACP Chemicals Inc.

3.2.2 Synthesis of NCs

NaYF₄, Er³⁺ or Tm³⁺ doped NaYF₄ nanoparticles were prepared using a high-temperature synthesis in a mixture of oleic acid and octadecene, following established protocols³⁰ with minor modifications. In a typical synthesis of NaYF₄:Er 2% nanoparticles, a mixture of 0.98 mmol YCl₃•6H₂O, 0.02 mmol ErCl₃•6H₂O, 6 mL oleic acid (OA) and 17 mL 1-octadecene (ODE) were added to a 100 mL three-neck flask. The mixture was heated to 130 °C while stirring under vacuum and kept at this temperature for about 40 minutes until a clear solution formed. The solution was then cooled down to room temperature, and a clear methanol solution (10 mL) containing 2.5 mmol NaOH and 4 mmol NH₄F was added dropwise into the flask and kept stirring overnight. The solution was slowly heated to 70 °C to remove methanol, before being quickly heated from 70 to 300 °C (20 °C/min) under an argon atmosphere. This temperature was maintained for 60 minutes and then the solution was cooled to room temperature. Finally, the NaYF₄:Er 2% nanoparticles were precipitated by adding absolute ethanol (~35 mL) and centrifuged for 5 minutes at 5,000 rpm (*g*-force = 2683). The supernatant was poured off and the washing process was repeated three times. Finally, the nanoparticles were dispersed in 10 mL of hexane for storage. Samples of NaY_(1-x)F₄: xEr (*x* = 0, 0.02, 0.05, 0.1) and NaY_(1-y)F₄: yTm (*y* = 0.02, 0.05, 0.1) nanocrystals were prepared with the same method.

3.2.3 Synthesis of Bulk Materials

A hydrothermal method³¹ was used to synthesize bulk Er or Tm doped NaYF₄ samples. Taking NaYF₄:Tm 2% as an example, 0.98 mmol Y(NO₃)₃•4H₂O, 0.02 mmol Tm(NO₃)₃•5H₂O, 2.5 mmol citric acid and 5 mmol NaOH were dissolved in 15 mL

deionized water and stirred for 30 minutes. 10 mL of a 1 M NaF solution was added to the above solution and stirred for 30 minutes. Next, the mixed solution was transferred to an electrically heated autoclave and heated at 180 °C for 24 hours. After the autoclave cooled to room temperature, the solution was washed with deionized water three times and ethanol once. The washed sample was dried at 110 °C for 4 hours, producing the bulk NaYF₄:Tm 2% sample. Samples of bulk NaY_(1-x)F₄: xEr ($x = 0, 0.02, 0.05, 0.1$) and NaY_(1-y)F₄: yTm ($y = 0.02, 0.05, 0.1$) were obtained with the same method.

3.2.4 Transmission Electron Microscopy (TEM)

A TEM (JEOL JEM-1400) operating at 80 kV was used to analyze the morphology and sizes of the prepared samples. Samples were prepared on TEM grid by dropping the NCs dispersed in hexane (or bulk samples dispersed in ethanol) onto a formvar carbon film supported by a 300 mesh copper grid. The size distribution of the NCs was obtained from more than 50 particles on average. The ImageJ software was used to measure the diameter of NCs by hand and the size distribution was obtained with a Gaussian fitting function.

3.2.5 Powder X-ray Diffraction (PXRD)

The phases of the Er- and Tm-doped NaYF₄ samples were characterized by a Rigaku bench-top X-ray diffractometer with a Cr K_α source ($\lambda = 2.2890 \text{ \AA}$) operating at 30 kV and 15 mA. Diffraction patterns were obtained by scanning from 20° to 100° (2 θ) at a rate of 1°/min, with a resolution of 0.05°.

3.2.6 Inductively Coupled Plasma Mass Spectrometry (ICP-MS)

The concentration of Er³⁺ and Tm³⁺ ions in NCs and bulk samples was measured with an ICP-MS spectrometer (Thermo X-Series II(X7)). The water dispersion of NC or

bulk samples (about 30–50 mg solution) was digested in concentrated nitric acid (about 2 mL of 16N HNO₃) at 125 °C in sealed Teflon vials for at least 24 hours. Then the digested solution was transferred to a larger plastic bottle and diluted by adding 100 g (~100 mL) ultrapure water. After that, about 2 g of the diluted solution was weighed and further diluted to ~10 g by adding 2% HNO₃. This solution was analyzed with the ICP-MS. Calibration was performed by analyzing serial dilutions of a mixed element synthetic standard containing a known amount of Er or Tm.

3.2.7 SSNMR Characterization

Ultra-fast magic angle spinning (UFMAS) ($\nu_{\text{rot}} = 60$ kHz) NMR experiments were conducted with a Bruker UFMAS 1.3 mm HX probe on a Bruker Avance III console with a $B_0 = 11.7$ T standard-bore magnet ($\nu_0(^1\text{H}) = 500.13$ MHz, $\nu_0(^{19}\text{F}) = 470.59$ MHz). All other MAS experiments (at slower spinning speeds) were conducted on a Bruker Avance III HD console with an Oxford $B_0 = 9.4$ T wide-bore magnet ($\nu_0(^1\text{H}) = 399.73$ MHz, $\nu_0(^{19}\text{F}) = 376.09$ MHz, $\nu_0(^{13}\text{C}) = 100.53$ MHz, $\nu_0(^{23}\text{Na}) = 105.74$ MHz, $\nu_0(^{89}\text{Y}) = 19.59$ MHz). ^{89}Y NMR experiments were conducted using a Varian/Chemagnetics 4 mm HXY probe equipped with a Varian/Chemagnetics low- γ tuning box. All other experiments conducted on this instrument used a Varian/Chemagnetics 4 mm HX probe. To conduct experiments on the bulk and NC materials, finely ground samples were packed into 1.3 mm or 4 mm o.d. zirconia rotors.

^{19}F chemical shifts were referenced with respect to neat CFC₃(l) ($\delta_{\text{iso}} = 0.0$ ppm) using neat fluorobenzene(l) (C₆H₅F, $\delta_{\text{iso}} = -113.15$ ppm) as a secondary reference. ^1H and ^{13}C chemical shifts were referenced to tetramethylsilane (TMS, $\delta_{\text{iso}} = 0.0$ ppm) using solid adamantane ($\delta_{\text{iso}} = 1.85$ and 38.57 ppm, respectively) as a secondary reference. ^{23}Na

chemical shifts were referenced with respect to a 1.0 M NaCl(aq) solution ($\delta_{\text{iso}} = 0.0$ ppm). ^{89}Y chemical shifts were referenced to a 1.0 M $\text{YCl}_3(\text{aq})$ solution ($\delta_{\text{iso}} = 0.0$ ppm) using $\text{Y}(\text{NO}_3)_3 \cdot 6\text{H}_2\text{O}(\text{s})$ ($\delta_{\text{iso}} = -53$ ppm) as a secondary reference.

Full details of the experimental parameters used for the SSNMR experiments are given in **Appendix B (Table B1-Table B6)**. ^1H , $^{13}\text{C}\{^1\text{H}\}$, ^{19}F , and $^{23}\text{Na}\{^{19}\text{F}\}$ direct-excitation MAS experiments were conducted using a rotor-synchronized Hahn echo pulse sequence of the form $(\pi/2)_x - \tau_1 - (\pi)_y - \tau_2 - \text{acq}$. High-power ^1H or ^{19}F decoupling was applied in all ^{23}Na , ^{89}Y , and ^{13}C experiments, using the two-pulse phase-modulation (TPPM) sequence.³² All cross-polarization (CP) experiments used a ramped-amplitude spin lock pulse on the ^{19}F channel between 50% and 100% of the maximum pulse amplitude.³³⁻³⁵ All SSNMR spectra were processed using TopSpin 3.5. Simulations of the processed spectra were generated with the Solid Lineshape Analysis (SOLA) module (v. 2.2.4) within TopSpin.

3.3 Results and Discussion

3.3.1 Transmission Electron Microscopy (TEM)

TEM images of the NC samples (**Figure B1**) confirm that they are spherical and monodisperse. All of the doped NC samples and one of the undoped samples have particle sizes of 18.0 ± 1.5 nm in diameter (**Table 3.1**). An additional undoped NC sample was prepared with a larger diameter ($27.9 \text{ nm} \pm 2.9 \text{ nm}$, based on the TEM) using the same method (see the **Experimental Methods** section for full synthetic details). Samples with larger particle sizes (*i.e.*, “bulk” samples) were prepared according to a distinct method, as previously reported.⁷ The TEM images of the bulk samples prepared

for the current work (**Figure B2**) indicate that the particles are microcrystalline, larger than 2 μm in diameter.

Table 3.1. Particle sizes of the NC NaYF_4 samples obtained from TEM measurements.

	Sample	Particle Size (nm) ^a
Undoped	NaYF_4 NC “small”	17.5(1.1)
	NaYF_4 NC “big”	27.9(2.9)
Er-Doped NC	NaYF_4 :Er 2% NC	18.0(0.6)
	NaYF_4 :Er 5% NC	19.5(0.6)
	NaYF_4 :Er 10% NC	17.0(0.6)
Tm-Doped NC	NaYF_4 :Tm 2% NC	17.0(0.8)
	NaYF_4 :Tm 5% NC	17.5(0.7)
	NaYF_4 :Tm 10% NC	19.5(0.5)

^aValues in parentheses are errors estimated from the FWHM of the particle size distribution obtained with TEM measurements.

3.3.2 Powder X-ray Diffraction (PXRD)

Experimental PXRD patterns of the NC and bulk samples are shown in **Figure B3**. These patterns are consistent with our previous reports on similar compounds, and with the reference pattern of hexagonal β - NaYF_4 .³⁶ Signals from impurities, including cubic α - NaYF_4 , are not observed. As is common with NC samples, the diffraction peaks from the NCs are broader than those of the corresponding bulk material due to the smaller grain sizes of the NCs and larger contributions from surface effects (*vide infra*).

3.3.3 Inductively Coupled Plasma Mass Spectrometry (ICP-MS)

The amounts of Er and Tm in the samples was quantified using ICP-MS. The results (**Table 3.2**) of this analysis show that in all cases, the dopant levels are within 2% of the expected values based on the at.% LnCl_3 used in the synthesis.

Table 3.2. Er and Tm content of the doped samples obtained from ICP-MS measurements.^a

	Sample Name	at.% Er	at.% Tm
NC Samples	Er 2%	1.8(3)	– ^b
	Er 5%	4.7(6)	–
	Er 10%	8.6(11)	–
	Tm 2%	–	1.9(3)
	Tm 5%	–	4.9(6)
	Tm 10%	–	11.1(14)
Bulk Samples	Er 2%	2.2(3)	–
	Er 5%	4.8(6)	–
	Er 10%	8.6(11)	–
	Tm 2%	–	1.9(3)
	Tm 5%	–	5.6(7)
	Tm 10%	–	11.6(15)

^aErrors are shown in parentheses, estimated from the instrument precision of $\pm 6\%$. ^bDashes indicate values below the detection limits.

3.3.4 Solid-State NMR

Our discussion of the multinuclear (¹⁹F, ²³Na, ⁸⁹Y, ¹H, ¹³C) SSNMR spectra of the NC and bulk samples (particle sizes of 17-28 nm and $> 2 \mu\text{m}$, respectively) is divided into three parts, in which we consider: (i) the effects of *dopant level and dopant identity* on the spectra of the NCs, (ii) spectra that reveal information on the molecular-level structure of the *NC surfaces*, and (iii) the influence of *particle size* on the spectra of undoped and doped materials.

3.3.5 Effects of NC Dopant Level and Identity

¹⁹F Ultra-Fast MAS (UFMAS) NMR experiments. The ¹⁹F UFMAS ($\nu_{\text{rot}} = 60 \text{ kHz}$) NMR spectra of the NC samples doped with Ln^{3+} (Ln = Er or Tm) are shown in **Figure 3.1**. These (and all other SSNMR spectra in this work) are presented with the spectra scaled to have the same maximum isotropic peak intensity in order to allow for clear comparison of peak widths and sideband intensities, unless otherwise noted. The spectrum of the undoped material has 5 features (see the deconvolution, **Figure B4**),

which result from (i) two distinct F environments in the crystal structure ($-86(1)$ and $-94(1)$ ppm, respectively),^{11,13} (ii) F environments near the surface of the particles (peaks at $-79(1)$ and $-89(1)$ ppm, respectively), and (iii) a trifluoroacetate impurity ($-74(3)$ ppm) (also observed in the ^{13}C experiments, *vide infra*). The data for the undoped NCs presented herein are consistent with those previously reported, in that the NMR spectra confirm that the bulk and NC materials have the same structure and hexagonal phase (see **Section 3.3.7 Particle Size effects** for more details).

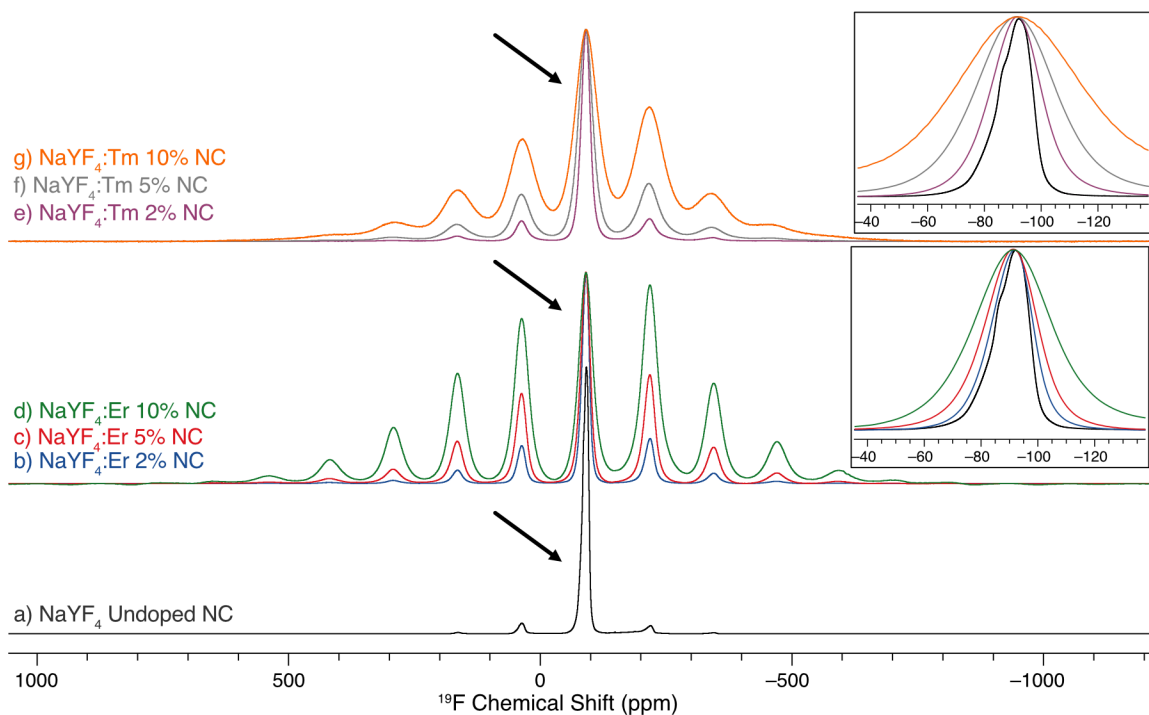


Figure 3.1. ^{19}F UFMAS ($v_{\text{rot}} = 60$ kHz) NMR spectra of a) undoped NaYF_4 NCs, b)-d) Er-doped NaYF_4 NCs and e)-g) Tm-doped NaYF_4 NCs. Percentages indicate the at.% Ln^{3+} dopant present in each sample. Arrows indicate the isotropic peaks; all other features in the spectra are spinning sidebands. The insets highlight the isotropic features of the spectra.

The spectra of the doped NCs each have only one, broad, isotropic peak with a center of gravity at $-90(1)$ ppm (see **Figure 3.1 insets**), such that none of the individual peaks discussed above can be resolved. However, there are no measurable chemical shift

differences in comparison to the undoped NC sample and no additional features are observed with the addition of more dopant, suggesting that peaks corresponding to the same two ^{19}F environments in the NaYF_4 crystals structure are present (consistent with the PXR data). The absence of peaks resulting from a strong paramagnetic-induced shift suggests that there is no substantial delocalization of the unpaired electron density onto the ^{19}F nuclei (*i.e.*, the Fermi contact interaction is small) and that the "through-space" pseudocontact interaction is likely dominant. The absence of a Fermi contact shift is common for compounds containing paramagnetic Ln^{3+} ions, because the unpaired electron is typically localized within the $4f$ inner shell and does not delocalize across multiple covalent bonds.³⁷ The similarities between the spectra of the undoped and doped materials indicate that the addition of dopants does not substantially change the crystal structure of the particles (*e.g.*, doping does not produce NCs with the cubic phase, α - NaYF_4 , which has substantially different chemical shifts).¹²

With higher dopant levels, two changes are apparent in the spectra of the particles: (i) the intensities of the spinning sidebands (SSBs) relative to the isotropic peaks increase and (ii) the isotropic peaks (and associated SSBs) broaden. The intensities of the SSBs result from a combination of chemical shift anisotropy (CSA) and an anisotropic contribution from the pseudocontact interaction, the dipolar shift anisotropy (DSA; this interaction is sometimes referred to in the literature as the dipolar shift). While the sources of these anisotropic interactions are different, they can both be described by non-traceless, second-rank tensors, which affect the spectra in a similar way.^{15,38} In the spectra obtained in this study, the DSA makes the largest contribution to the total shift anisotropy; the CSA is small (*i.e.*, the SSBs observed in the spectra of the

undoped materials are insignificant compared to those of the doped samples) and can be neglected. The increasing intensity of the SSBs relative to the isotropic peaks indicates an increased DSA in the samples with higher doping levels. The effects of the DSA can be quantified by fitting the sideband manifold with an analytical simulation (as was done here, see **Experimental Methods Section 3.2**) or using the isotropic peak and SSB intensities in a Herzfeld-Berger analysis.^{25,39} The values obtained for the spectra in the current work are listed in **Table 3.3**.

The span of the DS tensor,^{40,41} $\Delta_{\text{aniso}} = |\delta_{\text{zz}} - \delta_{\text{iso}}|$, is proportional to the electronic spin quantum number, S .¹⁴ The electronic spin quantum number of Er^{3+} is greater than that of Tm^{3+} ($S(\text{Er}^{3+}) = 3/2$, $S(\text{Tm}^{3+}) = 1$), which accounts for the larger Δ_{aniso} values and associated increased SSB intensities in the spectra of the Er^{3+} -doped materials (**Table 3.3**, **Figure 3.1**). As demonstrated by Ishii *et al.*,^{41,42} the Δ_{aniso} values (in ppm) can be related to the average distance between the observed nucleus and the unpaired electron density by **Eq. 3.1**:

$$|\Delta_{\text{aniso}}| = \frac{\mu_0 \mu_B g^2 \cdot S(S + 1)}{\langle R \rangle^3 k_B T} \cdot 10^6 \quad (3.1)$$

where μ_0 is the vacuum permittivity constant, μ_B is the Bohr magneton, g is the isotropic value of the electron g -tensor, S is the electron spin quantum number, $\langle R \rangle$ is the expectation value of the nuclear- Ln^{3+} distance (in meters), k_B is the Boltzmann constant, and T is the temperature (K). This model assumes an isotropic g -tensor and an axially symmetric DS tensor, and treats the paramagnetic electron density as a point charge at the metal centre.⁴³ Notably, this model does not account for spin-orbit interactions, which can play a significant role in the electronic properties of paramagnetic lanthanides.

Table 3.3. Experimental values of the span of the DS tensor (Δ_{aniso}) and corresponding calculated nuclear-Ln³⁺ distances obtained from fits of the SSNMR data.

Sample		¹⁹ F		²³ Na				¹ H		¹³ C	
		$\Delta_{\text{aniso}}^{\text{a}}$ (ppm)		Site 1 ($\delta_{\text{iso}} = -11.1$ ppm)		Site 2 ($\delta_{\text{iso}} = 0$ ppm)		$\Delta_{\text{aniso}}^{\text{a}}$ (ppm)		$\Delta_{\text{aniso}}^{\text{a}}$ (ppm)	
				$\langle R \rangle^{\text{b}}$ (Å)		$\Delta_{\text{aniso}}^{\text{a}}$ (ppm)					
		$\Delta_{\text{aniso}}^{\text{a}}$ (ppm)	$\langle R \rangle^{\text{b}}$ (Å)	$\Delta_{\text{aniso}}^{\text{a}}$ (ppm)	$\langle R \rangle^{\text{b}}$ (Å)	$\Delta_{\text{aniso}}^{\text{a}}$ (ppm)	$\langle R \rangle^{\text{b}}$ (Å)	$\Delta_{\text{aniso}}^{\text{a}}$ (ppm)	$\langle R \rangle^{\text{b}}$ (Å)	$\Delta_{\text{aniso}}^{\text{a}}$ (ppm)	$\langle R \rangle^{\text{b}}$ (Å)
NC Samples	Er 2%	202(10)	8.3(1)	146(20)	9.2(4)	274(20)	7.5(2)	90(10)	10.9(4)	83(20)	11.2(9)
	Er 5%	292(20)	7.4(2)	233(20)	7.9(2)	480(100)	6.2(4)	198(10)	8.4(1)	135(15)	9.5(4)
	Er 10%	396(60)	6.7(3)	483(50)	6.2(2)	910(100)	5.0(2)	312(20)	7.2(2)	216(20)	8.1(3)
	Tm 2%	142(15)	8.0(3)	113(10)	8.6(3)	185(20)	7.3(3)	61(15)	10.6(9)	55(20)	10.9(13)
	Tm 5%	220(30)	6.9(3)	117(20)	8.5(5)	320(50)	6.1(3)	133(10)	9.6(2)	100(20)	9.0(6)
	Tm 10%	305(50)	6.2(3)	272(50)	6.4(4)	653(200)	4.8(5)	312(20)	7.2(2)	174(10)	7.5(1)
Bulk Samples	Er 2%	219(20)	8.1(2)	113(20)	10.1(6)	301(50)	7.3(4)	— ^d	— ^d	— ^d	— ^d
	Er 5%	292(40)	7.4(3)	219(20)	8.1(2)	474(70)	6.3(3)	— ^d	— ^d	— ^d	— ^d
	Er 10%	402(60)	6.6(3)	— ^c	— ^c	— ^c	— ^c	— ^d	— ^d	— ^d	— ^d
	Tm 2%	164(30)	7.6(5)	146(20)	7.9(4)	170(20)	7.5(3)	— ^d	— ^d	— ^d	— ^d
	Tm 5%	234(40)	6.7(4)	142(20)	8.0(4)	376(50)	5.8(3)	— ^d	— ^d	— ^d	— ^d
	Tm 10%	321(50)	6.1(3)	262(100)	6.5(8)	621(250)	4.9(7)	— ^d	— ^d	— ^d	— ^d

^aThe span of the dipolar shift tensor is defined⁴⁰ as $\Delta_{\text{aniso}} = |\delta_{\text{zz}} - \delta_{\text{iso}}|$, where δ_{iso} is the isotropic shift, and δ_{zz} is the principal value of the dipolar shift tensor that gives the largest absolute difference from δ_{iso} . ^b $\langle R \rangle$ is the expectation value of the distance between the nucleus of interest and a point charge centered at the Ln³⁺ position. ^cLow resolution of this spectrum prevented an accurate measurement of the DSA. ^dThe bulk samples do not contain ¹H or ¹³C nuclei.

Coupling of the spin and orbital angular momenta requires that the system be described by the total angular momentum quantum number, J , rather than merely the spin quantum number, S . Furthermore, this coupling causes the isotropic lanthanide g -factor (g_J) to be a function of L , S , and J , as follows: $g_J = 1 + \frac{J(J+1) - L(L+1) + S(S+1)}{2J(J+1)}$.¹⁴ As such, to measure nuclear...Ln³⁺ distances in the current work, we have used a modified version of **Eq. 3.2**, shown below:

$$|\Delta_{\text{aniso}}| = \frac{(\mu_0 \mu_B) g_J^2 \cdot J(J+1)}{\langle R \rangle^3 k_B T} \cdot 10^6 \quad (3.2)$$

where we have treated the lanthanide as a free ion (*i.e.*, ignored ligand-field effects, which is reasonable as they are typically less than 100 cm⁻¹), replaced the isotropic g -tensor value (g) with g_J , and used the total angular momentum quantum number, J , in place of S .

The $\langle R \rangle$ values calculated from the experimental ¹⁹F Δ_{aniso} data correspond to the average distance between ¹⁹F nuclei and the nearest Ln³⁺ site (**Table 3.3**). For the 2% doped samples, the observed Δ_{aniso} values are the smallest of all of the doped materials; using **Eq. 3.2**, these values correspond to $\langle R \rangle \approx 8$ Å. At higher dopant levels, there are more Ln³⁺ ions in the sample; hence, the average distance between the ¹⁹F nuclei and Ln³⁺ ions is smaller (with 10 at.% dopant, $\langle R \rangle \approx 6$ Å). The shortest $\langle R \rangle$ measured for all of the samples (6.1 Å) is much longer than the F–Y bond lengths in the crystal structure (*ca.* 2.5 Å),¹³ and longer than the through-space F...Y distances to Y atoms in the second coordination sphere of a F (*ca.* 4-5 Å). This indicates that signal is not observed from ¹⁹F nuclei with Ln³⁺ in the first or second coordination spheres. Such patterns are not observed because of fast nuclear relaxation (*vide infra*). If such sites (with $\langle R \rangle \approx 3$ Å)

were detected, **Eq. 3.2** predicts they would have Δ_{aniso} values of *ca.* 4000 ppm, which would produce SSB manifolds on the order of 5000 ppm wide. Analyses of a 20% Er³⁺-doped sample were attempted, but the resulting S/N and resolution in the ¹⁹F NMR spectra was poor (**Figure B5**), which inhibited an accurate measurement of the ¹⁹F DSA (and prevented the acquisition of any signal from the other nuclei as well). Studying samples with this level of dopant or higher would require much faster MAS to further average the effects of the paramagnetic interaction.

The second effect of the increased dopant level on the spectra of the NCs is to broaden the peaks. Broad peaks are common in the spectra of paramagnetic materials,^{21,44,45} and arise from a combination of (i) fast transverse relaxation (T_2) resulting from a dominant contribution from the unpaired electron relaxation mechanism (T_2^{uc}) and (ii) inhomogeneous broadening due to the influence of the paramagnetic centers on the anisotropic bulk magnetic susceptibility (ABMS) of the sample.^{14,15,46} Given the lack of a substantial pseudocontact shift (*vide supra*), the magnetic susceptibility tensors must be nearly isotropic in the Ln³⁺-doped samples. Paramagnetic lanthanide ions are typically associated with highly anisotropic BMS; however, the ABMS is reduced in cases where the lanthanide ion has a high coordination number.⁴⁷ The lack of a substantial ABMS in the samples in this work is consistent with the Ln³⁺ ions occupying the Y³⁺ sites with 9-fold coordination in NaYF₄ and indicates *homogeneous* doping of the samples (as an inhomogeneous distribution would result in substantial ABMS and corresponding pseudocontact shifts). Therefore, the observed broadening in the ¹⁹F SSNMR spectra is predominantly influenced by fast T_2 relaxation, which becomes more efficient as the number of paramagnetic centres increases.

The peaks in the spectra of the Tm-doped samples (**Figure 3.1e-g**) are *broader* than those of the Er-doped materials (**Figure 3.1b-d**), indicating that T_2 relaxation is more efficient in the former. The rate of nuclear relaxation resulting from the paramagnetic interaction is primarily dictated by the relaxation of the unpaired electrons.^{14,48} The primary mechanisms of electronic relaxation in solids involve interactions of the electronic magnetic moments with phonons in the lattice; such coupling is stronger when there is increased overlap of the Ln $4f$ orbitals with those of the surrounding host lattice.^{49,50} Despite having stronger lanthanide contraction (which decreases the orbital overlap), the Tm $4f$ orbitals are less shielded by the $5s^2$ and $5p^6$ electrons than those of Er, which produces more efficient electronic relaxation in Tm^{3+} -containing compounds than in those with Er^{3+} .⁵⁰ The NMR peak breadths observed in the current work are consistent with this explanation, as well as studies on other compounds containing these dopants.⁵¹

Given the homogeneous distribution of the dopant ions, the dopant level can be used to calculate an approximate distance between the Ln^{3+} ions with a sphere-packing model (see **Appendix B** for details). Using this analysis, the predicted $\text{Ln}^{3+}\cdots\text{Ln}^{3+}$ distances range between 8.8 and 16.2 Å for 10% and 2%-doped NCs, respectively. For samples with low dopant levels, the average $\text{Ln}^{3+}\cdots^{19}\text{F}$ distances obtained from the SSNMR data (**Table 3.3**) are roughly half of the $\text{Ln}^{3+}\cdots\text{Ln}^{3+}$ distances calculated (as expected for a nucleus located between the lanthanides). However, with higher dopant levels, the average $\text{Ln}^{3+}\cdots^{19}\text{F}$ distances calculated from the SSNMR data become progressively larger relative to the distances calculated from the sphere packing model. For example, for the 10%-doped NCs, the measurement from the SSNMR is *ca.* 0.7×the calculated $\text{Ln}^{3+}\cdots\text{Ln}^{3+}$ value (*i.e.*, the SSNMR results indicate longer distances than are

expected from the sphere packing analysis). This result can be attributed to the fact that, as discussed above, ^{19}F sites with Ln^{3+} ions in their 1st or 2nd coordination spheres are not observed in the ^{19}F NMR spectra, and so the *average* $\text{Ln}^{3+}\cdots^{19}\text{F}$ distances are skewed to slightly higher distances.

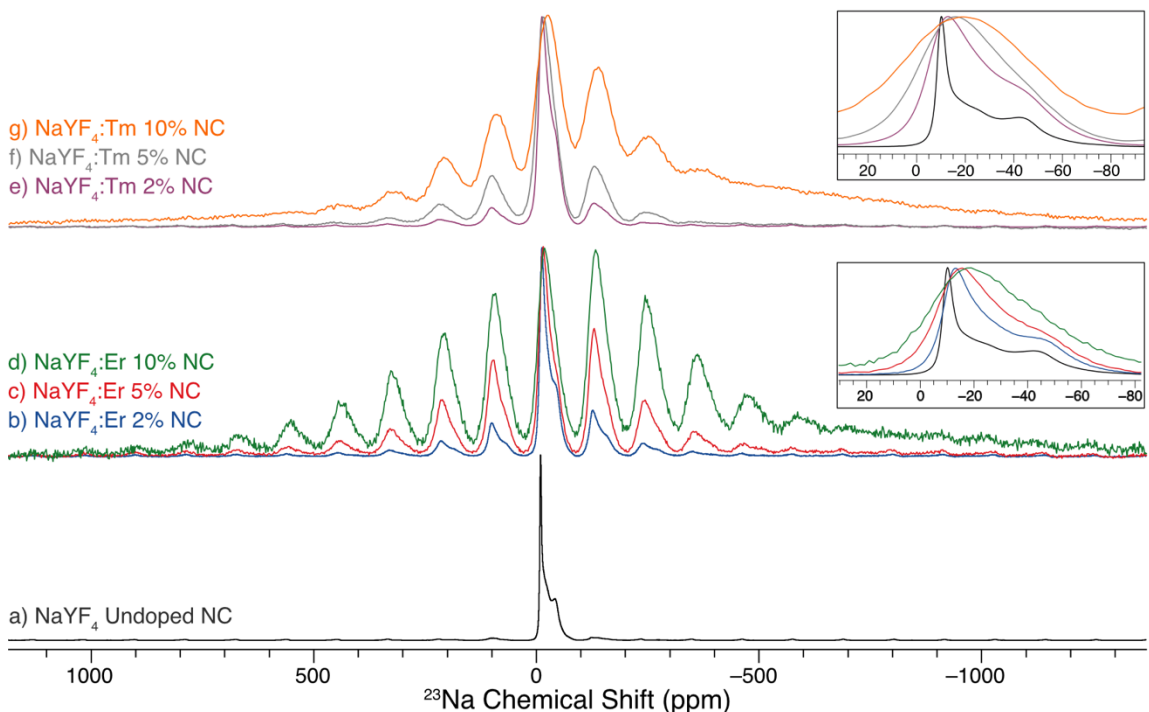


Figure 3.2. $^{23}\text{Na}\{^{19}\text{F}\}$ MAS ($\nu_{\text{rot}} = 12$ kHz) NMR spectra of a) undoped NaYF_4 NCs, b)-d) Er-doped NaYF_4 NCs and e)-g) Tm-doped NaYF_4 NCs. The insets highlight the isotropic features of the spectra.

^{23}Na MAS NMR Experiments. The paramagnetic Ln^{3+} dopants affect the ^{23}Na NMR spectra in a similar way (**Figure 3.2**). Consistent with our previous reports,¹¹ the spectra of the undoped materials have two ^{23}Na features, which correspond to the two crystallographically-distinct Na sites in the crystal structure; however, these sites cannot be independently resolved in the spectra of the doped samples (though the isotropic centerband and associated SSBs are skewed to low frequency, consistent with the presence of the underlying second-order quadrupolar pattern). Samples containing more

dopant ions produce spectra with increasingly broad features and intense SSBs due to DSA. Again, no additional peaks (or paramagnetic shifts) are observed for the doped samples, indicating that the ^{23}Na structural environments are consistent between the undoped and doped materials. Fitting the ^{23}Na NMR spectra is more challenging than the corresponding ^{19}F NMR spectra because the ^{23}Na sites are disordered¹³ and have a distribution of quadrupolar interactions, which decreases the resolution of the quadrupolar patterns and produces higher uncertainties in the measurement of DSA. However, the average $^{23}\text{Na}\cdots\text{Ln}^{3+}$ distances (**Table 3.3**) are similar to the $^{19}\text{F}\cdots\text{Ln}^{3+}$ values and support the measurements made from the ^{19}F NMR spectra.

^{19}F - ^{89}Y CP/MAS NMR Experiments. The ^{19}F - ^{89}Y CP/MAS ($\nu_{\text{rot}} = 5$ kHz) NMR spectra of the NC samples (**Figure 3.3**) are dominated by a single peak at $-75(5)$ ppm. This shift is the same for the undoped and doped samples (*i.e.*, there are no paramagnetic-induced shifts), and matches our previously published results.¹¹ The paramagnetic effects of the dopants on the sideband intensities and peak breadths are much less pronounced in the ^{89}Y NMR spectra than in the ^{19}F and ^{23}Na NMR spectra. While the strength of the pseudocontact interaction does not depend on the identity of the observed nucleus,¹⁴ DSA produces less intense sidebands in the spectra of nuclei with lower gyromagnetic ratios (*e.g.*, ^{89}Y).³⁹ The transverse nuclear relaxation from the unpaired electron relaxation mechanism, T_2^{uc} , is proportional to the square of the gyromagnetic ratio of the nucleus (γ_{I}^2);¹⁴ thus, the effects of the dopants on nuclear relaxation (and the associated peak broadening) are smaller for ^{89}Y than ^{19}F (by a factor of 365). Finally, the S/N in the ^{89}Y spectra decreases with increasing dopant level, as observed for all other nuclides discussed above. Here, lower S/N primarily results from decreased CP efficiency from

the presence of the paramagnetic dopants (the predominant effect is the reduction of the ^{19}F and ^{89}Y spin-lattice relaxation times in the rotating frame, $T_{1\rho}(^{19}\text{F})$ and $T_{1\rho}(^{89}\text{Y})$, respectively),^{14,52,53} but may also indicate fewer ^{89}Y sites (e.g., due to replacement by Ln^{3+} through substitutional doping).

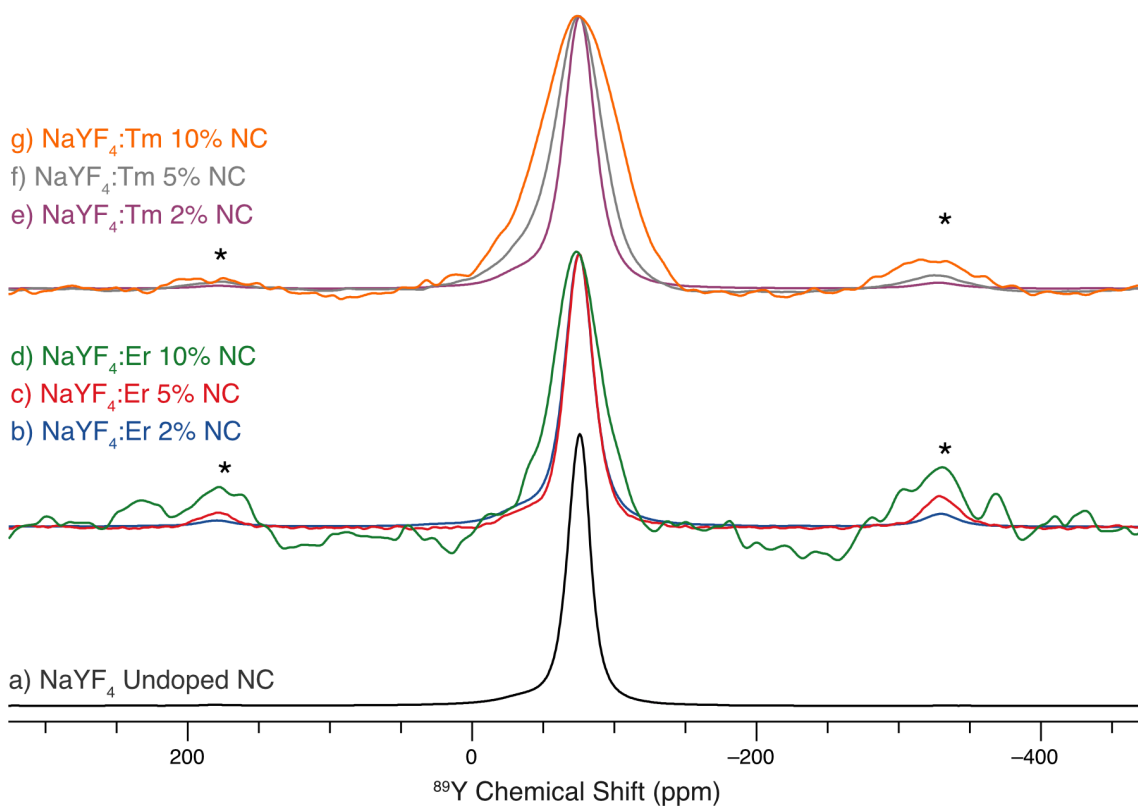


Figure 3.3. ^{19}F - ^{89}Y CP/MAS ($\nu_{\text{rot}} = 5$ kHz) NMR spectra of a) undoped NaYF_4 NCs, b)-d) Er-doped NaYF_4 NCs and e)-g) Tm-doped NaYF_4 NCs. Percentages indicate the at.% Ln^{3+} dopant present in each sample. Asterisks denote spinning sidebands.

3.3.6 NC Surfaces

As we demonstrated previously,¹¹ the NaYF_4 NCs produced using the synthetic method proposed by Li *et al.*⁵⁴ have an oleate surfactant bound to their surfaces, bound to their surfaces. The rest of the NC structure is entirely inorganic and does not contain ^1H or ^{13}C nuclei. As such, direct-excitation ^1H and ^{13}C NMR experiments, as well as CP

experiments involving these nuclei, can selectively probe the nuclear environments on and near the surfaces of the particles.

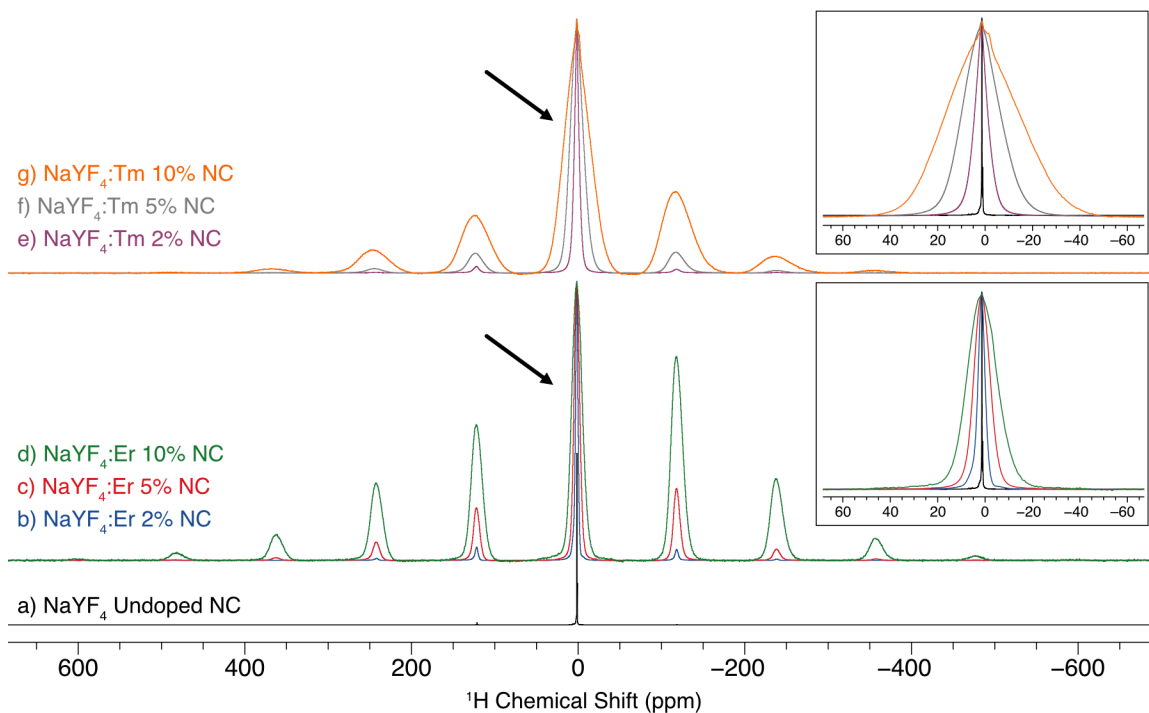


Figure 3.4. ^1H UFMAS ($\nu_{\text{rot}} = 60$ kHz) NMR spectra of a) undoped 19 nm NaYF_4 NCs, b)-d) Er-doped NaYF_4 NCs and e)-g) Tm-doped NaYF_4 NCs. Percentages indicate the at.% Ln^{3+} dopant present in each sample. Arrows indicate the isotropic peaks; all other features in the spectra are spinning sidebands. The insets highlight the isotropic features of the spectra.

^1H UFMAS NMR Experiments. The ^1H UFMAS ($\nu_{\text{rot}} = 60$ kHz) NMR spectra of the doped-NCs (**Figure 3.4**) each have a broad isotropic feature flanked by a manifold of SSBs. As with the ^{19}F results, the appearances of these spectra are strongly affected by interactions of protons with the paramagnetic centres in the sample, which produce broad isotropic peaks and increasingly intense SSBs. Even with fast MAS ($\nu_{\text{rot}} = 60$ kHz) the resolution in these spectra is insufficient to identify individual ^1H environments from oleic acid (as is possible with the spectrum of the undoped material, **Figure 3.4a and Figure B6**). There are some sharper features visible in the spectra of the doped materials

(**Figure 3.4 inset**), which may result from residual starting materials, *e.g.*, trifluoroacetate (*vide infra*).

The SSBs in these spectra can be analyzed to determine the expectation value of the internuclear $^1\text{H}\cdots\text{Ln}^{3+}$ distances using the same method described above for the ^{19}F and ^{23}Na NMR spectra. The results of this analysis (**Table 3.3**) show that Ln^{3+} dopants are, on average, within 10.9(4) Å of the ^1H nuclei in the 2%-doped samples, and the expectation value decreases to 7.2(2) Å for the 10%-doped samples. Such short distances indicate that Ln^{3+} dopants must be within close proximity of the surface of the structure.

Our NMR data provide constraints on the orientations of the oleates at the surfaces of the NCs. If the oleate chains point away from the surface of the NCs, the furthest ^1H in the kinked alkyl chain would be roughly 18 Å from the surface of the NC; however, our NMR data suggest much shorter average $^1\text{H}\cdots\text{Ln}^{3+}$ distances. There are two possible explanations for this observation: (i) the oleates could fold toward the surface of the NC resulting in more of the alkyl chain being closer to the surface, or (ii) they could stretch out and interact with Ln^{3+} ions in a neighboring NC. The latter possibility is supported by the inter-NC distances of $20 \text{ Å} \pm 4.6 \text{ Å}$ obtained from TEM images. While efficient spin-diffusion between the ^1H nuclei in the chain could influence the measured $^1\text{H}\cdots\text{Ln}^{3+}$ distances, the values measured are consistent with those obtained from the ^{13}C data (*vide infra*), where spin-diffusion should not have a substantial effect.

^{13}C MAS NMR Experiments. The $^{13}\text{C}\{^1\text{H}\}$ MAS ($\nu_{\text{rot}} = 12 \text{ kHz}$) spectra of the NC samples are shown in **Figure 3.5** (*N.B.* ^1H - ^{13}C CP/MAS experiments are affected by the presence of paramagnetic centers, *vide supra*). The most intense features in all of these spectra are between 0 ppm and 64 ppm, which correspond to the oleic acid chains on the

surface of the molecules.¹¹ A low intensity feature from the alkene functional group in the oleates is only present in the spectrum of the 2 at.% Er-doped NC sample (see **Figure 3.5, left inset**). For samples with more dopant ions, this peak is broadened beyond detection, providing further evidence of the presence of dopant ions at or near the surface of the particles. There is an additional sharp peak in all of the ^{13}C spectra at *ca.* 112 ppm, whose breadth remains constant regardless of the dopant level. This feature corresponds to an impurity of trifluoroacetate.⁵⁵

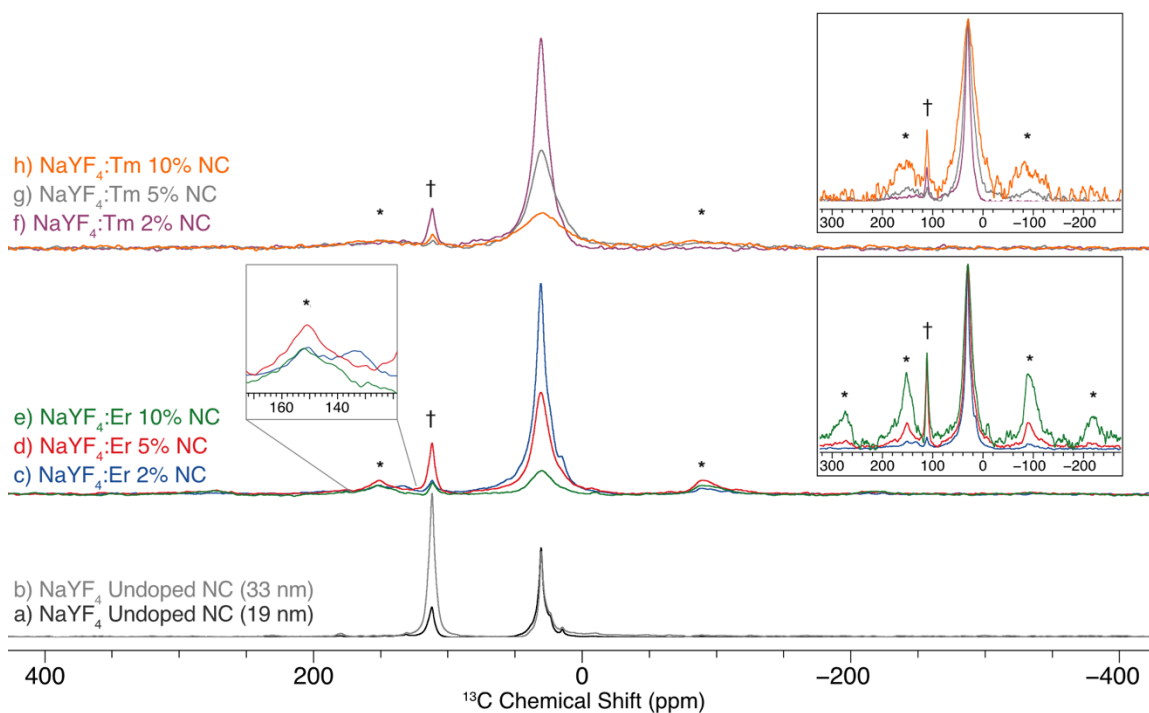


Figure 3.5. $^{13}\text{C}\{^1\text{H}\}$ MAS ($v_{\text{rot}} = 12$ kHz) NMR spectra of a) 19 nm and b) 33 nm undoped NaYF_4 NCs, c)-e) Er-doped NaYF_4 NCs and f)-h) Tm-doped NaYF_4 NCs. Percentages indicate the at.% Ln^{3+} dopant present in each sample. Asterisks denote spinning sidebands. Daggers indicate signal from an impurity of trifluoroacetate, as discussed in the text. The insets on the right highlight the difference in relative intensity of the SSBs, and are scaled such that the intensities of the isotropic peaks are the same. The inset on the left contains an expansion of the alkene region of the spectra of the Er-doped samples.

Like the ^1H results, the ^{13}C peaks are increasingly broadened in the spectra of samples with higher dopant levels. The presence of the paramagnetic dopants affects the

DSA of the ^{13}C nuclei, and the resulting intensities of the SSBs in the ^{13}C spectra (**Figure 3.5, right insets**) can be analyzed to yield average $^{13}\text{C}\cdots\text{Ln}^{3+}$ distances. As seen in **Table 3.3**, these values are consistent with those obtained from the ^1H data, and suggest that on average, the ^{13}C nuclei in the surfactant are between 7.5(1) and 11.2(9) Å of a Ln^{3+} dopant.

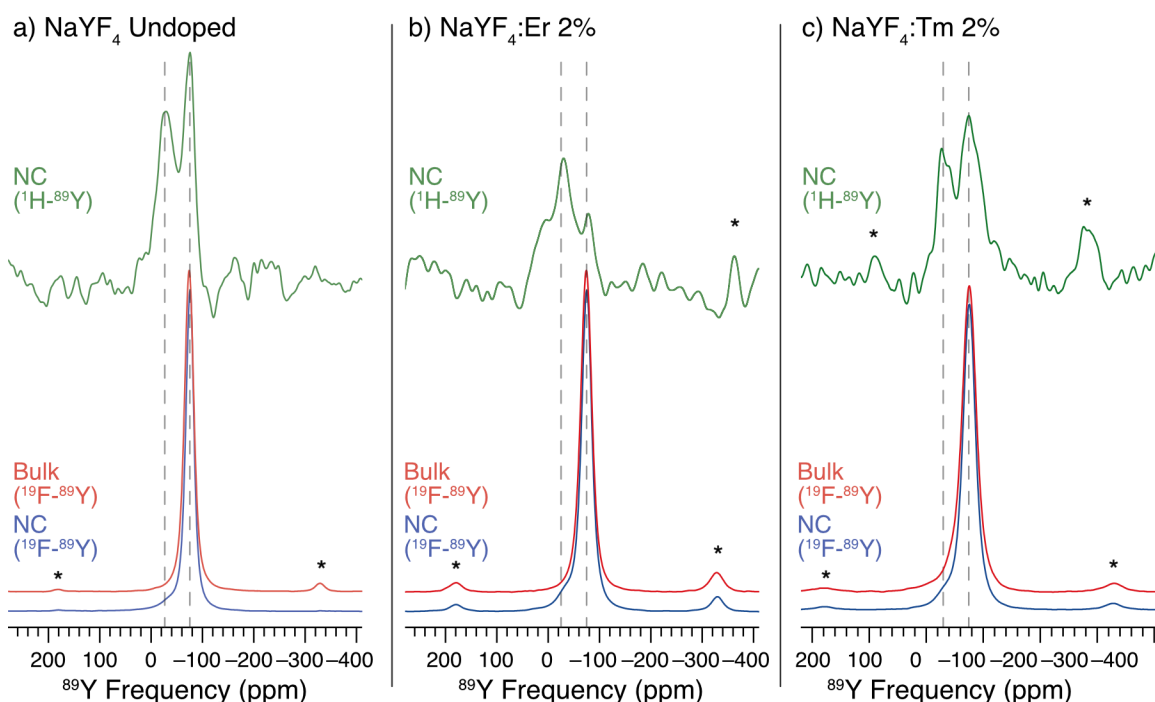


Figure 3.6. ^1H - ^{89}Y CP/MAS ($v_{\text{rot}} = 5$ kHz) NMR spectra (green, top row) of NC samples and ^{19}F - ^{89}Y CP/MAS ($v_{\text{rot}} = 5$ kHz) NMR spectra of bulk samples (red, middle row) and NC samples (blue, bottom row). Each column contains spectra of samples with the same amount of dopant: a) undoped samples, b) with 2 at.% Er^{3+} dopant, c) with 2 at.% Tm^{3+} dopant. Dashed lines indicate features that are present in the spectra of the NC samples.

^1H - ^{89}Y CP/MAS NMR Experiments. A comparison of the ^{19}F - ^{89}Y CP/MAS NMR spectra of the bulk and NC samples (red and blue traces in **Figure 3.6**) reveals that the spectra of the NCs have a second, low-intensity feature at $-42(2)$ ppm that is not present in the spectra of the bulk samples. This feature is much more intense in the ^1H - ^{89}Y CP/MAS NMR spectra of the NCs (green trace in **Figure 3.6**). Since polarization transfer

from ^1H nuclei (which are only present at the surface) occurs to proximate ^{89}Y nuclei, this feature results from yttrium atoms near or at the surface of the NCs, which have a distinct local environments in comparison to those within the deeper interior of the NC, due to surface reconstruction⁵⁶ and the presence of the oleic acid surfactant. Yttrium surface sites that are distinct from the core have been previously observed in these compounds using X-ray photoelectron spectroscopy (XPS),⁵⁷ and the shift to higher frequency in the SSNMR spectra is consistent with results observed for other yttrium fluoride NCs.⁵⁸ The apparent absence of the peak at -42 ppm in the ^{19}F - ^{89}Y CP/MAS NMR spectra of the bulk materials can be explained based on the relative number of ^{89}Y nuclei in the core versus those near the surface. Due to the high surface area of NCs, ^{89}Y nuclei in surface sites constitute a much larger portion of the sample in the NCs than in the bulk materials. As such, surface sites are more easily observed in the ^{89}Y NMR spectra of the NCs than in those of the bulk samples. The ^1H - ^{89}Y CP/MAS NMR spectra of the undoped and 2%-doped samples all have low S/N, despite extensive experimental time (*ca.* 24 hours per experiment). Similar experiments on samples with higher dopant levels were unsuccessful, likely due to decreased CP efficiency resulting from the presence of the paramagnetic ions.

3.3.7 Particle Size effects

In order to exclude variation in particle size as a cause of differences in the spectra of the NaYF_4 materials, three undoped samples were prepared: microcrystalline "bulk" samples (particles $> 2 \mu\text{m}$ in diameter), and two NC samples (17.5 nm and 27.9 nm in diameter, respectively). The ^{19}F MAS, ^{23}Na MAS, and ^{19}F - ^{89}Y CP/MAS NMR spectra of the two undoped NC samples are identical (**Figure 3.7 and Figures S8-S9**),

indicating that a small difference in particle size (*ca.* 10 nm) does not change the structure of the material.

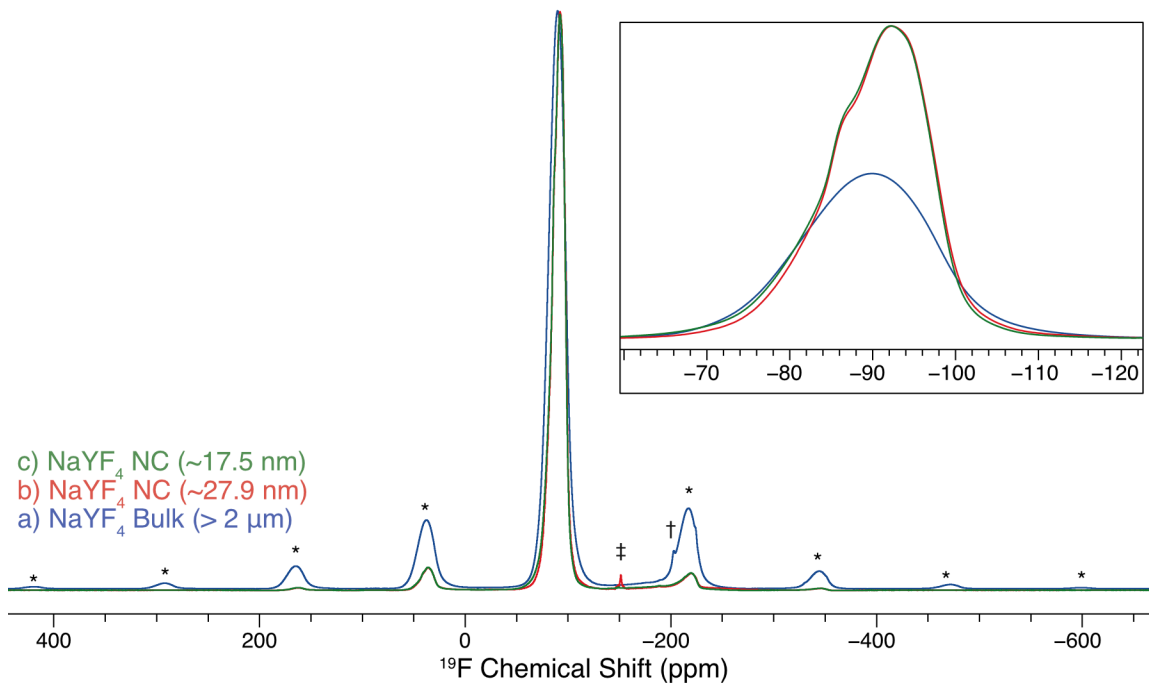


Figure 3.7. ^{19}F UFMAS ($\nu_{\text{rot}} = 60$ kHz) NMR spectra of the undoped NaYF_4 samples with different particle sizes: a) bulk samples ($> 2 \mu\text{m}$), b) NC (33 nm), c) NC (19 nm). Single and double daggers denote peaks from minor NaF and NH_4F impurities, respectively. Asterisks denote spinning sidebands. The insets highlight the isotropic features of the spectra.

In general, the spectral features produced by the bulk material have the same chemical shifts as those of the NCs (suggesting that the bulk material is isostructural with the NC samples). However, the spectra of the microcrystalline particles show subtle differences in the peak breadths and marked differences in the intensities of the SSB manifolds. These differences are most noticeable in the ^{19}F NMR spectra (**Figure 3.7 and inset**), in which only one broad featureless isotropic peak is observed in the spectrum of the bulk material, and the SSBs are more intense than those of the NC samples. The *decreased* resolution in the spectrum of the microcrystalline material relative to those of the NCs is contrary to what is typically observed.^{59,60} Bulk microcrystalline materials

have large core regions and small surface areas in comparison to analogous nanocrystalline materials; as such, the former normally have SSNMR spectra with sharp resonances (corresponding mainly to sites in the core regions), whereas the latter often have broad peaks arising from distributions of chemical shifts (due to the increased ratio of surface to core sites, and the differentiation of surface environments from those in the core due to the presence of defects at the surface, interactions with passivating ligands, or the presence of grain boundaries).

In contrast to the SSNMR data, the PXRD data (**Figure B3**) are consistent with the typical results for NC and microcrystalline samples (*i.e.*, the peak widths in the patterns of the bulk samples are dramatically narrower than those of the NCs). These data also indicate that the microcrystalline particles do not have lower crystallinity than the NC samples; therefore, the broadening in the SSNMR spectra of the bulk samples cannot be attributed to amorphization. However, unlike PXRD, SSNMR is sensitive to *local* disorder; therefore, the additional peak broadening and distinct SSB manifolds observed in the spectra of the bulk material may result from local defect sites in the microcrystals that produce a distribution of CSAs.

Defect sites are often associated with increased mobility at the molecular level, which can influence nuclear relaxation (*i.e.*, change the longitudinal, T_1 , and transverse, T_2 , relaxation time constants of a material).^{61,62} The relaxative processes in the bulk and NC samples are different, as the longitudinal relaxation in the bulk material ($T_{1,\text{bulk}}(^{19}\text{F}) \approx 850$ ms) is much more efficient than in the NCs ($T_{1,\text{NC}}(^{19}\text{F}) \approx 10$ s) (*N.B.* this result is also contrary to what is typically observed in comparisons of isostructural NC and bulk materials). The effective $T_2(^{19}\text{F})$ values measured under MAS ($\nu_{\text{rot}} = 60$ kHz) are far more

similar to each other (3.7 and 3.9 ms for the bulk and NC samples, respectively). Based on these values, T_2 makes an insignificant contribution to the observed peak breadths in the spectra (*i.e.*, for all of the samples $\Delta\nu_{1/2} \approx (2\pi T_2)^{-1} \approx 40$ Hz) and cannot explain the additional broadening observed in the spectrum of the bulk sample (on the order of kHz). As such, the low resolution produced by the bulk material must result from inhomogeneous broadening from a distribution of environments (*vide supra*).

TEM images of the bulk samples (**Figure B2**) also support the presence of defect sites in the bulk materials, as the particles have an inhomogeneous distribution of crystal sizes, morphologies, and irregular surface facets, all of which are associated with structures containing a high number of defect sites.^{62,63} Since the synthesis of the bulk material is distinct from that of the NCs, perhaps the mechanism by which the NCs are formed results in fewer defect sites within the crystal.

Incorporation of the dopant into the bulk samples. Since the bulk and NC samples are produced using different syntheses (see **Experimental Methods section**), it is possible that the Ln^{3+} ions incorporate differently into the two classes of samples. As such, bulk samples (*i.e.*, particle size $> 2 \mu\text{m}$) containing the same quantities of Er^{3+} and Tm^{3+} dopants as the NC samples were prepared and analyzed. ICP-MS results (**Table 3.2**) confirm that the dopant levels of the bulk and NC samples are identical. The ^{19}F , $^{23}\text{Na}\{^{19}\text{F}\}$, and ^{19}F - ^{89}Y SSNMR spectra of the Ln^{3+} -doped bulk samples are also remarkably similar to those of the Ln^{3+} -doped NC samples (**Figure B9-Figure B14**). For all three nuclei, the spectra of the doped materials have features with the same chemical shifts and SSB manifolds regardless of the particle size. Similar to the undoped materials discussed above, the spectra of the doped bulk materials have slightly more intense

sidebands and broader resonances than those of the NCs. These may result from a different distribution of CSAs in these samples (as noted for the undoped materials, *vide supra*), or slightly different average Ln³⁺···nuclear distances. For example, in the ¹⁹F NMR spectra, the Δ_{aniso} values for the bulk samples are within 50 ppm of those in the NCs, which correspond to changes in the average ¹⁹F···Ln³⁺ distance of < 0.3 Å (see **Table 3.3**). Nevertheless, these SSNMR results demonstrate that the incorporation of the dopant ions into the bulk materials produces doped materials that are essentially isostructural with their NC counterparts, even though they were prepared with very different synthesis methods.

3.4 Conclusions

Our multinuclear (¹⁹F, ²³Na, ⁸⁹Y, ¹H, ¹³C) SSNMR results demonstrate that the incorporation of paramagnetic Er³⁺ and Tm³⁺ dopants into NaYF₄ NCs at low dopant levels (2-10 at.%) does not appreciably change their molecular-level structures relative to the undoped diamagnetic materials. These results are consistent with dopants occupying the 9-coordinate Y sites in the structure through substitutional doping, since interstitial doping would cause larger changes in the local structure and would be reflected in substantial differences in the NMR spectra of the two classes of samples. The presence of paramagnetic lanthanides affects all of the NMR spectra by producing intense spinning sidebands (which result from dipolar shift anisotropy, DSA) and peak broadening (primarily from increased *T*₂ relaxation due to the electron relaxation mechanism). The lack of any large paramagnetic shifts indicates that the unpaired spin density is localized close to the lanthanide ions, and that the ABMS is small in these samples. Based on all of these results, the dopant ions are *homogeneously* dispersed throughout the NCs, in both

the core and surface regions. While there is evidence for a gradient of dopant ions between the core and surface in NaYF₄ samples containing larger Ln³⁺ dopants,^{64,65} our results contradict that model for the samples in the current study. Homogeneous doping is more likely for the lanthanides discussed herein because of the similarity between the ionic radii of the dopants (Er³⁺ or Tm³⁺) and Y³⁺.

Finally, we have shown that the long-range structure of NaYF₄ is consistent between nanocrystalline and microcrystalline particles, and that the dopants incorporate into the two classes of particles in the same way. Our NMR experiments show subtle, yet surprising differences in the SSB intensities and isotropic peak breadths in spectra of the bulk material relative to those of the NCs, contrary to what is typically observed. The appearances of these spectra can be explained by a wider distribution of distinct chemical environments in the bulk material (and associated distribution of CSA), which result from an increase in the number of defect sites in the bulk relative to the NC.

We have demonstrated that multinuclear SSNMR can be applied to the study of paramagnetically-doped NaYF₄ materials, and provide molecular level information on the structural effects of dopants. The SSNMR methods used in this work can be applied to samples containing other lanthanides, as well as different host materials, and may provide insight into the structural differences that produce either homogeneous or inhomogeneous dopant distributions. This information is useful for probing the molecular-level origins of upconversion efficiency, and aids in the systematic modification and design of new nanomaterials with improved quantum yields.

3.5 References

- (1) Sun, L.-D.; Dong, H.; Zhang, P.-Z.; Yan, C.-H. *Annu. Rev. Phys. Chem.* **2015**, *66*, 619–642.
- (2) Haase, M.; Schäfer, H. *Angew. Chemie Int. Ed.* **2011**, *50*, 5808–5829.
- (3) Wang, F.; Liu, X. *Chem. Soc. Rev.* **2009**, *38*, 976–989.
- (4) Zheng, W.; Huang, P.; Tu, D.; Ma, E.; Zhu, H.; Chen, X. *Chem. Soc. Rev.* **2015**, *44*, 1379–1415.
- (5) Chen, C.; Li, C.; Shi, Z. *Adv. Sci.* **2016**, *3*, 1600029.
- (6) Bünzli, J.-C. G.; Eliseeva, S. V. *J. Rare Earths* **2010**, *28*, 824–842.
- (7) Boyer, J.-C.; van Veggel, F. C. J. M. *Nanoscale* **2010**, *2*, 1417–1419.
- (8) Kar, A.; Kundu, S.; Patra, A. *ChemPhysChem* **2015**, *16*, 505–521.
- (9) Sommerdijk, J. L. *J. Lumin.* **1973**, *8*, 126–130.
- (10) Liu, X.; Deng, R.; Zhang, Y.; Wang, Y.; Chang, H.; Huang, L.; Liu, X. *Chem. Soc. Rev.* **2015**, *44*, 1479–1508.
- (11) Hirsh, D. A.; Johnson, N. J. J.; Van Veggel, F. C. J. M.; Schurko, R. W. *Chem. Mater.* **2015**, *27*, 6495–6507.
- (12) Arnold, A. A.; Terskikh, V.; Li, Q. Y.; Naccache, R.; Marcotte, I.; Capobianco, J. A. *J. Phys. Chem. C* **2013**, *117*, 25733–25741.
- (13) Krämer, K. W.; Biner, D.; Frei, G.; Güdel, H. U.; Hehlen, M. P.; Lüthi, S. R. *Chem. Mater.* **2004**, *16*, 1244–1251.
- (14) Bertini, Ivano; Luchinat, Claudio; Parigi, Giacomo; Ravera, E. *NMR of Paramagnetic Molecules. Applications to Metalloproteins and Models.*; 2016.
- (15) Pintacuda, G.; Kervern, G. In *Modern NMR Methodology*; Heise, H., Matthews, S., Eds.; Springer Berlin Heidelberg: Berlin, Heidelberg, **2013**; pp 157–200.
- (16) Kaupp, M.; Köhler, F. H. *Coord. Chem. Rev.* **2009**, *253*, 2376–2386.
- (17) Bertini, I.; Luchinat, C.; Parigi, G. *Prog. Nucl. Magn. Reson. Spectrosc.* **2002**, *40*, 249–273.
- (18) Wickramasinghe, N. P.; Shaibat, M.; Ishii, Y. *J. Am. Chem. Soc.* **2005**, *127*, 5796–5797.
- (19) Parthasarathy, S.; Nishiyama, Y.; Ishii, Y. *Acc. Chem. Res.* **2013**, *46*, 2127–2135.
- (20) Chacko, V. P.; Ganapathy, S.; Bryant, R. G. *J. Am. Chem. Soc.* **1983**, *105*, 5491–5492.
- (21) Nayeem, A.; Yesinowski, J. P. *J. Chem. Phys.* **1988**, *89*, 4600.
- (22) Grey, C. P.; Dobson, C. M.; Cheetham, A. K.; Jakeman, R. J. B. *J. Am. Chem. Soc.* **1989**, *111*, 505–511.
- (23) Grey, C. P.; Smith, M. E.; Cheetham, A. K.; Dobson, C. M.; Dupree, R. *J. Am. Chem. Soc.* **1990**, *112*, 4670–4675.
- (24) Bakhmutov, V. I. *Chem. Rev.* **2011**, *111*, 530–562.
- (25) Heise, H.; Köhler, F. H.; Xie, X. *J. Magn. Reson.* **2001**, *150*, 198–206.
- (26) Bertini, I.; Luchinat, C.; Parigi, G.; Pierattelli, R. *Dalt. Trans.* **2008**, 3782.
- (27) Knight, M. J.; Felli, I. C.; Pierattelli, R.; Emsley, L.; Pintacuda, G. *Acc. Chem. Res.* **2013**, *46*, 2108–2116.
- (28) Bhaumik, A.; Luchinat, C.; Parigi, G.; Ravera, E.; Rinaldelli, M. *CrystEngComm* **2013**, *15*, 8639–8656.
- (29) Nitsche, C.; Otting, G. *Prog. Nucl. Magn. Reson. Spectrosc.* **2017**, *98–99*, 20–49.

- (30) Li, Z.; Zhang, Y. *Nanotechnology* **2008**, *19*, 345606.
- (31) Lin, H.; Xu, D.; Teng, D.; Yang, S.; Zhang, Y. *New J. Chem.* **2015**, *39*, 2565–2572.
- (32) Bennett, A. E.; Rienstra, C. M.; Auger, M.; Lakshmi, K. V.; Griffin, R. G. *J. Chem. Phys.* **1995**, *103*, 6951–6958.
- (33) Peersen, O.; Wu, X.; Smith, S. *J. Magn. Reson.* **1994**, *106*, 127–131.
- (34) Peersen, O. B.; Wu, X. L.; Kustanovich, I.; Smith, S. O. *J. Magn. Reson.* **1993**, *104*, 334–339.
- (35) Metz, G.; Wu, X. L.; Smith, S. O. *J. Magn. Reson.* **1994**, *110*, 219–227.
- (36) Sobolev, B. P.; Mineev, D. A.; Pashutin, V. P. *Dokl. Akad. Nauk SSR* **1963**, *150*, 791–794.
- (37) Bertini, I.; Janik, M. B. L.; Lee, Y.-M.; Luchinat, C.; Rosato, A. *J. Am. Chem. Soc.* **2001**, *123*, 4181–4188.
- (38) Bertmer, M. *Solid State Nucl. Magn. Reson.* **2017**, *81*, 1–7.
- (39) Herzfeld, J.; Berger, A. E. *J. Chem. Phys.* **1980**, *73*, 6021–6030.
- (40) Antzutkin, O. N.; Lee, Y. K.; Levitt, M. H. *J. Magn. Reson.* **1998**, *135*, 144–155.
- (41) Wickramasinghe, N. P.; Shaibat, M. A.; Ishii, Y. *J. Phys. Chem. B* **2007**, *111*, 9693–9696.
- (42) Wickramasinghe, N. P.; Ishii, Y. *J. Magn. Reson.* **2006**, *181*, 233–243.
- (43) Golding, R. M.; Pascual, R. O.; McGarvey, B. R. *J. Magn. Reson.* **1982**, *46*, 30–42.
- (44) Köhler, F. H.; Storcheva, O. *Inorg. Chem.* **2015**, *54*, 6801–6806.
- (45) Kubo, A.; Spaniol, T. P.; Terao, T. *J. Magn. Reson.* **1998**, *133*, 330–340.
- (46) Nadaud, P. S.; Helmus, J. J.; Kall, S. L.; Jaroniec, C. P. *J. Am. Chem. Soc.* **2009**, *131*, 8108–8120.
- (47) Mironov, V. S.; Galyametdinov, Y. G.; Ceulemans, A.; Görrler-Walrand, C.; Binnemans, K. *J. Chem. Phys.* **2002**, *116*, 4673–4685.
- (48) Vega, A. J.; Fiat, D. *Mol. Phys.* **1976**, *31*, 347–355.
- (49) Bertini, I.; Martini, G.; Luchinat, C. In *Handbook of Electron Spin Resonance*; Poole, C. P., Farach, H. A., Eds.; New York, NY, 1999; pp 61–320.
- (50) Meijerink, A.; Blasse, G.; Sytsma, J.; de Mello Donega, C.; Ellens, A. *Acta Phys. Pol. A* **1996**, *90*, 109–119.
- (51) Zhang, Y.; Krylov, D.; Rosenkranz, M.; Schiemenz, S.; Popov, A. A. *Chem. Sci.* **2015**, *6*, 2328–2341.
- (52) Peng, W. K.; Samoson, A.; Kitagawa, M. *Chem. Phys. Lett.* **2008**, *460*, 531–535.
- (53) Konig, S. H. *J. Magn. Reson.* **1982**, *47*, 441–453.
- (54) Li, Z.; Zhang, Y.; Jiang, S. *Adv. Mater.* **2008**, *20*, 4765–4769.
- (55) Hasegawa, M.; Isogai, A.; Onabe, F.; Usuda, M. *J. Appl. Polym. Sci.* **1992**, *45*, 1857–1863.
- (56) Berrettini, M. G.; Braun, G.; Hu, J. G.; Strouse, G. F. *J. Am. Chem. Soc.* **2004**, *126*, 7063–7070.
- (57) Pichaandi, J.; Das, G. K.; Johnson, N. J. J.; Regier, T.; van Veggel, F. C. J. M. *J. Phys. Chem. C* **2014**, *118*, 21639–21646.
- (58) Lucier, B. E. G.; Johnston, K. E.; Arnold, D. C.; Lemyre, J.; Beaupré, A.; Blanchette, M.; Ritcey, A. M.; Schurko, R. W. *J. Phys. Chem. C* **2014**, *118*, 1213–1228.

- (59) Cadars, S.; Smith, B. J.; Epping, J. D.; Acharya, S.; Belman, N.; Golan, Y.; Chmelka, B. F. *Phys. Rev. Lett.* **2009**, *103*, 136802.
- (60) Lovingood, D. D.; Achey, R.; Paravastu, A. K.; Strouse, G. F. *J. Am. Chem. Soc.* **2010**, *132*, 3344–3354.
- (61) Berendt, R. T.; Sperger, D. M.; Munson, E. J.; Isbester, P. K. *Trends Anal. Chem.* **2006**, *25*, 977–984.
- (62) Dempah, K. E.; Lubach, J. W.; Munson, E. J. *Mol. Pharm.* **2017**, *14*, 856–865.
- (63) Lubach, J. W.; Xu, D.; Segmuller, B. E.; Munson, E. J. *J. Pharm. Sci.* **2007**, *96*, 777–787.
- (64) Dong, C.; Pichaandi, J.; Regier, T.; van Veggel, F. C. J. M. *J. Phys. Chem. C* **2011**, *115*, 15950–15958.
- (65) Xu, X.; Clarke, C.; Ma, C.; Casillas, G.; Das, M.; Guan, M.; Liu, D.; Wang, L.; Tadich, A.; Du, Y.; Ton-That, C.; Jin, D. *Nanoscale* **2017**, *9*, 7719–7726.

Chapter 4: Multinuclear Solid-State NMR as a Probe of the Molecular-Level Structure in Rare Earth-Doped Yttrium Fluoride Nanoparticles

4.1 Introduction

Inorganic materials containing lanthanide (Ln) elements have unique magnetic, electronic, and optical properties that have made them a fertile area of materials science research.¹ As such, these compounds have been used to develop numerous advanced materials, including magnets,²⁻⁴ catalysts,^{5,6} phosphors,⁷⁻¹⁰ and fuel cells.¹¹⁻¹³ While Sc and Y are not lanthanides, their ionic sizes are similar to those of the lanthanides (**Table 4.1**), they exhibit similar chemistry, and are found in nature in the same raw ores. Collectively, these compounds are called the rare-earth elements (RE = Ln, Y, Sc).

Table 4.1. Ionic radii of different RE ions with various coordination numbers as reported by Shannon *et al.*⁶³

RE Ion	Coordination Number			
	6	7	8 ^a	9
Sc ³⁺	0.75	– ^b	0.87	– ^b
Er ³⁺	0.89	0.95	1.00	1.06
Y ³⁺	0.90	0.96	1.02	1.08
Eu ³⁺	0.95	1.01	1.07	1.12
Eu ²⁺	1.17	1.20	1.25	1.30

^aThe (H₃O)Y₃F₁₀•xH₂O structure contains 8-coordinate Y sites. ^bData not available.

RE-containing microcrystalline materials (both natural and synthetic) have been known for over two centuries. More recently, there have been increased research efforts focusing on the synthesis and preparation of *nanoscale* RE-containing materials.

Nanoparticles (NPs, sometimes called nanocrystals) are of great interest, because of their large surface areas (which are beneficial for surface chemistry and catalysis), and their use in applications where the particle size of microcrystalline materials is prohibitive, such as in colloidal suspensions,¹⁴ or in spatially-restricted applications like photoswitches.¹⁵ Unlike analogous metallic nanoparticles and chalcogenide-based quantum dots, many lanthanide-containing materials have bulk properties (*e.g.*, luminescence wavelength and lifetimes) that are dependent on the identities, local structures, and concentrations of the RE elements.

One common way to incorporate RE-elements into nanomaterials is to use them in small quantities as dopants within a stable host lattice. RE ions are almost always most stable in the +3 oxidation state, and as such, the bonding and coordination about these ions is typically dictated by the relative ionic radii of RE³⁺ ions and atoms of surrounding ligands.¹⁶ Notably, the size of the RE³⁺ ion often determines how the dopant incorporates into a host structure: (i) *substitutionally* (where the RE dopant replaces elements in the host matrix), (ii) *interstitially* (where it occupies positions among the atoms of the host material without displacing them), or (iii) via *inclusion* (where the dopant occupies a pore or channel in the host structure). Dopants can influence the crystal structure, direct the formation of different products, and influence the bulk properties of the material. Even at low dopant levels, small amounts of doped RE³⁺ ions can serve as nucleation sites for the creation of distinct structures and new phases. Often, these consequences are difficult to predict, as they can vary depending on small differences in the size of the RE³⁺ ions, as well as the dopant level and nature of interactions between the RE³⁺ ions and surrounding atoms or ligands.

Nanoparticle syntheses are complex processes, and their outcomes are often determined by slight variations in reaction conditions. Minor changes in the concentrations of reactants, dopant level, reaction time, reaction volume, and/or temperature can produce different products with different particle sizes, crystallinity, and/or molecular structures. Clearly, structural characterization of these materials is essential for ensuring that the syntheses are robust, the desired products are obtained, and is critical for the rational design of novel particles. Often, careful studies of these reactions and the resulting NP structures and morphologies are lacking in the literature.

Previously, we reported the synthesis and characterization of yttrium fluoride NPs.¹⁷⁻²⁰ In these studies, we applied transmission electron microscopy (TEM), powder X-ray diffraction (PXRD), and solid-state NMR spectroscopy (SSNMR) to characterize materials made with YCl_3 and a F^- ion source. One of the surprising discoveries in this previous work was that rather than producing NPs with molecular-level core structure akin to bulk YF_3 , this synthesis produces NPs with the empirical formula $(\text{H}_3\text{O})\text{Y}_3\text{F}_{10}\cdot x\text{H}_2\text{O}$ (hereafter referred to as **YF**) that have a zeolitic structure with two perpendicular channels (**Figure 4.1**). These channels feature pores of *ca.* 5 Å in diameter that are separated by H_3O^+ ions, and each pore contains water molecules. The synthetic mechanism by which these materials are produced was the subject of a previous study.¹⁸ In brief, aqueous F^- ions are added to Y^{3+} ions dispersed in nonionic reverse micelles. As the micelles come into contact with the aqueous phase, they allow F^- ions to react with the Y^{3+} ions, generating nucleation sites of the **YF** structure. As is common for such syntheses, the organic surfactant molecules from the micelles are also present in the final material, likely bound to the surfaces of the particles.¹⁹

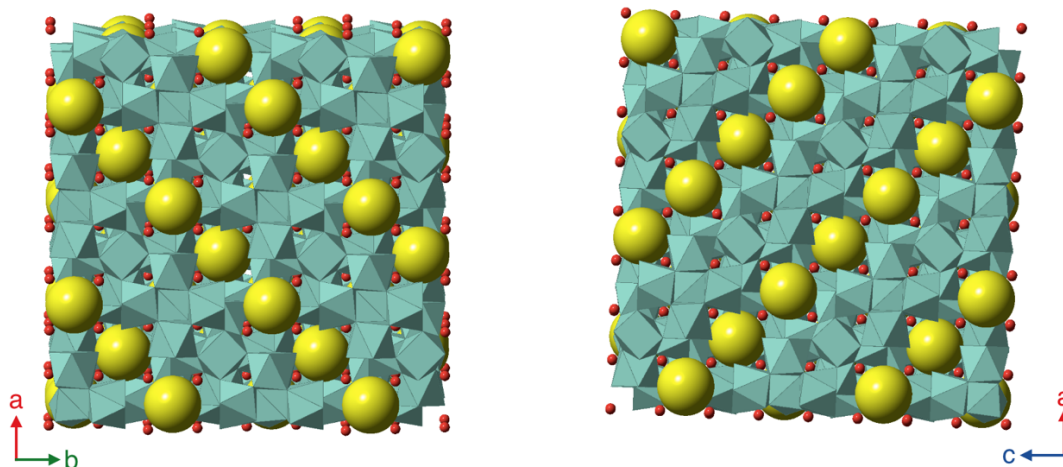


Figure 4.1. Crystal structure of **YF** shown from two views (rotated 90° from one another, as indicated by the crystallographic axes). This representation highlights the void spaces produced by the pores (yellow spheres) in the dual channel structure. The void spaces are connected by H_3O^+ ions, shown as red spheres. The $[\text{Y}_6\text{F}_{32}]^{14-}$ UOA octahedral-like building units are represented by green polyhedra.

In the current work, we expand on the previous studies of this synthesis to include reactions containing Sc^{3+} , Er^{3+} , and Eu^{3+} dopants at different concentrations (*i.e.*, by systematically replacing some of the YCl_3 in the synthesis with other $(\text{RE})\text{Cl}_3$ materials). As noted in **Table 4.1**, these ions have different ionic radii that are (i) smaller than (Sc^{3+}), (ii) roughly equal to (Er^{3+}), or (iii) larger than (Eu^{3+}) that of Y^{3+} . As such, these reactions provide insight into the impact of ionic radius on the incorporation of the dopants into the NPs. Through the use of multinuclear (^{19}F , ^{89}Y , ^1H , ^{45}Sc) SSNMR, PXRD, TEM, and EPR methods, the structures of these new materials are probed (including close examination of the homogeneity of the dopant within the core structures), distinct RE^{3+} ion environments are detected, and reaction by-products and impurities are identified. The discovery of numerous by-products serves to illustrate the complexity of the syntheses of this class of NPs, and highlights the great utility of SSNMR, in particular, for the identification of these species. Our results will help improve the understanding of

the mechanisms of dopant incorporation into the YF structure, and aid in increasing the control of the reactions involving these and other RE³⁺ dopants.

4.2 Methods

4.2.1 Chemicals

All chemicals were purchased from Sigma-Aldrich and used as received unless otherwise specified. Aqueous solutions employed in the synthesis of the nanoparticles were prepared with deionized water of nanopure quality (17.8 - 18.2 Mohms resistivity). Yttrium chloride hexahydrate was acquired with a purity of 99.99%, whereas erbium chloride hexahydrate, europium chloride hexahydrate and scandium chloride hexahydrate salts were acquired with purities of 99.9%. Ammonium hydrogen difluoride salt was purchased with purity equal or greater to 98%. ACS certified cyclohexane, supplied by Fisher Scientific, was used for the preparation of the microemulsions.

4.2.2 Synthesis of the Yttrium Fluoride Nanoparticles (YF NPs)

The synthesis of yttrium fluoride NPs was performed with a slight modification of a previously reported method using a reverse microemulsion.¹⁷ The procedure consists of first dissolving 36 g of polyoxyethylene (5) nonylphenyl ether (Igepal® CO-520) and 4 g of sodium bis(2-ethylhexyl) sulfosuccinate (AOT) in 300 mL of cyclohexane with an ultrasonic bath. A 10 mL aliquot of a 400 mM aqueous solution of yttrium chloride hexahydrate and the desired doping salt was then added under magnetic stirring. The desired dopant level was obtained by varying the molar ratio of the Eu, Er, or Sc and Y chlorides in this solution. The total molar concentration was held constant at 400 mM in order to maintain an equivalent amount of reagent from one synthesis to another.

Following the addition of the first aqueous solution, the system was allowed to stabilize

under continuous stirring for one hour to ensure the formation of uniform reverse micelles. Then, a 10 mL aliquot of a 400 mM ammonium hydrogen difluoride aqueous solution was added and the microemulsion was left to stir for one week.

4.2.3 Purification of the Yttrium Fluoride Nanoparticles

NPs were purified by ultrafiltration with a 75 mL Millipore Solvent Resistant Stirred Cell and Ultracel PL-100 membranes (100 kDa NMWL), both provided by Millipore EMD. Microemulsions containing the particles were first transferred to a rotary evaporator and the cyclohexane was completely removed. The resulting viscous mixtures were dispersed in methanol using an ultrasonic bath, passed through the ultrafiltration membrane and rinsed several times within the filtration cell with methanol and under nitrogen pressure of 10 psi. Once washed from excess surfactant, the samples were removed from the cell, dried in a vacuum oven at 80-85 °C overnight and finally cooled to room temperature and stored for further analysis.

4.2.4 Transmission Electron Microscopy (TEM) Experiments

Particle sizes of the prepared samples were determined by transmission electron microscopy (TEM) using the image processing software Image-J. The corresponding TEM images are shown in **Figure C1 and Figure C2**. TEM images were recorded at 80 kV using a JEOL 1230 microscope equipped with an Ultrascan 1000XP high resolution CCD camera. To enable sample deposition, nickel TEM grids were first coated with a thin Formvar film on which a carbon layer was subsequently deposited. Nanoparticle suspensions were then prepared by dispersing 10 mg of purified sample in 10 mL of methanol using an ultrasonic bath. Next, small amounts of chloroform were carefully poured onto the carbon-coated grids to remove the Formvar film. Two drops of

nanoparticle suspension were deposited per grid and these were dried overnight at room temperature before being observed. Mean size values were determined by individually measuring more than two hundred nanoparticles. Edge length was measured for polyhedral nanoparticles, whereas diameter was measured for more spherical ones and length for the 50% europium-doped specifically. The resulting particles sizes are summarized in **Table 4.2**.

Table 4.2. Particle sizes measured using TEM (**Figure C1**).

Sample	Particle Size (nm) ^a
YF	60(3)
YF:Sc10	19(4)
YF:Sc20^b	12(1)
YF:Sc50^b	13(1)
YF:Er5	62(6)
YF:Er10	60(6)
YF:Er20	59(6)
YF:Er50	57(6)
YF:Eu5	60(5)
YF:Eu10	62(4)
YF:Eu20	85(5)
YF:Eu50^b	362(16)

^aValues in parentheses are errors estimated from the FWHM of the particle size distribution obtained with TEM measurements. ^bTEM images show that the majority of the crystals in this sample do not have an octahedral shape.

4.2.5 Solid-State NMR (SSNMR) Experiments

¹H, ¹⁹F, and ⁴⁵Sc SSNMR experiments were conducted using a Bruker Avance II console equipped with a standard-bore $B_0 = 11.7$ T magnet ($\nu_0(^1\text{H}) = 500.13$ MHz, $\nu_0(^{19}\text{F}) = 470.59$ MHz, $\nu_0(^{45}\text{Sc}) = 121.49$ MHz) and a Bruker 1.3 mm HX probe. ⁸⁹Y NMR experiments were performed with a Bruker Avance III HD console, a wide-bore $B_0 = 9.4$ T magnet ($\nu_0(^1\text{H}) = 399.73$ MHz, $\nu_0(^{19}\text{F}) = 376.09$ MHz, $\nu_0(^{89}\text{Y}) = 19.59$ MHz), and a

Varian/Chemagnetics 4mm HXY probe. To prepare samples for SSNMR experiments, materials were ground and packed into 1.3 mm or 4mm o.d. zirconia rotors.

^1H chemical shifts were referenced to tetramethylsilane (TMS, $\delta_{\text{iso}} = 0.0$ ppm) using solid adamantane ($\delta_{\text{iso}} = 1.85$ ppm) as a secondary reference. ^{19}F chemical shifts were referenced to neat $\text{CFCl}_3(\text{l})$ ($\delta_{\text{iso}} = 0.0$ ppm) using neat fluorobenzene(l) ($\text{C}_6\text{H}_5\text{F}$, $\delta_{\text{iso}} = -113.15$ ppm) as a secondary reference. ^{45}Sc chemical shifts were referenced to a 0.2 M solution of ScCl_3 in H_2O ($\delta_{\text{iso}} = 0.0$ ppm). ^{89}Y chemical shifts were referenced to a 1.0 M $\text{YCl}_3(\text{aq})$ solution ($\delta_{\text{iso}} = 0.0$ ppm) using $\text{Y}(\text{NO}_3)_3 \cdot 6\text{H}_2\text{O}(\text{s})$ ($\delta_{\text{iso}} = -53$ ppm) as a secondary reference.

Full details of the experimental parameters used in this work are detailed in **Appendix C (Table C3-Table C5)**. All direct excitation experiments were conducted using a rotor-synchronized Hahn echo sequence: $(\pi/2)_x - \tau_1 - (\pi)_y - \tau_2 - \text{acq}$. For the ^{45}Sc experiments, central-transition selective pulse widths were used, calculated by scaling the non-selective $\pi/2$ pulse length by a factor of $(I + 1/2)$ (*i.e.*, dividing by 4). ^{19}F - and ^1H - ^{89}Y cross-polarization (CP) experiments were conducted with a ramped-amplitude spin lock pulse on the ^1H channel between 50% and 100% of the pulse power.²¹⁻²³ High power ^1H or ^{19}F decoupling was used in the ^{89}Y experiments with the swept field two-pulse phase-modulation (sw-TPPM) sequence.^{24,25}

SSNMR spectra were processed using TopSpin 3.5. Analytical simulations of the processed spectra were generated with the Solid Lineshape Analysis module (v. 2.2.4) within TopSpin.

4.2.6 Powder X-ray Diffraction (PXRD) Experiments

PXRD patterns were acquired with a Proto AXRD bench-top diffractometer equipped with a Cu K α ($\lambda = 1.540593 \text{ \AA}$) X-ray source and Proto DECTRIS hybrid pixel detector. For each experiment, roughly 20 mg of sample was packed onto a Proto plate sample holder and analyzed for 40 minutes. The detector scanned 2θ angles between 5° and 60° with a step size ($\Delta 2\theta$) of 8° and a dwell of 6 seconds per step. The resulting patterns were processed and compared with simulated data from previously reported crystal structures using the CrystalDiffract application (**Figure C3-Figure C6**).

4.2.7 Electron Paramagnetic Resonance (EPR) Experiments

Room temperature X-band (9.3–9.8 GHz) EPR spectra of the paramagnetic samples were acquired with a Bruker EMX-plus spectrometer with an ER041 microwave bridge. Spectra were acquired between 0 and 8000 G. Powdered samples were packed into quartz EPR tubes for analysis.

4.3 Results and Discussion

4.3.1 Undoped NP Material, YF

The analysis of the undoped $(\text{H}_3\text{O})\text{Y}_3\text{F}_{10}\cdot x\text{H}_2\text{O}$ NPs herein is consistent with the results of similar samples studied in our previous work.¹⁹ However, with the use of additional experiments and faster magic-angle spinning (MAS) speeds, we have been able to resolve additional features that were not apparent in the previous study, including signals indicating the presence of impurities, by-products, and/or unreacted starting reagents (*i.e.*, these NPs are very complex materials). Specifics pertaining to the spectra of the $(\text{H}_3\text{O})\text{Y}_3\text{F}_{10}\cdot x\text{H}_2\text{O}$ NPs (**Figure 4.2**) are discussed first, as they aid in the assignments of features in the spectra of materials prepared with other RE elements (*vide*

infra). For clarity, the undoped yttrium fluoride NPs with the $(\text{H}_3\text{O})\text{Y}_3\text{F}_{10}\cdot x\text{H}_2\text{O}$ structure will be referred to as **YF**.

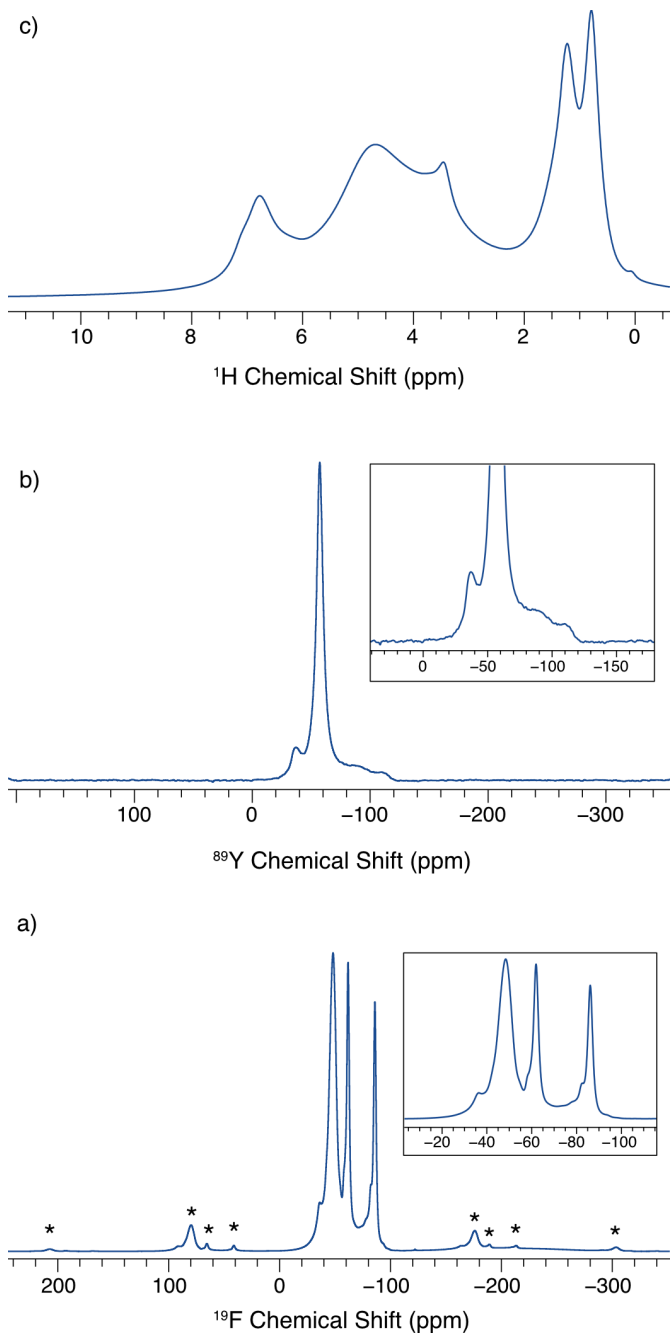


Figure 4.2. Multinuclear SSNMR spectra of the undoped **YF** NPs: a) ^{19}F UFMAS ($v_{\text{rot}} = 60$ kHz) (inset shows an expansion of the isotropic peaks), b) ^{19}F - ^{89}Y CP/MAS ($v_{\text{rot}} = 5$ kHz) (inset shows the peaks with increased vertical scaling), and c) ^1H UFMAS ($v_{\text{rot}} = 60$ kHz). These spectra are reproduced in the subsequent figures for comparison with those of the other samples.

Table 4.3. List of observed ^{19}F , ^{89}Y , and ^1H NMR chemical shifts and peak assignments for the undoped **YF** NP sample, as discussed in the text.

$\delta_{\text{iso}}(^{19}\text{F})$ (ppm) ^a	Peak Assignment
-36(2)	Unknown
-43(2)	YF , Site A (Surface) ^b
-48(2)	YF , Site A ^b
-55(2)	YF_3 , Site 1
-58(1)	YF , Site B (Surface) ^b
-62(1)	YF , Site B ^b
-67(2)	YF_3 , Site 2
-73(2)	$\text{Y}(\text{OH})_{(3-x)}\text{F}_x$ or hydrated YF_3 species
-78(2)	$\text{Y}(\text{OH})_{(3-x)}\text{F}_x$ or hydrated YF_3 species
-83(1)	YF , Site C (Surface) ^b
-86(1)	YF , Site C ^b
-122(1)	Aqueous F^-

$\delta_{\text{iso}}(^{89}\text{Y})$ (ppm) ^a	Peak Assignment
-12(7)	$\text{Y}(\text{H}_2\text{O})_6^{3+}$ or Y coordinated to surfactant molecules
-36(4)	YF , surface sites
-57(3)	YF , core sites
-90(7)	$\text{Y}(\text{OH})_{(3-x)}\text{F}_x$ or hydrated YF_3 species
-110(7)	YF_3

$\delta_{\text{iso}}(^1\text{H})$ (ppm) ^a	Peak Assignment
7.1(1)	surfactant
6.7(2)	surfactant
6.1(3)	YF , H_3O^+
4.6(6)	YF , zeolitic water
3.6(2)	surfactant
3.3(1)	surfactant
1.3(2)	surfactant
1.1(1)	surfactant
0.66(1)	surfactant
0.44(2)	surfactant
0.09(2)	monomeric water

^aUncertainties in the chemical shift values are listed in parentheses. ^b**YF** sites are defined with the nomenclature used in our previous report on similar materials.¹⁹

4.3.1.1 ^{19}F NMR Experiments on YF

The ^{19}F ultrafast MAS (UFMAS) ($\nu_{\text{rot}} = 60$ kHz) NMR spectrum of YF (**Figure 4.2a**) is complicated, and has at least 11 underlying features (see deconvolution in **Figure C7**, and a full listing of peak assignments in **Table 4.3**). First, consistent with previous observations, there are three features corresponding to the crystallographically-distinct fluorine sites in the YF crystal structure ($\delta_{\text{iso}}(^{19}\text{F}) = -48, -62, \text{ and } -86$ ppm, respectively) in a 3.0:1.2:1.0 integrated intensity ratio, close to the 3:1:1 ratio of the F sites.¹⁹ With UFMAS, three additional peaks are resolved ($\delta_{\text{iso}}(^{19}\text{F}) = -43, -58, \text{ and } -83$ ppm, respectively), with approximately the same intensity ratio (3.0:1.1:1.2). These less intense features, which are all shifted to higher frequencies compared to the first set, correspond to ^{19}F nuclei near the surfaces of the NPs.

There are several features that result from by-products or impurities. First, there are two peaks that correspond to the two F environments in bulk YF_3 (-55 and -67 ppm, respectively).^{19,26} Second, some low intensity signal is observed between -65 and -80 ppm, with at least two peaks resolved in the deconvolution (at -73 and -78 ppm, respectively, **Figure C7**). These features may correspond to $\text{Y}(\text{OH})_{(3-x)}\text{F}_x$ or hydrated YF_3 species.²⁷ The presence of yttrium hydroxide fluorides is supported by ^{89}Y NMR data (*vide infra*), but there may also be signal from amorphous YF_3 , as was previously suggested,¹⁹ which would appear as a broad feature in this range. There is also a sharp feature at -122 ppm, which is produced by residual aqueous F^- ions from the synthesis; this result is consistent with the chemical shift measured for aqueous KF .²⁸ Finally, there is a feature at -36 ppm. While the source of this feature is currently unknown, given the similarity of its intensity and linewidth to those of the surface sites (*i.e.*, at $-43, -58, \text{ and}$

–83 ppm, respectively), perhaps this feature results from a distinct environment at the surface of the particles (*e.g.*, near where the surfactant binds to the surface).

4.3.1.2 ^{89}Y NMR Experiments on YF

Consistent with previous reports,¹⁹ the predominant features in the ^{19}F - ^{89}Y CP/MAS NMR spectrum of YF (**Figure 4.2b**) correspond to distinct Y environments near the surface of the NPs (–36 ppm) and those in the core (–57 ppm). The ^{19}F - ^{89}Y CP/MAS NMR spectrum of YF (**Figure 4.2b**) also has features from impurities/by-products: a peak at –110 ppm corresponds to YF_3 ,^{26,29} and a feature at –90 ppm likely results from a different nine-coordinate Y environment,³⁰ which must be proximate to ^{19}F nuclei (since these signals are observed using ^{19}F - ^{89}Y cross polarization). The latter feature is also present in the ^1H - ^{89}Y CP/MAS ($v_{\text{rot}} = 5$ kHz) NMR spectrum of the same sample (**Figure C8**), indicating that the Y site is also proximate to ^1H nuclei. As such, this feature could result from hydrated or hydroxy species, possibly $\text{Y}(\text{OH})_{(3-x)}\text{F}_x$, which are known to crystallize with nine-coordinate Y environments.²⁷ Yttrium chemical shifts are sensitive to the identities of the next-nearest neighbor atoms.^{30,31} As previously discussed by Scholz *et al.*,²⁶ the replacement of F by O in the first coordination sphere of Y causes shifts to higher frequency in the ^{89}Y NMR spectra. This analysis is consistent with our results, which infer that the chemical shift of YF_3 is at a lower frequency than the signals we attribute to yttrium hydroxy fluorides or hydrates.

Finally, there is an additional low-intensity feature at –12 ppm in the ^1H - ^{89}Y CP/MAS NMR spectrum of YF. Since this feature is not observed in the ^{19}F - ^{89}Y CP/MAS NMR spectrum, it must come from an Y-containing species without ^{19}F nuclei, in which Y sites are proximate to ^1H nuclei. These Y sites might correspond to distinct

hydrated species (*e.g.*, $\text{Y}(\text{H}_2\text{O})_6^{3+}$) and/or Y atoms coordinated to the surfactant molecules, since known $\delta_{\text{iso}}(^{89}\text{Y})$ for Y atoms coordinated by six O atoms are similar (*e.g.*, $\delta_{\text{iso}}[\text{Y}(\text{NO}_3)_3 \cdot 6\text{H}_2\text{O}] = -53$ ppm; $\delta_{\text{iso}}[\text{Y}(\text{acac})_3 \cdot 3\text{H}_2\text{O}] = +22$ and $+28$ ppm).²⁹

4.3.1.3 ^1H NMR Experiments on YF

There are a variety of overlapping features in the ^1H UFMAS NMR spectrum of the YF NPs (**Figure 4.2c**). The spectrum acquired for the current work is consistent with previous reports.¹⁹ However, with the improved resolution afforded by UFMAS, we can resolve additional features from the surfactant molecules (see **Table 4.3**). Finally, the signal attributed to isolated water molecules (*i.e.*, those not interacting with their surroundings) at *ca.* 0.09 ppm is significantly less intense than those observed previously, suggesting that such water molecules are less prevalent in the YF sample described herein.

4.3.2 Preparation of Samples with Other RE Elements

The previously-reported synthesis of $(\text{H}_3\text{O})\text{Y}_3\text{F}_{10} \cdot x\text{H}_2\text{O}$ NPs^{17,19} provides a straightforward method for introducing other RE elements into the reaction by replacing some (or all) of the YCl_3 with another $(\text{RE})\text{Cl}_3$ compound. Herein, we describe the characterization of samples prepared using different amounts of ScCl_3 , ErCl_3 , or EuCl_3 (see **Section 4.2 Methods** for details on the syntheses). The following discussion is organized by the specific RE element, and the samples are referred to by the ratio of the number of dopant ions (Sc, Er, or Eu) to the total RE content in the sample (*i.e.*, dopant + Y^{3+}). For example, a sample prepared with a molar ratio of 1:9 $\text{ErCl}_3:\text{YCl}_3$ is referred to as **YF:Er10**. *N.B.* The spectra of the undoped YF NPs (shown in **Figure 4.2**) are

reproduced in the figures that follow (**Figure 4.3 - Figure 4.12**), so that comparisons with the spectra of the doped materials can be made.

4.3.3 Sc-Containing NPs

4.3.3.1 ^{45}Sc NMR Experiments on Sc-Containing Samples

The most direct way to study the local environments of the dopant sites is to conduct NMR experiments on the dopant ions themselves. For most RE elements, these experiments are not possible, however, due to their paramagnetic ground states, large quadrupole moments, and/or low receptivities (*N.B.* the only diamagnetic RE elements that have NMR-active nuclei are ^{45}Sc , ^{89}Y , ^{139}La , ^{153}Eu , ^{171}Yb , and ^{175}Lu). However, ^{45}Sc is a highly receptive quadrupolar nucleus ($I = 7/2$, 100% natural abundance, and a receptivity 1780 times that of ^{13}C), and it is particularly useful in the current work for probing the Sc-containing products. The ^{45}Sc UFMAS ($\nu_{\text{rot}} = 60$ kHz) spectra of the Sc-containing samples (**Figure 4.3a-c**) have two isotropic peaks, one at -55 ppm and the other at -40 ppm. The former is more intense in the spectra of samples with higher Sc-content, and is the only feature present in the spectrum of **YF:Sc100** (**Figure 4.3d**). It has a center of gravity and appearance consistent with ScF_3 (an assignment also supported by the ^{19}F data, *vide infra*).^{32,33} Second-order patterns are not observed for either site; instead, they appear as featureless peaks, suggesting that the $C_Q(^{45}\text{Sc})$ is small (*vide infra*) and that the Sc sites are somewhat disordered. Such disorder has been previously reported for ScF_3 , and has been used to justify its negative thermal expansion.³⁴ The lack of resolution makes an accurate measurement of the quadrupolar coupling constant, C_Q , difficult; however, based on a fit of the spinning sideband manifold, the estimated C_Q

values for both sites range between 0.5 and 1.1 MHz, consistent with previous reports.^{32,33}

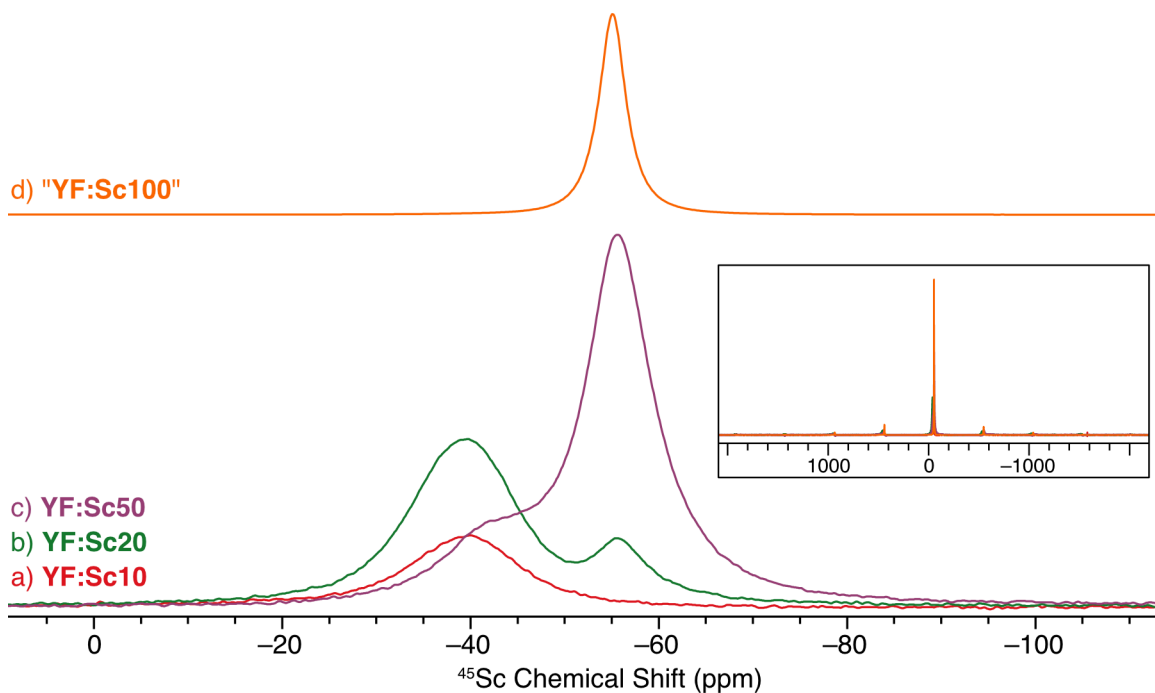


Figure 4.3. $^{45}\text{Sc}\{^{19}\text{F}\}$ UFMAS ($\nu_{\text{rot}} = 60$ kHz) NMR spectra of the Sc-containing samples. The inset shows the full spectral window and low intensity spinning sidebands.

The peak at -40 ppm is most intense in the spectrum of **YF:Sc20**, and its intensity is similar in the spectra of **YF:Sc50** and **YF:Sc10**. The chemical shift of this peak is consistent with an eight-coordinate Sc environment.^{35–37} Since the Y environment in undoped **YF** is eight-coordinate, the ^{45}Sc NMR results alone could suggest that Sc substitutionally replaces Y. However, multinuclear NMR experiments described below demonstrate that substitutional doping does not occur. Instead, it is likely that Sc^{3+} ions sit in the channels of the **YF** structure, interacting with F atoms and water molecules. Due to the geometry of the structure, eight-coordinate Sc atoms in the large pores (yellow spheres in **Figure 4.1**) would produce a highly distorted Sc coordination environment that is inconsistent with the small value of C_Q . A more likely position that is consistent

with the NMR data is for the Sc atoms to replace H_3O^+ between the pores (**Figure 4.1**). Such Sc atoms are eight coordinate (binding to six F atoms at the edge of a pore and two water molecules in adjacent pores, **Figure C9**). This geometry would produce a small electric field gradient at the ^{45}Sc nucleus, consistent with the small C_Q (^{45}Sc) value.

4.3.3.2 ^{19}F NMR Experiments on Sc-Containing Samples

With the exception of **YF:Sc100**, all of the ^{19}F UFMAS ($\nu_{\text{rot}} = 60$ kHz) NMR spectra of the Sc-containing compounds have features with similar shifts and appearances to those of **YF** (**Figure 4.4, Table 4.4**). However, a subtle, progressive shift (0.5 to 1.0 ppm) of the high- and low-frequency peaks is observed as the Sc content increases (**Figure C10**). In contrast, the central peak at -62 ppm does not shift. The fact that the observed shift differences are so slight suggests that the molecular-level structure remains largely the same (PXRD results also support the formation of **YF**-like NPs **Figure C4**). Previously, it was observed that the ^{19}F chemical shifts of **YF** are sensitive to the amount of water trapped in the pores of the zeolitic structure;¹⁹ such differences in chemical shifts are common in a variety of porous materials.^{38–40} Based on the ^1H NMR data (*vide infra*), **YF:Sc10** contains slightly more zeolitic water than **YF:Sc20** and undoped **YF**. Since the largest change in the ^{19}F NMR spectra is observed for **YF:Sc20**, however, differences in hydration levels cannot account for the observed ^{19}F chemical shift differences. A much more likely possibility, which is supported by the ^{45}Sc NMR results, is that some of the Sc^{3+} ions reside in the channels of the $(\text{H}_3\text{O})\text{Y}_3\text{F}_{10}\cdot x\text{H}_2\text{O}$ structure, coordinated to the F sites between the pores and water (**Figure C9**). RE elements have been shown to incorporate into the extra-framework spaces of various zeolites (producing so-called RE-exchanged zeolites).^{41–43} SSNMR spectra of these materials show that the chemical shifts

of nuclei in the framework (*e.g.*, ^{27}Al , ^{29}Si) shift moderately upon incorporation of the dopant due to slight changes in their bonding geometries.^{43–46} A careful examination of the $(\text{H}_3\text{O})\text{Y}_3\text{F}_{10}\cdot x\text{H}_2\text{O}$ crystal structure of **YF** shows that two of the F sites are adjacent to the channels of the zeolitic structure, while the other is not; hence, the ^{19}F peaks that shift with the addition of Sc are assigned to the former two sites (*ca.* -49 , and -86 ppm, respectively), while the peak at -62 that does not shift is assigned to the latter. It is unlikely that these shifts result from the substitution of Y sites by Sc, because all three of the F atoms are bound to Y; a change in the type of central RE^{3+} ion would affect each of the ^{19}F shifts, and very likely produce substantially greater chemical shift differences than those observed.

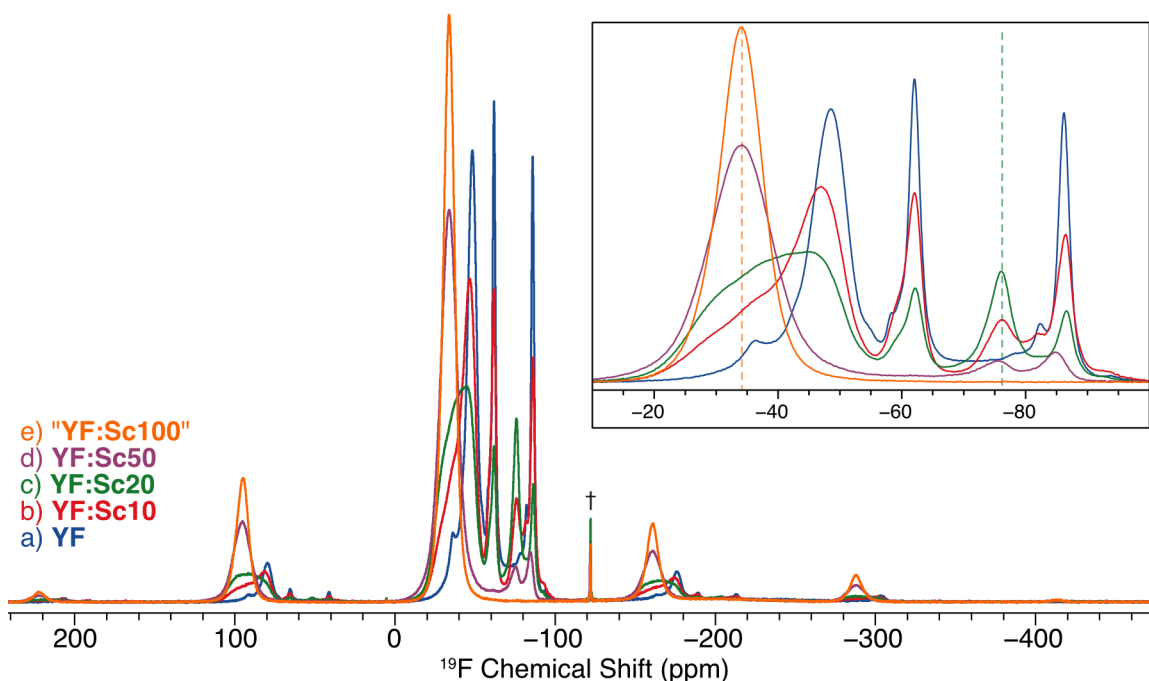


Figure 4.4. ^{19}F UFMAS ($\nu_{\text{rot}} = 60$ kHz) NMR spectra of the Sc-containing samples. The inset shows an expansion of the isotropic peaks. Dashed lines indicate distinct features that are not present in the spectrum of **YF**. The dagger symbol denotes a F^- impurity. All of the other features are spinning sidebands.

One of the most noticeable differences between the spectra of the Sc-containing samples and those of the undoped **YF** is the appearance of a new feature at -34 ppm, which increases in intensity with the amount of Sc in the synthesis. Consistent with the ^{45}Sc data, this feature results from ScF_3 ^{32,33} (*N.B.*, though there is a feature with a similar shift in the spectrum of the undoped material ($-36.0(3)$ ppm), there is no Sc in the undoped material; therefore, these features have different origins (*vide supra*). The peak at -34 ppm is the only one present in the spectrum of **YF:Sc100** (**Figure 4.4e**). As such, the NPs prepared with only ScCl_3 do not form a zeolitic Sc_3F_{10} structure analogous to that of **YF**, likely because of the smaller ionic radius of Sc^{3+} (**Table 4.1**). TEM images reveal that high Sc-levels produce crystals with a rectangular prism shape, rather than the octahedral crystals observed for **YF** NPs with the $(\text{H}_3\text{O})\text{Y}_3\text{F}_{10}\cdot x\text{H}_2\text{O}$ structure (**Figure C1** and **Figure C2**). The former is consistent with the appearance of ScF_3 crystals.^{47,48} Finally, with the exception of **YF:Sc100**, all of the spectra of the Sc-containing materials have a peak at -76 ppm. As with similar features in the spectrum of **YF** (**Table 4.3**, and *vide supra*), this peak likely results from $\text{Y}(\text{OH})_{(3-x)}\text{F}_x$ or hydrated YF_3 by-products. The presence of such materials is also supported by ^{89}Y and ^1H NMR data (*vide infra*).

4.3.3.3 ^{89}Y NMR Experiments on Sc-Containing Samples

The ^{19}F - ^{89}Y CP/MAS ($v_{\text{rot}} = 5$ kHz) NMR spectra of the Sc-containing samples are shown in **Figure 4.5**. As expected, the signal intensity decreases in the spectra of samples prepared with higher Sc content (*i.e.*, less Y). The spectra of **YF:Sc10** and **YF:Sc20** (**Figure 4.5b-c**) are similar to each other, both having three features: peaks at -36 , -56 , and -90 ppm. The shapes and relative intensity of the first two peaks are similar to those of **YF**, but while the center of gravity of the feature at *ca.* -36 ppm is

constant (and consistent with the undoped material), that of the other feature is shifted by about +1.2 ppm (see **Figure 4.5 inset**). The peak at -56 ppm is also roughly twice as broad as that of the undoped material, and the breadth increases slightly with the amount of Sc in the sample. These differences in breadth may indicate a distribution of ^{89}Y environments in the particle and/or the presence of additional underlying peaks (*vide infra*).

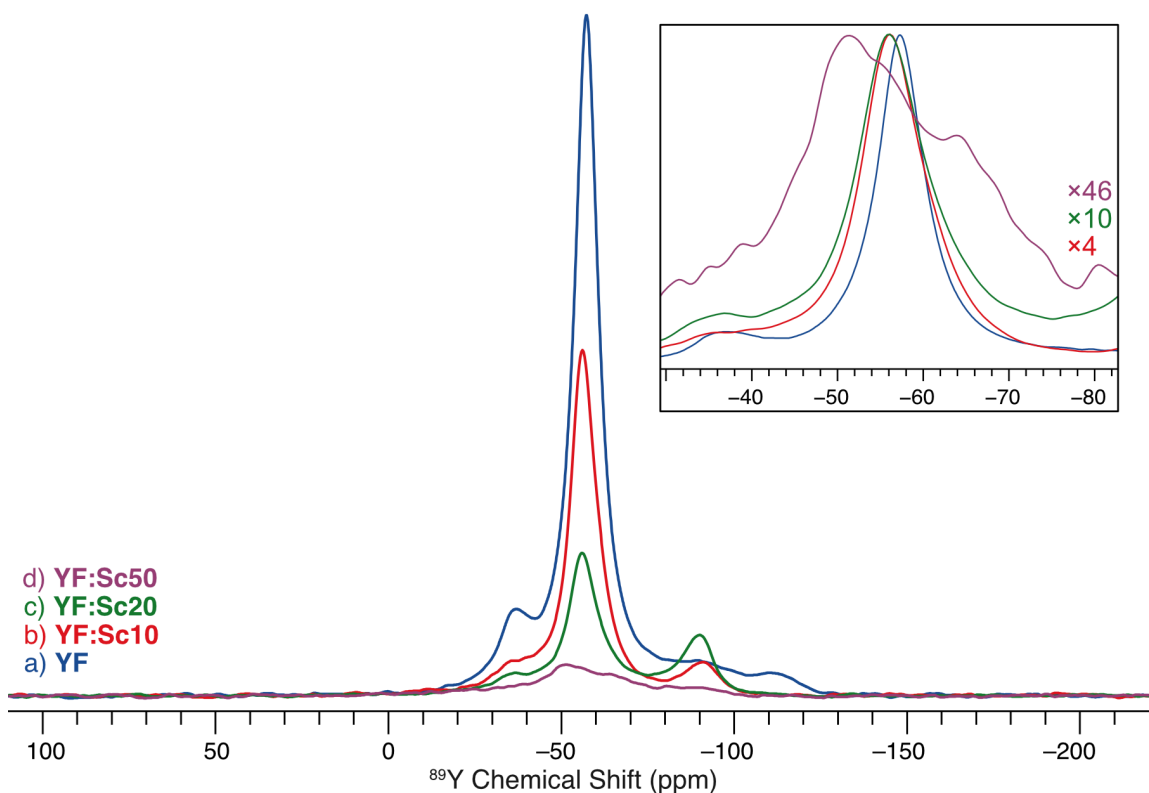


Figure 4.5. ^{19}F - ^{89}Y CP/MAS ($\nu_{\text{rot}} = 5$ kHz) NMR spectra of the Sc-containing samples and **YF**. The inset shows an expansion of the same spectra with the spectra scaled to have same maximum intensity. The corresponding scaling factors are listed in the inset.

The corresponding spectrum of **YF:Sc50** (**Figure 4.5d**) is dominated by a broad feature ($\Delta\nu_{1/2} \approx 475$ Hz) centered near -56 ppm and lopsided towards high frequency. It is likely that this feature is produced by multiple Y environments in the range of -42 to -75 ppm; such environments may be present in **YF:Sc10** and **YF:Sc20**, accounting for

the increased breadths and slight shifts in their ^{89}Y NMR spectra. However, the low S/N and resolution in the ^{89}Y NMR spectrum of **YF:Sc50** makes an accurate deconvolution and assignment of such features difficult. TEM images of **YF:Sc20** and **YF:Sc50** indicate that crystals with a rectangular prism shape are the dominant phase (likely ScF_3 , *vide supra*). Nonetheless, the ^{89}Y and ^{19}F SSNMR results (as well as PXRD patterns, **Figure C4**) indicate that these samples also contain some particles with the zeolitic $(\text{H}_3\text{O})\text{Y}_3\text{F}_{10}\cdot x\text{H}_2\text{O}$ structure.

Finally, the spectra of all of the Sc-containing samples have peaks at -90 ppm, which indicates the presence of $\text{Y}(\text{OH})_{(3-x)}\text{F}_x$ species, consistent with the ^{19}F and ^1H results. Unlike the spectrum of **YF**, signal from YF_3 (at -110 ppm) is not observed. As such, Sc^{3+} may promote the reaction of YF_3 with H_2O in the sample to form $\text{Y}(\text{OH})_{(3-x)}\text{F}_x$ instead. Interestingly, reaction mixtures containing Eu have the opposite behavior, in that YF_3 -like material is formed as a by-product rather than $\text{Y}(\text{OH})_{(3-x)}\text{F}_x$ species (*vide infra*).

Table 4.4. List of observed ^{45}Sc , ^{19}F , ^{89}Y , and ^1H NMR chemical shifts and peak assignments for the Sc-containing samples, as discussed in the text.

$\delta_{\text{iso}}(^{45}\text{Sc})$ (ppm) ^{a,b}				Peak Assignment
YF:Sc10	YF:Sc20	YF:Sc50	“YF:Sc100”	
-40(5.5)	-39(5.5)	-42(7)	–	YF:Sc, from Sc^{3+} ions in pores of YF ScF ₃
–	-56(3.5)	-55(4)	-55(1.3)	
$\delta_{\text{iso}}(^{19}\text{F})$ (ppm) ^{a,b}				Peak Assignment
YF:Sc10	YF:Sc20	YF:Sc50	“YF:Sc100”	
–	-34(5)	-34(6)	-34(5)	ScF ₃
-36(3)	-36(4)	–	–	Unknown
-47(3)	-46(4)	–	–	YF, Site A ^c
-59(1)	-59(2)	–	–	YF, Site B (Surface) ^c
-62(1.5)	-62(1)	-62(4)	–	YF, Site B ^c
-76(2.5)	-76(3.5)	-76(3)	–	Y(OH) _(3-x) F _x or hydrated YF ₃ species
-82(1.5)	-82(2)	–	–	YF, Site C (Surface) ^c
-86(1.5)	-87(2)	-85(2)	–	YF, Site C ^c
$\delta_{\text{iso}}(^{89}\text{Y})$ (ppm) ^a				Peak Assignment
YF:Sc10	YF:Sc20	YF:Sc50	“YF:Sc100”	
-36(5)	-37(5)	–	–	YF, surface sites
-56(5)	-56(5)	-55(10)	–	YF, core sites
-91(5)	-90(5)	-90(6)	–	Y(OH) _(3-x) F _x or hydrated YF ₃ species
$\delta_{\text{iso}}(^1\text{H})$ (ppm) ^a				Peak Assignment
YF:Sc10	YF:Sc20	YF:Sc50	“YF:Sc100”	
7.2(1)	7.1(1)	7.1(2)	7.1(2)	surfactant
6.8(2)	6.8(2)	6.8(2)	6.8(2)	surfactant
6.5(3)	6.5(3)	6.5(4)	–	YF, H ₃ O ⁺
4.8(6)	4.7(6)	4.7(8)	–	YF, zeolitic water
4.0(2)	3.9(3)	4.0(4)	4.0(4)	surfactant
3.6(1)	3.7(2)	3.7(3)	3.7(4)	surfactant
3.2(1)	3.1(1)	–	–	Y(OH) _(3-x) F _x or hydrated YF ₃ species
3.1(1)	3.0(1)	–	–	Y(OH) _(3-x) F _x or hydrated YF ₃ species
1.5(2)	1.6(2)	1.6(4)	1.5(2)	surfactant
1.3(1)	1.3(1)	1.3(2)	1.2(2)	surfactant
0.8(1)	0.9(1)	0.8(2)	0.8(2)	monomeric water

^aUncertainties in the chemical shift values are listed in parentheses. ^bDashes indicate features that are not present or cannot be resolved in the corresponding spectra. ^cYF sites are defined with the nomenclature used in our previous report on similar materials.¹⁹

4.3.3.4 ^1H NMR Experiments on Sc-Containing Samples

All of the peaks in the ^1H NMR spectrum of **YF** are also observed in ^1H UFMAS spectra of the Sc-containing samples (**Figure 4.6**), with the most intense features corresponding to the surfactant molecules. The intensities of the signals from H_2O within the zeolitic channels (*ca.* 5 ppm) vary, consistent with the samples having slightly different hydration levels.¹⁹ The **YF:Sc10** sample appears to be slightly more hydrated than **YF:Sc20** and **YF**. Almost no signal from zeolitic water is present in the spectrum of **YF:Sc50**, and the signal is completely absent from the spectrum of **YF:Sc100**. As discussed above, these samples contain limited or no zeolitic material, and therefore cannot bind water in the same way. There are two peaks between 3.0 and 3.2 ppm that are most noticeable in the spectra of **YF:Sc10** and **YF:Sc20**. These features may correspond to the yttrium hydroxide fluorides suggested by the ^{19}F and ^{89}Y NMR data.

4.3.3.5 Structural Conclusions (Sc-Containing Samples)

The addition of ScCl_3 to the previously-reported reverse micelle synthesis produces a mixture of products. Zeolitic **YF** NPs are present in all of the samples prepared with YCl_3 , and it is most probable that Sc^{3+} ions replace H_3O^+ sites in the channels rather than substitutionally replacing the Y atoms. ScF_3 is a major by-product of the reaction; it is detected in all of the Sc-containing samples, and at high levels of Sc, it is the sole product. Finally, hydroxylated (or hydrated) yttrium fluorides are observed and not YF_3 , which is a by-product of the reaction conducted without ScCl_3 .

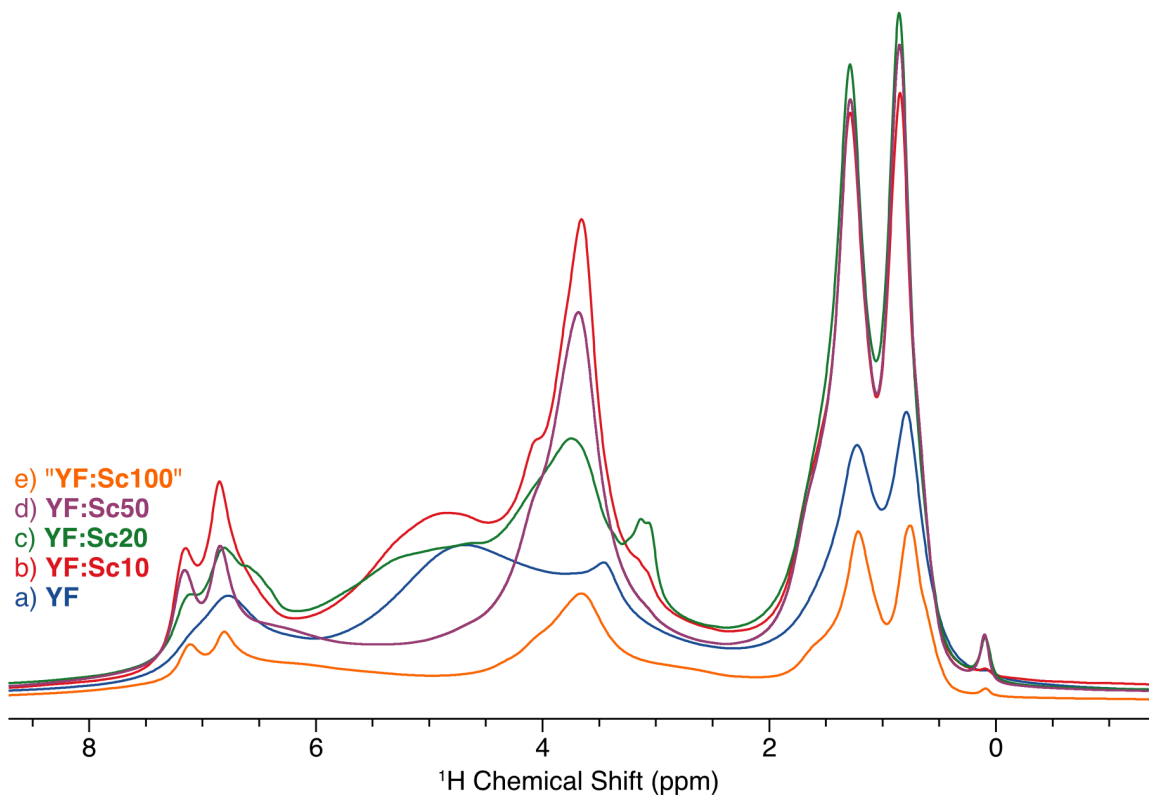


Figure 4.6. ^1H UFMAS ($\nu_{\text{rot}} = 60$ kHz) NMR spectra of the Sc-containing samples and YF.

4.3.4 Er-Containing Samples

Unlike Sc^{3+} , Er^{3+} has a paramagnetic ground state, which makes direct characterization of the ^{167}Er ($I = 7/2$) nuclei with NMR impossible. Paramagnetic centers can be studied using another magnetic resonance technique, electron paramagnetic resonance spectroscopy (EPR), which we have used here (**Figure C13**, *vide infra*). When paramagnetic nuclei incorporate into a diamagnetic host material, they also affect the other NMR-active nuclei in the structure. As such, NMR can be used as an *indirect* probe of the dopants, and provide additional information on the structure of the materials and dopant homogeneity.

4.3.4.1 ^{19}F NMR Experiments on Er-Containing Samples

The ^{19}F UFMAS ($\nu_{\text{rot}} = 60$ kHz) NMR spectra of the Er-containing samples (**Figure 4.7**) are strongly influenced by the presence of paramagnetic Er^{3+} ions. In these samples, the paramagnetic interaction causes (i) broadening of the isotropic peaks and associated spinning-sidebands (SSBs), and (ii) an increase in the intensity of the SSBs relative to the isotropic peaks; both effects intensify as the Er^{3+} concentration increases.

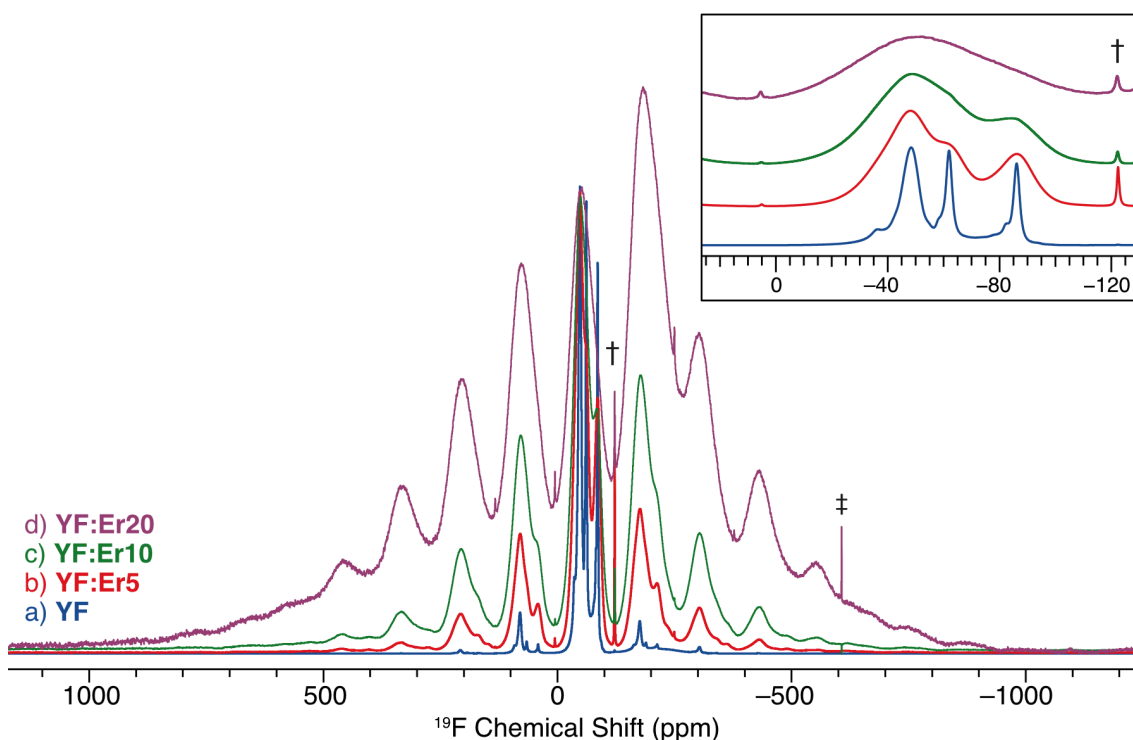


Figure 4.7. ^{19}F UFMAS ($\nu_{\text{rot}} = 60$ kHz) NMR spectra of the Er-containing samples and YF. The inset shows an expanded view of the isotropic peaks. The dagger and double dagger symbols denote a F^- impurity and background signal from the probe, respectively (see **Figure C11**). All of the other features are spinning sidebands.

The broadening results primarily from efficient transverse relaxation (T_2) due to the unpaired electron relaxation mechanism (T_2^{ue}).^{49–51} While the presence of paramagnetic ions can also affect the anisotropic bulk magnetic susceptibility (ABMS) of the sample (resulting in additional broadening),^{49,51,52} such effects would also produce a

noticeable shift in the isotropic peaks due to the "through-space" pseudocontact interaction, which is not observed. If much of the sample remains undoped (*e.g.*, if the Er doping was inhomogeneous within the NPs, or produced a mixture of doped and undoped particles), these spectra should show sharp features from the regions of undoped material. No sharp features are observed, indicating that the dopant affects all of the ^{19}F nuclei in the sample, and is homogeneously distributed throughout the particles. While it is possible that the broad spectral features resulting from the presence of paramagnetic ions may obscure a small amount of signal from undoped **YF** material, the amount of **YF** would have to be extremely small to be undetectable (*cf.* ^{19}F NMR spectrum of **YF:Er50**, **Figure C14**, *vide infra*).

The introduction of Er^{3+} ions also produces intense SSB manifolds, which are largely the result of the dipolar shift anisotropy (DSA), as well as a smaller contribution from the chemical shift anisotropy (CSA) (given its comparatively small magnitude, the latter can be neglected in the discussion of the spectra of the paramagnetic samples). DSA is described by a second-rank tensor, analogous to the CS tensor.^{49–51} As such, the spinning sideband (SSB) intensities in the spectra can be analyzed to determine the principal components of the DSA tensor using a Herzfeld-Berger analysis,⁵³ or analytical simulation (as was done here, see **Section 4.2 Methods**) in the same way as a CS tensor.⁵⁴

As previous work has demonstrated,^{55,56} the anisotropy of this tensor (in ppm),^{55,57} $\Delta_{\text{aniso}} = |\delta_{\text{zz}} - \delta_{\text{iso}}|$, is related to the average distance between the observed nucleus and the unpaired electron density from a paramagnetic lanthanide by **Eq. 1.1**:

$$|\Delta_{\text{aniso}}| = \frac{(\mu_0 \mu_{\text{B}}) g_J^2 \cdot J(J+1)}{\langle R \rangle^3 k_{\text{B}} T} \cdot 10^6 \quad (4.1)$$

where μ_0 is the vacuum permittivity constant, μ_B is the Bohr magneton, J is the total angular momentum quantum number, $\langle R \rangle$ is the expectation value of the nuclear-lanthanide distance (in meters), k_B is the Boltzmann constant, T is the temperature (in K), and g_J is the isotropic lanthanide g -factor, defined as:

$$g_J = 1 + \frac{J(J + 1) - L(L + 1) + S(S + 1)}{2J(J + 1)} \quad (4.2)$$

where J , L and S are the total, orbital, and spin momentum quantum numbers, respectively. This equation treats the lanthanide without ligand-field effects (*i.e.*, as a free ion) and models the unpaired electron density as a point charge. Both assumptions are common for lanthanides, and provide good approximations in most systems.^{58,59} The results of this analysis are shown in **Table 4.6**.

As the lanthanide concentration is increased, the average distance between the observed nuclei and the closest Er^{3+} ion decreases (*i.e.*, $\langle R \rangle$ gets smaller). The smallest value of $\langle R \rangle$ is 6.5(3) Å, which is larger than the second coordination sphere of F, indicating that ^{19}F nuclei with lanthanides in their first two coordination spheres are not detected due to fast nuclear relaxation. Moreover, the number of such ^{19}F environments grows as the amount of Er^{3+} in the sample increases, and results in decreased S/N in the spectra of samples with higher Er^{3+} concentrations. We have also attempted to characterize a sample made with 50% ErCl_3 (*i.e.*, **YF:Er50**), but with this much Er^{3+} , the unpaired electrons cause ^{19}F relaxation that is too fast to allow a meaningful spectrum to be obtained and analyzed (**Figure C11**).

Finally, the introduction of Er^{3+} ions into the synthesis of **YF** NPs does not produce observable shifts of the ^{19}F NMR peaks relative to those of the undoped **YF** NPs. The ^{19}F nuclei that produce the observed signal are not affected by the Fermi contact

interaction, indicating that there is limited delocalization of the unpaired spin density onto the observed ^{19}F nuclei.

Table 4.5. List of observed ^{19}F , ^{89}Y , and ^1H NMR chemical shifts and peak assignments for the Eu-containing samples, as discussed in the text.

$\delta_{\text{iso}}(^{19}\text{F})$ (ppm) ^{a,b}				Peak Assignment
YF:Eu5	YF:Eu10	YF:Eu20	YF:Eu50	
-37(3)	-37(3)	-38(5)	–	Unknown
-43(2)	-43(3)	-44(3)	–	YF, Site A (Surface) ^c
-47(3)	-48(3)	-49(5)	-49(10)	YF, Site A ^c
-54(3)	-54(3)	-55(4)	–	YF ₃ , Site 1
-59(1)	-59(1)	–	–	YF, Site B (Surface) ^c
-63(1)	-63(1)	-63(2)	-62(10)	YF, Site B ^c
-67(2)	-67(2)	-67(2)	–	YF ₃ , Site 2
-83(2)	-83(2)	–	–	YF, Site C (Surface) ^c
-87(1)	-87(2)	-87(3)	-87(10)	YF, Site C ^c
-122(1)	-122(1)	-122(1)	-122(1)	Aqueous F ⁻

$\delta_{\text{iso}}(^{89}\text{Y})$ (ppm) ^{a,b}				Peak Assignment
YF:Eu5	YF:Eu10	YF:Eu20	YF:Eu50	
-15(5)	-15(5)	-15(5)	–	Y-F impurity
-38(4)	-38(4)	-38(5)	–	YF, surface sites
-57(7)	-57(7)	-57(8)	–	YF:Eu ^d
-58(2.5)	-58(2.5)	-58(2.5)	–	YF, core sites ^d
-105(9)	-107(5)	-104(8)	–	YF ₃ , possibly containing some Eu ³⁺

$\delta_{\text{iso}}(^1\text{H})$ (ppm) ^{a,b}				Peak Assignment
YF:Eu5	YF:Eu10	YF:Eu20	YF:Eu50	
7.1(1)	7.1(2)	–	14(7)	surfactant
6.8(1)	6.8(2)	6.9(6)	–	surfactant
3.9(2)	3.9(3)	–	4(5)	surfactant
3.5(2)	3.6(3)	3.5(6)	–	surfactant
1.5(2)	–	–	–	surfactant
1.2(2)	1.1(2.5)	–	–	surfactant
0.7(2)	0.8(2.5)	0.9(8)	–	surfactant

^aUncertainties in the chemical shift values are listed in parentheses. ^bDashes indicate features that are not present or cannot be resolved in the corresponding spectra. ^cYF sites are defined with the nomenclature used in our previous report on similar materials. ^dAssignments based on the deconvolution shown in **Figure C15** where the narrow peak results from YF, and the broad from YF:Eu. These two features may also result from 1 peak corresponding to a lopsided distribution of chemical shifts. See text for details.

Table 4.6. Experimental values of the span of the DSA tensor (Δ_{aniso}) and corresponding calculated nuclear-Ln³⁺ distances obtained from fits of the ¹⁹F and ¹H SSNMR data.

Sample	¹⁹ F						¹ H					
	Site 1 ($\delta_{\text{iso}} = -47$ ppm)		Site 2 ($\delta_{\text{iso}} = -63$ ppm)		Site 3 ($\delta_{\text{iso}} = -86$ ppm)		Site 1 ($\delta_{\text{iso}} = 6.6$ ppm)		Site 2 ($\delta_{\text{iso}} = 3.5$ ppm)		Site 3 ($\delta_{\text{iso}} = 0.58$ ppm)	
	$\Delta_{\text{aniso}}^{\text{a}}$ [/ppm]	$\langle R \rangle^{\text{b}}$ [Å]	$\Delta_{\text{aniso}}^{\text{a}}$ [/ppm]	$\langle R \rangle^{\text{b}}$ [Å]	$\Delta_{\text{aniso}}^{\text{a}}$ [/ppm]	$\langle R \rangle^{\text{b}}$ [Å]	$\Delta_{\text{aniso}}^{\text{a}}$ [/ppm]	$\langle R \rangle^{\text{b}}$ [Å]	$\Delta_{\text{aniso}}^{\text{a}}$ [/ppm]	$\langle R \rangle^{\text{b}}$ [Å]	$\Delta_{\text{aniso}}^{\text{a}}$ [/ppm]	$\langle R \rangle^{\text{b}}$ [Å]
YF:Er5	232(10)	7.9(1)	247(40)	7.8(4)	246(20)	7.8(2)	135(20)	9.5(5)	134(20)	9.5(5)	119(10)	9.9(3)
YF:Er10	288(20)	7.4(2)	305(30)	7.3(2)	308(10)	7.2(1)	162(30)	9.0(6)	152(20)	9.1(4)	200(20)	8.3(3)
YF:Er20	425(50)	6.5(3)	425(50)	6.5(3)	425(50)	6.5(3)	456(20)	6.3(1)	– ^c	– ^c	– ^c	– ^c
YF:Er50	650(100)	5.6(3)	– ^c	– ^c	– ^c	– ^c	223(30)	7.1(3)	– ^c	– ^c	– ^c	– ^c
YF:Eu50^d	350(100)	6.1(6)	– ^c	– ^c	– ^c	– ^c	223(30)	7.1(3)	– ^c	– ^c	– ^c	– ^c

^aThe span of the dipolar shift tensor is defined as $\Delta_{\text{aniso}} = |\delta_{\text{zz}} - \delta_{\text{iso}}|$, where δ_{iso} is the isotropic shift, and δ_{zz} is the principal value of the dipolar shift tensor that gives the largest absolute difference from δ_{iso} . ^b $\langle R \rangle$ is the expectation value of the distance between the nucleus of interest and a point charge centered at the Ln position. ^cLow resolution of this spectrum prevented an accurate measurement of the DSA.

4.3.4.2 ^{89}Y NMR Experiments on Er-Containing Samples

The paramagnetic interaction also affects the ^{19}F - ^{89}Y CP/MAS ($v_{\text{rot}} = 5$ kHz) NMR spectra of the Er-containing samples (**Figure 4.8**), which all have a single broad feature centered at -58 ppm that increases in breadth with increasing Er^{3+} concentration. These spectra do not have large SSB manifolds because the effects of DSA are significantly smaller in the spectra of low- γ nuclei like ^{89}Y .⁵³ Unlike the spectrum of **YF** (**Figure 4.8a**), a separate feature corresponding to surface Y sites is not resolved. The centers of gravity of the broad features are consistent with that of the undoped material (*i.e.*, no large paramagnetic shifts are observed). As in the ^{19}F experiments, no sharp features are observed from undoped **YF** material or other by-products, confirming that all of the Y nuclei in the sample are affected by the presence of paramagnetic Er^{3+} ions (*i.e.*, that the doping is homogeneous). While the signal intensity clearly decreases in the spectra of materials with higher concentrations of Er^{3+} , this decrease is largely due to the interference of the paramagnetic interaction with the CP efficiency.^{49,60,61} For instance, ^{19}F - ^{89}Y CP/MAS NMR experiments were attempted on **YF:Er50**, but no signal could be obtained. From the SSNMR data alone, it is possible that strong paramagnetic impurities (*i.e.*, with high levels of Er^{3+} , like ErF_3) could be undetected. However, we do not see evidence for the production of an additional phase in the TEM images or PXRD data (**Figure C1** and **Figure C5**, respectively).

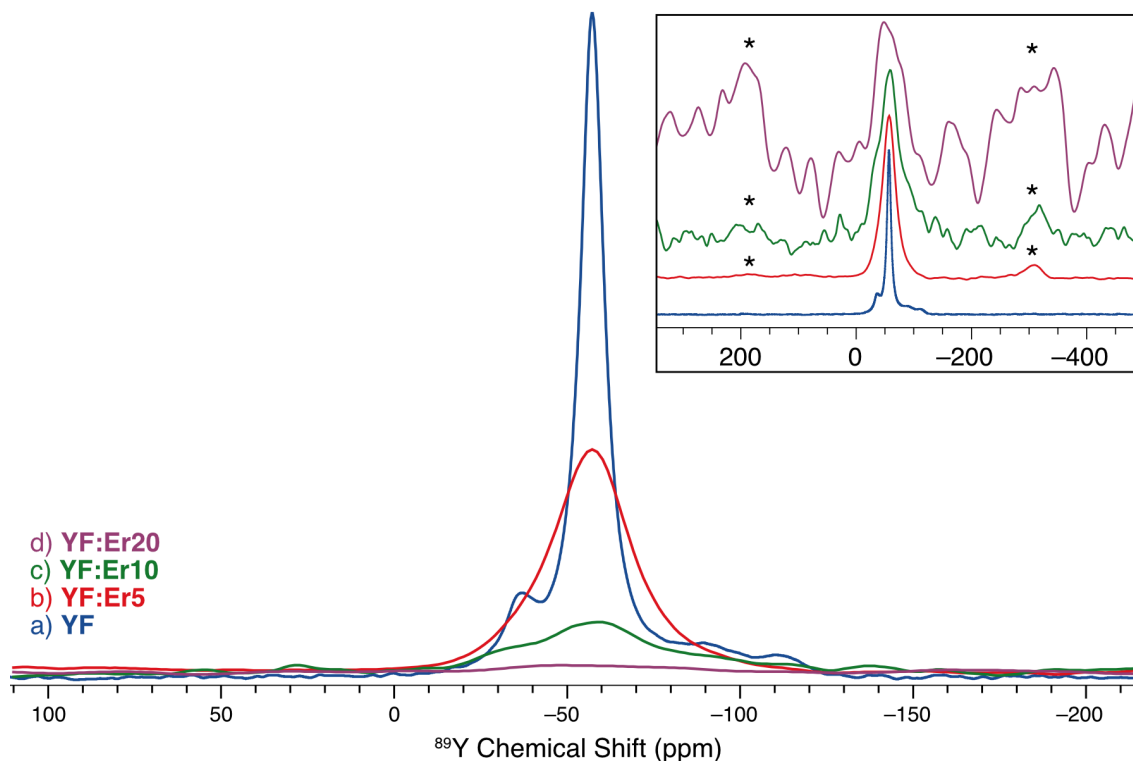


Figure 4.8. ^{19}F - ^{89}Y CP/MAS ($\nu_{\text{rot}} = 5$ kHz) NMR spectra of the Er-containing samples and YF. The inset shows the spectra scaled to the same maximum intensity. Asterisks denote spinning sidebands.

4.3.4.3 ^1H NMR Experiments on Er-Containing Samples

The ^1H UFMAS ($\nu_{\text{rot}} = 60$ kHz) NMR spectra of the Er-containing samples have broad isotropic peaks and intense SBBs (**Figure 4.9**). The isotropic peaks are broadened primarily due to relaxation from the paramagnetic centers, which prevents the resolution of much of the fine structure (*cf.*, the variety of ^1H sites detected in YF, **Figure 4.9a**).

The broad signal intensities are lopsided to low frequency, similar to the general shape of the spectrum of the undoped material. Interestingly, there appears to be some separation of features in the spectrum of YF:Er20 (**Figure 4.9d**, and **Figure C12**), as some of the peaks are shifted to negative ppm values (*ca.* -1 to -2 ppm). In the spectrum of YF:Er50, these peaks are shifted even further to low frequency (*ca.* -10 ppm, **Figure C12**). These features may indicate a Fermi or pseudocontact shift in the signal from the

surfactants, and indicate that the surfactants are in close proximity to some of the Er^{3+} ions near the surface of the particles. These results are consistent with homogeneous doping of the particles, which is difficult to detect using other methods.

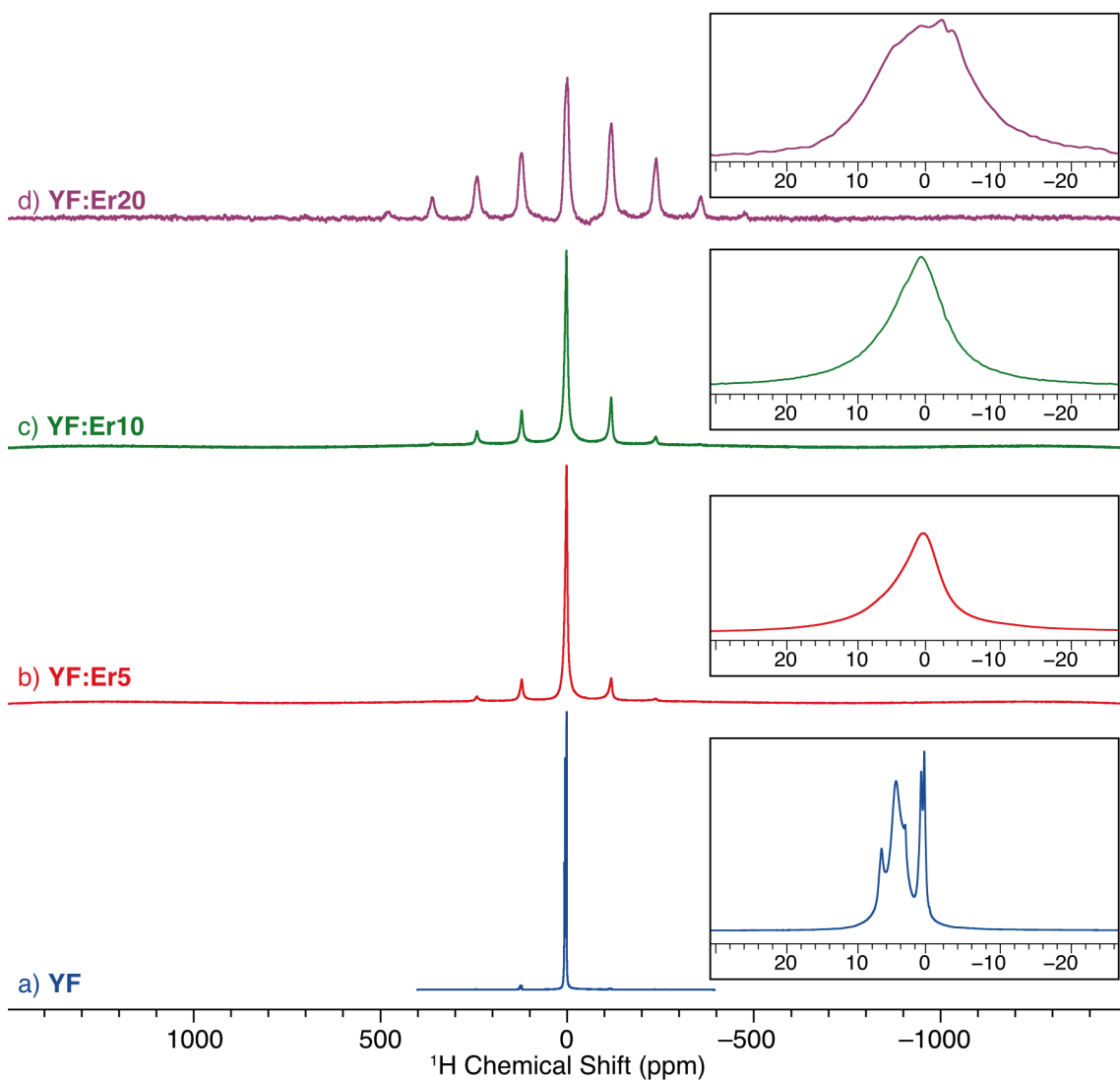


Figure 4.9. ^1H UFMAS ($\nu_{\text{rot}} = 60$ kHz) NMR spectra of the Er-containing samples and **YF**. The insets show expansions of the isotropic peaks. All other features are spinning sidebands.

As with the ^{19}F spectra, the SSB manifolds can be analyzed to obtain $\langle R \rangle$ values for the average $^1\text{H}\cdots\text{Er}^{3+}$ internuclear distances. While all of the individual ^1H environments could not be resolved, the fit of the broad pattern was improved by using 3

peaks at 6.6, 3.5, and 0.58 ppm, which largely arise from protons in the surfactant molecules. The results of this analysis are shown in **Table 4.6**. The three features have similar Δ_{aniso} values and therefore similar average $^1\text{H}\cdots\text{Er}^{3+}$ distances (ca. 8-10 Å).

With a homogeneous distribution of dopant, the probability, P , of at least one Er^{3+} ion being present within a given radius of a proton can be calculated using a binomial distribution as follows:⁶²

$$P = \sum_{k=0}^n x^k (1-x)^{n-k} \left(\frac{n!}{k! (n-k)!} \right) \quad (4.3)$$

where x is the dopant level and k is the number of dopant ions present in n possible dopant ion positions. This model can be used to measure probabilities for the $(\text{H}_3\text{O})\text{Y}_3\text{F}_{10}\cdot x\text{H}_2\text{O}$ structure with either: (i) Er^{3+} ions substitutionally replacing Y in the structure, or (ii) Er^{3+} ions occupying the pores of the structure. In the former case, there are eighteen Y sites in the first “shell” around the water atoms in the pore (*i.e.*, 5.0–5.6 Å from the ^1H) and an additional thirty-six within the second shell (*i.e.* 8.2-8.6 Å). For a 5 mol-% doping level, **Eq. 1.3** indicates that the probability that at least one Er replaces an Y site within the first and second coordination shells 60% and 93% of the time, respectively. At higher dopant levels, the probabilities increase further (*e.g.*, at 20 mol-% doping there is a 98% chance Er is located within the first shell). *N.B.* These probabilities can also be thought of as the proportion of the ^1H nuclei in the sample that are within the given radius (*i.e.*, 5.6 Å or 8.6 Å) of at least one Er. The pores of the structure are much less dense than the Y sites, so a homogeneous Er distributions with Er^{3+} ions in the pores would be much less concentrated than those where Er replaced Y substitutionally. As such, the analogous probabilities for Er within the first shell (6.7 Å radius, 4 sites) is

36%, and within the first two shells (12.8 Å, 31 sites) is 76%. At a 20% dopant level, the corresponding probabilities are 60% and 99.8%, respectively.

Regardless of the location of the dopants, NMR signals from ^1H nuclei with Er in their first shell (*i.e.*, *ca.* 5-6 Å) is not detected due to rapid nuclear relaxation caused by the paramagnetic interaction. If this signal could be acquired, it would produce a pattern with a very broad SSB manifold on the order of 2000 ppm or broader (such a pattern is not observed in the spectra of the NPs, **Figure 4.9**). Given the observed patterns, and the corresponding average $\text{Er}^{3+}\cdots^1\text{H}$ distances calculated from the SSB manifolds, it is likely that any signal from water molecules in the spectra of the Er-containing samples comes from ^1H sites with Er in their second shell. At higher dopant levels (*e.g.*, **YF:Er20**) it is unlikely that any signal from water in the **YF**-like structure is observed, and hence the signal results entirely from surfactant molecules.

4.3.4.4 Structural Conclusions (Er-Containing Samples)

Reactions conducted with a mixture of YCl_3 and ErCl_3 produce octahedral-shaped NPs that are isostructural with **YF** but contain Er^{3+} . The Er^{3+} dopant may incorporate directly into the $(\text{H}_3\text{O})\text{Y}_3\text{F}_{10}\cdot x\text{H}_2\text{O}$ structure (substituting for Y atoms) or be present in the channels. The former is consistent with the TEM images of these samples, which show that high Er^{3+} levels produce the same crystal shape as **YF**, indicating that Er^{3+} ions may incorporate less disruptively than Sc^{3+} (**Figure C1**) Unlike for the Sc-containing materials, where subtle shifts in the ^{19}F peaks indicate structural differences, the NMR analysis is inconclusive for the Er-containing samples largely due to paramagnetic broadening. However, SSNMR clearly demonstrates that regardless of the type of dopant incorporation, the doping throughout the sample is homogeneous as signals from

undoped materials are not observed. Finally, unlike the Sc-containing samples, the use of ErCl_3 does not result in substantial crystalline impurity phases or diamagnetic by-products (*e.g.*, YF_3) as indicated by the PXRD and SSNMR data. However, we cannot exclude the presence of a small amount of an amorphous, paramagnetic by-product that is undetected by both techniques.

4.3.5 Eu-Containing Samples

Eu^{3+} has a diamagnetic ground state, as well as an NMR-active isotope (^{153}Eu). However, ^{153}Eu is quadrupolar ($I = 5/2$) with an extremely large quadrupole moment (241.2 fm^2), which makes characterization with SSNMR impractical for most samples. However, as with the Er-containing samples, NMR spectra of the other NMR-active elements in the material can provide indirect information about the local structure of the Eu^{3+} ions.

4.3.5.1 ^{19}F NMR Experiments on Eu-Containing Samples

All of the ^{19}F UFMAS ($\nu_{\text{rot}} = 60 \text{ kHz}$) NMR spectra of the Eu-containing samples are similar to that of **YF** (**Figure 4.10**), with the exception of **YF:Eu50**, *vide infra*. At low Eu levels (5-20 mol-% Eu), the peaks broaden slightly as the doping levels increase, suggesting increased disorder of the F sites (*e.g.*, caused by incorporation of Eu^{3+} into the structure producing a distribution of F environments) or the presence of a small amount of a paramagnetic species that may influence ^{19}F transverse relaxation (*vide infra*). The three peaks corresponding to the zeolitic structure shift slightly relative to those of **YF**; however, these shift differences are within the limits of the estimated uncertainties of the chemical shifts. Furthermore, the shifts are affected by the presence of multiple underlying peaks that cannot be fully resolved. These features likely include those

resulting from surface sites as well as impurities like YF_3 (see **Figure 4.10 inset**, the presence of YF_3 and other species containing both Y and F is also supported by ^{89}Y NMR data, *vide infra*). Since these phases are not detected in the PXRD patterns (**Figure C6**), they are likely amorphous.

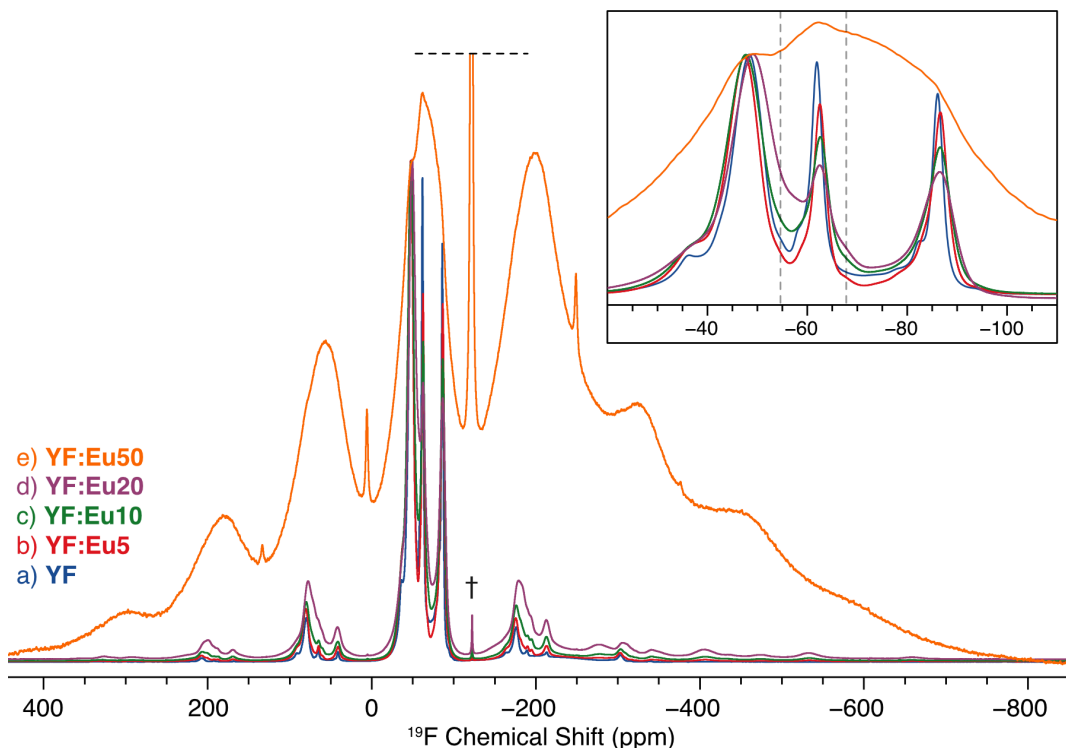


Figure 4.10. ^{19}F UFMAS ($\nu_{\text{rot}} = 60$ kHz) NMR spectra of the Eu-containing samples and **YF**. The inset shows an expanded view of the isotropic peaks, dashed lines indicate the locations of signals from YF_3 . The dagger symbol denotes a F^- impurity. All of the other features are spinning sidebands.

The ^{19}F NMR spectrum of **YF:Eu50** (**Figure 4.10e**) is distinct from the other samples, and features broad lineshapes and a much more intense SSB manifold. Some of the line broadening results from decreased sample crystallinity (PXRD results indicate the **YF:Eu50** sample contains mostly amorphous material, **Figure C6e**); however, the resulting disorder (and associated distribution of chemical shifts) does not account for the increase in the magnitude of the SSBs relative to the isotropic peaks. As with the Er-

doped materials, these changes result from the interaction of the ^{19}F nuclei with unpaired spin density centered at the Eu sites, indicating that the **YF:Eu50** sample is paramagnetic. The paramagnetic nature of this sample is also confirmed by EPR (**Figure C13**). Eu^{3+} has a diamagnetic ground state; however, it can be reduced to Eu^{2+} , which is paramagnetic. The latter is likely present in **YF:Eu50**, and produces much of the broadening observed in its ^{19}F SSNMR spectrum. PXRD results (**Figure C6**) suggest that this sample may contain both amorphous EuF_3 and EuF_2 , the latter of which supports the formation of Eu^{2+} species. The samples prepared with smaller amounts of Eu may also contain some paramagnetic Eu^{2+} material, as their ^{19}F SSNMR spectra (**Figure 4.10**) show slight line broadening and more intense SSBs in comparison to the spectrum of the undoped material. These features are most apparent in the spectrum of **YF:Eu20** (**Figure 4.10**), but the effect is significantly smaller than in that of **YF:Eu50**.

A notable difference between the ^{19}F spectrum of **YF:Eu50** and those of the paramagnetic Er-containing samples is that the isotropic peak region in the former appears to have some fine structure. As seen in the inset of **Figure 4.10** and in **Figure C14**, there are three features in the spectrum of **YF:Eu50** that are just barely resolved, with similar shifts to the three ^{19}F environments in **YF**. However, these features cannot be resolved in the SSBs, suggesting that this spectrum consists of features produced by multiple sites with different amounts of broadening and DSA. The deconvolution of this spectrum (**Figure C14**) shows a mixture of broad features with large SSB manifolds (due to the DSA produced by the paramagnetic centers) as well as narrower features with smaller Δ_{aniso} values (*e.g.*, from diamagnetic material, or regions with less unpaired spin

density). As such, this sample contains a mixture of paramagnetic material (containing Eu^{2+} ions) and diamagnetic material (similar to the undoped sample).

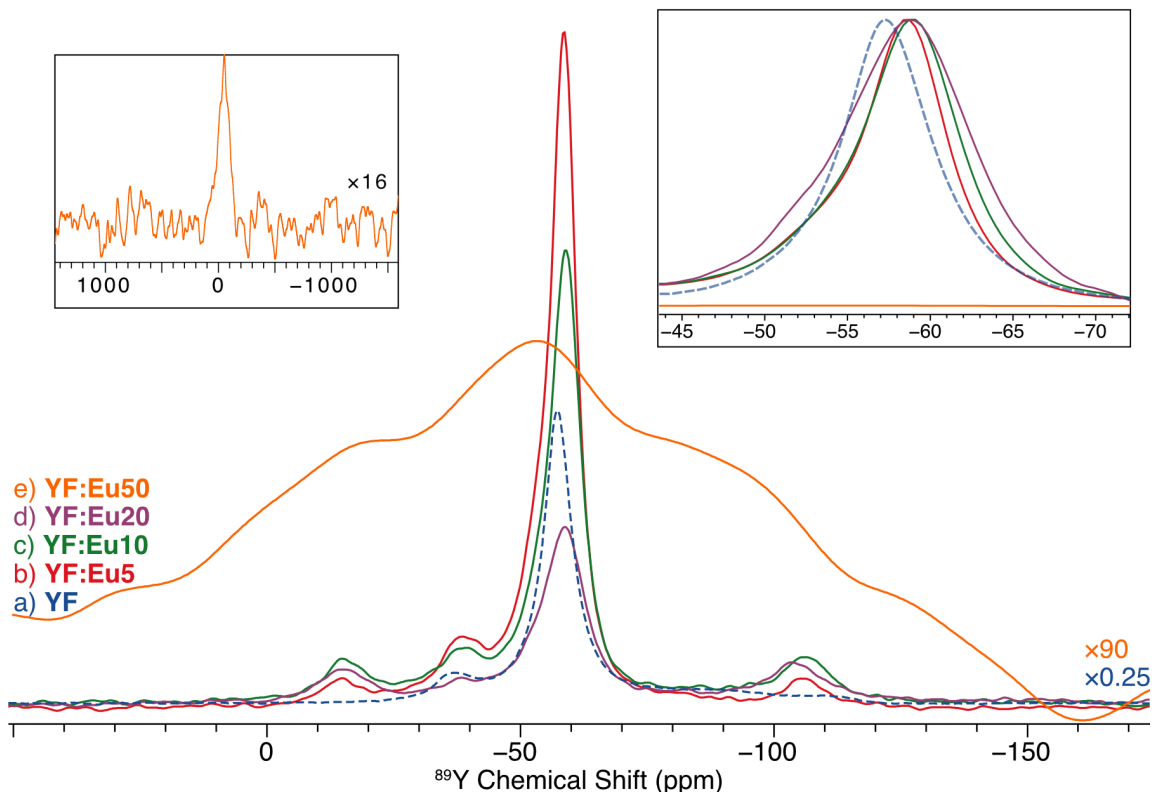


Figure 4.11. ^{19}F - ^{89}Y CP/MAS ($\nu_{\text{rot}} = 5$ kHz) NMR spectra of the Eu-containing samples (solid lines) and **YF** (dashed line). The latter is shown in the outset with *ca.* 0.25 vertical scaling, so that the lower intensity features from impurities in the Eu-containing samples can be seen. The right inset shows an expanded view of the most intense features in the spectra vertically scaled to have the same maximum intensity. The left inset shows the full spectrum of **YF:Eu50** with increased vertical scaling.

4.3.5.2 ^{89}Y NMR Experiments on Eu-Containing Samples

With the exception of **YF:Eu50** (*vide infra*), the ^{19}F - ^{89}Y CP/MAS ($\nu_{\text{rot}} = 5$ kHz) NMR spectra of the Eu-containing samples (**Figure 4.11**) are similar to each other. Each spectrum has four discernable features: (i) signals at roughly -36 and -57 ppm corresponding to **YF**-like material, (ii) a peak at -105 ppm resulting from YF_3 , and (iii) a feature from an additional impurity at -15 ppm. The most intense features in all of the

spectra are those from **YF**-like material, but their intensities decrease (relative to the signals from the impurities) with increasing amounts of dopant. Such a change is consistent with the replacement of Y by Eu in the reaction mixture. In contrast, the features from impurities (*i.e.*, at -105 ppm and -15 ppm) have roughly the same intensity in the spectra of all of the doped materials, suggesting that the amount of dopant does not affect how much of these by-products are produced. *N.B.* The NMR spectra shown in **Figure 4.11** are not quantitative, as they were acquired with CP/MAS. However, the CP efficiency should be consistent for the same type of ^{89}Y environment, and thus the intensities of a particular peak in several spectra can be compared.

As shown in the right inset of **Figure 4.11**, the peaks from the samples prepared with Eu are broader than those of the undoped **YF** material, and have centers of gravity that are shifted to a lower frequency. Such changes, which increase slightly with higher dopant level, indicate the presence of a distribution of chemical shifts, likely the result of incorporation of Eu in the samples. For all of the spectra, the distribution can be modeled as two Gaussian peaks, one broad and one narrow, centered at -57 and -58 ppm, respectively (see **Figure C15**). While the observed spectrum can be fit with other models (*e.g.*, a mixture of Gaussian/Lorentzian character), the presence of a narrow feature at -58 ppm is consistent with the ordered **YF**-like material indicated by PXRD (**Figure C6**).

The other features in the spectra (at -105 and -15 ppm) result from by-products of the reaction. The feature at -105 ppm is shifted by *ca.* $+5$ ppm relative to that of bulk YF_3 ; this shift could be due to the incorporation of Eu^{3+} ions, which is consistent with the observations of Bessada *et al.*, who noted a similar shift to high frequency in AlkF-YF_3

melts (Alk = Li, Na, K).³⁰ The peak at -15 ppm has a similar shift to one in the ^1H - ^{89}Y CP/MAS spectrum of **YF** (**Figure C8**, **Table 4.3**); however, the latter is not observed in the ^{19}F - ^{89}Y CP/MAS spectrum of **YF**, and thus is not the same material that produces the feature in the spectra of the Eu-containing samples. It is unlikely that either of the by-products identified in the ^{89}Y spectra are paramagnetic because paramagnetic centers strongly decrease CP efficiency^{49,60,61} (*cf.* ^{19}F - ^{89}Y spectra of the Er-containing samples, **Figure 4.8**). Unlike the Sc-containing samples, signal is not observed from yttrium hydroxy fluorides or hydrated YF_3 at -90 ppm, which implies that the role of water in this preparation is different when using Sc^{3+} or Eu^{3+} dopants (this conclusion is also supported by the ^1H NMR spectra, *vide infra*).

Consistent with the ^{19}F NMR results, the ^{19}F - ^{89}Y CP/MAS spectrum of **YF:Eu50** (**Figure 4.11e**) is distinct from those of the other Eu-containing samples. The paramagnetic interaction produces extensive line broadening in this spectrum, and severely decreases the CP efficiency such that the S/N is low (see left inset in **Figure 4.12**). The lack of sharp features suggests that all of the ^{89}Y nuclei in the sample are proximate to paramagnetic Eu^{2+} ions.

4.3.5.3 ^1H NMR Experiments on Eu-Containing Samples

The ^1H UFMAS ($v_{\text{rot}} = 60$ kHz) NMR spectra of the Eu-containing samples (**Figure 4.12**) are distinct from that of **YF**. While features from the surfactant molecules are present in the spectra, signal is not observed from the zeolitic water molecules in the $(\text{H}_3\text{O})\text{Y}_3\text{F}_{10}\cdot x\text{H}_2\text{O}$ structure.¹⁹ This result indicates that if any **YF**-like material is present, it is anhydrous, and something else (likely Eu^{3+} ions) occupies the pores of the NPs.

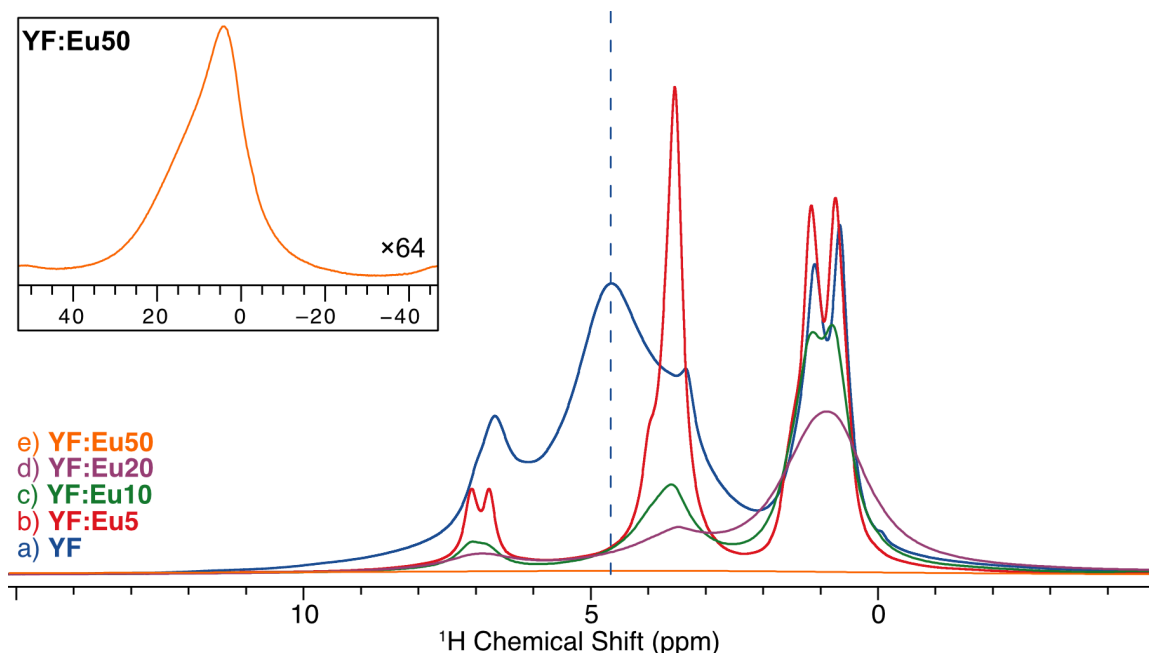


Figure 4.12. ^1H UFMAS ($\nu_{\text{rot}} = 60$ kHz) NMR spectra of the Eu-containing samples and **YF**. The inset shows the full spectrum of **YF:Eu50** with increased vertical scaling.

Consistent with the other spectra of the **YF:Eu50** sample, the paramagnetic interaction has a large effect on its ^1H UFMAS NMR spectrum (**Figure 4.12e**, **Figure C16**). This spectrum appears as a single peak that is lopsided to the low frequency side with a substantial SSB manifold. All of the fine structure observed in the spectra of the other samples is absent, which makes assignment of the spectrum to particular ^1H environments impossible. However, the lack of sharp features indicates that all of the ^1H nuclei in the sample are affected by the paramagnetic centers (*i.e.*, no signal from undoped material is observed). As such, any water and/or surfactant molecules must be within close proximity of the Eu^{2+} species. The paramagnetic interaction produces an increase in the intensity of the SSB manifold due to DSA (**Figure C16**). Using a two-site fit, the resulting Δ_{aniso} values indicate average $\text{Eu}^{2+\cdots 1}\text{H}$ distances of 7.1(3) Å and 7.9(3) Å, respectively. The resolution in the spectra of the other Eu-containing samples (**Figure 4.12b-d**) may also be affected by the presence of a small amount of paramagnetic Eu^{2+} .

For each sample, the resolution is poorer than that of **YF**, and gets progressively worse as the amount of Eu (and possibly Eu^{2+}) increases. An EPR study of these lower-concentration Eu samples is in progress.

4.3.5.4 Structural Conclusions on Eu-Containing Samples

Of the three RE elements studied in this work, the reactions involving Eu produce the most diverse collection of products. At low Eu levels, ^{19}F and ^{89}Y NMR data (supported by PXRD) suggest that **YF**-like material is produced, as well as two by-products that contain both Y and F atoms in close proximity to one another. The NMR features of the former are broader than those of the undoped **YF** material, consistent with a distribution of local F and Y environments produced by Eu incorporating into the channels of the structure; there is no evidence for Eu substitutionally replacing Y sites in the structure. Despite the structural similarities with **YF**, the ^1H NMR spectra indicate that the Eu-containing materials lack zeolitic water molecules. As such, Eu^{3+} ions present in the channels may block the diffusion of water into the structure, or affect the reaction conditions such that water is not present when the particle is forming. SSNMR experiments, supported by EPR data, reveal that at higher dopant levels, a paramagnetic material is formed, which contains a mixture of Y, F, and likely Eu^{2+} ions (as Eu^{3+} is diamagnetic). PXRD data suggest these products are amorphous, and that EuF_2 and EuF_3 may also be produced in the reaction.

4.3.6 General Structural Discussion (All Dopants)

Replacing some of the YCl_3 in the previously-reported synthesis of **YF** with another $(\text{RE})\text{Cl}_3$ forms a variety of products that depend on which $(\text{RE})\text{Cl}_3$ is used. With all but the highest doping levels (*i.e.*, > 50 mol-% RE^{3+} dopant), the syntheses produce

YF material as the primary product, as confirmed by multinuclear SSNMR (^{19}F , ^{89}Y , ^1H) and PXRD, with the dopant ions incorporating into the structures. Samples prepared with all of the YCl_3 replaced with ScCl_3 or EuCl_3 do not produce a product that is isostructural with **YF**, but rather the $(\text{RE})\text{F}_3$. The effects of dopant ions on the NMR spectra are most dramatic in the case of Er^{3+} , because the product is paramagnetic, which results in severely broadened spectra. Despite the lower resolution of isotropic peaks, these spectra provide additional structural information: namely, that the Er^{3+} dopants are homogeneously distributed throughout the NPs, and are even found proximate to the surfaces of the particles. The effects of Sc^{3+} and Eu^{3+} dopants are easier to compare, because both materials produce diamagnetic materials at low dopant levels. The ^{19}F and ^{89}Y NMR spectra of both samples have a distribution of chemical shifts, which is most consistent with ions sitting in the channels of the structure. The Sc^{3+} ions appear to replace H_3O^+ sites and are eight-coordinate, probably bound to water molecules in two neighboring pores. The Eu^{3+} ions may occupy different sites in the channels (*e.g.*, in the pores themselves), and/or inhibit the movement of water through the structure in some way. ^1H NMR results reveal that the incorporation of water is different in the Sc- and Eu-containing materials. The former have zeolitic water molecules (consistent with the undoped **YF** material), while the latter appear to be anhydrous. As such, it is likely that the location of the ions plays a role in the hydration of the material. Finally, different by-products are generated depending on which dopant is present. For the Eu-containing samples, PXRD results indicate EuF_3 and EuF_2 are formed, and NMR detects a YF_3 -like material, possibly with Eu^{3+} dopants incorporated into the structure. Similarly, with high Sc-content, ScF_3 is the major product; however Sc^{3+} ions also produce a hydrated Y-F

species (*e.g.*, $\text{Y(OH)}_{(3-x)}\text{F}_x$ or $\text{YF}_3 \cdot x\text{H}_2\text{O}$), which is not observed in the Eu-containing samples.

4.4 Conclusions

In this study, we have demonstrated that a combination of multinuclear SSNMR, PXRD, TEM, and EPR can be used to identify the structures and compositions of products in NPs prepared using different RE^{3+} ions dispersed in nonionic reverse micelles. These syntheses produce undoped **YF** NPs of high purity; however, when other RE^{3+} ions are introduced, they feature complicated reaction kinetics in solution that result in numerous by-products whose identities depend on both the nature and amount of the dopant ions. At lower doping levels (*i.e.*, < 20 mol-%), doped **YF**-like NPs are the dominant product. These dopant ions can incorporate themselves in a variety of different ways, including (i) by replacing Y sites in the host material substitutionally, (ii) replacing H_3O^+ sites in the channels, and (iii) binding to the sides of the pores that would otherwise contain water molecules. Our results suggest that SSNMR is uniquely capable of identifying these structurally distinct outcomes.

There are numerous factors that may play a role in determining the outcome of the syntheses including: (i) differences in ionic size (**Table 4.1**) and the associated differences bond lengths or coordination geometries, (ii) charge balance (*e.g.*, replacement of H_3O^+ with RE^{3+} would create a net-positively charged structure), (iii) differences in the interaction of the RE^{3+} ions with water (*e.g.*, enthalpies of solvation), (iv) reactivity of the RE^{3+} ions (which could affect the rate of NP nucleation vs. growth), and/or (v) differences in the mobility of water molecules within the zeolitic structures. Studies like the current work are the first steps in trying to isolate key factors in NP

preparation such that syntheses can be optimized to reliably yield the desired products with high purity. The methods discussed herein should be very useful for the continued study of these materials, as well as numerous other classes of NPs, to aid in the development of successful methods for the rational design of advanced materials.

4.5 References

- (1) *The Rare Earth Elements: Fundamentals and Applications*, 1st ed.; Atwood, D. A., Ed.; John Wiley & Sons Ltd: West Sussex, United Kingdom, 2012.
- (2) Sorace, L.; Benelli, C.; Gatteschi, D. *Chem. Soc. Rev.* **2011**, *40*, 3092.
- (3) Gutfleisch, O.; Willard, M. A.; Brück, E.; Chen, C. H.; Sankar, S. G.; Liu, J. P. *Adv. Mater.* **2011**, *23*, 821–842.
- (4) Herbst, J. F. *Rev. Mod. Phys.* **1991**, *63*, 819–898.
- (5) Arnold, P. L.; McMullon, M. W.; Rieb, J.; Kühn, F. E. *Angew. Chemie Int. Ed.* **2015**, *54*, 82–100.
- (6) McFarland, E. W.; Metiu, H. *Chem. Rev.* **2013**, *113*, 4391–4427.
- (7) Gai, S.; Li, C.; Yang, P.; Lin, J. *Chem. Rev.* **2014**, *114*, 2343–2389.
- (8) Huang, X.; Han, S.; Huang, W.; Liu, X. *Chem. Soc. Rev.* **2013**, *42*, 173–201.
- (9) Bünzli, J.-C. G. *Coord. Chem. Rev.* **2015**, *293–294*, 19–47.
- (10) Wang, X.; Liu, Q.; Bu, Y.; Liu, C.-S.; Liu, T.; Yan, X. *RSC Adv.* **2015**, *5*, 86219–86236.
- (11) Ormerod, R. M. *Chem. Soc. Rev.* **2003**, *32*, 17–28.
- (12) Antolini, E.; Perez, J. *Int. J. Hydrogen Energy* **2011**, *36*, 15752–15765.
- (13) Wang, H.-Q.; Batentschuk, M.; Osvet, A.; Pinna, L.; Brabec, C. J. *Adv. Mater.* **2011**, *23*, 2675–2680.
- (14) Zhao, Y.; Shang, L.; Cheng, Y.; Gu, Z. *Acc. Chem. Res.* **2014**, *47*, 3632–3642.
- (15) Zhang, Y.; Zhang, K.; Wang, J.; Tian, Z.; Li, A. D. Q. *Nanoscale* **2015**, *7*, 19342–19357.
- (16) Jia, Y. Q. *J. Solid State Chem.* **1991**, *95*, 184–187.
- (17) Lemyre, J.; Ritcey, A. M. *Chem. Mater.* **2005**, *17*, 3040–3043.
- (18) Lemyre, J.-L.; Lamarre, S.; Beaupré, A.; Ritcey, A. M. *Langmuir* **2011**, *27*, 11824–11834.
- (19) Lucier, B. E. G.; Johnston, K. E.; Arnold, D. C.; Lemyre, J.; Beaupré, A.; Blanchette, M.; Ritcey, A. M.; Schurko, R. W. *J. Phys. Chem. C* **2014**, *118*, 1213–1228.
- (20) Caron, C.; Boudreau, D.; Ritcey, A. M. *J. Mater. Chem. C* **2015**, *3*, 9955–9963.
- (21) Peersen, O.; Wu, X.; Smith, S. *J. Magn. Reson.* **1994**, *106*, 127–131.
- (22) Peersen, O. B.; Wu, X. L.; Kustanovich, I.; Smith, S. O. *J. Magn. Reson.* **1993**, *104*, 334–339.
- (23) Metz, G.; Wu, X. L.; Smith, S. O. *J. Magn. Reson.* **1994**, *110*, 219–227.
- (24) Bennett, A. E.; Rienstra, C. M.; Auger, M.; Lakshmi, K. V.; Griffin, R. G. *J. Chem. Phys.* **1995**, *103*, 6951–6958.
- (25) Thakur, R. S.; Kurur, N. D.; Madhu, P. K. *J. Magn. Reson.* **2008**, *193*, 77–88.
- (26) Scholz, G.; Dreger, M.; Bertram, R.; Kemnitz, E. *Dalt. Trans.* **2015**, *44*, 13522–13529.
- (27) Nishizawa, H.; Okumoto, K.; Mitsushio, T. *J. Solid State Chem.* **1991**, *92*, 370–379.
- (28) Kołodziejwski, W.; Kęcki, Z. *J. Mol. Struct.* **1975**, *29*, 27–31.
- (29) Wu, J.; Boyle, T. J.; Shreeve, J. L.; Ziller, J. W.; Evans, W. J. *Inorg. Chem.* **1993**, *32*, 1130–1134.
- (30) Bessada, C.; Rakhmatullin, A.; Rollet, A.; Zanghi, D. *J. Fluor. Chem.* **2009**, *130*,

- 45–52.
- (31) Dupree, R.; Smith, M. E. *Chem. Phys. Lett.* **1988**, *148*, 41–44.
 - (32) Lo, A. Y. H.; Sudarsan, V.; Sivakumar, S.; van Veggel, F.; Schurko, R. W. *J. Am. Chem. Soc.* **2007**, *129*, 4687–4700.
 - (33) Sadoc, A.; Body, M.; Legein, C.; Biswal, M.; Fayon, F.; Rocquefelte, X.; Boucher, F. *Phys. Chem. Chem. Phys.* **2011**, *13*, 18539.
 - (34) Greve, B. K.; Martin, K. L.; Lee, P. L.; Chupas, P. J.; Chapman, K. W.; Wilkinson, A. P. *J. Am. Chem. Soc.* **2010**, *132*, 15496–15498.
 - (35) Alba, M. D.; Chain, P.; Florian, P.; Massiot, D. *J. Phys. Chem. C* **2010**, *114*, 12125–12132.
 - (36) Kim, N.; Hsieh, C.-H.; Stebbins, J. F. *Chem. Mater.* **2006**, *18*, 3855–3859.
 - (37) Rossini, A. J.; Schurko, R. W. *J. Am. Chem. Soc.* **2006**, *128*, 10391–10402.
 - (38) Loiseau, T.; Serre, C.; Huguenard, C.; Fink, G.; Taulelle, F.; Henry, M.; Bataille, T.; Férey, G. *Chem. Eur. J.* **2004**, *10*, 1373–1382.
 - (39) Buchholz, A.; Wang, W.; Arnold, A.; Hunger, M. *Microporous Mesoporous Mater.* **2003**, *57*, 157–168.
 - (40) Li, S.; Zheng, A.; Su, Y.; Fang, H.; Shen, W.; Yu, Z.; Chen, L.; Deng, F. *Phys. Chem. Chem. Phys.* **2010**, *12*, 3895.
 - (41) Ward, J. W. *J. Phys. Chem.* **1968**, *72*, 4211–4223.
 - (42) Reddy, T. I.; Varma, R. S. *Tetrahedron Lett.* **1997**, *38*, 1721–1724.
 - (43) Frising, T.; Leflaive, P. *Microporous Mesoporous Mater.* **2008**, *114*, 27–63.
 - (44) Nery, J. G.; Mascarenhas, Y. P.; Bonagamba, T. J.; Mello, N. C.; Souza-Aguiar, E. *F. Zeolites* **1997**, *18*, 44–49.
 - (45) van Bokhoven, J. a; Roest, A. L.; Koningsberger, D. C.; Miller, J. T.; Nachttegaal, G. H.; Kentgens, A. P. M. *J. Phys. Chem. B* **2000**, *104*, 6743–6754.
 - (46) Thomas, B.; Das, B. B.; Sugunan, S. *Microporous Mesoporous Mater.* **2006**, *95*, 329–338.
 - (47) Han, L.; Wang, Y.; Guo, L.; Zhao, L.; Tao, Y. *Nanoscale* **2014**, *6*, 5907–5917.
 - (48) Hu, L.; Chen, J.; Pan, Z.; Deng, J.; Yu, R.; Xing, X. *J. Am. Ceram. Soc.* **2014**, *97*, 1386–1388.
 - (49) Bertini, Ivano; Luchinat, Claudio; Parigi, Giacomo; Ravera, E. *NMR of Paramagnetic Molecules. Applications to Metalloproteins and Models.*; 2016.
 - (50) Pintacuda, G.; Kervern, G. In *Modern NMR Methodology*; Heise, H., Matthews, S., Eds.; Springer Berlin Heidelberg: Berlin, Heidelberg, 2013; pp 157–200.
 - (51) Bertmer, M. *Solid State Nucl. Magn. Reson.* **2017**, *81*, 1–7.
 - (52) Nayeem, A.; Yesinowski, J. P. *J. Chem. Phys.* **1988**, *89*, 4600.
 - (53) Herzfeld, J.; Berger, A. E. *J. Chem. Phys.* **1980**, *73*, 6021–6030.
 - (54) Harris, R. K.; Olivieri, A. C. *ChemInform* **2003**, *34*, 1–10.
 - (55) Wickramasinghe, N. P.; Shaibat, M. A.; Ishii, Y. *J. Phys. Chem. B* **2007**, *111*, 9693–9696.
 - (56) Hirsh, D. A.; Zhang, X.; van Veggel, F. C. J. M.; Schurko, R. W. **2017**, In preparation.
 - (57) Antzutkin, O. N.; Lee, Y. K.; Levitt, M. H. *J. Magn. Reson.* **1998**, *135*, 144–155.
 - (58) Golding, R. M.; Pascual, R. O.; McGarvey, B. R. *J. Magn. Reson.* **1982**, *46*, 30–42.
 - (59) Bertini, I.; Janik, M. B. L.; Lee, Y.-M.; Luchinat, C.; Rosato, A. *J. Am. Chem. Soc.*

- 2001**, *123*, 4181–4188.
- (60) Peng, W. K.; Samoson, A.; Kitagawa, M. *Chem. Phys. Lett.* **2008**, *460*, 531–535.
- (61) Konig, S. H. *J. Magn. Reson.* **1982**, *47*, 441–453.
- (62) Palke, A. C.; Stebbins, J. F.; Boatner, L. A. *Inorg. Chem.* **2013**, *52*, 12605–12615.
- (63) Shannon, R. D. *Acta Crystallogr. Sect. A* **1976**, *32*, 751–767.
- (64) Zinchenko, V. .; Efyushina, N. .; Eryomin, O. .; Markiv, V. Y.; Belyavina, N. .; Mozkova, O. .; Zakharenko, M. . *J. Alloys Compd.* **2002**, *347*, L1–L3.
- (65) Kunkel, N.; Meijerink, A.; Kohlmann, H. *Inorg. Chem.* **2014**, *53*, 4800–4802.

Chapter 5: ³⁵Cl Dynamic Nuclear Polarization Solid-State NMR of Active Pharmaceutical Ingredients

5.1 Introduction

The identification of solid forms of active pharmaceutical ingredients (APIs) plays an important role in drug development, both in the discovery of new forms and quality control.¹⁻³ Each polymorph, pseudopolymorph (such as a hydrate or solvate), cocrystal, or salt of an API is uniquely patentable,^{4,5} and can have substantially different physicochemical properties (stability, solubility, bioavailability etc.).⁶⁻¹¹ Undesired phases or impurities in dosage forms are potentially dangerous or costly; hence, new and innovative methods are needed for characterizing APIs, both in the bulk phase and especially within solid dosage forms.

Solid APIs are commonly characterized using X-ray diffraction (powder or single-crystal), ¹H and ¹³C solid-state NMR (SSNMR), thermogravimetric methods, and other spectroscopic techniques.¹²⁻¹⁸ In many cases, these techniques provide adequate characterization of the bulk forms of APIs; however, they are often of limited use for dosage forms (especially those with low weight percentages, wt-%, of the API). In particular, both PXRD patterns and ¹³C SSNMR spectra of dosage forms often display interfering signals from the excipient (*e.g.*, binding ingredients and fillers), which obscure signals arising from the API.

Prior studies by our group¹⁹⁻²¹ and others^{22,23} have demonstrated that ³⁵Cl SSNMR is a valuable tool for characterizing the bulk and dosage forms of APIs that have been synthesized as HCl salts (excipients do not contain chloride ions, and thus do not produce interfering signals in the ³⁵Cl SSNMR spectra of dosage forms). Since ³⁵Cl is a

quadrupolar nucleus ($I = 3/2$), its spectra are influenced by a combination of anisotropic chemical shift and quadrupolar interactions. The latter are particularly sensitive to small structural differences in the local Cl^- anion environments arising from variations in local hydrogen bonding.^{19,20,24–27} As a result, each solid phase of an API produces a distinct ^{35}Cl SSNMR spectral fingerprint. Given the importance of identifying low concentrations of API phases within dosage forms (including impurities), it is crucial to improve the lower detection limit (LDL) of ^{35}Cl SSNMR experiments.

Our research group has developed pulse sequences that enable the rapid acquisition of broad ^{35}Cl SSNMR patterns (hundreds of kHz or more) with high S/N, even at moderate field strengths (*e.g.*, 9.4 T). Unlike older methods,^{28–30} these pulse sequences rely on phase-modulated frequency-swept WURST (wideband uniform-rate smooth truncation) pulses^{31,32} for broadband excitation and polarization transfer. The WURST-CPMG^{33,34} and broadband adiabatic inversion cross-polarization (BRAIN-CP)³⁵ pulse sequences are used for direct (^{35}Cl) and indirect (^1H - ^{35}Cl) broadband excitation of ^{35}Cl SSNMR spectra, respectively. The BRAIN-CP-WURST-CPMG sequence (BCP for short) uses BRAIN-CP to transfer spin polarization from abundant nuclides (*e.g.*, ^1H) to dilute nuclides (*e.g.*, ^{35}Cl), and a subsequent WURST-CPMG pulse and windowed acquisition train for further signal enhancement (**Figure D1**).

Over the past few years, high-field dynamic nuclear polarization (DNP) has become a prominent method for achieving high gains in S/N for SSNMR experiments.^{36–39} Recent developments in DNP NMR instrumentation (*e.g.*, high-frequency gyrotrons,^{40,41} low-temperature MAS probes^{42,43}), optimized radical polarizing agents,^{44–48} and the availability of commercial DNP NMR spectrometers^{49,50} have enabled signal

increases in excess of 300, representing potential time savings by a factor of 90,000. DNP has enabled SSNMR experiments that were previously considered challenging or impossible, allowing the detailed study of materials that were previously inaccessible to SSNMR.⁵¹⁻⁶⁰ Most materials are prepared for DNP experiments by using a simple incipient wetness impregnation procedure to coat the surface of the particles, or fill the porous volume with a radical polarizing agent solution.^{47,61} Saturation of the EPR transitions of the radicals with microwaves results in enhanced polarization of the nuclei (most often protons) that are in close proximity to the polarizing agents.⁴⁶ In the case of micro-particulate organic solids (*e.g.*, APIs), DNP-enhanced polarization can be relayed from the surface of the particles into the interiors of the solids by ^1H - ^1H spin diffusion without perturbing their macroscopic structure.^{62,63} With this technique, DNP-enhanced solid-state NMR can be applied to organic solids,⁶³⁻⁶⁶ pure APIs,^{63,66-69} and low API wt-% dosage forms.⁶⁹ These developments have enabled natural isotopic abundance ^{13}C - ^{13}C , ^1H - ^{15}N and ^{13}C - ^{15}N correlation SSNMR experiments which would be difficult or impossible without DNP.

To date, most DNP SSNMR studies have been limited to the characterization of nuclei with fairly narrow powder patterns (*i.e.*, breadths on the order of tens of kHz or less). These reports include the spectral acquisition of a variety of spin-1/2 nuclei as well as quadrupolar nuclei in highly symmetric environments (*e.g.*, ^2H , ^{14}N overtone, ^{17}O , ^{27}Al , and ^{51}V).^{55,56,64,66,70-75} However, the enhancements afforded by DNP also make it an attractive technique for the acquisition of NMR spectra of broader patterns (*e.g.*, ^{35}Cl SSNMR) due to their inherently low S/N that largely results from the distribution of NMR signal across a wide frequency range. During the final preparation of this work,

Kobayashi *et al.* published one such example in a report on DNP-enhanced ultra-wideline ^{195}Pt SSNMR.⁷⁶ One factor that hinders the acquisition of DNP-enhanced wideline spectra from stationary samples is that moderate- and fast-magic angle spinning (MAS) results in substantially higher DNP and sensitivity enhancements.^{47,50,77-79} MAS rates of ca. 6 to 40 kHz provide DNP enhancements (ϵ) that are *ca.* 3 to 5 times higher than those obtained from static (*i.e.*, stationary sample) experiments.^{47,50,77,78} Unfortunately, MAS experiments are not generally useful for patterns with breadths on the order of 100 kHz or more, especially for quadrupolar nuclides. First, MAS only results in partial averaging of the effects of the second-order quadrupolar interaction, and second, even very fast MAS may not result in the separation of the spinning sidebands from the isotropic centerband.⁸⁰ Matters are further complicated by the effects of first-order quadrupolar interactions and/or large chemical shift anisotropies. In many cases, MAS spectra of broad patterns are distorted and have low S/N, which prevents the accurate determination of quadrupolar and chemical shift tensor parameters.

Herein, we show that DNP can be used to enhance S/N in static wideline ^{35}Cl SSNMR patterns of APIs acquired with BCP methods. We detail a new protocol, called spinning-on spinning-off (**SOSO**) acquisition, for enhancing the DNP polarization under MAS and subsequently acquiring a wideline ^{35}Cl pattern free from spinning sidebands under static conditions. These techniques result in DNP enhancements in ^{35}Cl SSNMR spectra of up to a factor of 110 at 100 K and $B_0 = 9.4$ T. We demonstrate the application of ^{35}Cl DNP SSNMR for the characterization of APIs in their bulk forms, as well as in dosage forms with Cl contents of as low as 0.45 wt-%. The application of these

techniques for polymorph differentiation, impurity identification, and the discovery of new solid phases are also demonstrated.

5.2 Methods

5.2.1 Sample Preparation

Bulk samples of histidine hydrochloride monohydrate (**hist**), ambroxol hydrochloride (**ambr**), isoxsuprine hydrochloride (**isox**), diphenhydramine hydrochloride (**diph**), and cetirizine dihydrochloride (**ceti**), with purities ranging between 98 and 99 wt-%, were purchased from Sigma-Aldrich Canada, Ltd. and used without further purification (**Figure 5.1**).

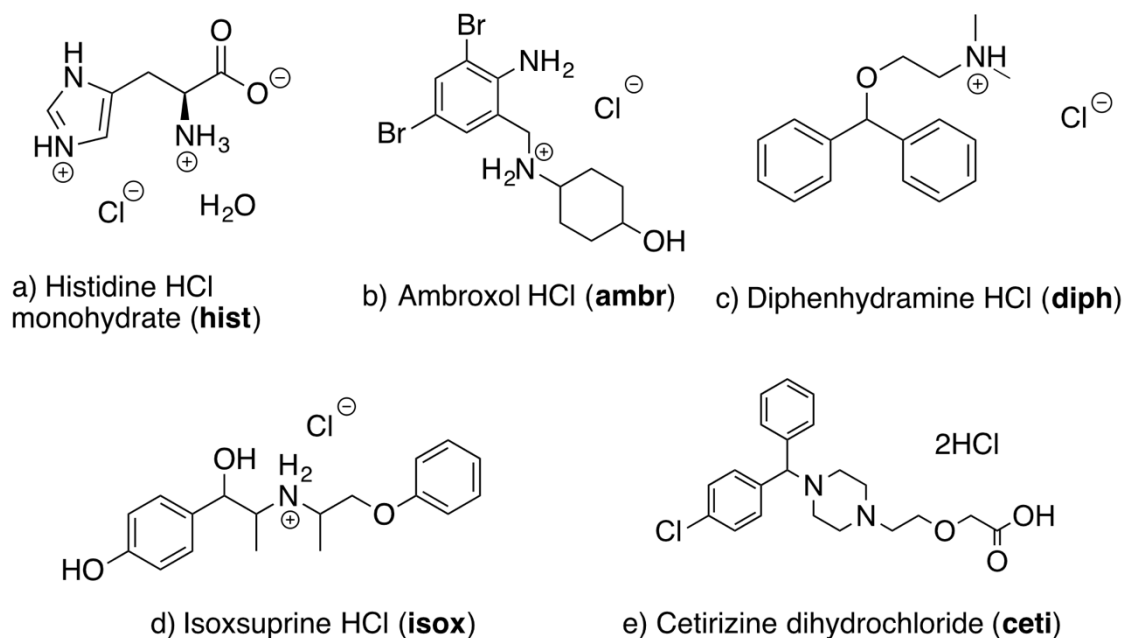


Figure 5.1. Molecular structures of APIs.

A 10 mg tablet of isoxsuprine and a 25 mg tablet of Life Brand diphenhydramine obtained at local pharmacies were used as the dosage forms of **isox** and **diph**, respectively. The weight percentages of chlorine in the bulk and dosage samples are

tabulated in **Appendix D (Table D2)**. To prepare the samples for DNP SSNMR experiments, the bulk powders were ground by hand for several minutes in a mortar and pestle to reduce particle sizes, while the dosage form tablets were only lightly crushed to break the tablets into a fine powder. The samples were then impregnated^{52,61} with *ca.* 15 μL of 15 mM TEKpol in 1,1,2,2-tetrachloroethane (TCE)⁴⁷ (**hist**, **ambr**, **isox**) or 1,3-dibromobutane (DBB) (**ceti**, **diph**) and packed into 3.2 mm sapphire rotors.

5.2.2 VT PXRD

Variable-temperature powder X-ray diffraction (PXRD) experiments were conducted using the APEX III software suite and a Bruker Photon 100 CMOS diffractometer with a graphite monochromator with $\text{CuK}\alpha$ ($\lambda = 1.5406 \text{ \AA}$). Samples were ground, packed into glass capillary tubes, and then cooled with a stream of cold N_2 from an Oxford cryostream attached to the diffractometer. PXRD patterns were acquired for all of the samples and the identities of the samples with known crystal structures were confirmed by comparison to simulated patterns (**Figure D13**).^{81–84}

5.2.3 NMR

^{13}C and ^{35}Cl SSNMR DNP experiments were conducted on a 9.4 T (400 MHz)/263 GHz Bruker Avance III solid-state DNP NMR spectrometer⁵⁰ using a 3.2 mm HXY probe configured for ^1H - ^{13}C - ^{35}Cl experiments located at the DOE Ames Laboratory. Carbon and ^{chlorine} chemical shifts were referenced to TMS at 0 ppm, using the unified scale in the IUPAC standard.⁸⁵ Preliminary DNP NMR experiments were conducted at the EPFL (Lausanne) on a Bruker Avance I solid-state DNP NMR spectrometer equipped with a 3.2 mm HXY probe configured for ^1H - ^{13}C - ^{35}Cl .

The full experimental parameters used for the ^{13}C and ^{35}Cl experiments are given in **Appendix D (Table D3 to Table D6)**. **NMR - ^{13}C :** All ^1H - ^{13}C CP/MAS experiments used a CP contact time of 2 ms, and a constant ^{13}C spin lock rf field of *ca.* 74 kHz. An MAS frequency of 8 kHz (or 9 kHz for **isox**) was used. The ^1H spin lock amplitude was linearly ramped⁸⁶⁻⁸⁸ from *ca.* 75 kHz to 83 kHz. Proton decoupling was applied for each acquisition using an rf field of 100 kHz and the SPINAL-64 pulse sequence.⁸⁹ **NMR - ^{35}Cl :** ^1H - ^{35}Cl CP-CPMG and CP-echo spectra of **hist** were acquired using conventional rectangular pulses with *ca.* 70 kHz rf on both channels. The ^1H - ^{35}Cl BRAIN-CP-WURST-CPMG (BCP) pulse sequence³⁵ was used to acquire the spectra of all of the other samples. The sweep direction of the WURST pulse applied during the BCP contact period can result in lopsided powder patterns; to minimize these effects on the ^{35}Cl powder patterns of **isox** and **diph**, two sub-spectra were acquired with opposite sweep directions for the BCP contact pulses. These sub-spectra were then co-added together to form the final spectrum (**Figure D10**). With the exception of the spectra of **hist**, all of the ^{35}Cl spectra were acquired using WURST-CPMG refocusing pulses.^{33,34} To process these spectra, the echoes in each FID were co-added to form a single echo, which was then Fourier transformed and magnitude processed.

Because of the breadth of the ^{35}Cl powder pattern of **ceti** (*vide infra*), its ^1H - ^{35}Cl BCP spectrum was acquired using frequency-stepped acquisition.^{28,29,90} Four pieces were acquired with the transmitter frequencies separated by 50 kHz increments. These pieces were then co-added together to produce the final spectrum.

The dipolar hetero-nuclear multiple-quantum correlation rotatory-resonance recoupling (D-HMQC-R₃) pulse sequence^{91,92} was used to obtain a 2D dipolar ¹³C-³⁵Cl correlation spectrum in the **hist** sample. See **Table D4** for the experimental parameters.

5.2.4 Software

All spectra were processed using the TopSpin 3.2 software package. Analytical simulations of the processed ³⁵Cl SSNMR spectra (**Figures S5-S9**) were generated using the Solid Lineshape Analysis module (v. 2.2.4) within TopSpin. The resulting quadrupolar and chemical shift parameters are listed in **Table D7**. Simulated ³⁵Cl MAS NMR spectra were obtained using the simulation program for solid-state NMR spectroscopy (SIMPSON).^{93,94}

5.3 Results and Discussion

5.3.1 Histidine HCl

Histidine HCl (**hist**) is an excellent setup standard for DNP experiments due to its long $T_1(^1\text{H})$, which is *ca.* 284 s at 100 K. Slow longitudinal relaxation is advantageous for remote DNP, as it allows for increased ¹H polarization buildup and greater DNP enhancements.⁴⁷ The ¹H-¹³C CP/MAS NMR spectra of **hist** obtained with and without microwaves are shown in **Figure 5.2a**. The corresponding ¹³C DNP enhancement ($\epsilon_{\text{CP}}(^{13}\text{C}) = 260$) is the highest measured for all of the compounds in this study. All ¹³C signals from histidine are easily resolved and differentiated from the broad 1,1,2,2-tetrachloroethane (TCE) solvent peak at *ca.* 75 ppm. The ¹H-³⁵Cl CP-CPMG NMR spectra of **hist** acquired with and without DNP are shown in **Figure 5.2b**. Even under completely static sample conditions, a large DNP enhancement is observed when the microwaves are turned on ($\epsilon_{\text{CP}}(^{35}\text{Cl}) = 50$) (**Figure 5.2b**). However, when the sample is

rotated during part of the 30 s recycle/polarization delay, an additional 2.2-fold signal gain over the static DNP experiment is observed (**Figure 5.2b**). We call this technique spinning-on spinning-off (SOSO). To acquire the spectrum with SOSO, we manually controlled the sample spinning at *ca.* 200 to 2000 Hz during the recycle delay and stopped the sample spinning several seconds before collecting a spectrum under static conditions (see **Figure D1** for a schematic diagram of the pulse sequence timings). This procedure was repeated for each of the 4 to 8 scans in the experiment. SOSO allows for a larger ^1H polarization build-up due to improved DNP while the sample is spinning and acquisition of a distortion-free wideline spectrum under static conditions. The improved DNP enhancement with spinning is consistent with previous results that show increased DNP enhancements in ^1H - ^{13}C CP/MAS NMR spectra with increasing sample spinning speeds up to *ca.* 10-15 kHz.^{47,50,77,78}

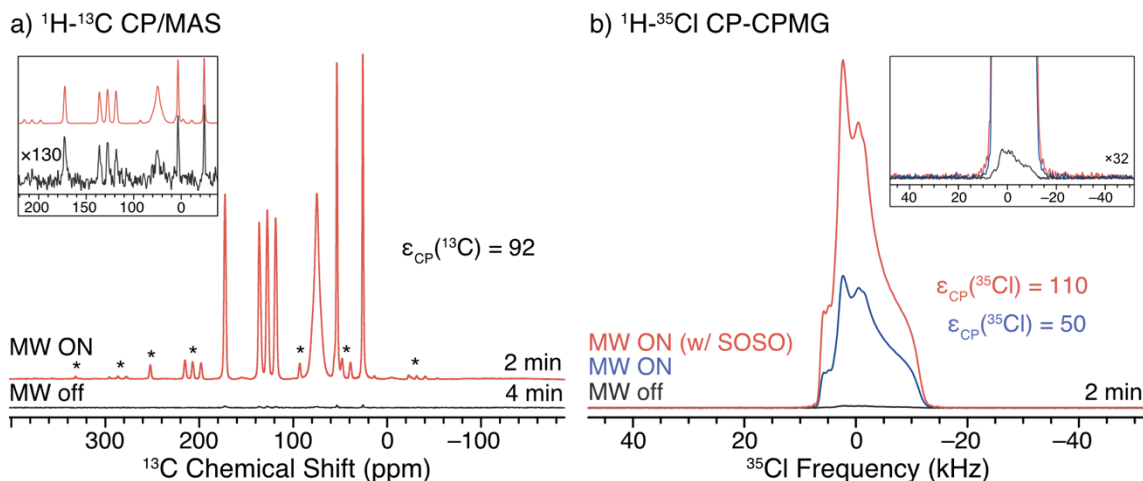


Figure 5.2. ^{13}C and ^{35}Cl SSNMR spectra of finely ground **hist** impregnated with a 15 mM TEKPol/TCE solution acquired at 100 K and $B_0 = 9.4$ T. a) ^1H - ^{13}C CP/MAS spectra acquired with and without microwaves. The top inset shows the two ^{13}C spectra scaled to the same maximum intensity. Asterisks denote spinning sidebands. b) ^1H - ^{35}Cl CP-CPMG spectra acquired with microwaves and rotation during part of the recycle delay period (SOSO conditions, red), with microwaves and a stationary sample (blue), and a stationary sample without microwaves (black). The inset shows a vertical expansion of the ^{35}Cl SSNMR spectra.

In order to examine the effects of slow MAS on DNP efficiency (without the application of SOSO), a ^{35}Cl SSNMR spectrum was acquired with uninterrupted slow MAS at 250 Hz and the CP-echo pulse sequence (**Figure 5.3a**). Slow MAS yields a central transition powder pattern that is very similar in appearance to that obtained from a corresponding experiment on a static sample (**Figure 5.3a** and **Figure D2**). The signal in the spectrum acquired with continuous slow MAS is *ca.* 3.1 times greater than that acquired under static conditions (**Figure 5.3a**). Thus, the DNP enhancement under continuous MAS is slightly greater than that obtained with SOSO (2.2 times, *vide supra*). The ^{35}Cl DNP enhancements in these spectra are lower than the enhancements seen in the ^{13}C NMR spectra, due in part to the slower MAS frequencies used in both the SOSO and slow MAS ^{35}Cl SSNMR experiments.

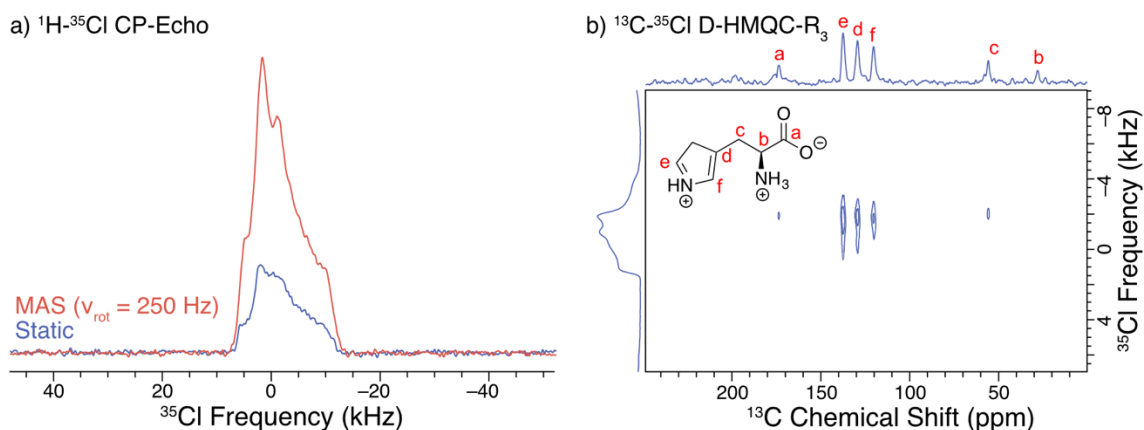


Figure 5.3. a) DNP-enhanced ^{35}Cl SSNMR spectra of finely ground **hist** impregnated with a 15 mM TEKPol/TCE solution acquired with the CP-Echo pulse sequence under continuous slow MAS ($v_{\text{rot}} = 250 \text{ Hz}$) (red) and with the sample stationary at all times (blue). b) 2D ^{13}C - ^{35}Cl D-HMQC- R_3 correlation spectrum of **hist** acquired under MAS ($v_{\text{rot}} = 8 \text{ kHz}$) with a projection of the 2D data along the direct dimension axis and the ^{35}Cl CPMAS-echo spectrum shown along the indirect dimension axis.

Since **hist** has a small quadrupolar coupling constant, a high-quality DNP enhanced CP-echo spectrum was also acquired at a faster MAS frequency of 8 kHz (**Figure D3**), resulting in a powder pattern free of overlapping spinning sidebands. The

DNP enhancement of this MAS spectrum ($\epsilon_{\text{CP}}(^{35}\text{Cl}) = 230$) is comparable to the enhancements seen in the ^{13}C NMR spectra ($\epsilon_{\text{CP}}(^{13}\text{C}) = 260$, *vide supra*). While slow or moderate MAS experiments may be useful for acquiring spectra of narrow central transition patterns that can be partially averaged (*i.e.*, static pattern breadths < 50 kHz, **Figure D3**), overlap of the MAS powder patterns with spinning sidebands is problematic for spectra with broader central transition patterns. Such overlap yields spectra without clearly defined discontinuities, which are difficult to analyze (**Figure D4** and *vide infra*). Given that the ^{35}Cl SSNMR spectra of anionic chlorides in hydrochloride salts of APIs typically have powder patterns with breadths spanning 100-300 kHz at moderate field strengths,¹⁹⁻²¹ MAS ^{35}Cl experiments with spinning rates between 5 and 15 kHz are not suitable for the characterization of most APIs. Furthermore, the polarization transfer from ^1H to quadrupolar nuclei is often challenging to optimize and inefficient under MAS conditions.⁹⁵

All of the ^{35}Cl SSNMR spectra of **hist** can be simulated with the same quadrupolar tensor parameters: $C_{\text{Q}} = 1.8(1)$ MHz, $\eta_{\text{Q}} = 0.72(2)$, $\delta_{\text{iso}} = 16(5)$ ppm (spectral simulations of these and all other ^{35}Cl powder patterns in this work can be found in **Appendix D, Figure D5-Figure D9** and **Table D7**). While these parameters agree with those reported in a recent study by Pandey *et al.* ($C_{\text{Q}} = 1.8$ MHz and $\eta_{\text{Q}} = 0.66$),²² they do not match those reported by Bryce *et al.* for the room temperature spectrum of **hist** ($C_{\text{Q}} = 4.59$ MHz, $\eta_{\text{Q}} = 0.46$, $\delta_{\text{iso}} = 93$ ppm).²⁴ It is possible that the study by Bryce *et al.* involved a different polymorph of **hist**.

DNP enhancement also provides access to two-dimensional experiments that would otherwise be challenging or impossible. One such example is a 2D heteronuclear

dipolar correlation spectrum of proximate ^{13}C and ^{35}Cl nuclei. As a proof of concept, we obtained a ^{13}C - ^{35}Cl dipolar heteronuclear multiple-quantum correlation spectrum (**Figure 5.3b**) with rotatory-resonance recoupling (D-HMQC- R^3).^{91,92} This 2D spectrum shows correlations between the ^{13}C and ^{35}Cl nuclei that are close to each other. Such results may provide valuable distance constraints on the structure of the molecule that may be useful for NMR crystallography.⁹⁶ With DNP at higher magnetic fields and/or with faster sample spinning rates, it should be possible to acquire ^{13}C - ^{35}Cl correlation spectra for APIs with larger values of C_Q . 2D ^{13}C - ^{35}Cl correlation NMR spectra could enable overlapping ^{35}Cl powder patterns in APIs with multiple ^{35}Cl sites to be resolved by correlation to high resolution ^{13}C resonances.

5.3.2 Ambroxol HCl

Ambroxol HCl (**ambr**) is an API that is used to treat a myriad of respiratory diseases by clearing mucus from the respiratory tract. It is sold under a variety of trade names, including Mucosolvan, Mucobrox, Mucol, Lasolvan, Mucoangin, Surbronc, Ambolar, and Lysopain. A substantial DNP-enhancement ($\epsilon_{\text{CP}}(^{13}\text{C}) = 92$) was measured for the ^1H - ^{13}C CP/MAS NMR spectra of **ambr** (**Figure 5.4a**). The decreased enhancement relative to **hist** could result from less favorable relaxation characteristics; the $T_1(^1\text{H})$ of **ambr** at 100 K (*ca.* 30 s) is far less than that of **hist** (*ca.* 284 s), which limits the DNP enhancements of **ambr**.^{62,63}

As with **hist**, DNP provides a considerable signal enhancement ($\epsilon_{\text{CP}}(^{35}\text{Cl}) = 15$) in the ^1H - ^{35}Cl BCP NMR spectra acquired under static conditions (**Figure 5.4b**). If the SOSO procedure is used (*i.e.*, where the sample is spun slowly during most of the recycle delay and then is stationary during the pulse and acquisition periods), the DNP

enhancement is further increased by a factor 2 and $\epsilon_{\text{CP}}(^{35}\text{Cl}) = 30$ is observed (**Figure 5.4b**). The combination of DNP and BCP produces a high S/N spectrum, spanning roughly 200 kHz, (*ca.* 10 times broader than that of **hist**).

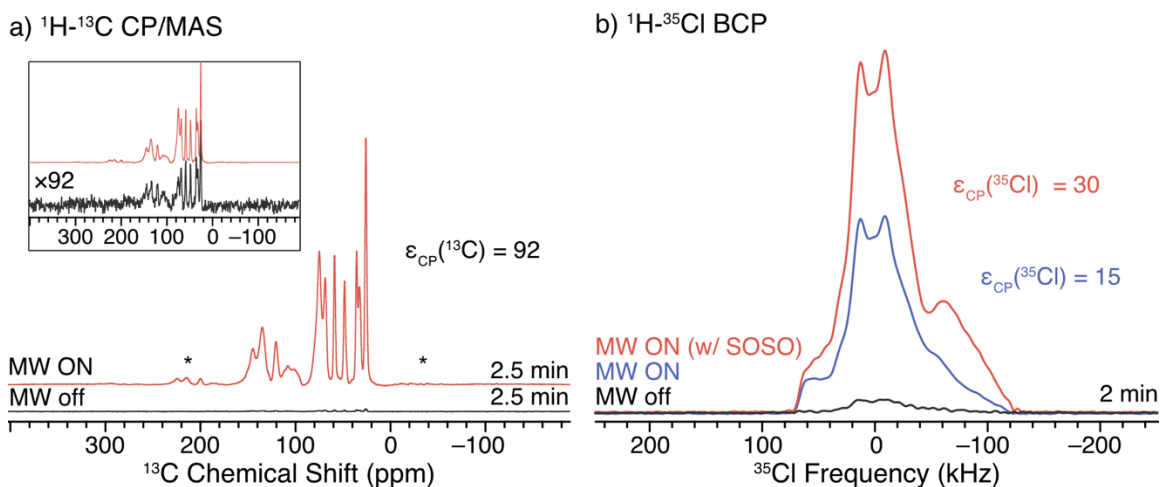


Figure 5.4. ^{13}C and ^{35}Cl SSNMR spectra of finely ground **ambr** impregnated with 15 mM TEKPol/TCE solution acquired at 100 K and $B_0 = 9.4$ T. a) ^1H - ^{13}C CP/MAS spectra acquired with and without microwaves to drive DNP. The top inset shows the two ^{13}C spectra scaled to the same maximum intensity. The asterisks denote spinning sidebands. b) ^1H - ^{35}Cl BCP spectra acquired with microwaves and slow MAS rotation during most of recycle delay period (SOSO condition, red), with microwaves and with the sample stationary at all times (blue), and with the sample stationary without microwaves (black).

Given the breadth of the ^{35}Cl powder pattern of **ambr** at 9.4 T, it is not possible to use conventional MAS (*i.e.*, constant spinning throughout the experiment). At the spinning speeds typically used for DNP-enhanced ^{13}C NMR experiments (*i.e.*, between 8 and 15 kHz), the presence of spinning sidebands distorts the ^{35}Cl pattern and makes analysis of the powder pattern challenging (**Figure D4**). These issues result because (i) slower MAS rates do not average the effects of the second-order quadrupolar interaction, leading to patterns with many overlapping sidebands that are difficult to simulate, and (ii) spinning speeds exceeding 40 to 50 kHz are necessary to separate the spinning sidebands from the isotropic centerband for typical values of ^{35}Cl C_Q at 9.4 T (or hundreds of kHz

for other quadrupolar nuclides).⁸⁰ However, DNP MAS probes with faster spinning rates have recently become available,⁷⁹ and may enable acquisition of spectra exhibiting undistorted isotropic centerbands for ³⁵Cl sites with larger values of C_Q .

There is a slight distortion in the low-frequency shoulder (at *ca.* -70 kHz) of the pattern acquired with the SOSO method. This distortion may arise from an improperly refocused CPMG echo train, which results from the sample not coming to a complete stop after spinning during the recycle delay – even very slow spinning can be disastrous for these experiments (**Figure D10**). The starting and stopping of the sample spinning was performed manually for this preliminary set of experiments. In the future, these issues could be addressed with the addition of specialized hardware to precisely control the spinning rate and stop/start timings of the sample. Alternatively, longer recycle delays could be employed, at the expense of a slight reduction in sensitivity.

5.3.3 Isoxsuprine HCl

The API isoxsuprine HCl (**isox**), commonly sold as Duvadilan, is a vasodilator used for both human and equine treatments. We have previously characterized **isox** in its bulk and dosage forms using ³⁵Cl static NMR experiments without DNP.²¹ The ¹H-¹³C CP/MAS NMR spectra of both the bulk and dosage forms of **isox** (**Figure 5.5a** and **Figure 5.5b**, respectively) can be acquired in only a few minutes with DNP ($\epsilon_{CP}(^{13}C) = 86$ and 32, respectively). The DNP enhancement of the signal from the API in the dosage form is much less than that from the bulk form of the API (a trend that continues with the other dosage form samples in this study, *vide infra*). Such lower DNP enhancements for dosage forms are likely due to: (i) differences in the particle sizes of the API in the bulk

and dosage forms, (ii) the distribution of the radical solution in the sample, (iii) the presence of the excipient, or (iv) some combination of these factors.

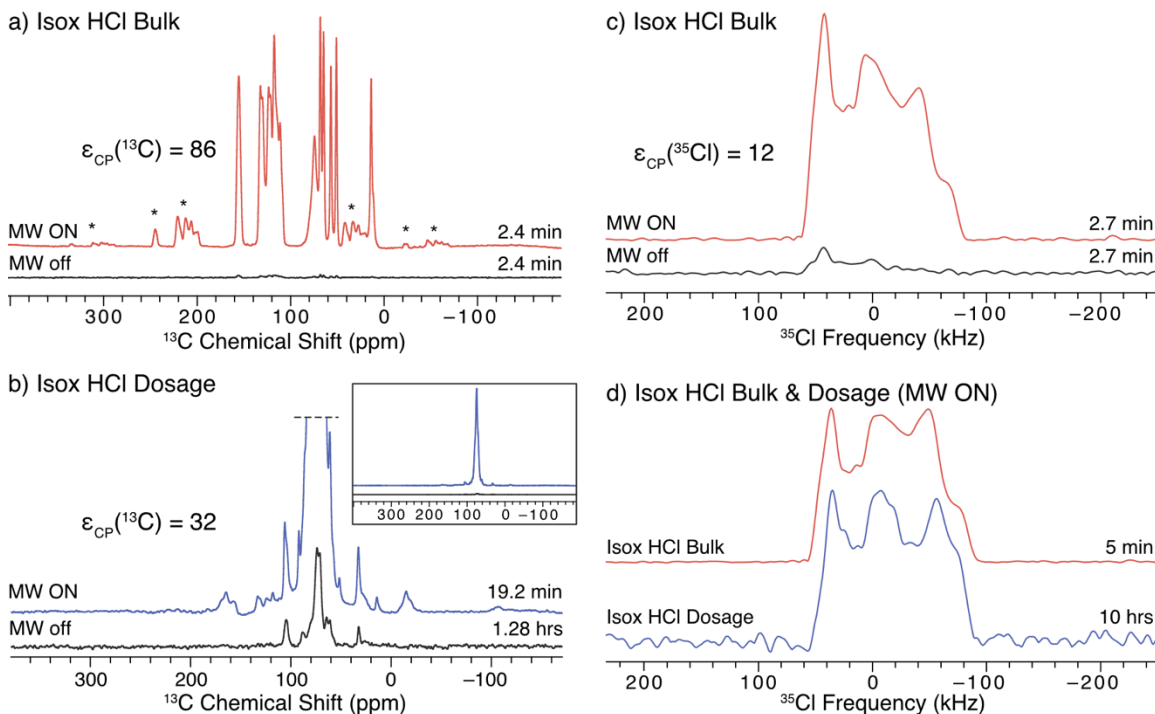


Figure 5.5. SSNMR spectra of the bulk and dosage forms of **isox** impregnated with a 15 mM TEKPol/TCE solution acquired at 100 K and $B_0 = 9.4$ T. The left column has ^1H - ^{13}C CP/MAS spectra of a) the bulk API and b) the dosage samples acquired with microwaves on and off. The bottom inset shows the full spectra of the dosage form without vertical clipping. The right column has ^1H - ^{35}Cl BCP spectra of c) the bulk API with and without microwaves and d) the bulk API and dosage samples with DNP enhancement. The lineshapes in c) are lopsided to the high frequency side because only one sweep direction of the BCP contact pulse was used (see **Figure D10** for more details).

First, there are likely differences in the size of the API particles in the bulk and dosage forms due to the processing the API undergoes during tablet manufacturing. Second, the radical solution may be adsorbed preferentially by excipients during the impregnation step, or, if most of the API particles were coated with an excipient (*e.g.*, a polymer) during production of the dosage form, the radical solution may not penetrate the excipient.⁶⁹ Finally, the API particles may be coated with an excipient phase having an intrinsically short $T_1(^1\text{H})$, a very high concentration of protons, or unfavorable dielectric

properties that reduce local microwave fields. All of these effects would reduce DNP enhancements of the ^1H nuclei at the surface of the API particles and subsequently inside the cores of the API particles. DNP enhancements could probably be further improved on a case-by-case basis by optimizing the solvent used for impregnation (including investigating the use of fully- and partially-deuterated solvents), the concentration of radical in the solution, and the amount of radical solution used for the impregnation step.^{62,63}

Another complication is that the DNP enhancements of signals arising from the API, solvent, and excipient molecules are not the same, as was observed in a prior study of several cetirizine dosage forms using DNP-enhanced ^{13}C SSNMR.⁶⁹ In the case of **isox** (**Figure 5.5b, inset**), the strongest signal is observed for a feature at 74.8(2) ppm, which corresponds to the solvent, TCE ($\epsilon_{\text{CP}}(^{13}\text{C}) = 104$). This intense feature dominates the spectrum of the dosage form and obscures several peaks from the API. The DNP enhancement of the unobscured API signal (*e.g.*, peaks at *ca.* 110-135 ppm), $\epsilon_{\text{CP}}(^{13}\text{C}) = 32$, is less than that of the solvent. Finally, there are features that correspond to various types of excipient molecules,^{69,97,98} which have enhancements ranging from 12 to 50. Overlapping signals from the API and excipient make it challenging to determine the phase of an API in ^{13}C NMR spectra even without the use of DNP;²¹ however, the differences in the DNP-enhancement such as those observed in the spectra of **isox** can further complicate the analysis. While the signal from the solvent can be decreased by adding a spin-echo to the pulse sequence⁹⁹ doing so only marginally improves the resolution of the features from **isox** (**Figure D14**).

^{35}Cl SSNMR can selectively probe the API in the dosage form without interfering signals from the excipients, since chloride ions are only found in the API and the ^{35}Cl signal from covalently-bound chlorines would be extremely broad and of too low intensity to be detected.^{100–102} A comparison of the DNP-enhanced ^1H - ^{35}Cl BCP NMR spectra of bulk and dosage forms of **isox** is shown in **Figure 5.5d**. The DNP enhancement observed for **isox** under static conditions (**Figure 5.5c**, $\epsilon_{\text{CP}}(^{35}\text{Cl}) = 12$) is comparable to that of **ambr** (*cf.* **Figure 5.4b**). Both the ^{35}Cl SSNMR spectra of the bulk and dosage forms of **isox** are consistent with spectra acquired without DNP¹⁹ (see **Figure D7** for the spectral simulation and associated quadrupolar parameters). The fact that the powder pattern of the tablet matches that of the bulk compound confirms that both samples contain the same polymorph of **isox**. There are additional features in the centers of both patterns (with centers of gravity at *ca.* 0 ppm). While the origin of this feature is still under study, it may result from Cl^- anions coordinated to H_2O (*e.g.*, as a result of disproportionation of the HCl salt), or some other chemical or physical alteration of the sample (see VT-PXRD patterns in **Figure D11**).

A primary advantage of DNP experiments is that dosage forms of APIs can be studied even if the wt-% of the API is very low, as is the case for **isox** (4.95 wt-% API, 0.52 wt-% Cl). Here, the combined acquisition time of the ^{35}Cl spectra of the pure and dosage forms of **isox** with DNP was just over 10 hours, roughly half the experiment time necessary to acquire a comparable set of spectra at room temperature.²¹ Such time savings are critical in the high-throughput screening of dosage forms with low wt-% APIs. Given the long acquisition times required to obtain sufficient ^{35}Cl signal without

microwaves, we have not attempted to acquire these spectra, and cannot report an enhancement in the spectrum of dosage **isox** (or the other dosage forms, *vide infra*).

SOSO experiments were not conducted on **isox** because of its short $T_1(^1\text{H})$ of 15 s. The short $T_1(^1\text{H})$ limits the amount of time available for ^1H polarization build up before the polarization is lost to longitudinal relaxation. Roughly 25 s were required to start the sample spinning and completely stop rotation, which was not fast enough to fit within the optimal polarization time (20 s) for the experiments with **isox**. Of course, a longer polarization time could be applied to perform the SOSO method; however, the gains from increased DNP enhancement would be partially offset from reduced sensitivity arising from use of a recycle delay longer than $1.3 \times T_1$. As with **ambr** (*vide supra*), the ^{35}Cl powder pattern is too broad for conventional MAS to be used.

5.3.4 Diphenhydramine HCl

Diphenhydramine HCl (**diph**) is a widely used antihistamine, most commonly sold under the trade name Benadryl. The ^1H - ^{13}C CP/MAS NMR spectra of both bulk **diph** (**Figure 5.6a**) and the dosage form (**Figure 5.6b**) show fair DNP enhancement ($\epsilon_{\text{CP}}(^{13}\text{C}) = 25$ and 16, respectively) and can be acquired in 2 minutes or less. The most intense feature in both of these spectra is a broad feature at *ca.* 50(2) ppm, which corresponds to the solvent, 1,3-dibromobutane (DBB). DBB was used for these experiments because **diph** was found to be soluble in TCE. Distinct features corresponding to the API (*e.g.*, at 128(1) ppm) can be distinguished from those of the solvent and excipient in the spectrum of the dosage form (**Figure 5.6b**).

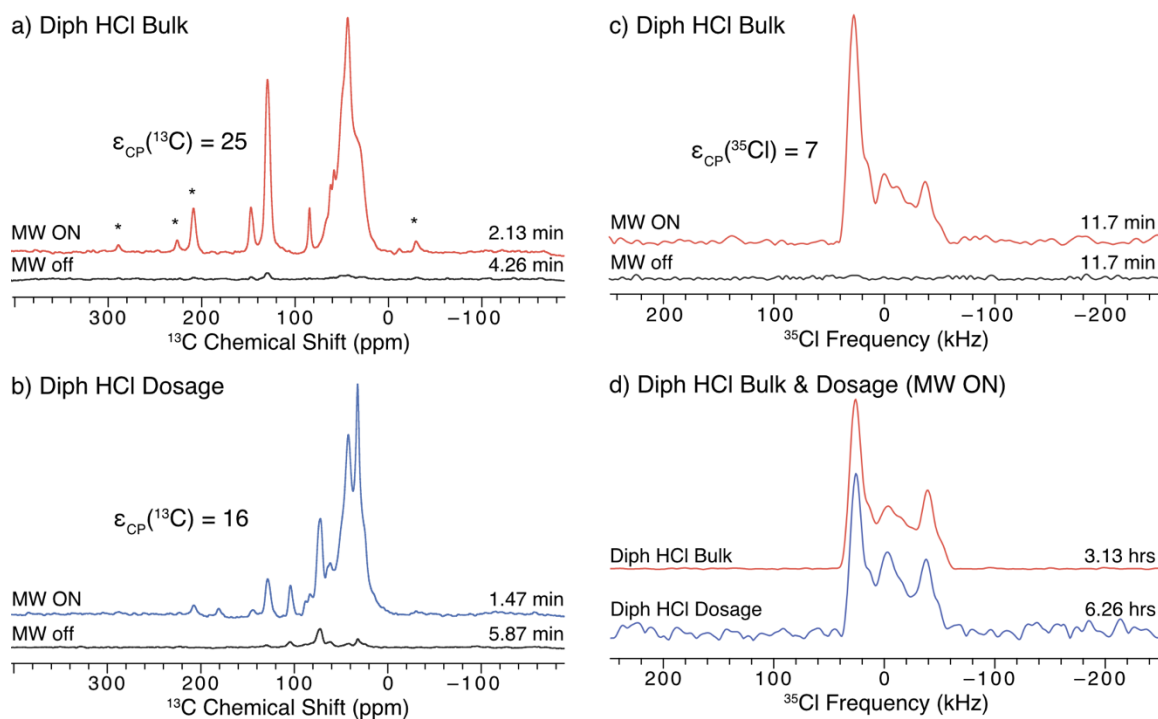


Figure 5.6. ^{13}C and ^{35}Cl SSNMR spectra of the bulk and dosage forms of **diph** impregnated with a 15 mM TEKPol/1,3-dibromobutane solution acquired at 100 K and $B_0 = 9.4$ T. The left column has ^1H - ^{13}C CP/MAS spectra of a) the bulk API and b) the dosage samples acquired with microwaves on and off. Asterisks denote spinning sidebands. The right column has ^1H - ^{35}Cl BCP spectra of c) the bulk API with and without microwaves and d) the bulk API and dosage samples with DNP enhancement. The lineshape in c) is lopsided to the high frequency side because only one sweep direction of the BCP contact pulse was used (see **Figure D11** for more details).

The DNP enhancement observed in these spectra is not as high as those observed in the spectra of the other samples (**Figure 5.2**, **Figure 5.4**, and **Figure 5.5**). One contributing factor is that **diph**, like **isox**, has a relatively short $T_1(^1\text{H})$ (*ca.* 18 s), which limits the build-up of enhanced polarization in the microcrystalline solid. The choice of solvent for the radical also plays an important role, as prior studies have reported decreased enhancements when using DBB rather than TCE, however, DBB was required for solubility reasons.^{47,48,103} Another disadvantage of the use of DBB is that it produces a broad solvent peak in the ^{13}C SSNMR spectra, which can obscure features from the API and excipient and make confirmation of the phase and purity even more difficult. Clearly,

the identification of other compatible solvents is an important future step for the further optimization of DNP experiments on APIs.

Unlike the ^{13}C spectra, the ^1H - ^{35}Cl BCP NMR spectra of **diph** (**Figure 5.6d**) are free from signal interference from the excipient and solvent. The breadths of the powder patterns and locations of the discontinuities are identical, which confirm that the same phase of **diph** is present in both the bulk and dosage forms. These features are also consistent with previous work done at room temperature.²¹ As with the spectra of **isox**, there is an additional low-intensity feature at *ca.* $-4(2)$ ppm that may result from disproportionation of the API. It is difficult to measure the DNP enhancement of these spectra due to the low S/N in the spectrum acquired without microwaves (**Figure 5.6c**). The *estimated* minimum value of $\epsilon_{\text{CP}}(^{35}\text{Cl}) = 7$ was obtained by comparing the spectra after applying a Fourier transform directly to the CPMG echo train (see **Figure D12**).

Prior ^{35}Cl SSNMR studies of this compound have relied on direct excitation experiments (*e.g.*, WURST-CPMG)²¹ because attempts to use CP at room temperature were unsuccessful due to poor CP efficiency. While CP experiments are still a challenge at low temperature, they are possible with the use of DNP. Unfortunately, the variation of CP efficiency with temperature when using the BCP pulse sequence is not well understood. DNP experiments, such as those reported here, could provide opportunities for further understanding the CP dynamics, and lead to improvements to the BCP sequence and related experiments under DNP conditions.

5.3.5 Cetirizine HCl

SSNMR is extremely useful for the study of APIs that form solid amorphous phases.^{104,105} One such API is cetirizine dihydrochloride (**ceti**), an antihistamine that is commonly sold under the trade names Zyrtec and Reactine.

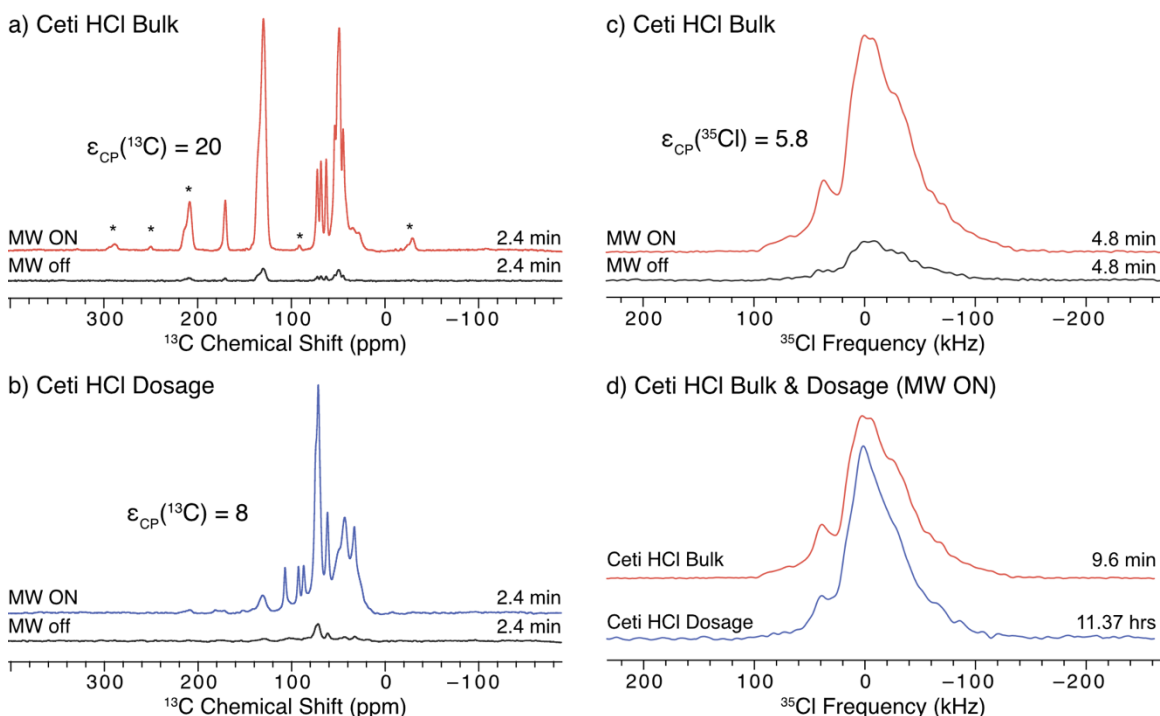


Figure 5.7. ^{13}C and ^{35}Cl SSNMR spectra of the bulk and dosage forms of **ceti** impregnated with 15 mM TEKPol/1,3-dibromobutane solution acquired at 100 K and $B_0 = 9.4$ T. The left column has ^1H - ^{13}C CP/MAS spectra of a) the bulk API and b) the dosage samples acquired with and without microwaves. Asterisks denote spinning sidebands. The right column shows the ^1H - ^{35}Cl BCP spectra of c) the bulk API with and without microwaves and d) the bulk API and dosage samples with DNP enhancement.

The ^1H - ^{13}C CP/MAS NMR spectra of the bulk and dosage samples of **ceti** are shown in **Figure 5.7a** and **Figure 5.7b**, respectively, and are consistent with previous studies of this compound using DNP-enhanced ^{13}C SSNMR.⁶⁹ Several distinct features from the API are apparent in the spectrum of bulk **ceti** (e.g., peaks at 60-70 ppm and 130-200 ppm). However, only the strongest signal from the API (at ca. 130 ppm) can be distinguished in the spectrum of the dosage form due to interference from the excipients.

In both spectra of **ceti**, there is less interference from the solvent than was observed in the spectra of **diph** (*cf.* **Figure 5.6a** and **Figure 5.6b**), because the DNP enhancement of the solvent peak is not as large ($\epsilon(\text{DBB}, \text{ceti}) = 24$, $\epsilon(\text{DBB}, \text{diph}) = 50$). The enhancement of the solvent varies from sample to sample, which may depend on the types and concentrations of different excipients, the quality of the glass formation when the radical-containing solution freezes, the amount of dissolved $\text{O}_2(\text{g})$, the dielectric properties of the sample that affect the microwave field,¹⁰⁶ or the other factors discussed above.

The enhancement observed in the spectrum of bulk **ceti** ($\epsilon_{\text{CP}}(^{13}\text{C}) = 20$) is close to what was previously reported for this compound ($\epsilon_{\text{CP}}(^{13}\text{C}) = 31$).⁶⁹ However, for **ceti** in the dosage form we measured $\epsilon_{\text{CP}}(^{13}\text{C}) = 8$, which is lower than the 55-fold enhancement previously reported. We attribute these decreased enhancements to the use of DBB as the radical solvent. In the previous DNP SSNMR study, **ceti** was found to be sparingly soluble in TCE.⁶⁹ We chose to use DBB (in which **ceti** is insoluble) to maximize the amount of solid sample in the rotor and to better maintain the structure of the API in the dosage form. Given that the discrepancy in enhancements is particularly apparent in the spectra of the dosage form, it is possible that DBB does not penetrate the excipients as well as TCE. Further optimization of the sample preparation could likely yield improved enhancements.

Ceti is a dihydrochloride, and its ^{35}Cl SSNMR spectra should show two distinct ^{35}Cl patterns corresponding to structurally unique Cl^- anion sites. With the use of DNP, it is possible to identify two overlapping powder patterns in the ^{35}Cl spectrum of the bulk form in just 5 minutes ($\epsilon_{\text{CP}}(^{35}\text{Cl}) = 5.8$, **Figure 5.7c**). Due to hardware limitations, it is challenging to uniformly excite the entire breadth of the two ^{35}Cl patterns of **ceti**, even

with BCP. As such, we used frequency-stepped acquisition^{28,29} and combined 4 sub-spectra at evenly spaced transmitter frequencies to obtain the full pattern (which is *ca.* 250 kHz broad, **Figure D9**). The two overlapping ³⁵Cl powder patterns with distinct quadrupolar parameters can be readily distinguished using analytical simulations. Nonetheless, the most important discontinuities in the two patterns can be observed in the central sub-spectrum (as in **Figure 5.7c** and **Figure 5.7d**).

Acquiring a ³⁵Cl SSNMR spectrum of the dosage form with similar signal-to-noise ratio takes more than 11 hours, due to the extremely low wt-% Cl in this sample (5.78 wt-% API, 0.45 wt-% Cl), which is the lowest discussed herein. Comparison of the ³⁵Cl spectra of the bulk and dosage forms (**Figure 5.7d**) shows that the dosage form likely contains two ³⁵Cl environments that are similar to those of the bulk form. However, the poorer resolution of the discontinuities in the ³⁵Cl spectrum of the dosage form (most evident at the center of the pattern) is consistent with the lower crystallinity of the API within the formulation. This API was previously confirmed to exist as an amorphous form in all formulations using DNP-enhanced ¹³C and ¹⁵N SSNMR in the previous study.⁶⁹

5.4 Conclusions

We have demonstrated the acquisition of high-quality static wide-line ³⁵Cl SSNMR spectra of APIs using the ¹H-³⁵Cl BRAIN-CP-WURST-CPMG pulse sequence under DNP conditions. DNP has been observed to enhance the ³⁵Cl SSNMR signal by as much as 110 times for stationary samples. This enhancement is achieved by using a new spinning-on spinning-off (SOSO) protocol, in which the sample is spun during the recycle delay and halted shortly before the pulse/acquisition periods. The use of SOSO

results in a build-up in ^1H polarization under MAS conditions and allows for the acquisition of a wide-line ^{35}Cl spectrum free of spinning sidebands under static conditions. This method provides an additional two-fold signal enhancement over the spectra acquired with DNP under purely static conditions. The use of DNP dramatically decreases the lower detection limit for ^{35}Cl SSNMR spectra of dosage forms; we report successful characterization of APIs in bulk and dosage forms with Cl contents as low as 0.45 wt-%. These ^{35}Cl NMR spectra are particularly useful for the identification of the API within the dosage form because they are not affected by interfering signals from excipient molecules in the pill. In this respect, the DNP-enhanced ^1H - ^{13}C CP/MAS spectra of the dosage forms are limited, despite having higher signal enhancements than the corresponding ^{35}Cl NMR spectra. For all of the systems in this study, we observed lower DNP enhancements in the spectra of the dosage forms than in those of the bulk API, possibly due to the presence of excipients that reduce DNP efficiency via a number of different mechanisms, or due to differences in the particle size of the API in the bulk and dosage samples. These techniques show potential for investigating the sizes of micro- and nanoparticles of APIs in dosage forms.⁶⁹ Finally, we have demonstrated the use of DNP signal enhancement for the acquisition of a two-dimensional ^{13}C - ^{35}Cl correlation NMR spectrum of histidine HCl monohydrate. The increasing availability of DNP MAS probes with faster spinning rates⁷⁹ will allow for the acquisition of 1D and 2D ^{35}Cl MAS NMR spectra of most chloride salts of APIs and other organic molecules, with C_Q values as high as 7 to 8 MHz at 9.4 T.

The techniques we have reported in this study will help expand the use of DNP to the study of other wide-line and ultra-wide-line (breadths > 250 kHz) powder patterns.

While the spectra reported herein are dominated by the second-order quadrupolar interaction, the techniques described should would work equally well for patterns that are broadened by the first-order quadrupolar interaction, chemical shift anisotropy, or combinations thereof. These developments make DNP useful for the study of a wide range of materials whose NMR spectra suffer from inherently low S/N largely due to the wide breadth of the signal.

5.5 References

- (1) Kesisoglou, F.; Panmai, S.; Wu, Y. *Adv. Drug Deliv. Rev.* **2007**, *59*, 631–644.
- (2) Aaltonen, J.; Alleso, M.; Mirza, S.; Koradia, V.; Gordon, K.; Rantanen, J. *Eur. J. Pharm. Biopharm.* **2009**, *71*, 23–37.
- (3) Newman, A.; Knipp, G.; Zografí, G. *J. Pharm. Sci.* **2012**, *101*, 1355–1377.
- (4) Vogt, F. G. In *eMagRes*; John Wiley & Sons, Ltd: Chichester, UK, 2015; Vol. 4, pp 181–188.
- (5) Trask, A. V. *Mol. Pharm.* **2007**, *4*, 301–309.
- (6) Chemburkar, S. R.; Bauer, J.; Deming, K.; Spiwek, H.; Patel, K.; Morris, J.; Henry, R.; Spanton, S.; Dziki, W.; Porter, W.; Quick, J.; Bauer, P.; Donaubauer, J.; Narayanan, B. A.; Soldani, M.; Riley, D.; McFarland, K. *Org. Process Res. Dev.* **2000**, *4*, 413–417.
- (7) Caira, M. R. *Des. Org. Solids* **1998**, *198*, 163–208.
- (8) Bauer, J.; Morley, J.; Spanton, S.; Leusen, F. J. J.; Henry, R.; Hollis, S.; Heitmann, W.; Mannino, A.; Quick, J.; Dziki, W. *J. Pharm. Sci.* **2006**, *95*, 917–928.
- (9) Hörter, D.; Dressman, J. B. *Adv. Drug Deliv. Rev.* **1997**, *25*, 3–14.
- (10) Langham, Z. A.; Booth, J.; Hughes, L. P.; Reynolds, G. K.; Wren, S. A. C. *J. Pharm. Sci.* **2012**, *101*, 2798–2810.
- (11) Huang, L.-F.; Tong, W.-Q. *Adv. Drug Deliv. Rev.* **2004**, *56*, 321–334.
- (12) Bugay, D. E. *Adv. Drug Deliv. Rev.* **2001**, *48*, 43–65.
- (13) Datta, S.; Grant, D. J. W. *Nat. Rev. Drug Discov.* **2004**, *3*, 42–57.
- (14) Harris, R. K. *Analyst* **2006**, *131*, 351.
- (15) Harris, R. K. *J. Pharm. Pharmacol.* **2007**, *59*, 225–239.
- (16) Vogt, F. G. In *New Applications of NMR in Drug Discovery and Development*; 2013; pp 43–100.
- (17) Monti, G. A.; Chattah, A. K.; Linck, Y. G. In *Annual Reports on NMR Spectroscopy*; Elsevier Ltd., 2014; Vol. 83, pp 221–269.
- (18) Vogt, F. G. *eMagRes* **2015**, *4*, 255–268.
- (19) Hildebrand, M.; Hamaed, H.; Namespetra, A. M.; Donohue, J. M.; Fu, R.; Hung, I.; Gan, Z.; Schurko, R. W. *CrystEngComm* **2014**, *16*, 7334.
- (20) Hamaed, H.; Pawlowski, J. M.; Cooper, B. F. T.; Fu, R.; Eichhorn, S. H.; Schurko, R. W. *J. Am. Chem. Soc.* **2008**, *130*, 11056–11065.
- (21) Namespetra, A. M.; Hirsh, D. A.; Hildebrand, M. P.; Sandre, A. R.; Hamaed, H.; Rawson, J. M.; Schurko, R. W. *CrystEngComm* **2016**, *18*, 6213–6232.
- (22) Pandey, M. K.; Kato, H.; Ishii, Y.; Nishiyama, Y. *Phys. Chem. Chem. Phys.* **2016**, *18*, 6209–6216.
- (23) Vogt, F. G.; Williams, G. R.; Strohmeier, M.; Johnson, M. N.; Copley, R. C. B. *J. Phys. Chem. B* **2014**, *118*, 10266–10284.
- (24) Bryce, D. L.; Sward, G. D. *J. Phys. Chem. B* **2006**, *110*, 26461–26470.
- (25) Butler, B. J.; Hook, J. M.; Harper, J. B. *Recent Advances in the NMR Spectroscopy of Chlorine, Bromine and Iodine*, 1st ed.; Elsevier Ltd., 2011; Vol. 73.
- (26) Widdifield, C. M.; Chapman, R. P.; Bryce, D. L. In *Annual Reports on NMR Spectroscopy*; Elsevier Ltd., 2009; Vol. 66, pp 195–326.
- (27) Bryce, D. L.; Bultz, E. B. *Chem. Eur. J.* **2007**, *13*, 4786–4796.
- (28) Clark, W. G.; Hanson, M. E.; Lefloch, F.; Ségransan, P. *Rev. Sci. Instrum.* **1995**,

- 66, 2453–2464.
- (29) Massiot, D.; Farnan, I.; Gautier, N.; Trumeau, D.; Trokner, A.; Coutures, J. P. *Solid State Nucl. Magn. Reson.* **1995**, *4*, 241–248.
 - (30) Schurko, R. W. *Acc. Chem. Res.* **2013**, *46*, 1985–1995.
 - (31) Kupce, E.; Freeman, R. *J. Magn. Reson.* **1995**, *115*, 273–276.
 - (32) Bhattacharyya, R.; Frydman, L. *J. Chem. Phys.* **2007**, *127*, 194503.
 - (33) O'Dell, L. A.; Rossini, A. J.; Schurko, R. W. *Chem. Phys. Lett.* **2009**, *468*, 330–335.
 - (34) O'Dell, L. A.; Schurko, R. W. *Chem. Phys. Lett.* **2008**, *464*, 97–102.
 - (35) Harris, K. J.; Lupulescu, A.; Lucier, B. E. G.; Frydman, L.; Schurko, R. W. *J. Magn. Reson.* **2012**, *224*, 38–47.
 - (36) Hall, D. A.; Maus, D. C.; Gerfen, G. J.; Inati, S. J.; Becerra, L. R.; Dahlquist, F. W.; Griffin, R. G. *Science* **1997**, *276*, 930–932.
 - (37) Griffin, R. G.; Prisner, T. F. *Phys. Chem. Chem. Phys.* **2010**, *12*, 5737–5740.
 - (38) Maly, T.; Debelouchina, G. T.; Bajaj, V. S.; Hu, K.-N.; Joo, C.-G.; Mak-Jurkauskas, M. L.; Sirigiri, J. R.; van der Wel, P. C. a; Herzfeld, J.; Temkin, R. J.; Griffin, R. G. *J. Chem. Phys.* **2008**, *128*, 52211.
 - (39) Becerra, L. R.; Gerfen, G. J.; Temkin, R. J.; Singel, D. J.; Griffin, R. G. *Phys. Rev. Lett.* **1993**, *71*, 3561–3564.
 - (40) Becerra, L. R.; Gerfen, G. J.; Bellew, B. F.; Bryant, J. A.; Hall, D. A.; Inati, S. J.; Weber, R. T.; Un, S.; Prisner, T. F.; McDermott, A. E.; Fishbein, K. W.; Kreisler, K. E.; Temkin, R. J.; Singel, D. J.; Griffin, R. G. *J. Magn. Reson.* **1995**, *117*, 28–40.
 - (41) Joye, C. D.; Griffin, R. G.; Hornstein, M. K.; Kan-Nian Hu; Kreisler, K. E.; Rosay, M.; Shapiro, M. A.; Sirigiri, J. R.; Temkin, R. J.; Woskov, P. P. *IEEE Trans. Plasma Sci.* **2006**, *34*, 518–523.
 - (42) Barnes, A. B.; Mak-Jurkauskas, M. L.; Matsuki, Y.; Bajaj, V. S.; van der Wel, P. C. A.; DeRocher, R.; Bryant, J.; Sirigiri, J. R.; Temkin, R. J.; Lugtenburg, J.; Herzfeld, J.; Griffin, R. G. *J. Magn. Reson.* **2009**, *198*, 261–270.
 - (43) Rosay, M.; Lansing, J. C.; Haddad, K. C.; Bachovchin, W. W.; Herzfeld, J.; Temkin, R. J.; Griffin, R. G. *J. Am. Chem. Soc.* **2003**, *125*, 13626–13627.
 - (44) Song, C.; Hu, K.-N.; Joo, C.-G.; Swager, T. M.; Griffin, R. G. *J. Am. Chem. Soc.* **2006**, *128*, 11385–11390.
 - (45) Sauvée, C.; Rosay, M.; Casano, G.; Aussenac, F.; Weber, R. T.; Ouari, O.; Tordo, P. *Angew. Chemie Int. Ed.* **2013**, *52*, 10858–10861.
 - (46) Hu, K.-N.; Yu, H.; Swager, T. M.; Griffin, R. G. *J. Am. Chem. Soc.* **2004**, *126*, 10844–10845.
 - (47) Zagdoun, A.; Casano, G.; Ouari, O.; Schwarzwälder, M.; Rossini, A. J.; Aussenac, F.; Yulikov, M.; Jeschke, G.; Copéret, C.; Lesage, A.; Tordo, P.; Emsley, L. *J. Am. Chem. Soc.* **2013**, *135*, 12790–12797.
 - (48) Kubicki, D. J.; Casano, G.; Schwarzwälder, M.; Abel, S.; Sauvée, C.; Ganesan, K.; Yulikov, M.; Rossini, A. J.; Jeschke, G.; Copéret, C.; Lesage, A.; Tordo, P.; Ouari, O.; Emsley, L. *Chem. Sci.* **2016**, *7*, 550–558.
 - (49) Rosay, M.; Blank, M.; Engelke, F. *J. Magn. Reson.* **2016**, *264*, 88–98.
 - (50) Rosay, M.; Tometich, L.; Pawsey, S.; Bader, R.; Schauwecker, R.; Blank, M.; Borchard, P. M.; Cauffman, S. R.; Felch, K. L.; Weber, R. T.; Temkin, R. J.;

- Griffin, R. G.; Maas, W. E. *Phys. Chem. Chem. Phys.* **2010**, *12*, 5850–5860.
- (51) Kobayashi, T.; Perras, F. A.; Slowing, I. I.; Sadow, A. D.; Pruski, M. *ACS Catal.* **2015**, *5*, 7055–7062.
- (52) Rossini, A. J.; Zagdoun, A.; Lelli, M.; Lesage, A.; Copéret, C.; Emsley, L. *Acc. Chem. Res.* **2013**, *46*, 1942–1951.
- (53) Lafon, O.; Thankamony, A. S. L.; Kobayashi, T.; Carnevale, D.; Vitzthum, V.; Slowing, I. I.; Kandel, K.; Vezin, H.; Amoureux, J.-P.; Bodenhausen, G.; Pruski, M. *J. Phys. Chem. C* **2013**, *117*, 1375–1382.
- (54) Gunther, W. R.; Michaelis, V. K.; Caporini, M. A.; Griffin, R. G.; Román-Leshkov, Y. *J. Am. Chem. Soc.* **2014**, *136*, 6219–6222.
- (55) Perras, F. A.; Kobayashi, T.; Pruski, M. *J. Am. Chem. Soc.* **2015**, *137*, 8336–8339.
- (56) Blanc, F.; Sperrin, L.; Jefferson, D. A.; Pawsey, S.; Rosay, M.; Grey, C. P. *J. Am. Chem. Soc.* **2013**, *135*, 2975–2978.
- (57) Lund, A.; Hsieh, M.-F.; Siaw, T.-A.; Han, S. *Phys. Chem. Chem. Phys.* **2015**, *17*, 25449–25454.
- (58) Takahashi, H.; Lee, D.; Dubois, L.; Bardet, M.; Hediger, S.; De Paëpe, G. *Angew. Chemie Int. Ed.* **2012**, *51*, 11766–11769.
- (59) Lee, D.; Monin, G.; Duong, N. T.; Lopez, I. Z.; Bardet, M.; Mareau, V.; Gonon, L.; De Paëpe, G. *J. Am. Chem. Soc.* **2014**, *136*, 13781–13788.
- (60) Guo, Z.; Kobayashi, T.; Wang, L.-L.; Goh, T. W.; Xiao, C.; Caporini, M. A.; Rosay, M.; Johnson, D. D.; Pruski, M.; Huang, W. *Chem. Eur. J.* **2014**, *20*, 16308–16313.
- (61) Lesage, A.; Lelli, M.; Gajan, D.; Caporini, M. A.; Vitzthum, V.; Miéville, P.; Alauzun, J. G.; Roussey, A.; Thieuleux, C.; Mehdi, A.; Bodenhausen, G.; Coperet, C.; Emsley, L. *J. Am. Chem. Soc.* **2010**, *132*, 15459–15461.
- (62) van der Wel, P. C. A.; Hu, K.-N.; Lewandowski, J.; Griffin, R. G. *J. Am. Chem. Soc.* **2006**, *128*, 10840–10846.
- (63) Rossini, A. J.; Zagdoun, A.; Hegner, F.; Schwarzwälder, M.; Gajan, D.; Copéret, C.; Lesage, A.; Emsley, L. *J. Am. Chem. Soc.* **2012**, *134*, 16899–16908.
- (64) Rossini, A. J.; Emsley, L.; O'Dell, L. A. *Phys. Chem. Chem. Phys.* **2014**, *16*, 12890–12899.
- (65) Märker, K.; Pingret, M.; Mouesca, J. M.; Gasparutto, D.; Hediger, S.; De Paëpe, G. *J. Am. Chem. Soc.* **2015**, *137*, 13796–13799.
- (66) Rossini, A. J.; Schlagnitweit, J.; Lesage, A.; Emsley, L. *J. Magn. Reson.* **2015**, *259*, 192–198.
- (67) Mollica, G.; Dekhil, M.; Ziarelli, F.; Thureau, P.; Viel, S. *Angew. Chemie Int. Ed.* **2015**, *54*, 6028–6031.
- (68) Pinon, A. C.; Rossini, A. J.; Widdifield, C. M.; Gajan, D.; Emsley, L. *Mol. Pharm.* **2015**, *12*, 4146–4153.
- (69) Rossini, A. J.; Widdifield, C. M.; Zagdoun, A.; Lelli, M.; Schwarzwälder, M.; Copéret, C.; Lesage, A.; Emsley, L. *J. Am. Chem. Soc.* **2014**, *136*, 2324–2334.
- (70) Maly, T.; Andreas, L. B.; Smith, A. A.; Griffin, R. G. *Phys. Chem. Chem. Phys.* **2010**, *12*, 5872–5878.
- (71) Michaelis, V. K.; Markhasin, E.; Daviso, E.; Herzfeld, J.; Griffin, R. G. *J. Phys. Chem. Lett.* **2012**, *3*, 2030–2034.
- (72) Perez Linde, A. J.; Carnevale, D.; Miéville, P.; Sienkiewicz, A.; Bodenhausen, G.

- Magn. Reson. Chem.* **2015**, *53*, 88–92.
- (73) Lee, D.; Takahashi, H.; Thankamony, A. S. L.; Dacquin, J.-P.; Bardet, M.; Lafon, O.; Paëpe, G. De. *J. Am. Chem. Soc.* **2012**, *134*, 18491–18494.
- (74) Valla, M.; Rossini, A. J.; Caillot, M.; Chizallet, C.; Raybaud, P.; Digne, M.; Chaumonnot, A.; Lesage, A.; Emsley, L.; van Bokhoven, J. A.; Copéret, C. *J. Am. Chem. Soc.* **2015**, *137*, 10710–10719.
- (75) Vitzthum, V.; Miéville, P.; Carnevale, D.; Caporini, M. A.; Gajan, D.; Copéret, C.; Lelli, M.; Zagdoun, A.; Rossini, A. J.; Lesage, A.; Emsley, L.; Bodenhausen, G. *Chem. Commun.* **2012**, *48*, 1988–1990.
- (76) Kobayashi, T.; Perras, F. A.; Goh, T. W.; Metz, T. L.; Huang, W.; Pruski, M. *J. Phys. Chem. Lett.* **2016**, *7*, 2322–2327.
- (77) Thurber, K. R.; Tycko, R. *J. Chem. Phys.* **2012**, *137*, 84508.
- (78) Mentink-Vigier, F.; Akbey, Ü.; Hovav, Y.; Vega, S.; Oschkinat, H.; Feintuch, A. *J. Magn. Reson.* **2012**, *224*, 13–21.
- (79) Chaudhari, S. R.; Berruyer, P.; Gajan, D.; Reiter, C.; Engelke, F.; Silverio, D. L.; Copéret, C.; Lelli, M.; Lesage, A.; Emsley, L. *Phys. Chem. Chem. Phys.* **2016**, *18*, 10616–10622.
- (80) Jerschow, A. *Prog. Nucl. Magn. Reson. Spectrosc.* **2005**, *46*, 63–78.
- (81) Fuess, H.; Hohlwein, D.; Mason, S. A. *Acta Crystallogr. Sect. B Struct. Crystallogr. Cryst. Chem.* **1977**, *33*, 654–659.
- (82) Schollmeyer, D.; Henk, M. CCDC 189162: Private communication to the Cambridge Structural Database 2002.
- (83) Yathirajan, H. S.; Nagaraj, B.; Narasegowda, R. S.; Nagaraja, P.; Bolte, M. *Acta Crystallogr. Sect. E* **2004**, *60*, o2228–o2229.
- (84) Glaser, R.; Maartmann-Moe, K. *J. Chem. Soc. Perkin Trans. 2* **1990**, 1205–1210.
- (85) Harris, R. K.; Becker, E. D.; Cabral de Menezes, S. M.; Goodfellow, R.; Granger, P. *Pure Appl. Chem.* **2001**, *73*, 1795–1818.
- (86) Peersen, O.; Wu, X.; Smith, S. *J. Magn. Reson.* **1994**, *106*, 127–131.
- (87) Peersen, O. B.; Wu, X. L.; Kustanovich, I.; Smith, S. O. *J. Magn. Reson.* **1993**, *104*, 334–339.
- (88) Metz, G.; Wu, X. L.; Smith, S. O. *J. Magn. Reson.* **1994**, *110*, 219–227.
- (89) Fung, B. M.; Khitrin, A. K.; Ermolaev, K. *J. Magn. Reson.* **2000**, *142*, 97–101.
- (90) Tang, J. A.; Masuda, J. D.; Boyle, T. J.; Schurko, R. W. *ChemPhysChem* **2006**, *7*, 117–130.
- (91) Gan, Z.; Amoureux, J.-P.; Trébosc, J. *Chem. Phys. Lett.* **2007**, *435*, 163–169.
- (92) Hu, B.; Amoureux, J.-P.; Trébosc, J.; Hafner, S. *J. Magn. Reson.* **2008**, *192*, 8–16.
- (93) Bak, M.; Rasmussen, J. T.; Nielsen, N. C. *J. Magn. Reson.* **2000**, *147*, 296–330.
- (94) Tošner, Z.; Andersen, R.; Stevansson, B.; Edén, M.; Nielsen, N. C.; Vosegaard, T. *J. Magn. Reson.* **2014**, *246*, 79–93.
- (95) Vega, A. J. *J. Magn. Reson.* **1992**, *96*, 50–68.
- (96) Martineau, C.; Senker, J.; Taulelle, F. In *Annual Reports on NMR Spectroscopy*; 2014; Vol. 82, pp 1–57.
- (97) Pisklak, D. M.; Zielińska-Pisklak, M. A.; Szeleszczuk, Ł.; Wawer, I. *J. Pharm. Biomed. Anal.* **2016**, *122*, 81–89.
- (98) Sperger, D. M.; Munson, E. J. *AAPS PharmSciTech* **2011**, *12*, 821–833.
- (99) Grüning, W. R.; Rossini, A. J.; Zagdoun, A.; Gajan, D.; Lesage, A.; Emsley, L.;

- Copéret, C. *Phys. Chem. Chem. Phys.* **2013**, *15*, 13270.
- (100) Bryce, D. L.; Sward, G. D. *Magn. Reson. Chem.* **2006**, *44*, 409–450.
- (101) Johnston, K. E.; O’Keefe, C. A.; Gauvin, R. M.; Tr??bosc, J.; Delevoye, L.; Amoureux, J. P.; Popoff, N.; Taoufik, M.; Oudatchin, K.; Schurko, R. W. *Chem. Eur. J.* **2013**, *19*, 12396–12414.
- (102) O’Keefe, C. A.; Johnston, K. E.; Sutter, K.; Autschbach, J.; Delevoye, L.; Popo, N.; Taou, M.; Oudatchin, K.; Schurko, R. W. *Inorg. Chem.* **2014**, *53*, 9581–9597.
- (103) Zagdoun, A.; Rossini, A. J.; Gajan, D.; Bourdolle, A.; Ouari, O.; Rosay, M.; Maas, W. E.; Tordo, P.; Lelli, M.; Emsley, L.; Lesage, A.; Coperet, C. *Chem. Commun.* **2012**, *48*, 654–656.
- (104) Geppi, M.; Mollica, G.; Borsacchi, S.; Veracini, C. A. *Appl. Spectrosc. Rev.* **2008**, *43*, 202–302.
- (105) Berendt, R. T.; Sperger, D. M.; Munson, E. J.; Isbester, P. K. *Trends Anal. Chem.* **2006**, *25*, 977–984.
- (106) Kubicki, D. J.; Rossini, A. J.; Porea, A.; Zagdoun, A.; Ouari, O.; Tordo, P.; Engelke, F.; Lesage, A.; Emsley, L. *J. Am. Chem. Soc.* **2014**, *136*, 15711–15718.

Chapter 6: Quantifying Disproportionation in Pharmaceutical Formulations with ^{35}Cl Solid-State NMR

6.1 Introduction

Active pharmaceutical ingredients (APIs) in dosage formulations are typically manufactured as salts, in which a weakly basic or acidic form of the API is charge balanced by a counterion. Salts are advantageous because they typically have high bioavailability and aqueous solubility, properties that are desirable for formulations.¹⁻⁴ However, a pharmaceutical product containing an API salt can be problematic: under certain circumstances, an API salt can undergo a proton exchange process and convert to a neutral form, which often has less desirable physicochemical properties. This process is known as *disproportionation*.⁵⁻¹⁰

Several factors have been shown to influence the extent and rate of salt disproportionation in drug products, including the: (i) storage conditions, (ii) physicochemical properties of the API salt (*e.g.*, $\text{p}K_{\text{a}}$ or intrinsic solubility), and (iii) properties of excipients (*e.g.*, acidity or alkalinity or presence of a proton accepting group).⁵⁻¹⁴ In particular, disproportionation is known to be solution-mediated and even small amounts of moisture can initiate the reaction (*e.g.*, adsorption from the atmosphere).⁴ The stability of an API within a dosage formulation is a major concern throughout the manufacturing process;¹⁵ therefore, efficient methods for detecting disproportionation in formulations are imperative. In particular, these methods must also be able to *quantify* the amount of disproportionation in a sample.

Quantification is important for demonstrating drug stability under typical manufacturing and storage conditions, but it is also crucial for the study of the

mechanisms of disproportionation (*e.g.*, reaction kinetics, thermodynamic effects) and to identify the sources of problematic formulations early in their development. Several methods have been applied successfully to quantitatively detect disproportionation in model formulations, including near infrared (NIR) and Raman spectroscopies, as well as X-ray and synchrotron diffraction methods.^{5,10,16–18} However, these techniques may not be applicable to all formulations. Signal overlap can complicate identification of signals from the salt or disproportionation by-products. Diffraction techniques rely on long-range order, which may not be useful in samples where the free base or salt are amorphous, or in cases where interfering signals from the excipient matrix obscure those from the API.¹⁹ Therefore, alternative methods of detecting disproportionation are desirable.

Solid-state nuclear magnetic resonance (SSNMR) spectroscopy is a useful method for characterizing drugs in bulk and dosage formulations.^{20–23} One of its primary advantages is an ability to detect signals from crystalline, amorphous, and aqueous phases, which is important for studying solvent-mediated processes like disproportionation. NMR is also inherently quantitative because the amount of signal is directly proportional to the number of NMR-active nuclei in the sample. Unlike some other quantification methods, quantitative NMR (qNMR) experiments do not generally require extensive instrument calibration or elaborate sample preparation,^{24–28} though some calibration of experimental conditions is often necessary (*vide infra*). Quantitative SSNMR studies have been used previously to measure relative amounts of crystalline or amorphous pharmaceutical components,^{29–32} and mixtures of crystalline pharmaceutical phases (*e.g.*, different solid API forms);^{27,33–38} however, despite the potential advantages, there are relatively few examples of the use of SSNMR to study disproportionation.^{10,39}

Pharmaceuticals are most commonly studied using ^1H or ^{13}C SSNMR; however, these nuclei can be challenging targets when studying dosage formulations that contain numerous environments (from the API and excipients) with overlapping signals (a problem similar to that mentioned above).¹⁹ Fortunately, many API formulations contain numerous other NMR-active nuclides that can act as useful NMR handles for probing molecular-level structure, API integrity, and the production of impurities (*e.g.*, disproportionation by-products).

^{35}Cl SSNMR is an excellent method to characterize APIs that are formulated as HCl salts, given that the excipients do not contain Cl^- ions, and therefore do not interfere with signal from the API salt. Additionally, such spectra are not influenced by the broad patterns arising from covalently bound Cl atoms.¹⁹ This technique is particularly well-suited for studying disproportionation, as it can directly probe the salt counter anion, a chemical target that is not explored by other methods. Chlorine-35 is a quadrupolar nucleus ($I = 3/2$), and its SSNMR spectra are affected by a combination of anisotropic quadrupolar and chemical shift interactions.^{40,41} The former has been shown to be particularly sensitive to the local Cl^- anion environment,^{19,42-44} producing unique ^{35}Cl NMR spectra that serve as spectral fingerprints of each API and API phase.

Primarily due to the strength of the quadrupolar interaction, central transition (CT, $m_I = +1/2 \leftrightarrow -1/2$) ^{35}Cl NMR spectra of solids typically have broad powder patterns on the order of 100s of kHz or larger, so-called ultra-wideline (UW) spectra;⁴⁵ the breadths of these patterns necessitate the use of specialized pulse sequences that can improve the inherently low S/N of the broad signals and excite the entire breadth evenly.⁴⁶⁻⁴⁸ One of the most common signal enhancement methods is the Carr-Purcell-Meiboom-Gill

(CPMG) sequence,^{49,50} which consists of repeated π -pulses that refocus the signal, producing a series of echoes called an echo train. Broadband excitation of UW patterns can be achieved using wideband uniform-rate smooth truncation (WURST) pulses.^{51,52} These pulses employ phase- and amplitude-modulated shapes to create an effective frequency-sweep of the transmitter across the pattern. WURST pulses are often combined with CPMG in a pulse sequence known as WURST-CPMG.^{53,54}

Quantification using SSNMR can be complicated by several factors, including: temperature, sample filling factor and positioning, and the presence of spectral artifacts (*e.g.*, probe background). These concerns, and methods to reduce their impact, have been discussed previously.^{26,31,34,55} The intensities of peaks in an NMR spectrum are also influenced by multiple relaxation mechanisms; specifically, the chemical environments of nuclei/atoms determine the relative contributions to relaxation arising from distinct NMR interactions. As such, the nuclear relaxation rates (and associated peak intensities) can vary between sites, regardless of whether they are in the same molecule, same sample, or a mixture of constituents. In order to circumvent this problem, it is often necessary to compare the signal obtained from a peak of interest to one produced by a standard.^{26,28}

There are a number of concerns associated with quantitative comparison of powder patterns acquired with UW NMR methods, most of which remain unexplored to date. First, the observed signal intensity in spectra acquired using CPMG is strongly related to the transverse relaxation (T_2) of the nuclei. The primary source of $T_2(^{35}\text{Cl})$ relaxation in HCl APIs is ^1H - ^{35}Cl heteronuclear dipolar coupling; in most cases, the intensity of the ^{35}Cl NMR signal can be improved dramatically with the use of high-power ^1H decoupling (producing an effective $T_2(^{35}\text{Cl})$, called T_2^{eff} , where $T_2^{\text{eff}} > T_2$).

However, decoupling efficiency (and the resulting T_2^{eff}) can vary for different sites in a sample. A second concern relates to quantifying signals from *quadrupolar* nuclei ($I > 1/2$), which stems from differences in the nutation behavior of nuclei in distinct sites. Nutations of quadrupolar spins depend on the strength of the quadrupolar interaction, which varies depending on the local nuclear environment.^{56,57} This problem can be avoided with the use of CT selective pulses (*i.e.*, $\tau_{\text{selective}} = \tau_{\text{nonselective}} \times (I + 1/2)^{-1}$) or pulses with low-RF powers.^{58,59} Fortunately, nutation rates are not a concern when the pattern is excited with low-RF WURST pulses (*vide infra*).⁶⁰

Despite these additional considerations, useful quantitative information can be obtained from UW NMR spectra by comparing the integrated signal intensity from a sample in a mixture to that of an external reference (*e.g.*, the pure material). Similar techniques have been used in ^1H - ^{13}C CP/MAS NMR studies, where a variety of relaxation rates and processes can complicate quantification^{27,31} Therefore, comparison of a ^{35}Cl SSNMR spectrum of a sample in which disproportionation has occurred to that of the pure salt, can be used to measure the amount of disproportionation (*i.e.*, %-conversion of the salt).

Recently, the HCl salt form of pioglitazone (**PiogHCl**), a thiazolidinedione used for treating type-II diabetes, has been a popular test case for various proof-of-concept methods to detect disproportionation.^{10,16,17,61,62} **PiogHCl** is known to disproportionate in mixtures with salt stearates such as magnesium stearate (**MgSt**) and sodium stearate (**NaSt**), according to the proposed reaction scheme shown in **Figure 6.1**.^{8,10,16} Such stearates are common lubricants in a variety of formulations, and are typically present in small quantities (*e.g.*, 2-3 wt-% of the final dosage form).

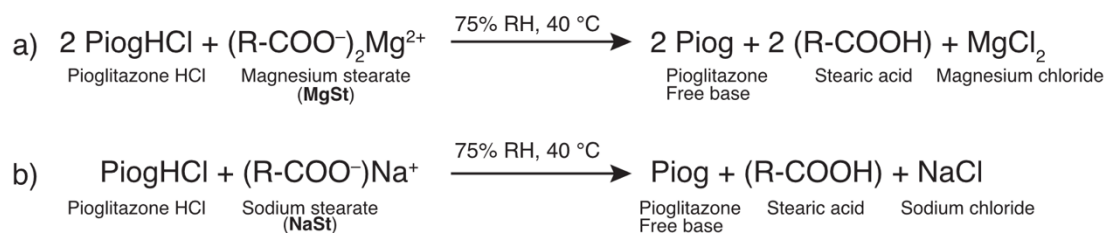


Figure 6.1. Proposed disproportionation reactions of PiogHCl with a) MgSt and b) NaSt.

Herein, we describe the use of ^{35}Cl SSNMR to study disproportionation reactions in **PiogHCl** mixtures with stearate salts. Qualitatively, comparisons of ^{35}Cl NMR spectra of the sample mixtures before and after treatment at high temperature and relative humidity (RH) can reveal the identity of disproportionation products involving the Cl^- anion, which are not adequately characterized using other methods. We propose a simple quantitative method for measuring the amount of HCl salt in a dosage formulation, and demonstrate its utility by measuring the amount of disproportionation in treated **PiogHCl** samples containing different stearate salts.

6.2 Experimental Methods

6.2.1 Chemicals

The salt and free-base forms of pioglitazone (**PiogHCl**, and **PiogFB**, respectively) were ordered from Tokyo Chemical Industry (TCI) Co, Ltd. (Portland, OR). Magnesium stearate (**MgSt**) was purchased from Mallinckrodt (St. Louis, MO). Sodium stearate (**NaSt**) was provided by Acme-Hardesty Co. (Blue Bell, PA). Chemical structures of the materials used in this study are shown in **Figure C1**. Samples were stored at 5°C with desiccant to avoid water intake and degradation while not in use.

6.2.2 Sample Preparation

Quantification standards were prepared by mixing various amounts of **PiogHCl** with the free base form to produce samples ranging from 3% to 100% HCl salt (wt/wt). These samples are referred to in the text using the wt-% **PiogHCl** present in the sample (*e.g.*, **PiogHCl 3%**, **PiogHCl 100%**). Sample mixtures of **PiogHCl** with **MgSt** or **NaSt** were prepared with 90% API wt/wt. As discussed previously,⁶¹ this weight ratio is representative of a typical tablet formulation. Samples were weighed and prepared under an inert atmosphere to minimize water uptake. The sample codes and masses are listed in **Table 6.1**. Samples to be used as controls (*i.e.*, API/stearate mixtures not exposed to high temperature or humidity, **NaSt_C** and **MgSt_C**) and the quantification standards were mixed for 5 minutes with a vortex mixer before the samples were packed. Treated samples (**NaSt_X** and **MgSt_X**, respectively) were prepared using binary mixtures of **PiogHCl** and **MgSt** or **NaSt** placed into petri dishes, which were subjected to 40°C/75% RH stability chamber for 5 days in an open dish condition.

Prior work on similar materials has demonstrated that the binary mixtures can be highly hygroscopic.⁶³ As such, two rehydrated samples (**NaSt_XH**, and **MgSt_XH**, respectively), were prepared by placing approximately 300 mg of the **NaSt_X** or **MgSt_X** samples in a 75% RH environment at 22 °C for 4 hours. Preliminary ¹H and ³⁵Cl NMR experiments (as well as previous work on this sample)⁶³ demonstrated that **NaSt_X** did not absorb significant amounts of H₂O upon rehydration; therefore, the **NaSt_XH** sample was not examined further.

Table 6.1. Sample masses used to prepare materials for quantification with ^{35}Cl SSNMR.

Sample Name	Amount of compound added (mg) ^b					Packed Sample Wt. ^{b,c}
	Wt-% Piog HCl Salt ^a	Piog HCl	Piog FB	MgSt	NaSt	
PiogHCl 100%	100%	300.0	–	–	–	137.2
PiogHCl 90%	90.0%	271.1	30.1	–	–	139.6
PiogHCl 60%	60.3%	181.8	119.9	–	–	151.2
PiogHCl 30%	29.9%	90.1	210.8	–	–	146.0
PiogHCl 10%	10.1%	30.2	270	–	–	145.8
PiogHCl 5%	5.2%	15.7	284.9	–	–	150.8
PiogHCl 3%	3.0%	8.9	291.3	–	–	143.5
MgSt_C	90.1%	273.0	–	30	–	191.2
MgSt_X (Treated at 40 °C, 45% RH)	90.0%	270.0	–	30.0	–	136.3
MgSt_XH (rehydrated for 4 hours at 75% RH) ^d	90.0%	270.0	–	30.0	–	148.8
NaSt_C	90.1%	272.0	–	–	30.0	146.0
NaSt_X (Treated at 40 °C, 45% RH)	90.0%	270.0	–	–	30.0	132.6

^aWt-% **PiogHCl** salt calculated from the masses of the materials in the sample mixture. ^bAll reported masses are accurate to within 0.1 mg. ^cMass of the packed sample used for ^{35}Cl SSNMR experiments. ^dThe **MgSt_XH** sample was prepared by placing 300 mg of the **MgSt_X** sample in a 75% RH humidity chamber for 4 hours immediately before packing the sample.

All samples were ground with a mortar and pestle before being packed and weighed under an inert atmosphere. For magic-angle spinning (MAS) experiments, samples were packed into 4 mm o.d. zirconia rotors sealed with air-tight Teflon® screws. For experiments conducted under static sample conditions, samples were packed into glass tubes with one open end, which was then sealed using Teflon® tape and vacuum grease.

6.2.3 Solid-State NMR (SSNMR) Experiments

All solid-state NMR (SSNMR) experiments were conducted on a Bruker Avance III HD console with an Oxford $B_0 = 9.4$ T wide-bore magnet ($\nu_0(^1\text{H}) = 399.73$ MHz, $\nu_0(^{13}\text{C}) = 100.53$ MHz, $\nu_0(^{23}\text{Na}) = 105.74$ MHz, $\nu_0(^{35}\text{Cl}) = 39.16$ MHz). ^1H and ^{35}Cl experiments used a Varian/Chemagnetics 5mm HX static probe with a horizontal coil alignment. All other experiments used a Varian/Chemagnetics 4 mm HX MAS probe. ^{35}Cl chemical shifts were referenced with respect to NaCl(s) ($\delta_{\text{iso}} = 0.0$ ppm). ^1H and ^{13}C chemical shifts were referenced to tetramethylsilane (TMS, $\delta_{\text{iso}} = 0.0$ ppm) using adamantane ($\delta_{\text{iso}} = 1.85$ and 38.57 ppm, respectively) as a secondary reference. ^{23}Na chemical shifts were referenced with respect to a 1.0 M NaCl(aq) solution ($\delta_{\text{iso}} = 0.0$ ppm).

A full list of experimental parameters used for the SSNMR experiments is given in **Appendix E Table E1-Table E4**. $^{35}\text{Cl}\{^1\text{H}\}$ spectra were acquired using the WURST-CPMG sequence.^{53,54} ^1H and $^{23}\text{Na}\{^1\text{H}\}$ direct-excitation MAS experiments were conducted using a rotor-synchronized Hahn echo pulse sequence of the form $(\pi/2)_x - \tau_1 - (\pi)_y - \tau_2 - \text{acq}$. ^1H - ^{13}C cross-polarization (CP) experiments used a ramped-amplitude spin lock pulse on the ^1H channel.⁶⁴⁻⁶⁶ High power ^1H decoupling was applied in all ^{35}Cl , ^{23}Na , and ^{13}C experiments, using either continuous wave (for ^{35}Cl) or swept field two-pulse phase-modulation (sw-TPPM)^{67,68} (for ^{23}Na and ^{13}C) decoupling sequences. All experiments were conducted at 20 °C with temperature control provided by a Varian VT stack and Bruker BCU II 80/60 chiller.

6.2.4 Powder X-ray Diffraction (PXRD) Experiments

PXRD patterns for all of the samples were collected using a Bruker DISCOVER X-ray diffractometer with a Cu-K α ($\lambda = 1.54056 \text{ \AA}$) radiation source and Bruker AXS HI-STAR area detector. Samples were packed into 0.9 mm o.d. glass capillary tubes and analyzed for 30 minutes with the detector set at $2\theta = 18^\circ$. Diffraction patterns were processed using the CrystalDiffract software package.

6.3 Results and Discussion

6.3.1 Pioglitazone HCl

The $^{35}\text{Cl}\{\text{}^1\text{H}\}$ WURST-CPMG NMR spectrum of pioglitazone HCl (**PiogHCl**) acquired under static sample conditions is shown in **Figure 6.2**. The spectrum has a powder pattern spanning roughly 150 kHz with a shape typical of the second-order quadrupolar interaction. This pattern can be simulated with NMR tensor parameters as follows: $\delta_{\text{iso}} = 100(20)$ ppm, $C_Q = 4.8(1)$ MHz, and $\eta_Q = 0.63(5)$. The shape of the pattern, and associated tensor parameters, are unique to the Cl^- environment in **PiogHCl**, and therefore serve as a spectra fingerprint of the API.^{19,42,43} The data can be processed by either performing a Fourier transform (FT) of the echo train itself (producing a spectrum with a series of spikelets), or by coadding the echoes together to form a single echo before the FT (producing a spectrum with a continuous line that traces the edge of the powder pattern, so-called *echo coaddition*).⁶⁹ As seen in **Figure 6.2**, both processing methods yield patterns with the same shape.

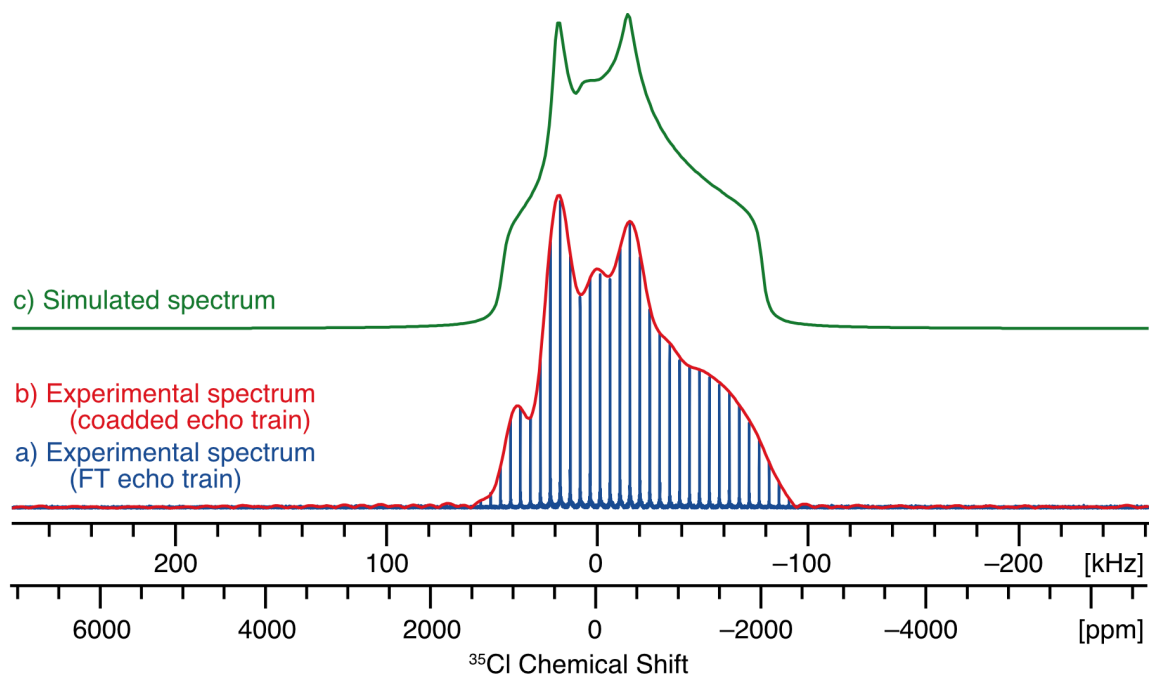


Figure 6.2. Experimental $^{35}\text{Cl}\{^1\text{H}\}$ WURST-CPMG NMR spectra of pure **PiogHCl** under static sample conditions, a) and b), and the corresponding analytical simulation, c). Experimental data were processed by a) applying a Fourier transform (FT) to the entire echo train (blue), or b) coadding the echoes together before performing a FT (red), see details in the text.

6.3.2 PiogHCl:NaSt mixture

^{35}Cl NMR Spectra. The $^{35}\text{Cl}\{^1\text{H}\}$ WURST-CPMG NMR spectra of the NaSt-containing samples are shown in **Figure 6.3**. The spectrum of the control mixture (NaSt_C, **Figure 6.3a**) has the same shape as the spectrum of pure **PiogHCl**, indicating that without treatment the local structure of the Cl^- ion does not change (*e.g.*, disproportionation has not occurred). The spectrum of the treated sample (NaSt_X, **Figure 6.3b**) has the same breadth and all of the discontinuities present in the spectrum of pure **PiogHCl**; however, this spectrum also has a distinct feature that results from the disproportionation reaction: a sharp peak at roughly 0 ppm (see **Figure E2** for a deconvolution). As shown in the deconvolution, the pattern arising from pure **PiogHCl** accounts for most of the integrated intensity, indicating that most of the **PiogHCl** does

not disproportionate when the sample is treated (*vide infra*). The signal from disproportionation products can be isolated by examining the difference between the spectra of the control and treated samples (*i.e.*, by subtracting one spectrum from the other, **Figure 6.3c**). (*N.B.* difference spectra obtained in this way are *not* quantitative, *vide infra*). This signal is largely negative, because the amount of **PiogHCl** decreases in the disproportionation process.

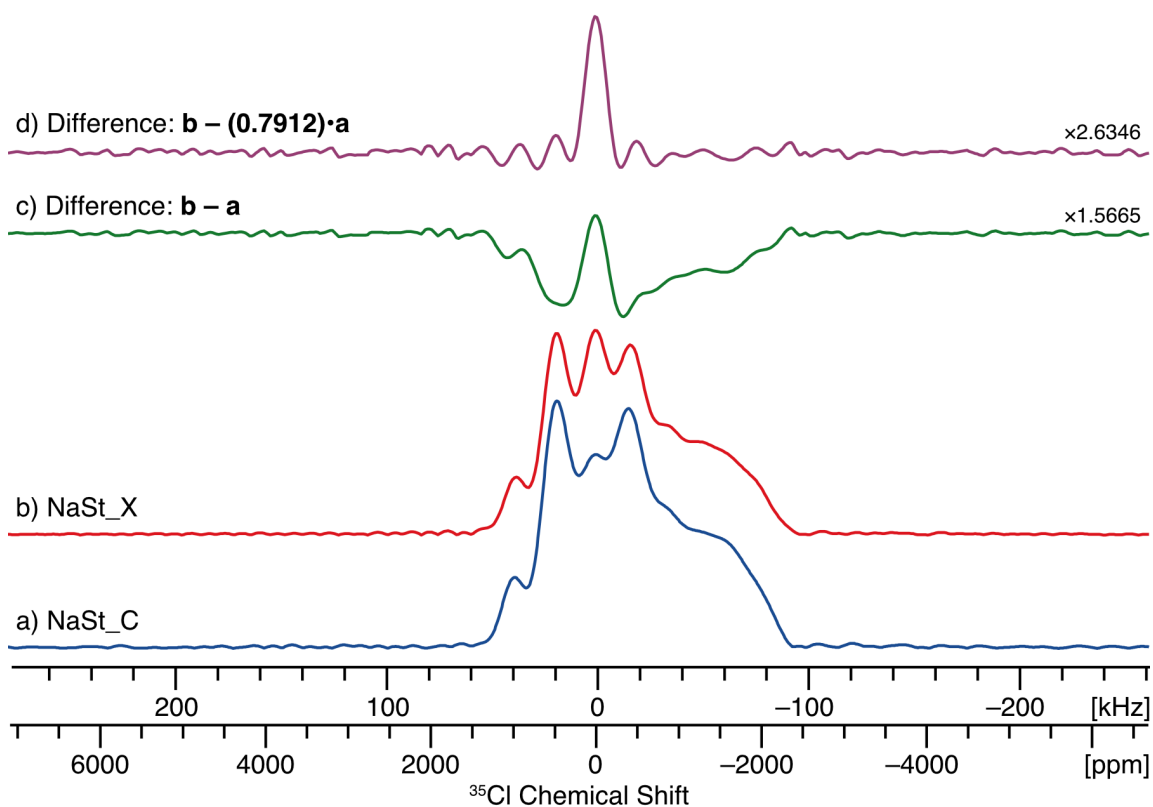


Figure 6.3. $^{35}\text{Cl}\{^1\text{H}\}$ WURST-CPMG NMR spectra of **PiogHCl** samples mixed with NaSt (9:1 wt/wt), a) is the spectrum of the untreated control sample, and b) is the spectrum of the sample treated at 40 °C/75% RH for 5 days. The difference between the spectra (control – treated) is shown in c) and d). When calculating the latter, the intensity of the spectrum of the control (a) was decreased to produce only positive signal (see text for details).

Decreasing the scale of the spectrum of **NaSt_C** to account for the decreased amount of **PiogHCl** before taking the difference produces a spectrum with entirely positive signal corresponding to the disproportionation product (**Figure 6.3d**). The result

is a sharp feature, which indicates a site with a small quadrupolar interaction, such as an ionic chloride in an environment of high spherical (Platonic) symmetry.^{44,70,71} The narrow breadth of this pattern, and its shift (0 ppm) are consistent with NaCl(s), which has previously been proposed as a by-product of the disproportionation reaction.^{10,61} No other peaks are observed in the ³⁵Cl NMR spectrum, which suggests that the Cl⁻ ions that separate from the API salt exclusively react with Na⁺ ions in the stearate to form NaCl (a result that is also confirmed by ²³Na NMR and PXRD, *vide infra*).

The magnitudes of the quadrupolar coupling constants, C_Q , are very different for Cl⁻ ions in the API salt and the disproportionation product; these produce distinct ³⁵Cl nutation behavior for the CT patterns corresponding to each environment.^{56,57} Such differences in nutation frequencies can be exploited to isolate signal from the narrow disproportionation products. For example, using a Hahn echo sequence with non-selective excitation pulses (*i.e.*, where the applied rf amplitude, ν_1 , is greater than the quadrupolar frequency, $\nu_Q = C_Q/[4I(2I - 1)2\pi]$) of the narrow pattern, results in a spectrum with only the narrow signal from the disproportionation product (**Figure E3**). ³⁵Cl NMR spectra of this type provide a rapid means of detecting the disproportionation products, because the signal from the intact API is effectively filtered by the experiment. Finally, the Hahn-echo spectrum confirms that no signal from NaCl(aq) is observed, as the ³⁵Cl chemical shifts of NaCl(s) and NaCl(aq) are distinct (**Figure E4**). While the disproportionation process may be solvent mediated, storage under dry conditions removes any aqueous NaCl by-products.

²³Na NMR Spectra. ²³Na SSNMR is an alternative approach for characterizing these samples, and is particularly advantageous given that ²³Na is a highly receptive

nucleus (100% abundant, with a gyromagnetic ratio comparable to ^{13}C , but a receptivity 545 times larger). The $^{23}\text{Na}\{^1\text{H}\}$ MAS SSNMR spectra of the control (**NaSt_C**) and treated (**NaSt_X**) samples (**Figure 6.4a** and **Figure 6.4b**, respectively) show two features: (i) a broad second-order pattern with a center of gravity at -7 ppm, and (ii) a sharp feature at $7.3(1)$ ppm. The broad feature is more prominent in the spectrum of **NaSt_C**, and corresponds to pure **NaSt** (**Figure 6.4c**) (the presence of **NaSt** is also confirmed by ^{13}C SSNMR and PXRD, **Figure E5** and **Figure E7**, respectively). The sharp feature is more pronounced in the spectrum of **NaSt_X**, and results from the **NaCl(s)** produced by disproportionation. Sample treatment affects the intensities of these two features in opposite ways (*cf.* **Figure 6.4a** and **Figure 6.4b**); the broad feature decreases in intensity and is almost completely absent in the spectrum of **NaSt_X** (**Figure 6.4b**, inset), while the sharp feature intensifies. These spectra clearly demonstrate that the Na^+ ions from the **NaSt** are involved in the disproportionation reaction, and form **NaCl(s)** with Cl^- ions from **PiogHCl**. The ^{23}Na spectra also confirm that solvated **NaCl** is not present in these samples, as no ^{23}Na signal at 0 ppm is observed (**Figure E9**). Both results are consistent with the ^{35}Cl SSNMR data. The ^{23}Na NMR spectrum of **NaSt_C** (**Figure 6.4a**) also has a small peak at 7.3 ppm, indicating that some disproportionation has occurred in the control sample. This sample may have been exposed to a small amount of water during storage, or residual water in the API (which was not dried prior to sample preparation to protect the API integrity). ^{23}Na NMR is extremely sensitive to disproportionation in these samples, and is well suited to study **PiogHCl** mixtures with **NaSt**.

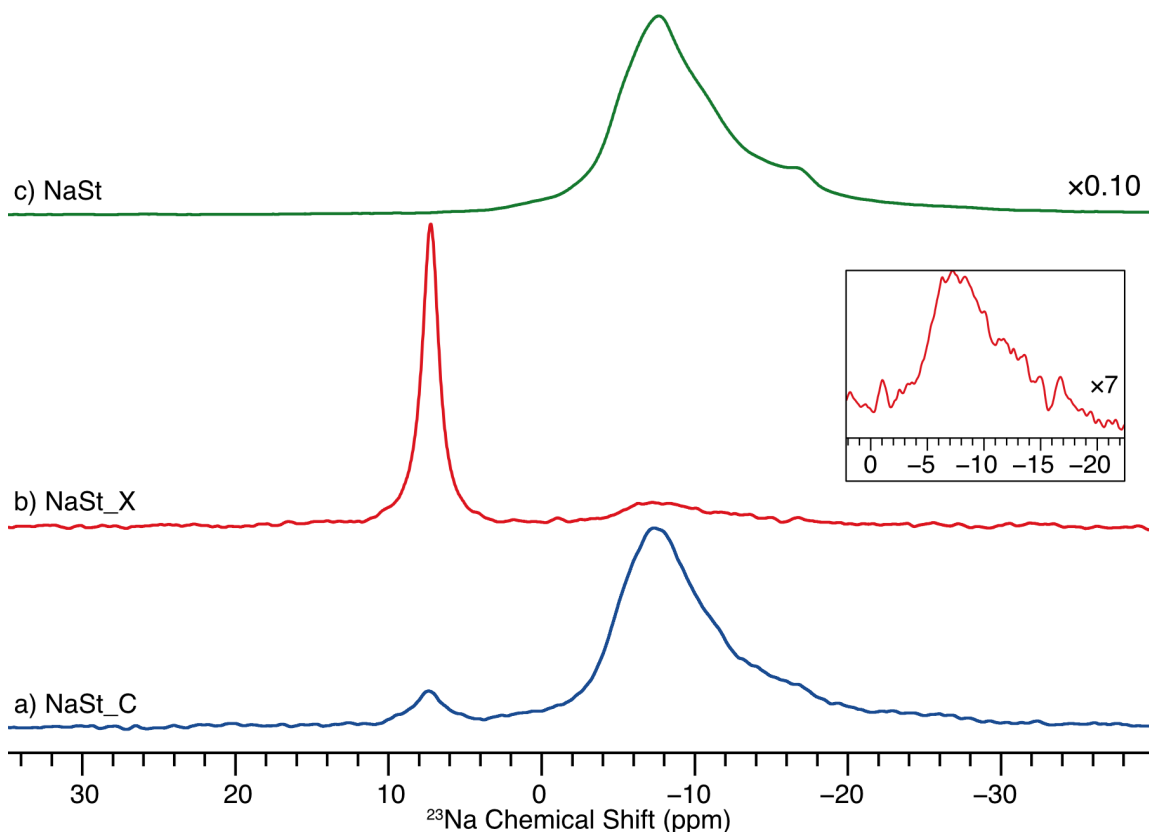


Figure 6.4. $^{23}\text{Na}\{^1\text{H}\}$ MAS ($v_{\text{rot}} = 12$ kHz) NMR spectra of a) **NaSt_C**, b) **NaSt_X**, and c) pure **NaSt**. The inset shows the **NaSt** region of the spectrum of **NaSt_X** with increased intensity.

6.3.3 PiogHCl:MgSt Mixture

At first glance, the ^{35}Cl NMR spectra of the control and treated samples containing **MgSt** (**Figure 6.5a** and **Figure 6.5b**) are more similar to each other than those of their **NaSt**-containing counterparts. However, the effects of disproportionation are apparent when looking at the differences between the spectra (**Figure 6.5d** and **Figure 6.5e**). Disproportionation in the **MgSt** samples produces a pattern with distinct second-order quadrupolar features, which is much broader than the narrow feature from NaCl(s) discussed above. It has been suggested that MgCl_2 is formed in the disproportionation reaction of **PiogHCl** and **MgSt**,^{10,16,17,61} and the presence of MgCl_2 in the samples in this work is supported by PXRD (**Figure E6**). ^{35}Cl NMR spectra of

anhydrous MgCl_2 and the more common hydrated form ($\text{MgCl}_2 \cdot 6\text{H}_2\text{O}$) have been published.^{72,73} Each compound has a distinct second-order pattern, which can be used to simulate the difference spectrum obtained here (**Figure E10**). The combined simulation matches the observed spectrum, suggesting that the disproportionation products may involve multiple MgCl_2 hydrates.

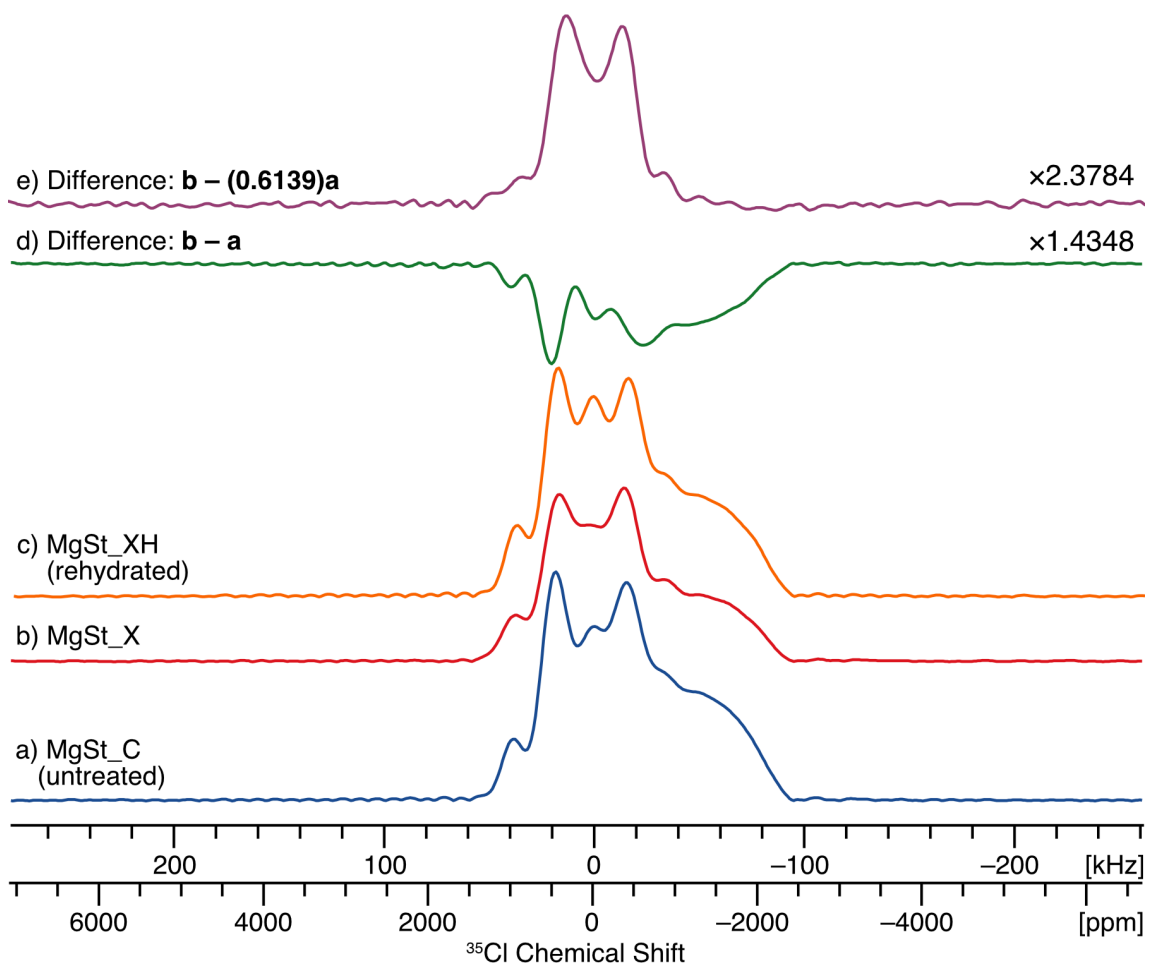


Figure 6.5. $^{35}\text{Cl}\{^1\text{H}\}$ WURST-CPMG NMR spectra of **PiogHCl** samples mixed with MgSt (9:1 wt/wt), a) the untreated control sample, b) the sample treated at 40 °C/75% RH for 5 days, and c) the treated sample immediately after being rehydrated at 20 °C/75% RH for 4 hours. The difference between the spectra (control – treated) is shown in d) and e). When calculating the latter, the intensity of the spectrum of the control (a) was decreased to produce only positive signal.

MgCl₂ and MgCl₂•6H₂O are extremely hygroscopic and deliquescent, and their presence is a major contributor to the high water adsorption previously reported for **MgSt_X**.^{10,61} To examine the effects of water exposure on the SSNMR spectra, 300 mg of the **MgSt_X** sample was exposed to moisture for a second time (75% RH for 4 hours at 20 °C), to produce a sample hereafter referred to as **MgSt_XH**. Preliminary ¹H SSNMR experiments demonstrated that **MgSt_XH** retains a considerable amount of water from the humid environment (**Figure E11**), consistent with the presence of MgCl₂. Rehydration has a significant effect on the ³⁵Cl NMR spectrum of **MgSt_XH** as well (**Figure 6.5c**), resulting in a sharp feature in the center of the spectrum, similar to that of **NaSt_X**. As with the **NaSt**-containing samples, using a Hahn echo experiment with non-selective pulses can isolate this feature from the underlying broad signals produced by **PiogHCl** and MgCl₂ (**Figure E12**). The corresponding ³⁵Cl Hahn echo NMR spectrum of the rehydrated sample (**MgSt_XH**) has a single sharp feature, while the spectrum of the sample before rehydration (**MgSt_X**) does not. The shift and breadth of this peak is consistent with that of a MgCl₂•6H₂O sample that has been exposed to moisture in the air (**Figure E13b**), confirming that MgCl₂•6H₂O is a product of the disproportionation reaction. The spectrum of "wet" MgCl₂•6H₂O is far narrower than the second order pattern observed for "dry" MgCl₂•6H₂O(s) (**Figure E10**),⁷² suggesting that the adsorption of water begins to dissolve the material and produces a distribution of ³⁵Cl environments.

Unlike the rehydrated sample, **MgSt_X** does not yield any signal in the ³⁵Cl Hahn-echo NMR experiment (*cf.* **Figure E12a** and **Figure E12c**). This result suggests that the **MgSt_X** sample does not contain solvated Cl⁻ ions or other chlorides in environments of high spherical symmetry, which would appear as sharp features near 0

ppm.^{44,73} Consequently, any products of the disproportionation reaction must associate with Mg^+ counterions rather than H_2O molecules alone, and the limiting reagent in the disproportionation reaction is likely **MgSt**. Solvated phases (*e.g.*, “wet” $\text{MgCl}_2 \cdot 6\text{H}_2\text{O}(\text{s})$ or hexaaqua-coordinated Cl^- ions) may exist during the disproportionation process, but are dehydrated during the dry storage conditions used in this study. Future NMR experiments on samples subjected to various conditions throughout the disproportionation process should help isolate these or other intermediates.

6.3.4 Quantification of ^{35}Cl SSNMR Spectra

SSNMR spectra are inherently quantitative, as the amount of signal is directly proportional to the number of spins present in the sample; however, as discussed above, accurate quantification of components in a series of mixtures using SSNMR requires the careful control of other factors that affect the signal intensity, namely: (i) temperature (to avoid differences in Boltzmann population), (ii) sample volume (to ensure the NMR coil is filled consistently and uniformly), and (iii) identical experimental parameters (*i.e.*, rf amplitudes, phases, and all timings).^{27,34} As a proof-of-concept for testing quantification with ^{35}Cl SSNMR experiments, standard mixtures were prepared with different ratios of **PiogHCl** and the free base form of pioglitazone (**PiogFB**). $^{35}\text{Cl}\{^1\text{H}\}$ NMR spectra of these samples were obtained under identical experimental conditions with a regulated sample temperature. Qualitatively, the intensity of the resulting ^{35}Cl NMR patterns (**Figure 6.6**) decreases as the amount of API salt decreases.

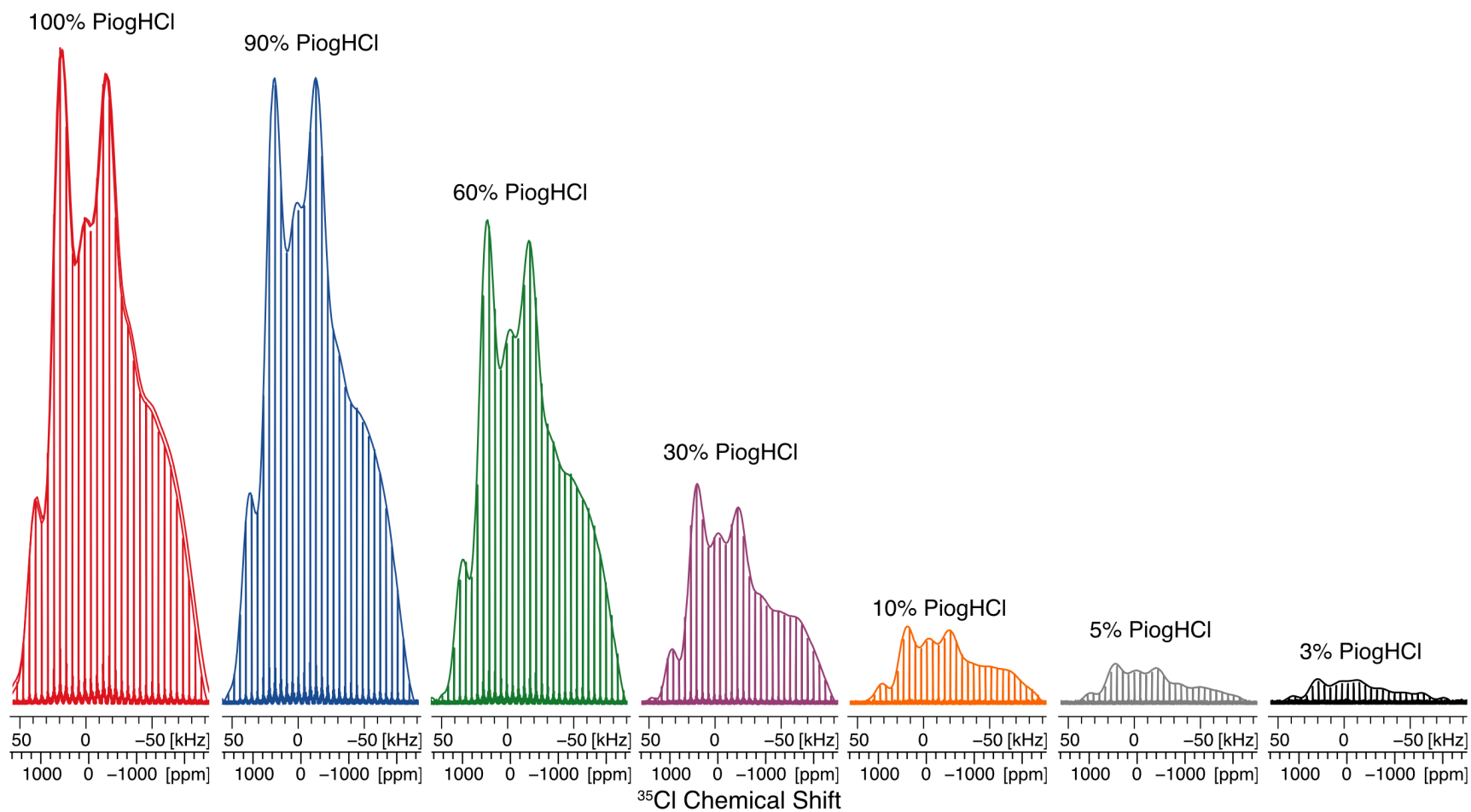


Figure 6.6. $^{35}\text{Cl}\{^1\text{H}\}$ WURST-CPMG NMR spectra of the **PiogHCl/PiogFB** mixtures. The data are shown after processing by either (i) applying a FT to the entire echo train (“spikelet spectrum”) or (ii) combining the echoes together before performing the FT.

In order to *quantitatively* compare these spectra, we have used the spikelet spectra (those obtained by processing the data with a Fourier transform of the entire echo train). Such spectra are advantageous for the study of disproportionation because spikelets that correspond solely to signal from the intact salt can be compared (*i.e.*, those outside the range of signal from the disproportionation products). Furthermore, the presence of sharp peaks provides two simple approaches to measure intensity at different parts of the pattern: (i) by measuring the spikelet intensity or (ii) integrating the area of the spikelet. Our quantification method can be summarized in the following 3 steps:

1. Measure the spikelet intensities by using either maximum spikelet intensity or integrated area.
2. Scale the data to account for variation in the mass of the sample.
3. Divide the scaled intensity for a sample by the intensity obtained from a pure sample (*i.e.*, normalize the results to values obtained from the spectrum of **PiogHCl 100%**).

The results of this analysis can be compared to the relative wt-% of **PiogHCl** measured when preparing the sample.

There are many ways to process UW ^{35}Cl spectra, all of which might affect the accuracy of the measured intensities, such as the addition of line broadening, or use of absolute magnitude processing (as opposed to phasing) of the spectra. As discussed in **Appendix E**, we have examined these factors using the ^{35}Cl NMR spectrum of **PiogHCl 90%**. Based on this analysis, we conclude that the best quantification results are obtained when using 100 Hz of line broadening and that taking the absolute magnitude of the spectra (rather than applying phase corrections) is sufficient.

Table 6.2. Experimental and calculated amounts of **PiogHCl** in the standard samples.

Sample	Wt-% PiogHCl ^a	Measurement method ^b	Measured wt-% PiogHCl ^c	RMSD (wt-%) ^d	Standard deviation, σ (wt-%) ^e
PiogHCl 90%	90.0%	MSI	90.4%	1.81%	1.81%
		ISI	90.2%	1.95%	1.98%
PiogHCl 60%	60.3%	MSI	59.4%	2.42%	2.06%
		ISI	59.4%	2.80%	2.71%
PiogHCl 30%	29.9%	MSI	30.0%	3.15%	3.22%
		ISI	30.0%	3.98%	4.05%
PiogHCl 10%	10.1%	MSI	11.0%	1.34%	0.95%
		ISI	11.4%	2.51%	2.14%
PiogHCl 5%	5.2%	MSI	5.8%	0.81%	0.50%
		ISI	5.8%	4.25%	0.52%
PiogHCl 3%	3.0%	MSI	3.9%	1.15%	1.74%
		ISI	3.9%	6.22%	1.13%

^aCalculated from the masses of **PiogHCl** and **PiogFB** used in the sample mixture, see **Table 6.1**. ^bDenotes the method used to measure spikelet intensity, either: (i) maximum spikelet intensity (MSI) or integrated spikelet intensity (ISI). ^cMeasured values from ³⁵Cl SSNMR experiments, reported as the average value obtained from spikelets between 39 kHz and -84 kHz, see text for details. ^dRoot mean square deviation,

$$\text{RMSD} = \sqrt{\frac{1}{N} \sum_{i=1}^N (\hat{x} - x_i)^2}$$

calculated using the formula:

where N = number of spikelets, \hat{x} = the wt-%

PiogHCl measured by sample mass, and x_i = the measured wt-% **PiogHCl** of spikelet i . ^eStandard deviation,

$$\sigma = \sqrt{\frac{1}{(N-1)} \sum_{i=1}^N (x_i - \bar{x})^2}$$

σ , calculated using the formula:

where N = number of spikelets, \bar{x} = the

average measured wt-% **PiogHCl**, and x_i = the measured wt-% **PiogHCl** of spikelet i .

Standardization curves obtained when using either the maximum spikelet intensity (**MSI**) or integrated spikelet intensity (**ISI**) are shown in **Figure 6.7** (the corresponding numerical data are listed in **Table 6.2**). Points on these plots correspond to the average wt-% **PiogHCl** measured from spikelets between 39 and -84 kHz (as demonstrated in **Appendix E**, spikelets outside this range have low S/N, which decreases their accuracy). Both plots show very good agreement with the expected values ($R^2 > 0.999$); using either measure of spikelet intensity, the measured salt contents are within 1

wt-% of the expected value. The root mean square deviation (RMSD) and standard deviations (σ) of the measurements (**Table 6.2**) are larger when using ISI (primarily at low wt-% **PiogHCl**), due to low S/N of these spectra. Thus, MSI seems to be preferable for quantification of these patterns (especially for low salt contents), and is the method we used for all further quantification experiments (*vide infra*).

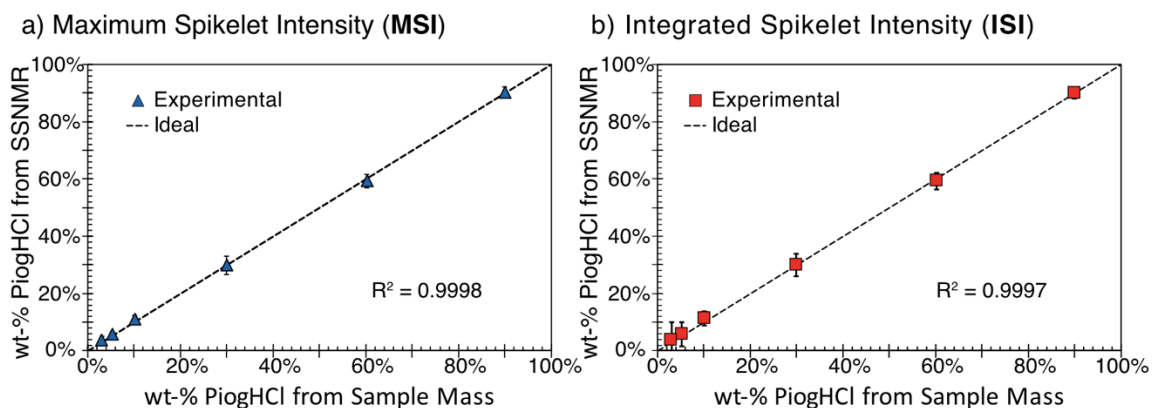


Figure 6.7. Plots of PiogHCl wt-% measured experimentally using ^{35}Cl SSNMR (y -axis) and the wt-% determined from the salt : free base mass ratio of the sample (x -axis). Data were obtained from spikelets in the spectra by measuring a) the peak intensity or b) the integrated intensity of each spikelet. The plotted values are the average measurement obtained from the spikelets in a given spectrum between 39 and -84 kHz, and the error bars represent the root mean square deviation (RMSD). Standard deviations, σ , in the measured values (not shown) are smaller than the point markers. (See **Table 6.2** for definitions of these two statistical values).

6.3.5 Quantification of Disproportionation

Given the success of our procedure for quantifying **PiogHCl** in standard samples using ^{35}Cl SSNMR, we applied the same method to measure the amount of **PiogHCl** in the stearate-containing sample mixtures. In order to avoid interfering signal from the disproportionation products, we analyzed spikelets between -40 and -65 kHz, which are outside of the range of signals from NaCl or MgCl_2 (see the difference spectra, **Figure 6.3c** and **Figure 6.5d**, respectively). The amounts of **PiogHCl** measured are listed in

Table 4.3. As discussed above, all of the Cl^- anions involved in disproportionation react with the cation of the stearate to produce either NaCl or MgCl_2 (and its hydrates); therefore, the limiting reagent in the disproportionation reaction is the stearate. With a 9:1 wt/wt ratio of API to stearate, the maximum stoichiometric limits of **PiogHCl** conversion are 14.77% and 14.25% in mixtures with **MgSt** and **NaSt**, respectively. The former value is within 0.5 %-conversion of what we have determined using ^{35}Cl SSNMR, supporting our measured value. Interestingly, the values measured previously with other techniques^{10,17,61} range between 20-30 %-conversion for the **MgSt** mixture, which may indicate the presence of Cl^- ions that are not bound to stearate cations (*e.g.*, hexaaqua-coordinated Cl^- species), but we have not observed these species in our work. **MgSt** seems to cause a substantially larger loss of **PiogHCl** than **NaSt** (*vide infra*), in agreement with the previous observations.^{10,61}

Table 6.3. Experimental and calculated amounts of **PiogHCl** in the stearate mixture samples.

Sample	Measured wt-% PiogHCl (%) ^a	Measured % Conversion of PiogHCl (%) ^b	Theoretical Max. % Conversion of PiogHCl (%) ^c
NaSt_C	93(2)	–	–
NaSt_X	84(2)	7(2)	14.25
MgSt_C	92(3)	–	–
MgSt_X	77(2)	15(2)	14.77

^aMeasured values from ^{35}Cl SSNMR experiments, reported as the average value obtained from spikelets between –40 and –65 kHz with the standard deviation listed in parentheses, see text for details. ^bCalculated using the formula: % conversion = $\frac{\text{amount of PiogHCl consumed}}{\text{amount of PiogHCl supplied}} = \left(\frac{90\% - \text{measured wt-\% PiogHCl}}{90\%} \right)$

^cConversion of **PiogHCl** that would occur if all of the stearate cations reacted stoichiometrically with Cl^- anions from the salt.

The amount of disproportionation measured in the **NaSt**-containing sample, 7(2) %-conversion, is roughly half what is predicted based on the stoichiometry of the mixture, indicating a partial conversion of the stearate. This result is supported by the ^{23}Na NMR data (**Figure 6.4b**), which reveal that some of the **NaSt** remains in the **NaSt_X** sample after it has been treated (*i.e.*, some of the **NaSt** does not react with the API). As was previously noted,⁶¹ the decreased %-conversion of **NaSt_X** relative to **MgSt_X** is counterintuitive; **NaSt** has a higher surface area, alkalinity, and stronger hygroscopicity than **MgSt**, all of which are factors that are thought to increase disproportionation. However, as verified in the current work, the disproportionation in **MgSt_X** produces MgCl_2 , whose strong hygroscopicity is a driving force for the reaction. Such conclusions require further study, for which NMR should be helpful, given its ability to study both solid and solution products of disproportionation.

6.4 Conclusions

In this work, we demonstrate the use of ^{35}Cl SSNMR for qualitative and quantitative assessment of the disproportionation reaction of **PiogHCl** in model formulations with metallic stearates. While this system has been studied previously from the perspective of the salt and free base, our results are the first to examine the reaction by characterizing the Cl^- counterions, which play a key role in disproportionation. The chlorine-containing disproportionation products produce unique ^{35}Cl powder patterns that are distinct from that of **PiogHCl** and each other. Our SSNMR spectra provide conclusive proof of the reactions between the chloride anions in the API salt and the metal cations in the stearates to produce solid salts (*i.e.*, NaCl or MgCl_2). The data reveal that these are the only Cl-containing by-products of the reaction (*e.g.*, no hexaaqua-

coordinated Cl^- species are observed). The presence of NaCl(s) is confirmed with ^{23}Na SSNMR experiments, while the strong deliquescent properties of MgCl_2 have been exploited to verify its presence. With judicious choice of pulse sequences, we can selectively excite signal from the disproportionation products, and filter signal from the intact API salt. Such spectra provide rapid detection of disproportionation (i) with a much greater efficiency than ^{13}C NMR and (ii) without interfering signal from excipient molecules; therefore, the acquisition of such spectra holds much promise for the high-throughput screening of formulations.

We also present a novel method for quantification of ultra-wideline (UW) NMR spectra. We have illustrated how, with careful sample preparation and experimental setup, ^{35}Cl SSNMR experiments can be used to accurately determine the amount of **PiogHCl** present in standardized binary mixtures containing the free base form (within 1 wt-% of the expected value). To the best of our knowledge, this is the first demonstration of quantification using UW NMR spectra of any nucleus.

This method has been used to quantitatively measure disproportionation in **PiogHCl** mixtures with metal stearates. By using spikelet spectra obtained from a Fourier transform of the entire CPMG echo train, our method can be used to selectively quantify peaks from the API salt without interference from the disproportionation products. Our results suggest that sample mixtures with **NaSt** and **MgSt** that have been treated at 75% RH and 40 °C for 5 days produce disproportionation (%-conversion of **PiogHCl**) of roughly 7(2)% and 15(2)%, respectively. The results obtained herein are consistent with those predicted based on the stoichiometry of the proposed reaction scheme (**Figure 6.1**).

Our results will aid in the mechanistic understanding of disproportionation, facilitating the risk assessment of API stabilities in the development of salt-containing pharmaceutical dosage formulations. Furthermore, with the novel approach for quantification of UW NMR spectra, we hope to encourage the use of quadrupolar nuclei and UW spectra in quantification studies of pharmaceuticals, as well as the wide variety of other important materials containing such nuclei.

6.5 References

- (1) Berge, S. M.; Bighley, L. D.; Monkhouse, D. C. *J. Pharm. Sci.* **1977**, *66*, 1–19.
- (2) Elder, D. P.; Holm, R.; Lopez de Diego, H. *Int. J. Pharm.* **2013**, *453*, 88–100.
- (3) Nelson, E. *J. Am. Pharm. Assoc.* **1958**, *47*, 297–299.
- (4) Serajuddin, A. T. M. *Adv. Drug Deliv. Rev.* **2007**, *59*, 603–616.
- (5) Guerrieri, P.; Taylor, L. S. *Pharm. Res.* **2009**, *26*, 2015–2026.
- (6) Thakral, N. K.; Kelly, R. C. *Int. J. Pharm.* **2017**, *520*, 228–240.
- (7) Thakral, N. K.; Behme, R. J.; Aburub, A.; Peterson, J. A.; Woods, T. A.; Diseroad, B. A.; Suryanarayanan, R.; Stephenson, G. A. *Mol. Pharm.* **2016**, *13*, 4141–4151.
- (8) Nie, H.; Byrn, S. R.; Zhou, Q. *Drug Dev. Ind. Pharm.* **2017**, *43*, 1215–1228.
- (9) Stephenson, G. A.; Aburub, A.; Woods, T. A. *J. Pharm. Sci.* **2011**, *100*, 1607–1617.
- (10) John, C. T.; Xu, W.; Lupton, L. K.; Harmon, P. A. *Pharm. Res.* **2013**, *30*, 1628–1641.
- (11) Hsieh, Y.-L.; Taylor, L. S. *Pharm. Res.* **2015**, *32*, 549–561.
- (12) Serajuddin, A. T. M.; Rosoff, M. *J. Pharm. Sci.* **1984**, *73*, 1203–1208.
- (13) Serajuddin, A. T. M.; Jarowski, C. I. *J. Pharm. Sci.* **1985**, *74*, 148–154.
- (14) Hsieh, Y.-L.; Merritt, J. M.; Yu, W.; Taylor, L. S. *Pharm. Res.* **2015**, *32*, 3110–3118.
- (15) Shah, A. K.; Agnihotri, S. A. *J. Control. Release* **2011**, *156*, 281–296.
- (16) Nie, H.; Liu, Z.; Marks, B. C.; Taylor, L. S.; Byrn, S. R.; Marsac, P. J. *J. Pharm. Biomed. Anal.* **2016**, *118*, 328–337.
- (17) Koranne, S.; Govindarajan, R.; Suryanarayanan, R. *Mol. Pharm.* **2017**, *14*, 1133–1144.
- (18) Skrdla, P. J.; Zhang, D. *J. Pharm. Biomed. Anal.* **2014**, *90*, 186–191.
- (19) Namespetra, A. M.; Hirsh, D. A.; Hildebrand, M. P.; Sandre, A. R.; Hamaed, H.; Rawson, J. M.; Schurko, R. W. *CrystEngComm* **2016**, *18*, 6213–6232.
- (20) Tishmack, P. A.; Bugay, D. E.; Byrn, S. R. *J. Pharm. Sci.* **2003**, *92*, 441–474.
- (21) Geppi, M.; Mollica, G.; Borsacchi, S.; Veracini, C. A. *Appl. Spectrosc. Rev.* **2008**, *43*, 202–302.
- (22) Vogt, F. G. *eMagRes* **2015**, *4*, 255–268.
- (23) Harris, R. K. *Analyst* **2006**, *131*, 351.
- (24) Holzgrabe, U.; Deubner, R.; Schollmayer, C.; Waibel, B. *J. Pharm. Biomed. Anal.* **2005**, *38*, 806–812.
- (25) Stephenson, G. A.; Forbes, R. A.; Reutzel-Edens, S. M. *Adv. Drug Deliv. Rev.* **2001**, *48*, 67–90.
- (26) Harris, R. K. *Analyst* **1985**, *110*, 649.
- (27) Harris, R. K.; Hodgkinson, P.; Larsson, T.; Muruganatham, A. *J. Pharm. Biomed. Anal.* **2005**, *38*, 858–864.
- (28) Ziarelli, F.; Caldarelli, S. *Solid State Nucl. Magn. Reson.* **2006**, *29*, 214–218.
- (29) Offerdahl, T. J.; Salsbury, J. S.; Dong, Z.; Grant, D. J. W.; Schroeder, S. A.; Prakash, I.; Gorman, E. M.; Barich, D. H.; Munson, E. J. *J. Pharm. Sci.* **2005**, *94*, 2591–2605.
- (30) Liu, J.; Nagapudi, K.; Kiang, Y.-H.; Martinez, E.; Jona, J. *Drug Dev. Ind. Pharm.* **2009**, *35*, 969–975.

- (31) Lefort, R.; De Gusseme, A.; Willart, J.-F.; Danède, F.; Descamps, M. *Int. J. Pharm.* **2004**, *280*, 209–219.
- (32) Nasu, M.; Nemoto, T.; Mimura, H.; Sako, K. *J. Pharm. Sci.* **2013**, *102*, 154–161.
- (33) Suryanarayanan, R.; Wiedmann, T. S. *Pharm. Res.* **1990**, *7*, 184–187.
- (34) Gao, P. *Pharm. Res.* **1996**, *13*, 1095–1104.
- (35) Tozuka, Y.; Ito, A.; Seki, H.; Oguchi, T.; Yamamoto, K. *Chem. Pharm. Bull.* **2002**, *50*, 1128–1130.
- (36) Vickery, R. D.; Nemeth, G. A.; Maurin, M. B. *J. Pharm. Biomed. Anal.* **2002**, *30*, 125–129.
- (37) Stueber, D.; Jehle, S. *J. Pharm. Sci.* **2017**, *106*, 1828–1838.
- (38) Tinmanee, R.; Larsen, S. C.; Morris, K. R.; Kirsch, L. E. *J. Pharm. Biomed. Anal.* **2017**, *146*, 29–36.
- (39) Rohrs, B. R.; Thamann, T. J.; Gao, P.; Stelzer, D. J.; Bergren, M. S.; Chao, R. S. *Pharm. Res.* **1999**, *16*, 1850–1856.
- (40) Ashbrook, S. E.; Duer, M. J. *Concepts Magn. Reson. Part A* **2006**, *28A*, 183–248.
- (41) Bryce, D. L.; Sward, G. D. *Magn. Reson. Chem.* **2006**, *44*, 409–450.
- (42) Hamaed, H.; Pawlowski, J. M.; Cooper, B. F. T.; Fu, R.; Eichhorn, S. H.; Schurko, R. W. *J. Am. Chem. Soc.* **2008**, *130*, 11056–11065.
- (43) Hildebrand, M.; Hamaed, H.; Namespetra, A. M.; Donohue, J. M.; Fu, R.; Hung, I.; Gan, Z.; Schurko, R. W. *CrystEngComm* **2014**, *16*, 7334.
- (44) Widdifield, C. M.; Chapman, R. P.; Bryce, D. L. In *Annual Reports on NMR Spectroscopy*; Elsevier Ltd., 2009; Vol. 66, pp 195–326.
- (45) Schurko, R. W. *Acc. Chem. Res.* **2013**, *46*, 1985–1995.
- (46) Perras, F. A.; Viger-Gravel, J.; Burgess, K. M. N.; Bryce, D. L. *Solid State Nucl. Magn. Reson.* **2013**, *51–52*, 1–15.
- (47) Ashbrook, S. E.; Sneddon, S. *J. Am. Chem. Soc.* **2014**, *136*, 1–60.
- (48) Schurko, R. W. In *Encyclopedia of Magnetic Resonance*; John Wiley & Sons, Ltd: Chichester, UK, 2011; pp 77–93.
- (49) Carr, H. Y.; Purcell, E. M. *Phys. Rev.* **1954**, *94*, 630–638.
- (50) Meiboom, S.; Gill, D. *Rev. Sci. Instrum.* **1958**, *29*, 688–691.
- (51) Kupce, E.; Freeman, R. *J. Magn. Reson.* **1995**, *115*, 273–276.
- (52) Bhattacharyya, R.; Frydman, L. *J. Chem. Phys.* **2007**, *127*, 194503.
- (53) O’Dell, L. A.; Schurko, R. W. *Chem. Phys. Lett.* **2008**, *464*, 97–102.
- (54) O’Dell, L. A.; Rossini, A. J.; Schurko, R. W. *Chem. Phys. Lett.* **2009**, *468*, 330–335.
- (55) Ziarelli, F.; Viel, S.; Sanchez, S.; Cross, D.; Caldarelli, S. *J. Magn. Reson.* **2007**, *188*, 260–266.
- (56) Samoson, A.; Lippmaa, E. *Phys. Rev. B* **1983**, *28*, 6567–6570.
- (57) Kentgens, A. P. M.; Lemmens, J. J. M.; Geurts, F. M. M.; Veeman, W. S. *J. Magn. Reson.* **1987**, *71*, 62–74.
- (58) Vega, A. J. In *Encyclopedia of NMR*; Grant, D. M., Harris, R. K., Eds.; Wiley: Chichester, 1996; Vol. 4, pp 3869–3888.
- (59) Man, P. P.; Klinowski, J.; Trokiner, A.; Zanni, H.; Papon, P. *Chem. Phys. Lett.* **1988**, *151*, 143–150.
- (60) O’Dell, L. A. *Solid State Nucl. Magn. Reson.* **2013**, *55–56*, 28–41.
- (61) Nie, H.; Xu, W.; Ren, J.; Taylor, L. S.; Marsac, P. J.; John, C. T.; Byrn, S. R. *Mol.*

- Pharm.* **2016**, *13*, 3541–3552.
- (62) Nie, H.; Xu, W.; Taylor, L. S.; Marsac, P. J.; Byrn, S. R. *Int. J. Pharm.* **2017**, *517*, 203–215.
- (63) Nie, H.; Su, Y.; Zhang, M.; Song, Y.; Leone, A.; Taylor, L. S.; Marsac, P. J.; Li, T.; Byrn, S. R. *Mol. Pharm.* **2016**, *13*, 3964–3975.
- (64) Peersen, O.; Wu, X.; Smith, S. *J. Magn. Reson.* **1994**, *106*, 127–131.
- (65) Peersen, O. B.; Wu, X. L.; Kustanovich, I.; Smith, S. O. *J. Magn. Reson.* **1993**, *104*, 334–339.
- (66) Metz, G.; Wu, X. L.; Smith, S. O. *J. Magn. Reson.* **1994**, *110*, 219–227.
- (67) Bennett, A. E.; Rienstra, C. M.; Auger, M.; Lakshmi, K. V.; Griffin, R. G. *J. Chem. Phys.* **1995**, *103*, 6951–6958.
- (68) Thakur, R. S.; Kurur, N. D.; Madhu, P. K. *J. Magn. Reson.* **2008**, *193*, 77–88.
- (69) Lefort, R.; Wiench, J. W.; Pruski, M.; Amoureux, J.-P. *J. Chem. Phys.* **2002**, *116*, 2493.
- (70) Akitt, J. W.; McDonald, W. S. *J. Magn. Reson.* **1984**, *58*, 401–412.
- (71) Autschbach, J.; Zheng, S.; Schurko, R. W. *Concepts Magn. Reson. Part A* **2010**, *36A*, 84–126.
- (72) Blaakmeer, E. S. (Merijn); Antinucci, G.; Busico, V.; van Eck, E. R. H.; Kentgens, A. P. M. *J. Phys. Chem. C* **2016**, *120*, 6063–6074.
- (73) Bryce, D. L.; Bultz, E. B. *Chem. Eur. J.* **2007**, *13*, 4786–4796.

Chapter 7: *In Situ* Characterization of Water in a Channel Hydrate API using ^{35}Cl SSNMR

7.1 Introduction

Active pharmaceutical ingredient (API) hydrates are solid phases of APIs formed by inclusion of water molecules.¹⁻⁵ Due to its small molecular size and propensity to form hydrogen bonds, water is capable of incorporating into a wide range of APIs (it is estimated that roughly one third of all APIs are hydrates).⁶ Hydration or dehydration of an API can occur as a response to changes in environment (*e.g.*, humidity, temperature) or manufacturing conditions (*e.g.*, pressure, temperature), or merely as a result of the passage of time (in the case of metastable hydrates). Such processes can produce APIs with multiple distinct crystalline or amorphous hydrated phases (called solvatomorphs or pseudopolymorphs). These forms can have different solid-state properties, which can affect the stability and bioavailability of the API, as well as the manufacture of stable and effective dosage formulations.

In many cases, waters of hydration are present in well-defined stoichiometric amounts, with mono- and di-hydrates being the most common;¹ however, *non-stoichiometric* hydrates also exist.⁷ An interesting sub-class of API hydrates, known as *variable hydrates*, can have a continuous range of non-stoichiometric hydration levels, often without significant changes in their crystal structures (*N.B.* the terms “variable” and “non-stoichiometric” hydrates are often used interchangeably in the literature).⁵ For this work, we define non-stoichiometric hydrates as those materials that crystallize with a fractional equivalent of water in their unit cells. By this definition, all variable hydrates are also non-stoichiometric hydrates, but not the reverse. Some *variable hydrate* APIs are

also *isomorphic desolvates*, (*i.e.*, the addition or removal of water does not produce a substantial phase change). Finally, *channel hydrates* are so-named because their crystal structures have one-, two-, or three-dimensional arrays of channels through which water molecules can move.⁸

The formation of a variable hydrate can be problematic for dosage form manufacturing. First, such materials are particularly sensitive to changes in the environment during the manufacturing process, which can produce unpredictable deviations in the hydration level. Second, since the water content affects the mass of the sample, variable hydrates can affect the dispensing amounts used in the tableting, thereby compromising the uniformity of the drug product. Finally, it is possible for some variable hydrates that the uptake or loss of water may result in a material that is more susceptible to a phase change, or even a molecular transformation that can occur in the bulk API or dosage form during manufacturing. Clearly, a careful understanding of the hydration level and its effects on molecular-level structure and stability is imperative for maintaining a predictable composition of both bulk and dosage forms APIs, such that the drug can be delivered safely and reliably.

Several complementary techniques are used to characterize variable hydrates. First, the existence of a variable hydrates is most commonly identified using thermal measurements. Differential scanning calorimetry (DSC) and thermogravimetric analysis (TGA) show characteristic endotherm shapes for such materials, and provide information on the total water content in the sample and the temperature and/or humidity ranges where dehydration occurs.^{5,7,9} Diffraction methods can be useful for identifying the changes in crystal structures that occur with hydration or dehydration.¹⁰⁻¹³ Such studies

are usually limited to the characterization of microcrystalline powders, as many hydration states of variable hydrates are metastable and cannot be isolated as single crystals. ^1H and ^{13}C solid-state NMR are also commonly used for studying hydrates, and can be particularly useful for the study of amorphous systems, in addition to microcrystalline materials. Like XRD, SSNMR spectra provide confirmation of the molecular structure, identification of crystallographically-distinct molecules in the unit cell, as well as detection of subtle or significant structural alterations that result from hydration or dehydration.¹⁴⁻¹⁹ SSNMR methods are especially useful as they can characterize the *in situ* hydration of the dosage formulations (even those of low wt-%), and enable the study of metastable phases like partially hydrated or amorphous materials.

Recently, ^{35}Cl SSNMR has emerged as a powerful method for characterizing APIs that are formed as HCl salts, including hydrates.²⁰⁻²⁵ Hydrated HCl salts of APIs are common, due to the interactions between the Cl^- anions and water molecules.^{26,27} ^{35}Cl is a quadrupolar nucleus ($I = 3/2$), and as such, its SSNMR spectra are influenced by the quadrupolar interaction in addition to chemical shift anisotropy. The former is extraordinarily sensitive to the local structural environments of the Cl^- anions;^{28,29} in particular, the nature of the $\text{H}\cdots\text{Cl}$ hydrogen bonds (*i.e.*, the number and arrangement of short $\text{H}\cdots\text{Cl}$ contacts $< 2.2 \text{ \AA}$, $\text{H}\cdots\text{Cl}$ distances, and identities of the hydrogen bonded moieties) has an enormous effect on the ^{35}Cl electric field gradient (EFG) tensor parameters and orientations, which in turn produce distinct power patterns in the ^{35}Cl NMR spectra. As such, each API (and each of its unique polymorphic or pseudopolymorphic forms) has a spectrum with a unique spectral fingerprint that can be simulated utilizing an eight-parameter fit (*i.e.*, quadrupolar parameters, CS tensor

parameters, and Euler angles describing the relative orientation of the EFG and CS tensors). To our knowledge, there are no extensive studies of variable hydrates of HCl salts with ^{35}Cl SSNMR. This technique should be well-suited for their study, given that the Cl^- anions are the most prevalent binding sites for water molecules.

Given the importance of understanding the effects of hydration in both bulk and dosage formulations and the need for new methods to unambiguously characterize the molecular-level structures of APIs (including variable hydrates), herein, we present a study on the effects of hydration on a Genentech development compound, GNE-A, which is an HCl salt hydrate (**Figure 7.1**). ^{35}Cl SSNMR is the primary characterization tool in this work, as it can probe the local structures of hydrated and dehydrated Cl^- anions in samples with different hydration levels. Additional multinuclear (^{19}F , ^1H , ^{13}C , ^2H) SSNMR experiments are utilized to analyze the unique nuclear environments in the hydrated and dehydrated phases. These experiments are supported by complementary TGA and X-ray diffraction data. The methods demonstrated in this work are invaluable for the study of hydration in variable hydrates, and can easily be adapted to the study of dosage formulations.

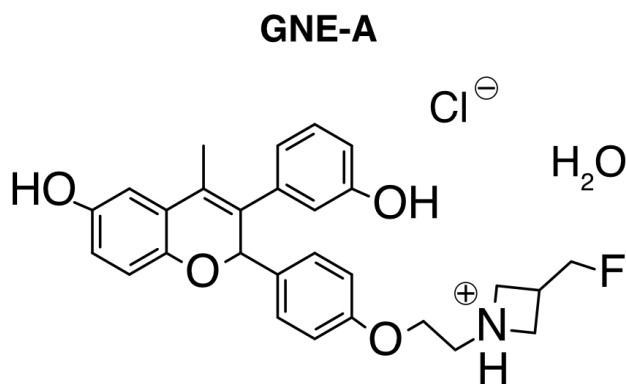


Figure 7.1. Molecular structure of GNE-A.

7.2 Methods

7.2.1 Chemicals

GNE-A was obtained from Genentech Inc. and used without further purification. 99.9%-labeled D₂O(ℓ) was obtained from Cambridge Isotope Labs.

7.2.2 Sample Preparation

Samples of GNE-A with different hydration levels were prepared *ex situ* by drying the **As Received** sample for 18 hours at 100 °C in an oven and then rehydrating for different amounts of time at 65% relative humidity (RH). These samples are referred to in the text by the amount of time they were exposed to moisture after drying: (i) **Dry** was packed under inert atmosphere immediately after removal from the oven, (ii) **Rehydrate Short** was packed immediately under 65% RH conditions, and (iii) **Rehydrate Long** was packed after rehydration in a humidity chamber for 40 hours. Finally, a **Rehydrate-D₂O** sample was prepared with the same method as **Rehydrate Long**, except that a humidity chamber containing 100% RH D₂O was used for the rehydration.

Samples were packed into 5 mm o.d. glass tubes plugged with Teflon tape (for static experiments) and packed into 4 mm o.d. zirconia rotors closed with air-tight Teflon screws (for magic-angle spinning (MAS) experiments). In order to prevent exposure to additional atmospheric moisture, all NMR experiments were conducted by passing a nitrogen gas stream over the sample holders (this was done for variable-temperature (VT) experiments, MAS drive and bearing gases, and probe cooling).

7.2.3 Solid-State NMR Experiments

Solid-state NMR (SSNMR) experiments at $B_0 = 9.4$ T were conducted using a Bruker Avance III HD console and an Oxford wide-bore magnet ($\nu_0(^1\text{H}) = 399.73$ MHz, $\nu_0(^{13}\text{C}) = 100.53$ MHz, $\nu_0(^2\text{H}) = 61.36$ MHz, $\nu_0(^{35}\text{Cl}) = 39.16$ MHz). ^1H and ^{13}C NMR experiments were conducted with a Varian/Chemagnetics 4 mm HX MAS probe.

Variable-temperature ^{35}Cl and ^2H NMR experiments were performed with a Varian/Chemagnetics 5 mm HX static probe and temperature control was provided by a Varian VT stack and Bruker BCU II 80/60 chiller. Supplementary ^{35}Cl experiments were conducted at $B_0 = 21.1$ T ($\nu_0(^{35}\text{Cl}) = 88.2$ MHz) at the National Ultrahigh-field NMR Facility for Solids in Ottawa, Ontario, Canada. These experiments used a Bruker Avance II spectrometer equipped with a standard-bore magnet. Experiments were conducted with a home-built 5 mm HX probe using a quadrupolar-echo pulse sequence of the form $(\pi/2)_x - \tau_1 - (\pi/2)_y - \tau_2 - \text{acq.}$ Ultra-fast MAS (UFMAS) ^1H and ^{19}F NMR experiments were conducted using a Bruker Avance II console equipped with a standard-bore $B_0 = 11.7$ T magnet ($\nu_0(^1\text{H}) = 500.13$ MHz, $\nu_0(^{19}\text{F}) = 470.59$ MHz) and a Bruker 1.3 mm HX probe.

^1H and ^{13}C chemical shifts were referenced to tetramethylsilane (TMS, $\delta_{\text{iso}} = 0.0$ ppm) using adamantane ($\delta_{\text{iso}} = 1.85$ and 38.57 ppm, respectively) as a secondary reference. ^{35}Cl chemical shifts were referenced with respect to NaCl(s) ($\delta_{\text{iso}} = 0.0$ ppm). ^2H chemical shifts were referenced with respect to C_6D_6 ($\delta_{\text{iso}} = 0.0$ ppm) using a 9:1 $\text{D}_2\text{O}:\text{H}_2\text{O}$ solution ($\delta_{\text{iso}} = 2.5$ ppm) as a secondary reference. ^{19}F chemical shifts were referenced to neat $\text{CFCl}_3(\text{l})$ ($\delta_{\text{iso}} = 0.0$ ppm) using neat fluorobenzene(l) ($\text{C}_6\text{H}_5\text{F}$, $\delta_{\text{iso}} = -113.15$ ppm) as a secondary reference.

Details of the SSNMR experimental parameters are listed in **Appendix F (Table F6)**. $^{35}\text{Cl}\{^1\text{H}\}$ spectra were acquired using the WURST-CPMG sequence.^{30,31} ^1H - ^{13}C cross-polarization (CP) experiments used a ramped-amplitude spin-lock pulse on the ^1H channel.^{32–34} ^2H NMR spectra were obtained with a quadrupolar-echo pulse sequence of the form $(\pi/2)_x - \tau_1 - (\pi/2)_y - \tau_2 - \text{acq.}$ ^1H and ^{19}F direct-excitation MAS experiments were conducted using a rotor-synchronized Hahn-echo pulse sequence of the form $(\pi/2)_x - \tau_1 - (\pi)_y - \tau_2 - \text{acq.}$ High-power ^1H decoupling was applied in all ^{35}Cl , ^{13}C , and ^2H experiments, using either continuous wave (for ^{35}Cl and ^2H) or swept-field two-pulse phase-modulation (sw-TPPM)^{35,36} (for ^{13}C) decoupling sequences.

SSNMR spectra were obtained and processed using TopSpin 3.5. Analytical simulations of the ^{35}Cl and ^2H powder patterns were prepared using the Solid Lineshape Analysis (SOLA) module within TopSpin. The effects of molecular dynamics on the ^2H powder patterns were modelled using EXchange Program for RELaxing Spin Systems (EXPRESS).³⁷

7.2.4 NMR Tensor Calculations

First-principles calculations were conducted using plane-wave density functional theory (DFT)³⁸ in the CASTEP software package.^{39,40} All calculations used the generalized gradient approximation (GGA) Perdew, Burke, and Ernzerhof (rPBE) functional,⁴¹ with ultrasoft pseudopotentials generated on-the-fly.⁴² The positions of all of the atoms in the crystal structure of GNE-A were refined using the Broyden-Fletcher-Goldfarb-Shanno (BFGS) energy-minimizing scheme,⁴³ while keeping the lattice parameters fixed. These optimizations employed a Grimme semi-empirical, two-body, force-field dispersion correction⁴⁴ with a reparametrized damping function developed in

our group (DFT-D2*).⁴⁵ After optimizing the structures, ³⁵Cl NMR tensor parameters were calculated using the gauge-including projector augmented wave algorithm (GIPAW)³⁹ implemented in CASTEP. A full list of parameters for these calculations is presented in **Table F7**.

7.3 Results and Discussion

7.3.1 Crystal Structure of GNE-A

The crystal structure of GNE-A is shown from two different perspectives in **Figure 3.1**. There are a total of four GNE-A molecules in the unit cell, which contains two asymmetric units ($Z = 2$), each with two crystallographically-distinct molecules of GNE-A ($Z' = 2$). As highlighted in **Figure 3.1a**, the structure features organic API molecules arranged in layers running parallel to each other. When viewed along the b axis of the unit cell (**Figure 3.1b**), it is apparent that there is also a channel containing Cl^- ions and water molecules parallel to the b axis, which may allow water to enter and exit under certain conditions (*vide infra*). There is some positional disorder in the structure, which can be modelled using two conformers (**Conformers A and B, Figure F1**). The primary difference between these structures is in the orientation of the F atoms in the fluoromethyl groups, which either point towards or away from the Cl^- sites in the hydrated channels. The crystal structure predicts fractional occupancy of these two conformers in a ratio of 2:1 for **A:B**. Simulated PXRD patterns for the two conformers are nearly identical, and match the experimental PXRD pattern obtained from the powder samples of GNE-A used in this work (**Figure F2**).

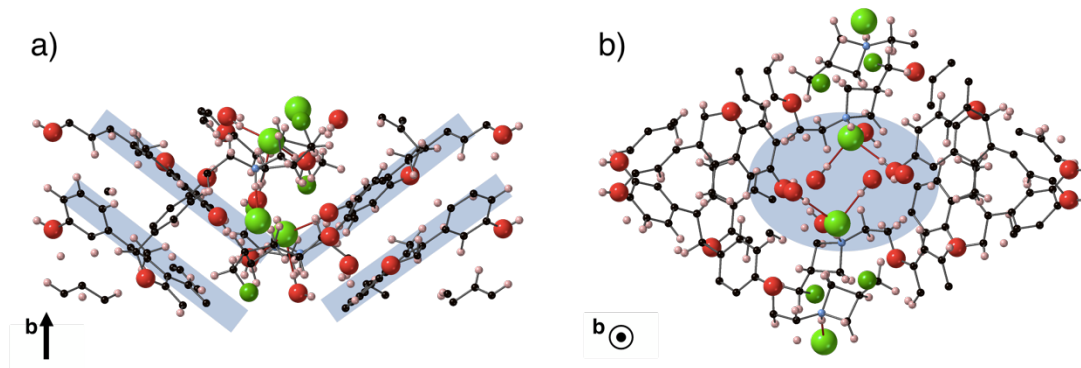


Figure 7.2. Crystal structure of GNE-A shown in two perpendicular orientations, as indicated by the orientation of the crystallographic *b*-axis. Shading highlights features of the structure that are discussed in the text. The crystal structure of GNE-A was solved by A. DiPasquale at Genentech. A full accounting of the solution of this structure will be released with the submission of a manuscript on this topic.

The primary focus of this work is to use ^{35}Cl SSNMR to characterize the hydration states of this material. As such, the local Cl^- environments in the conformer are particularly important for our analysis. There are two crystallographically-distinct Cl sites in the crystal structure, which have different sets of $\text{H}\cdots\text{Cl}$ close contacts, which are defined as $\text{H}\cdots\text{Cl}$ distances of *ca.* 2.2 Å or less (see **Table 6.1**). One of the two Cl sites does not have any close contacts with water molecules, whereas the other is present in the hydrated core of the conformer and has close contacts with H atoms in two water molecules. Herein, these anhydrous and hydrated sites are referred to as **Site I** and **Site II**, respectively. As summarized in **Table 6.1**, the lengths of the $\text{H}\cdots\text{Cl}$ contacts differ slightly (≈ 0.1 Å) between the two GNE-A conformers for **Sites I** and **II**; however, the identities and number of the hydrogen bond donors are the same in both cases.

Table 7.1. Close H \cdots Cl contacts (< 2.2 Å) for the two crystallographically distinct Cl sites in GNE-A.

	Conformer A		Conformer B	
	H-Bond Donor	H \cdots Cl Length (Å)	H-Bond Donor	H \cdots Cl Length (Å)
Site 1	R ₃ N-H	2.039	R ₃ N-H	2.096
	O-H	2.193	O-H	2.279
	O-H	2.268	O-H	2.293
Site 2	O-H	2.079	O-H	2.113
	H-O-H	2.100	H-O-H	2.124
	H-O-H	2.128	H-O-H	2.176

7.3.2 Thermogravimetric Analysis (TGA)

The TGA data obtained for GNE-A (**Figure F3**) show that the material loses 3.41% of its mass when heated to 100 °C, slightly less than one equivalent of water (3.5 wt-%). If the dried sample is cooled and exposed to ambient conditions for 10 minutes, it absorbs 2.3 wt-% water. This behavior is typical of a channel hydrate,^{1,2} and suggests water may pass into and out of the structure through the channels highlighted in **Figure 3.1**. While TGA can reveal the total water content of a sample, it does not provide information on the local molecular structure of the water molecules or any structural changes that may occur with dehydration and rehydration. As such, alternative characterization techniques are necessary.

7.3.3 ³⁵Cl SSNMR of GNE-A

Given the interaction of Cl⁻ anions with water molecules in the structure (**Figure 3.1, Table 6.1**), and the sensitivity of ³⁵Cl EFG tensors to differences and/or changes in hydrogen bonding, ³⁵Cl SSNMR experiments were conducted in order to probe the hydration levels of this material, and the effects on the local environments of the Cl⁻ anions in both **Sites I and II**.

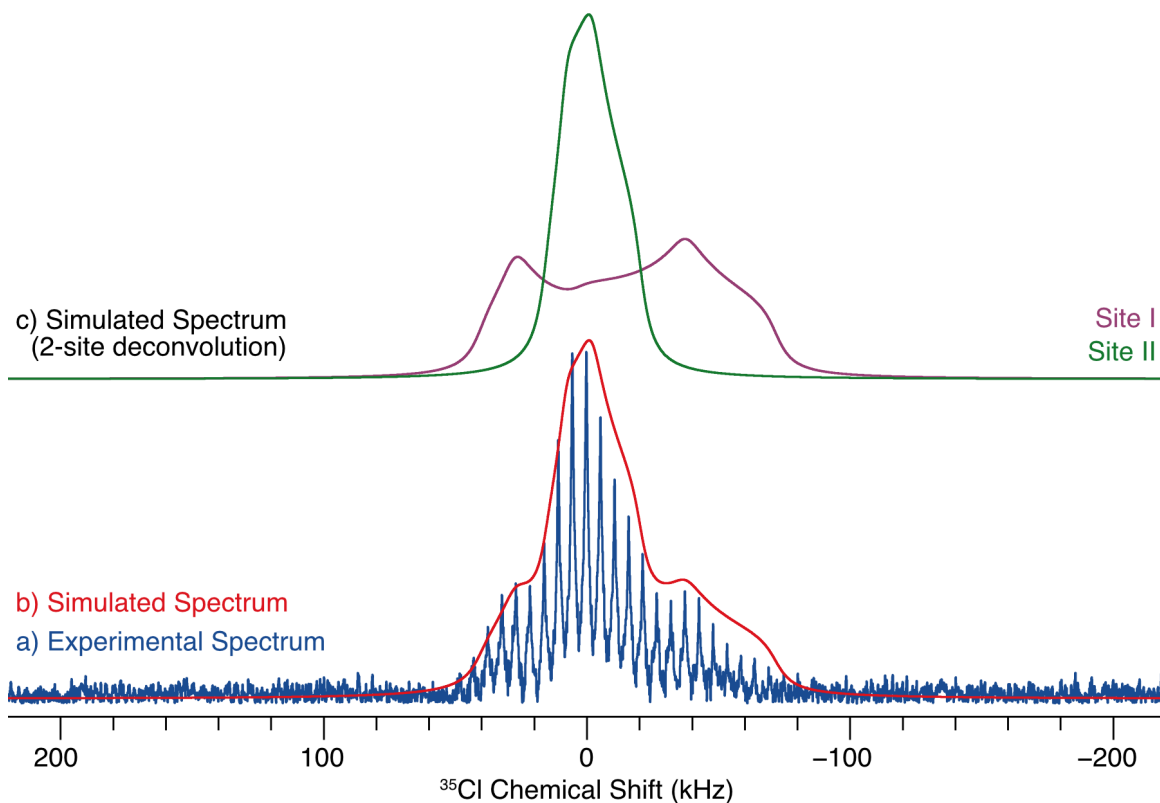


Figure 7.3. a) Experimental $^{35}\text{Cl}\{^1\text{H}\}$ WURST-CPMG NMR spectrum of GNE-A acquired under static sample conditions at 22 °C and b) the corresponding two-site analytical simulation. A deconvolution of the simulated spectrum is shown in c).

The $^{35}\text{Cl}\{^1\text{H}\}$ WURST-CPMG NMR spectrum of GNE-A acquired at 22 °C is shown in **Figure 7.3a**. In comparison to the numerous high-quality spectra of HCl APIs that have been acquired with this pulse sequence, the S/N in this spectrum is low (despite lengthy experimental times) and the two second-order quadrupolar patterns are not easily resolved. The WURST pulses provide uniform excitation of the broad central transition (*i.e.*, $+1/2 \leftrightarrow -1/2$, CT) pattern; however, due to the short ^{35}Cl transverse relaxation time constant, $T_2(^{35}\text{Cl})$, relatively few CPMG echoes are collected – this is the main factor resulting in the low S/N. Even the application of increased ^1H decoupling amplitudes failed to yield an longer effective $T_2(^{35}\text{Cl})$ that would serve to substantially increase S/N. Furthermore, the CT patterns are poorly defined, in that they do not have the sharp

discontinuities associated with CT patterns of highly crystalline samples; this is suggestive of some degree of disorder at the Cl⁻ sites, or perhaps a lack of long-range order in the sample. Nonetheless, two distinct ³⁵Cl patterns can be resolved (**Figure 7.3c**) and the combined simulated spectrum (**Figure 7.3b**) matches the experimental data well (NMR tensor parameters are listed in **Table 7.2**). In order to refine the experimental NMR tensor parameters, a second spectrum of GNE-A was acquired (**Figure F4**) using a higher magnetic field strength ($B_0 = 21.1$ T). This additional spectrum, which is acquired with a quadrupolar-echo pulse sequence, has higher S/N, and features narrower CT patterns that can be simulated using the same EFG and CS tensor parameters, increasing the confidence in the fit for both patterns.

Table 7.2. Experimental and calculated ³⁵Cl NMR tensor parameters of GNE-A.^a

	Experimental		Calculated			
			Conformer A		Conformer B	
	Site I	Site II	Site I	Site II	Site I	Site II
C_Q (MHz) ^b	5.5(2)	3.3(1)	6.4	-3.3	5.2	3.5
η_Q ^c	0.3(2)	0.6(1)	0.48	0.53	0.58	0.66
δ_{iso} (ppm) ^d	81(20)	68(20)	18	30	25	28
Ω (ppm) ^e	165(20)	75(25)	101	53	79	45
κ ^f	-1.0(2)	-1.0(2)	-0.20	-0.77	-0.34	-0.35
α (°) ^g	0	0	104	104	94	242
β (°) ^g	0	0	84	46	82	79
γ (°) ^g	0	0	186	52	180	68

^aThe experimental uncertainty in the last digit(s) for each value is indicated in parentheses. ^b $C_Q = eQV_{33}/h$; ^c $\eta_Q = (V_{11} - V_{22})/V_{33}$; ^d $\delta_{\text{iso}} = (\delta_{11} + \delta_{22} + \delta_{33})/3$, where $\delta_{jj} \approx \sigma_{\text{iso,ref}} - \sigma_{jj}$, where $jj = 11, 22, 33$ and $\delta_{11} \geq \delta_{22} \geq \delta_{33}$. $\sigma_{\text{iso,ref}}$ is the reference nuclear shielding, 971.22 ppm for ³⁵Cl, determined from calculations on NaCl. ^e $\Omega = \delta_{11} - \delta_{33}$; ^f $\kappa = 3(\delta_{22} - \delta_{\text{iso}})/\Omega$. ^gThe Euler angles, α , β , and γ , define the relative orientation of the CS and EFG tensors.

7.3.4 DFT-Calculations using CASTEP

The assignment of overlapping ^{35}Cl powder patterns in an ultra-wideline NMR spectrum to distinct Cl^- sites can be difficult without *a priori* knowledge of the NMR tensor parameters associated with each site. Previous work by our group²¹ identified trends that correlate the ^{35}Cl EFG tensor parameters of Cl^- environments with the numbers and types of short $\text{H}\cdots\text{Cl}$ contacts present at these sites; these trends can serve as an aid in making structural assignments for systems with multiple Cl^- anion sites. However, the structural trends identified to date are only useful for non-hydrated Cl^- anion sites; analysis of sites featuring hydrogen bonds between Cl^- anions and water molecules are hampered by inaccuracies in the hydrogen atom positions of the water molecules (both from experimental structures and theoretical computations). Hence, in the case of the patterns arising from **Sites I** and **II** in GNE-A, it is not possible to make a clear assignment using these trends.

Recently, our group has developed a dispersion-corrected plane-wave density functional theory (DFT) method for the refinement of atomic coordinates determined by experimental diffraction methods via an empirical parameterization of Grimme's two-body dispersion force field.⁴⁵ This method, known as **DFT-D2***, yields ^{35}Cl EFG tensors that are in excellent agreement with experimentally determined values, and has been demonstrated to optimize the positions of hydrogen atoms involved in hydrogen bonding with a precision rivaling that of neutron diffraction.

As such, plane-wave DFT-D2* calculations of the NMR tensors in GNE-A were performed using the CASTEP software package.^{39,40} Calculations were performed separately on the two conformers (**Conformers A** and **B**, **Figure F1**), since a calculation

on a supercell containing both conformers is computationally expensive. While these conformations co-exist in the real material, the Cl sites are close to a single F site in one conformer (**Conformer A**); as such, the ^{35}Cl EFG tensor is only affected by this neighboring F site. Preliminary ^{19}F NMR experiments (**Figure F6**) confirm that there are four crystallographically distinct F sites in the unit cell, which is consistent with CASTEP results that show each of the two conformers has two distinct F environments. The ^{19}F NMR patterns have a 2:1 intensity ratio, consistent with the relative occupancies of the two conformers determined using SCXRD. Additional ^{19}F NMR experiments to confirm this assignment are ongoing in our laboratory.

As seen in **Table 7.2**, there is remarkably good agreement between the calculated and experimental ^{35}Cl NMR tensor parameters, particularly for the EFG tensor parameters (C_Q and η_Q). From these results, we assign the broad pattern in **Figure 7.3** to the anhydrous site in the crystal structure (**Site I**) and the narrow pattern to the hydrated site (**Site II**). While there are deviations between the experimental and theoretical values of the CS tensor parameters (δ_{iso} , Ω , and κ), these likely result from the large uncertainties in the associated experimental values.

There are some key differences in the calculated results for the two conformers. While the calculated values for the anhydrous sites (**Site I**) in each conformer are similar to each other, those for the hydrated sites (**Site II**) have C_Q values with similar magnitudes but opposite signs. This sign change corresponds to a large difference in C_Q (*ca.* 6 MHz) between the two conformers, and results from differences in ^{35}Cl EFG tensor orientations due to interactions between the F site in the CH_2F group and the nearest Cl^- ion (**Figure F5**). In **Conformer A**, the C-F bond is oriented towards the neighboring Cl^-

site (F...Cl distance of 3.76 Å); but, in **Conformer B**, the C-F bond points away from the Cl (F...Cl distance of 4.38 Å), therefore having a lesser effect on the ^{35}Cl EFG tensor parameters. In **Conformer A**, the largest component of the EFG tensor, V_{33} , is oriented perpendicular to the direction of the Cl...F contact, whereas in **Conformer B**, V_{33} is directed towards the water molecules (*i.e.*, it is not strongly influenced by the F atom, see **Figure F5**). Unfortunately, it is not possible to determine the sign of C_Q from the experimental NMR spectra, but only its magnitude. Hence, if the two conformers exist in the sample, the ^{35}Cl NMR spectra likely represent an average of the magnitude of the quadrupolar interactions, which would partially explain the poor resolution of the discontinuities observed therein.

7.3.5 Variable-Temperature ^{35}Cl NMR of GNE-A

The removal or addition of water in variable hydrates of HCl APIs should dramatically affect the chlorine environments in the structure (and their associated ^{35}Cl SSNMR spectra), particularly that of the hydrated site (**Site II**). As such, variable-temperature experiments were conducted to probe the change in ^{35}Cl NMR spectra with dehydration of the sample; the resulting spectra are shown in **Figure 7.4** and **Figure F7**.

While there are some changes in the shapes of the pattern with temperature (**Figure F7**, *vide infra*), the primary difference between the spectra is their intensities, even though the spectra were acquired using the same sample and identical experimental parameters (**Figure 7.4**). The magnitude of NMR signals are influenced by temperature (*i.e.*, due to Boltzmann weighting of the spin state populations); however, the spectra acquired at the same temperature before and after heating also have different intensities.

Furthermore, if the spectra are scaled to account for the differences in temperature (as was done in **Figure 7.4**), there are still substantial differences in intensity.

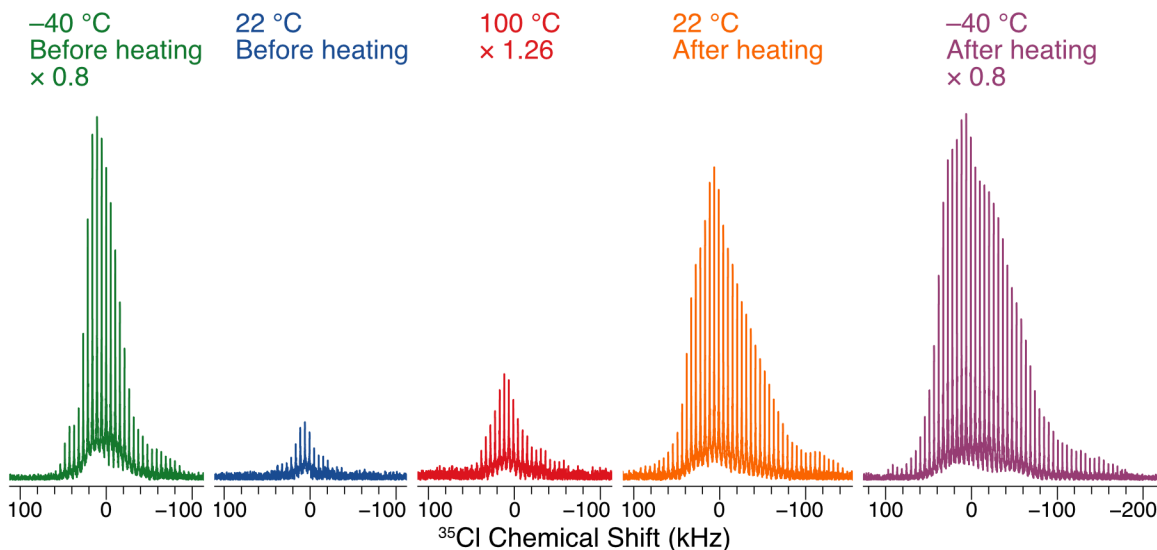


Figure 7.4. Experimental $^{35}\text{Cl}\{^1\text{H}\}$ WURST-CPMG NMR spectra of GNE-A acquired at various temperatures. Spectra were acquired on the same sample in the order shown from left to right. The spectra have been vertically scaled to account for the Boltzmann enhancement of the spin energy level populations due to temperature (*i.e.*, scaling factor = $T \times (295.15 \text{ K})^{-1}$).

Such a variation in signal intensity suggests a change in the nuclear relaxation constants (either longitudinal, T_1 , or transverse, T_2). However, substantial changes in $T_1(^{35}\text{Cl})$ were not observed for this sample (the recycle delay was optimized at each temperature, and was found to range from 0.5 to 1 s). Instead, the largest effect on the signal intensities comes from a change in the $T_2(^{35}\text{Cl})$ values, which can be measured using the FIDs from the WURST-CPMG experiments (**Figure F8**). The major contribution to $T_2(^{35}\text{Cl})$ relaxation in these samples is the ^1H - ^{35}Cl heteronuclear dipolar coupling mechanism. When spectra are acquired with strong ^1H decoupling (as was done here) the measured T_2 is an “effective” value, a so-called T_2^{eff} (because the actual T_2 measured without ^1H decoupling would have a smaller value). As shown in **Table 7.3**, the $T_2^{\text{eff}}(^{35}\text{Cl})$ doubles

when the sample is heated and then cooled, producing the intensity variations observed in **Figure 7.4**. Clearly, the removal of water causes a net increase in the $T_2^{\text{eff}}(^{35}\text{Cl})$, due to the removal of ^1H proximate to the ^{35}Cl nuclei (*vide infra*).

Table 7.3. Experimental $T_2^{\text{eff}}(^{35}\text{Cl})$ constants obtained from the WURST-CPMG spectra of GNE-A acquired at different temperatures before and after heating in the magnet.^a

Sample Temperature	$T_2^{\text{eff}}(^{35}\text{Cl})$ Constant ^{b,c}	
	Before Hot VT	After Hot VT
-40 °C	0.58(4) ms	1.69(9) ms
22 °C	0.50(4) ms	1.12(8) ms

^aThe experimental uncertainty in the last digit(s) for each value is indicated in parentheses. ^bMeasured values are “effective” values because they were determined from the WURST-CPMG echo train acquired with ^1H decoupling; the true $T_2(^{35}\text{Cl})$ values are shorter, see text for details. ^cEcho trains were fit using a mono-exponential decay.

7.3.6 Characterization of Samples with Different Hydration Levels

In order to characterize the local structural effects of water in GNE-A, three additional samples were prepared. In each case, the samples were first dried in the oven for 18 hours at 100 °C to ensure that as much water as possible was removed. Then, some of the dried sample was packed under inert atmosphere (hereafter referred to as the **Dry** sample). Finally, two dried samples were rehydrated at 65% RH for *ca.* 10 minutes (**Rehydrate Short**) and 40 hours (**Rehydrate Long**), respectively (see **Section 7.2.2** for full details).

Variable-temperature ^{35}Cl SSNMR spectra of the three prepared samples were acquired in the same way as those of the **As Received** sample shown in **Figure 7.4** (*i.e.*, at -40 °C, 22 °C, and 100 °C before cooling back down to 22 °C and -40 °C). While comparison of these samples using ^{35}Cl NMR spectra acquired at room temperature is possible, the S/N ratios are low in some cases (**Figure F9**), which makes the analysis

challenging. However, as previously shown for the **As Received** sample (**Figure 7.4**), a considerable increase in S/N can be obtained by decreasing the temperature. While temperature changes can induce polymorphic phase transitions in some APIs, none is observed for GNE-A when it is cooled to $-40\text{ }^{\circ}\text{C}$, as verified by PXRD (**Figure F10**).

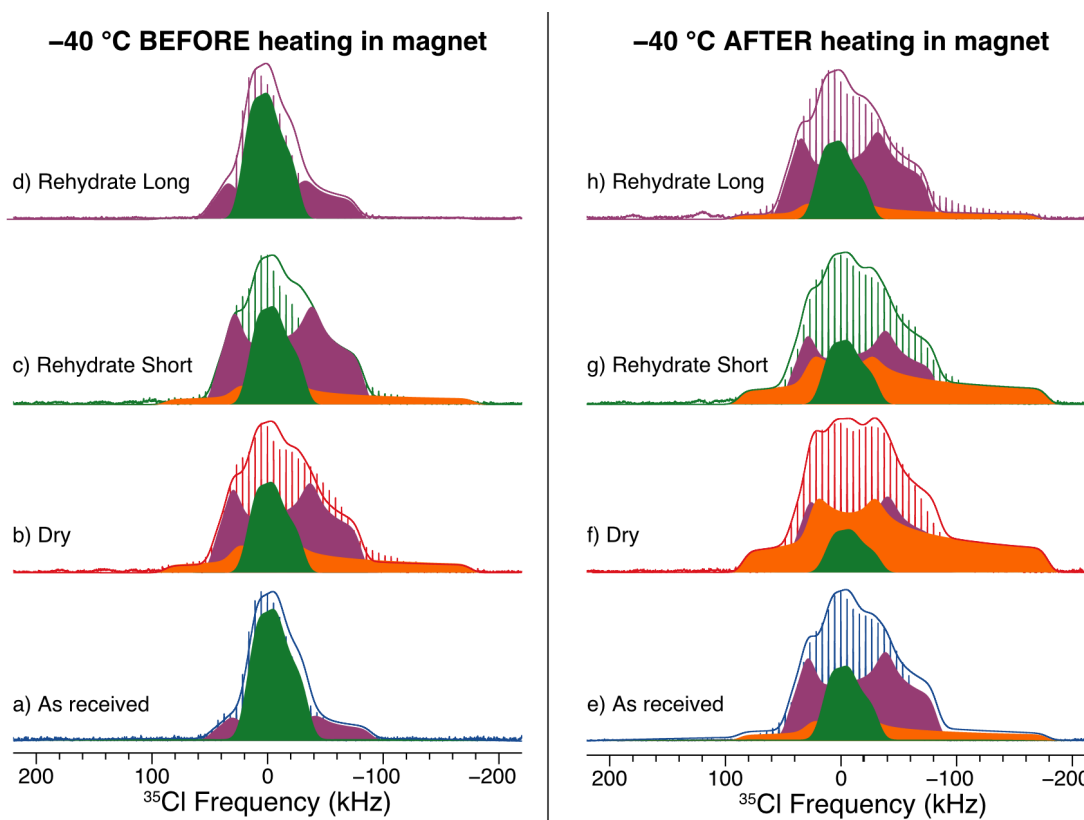


Figure 7.5. $^{35}\text{Cl}\{^1\text{H}\}$ WURST-CPMG NMR spectra of the GNE-A samples prepared with different hydration levels acquired at $-40\text{ }^{\circ}\text{C}$ (see text for details of the sample preparations). The left and right columns show spectra acquired before and after heating in the magnet, respectively. Overlaid on top of the experimental spectra are simulated spectra generated with three distinct ^{35}Cl NMR tensor parameters. The subspectra are shown as solid shapes (**Site I** = purple, **Site II** = green, **Site III** = orange).

The ^{35}Cl NMR spectra of the samples acquired at $-40\text{ }^{\circ}\text{C}$ *before* and *after* heating to $100\text{ }^{\circ}\text{C}$ in the magnet are shown in **Figure 7.5** with an overlay of their simulated deconvolutions (*vide infra*) and in **Figure F11** without the overlay. The spectra in the left column of **Figure 7.5** represent the changes that occur when the **As Received** sample is

heated in the oven and then rehydrated. Comparison of the spectra of the **As Received** and **Dry** samples (**Figure 7.5a and b**, respectively) reveal that the signal from **Site II** decreases relative to that of **Site I** when the sample is dried. Removal of water from the hydrated site should increase its $T_2^{\text{eff}}(^{35}\text{Cl})$, but it also substantially changes the local environment of the Cl, producing a distinct dehydrated ^{35}Cl environment (hereafter referred to as **Site III**) with $C_Q = 6.9(2)$ MHz and $\eta_Q = 0.72(10)$ (see **Figure F12** and *vide infra*). CASTEP calculations on model dehydrated GNE-A structures to support this assignment have proven difficult, but are currently in progress. The spectrum of **Rehydrate Short** is largely the same as that of **Dry** (**Figure 7.5c and b**, respectively), indicating that rehydration for a brief period of time (10 minutes or less) is insufficient to fully hydrate the material (as verified by the TGA results, **Figure F3**). When the material is rehydrated for a longer time, as represented by **Rehydrate Long**, the resulting ^{35}Cl spectrum is very similar to that of the **As Received** sample (*i.e.*, only two patterns corresponding to **Site I** and **Site II** are observed). As such, rehydrating the material produces the same Cl environments that are present before drying the sample (rather than generating a new polymorph or solvatomorph) and the removal of water is reversible.

Heating the samples in the magnet also produces changes in the spectra. The spectra of the **As Received** and **Rehydrate Long** materials acquired after heating in the magnet (**Figure 7.5e and h**, respectively) are similar to that of the **Dry** sample acquired before heating in the magnet (**Figure 7.5b**) (*i.e.*, all three spectra have decreased signal intensity from **Site II** relative to **Site I**, and some signal from **Site III** is observed). This result indicates that heating these samples in the magnet has a similar drying effect to heating in the oven. The spectra of all of the other samples in the right column of **Figure**

7.5 (f-h) represent the results of a second sample heating cycle. This second cycle appears to drive off even more water, as observed in the spectra of **Dry** and **Rehydrate Short**, which were acquired after heating in the magnet (**Figure 7.5f** and **Figure 7.5g**, respectively). In both cases, the intensity of the pattern corresponding to **Site II** decreases, while that of **Site III** increases).

Since each distinct Cl environment can have different nuclear relaxation properties (most importantly different effective transverse relaxation constants, $T_2^{\text{eff}}(^{35}\text{Cl})$), the relative intensities of patterns corresponding to distinct Cl^- sites are not necessarily quantitative. However, the relaxation of a given site should be the same in all of the samples, and thus, the relative intensities of each pattern can be compared.

7.3.7 ^{35}Cl SSNMR of a Partially Deuterated sample

An additional sample of GNE-A was prepared using the same drying and rehydration procedure used to make the **Rehydrate Long** sample, but using a rehydration chamber saturated with D_2O (this sample is referred to as **Rehydrate- D_2O**). As shown in **Figure F13**, the addition of D_2O produces a large increase in the ^{35}Cl NMR signal intensity from the hydrated **Site II** with respect to that of the analogous non-deuterated sample. This change occurs because replacing the ^1H nuclei in the water molecules with ^2H decreases the degree of ^1H - ^{35}Cl dipolar coupling, which in turn increases the $T_2^{\text{eff}}(^{35}\text{Cl})$ and the associated ^{35}Cl NMR signal. The signal from **Site I**, however, does not change noticeably between the two samples. Such a substantial change in the ^{35}Cl NMR spectrum with deuteration is consistent with the D_2O incorporating into the structure. Finally, the fact that a pattern consistent with **Site III** is not observed in the ^{35}Cl NMR

spectrum of **Rehydrate-D₂O**, supports its assignment to a dehydrated Cl⁻ site (*i.e.*, not a site that is present in the As Received material but has an extremely short $T_2^{\text{eff}}(^{35}\text{Cl})$).

7.3.8 Multinuclear NMR

Multinuclear SSNMR spectra can provide distinct and complementary information on the structure of GNE-A; for this work, ¹³C, ¹H, and ²H SSNMR experiments were conducted to support the data from our ³⁵Cl SSNMR experiments. For example, ¹³C NMR results can reveal structural changes in the organic API molecules that occur with the dehydration of the material, and both ¹H and ²H NMR spectra are sensitive to the local structures of the water molecules themselves. In this section, experiments and spectra for each of these nuclides are discussed separately.

7.3.9 ¹³C SSNMR

¹³C SSNMR is a common method for studying organic APIs; however, since the water molecules in hydrates like GNE-A do not directly interact with carbon atoms (*i.e.*, the carbon atoms do not participate in the hydrogen bonding), ¹³C NMR is not a direct probe of structural interactions with water. Nonetheless, ¹³C NMR spectra can provide information on the structural changes to the API molecules that occur as the result of water removal.^{12,46-48}

The ¹H-¹³C CP/MAS ($\nu_{\text{rot}} = 12$ kHz) spectra of the GNE-A samples are shown in **Figure 7.6**, and peak assignments based on solution NMR data are shown in **Figure F14**. Close examination of this spectrum reveals that some of the sites in the molecular structure produce two or more resonances in the SSNMR spectrum (*e.g.*, the peaks at *ca.* 12-15 ppm, and *ca.* 160 ppm). These additional resonances arise from

magnetically-distinct sites associated with the 2 crystallographically-distinct API molecules in the unit cell and/or from the presence of the two conformers.

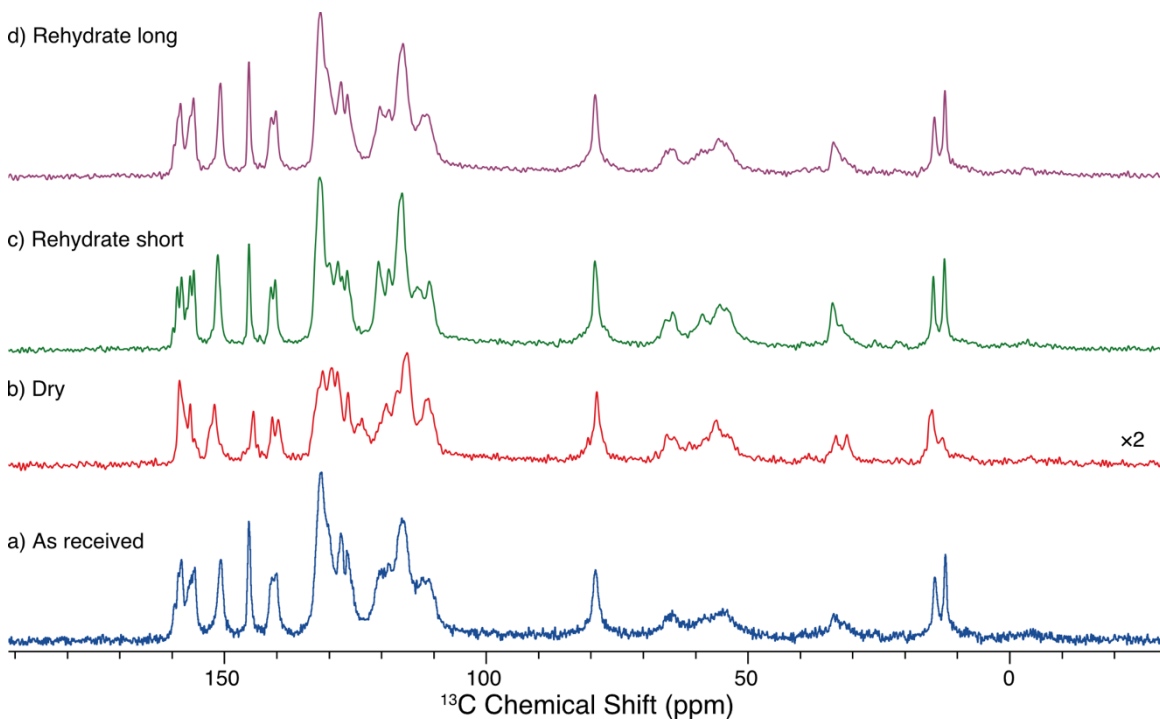


Figure 7.6. ^1H - ^{13}C CP/MAS ($\nu_{\text{rot}} = 12$ kHz) NMR spectra of the GNE-A samples prepared with different levels of hydration. See text for details of the sample preparations.

Consistent with the ^{35}Cl NMR results, the largest differences in the ^{13}C NMR spectra of the four GNE-A samples are observed in those of the **As Received** and **Dry** samples (**Figure 7.6a** and **Figure 7.6b**, respectively). There are subtle differences in the shifts, especially in the region corresponding to carbons in the phenyl ring closest to the four-membered azetidinium ring (*ca.* 125-135 ppm). These changes may indicate a slight change in the orientations of the ring to fill the void space produced by water removal. The shift of the ^{13}C site that is closest to the water molecules (at 150.7(2) ppm in **Figure 7.6a**), which might be expected to be most affected by the removal of water, does not change significantly with heating. In fact, all of the chemical shifts from the hydrated and

dehydrated materials are quite similar to each other, and as such, it would be difficult to discriminate them in a ^{13}C SSNMR spectrum of a physical mixture of the hydrated and dehydrated materials. Furthermore, ^{13}C NMR spectra would likely not be useful for probing the structure in dosage forms containing GNE-A, because the subtle chemical shift differences would likely be obscured by signals from excipient molecules.²² Nonetheless, ^{13}C SSNMR experiments are very useful for characterizing the bulk materials here, and are consistent with the results obtained from other nuclei and characterization methods.

The spectra of rehydrated samples (**Figure 7.6c** and **Figure 7.6d**) are nearly identical to the **As Received** sample, indicating that with rehydration, the ^{13}C environments from the **As Received** sample are restored. This observation is also consistent with the ^{35}Cl NMR and PXRD results (**Figure F15**).

7.3.10 ^1H SSNMR

Given the importance of water in the structure of GNE-A, studying the water molecules directly is desirable. Without expensive ^{17}O isotopic labeling (natural abundance = 0.0373%), the only options for probing the water molecules with NMR involve the hydrogens (*i.e.*, ^1H or ^2H SSNMR, *vide infra*). *N.B.* We note that the future application of DNP-enhanced ^{17}O NMR may allow the study of the water molecules at natural abundance in materials such as this (*i.e.*, where it is not feasible to use ^{17}O -labeled H_2O due to the large amount necessary to rehydrate the samples).

^1H NMR spectra obtained at a moderate MAS rate ($v_{\text{rot}} = 12$ kHz) are shown in **Figure 6.1**. In each case, the spectra feature broad peaks due to strong ^1H - ^1H homonuclear dipolar coupling, and the high number of crystallographically-distinct ^1H

environments in the sample (*i.e.*, > 30 sites). While the resolution can be improved slightly with faster spinning speeds (**Figure F16**), these experiments also produce frictional heating that can cause the dehydration of the sample. Due to hardware constraints, sample cooling during the UFMAS experiments was not possible. It is likely that homonuclear decoupling or 2D-correlation experiments could also improve the resolution, but these techniques may not be useful for looking at dosage formulations, where the number of ^1H environments would be even higher due to the presence of the excipients.

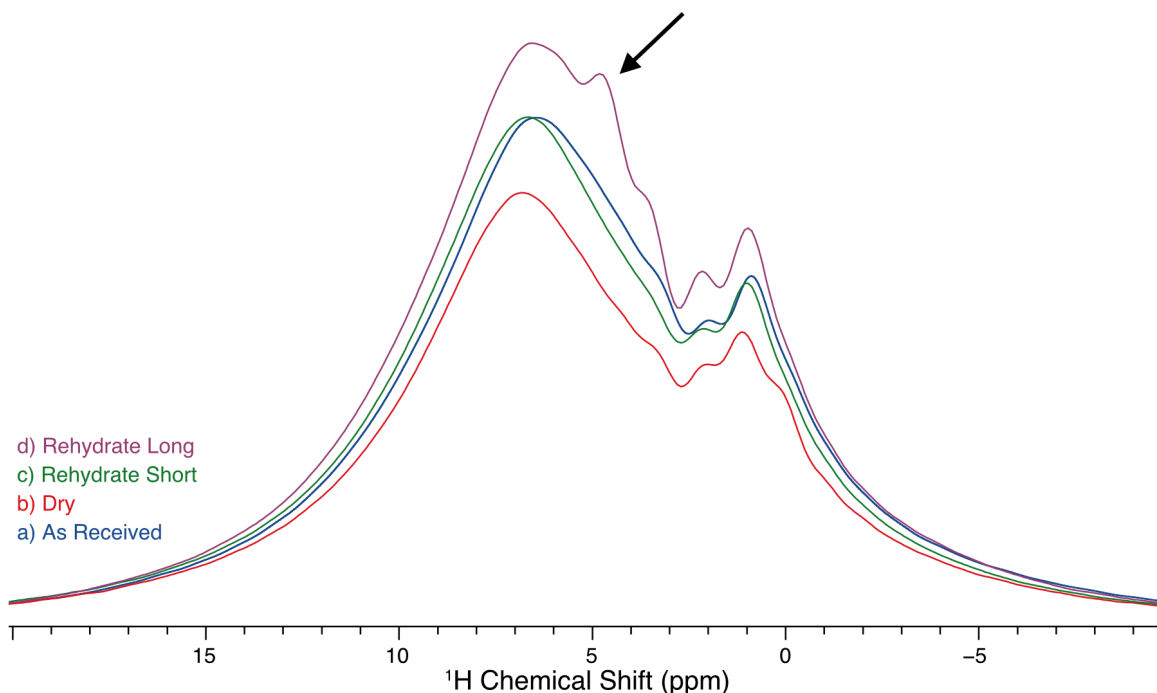


Figure 7.7. ^1H MAS ($\nu_{\text{rot}} = 12$ kHz) NMR spectra of the GNE-A samples prepared with different levels of hydration. See text for details of the sample preparations. The arrow indicates the position of a distinct feature in the spectrum of **Rehydrate Long** that is discussed in the text.

Despite the low resolution, some distinct features can be resolved in the spectra, and are consistent between the samples. One exception is a distinct peak at *ca.* 4.8(2) ppm that occurs in the spectrum of **Rehydrate Long**. This feature likely results from

additional water in the sample, perhaps located at the surfaces of the API particles (as may also be the case for the **Rehydrate-D₂O** sample which was prepared in a similar manner, *vide infra*). In general, the primary difference between all of the spectra is in their overall integrated signal intensities. The lowest intensity is observed in the spectrum of the **Dry** sample, and the highest in that of the **Rehydrate Long** sample. The spectra of the **As Received** and **Rehydrate Short** samples are similar. We attribute these differences primarily to variation in the amount of water present in the samples. This interpretation suggests that the **As Received** and **Rehydrate Short** samples have roughly the same water content, in contrast to the ³⁵Cl NMR results (which indicate the **Rehydrate Long** sample is most similar to **As Received**). *N.B.* these samples were prepared with the same amount of sample (± 5 mg) and so the corresponding spectra should be quantitative.

7.3.11 ²H SSNMR

Given the broadening observed in the ¹H SSNMR spectra, ²H SSNMR is an attractive complementary method for probing the water molecules. ²H, like ¹⁷O, has low natural abundance (0.0115%); however, it is relatively inexpensive and facile to introduce into GNE-A by rehydrating the sample with D₂O vapor (see **Section 7.2.2**). ²H is a spin-1 quadrupolar nucleus, which produces moderately broad NMR powder patterns on the order of tens to hundreds of kHz in breadth (so-called "wideline" patterns). ²H SSNMR spectra are particularly useful for the study of hydrates, as their lineshapes are sensitive to the dynamics of the water molecules in the solid state. The ²H EFG tensor in an D₂O molecule has high axial symmetry ($\eta_Q \approx 0$) and its largest component, V_{33} , is collinear with the O-D bond. Reorientation of this bond produces distinct lineshapes that

can be simulated to obtain the rate and type of motion water molecules.^{49–51} Prior work with crystalline and polycrystalline ice has shown that in the solid state, water flips 180° about its C_{2v} axis at a rate that varies with the temperature of the sample.^{52–54} Such motion has also been observed in the ^2H SSNMR spectra of many organic and inorganic hydrates.^{55–58}

^2H SSNMR spectra of **Rehydrate-D₂O** were acquired at several temperatures to examine changes in the motion of the water molecules (**Figure 7.8**). The S/N of these spectra is fairly low, primarily due to the low level of water in the sample (the D₂O accounts for a maximum of 3.5 wt-%, assuming 100% D₂O incorporation). The signal is particularly low for the spectra acquired at 40 °C and 100 °C, because they were acquired for shorter time periods (15 minutes vs. more than 1 hour for the other spectra) to ensure that signal from mobile water species could be obtained before they were removed from the sample (the TGA data, **Figure F3**, indicate that the sample loses water when heated to *ca.* 50 °C).

Table 7.4. Experimental ^2H EFG tensor parameters from the spectrum of **Rehydrate-D₂O** acquired at –125 °C.^{a,b}

	Site DI	Site DII	Site DIII
C_Q (MHz)	230(10)	200(10)	155(10)
η_Q	0.10(5)	0.10(5)	0.10(5)

^aThe experimental uncertainty in the last digit(s) for each value is indicated in parentheses. ^bSee **Table 7.2** for definitions of the EFG tensor parameters.

The spectrum acquired at –125 °C (**Figure C1**) can be simulated using three sites (denoted **Sites DI**, **DII**, and **DIII**, respectively), all with high axial symmetry (η_Q values ≈ 0.1); the corresponding ^2H EFG tensor parameters are listed in **Table 7.4**. **Site DIII** has parameters that are consistent with those previously-reported for ice.^{52–54} Ice may exist in

this sample at the surfaces of the API particles or in between them. The presence of ice is also supported by observations made during the preparation of this sample (see **Figure F19**). The other two powder patterns have distinct quadrupolar parameters from D₂O, and thus result from two distinct ²H environments in the GNE-A material.

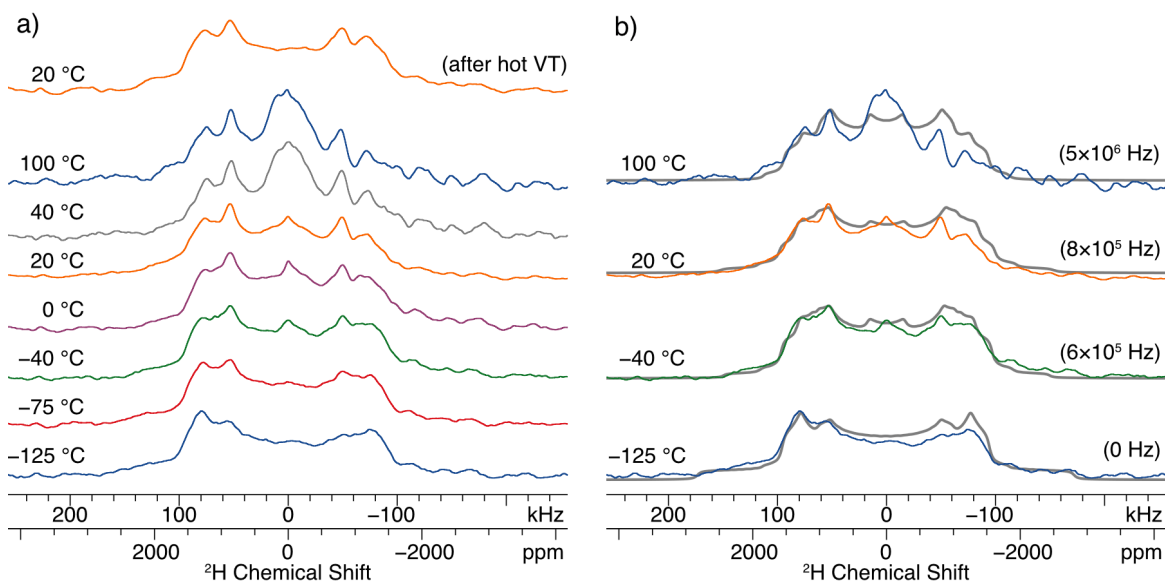


Figure 7.8. ²H quadrupolar-echo spectra of the **Rehydrate-D₂O** sample acquired under static sample conditions at various temperatures. In a) experimental spectra acquired at different temperatures, as indicated. In b) four of the same experimental spectra overlaid with simulated spectra generated using a three-site simulation with dynamical motion. The rates of motion of **Site DI** are listed in parentheses (see text for details). Previously-published⁵⁴ rates of motion for ice were used to simulate **Site DIII**.

At -125 °C, the motion of the deuterons is slow enough that it does not affect the appearance of the spectra (*i.e.*, the molecules are in the slow-motion limit). However, the appearances of the spectra change as the sample is heated (**Figure 7.8**). The most noticeable change is the increase of the signal intensity in the center of the patterns, especially in the spectra acquired at 40 °C and 100 °C. This change is accompanied by a slight shift in the most intense discontinuities of **Site DI** (called the “horns” of the pattern) towards the center and a disappearance of the outer-most discontinuities (called

the "feet" of the pattern). These changes can be attributed to an increase in the rate of motion of the D₂O molecules in the samples as the temperature is increased. While the simulation of these patterns is complicated by low S/N and the presence of multiple sites (with potentially different rates of motion), the simulations (**Figure 7.8b**) indicate that the D₂O molecules flip about their C₂ axis at a rate on the order of MHz.

In contrast to the other sites, the discontinuities associated with **Site DII** do not shift when the sample temperature is changed. This result indicates that this pattern is produced by a ²H environment that either does not move at a rate that can be detected with these experiments (between *ca.* 10³ and 10⁷ Hz), or whose motions do not affect the orientation of V₃₃. More likely, this pattern may result from deuterium exchange of the protonated-amine site in GNE-A (**Figure 7.1**). Deuteration of this site is likely given its relatively high acidity (pK_a ~7.75); in addition, the ²H EFG tensor parameters, which are consistent with previous reports for analogous R₃N-D⁺ environments.⁵⁹

Finally, there is a sharp signal at the center of the patterns that is consistent with highly mobile water molecules (*e.g.*, molecules moving through the channels, or perhaps at the surface). This signal is more intense in the spectra acquired above 0 °C, where there is also a contribution from liquid water, but even in these spectra it has low integrated intensity relative to the broad patterns.

²H NMR can also be used to monitor the dehydration of the material. To that end, spectra were acquired in 15 minute increments at 40 °C and 100 °C (**Figure F20**). As shown, the signal from the highly mobile species decreases after heating the sample, and is completely gone after 15 minutes of heating in the magnet. After the sample was heated, an additional spectrum of the sample was acquired at 22 °C (*i.e.*, the top spectrum

in **Figure 7.8**). Though this spectrum does not contain signal from the highly mobile D₂O species, there are still signals from **Site DI** and **Site DII**. Consistent with the ³⁵Cl NMR spectra, this result suggests tightly-bound D₂O molecules are still present in the materials even after they are heated.

7.4 Conclusions

In this chapter, we have demonstrated that multinuclear (³⁵Cl, ¹³C, ¹H, ²H, ¹⁹F) SSNMR is a valuable method for characterizing the hydration of channel hydrates, with a particular focus on the utility of ³⁵Cl SSNMR. Consistent with the proposed crystal structure, these spectra reveal three distinct Cl environments in GNE-A, two of which are present in the **As Received** sample, and a third that is generated by the dehydration process. Plane-wave DFT calculations using CASTEP aid in the assignment of the observed powder patterns to Cl environments in the structure. The ³⁵Cl NMR spectra of four GNE-A samples (with different hydration levels), obtained before and after heating in the magnet, reveal valuable information about the dehydration and rehydration of the material. First, dehydrating the sample is surprisingly challenging: dehydration does not go to completion even when the sample is heated repeatedly, or for long periods of time (*e.g.*, >18 hours). This result may explain why the TGA data detect less than one equivalent of water, since not all of the water is removed during the TGA experiment. Second, fully rehydrating the material requires more than 10 minutes to complete under ambient humidity. However, when the sample is exposed to humidity for a longer period (*e.g.*, 40 hours) water reincorporates into the channels, occupying the same binding sites as in the **As Received** material; our ³⁵Cl SSNMR spectra confirm that the local Cl⁻ environments in a fully rehydrated sample (*i.e.*, **Rehydrate Long**) are indistinguishable

from those of the **As Received** material. In contrast to more conventional techniques (*e.g.*, TGA) that only probe the *total* water content in the sample, ^{35}Cl SSNMR is well-equipped to determine the *in situ* hydration state of nuclei within the material, and verify the reincorporation of water into the structure.

NMR studies of other nuclides provide complementary information to what has been obtained with ^{35}Cl SSNMR. ^1H and ^2H NMR spectra provide a means to directly study the water molecules in these materials, with the latter providing additional information on the dynamics of the water molecules in the channels. ^{13}C and ^{19}F SSNMR spectra also provide information on these materials. While these additional nuclides are not directly sensitive to the locations of the water molecules (*i.e.*, unlike Cl, they are not involved in hydrogen bonding with the water), they support the proposed crystal structure, as well as the ability for the material to reversibly dehydrate and rehydrate.

The methods used in this work can easily be adapted to the study of dosage formulations containing GNE-A, with the ^{35}Cl SSNMR experiments being particularly well-suited to such samples (due to the lack of interfering signals from excipients, and the direct connection between the appearance of the ^{35}Cl NMR spectra and the hydration of the Cl sites). Due to the lower Cl wt-% of dosage forms, it is possible that such experiments might require signal enhancement methods, like DNP (as discussed in Chapter 5). More broadly speaking, such methods should be applicable to a wide range of API salt hydrates, including stoichiometric hydrates and non-stoichiometric hydrates whose structures change with dehydration. The latter class should be interesting to study with ^{35}Cl NMR, as the spectra should reveal changes in the local Cl^- environments

associated with the removal of water, and potentially reveal new hydrated phases not detected by other techniques.

7.5 References

- (1) Brittain, H. G.; Morris, K. R.; Boerrigter, S. X. M. In *Polymorphism in Pharmaceutical Solids*; Brittain, H. G., Ed.; 2009; pp 233–281.
- (2) Byrn, S. R.; Zografu, G.; Chen, X. S. In *Solid State Properties of Pharmaceutical Materials*; John Wiley & Sons, Inc.: Hoboken, 2017; pp 38–47.
- (3) Khankari, R. K.; Grant, D. J. W. *Thermochim. Acta* **1995**, *248*, 61–79.
- (4) Griesser, U. J. In *Polymorphism*; Wiley-VCH Verlag GmbH & Co. KGaA: Weinheim, FRG, 2006; pp 211–233.
- (5) Morris, K. R. In *Drugs and the pharmaceutical sciences*; Dekker: New York, NY, 1999; pp 125–181.
- (6) Stahl, H. In *Towards Better Safety of Drugs and Pharmaceutical Products*; Braimar, D., Ed.; Elsevier: New York, NY, 1980; pp 265–280.
- (7) Authelin, J.-R. *Int. J. Pharm.* **2005**, *303*, 37–53.
- (8) Vippagunta, S. R.; Brittain, H. G.; Grant, D. J. W. *Adv. Drug Deliv. Rev.* **2001**, *48*, 3–26.
- (9) Khankari, R. K.; Law, D.; Grant, D. J. W. *Int. J. Pharm.* **1992**, *82*, 117–127.
- (10) Evans, J. S. O.; Radosavljević, I. *Chem. Soc. Rev.* **2004**, *33*, 539.
- (11) Berziņš, A.; Skarbulis, E.; Reķis, T.; Actiņš, A. *Cryst. Growth Des.* **2014**, *14*, 2654–2664.
- (12) Kiang, Y. -H.; Cheung, E.; Stephens, P. W.; Nagapudi, K. *J. Pharm. Sci.* **2014**, *103*, 2809–2818.
- (13) Braun, D. E.; Gelbrich, T.; Kahlenberg, V.; Griesser, U. J. *Mol. Pharm.* **2014**, *11*, 3145–3163.
- (14) Vogt, F. G.; Dell’Orco, P. C.; Diederich, A. M.; Su, Q.; Wood, J. L.; Zuber, G. E.; Katrincic, L. M.; Mueller, R. L.; Busby, D. J.; DeBrosse, C. W. *J. Pharm. Biomed. Anal.* **2006**, *40*, 1080–1088.
- (15) Mafra, L.; Santos, S. M.; Siegel, R.; Alves, I.; Almeida Paz, F. A.; Dudenko, D.; Spiess, H. W. *J. Am. Chem. Soc.* **2012**, *134*, 71–74.
- (16) Vogt, F. G.; Copley, R. C. B.; Mueller, R. L.; Spoons, G. P.; Cacchio, T. N.; Carlton, R. A.; Katrincic, L. M.; Kennady, J. M.; Parsons, S.; Chetina, O. V. *Cryst. Growth Des.* **2010**, *10*, 2713–2733.
- (17) Stephenson, G. A.; Groleau, E. G.; Kleemann, R. L.; Xu, W.; Rigsbee, D. R. *J. Pharm. Sci.* **1998**, *87*, 536–542.
- (18) Te, R. L.; Griesser, U. J.; Morris, K. R.; Byrn, S. R.; Stowell, J. G. *Cryst. Growth Des.* **2003**, *3*, 997–1004.
- (19) Harris, R. K. *J. Pharm. Pharmacol.* **2007**, *59*, 225–239.
- (20) Hamaed, H.; Pawlowski, J. M.; Cooper, B. F. T.; Fu, R.; Eichhorn, S. H.; Schurko, R. W. *J. Am. Chem. Soc.* **2008**, *130*, 11056–11065.
- (21) Hildebrand, M.; Hamaed, H.; Namespetra, A. M.; Donohue, J. M.; Fu, R.; Hung, I.; Gan, Z.; Schurko, R. W. *CrystEngComm* **2014**, *16*, 7334.
- (22) Namespetra, A. M.; Hirsh, D. A.; Hildebrand, M. P.; Sandre, A. R.; Hamaed, H.; Rawson, J. M.; Schurko, R. W. *CrystEngComm* **2016**, *18*, 6213–6232.
- (23) Widdifield, C. M.; Chapman, R. P.; Bryce, D. L. In *Annual Reports on NMR Spectroscopy*; Elsevier Ltd., 2009; Vol. 66, pp 195–326.

- (24) Hirsh, D. A.; Rossini, A. J.; Emsley, L.; Schurko, R. W. *Phys. Chem. Chem. Phys.* **2016**, *18*, 25893–25904.
- (25) Vogt, F. G.; Williams, G. R.; Strohmeier, M.; Johnson, M. N.; Copley, R. C. B. *J. Phys. Chem. B* **2014**, *118*, 10266–10284.
- (26) Stahly, G. P. *Cryst. Growth Des.* **2007**, *7*, 1007–1026.
- (27) Infantes, L.; Chisholm, J.; Motherwell, S. *CrystEngComm* **2003**, *5*, 480.
- (28) Ashbrook, S. E.; Duer, M. J. *Concepts Magn. Reson. Part A* **2006**, *28A*, 183–248.
- (29) Bryce, D. L.; Sward, G. D. *Magn. Reson. Chem.* **2006**, *44*, 409–450.
- (30) O'Dell, L. A.; Schurko, R. W. *Chem. Phys. Lett.* **2008**, *464*, 97–102.
- (31) O'Dell, L. A.; Rossini, A. J.; Schurko, R. W. *Chem. Phys. Lett.* **2009**, *468*, 330–335.
- (32) Peersen, O.; Wu, X.; Smith, S. J. *Magn. Reson.* **1994**, *106*, 127–131.
- (33) Peersen, O. B.; Wu, X. L.; Kustanovich, I.; Smith, S. O. *J. Magn. Reson.* **1993**, *104*, 334–339.
- (34) Metz, G.; Wu, X. L.; Smith, S. O. *J. Magn. Reson.* **1994**, *110*, 219–227.
- (35) Bennett, A. E.; Rienstra, C. M.; Auger, M.; Lakshmi, K. V.; Griffin, R. G. *J. Chem. Phys.* **1995**, *103*, 6951–6958.
- (36) Thakur, R. S.; Kurur, N. D.; Madhu, P. K. *J. Magn. Reson.* **2008**, *193*, 77–88.
- (37) Vold, R. L.; Hoatson, G. L. *J. Magn. Reson.* **2009**, *198*, 57–72.
- (38) Bonhomme, C.; Gervais, C.; Babonneau, F.; Coelho, C.; Pourpoint, F.; Azaïs, T.; Ashbrook, S. E.; Griffin, J. M.; Yates, J. R.; Mauri, F.; Pickard, C. J. *Chem. Rev.* **2012**, *112*, 5733–5779.
- (39) Clark, S. J.; Segall, M. D.; Pickard, C. J.; Hasnip, P. J.; Probert, M. I. J.; Refson, K.; Payne, M. C. *Zeitschrift für Krist. - Cryst. Mater.* **2005**, *220*, 567–570.
- (40) Pickard, C. J.; Mauri, F. *Phys. Rev. B* **2001**, *63*, 245101.
- (41) Hammer, B.; Hansen, L. B.; Nørskov, J. K. *Phys. Rev. B* **1999**, *59*, 7413–7421.
- (42) Yates, J. R.; Pickard, C. J.; Mauri, F. *Phys. Rev. B - Condens. Matter Mater. Phys.* **2007**, *76*, 1–11.
- (43) Pfrommer, B. G.; Côté, M.; Louie, S. G.; Cohen, M. L. *J. Comput. Phys.* **1997**, *131*, 233–240.
- (44) Risthaus, T.; Grimme, S. *J. Chem. Theory Comput.* **2013**, *9*, 1580–1591.
- (45) Holmes, S. T.; Schurko, R. W. **2017**, Submitted.
- (46) Leung, S. S.; Padden, B. E.; Munson, E. J.; Grant, D. J. W. *J. Pharm. Sci.* **1998**, *87*, 508–513.
- (47) Zhu, H.; Halfen, J. A.; Young, V. G.; Padden, B. E.; Munson, E. J.; Menon, V.; Grant, D. J. W. *J. Pharm. Sci.* **1997**, *86*, 1439–1447.
- (48) Harris, R. K. *Analyst* **2006**, *131*, 351.
- (49) O'Dell, L. A.; Ratcliffe, C. I. In *eMagRes*; John Wiley & Sons, Ltd: Chichester, UK, 1996; pp 1–16.
- (50) Batchelder, L. S. *Encycl. Magn. Reson.* **2007**, 1–8.
- (51) Spiess, H. W.; Sillescu, H. *J. Magn. Reson.* **1981**, *42*, 381–389.
- (52) Waldstein, P.; Rabideau, S. W.; Jackson, J. A. *J. Chem. Phys.* **1964**, *41*, 3407–3411.
- (53) Jackson, J. A.; Rabideau, S. W. *J. Chem. Phys.* **1964**, *41*, 4008–4008.
- (54) Wittebort, R. J.; Usha, M. G.; Ruben, D. J.; Wemmer, D. E.; Pines, A. *J. Am. Chem. Soc.* **1988**, *110*, 5668–5671.

- (55) Aliev, A. E.; Harris, K. D. M. In *Structure and Bonding*; 2003; Vol. 108, pp 1–53.
- (56) Larsson, K.; Tegenfeldt, J.; Hermansson, K. *J. Chem. Soc. Faraday Trans.* **1991**, 87, 1193.
- (57) Berglund, B.; Lindgren, J.; Tegenfeldt, J. *J. Mol. Struct.* **1978**, 43, 179–191.
- (58) Berglund, B.; Vaughan, R. W. *J. Chem. Phys.* **1980**, 73, 2037–2043.
- (59) Hunt, M. J.; Mackay, A. L. *J. Magn. Reson.* **1976**, 22, 295–301.

Chapter 8: Conclusions and Future Outlook

8.1 General Overview

Two classes of complex, real-world materials have been studied in this thesis: nanoparticles and active pharmaceutical ingredients (APIs). As demonstrated herein, SSNMR is well-suited to the study both of these disparate categories of materials, a testament to the general utility of SSNMR for solid-state characterization; by extension, it is easy to rationalize the use of similar SSNMR methods for the study of a much broader array of materials. SSNMR can be used in tandem with other more common solid-state characterization techniques (like XRD, TEM, or TGA) to provide complementary structural information and also to probe materials with properties that make them unamenable for study by these other techniques (*e.g.*, amorphous phases). However, in many cases, it has been shown that SSNMR can stand alone, providing a direct fundamental understanding of matter on a molecular level; such information is imperative for the rational design of materials with interesting bulk properties.

All of the studies in this thesis have involved multinuclear NMR experiments. Most materials contain multiple NMR-active nuclei, which can potentially be studied from the perspectives of different elements in the periodic table; this opens up possibilities for directly and indirectly probing these elements in the numerous ways they incorporate into complex materials (*e.g.*, directly probing Cl^- sites with ^{35}Cl SSNMR to study complicated hydrogen bonding networks, observing ^{19}F and ^{89}Y nuclei in order to indirectly obtain information on paramagnetic dopants). In this respect, multinuclear NMR is itself a "tandem" approach to characterizing materials. In some cases, the nuclides of interest can be unreceptive to the NMR experiment; fortunately, there are

usually methods that can surmount such obstacles, including some that are detailed in this work. Given the wealth of information that can be obtained, the experiments and concomitant results are worth the added effort, and the continued development and application of techniques for observation of unreceptive NMR nuclides should continue to be pursued.

8.2 Nanoparticles

The first projects in this thesis (**Chapters 2, 3, and 4**) involve the study of inorganic nanomaterials containing rare-earth (RE) elements, with a focus on the structural effects of using mixtures of RE elements in their synthetic preparations.

The molecular structures of NPs are often not well understood. For example, the crystal structure of β -NaYF₄, one of the most widely used host materials for RE-doping, has been a source of debate for over 50 years. In **Chapter 2**, multinuclear (¹⁹F, ²³Na, and ⁸⁹Y) SSNMR experiments definitively show that the bulk phase of this material crystallizes in a *P*6₃/*m* structure.¹ Similar experiments on NaYF₄/NaLuF₄ core/shell NCs reveal that the NCs have the same β -NaYF₄ and β -NaLuF₄ phases as the bulk compounds. Finally, a series of ¹H-X cross-polarization NMR experiments confirm the presence of oleates on the surfaces of the particles, via their proximity to surface Na⁺ sites.

Lanthanide dopants are the source of the interesting luminescent properties in RE nanomaterials, which are closely tied to the local structures and distributions of the dopant ions. **Chapter 3** details the application of SSNMR to characterize NaYF₄ NCs doped with paramagnetic Er³⁺ and Tm³⁺ ions. Such samples have been problematic to study with SSNMR in the past, due to broad patterns and low S/N ratios caused by the

paramagnetic interaction. However, with the use of UFMAS, we have been able to measure average nuclear-Ln³⁺ distances, determine that the dopants substitute for the Y sites in the core structures, and prove that the dopants are distributed homogeneously throughout the particles. Such determinations are difficult to make using other techniques.

The third and final chapter on nanomaterials is an extension of previous work by our group that uncovered a serendipitous zeolitic yttrium fluoride structure. In **Chapter 4**, we address the effects of replacing some of the Y atoms in the reaction mixture that with other RE ions. When the dopant ions can be probed directly (*e.g.*, Sc³⁺), SSNMR provides direct information on the dopant coordination environments. In cases where the dopants are not amenable to direct study by NMR (*e.g.*, Er³⁺, Eu³⁺), SSNMR can still indirectly provide information on the dopant ions by using spectra of other nuclides in the sample. In this study, subtle shifts in the ¹⁹F and ⁸⁹Y SSNMR spectra demonstrate that Sc³⁺ and Eu³⁺ ions incorporate into the channels of the porous zeolitic structure, rather than substitutionally replacing Y atoms. This demonstrates that the common assumption that RE dopants always incorporate substitutionally may be inaccurate.

8.2.1 Future work - Nanomaterials

Several additional NMR methods may be useful for further study of the nanomaterials in this work, as well as other related compounds and nanomaterials. First, signal enhancement from DNP NMR methods would be invaluable, especially given that DNP can enhance signals from the surfaces of NPs,²⁻⁴ which are not easily detected otherwise (see examples in **Chapters 2, 3, 4**). It is possible that these techniques might lead to the detection of novel surface environments, unique ligand topologies, and defect

sites. The latter are particularly important in the study of luminescent NPs, as they are thought to be a major source of the quenching of fluorescence. Two-dimensional correlation experiments would supplement the one-dimensional experiments described in the current work. Such experiments would almost certainly require the use of DNP NMR methods, as the experimental time required to obtain useful spectra of unreceptive nuclides without it would be prohibitive. Such correlations could provide information on the proximities of dopant ions to particular sites in the host structure, for example.

The studies of doped NPs described herein could be easily extended to include other RE dopants with different ionic radii (which may incorporate differently into the NP structures). SSNMR experiments could also be used to isolate other factors that affect the outcomes of the synthesis (*e.g.*, dopant level, reactant concentrations, reaction times, temperatures, stabilizing surface ligands, and templating agents). Knowledge of these factors should enable the development of improved synthetic procedures with increased yields, higher purities, and most importantly, tunability of the structures and bulk properties of the final products. For porous materials like those described in **Chapter 3**, it might be possible to facilitate the synthesis of a material with one RE ion, followed by an ion exchange process to replace it with another (this might be a much better pathway for the production of NPs with minimal by-products and/or impurities). Finally, core/shell structures containing dopants in either the core, shell, or both, would be another avenue of pursuit; in particular, NPs with a broader range of NMR active nuclides in the shell would be crucial for the study of interfaces between the core and shell, as well as the shell and stabilizing surface ligands.

8.3 Active pharmaceutical ingredients

Chapters 5, 6, and 7 focus on the use of ^{35}Cl SSNMR to structurally characterize API HCl salts, which are the most common solid phase of APIs. While ^{35}Cl SSNMR is ideal for studying most systems in this class of materials, it can be difficult to analyze some samples in a timely fashion due to low S/N (*e.g.*, low wt-% Cl APIs or poor relaxation characteristics). If such methods are to be used in the pharmaceutical industry for purposes of high-throughput screening, quality assurance, quantification of products and by-products, and structural prediction, improving both the unambiguity of spectral analysis and the rapidity of spectral acquisition are of paramount importance.

Chapter 5 addresses some of these concerns via the testing and application of ^1H - ^{35}Cl BRAIN-CP/WURST-CPMG methods under DNP conditions, and the development of a hybrid MAS/static technique known as spinning-on-spinning-off (SOSO).⁵ The combination of these methods provides DNP enhancements of as high as 110, enabling rapid acquisition of ^{35}Cl SSNMR spectra of APIs. This study also demonstrates that these methods can be used with real-world samples like commercial dosage formulations of Benadryl®, Zyrtec®, and isoxsuprine tablets; there are clear implications that these methods can be used to study the many thousands of different commercial forms of APIs that are presently manufactured, as well as new formulations of APIs (*e.g.*, HCl API salts in amorphous solid dispersions).

NMR spectra are inherently quantitative; however, ^{35}Cl UWNMR spectra, have not been used previously for quantification. Such spectra are very useful for the study of dosage formulations, as they are not influenced by interfering signals from the materials in excipients. In **Chapter 6**, it is shown that ^{35}Cl SSNMR can be used to quantify the

amount of an API salt (pioglitazone HCl) in bulk and model dosage formulations with a high degree of accuracy (RMSD > 0.999). This method has been applied to quantify the amount of PiogHCl in problematic dosage formulations with metal stearates (*i.e.*, those that disproportionate when treated at high temperature and relative humidity).

Finally, **Chapter 7** presents a case study of a Genentech development compound, GNE-A, which is a variable-hydrate HCl salt. ^{35}Cl SSNMR spectra of various preparations of this compound indicate that the material is difficult to fully dehydrate; however, when exposed to moisture for a sufficient period of time, water reincorporates into the channels, occupying the same binding sites as in the original material. NMR studies of other nuclei provide additional information on the material, including ^1H and ^2H spectra, which directly probe the water molecules and their dynamical motions in the materials. Such studies of the uptake/loss of water are crucial at every level of pharmaceutical discovery and manufacture, since water can play an enormous role in structural stabilization, and in some cases, can even influence the very chemical nature of the API itself.

8.3.1 Future Work - APIs

The most direct extension of the work on APIs detailed in this thesis is to the study of other solid phases of APIs. One example is *cocrystals*, structures in which the API molecule is coordinated through intermolecular interactions (usually hydrogen bonding) with other molecules in the unit cell (called *coformers*).⁶⁻⁹ In HCl salt cocrystals, Cl is usually directly involved in the intermolecular interactions between the API and coformer. As such, ^{35}Cl SSNMR should act as a highly sensitive probe of any structural changes or differences that may occur when different coformers are used, and

should provide spectral fingerprints that verify the production of pure cocrystals with desired structures and properties. Given the importance of hydrogen bonding in the formation and stability of these systems, they could also be studied from the perspective of the hydrogen bond donor, *e.g.*, using ^{15}N , or ^{17}O . Due to the low natural abundance of both nuclei ($^{15}\text{N} = 0.4\%$, $^{17}\text{O} = 0.0373\%$), DNP enhancement would likely be necessary for such studies.

Another promising class of materials that could be studied with ^{35}Cl SSNMR is amorphous solid dispersions (ASDs). These materials are essentially amorphous glasses formed with a non-crystalline API stabilized in a polymer matrix.¹⁰⁻¹³ Due to the amorphous nature of the drug, SSNMR is likely the only technique that can probe the structures of these materials. Such studies could characterize distributions of the API within the structure, and look for phase separation (*e.g.*, the formation of regions of crystalline products), examine the domain sizes of the API, and probe interactions of the API and surrounding polymer matrix.

In addition to the methods discussed in the current work, there are other NMR techniques that show promise for the study of APIs. For example, the combination of UFMAS experiments with (indirect) ^1H detection of ^{35}Cl nuclei can provide dramatic improvements in sensitivity.¹⁴ Such experiments also provide additional correlation information, since the ^{35}Cl NMR signals can be connected with signals from with proximate heteronuclei. Such information might be particularly useful for the study of hydrogen bonding. Following the success of the ^{13}C - ^{35}Cl HMQC experiment documented in **Chapter 5**, other correlation experiments that were hitherto impractical due to excessive experimental time requirements may now be possible with use of DNP.

A direct follow-up to the work described in **Chapter 6** would be to study the kinetics and mechanisms of disproportionation using ^{35}Cl SSNMR. Disproportionation is likely affected by multiple factors, including particle size, hygroscopicity, and the molecular structures of the API and/or excipients. PiogHCl is an excellent model system for proof-of-concept studies to identify the relative importance of these factors. More broadly, quantification using ^{35}Cl SSNMR shows much promise for the analysis of dosage formulations, especially for purposes of quality assurance and structural prediction (*vide infra*).

The application of NMR crystallography¹⁵⁻¹⁷ to APIs is an exciting possibility for the drug development and manufacturing processes. With crystal structure prediction,^{18,19} powders of API molecules could be screened using NMR data, rather than requiring the sometimes arduous task of growing a single crystal (which may not crystallize in the same solid form as the API in a dosage formulation). Instead, it may soon be possible to take a tablet from the assembly line, acquire a set of multinuclear SSNMR spectra, and obtain full crystal structures of the API *in situ*, within the dosage form. Such methods provide unparalleled detail of the phases present in dosage formulations, including essential information on the stability of the API, as well as assist in the detection of by-products and impurities *in situ*.

8.4 Final Thoughts

In summary, SSNMR is a versatile technique, that is well-suited to the study of many complex real-world materials. The techniques described in the current work should be applicable to many other classes of related materials, including nanomaterials with other host structures and/or dopant ions, as well as other solid forms of HCl salt APIs.

Future developments, especially with the support of DNP, will undoubtedly continue to improve the study of such materials and their bulk properties. It is hoped that this thesis encourages further experimentation with complex systems, which reflect the myriad materials present in our daily lives.

8.5 References

- (1) Hirsh, D. A.; Johnson, N. J. J.; Van Veggel, F. C. J. M.; Schurko, R. W. *Chem. Mater.* **2015**, *27*, 6495–6507.
- (2) Rossini, A. J.; Zagdoun, A.; Lelli, M.; Canivet, J.; Aguado, S.; Ouari, O.; Tordo, P.; Rosay, M.; Maas, W. E.; Copéret, C.; Farrusseng, D.; Emsley, L.; Lesage, A. *Angew. Chemie Int. Ed.* **2012**, *51*, 123–127.
- (3) Protesescu, L.; Rossini, A. J.; Kriegner, D.; Valla, M.; De Kergommeaux, A.; Walter, M.; Kravchyk, K. V.; Nachttegaal, M.; Stangl, J.; Malaman, B.; Reiss, P.; Lesage, A.; Emsley, L.; Copéret, C.; Kovalenko, M. V. *ACS Nano* **2014**, *8*, 2639–2648.
- (4) Johnson, R. L.; Perras, F. A.; Kobayashi, T.; Schwartz, T. J.; Dumesic, J. A.; Shanks, B. H.; Pruski, M. *Chem. Commun.* **2016**, *52*, 1859–1862.
- (5) Hirsh, D. A.; Rossini, A. J.; Emsley, L.; Schurko, R. W. *Phys. Chem. Chem. Phys.* **2016**, *18*, 25893–25904.
- (6) Sun, C. C. *Expert Opin. Drug Deliv.* **2013**, *10*, 201–213.
- (7) Blagden, N.; Coles, S. J.; Berry, D. J. *CrystEngComm* **2014**, *16*, 5753.
- (8) Aakeröy, C. B.; Fasulo, M. E.; Desper, J. *Mol. Pharm.* **2007**, *4*, 317–322.
- (9) Friščič, T.; Jones, W. *Cryst. Growth Des.* **2009**, *9*, 1621–1637.
- (10) Baghel, S.; Cathcart, H.; O'Reilly, N. J. *J. Pharm. Sci.* **2016**.
- (11) Newman, A.; Knipp, G.; Zografí, G. *J. Pharm. Sci.* **2012**, *101*, 1355–1377.
- (12) Langham, Z. A.; Booth, J.; Hughes, L. P.; Reynolds, G. K.; Wren, S. A. C. *J. Pharm. Sci.* **2012**, *101*, 2798–2810.
- (13) Sawant, S.; Singh, M.; Sayyad, A. *J. Pharm. Res.* **2010**, *3*, 2494–2501.
- (14) Venkatesh, A.; Hanrahan, M. P.; Rossini, A. J. *Solid State Nucl. Magn. Reson.* **2017**.
- (15) *NMR Crystallography*, 1st ed.; Harris, R. K., Wasylshen, R. E., Duer, M. J., Eds.; John Wiley & Sons Ltd.: Chichester, UK, 2010.
- (16) Martineau, C.; Senker, J.; Taulelle, F. *Annu. Reports NMR Spectrosc.* **2014**, *82*, 1–57.
- (17) Taulelle, F. In *Encyclopedia of Magnetic Resonance*; John Wiley & Sons, Ltd: Chichester, UK, 2009; pp 1–14.
- (18) Day, G. M. *Crystallogr. Rev.* **2011**, *17*, 3–52.
- (19) Zilka, M.; Dudenko, D. V.; Hughes, C. E.; Williams, P. A.; Sturniolo, S.; Franks, W. T.; Pickard, C. J.; Yates, J. R.; Harris, K. D. M.; Brown, S. P. *Phys. Chem. Chem. Phys.* **2017**, *19*, 25949–25960.

Appendix A: Supporting Tables and Figures for Chapter 2

Table A1. Crystallographic Data for bulk NaYF₄ Structure I (Space Group: $P\bar{6}2m$)^{a,b}

Atom	Site	<i>x</i>	<i>y</i>	<i>z</i>	Frac. Occ.	Coordination
F	3f	0.618	0	0	1	-
F	3g	0.223	0	1/2	1	-
Na	2d	1/3	2/3	1/2	0.75	9
Y	2d	1/3	2/3	1/2	0.25	9
Y	1a	0	0	0	1	9

^aReported by Roy, D. M.; Roy, R. *J. Electrochem. Soc.* **1964**, 111, 421. ^bLattice parameters: *a* = 5.9148 Å, *c* = 3.496 Å.

Table A2. Crystallographic Data for bulk NaYF₄ Structure II (Space Group: $P6_3/m$)^{a,b}

Atom	Site	<i>x</i>	<i>y</i>	<i>z</i>	Frac. Occ.	Coordination
F	6h	0.3905	0.3092	0.25	1	-
Na	2b	0	0	0	0.434	6
Na	2c	1/3	2/3	1/4	0.566	9
Y	2c	1/3	2/3	1/4	0.434	9

^aReported by Sobolev, V. P. P. B. P.; Mineev, D. A. *Dokl. Akad. Nauk.* **1963**, 150, 791. ^bLattice parameters: *a* = 5.97567 Å, *c* = 3.53053 Å.

Table A3. ²³Na{¹⁹F} Hahn Echo MAS (*v*_{rot} = 12 kHz) NMR Experimental Parameters.

Sample	NaYF ₄	NaLuF ₄	27 nm NC	37 nm NC
Number of scans	256	256	256	256
Expt. time (min)	43	43	43	43
Recycle delay (s)	10	10	10	10
²³ Na rf field (kHz)	100	100	100	100
¹⁹ F decoupling rf (kHz)	84.7	84.7	84.7	84.7
²³ Na pulse width [$\pi/2$] (μ s)	1.25	1.25	1.25	1.25
Inter-pulse delay [τ] (us)	83.33	83.33	83.33	83.33
Spectral width (kHz)	200	200	200	200

Table A4. ^{23}Na MQMAS ($\nu_{\text{rot}} = 12$ kHz) NMR Experimental Parameters.

Sample	NaYF ₄	NaLuF ₄	27 nm NC	37 nm NC
Number of scans	96	96	96	96
Number of t_1 increments	256	256	256	256
Expt. time (hrs)	6.8	6.8	6.8	6.8
Recycle delay (s)	1	1	1	1
^{23}Na rf field (kHz)	152	152	152	152
Z-Filter rf (kHz)	26	26	26	26
Excitation pulse width (μs)	3.09	3.09	3.09	3.09
Conversion pulse width (μs)	1.03	1.03	1.03	1.03
Z-filter pulse width (μs)	40	40	40	40
Z-filter delay (μs)	12	12	12	12
Indirect dimension t_1 increment (μs)	11.25	11.25	11.25	11.25
Spectral width direct dimension, t_2 (kHz)	25	25	25	25
Spectral width indirect dimension, t_1 (kHz)	89	89	89	89

Table A5. ^{19}F - ^{89}Y CP Static and MAS ($\nu_{\text{rot}} = 6$ kHz) NMR Experimental Parameters.

Sample		NaYF ₄	27 nm NC	37 nm NC
Static sample	Number of scans	1644	1808	1722
	Experimental time (hrs)	18.3	20	19
MAS $\nu_{\text{rot}} = 6$ kHz	Number of scans	2072	2072	2072
	Experimental time (hrs)	23	23	23
Recycle delay (s)		40	40	40
^{19}F 90° pulse width [$\pi/2$] (μs)		2.9	2.9	2.9
Contact time (ms)		9	9	9
^{19}F rf field during contact pulse (kHz)		27.4	27.4	27.4
^{89}Y rf field during contact pulse (kHz)		21	21	21
^{19}F decoupling field (kHz)		41	41	41
Spectral width (kHz)		20	20	20
Acquisition length (number of points)		512	512	512

Table A6. ^{19}F Hahn Echo MAS ($v_{\text{rot}} = 6$ kHz) NMR Experimental Parameters.

Sample	NaYF ₄	NaLuF ₄	27 nm NC		37 nm NC
Number of scans	1152	1152	1655	1360	1632
Expt. time (min)	12.8	12.8	18.4	15.1	18.2
Recycle delay (s)	40	40	40	40	40
^{19}F rf field (kHz)	130	130	130	154	130
^{19}F pulse width [$\pi/2$] (μs)	1.93	1.93	1.93	1.63	1.93
Inter-pulse delay [τ] (μs)	40	40	40	12.94	40
Spectral width (kHz)	200	200	200	200	200
MAS rate (kHz)	25	25	25	65	25

Table A7. ^1H Bloch Decay MAS ($v_{\text{rot}} = 11$ kHz) NMR Experimental Parameters.

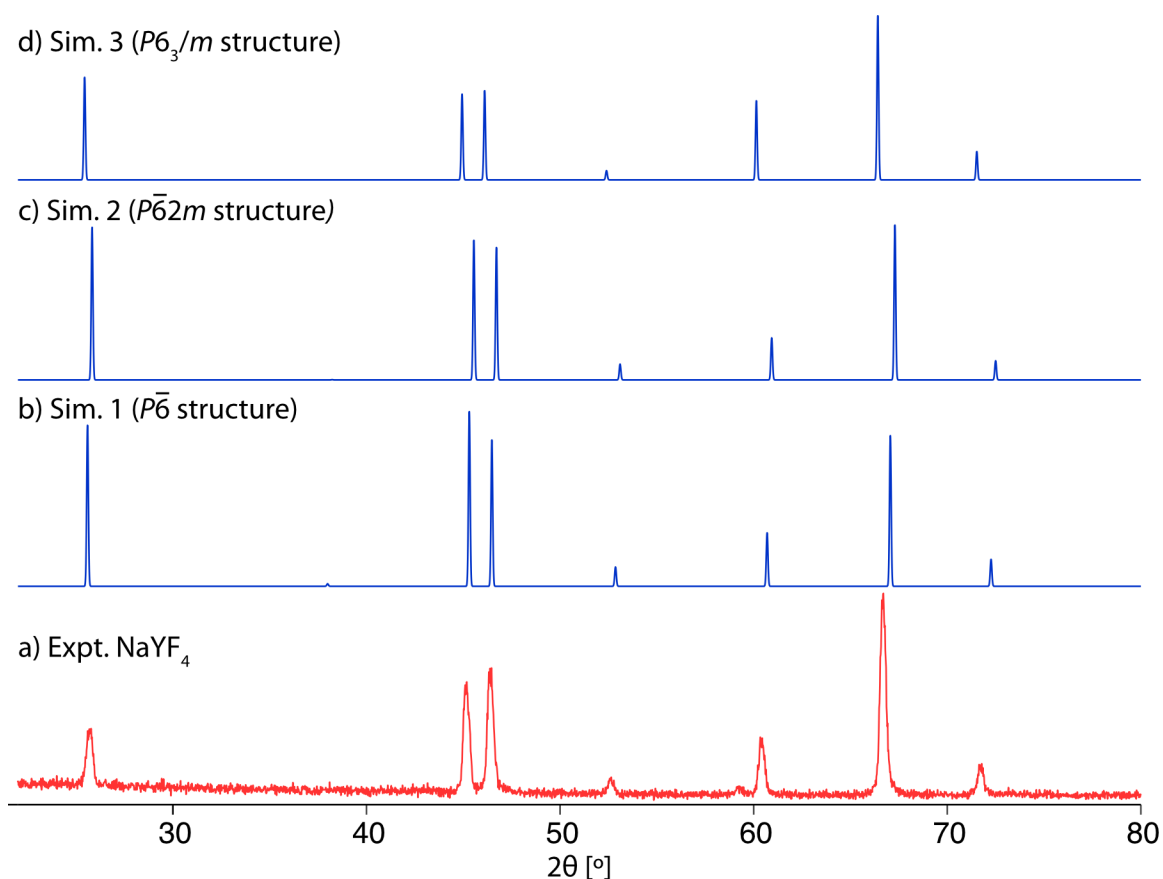
Sample	27 nm NC	37 nm NC
Number of scans	16	16
Expt. time (min)	32	32
Recycle delay (s)	120	120
^1H rf field (kHz)	90.9	90.9
^1H pulse width [$\pi/2$] (μs)	2.75	2.75
Spectral width (kHz)	200	200
Acquisition length (number of points)	5120	5120

Table A8. ^1H - ^{13}C CP/MAS ($v_{\text{rot}} = 12$ kHz) NMR Experimental Parameters.

Sample	27 nm NC	37 nm NC
Number of scans	12600	12600
Experimental time (hrs)	7	7
Recycle delay (s)	2	2
^1H 90° pulse width [$\pi/2$] (μs)	2.95	2.95
Contact time (ms)	3	3
^1H rf field during contact pulse (kHz)	42.5	42.5
^{13}C rf field during contact pulse (kHz)	73.5	73.5
^1H decoupling field (kHz)	34.5	34.5
Spectral width (kHz)	50	50
Acquisition length (number of points)	1024	1024

Table A9. $^1\text{H}/^{19}\text{F}$ - ^{23}Na CP/MAS ($\nu_{\text{rot}} = 6$ kHz) NMR Experimental Parameters.

CP Polarization Source	Low Power CP		High Power CP	
	^1H	^{19}F	^1H	^{19}F
Number of scans	175319	2108	71508	2108
Experimental time (hrs)	48.7	11.7	19.8	11.7
Recycle delay (s)	1	20	1	20
$^1\text{H}/^{19}\text{F}$ 90° pulse width [$\pi/2$] (μs)	2.5	3.18	2.5	3.18
Contact time (ms)	2	0.25	2	0.25
$^1\text{H}/^{19}\text{F}$ rf field during contact pulse (kHz)	27.9	56.8	27.9	56.8
^{23}Na rf field during contact pulse (kHz)	17.9	79.5	17.9	79.5
$^1\text{H}/^{19}\text{F}$ decoupling field (kHz)	78.1	78.1	78.1	78.1
Spectral width (kHz)	200	200	200	200
Acquisition length (number of points)	1024	1024	1024	1024

**Figure A1.** Comparison of a) the experimental PXR pattern of bulk NaYF_4 (red) with simulated patterns (blue) created using the proposed crystal structures with space groups b) $\text{P}\bar{6}$, c) $\text{P}\bar{6}2\text{m}$, and d) $\text{P}6_3/\text{m}$.

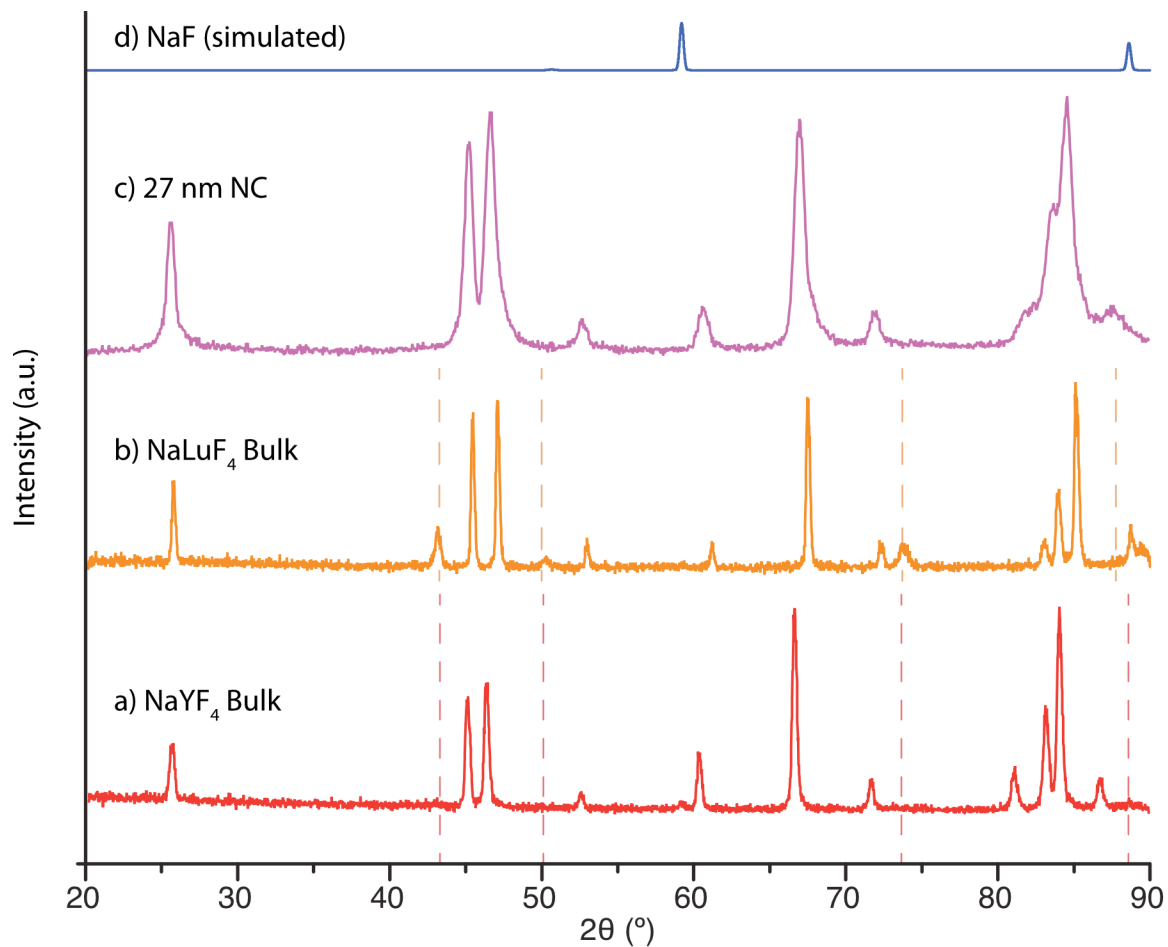


Figure A2. Comparison of experimental PXRD patterns of a) bulk NaYF₄, b) bulk NaLuF₄, and c) the 27 nm NC with d) a simulated diffraction pattern of NaF calculated from the crystal structure by Shirako, Y. *et al.*⁶² The red and orange dashed lines indicate features in the JCPDS reference patterns of cubic phase α -NaYF₄ (JCPDS: 6-0342) and α -NaLuF₄ (JCPDS: 27-0725), respectively.

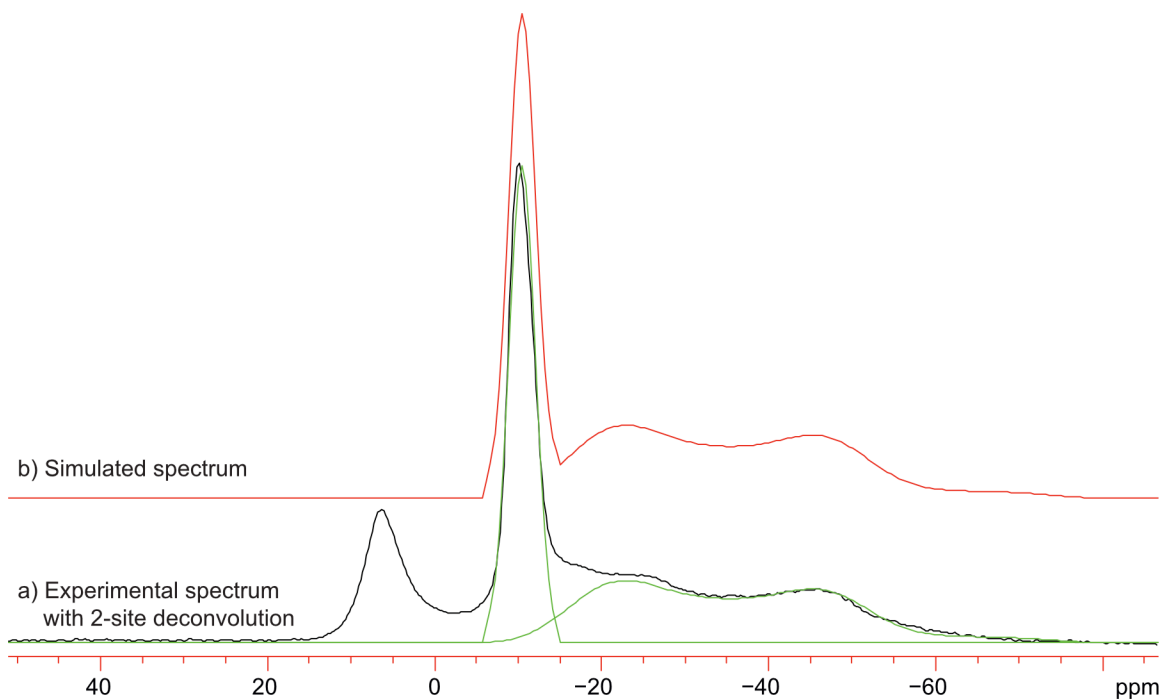


Figure A3. Two-site deconvolution of the $^{23}\text{Na}\{^{19}\text{F}\}$ MAS NMR spectrum of bulk NaYF_4 : a) the experimental spectrum (black) with 2-site deconvolution (green), and b) the simulated spectrum (red).

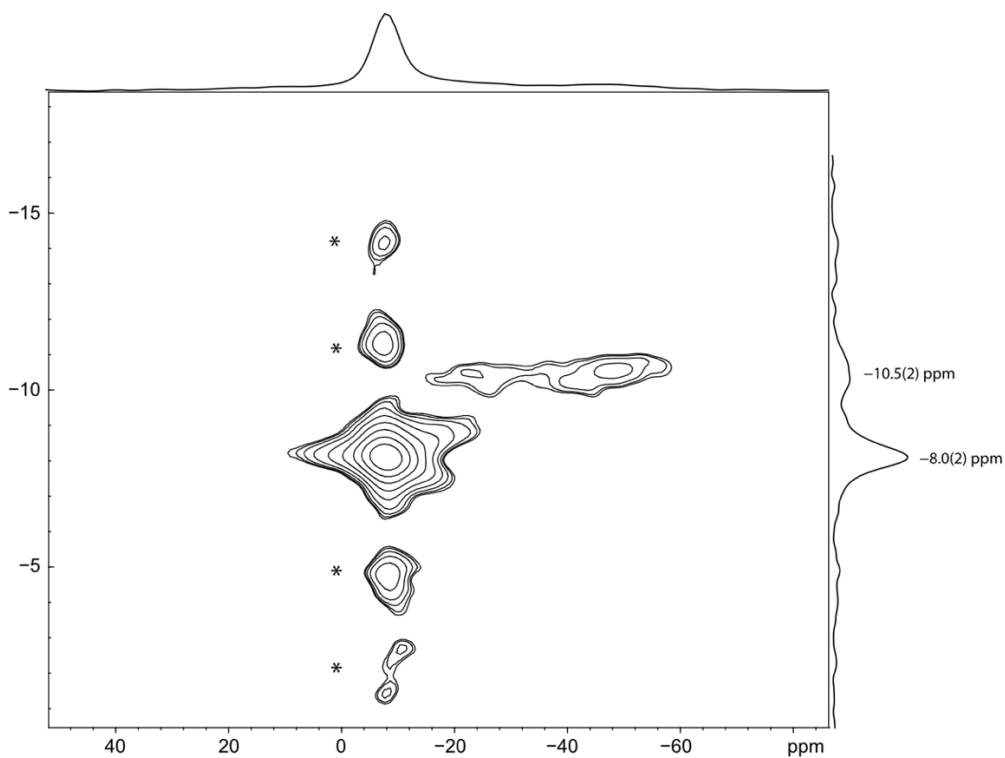


Figure A4. ^{23}Na MQMAS NMR spectrum of bulk NaLuF_4 ($\nu_{\text{rot}} = 12$ kHz). Asterisks denote spinning sidebands.

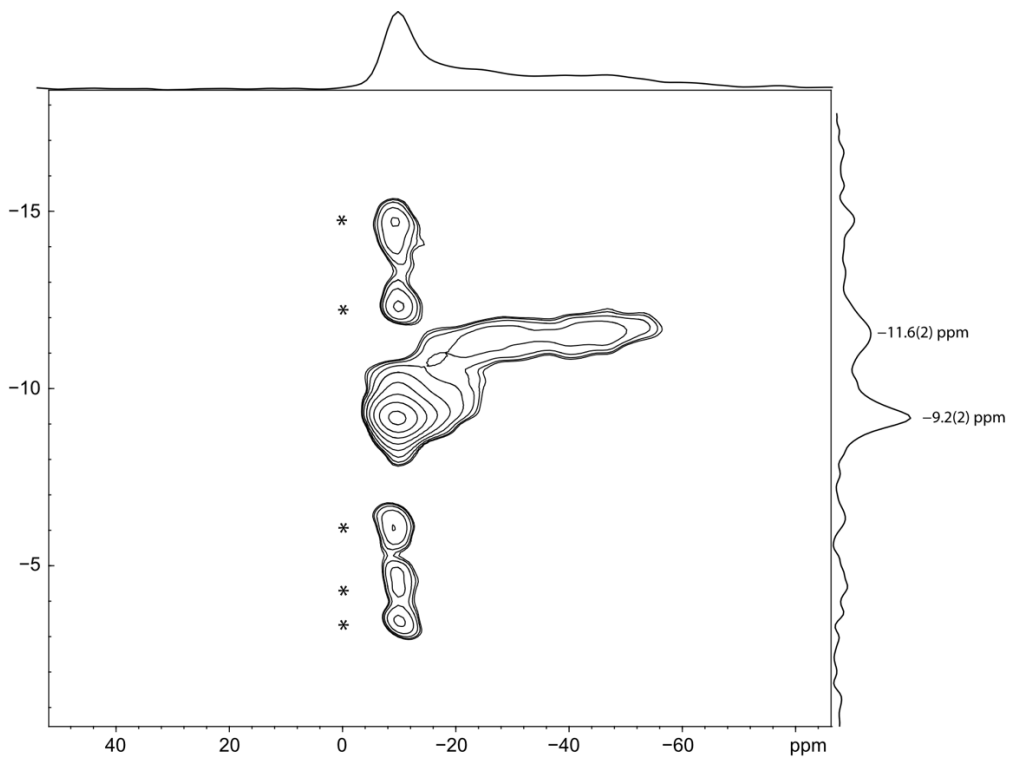


Figure A5. ^{23}Na MQMAS NMR spectrum of the 23 nm NC. Asterisks denote spinning sidebands.

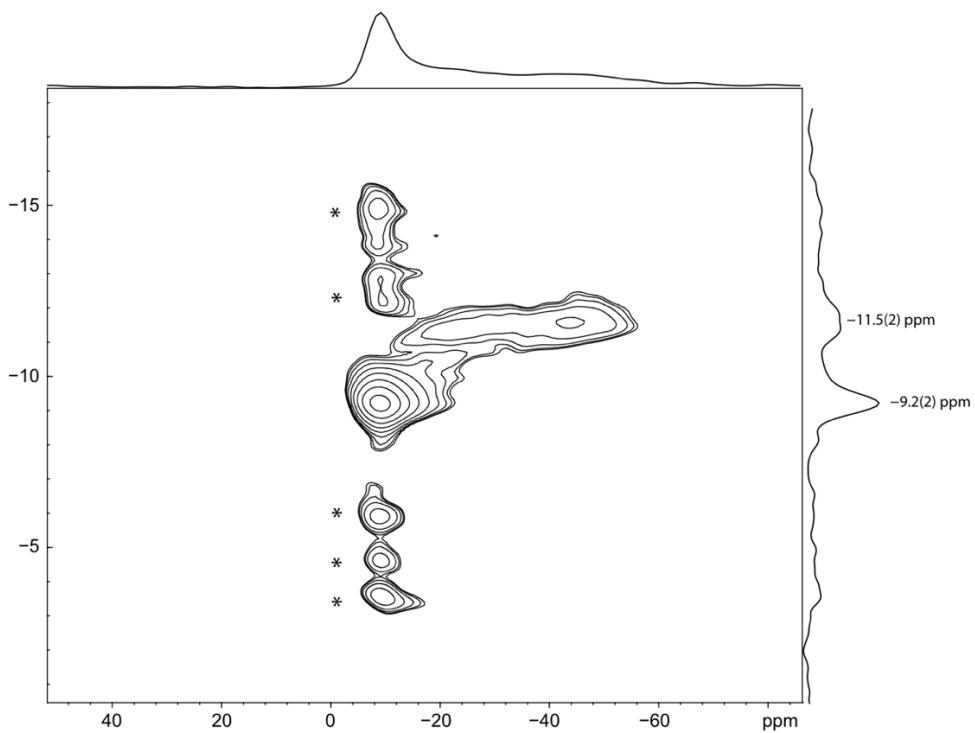


Figure A6. ^{23}Na MQMAS NMR spectrum of the 37 nm NC. Asterisks denote spinning sidebands.

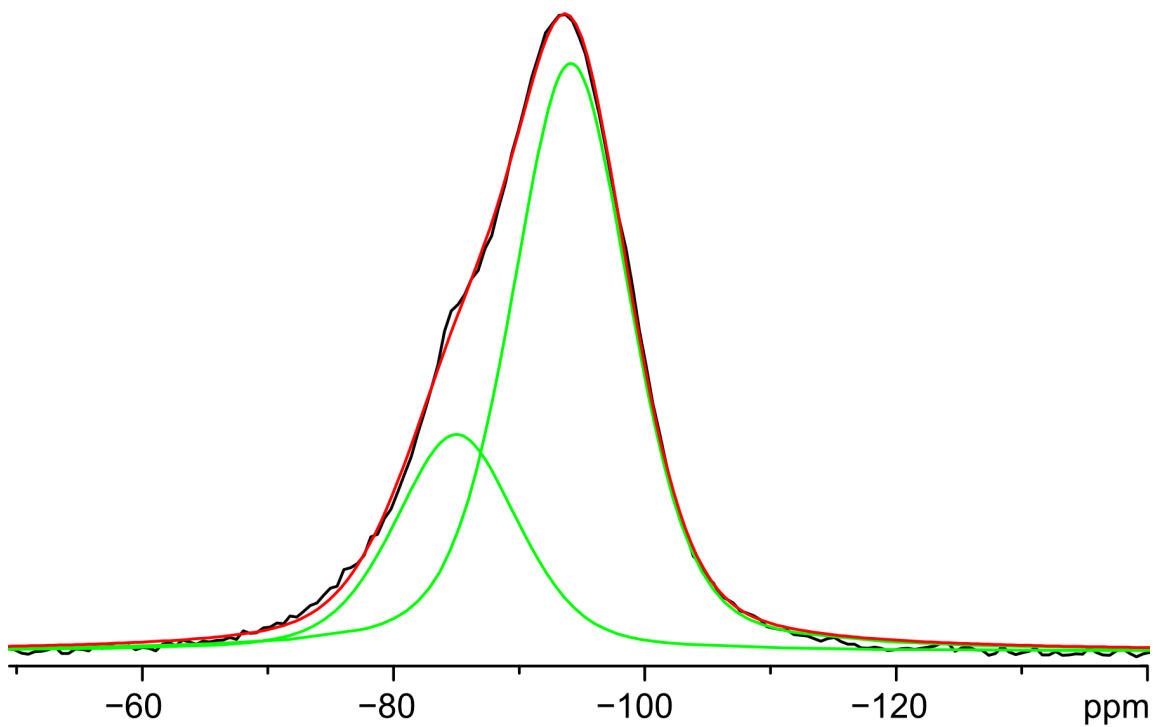


Figure A7. Two-site deconvolution of the ^{19}F MAS NMR spectrum of bulk NaYF_4 . The experimental spectrum is shown in black, the deconvoluted sites are shown in green, and the red trace shows the combined pattern.

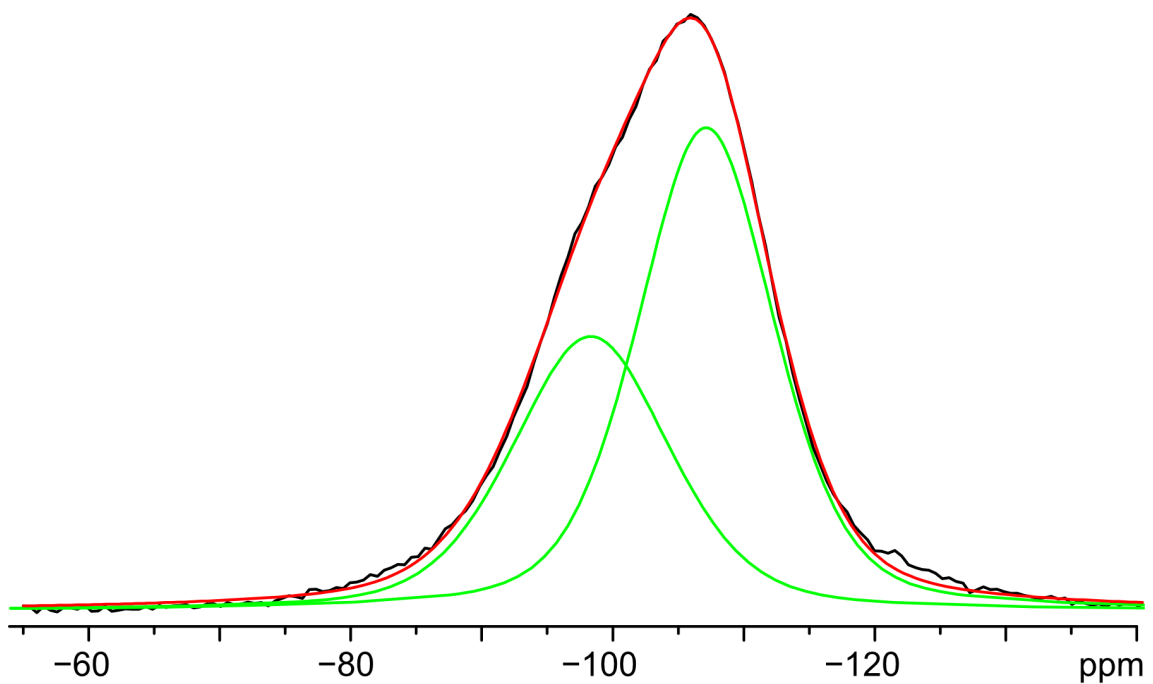


Figure A8. Two-site deconvolution of the ^{19}F MAS NMR spectrum of bulk NaLuF_4 . The experimental spectrum is shown in black, the deconvoluted sites are shown in green, and the red trace shows the combined pattern.

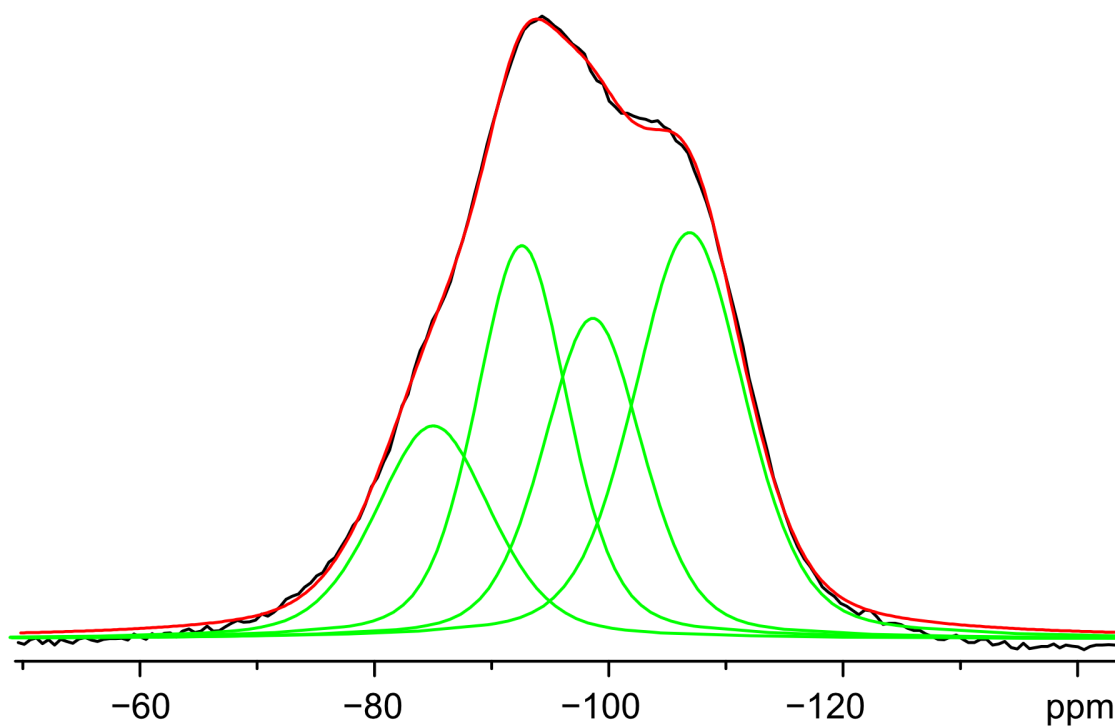


Figure A9. Four-site deconvolution of the ^{19}F MAS NMR spectrum of the 27 nm NC. The experimental spectrum is shown in black, the deconvoluted sites are shown in green, and the red trace shows the combined pattern.

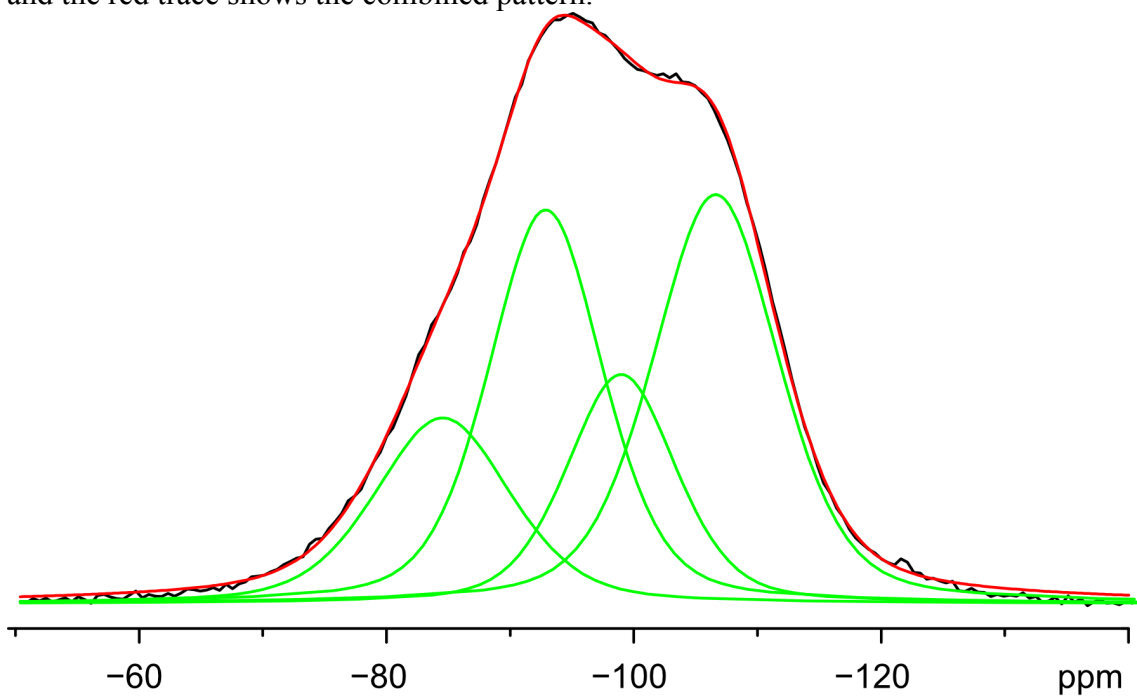


Figure A10. Four-site deconvolution of the ^{19}F MAS NMR spectrum of the 37 nm NC. The experimental spectrum is shown in black, the deconvoluted sites are shown in green, and the red trace shows the combined pattern.

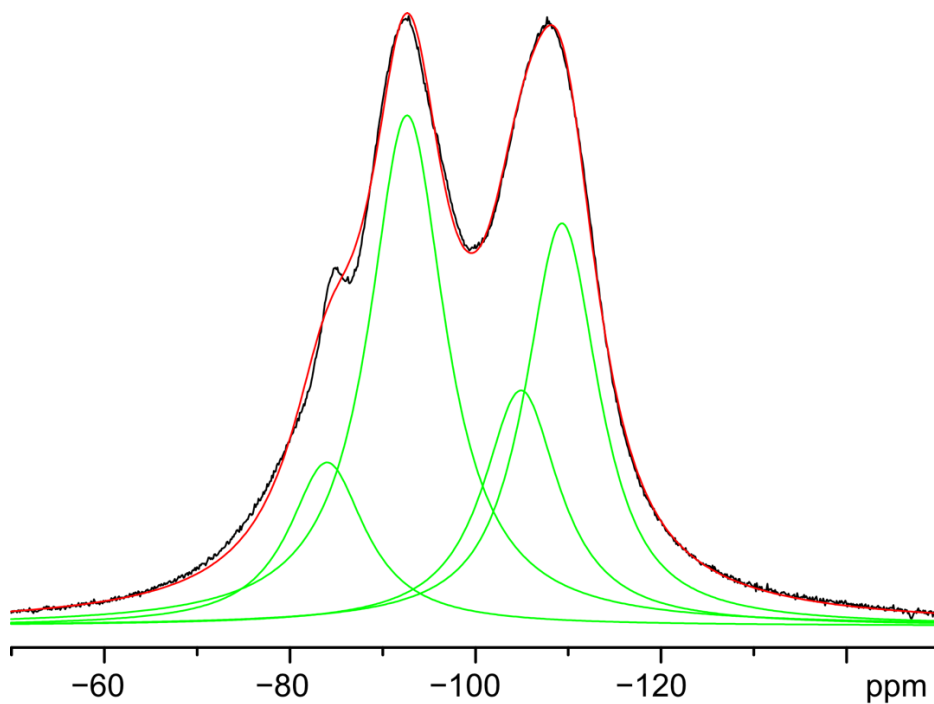


Figure A11. Four-site deconvolution of the ^{19}F UFMAS NMR spectrum of the 27 nm NC acquired at $B_0 = 11.7$ T. The experimental spectrum is shown in black, the deconvoluted sites are shown in green, and the red trace shows the combined pattern.

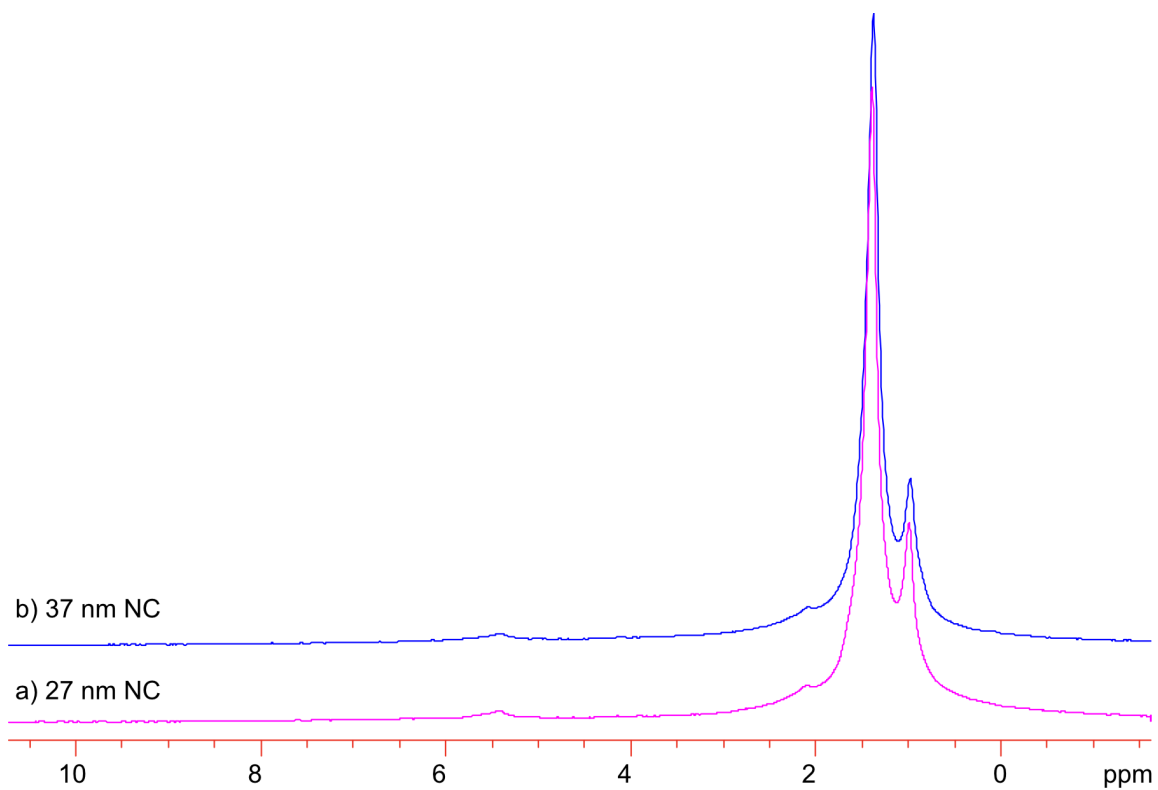


Figure A12. ^1H MAS NMR spectra of a) 27 nm NC and b) 37 nm NC ($\nu_{\text{rot}}=12$ kHz).

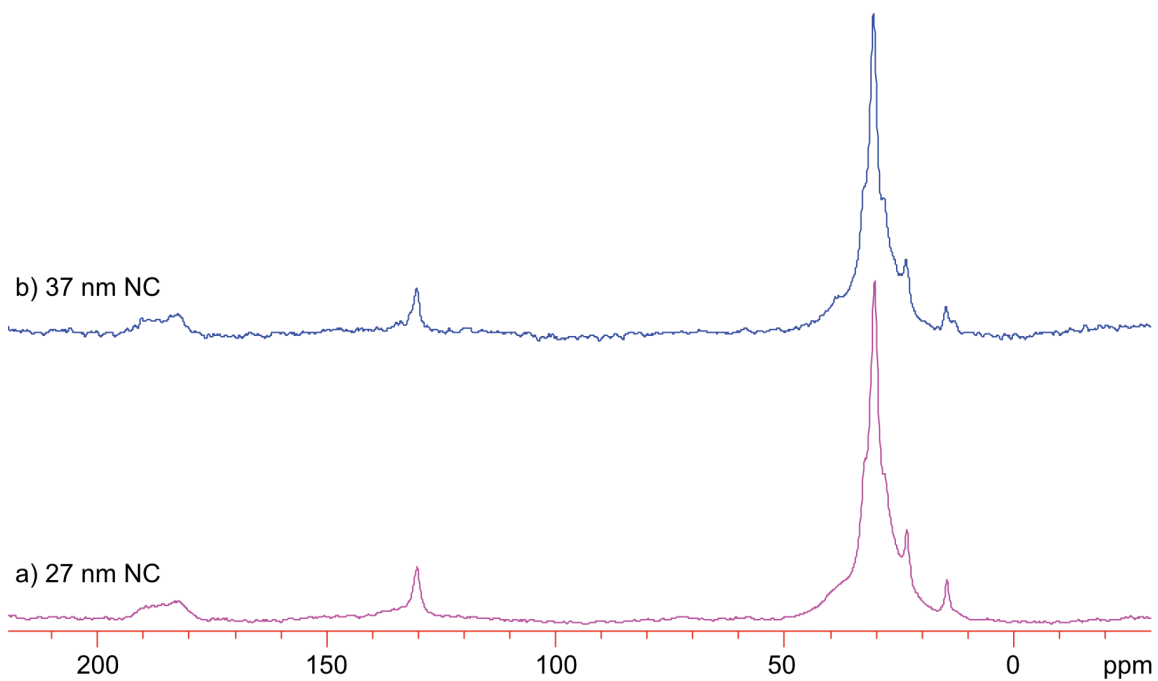


Figure A13. ^1H - ^{13}C CP/MAS NMR spectra of a) 27 nm NC and b) 37 nm NC ($\nu_{\text{rot}}=12$ kHz).

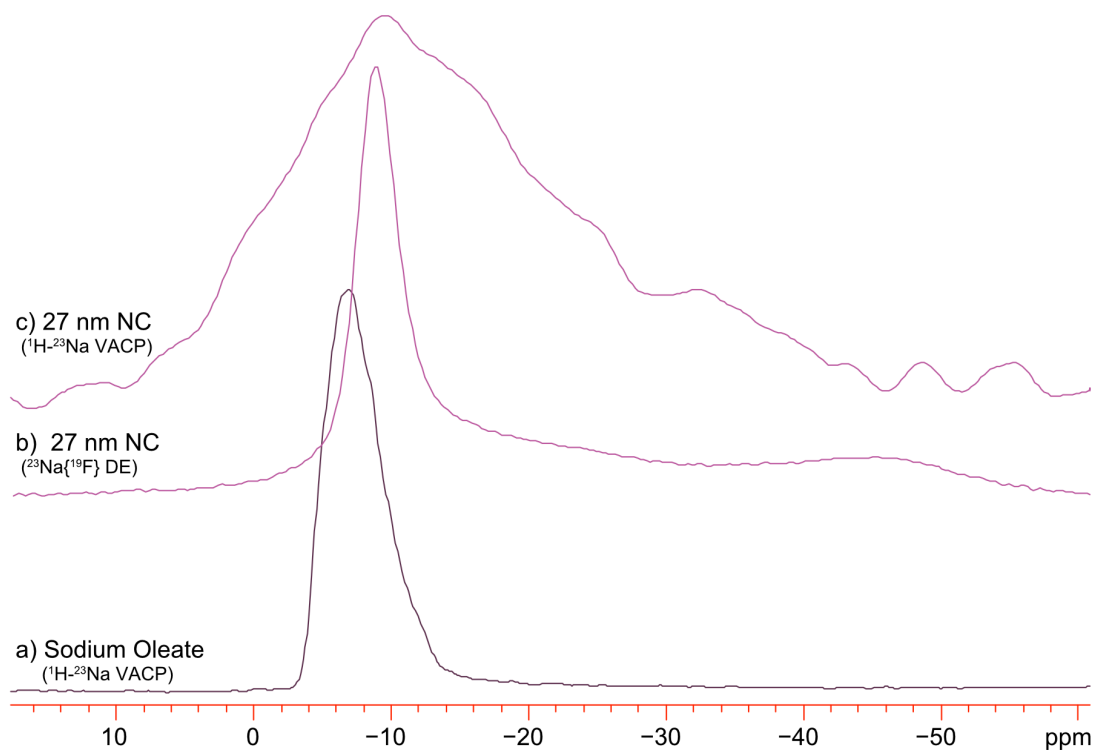


Figure A14. ^{23}Na MAS ($\nu_{\text{rot}} = 6$ kHz) NMR spectra of a) sodium oleate, b) and c) the 27 nm NC. The spectra in a) and c) were acquired using ^1H - ^{23}Na CP/MAS, the spectrum in b) was acquired using direct excitation of the ^{23}Na nuclei.

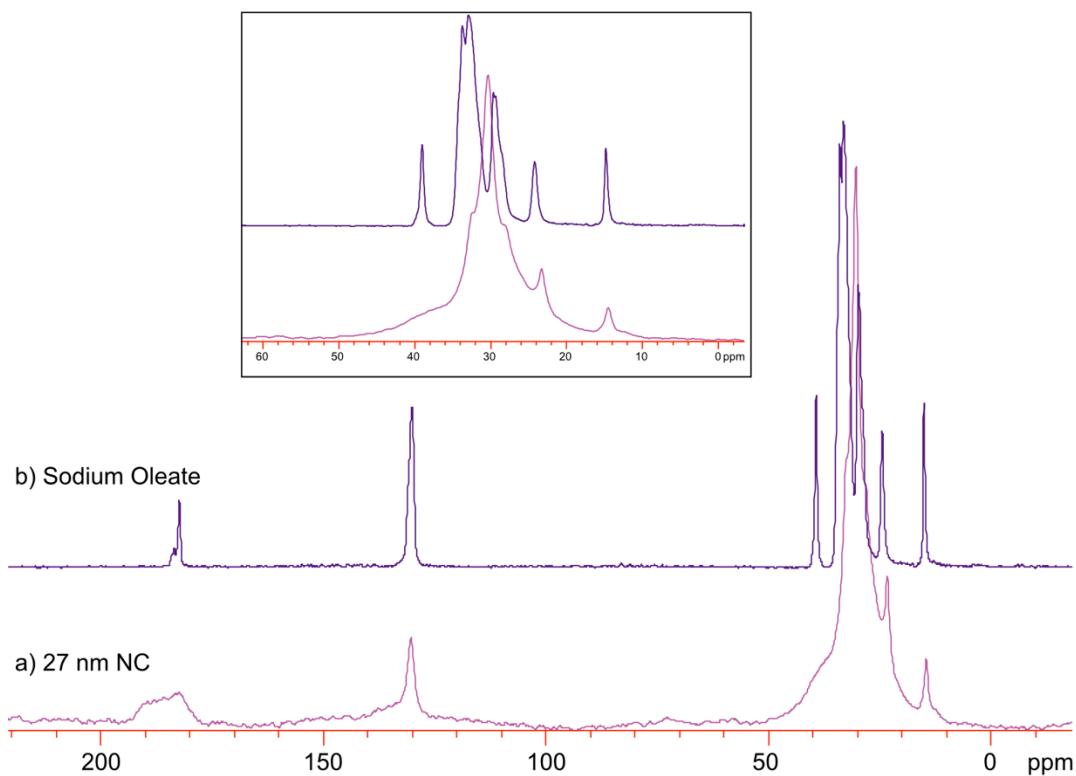


Figure A15. ^1H - ^{13}C CP/MAS ($\nu_{\text{rot}} = 10$ kHz) NMR spectra of a) sodium oleate and b) the 27 nm NC. The inset shows the low frequency regions of the spectra.

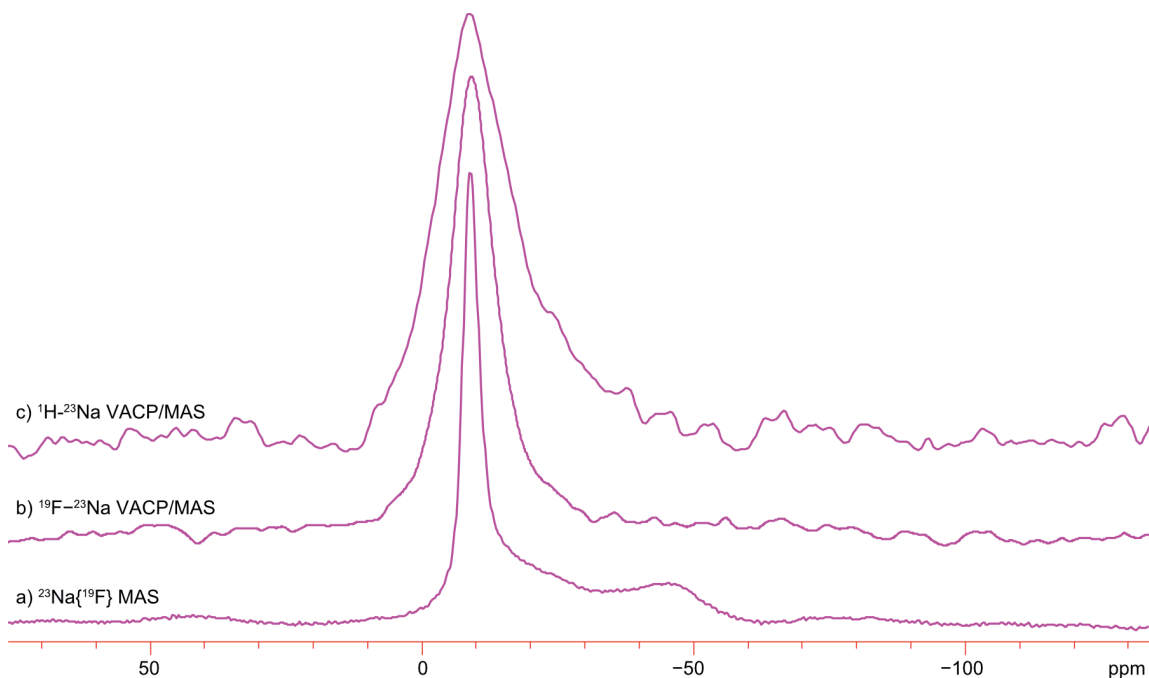


Figure A16. ^{23}Na MAS spectra of the 27 nm NC ($\nu_{\text{rot}} = 6$ kHz). a) direct excite, b) ^{19}F - ^{23}Na CP, and c) ^1H - ^{23}Na CP. The CP spectra were acquired using high power contact pulses (56.8 kHz and 79.5 kHz for ^{19}F or ^1H and ^{23}Na , respectively).

Appendix B: Supporting Tables and Figures for Chapter 3

Table B1. Acquisition parameters for ^1H UFMAS ($\nu_{\text{rot}} = 60$ kHz) Hahn echo experiments on the NC samples.

	Undoped Samples		Doped NC samples					
	19 nm	33 nm	Er 2%	Er 5%	Er 10%	Tm 2%	Tm 5%	Tm 10%
Number of scans	1024	1024	256	256	256	1024	1024	1024
Experimental time (min)	38.4	38.4	2.1	2.1	2.1	32.4	25.6	18.8
Recycle delay (s)	2.25	2.25	0.5	0.5	0.5	1.9	1.5	1.1
^1H $\pi/2$ pulse width (μs)	1.273	1.273	1.2	1.066	1.066	1.066	1.066	1.066
Inter-pulse delay [τ] (us)	16.47	16.47	16.49	16.51	16.51	16.49	16.49	16.49
^1H π pulse width (μs)	2.546	2.546	2.5	2.132	2.132	2.132	2.132	2.132
^1H rf field (kHz)	196	196	100	234	234	234	234	234
Spectral width (MHz)	0.039	0.039	1.25	1.25	1.25	1.25	1.25	1.25
Acquisition length (# of points)	32728	32728	8152	8152	8152	131032	65496	65496

Table B2. Acquisition parameters for $^{23}\text{Na}\{^{19}\text{F}\}$ MAS ($\nu_{\text{rot}} = 12$ kHz) Hahn echo experiments on the NC and bulk samples.

	All Samples (NC and Bulk)
Number of scans	3600
Experimental time (min)	60
Recycle delay (s)	1
^{23}Na $\pi/2$ (CT-selective) pulse width (μs)	1.25
Inter-pulse delay [τ] (us)	8.15
^{23}Na π (CT-selective) pulse width (μs)	2.5
^{23}Na rf field (kHz)	100
^{19}F rf decoupling strength (kHz)	85
Spectral width (MHz)	1.5
Acquisition length (number of points)	16344

Table B3. Acquisition parameters for ^{19}F UFMAS ($\nu_{\text{rot}} = 60$ kHz) Hahn echo experiments on the NC and bulk samples.

	Undoped Samples			Doped NC samples						Doped Bulk Samples					
	19 nm	33 nm	> 2 μm	Er 2%	Er 5%	Er 10%	Tm 2%	Tm 5%	Tm 10%	Er 2%	Er 5%	Er 10%	Tm 2%	Tm 5%	Tm 10%
Number of scans	4096	4096	4096	4096	4096	4096	1024	1024	1024	4096	4096	4096	1024	1024	1024
Experimental time (min)	867	887	75	51	34	34	20.5	8.5	8.5	34.1	17.1	17.1	17.1	8.54	8.54
Recycle delay (s)	12.7	13	1.1	0.75	0.5	0.5	1.2	0.5	0.5	0.5	0.25	0.25	1	0.5	0.5
^{19}F $\pi/2$ pulse width (μs)	1.2	1.2	1.2	1.2	1.2	1.2	1.2	1.2	1.2	1.2	1.2	1.2	1.25	1.25	1.25
Inter-pulse delay [τ] (μs)	14.8	14.8	14.8	14.8	14.8	14.8	14.8	14.8	14.8	14.8	14.8	14.8	14.8	14.8	14.8
^{19}F π pulse width [π] (μs)	2.4	2.4	2.4	2.4	2.4	2.4	2.4	2.4	2.4	2.4	2.4	2.4	2.5	2.5	2.5
^{19}F rf field (kHz)	208	208	208	208	208	208	208	208	208	208	208	208	200	200	200
Spectral width (MHz)	2	2	2	2	2	2	2	2	2	2	2	2	2	2	2
Acquisition length (# of points)	4096	4096	4096	4096	4096	4096	4096	4096	4096	4056	4056	4056	4056	16344	16344

Table B4. Acquisition parameters for ^1H - ^{89}Y MAS ($\nu_{\text{rot}} = 5$ kHz) experiments on the NC samples.

	Undoped NC Sample	Doped NC Samples	
	19 nm	Er 2%	Tm 2%
Number of scans	158440	204800	132896
Experimental time (hrs)	22	28.4	18.46
Recycle delay (s)	0.5	0.5	0.5
^1H $\pi/2$ pulse width (μs)	2.5	2.5	2.5
Contact time (ms)	10	15	15
^1H rf field during contact pulse (kHz)	38	38	38
^{89}Y rf field during contact pulse (kHz)	28	28	28
^1H decoupling field (kHz)	45	45	45
Spectral width (kHz)	50	50	50
Acquisition length (number of points)	2048	2048	2048

Table B5. Acquisition parameters for ^{19}F - ^{89}Y CP/MAS ($\nu_{\text{rot}} = 5$ kHz) experiments on the NC and Bulk samples.

	NC Samples						Bulk Samples						
	Er 2%	Er 5%	Er 10%	Tm 2%	Tm 5%	Tm 10%	Er 2%	Er 5%	Er 10%	Tm 2%	Tm 5%	Tm 10%	
Number of scans	28256	50912	22046	18000	18000	43841	–	39488	29744	50304	41327	25615	66296
Experimental time (hrs)	7.8	14.14	6.1	5	5	12.71	–	11	8.26	14	11.48	7.12	18.4
Recycle delay (s)	1	1	1	1	1	1	–	1	1	1	1	1	1
^{19}F $\pi/2$ pulse width (μs)	2.5	2.5	2.5	2.5	2.5	2.5	–	2.5	2.5	2.5	2.5	2.5	2.5
Contact time (ms)	8	8	8	8	8	8	–	8	8	8	8	8	8
^{19}F rf field during contact pulse (kHz)	40	40	40	39	39	39	–	40	40	40	40	40	40
^{89}Y rf field during contact pulse (kHz)	28	28	28	28	28	28	–	28	28	28	28	28	28
^{19}F decoupling field (kHz)	48	48	48	48	48	48	–	48	48	48	48	48	48
Spectral width (kHz)	50	50	50	50	50	50	–	50	50	50	50	50	50
Acquisition length (number of points)	2048	2048	2048	2048	2048	2048	–	2048	2048	2048	2048	2048	2048

Table B6. Acquisition parameters for $^{13}\text{C}\{^1\text{H}\}$ MAS ($\nu_{\text{rot}} = 12$ kHz) Hahn echo experiments on the NC samples.

	Undoped Samples		Doped NC samples					
	19 nm	33 nm	Er 2%	Er 5%	Er 10%	Tm 2%	Tm 5%	Tm 10%
Number of scans	35808	8960	35808	35808	35808	8192	8192	8192
Experimental time (hrs)	4.97	1.24	4.97	4.97	4.97	1.14	1.14	1.14
Recycle delay (s)	0.5	0.5	0.5	0.5	0.5	0.5	0.5	0.5
^{13}C $\pi/2$ pulse width (μs)	2.5	2.5	2.5	2.5	2.5	2.5	2.5	2.5
Inter-pulse delay [τ] (us)	7.95	7.95	7.95	7.95	7.95	7.95	7.95	7.95
^{13}C π pulse width (μs)	5	5	5	5	5	5	5	5
^{13}C rf field (kHz)	100	100	100	100	100	100	100	100
^1H rf decoupling strength (kHz)	50	50	50	50	50	50	50	50
Spectral width (kHz)	250	250	250	250	250	250	250	250
Acquisition length (# of points)	40960	40960	8054	8054	8054	8054	8054	8054

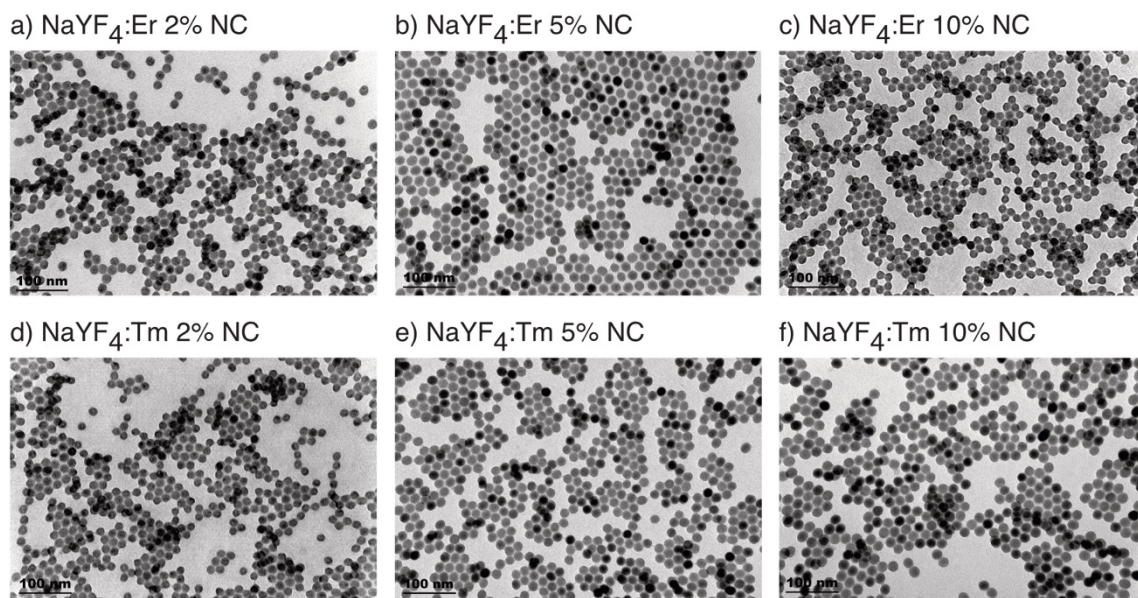


Figure B1. TEM images of the doped NC samples used to measure the particle size.

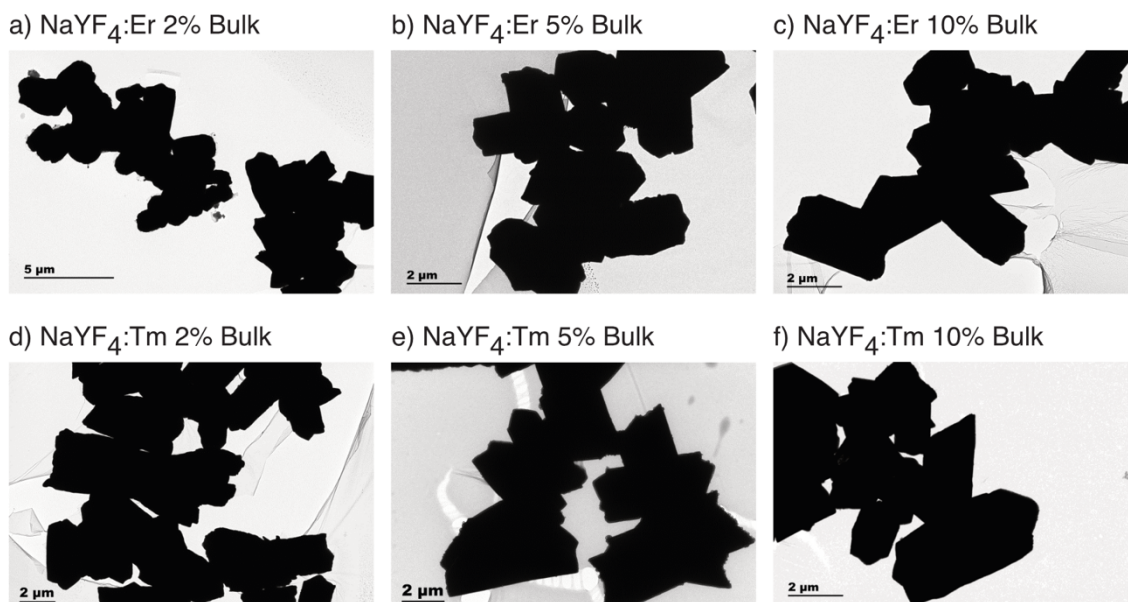


Figure B2. TEM images of the doped bulk samples used to measure the particle size.

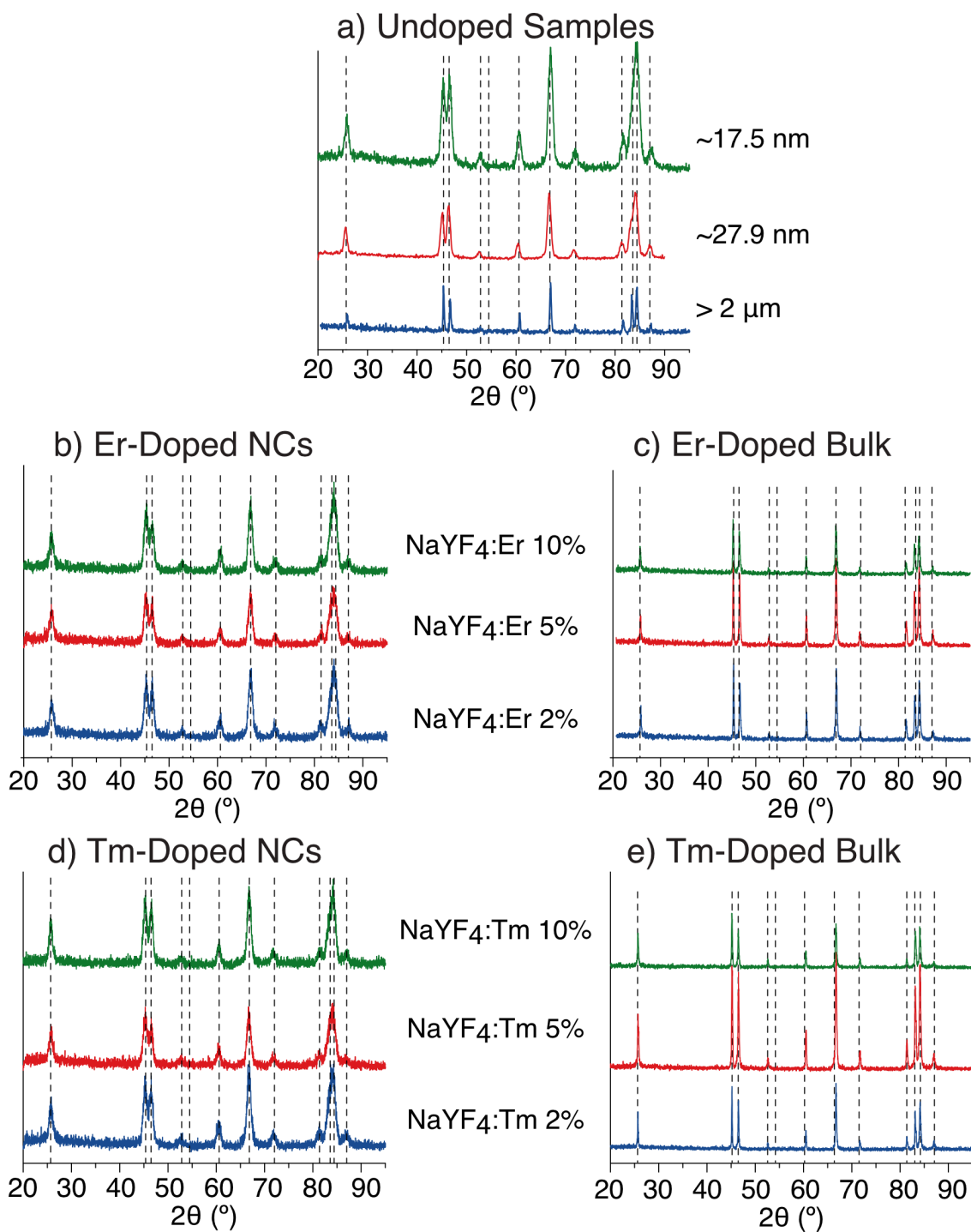


Figure B3. Powder X-ray diffraction patterns of a) undoped NaYF₄ samples b) Er-doped NaYF₄ NC samples, c) Er-doped bulk samples, d) Tm-doped NaYF₄ NC samples, and e) Tm-doped NaYF₄ bulk samples. Dashed lines indicate features in the JCPDS reference patterns of hexagonal-phase β -NaYF₄ (JCPDS: 16-0334).

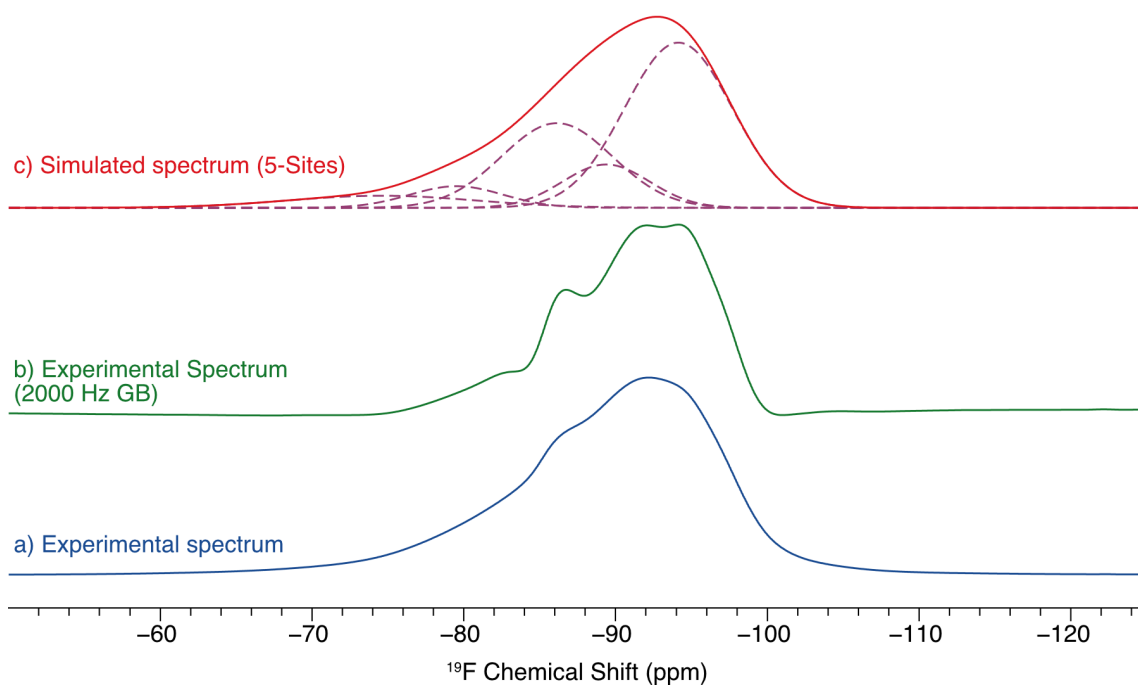


Figure B4. Experimental ^{19}F UFMAS ($\nu_{\text{rot}} = 60$ kHz) NMR spectra of the 17.5 nm NC processed with a) no line broadening and b) 2 kHz Gaussian line broadening (which enhances the resolution of the ^{19}F signal and reveals at least 4 distinct features). A simulated spectrum is shown in c), the deconvoluted sites are purple, and the red trace shows the combined pattern.

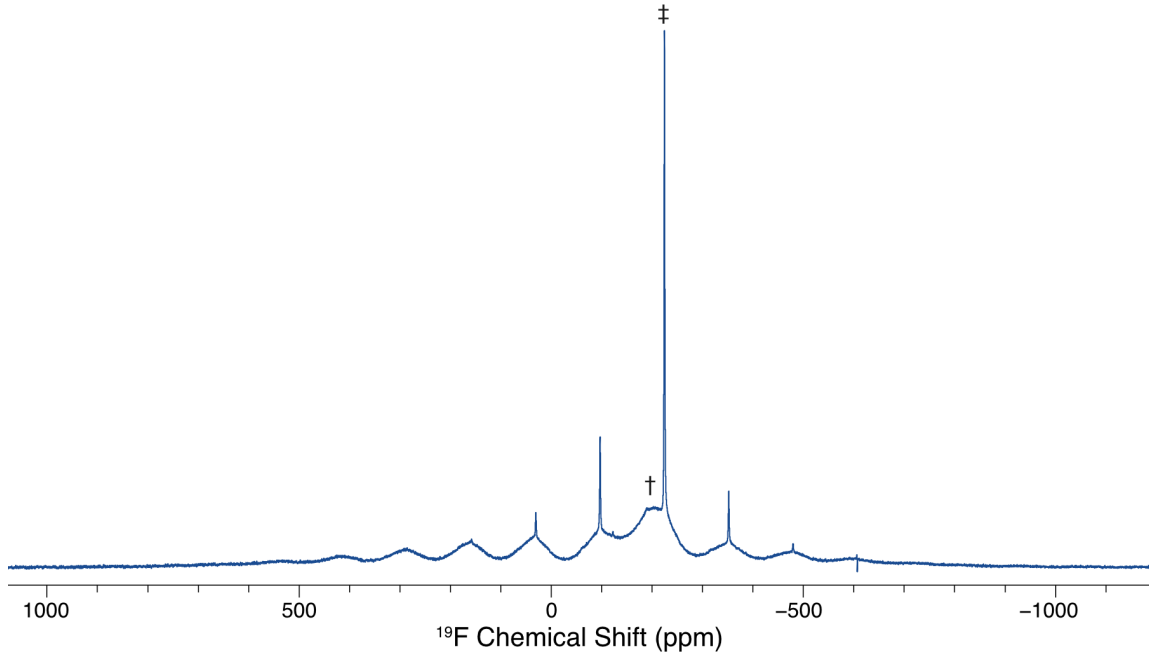


Figure B5. ^{19}F UFMAS ($\nu_{\text{rot}} = 60$ kHz) NMR spectrum of the 20% Er-doped NaYF_4 bulk sample. The single and double daggers correspond to isotropic peaks from the NaYF_4 material, and NaF impurity, respectively. All other features in the spectrum are spinning sidebands.

Calculation of Average $\text{Ln}^{3+}\dots\text{Ln}^{3+}$ Distances from Dopant Level

The dopant sites in the NCs can be modeled as spheres centered at the dopant ion, with diameters equal to the distance between dopants. Using a spherical packing model, the number of spheres (and therefore Ln^{3+} ions) that fit within the NC volume is related to the dopant level:

$$\text{Dopant Level} \approx \frac{(\text{Packing density}) \times (\text{Volume of NC})}{\text{Volume of } \text{Ln}^{3+} \text{ sphere}} = \frac{\text{Packing density}}{(\text{Volume of } \text{Ln}^{3+} \text{ sphere}) \rho_Y} \quad (8.1)$$

where the number of dopant sites can be calculated by multiplying the density of Y atoms in the structure, ρ_Y , by the volume of the NC.

With the assumption that Ln^{3+} ions are evenly distributed throughout the particles, the percentage of the total NC volume that is occupied by Ln^{3+} spheres (the packing density) is equal to the maximum possible for optimally packed spheres, which has been

mathematically proven to be 74.05%. By re-arranging **Eq. 3.3**, and using the formula for a volume of a sphere, the $\text{Ln}^{3+}\cdots\text{Ln}^{3+}$ distance, $D_{\text{Ln}^{3+}}$, can be calculated using **Eq. 3.4**:

$$D_{\text{Ln}^{3+}} = \sqrt[3]{\frac{0.7405}{\left(\frac{4}{3}\pi\right) (\text{Dopant level})(\rho_Y)}} \quad (8.2)$$

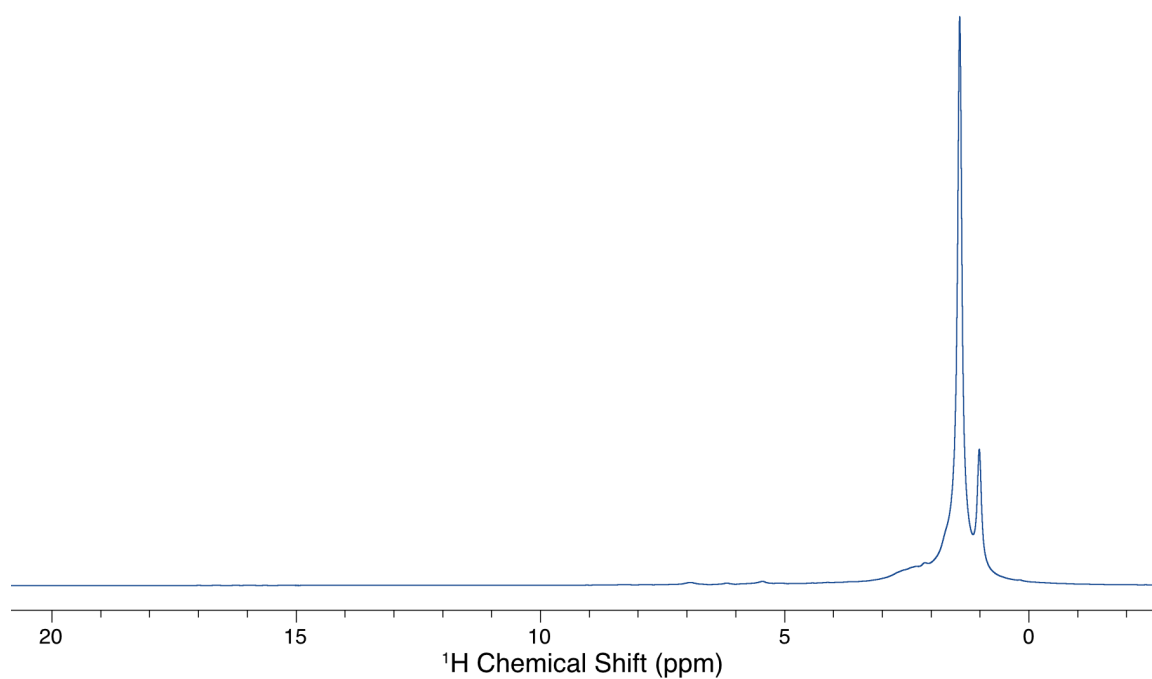


Figure B6. ^1H MAS ($\nu_{\text{rot}} = 60$ kHz) NMR spectrum of the 17.5 nm undoped NC.

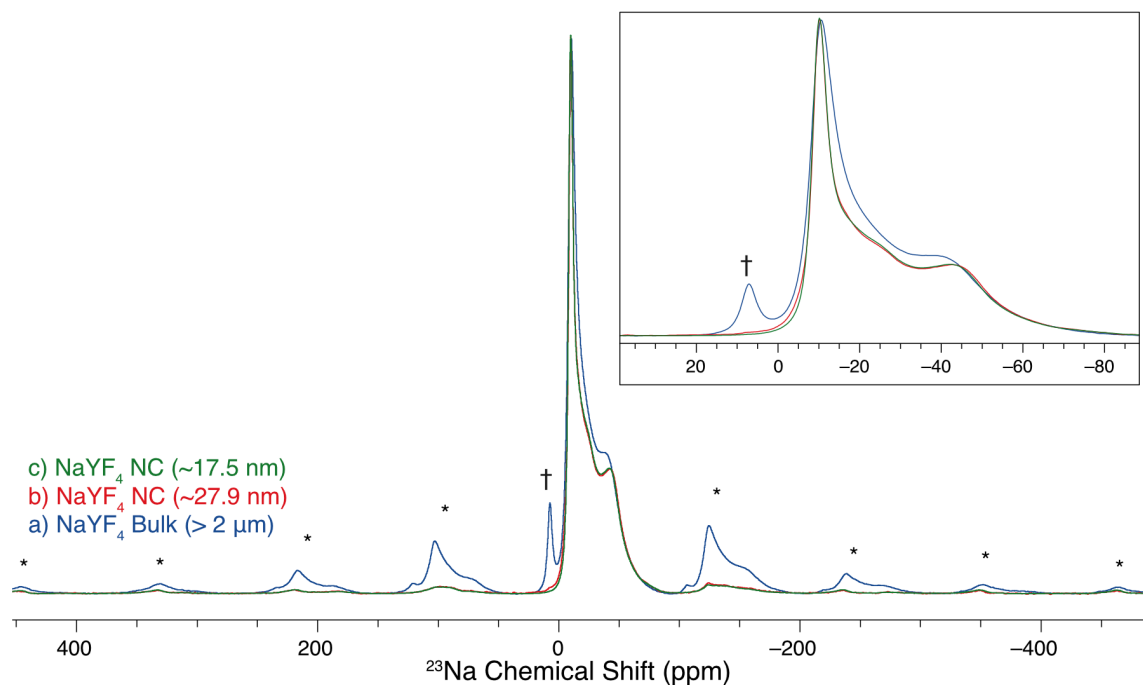


Figure B7. ^{23}Na MAS ($\nu_{\text{rot}} = 12$ kHz) NMR spectra of the undoped NaYF_4 samples with different particle size: a) bulk samples ($> 2 \mu\text{m}$), b) NC (33 nm), c) NC 19 nm. Daggers denote a peak from a minor NaF impurity at 7.2 ppm in a). Asterisks denote spinning sidebands.

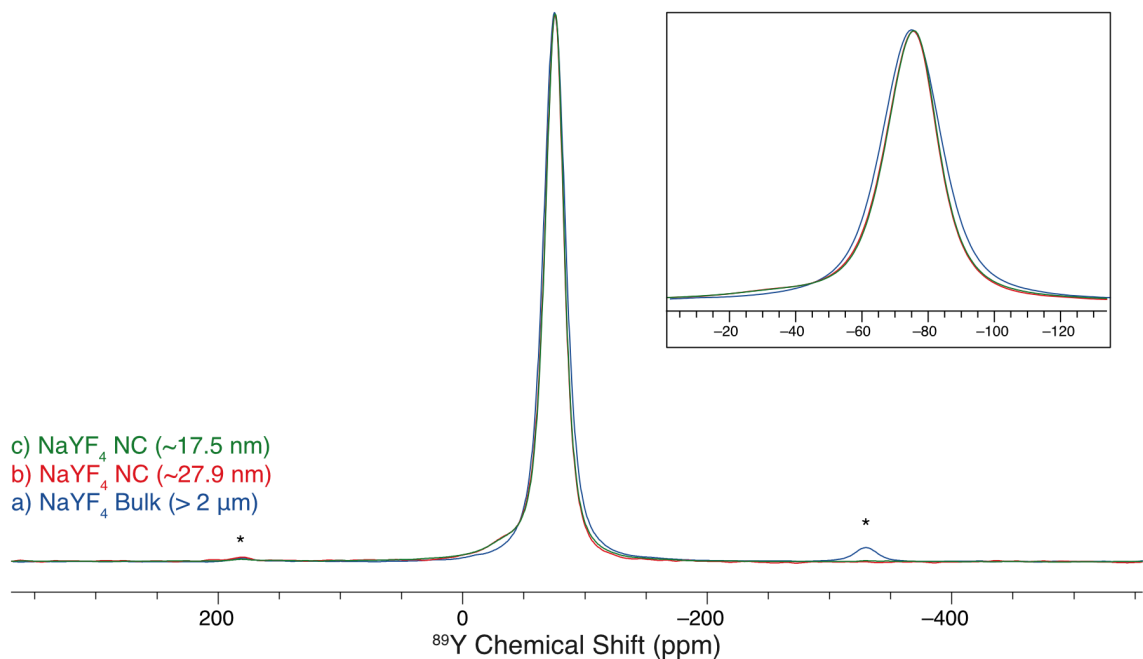


Figure B8. ^{19}F - ^{89}Y CP/MAS ($\nu_{\text{rot}} = 5$ kHz) NMR spectra of the undoped NaYF_4 samples with different particle size: a) bulk samples ($> 2 \mu\text{m}$), b) NC (33 nm), c) NC 19 nm. Asterisks denote spinning sidebands.

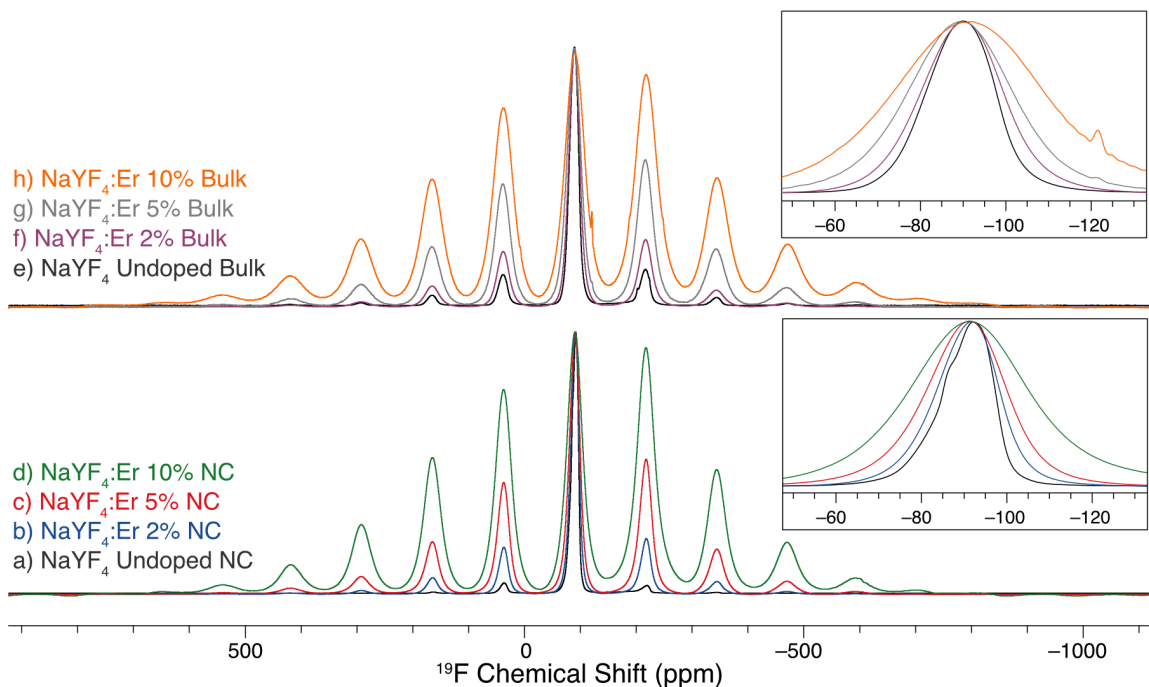


Figure B9. ¹⁹F UFMAS ($v_{\text{rot}} = 60$ kHz) NMR spectra of the undoped and Er-doped NC samples (bottom) and corresponding bulk samples (top). A minor F⁻ impurity produces a peak at -122 ppm in the spectrum of the NaYF₄: Er 10% bulk sample.

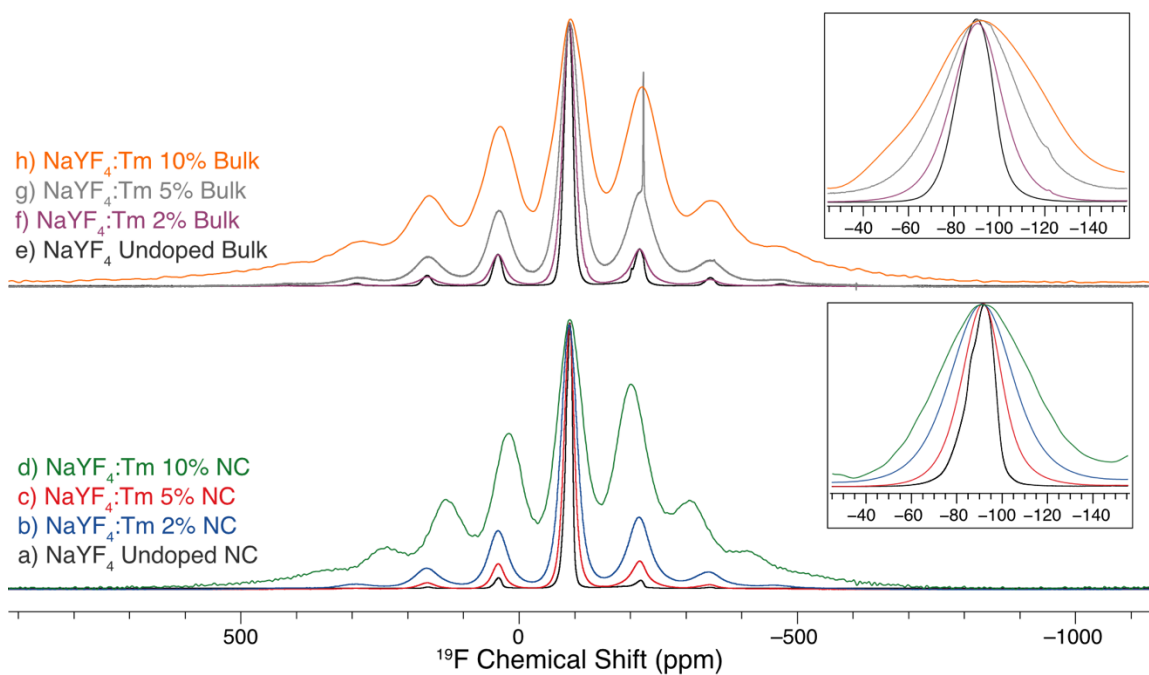


Figure B10. ¹⁹F UFMAS ($v_{\text{rot}} = 60$ kHz) NMR spectra of the undoped and Tm-doped NC samples (bottom) and corresponding bulk samples (top). A minor NaF impurity produces a peak at -222 ppm in the spectrum of the NaYF₄: Er 5% bulk sample.

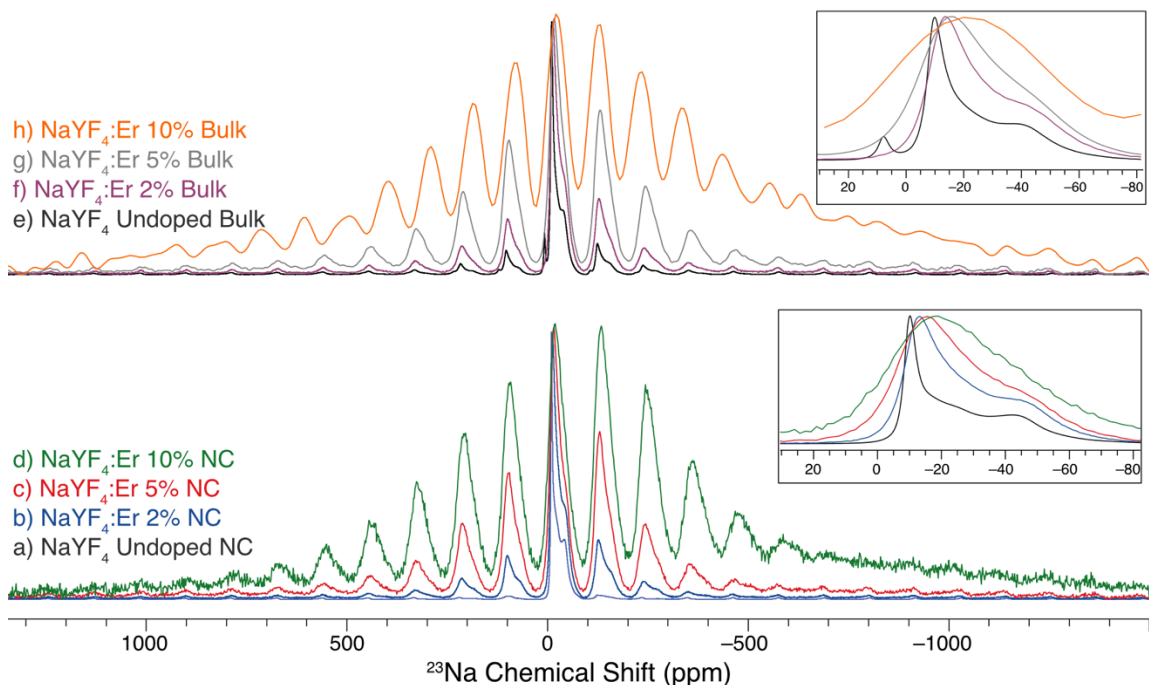


Figure B11. $^{23}\text{Na}\{^{19}\text{F}\}$ MAS ($\nu_{\text{rot}} = 12$ kHz) NMR spectra of the undoped and Er-doped NC samples (bottom) and corresponding bulk samples (top). A minor NaF impurity produces a peak at 7.2 ppm in the spectrum of the undoped bulk material.

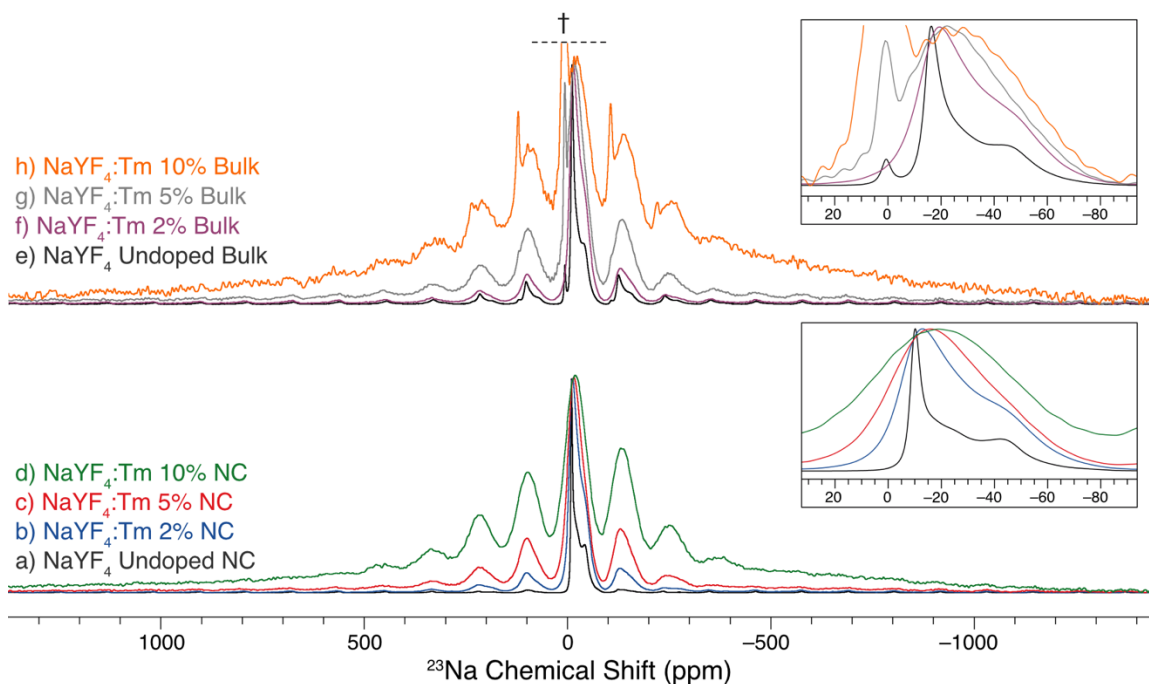


Figure B12. $^{23}\text{Na}\{^{19}\text{F}\}$ MAS ($\nu_{\text{rot}} = 12$ kHz) NMR spectra of the undoped and Tm-doped NC samples (bottom) and corresponding bulk samples (top). A NaF impurity produces a peak (marked with a dagger) in the spectra of the undoped, 5%, and 10%-doped Tm bulk samples.

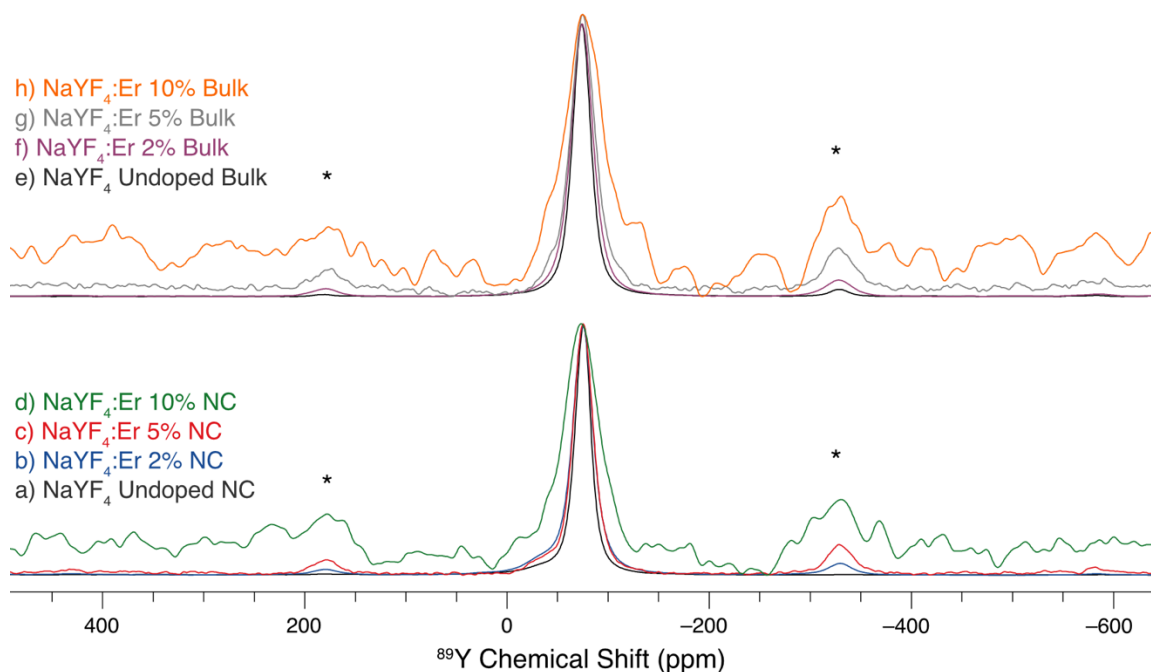


Figure B13. ^{19}F - ^{89}Y CP/MAS ($v_{\text{rot}} = 5$ kHz) NMR spectra of the undoped and Er-doped NC samples (bottom) and corresponding bulk samples (top). Asterisks denote spinning sidebands.

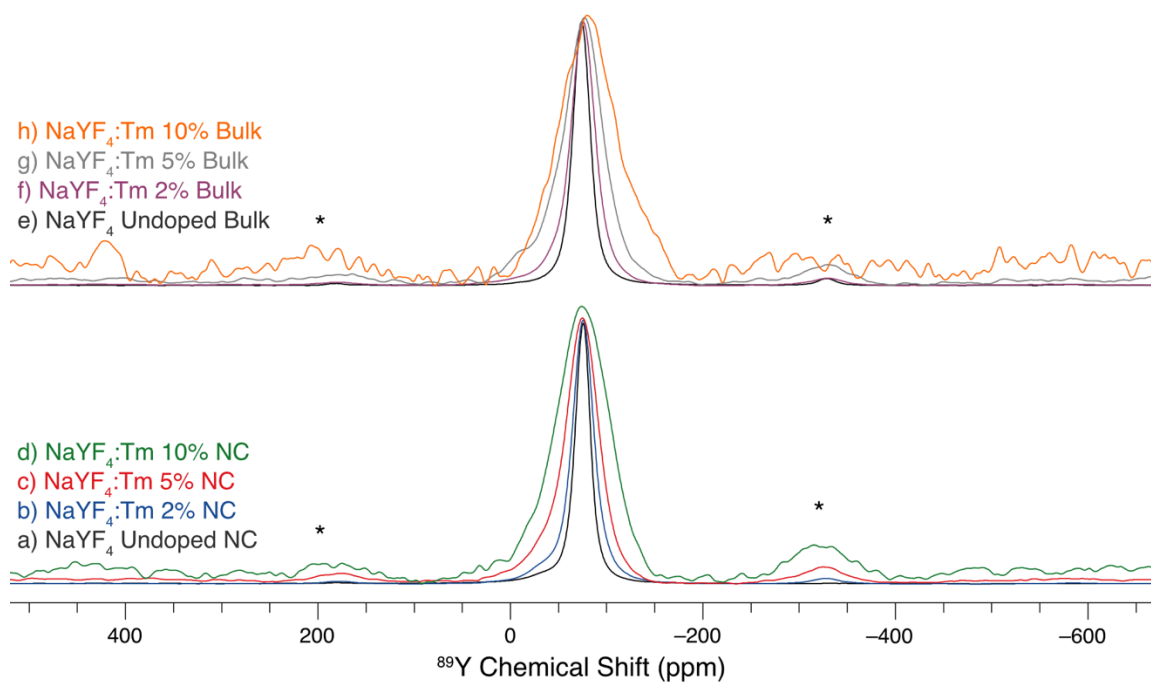


Figure B14. ^{19}F - ^{89}Y CP/MAS ($v_{\text{rot}} = 5$ kHz) NMR spectra of the undoped and Tm-doped NC samples (bottom) and corresponding bulk samples (top). Asterisks denote spinning sidebands.

Appendix C: Supporting Tables and Figures for Chapter 4

Table C1. Acquisition parameters for ^{19}F UFMAS ($\nu_{\text{rot}} = 60$ kHz) Hahn echo experiments on the NP samples.

	YF	Sc-Containing Samples				Er-Containing Samples				Eu-containing Samples			
		YF:Sc 10	YF:Sc 20	YF:Sc 50	YF:Sc 100	YF:Er 5	YF:Er 10	YF:Er 20	YF:Er 50	YF:Eu 5	YF:Eu 10	YF:Eu 20	YF:Eu 50
Number of scans	1024	1024	1024	1024	1024	4096	4096	4096	4096	4096	4096	4096	4096
Experimental time (min)	85	99	136	188	154	69	69	69	69	69	69	69	69
Recycle delay (s)	5	5.78	7.93	11	9	1	1	1	1	1	1	1	1
^{19}F $\pi/2$ pulse width (μs)	1.2	1.2	1.2	1.2	1.2	1.25	1.25	1.25	1.25	1.25	1.25	1.25	1.25
Inter-pulse delay [τ] (us)	14.9	14.9	14.9	14.9	14.9	14.8	14.8	14.8	14.8	14.8	14.8	14.8	14.8
^{19}F π pulse width (μs)	2.4	2.4	2.4	2.4	2.4	2.5	2.5	2.5	2.5	2.5	2.5	2.5	2.5
^{19}F rf field (kHz)	208	208	208	208	208	200	200	200	200	200	200	200	200
Spectral width (MHz)	2	2	2	2	2	2	2	2	2	2	2	2	2
Acquisition length (# of points)	65496	16344	16384	16344	16344	65496	65496	65496	65496	65496	65496	65496	65496

Table C2. Acquisition parameters for ^1H UFMAS ($\nu_{\text{rot}} = 60$ kHz) Hahn echo experiments on the NP samples.

	YF	Sc-Containing Samples				Er-Containing Samples				Eu-Containing Samples			
		YF:Sc 10	YF:Sc 20	YF:Sc 50	YF:Sc 100	YF:Er 5	YF:Er 10	YF:Er 20	YF:Er 50	YF:Eu 5	YF:Eu 10	YF:Eu 20	YF:Eu 50
Number of scans	1024	1024	1024	1024	1024	1024	1024	1024	2048	1024	1024	1024	1024
Experimental time (min)	17	25	33	26	154	17	17	17	34	17	17	17	17
Recycle delay (s)	1	1.46	1.95	1.54	9	1	1	1	1	1	1	1	1
^1H $\pi/2$ pulse width (μs)	1.2	1.275	1.275	1.275	1.2	1.275	1.275	1.275	1.2	1.275	1.275	1.2	1.275
Inter-pulse delay [τ] (us)	14.9	14.8	14.8	14.8	14.9	14.8	14.8	14.8	14.8	14.8	14.8	16.5	14.8
^1H π pulse width (μs)	2.4	2.55	2.55	2.55	2.4	2.55	2.55	2.55	2.4	2.55	2.55	2.4	2.55
^1H rf field (kHz)	208	196	196	196	208	196	196	196	208	196	196	208	196
Spectral width (MHz)	50	50	50	50	2	1500	1500	1500	5000	50	50	50	50
Acquisition length (# of points)	4096	4096	4096	16384	16344	8192	8192	8192	8192	4096	4096	4096	8192

Table C3. Acquisition parameters for ^{19}F - ^{89}Y CP/MAS ($\nu_{\text{rot}} = 5$ kHz) experiments on the NP samples.

	YF	Sc-Containing Samples				Er-Containing Samples				Eu-Containing Samples			
		YF:Sc 10	YF:Sc 20	YF:Sc 50	YF:Sc 100	YF:Er 5	YF:Er 10	YF:Er 20	YF:Er 50	YF:Eu 5	YF:Eu 10	YF:Eu 20	YF:Eu 50
Number of scans	1024	1024	1024	1024	–	65536	65536	57168	–	17086	17086	17086	17086
Experimental time (hrs)	1.4	1.6	2.25	2.3	–	18.2	18.2	15.9	–	4.75	4.75	4.75	4.75
Recycle delay (s)	5	5.78	7.93	8	–	1	1	1	–	1	1	1	1
^{19}F $\pi/2$ pulse width (μs)	2.5	2.5	2.5	2.5	–	2.5	2.5	2.5	–	2.5	2.5	2.5	2.5
Contact time (ms)	8	9	9	9	–	8	8	8	–	8	8	8	8
^{19}F rf field during contact pulse (kHz)	40	40	40	40	–	40	40	40	–	40	40	40	40
^{89}Y rf field during contact pulse (kHz)	28	28	28	28	–	28	28	28	–	28	28	28	28
^{19}F decoupling field (kHz)	50	50	50	50	–	50	50	50	–	50	50	50	50
Spectral width (kHz)	50	50	50	50	–	60	60	60	–	60	60	60	60
Acquisition length (number of points)	4096	2048	2048	2048	–	2048	2048	2048	–	2048	2048	2048	2048

Table C4. Acquisition parameters for ^1H - ^{89}Y CP/MAS ($\nu_{\text{rot}} = 5$ kHz) experiments on the undoped YF NP sample.

	YF
Number of scans	151120
Experimental time (hrs)	16.4
Recycle delay (s)	0.5
^1H 90° pulse width [$\pi/2$] (μs)	2.5
Contact time (ms)	10
^1H rf field during contact pulse (kHz)	34
^{89}Y rf field during contact pulse (kHz)	28
^1H decoupling field (kHz)	55
Spectral width (kHz)	50
Acquisition length (number of points)	2048

Table C5. Acquisition parameters for ^{45}Sc MAS ($\nu_{\text{rot}} = 60$ kHz) Hahn echo experiments on the Sc-containing samples.

	Sc-Containing Samples			
	YF:Sc10	YF:Sc20	YF:Sc50	YF:Sc100
Number of scans	4096	4096	4096	4096
Experimental time (hrs)	34	34	34	34
Recycle delay (s)	0.5	0.5	0.5	2.5
^{45}Sc CT-selective $\pi/2$ pulse width (μs)	2.431	2.431	2.431	2.431
Inter-pulse delay [τ] (us)	13	13	13	13
^{45}Sc CT-selective π pulse width (μs)	4.862	4.862	4.862	4.862
^{45}Sc rf field (kHz)	25.7	25.7	25.7	25.7
Spectral width (MHz)	1	1	1	1
Acquisition length (# of points)	20480	20480	20480	20480

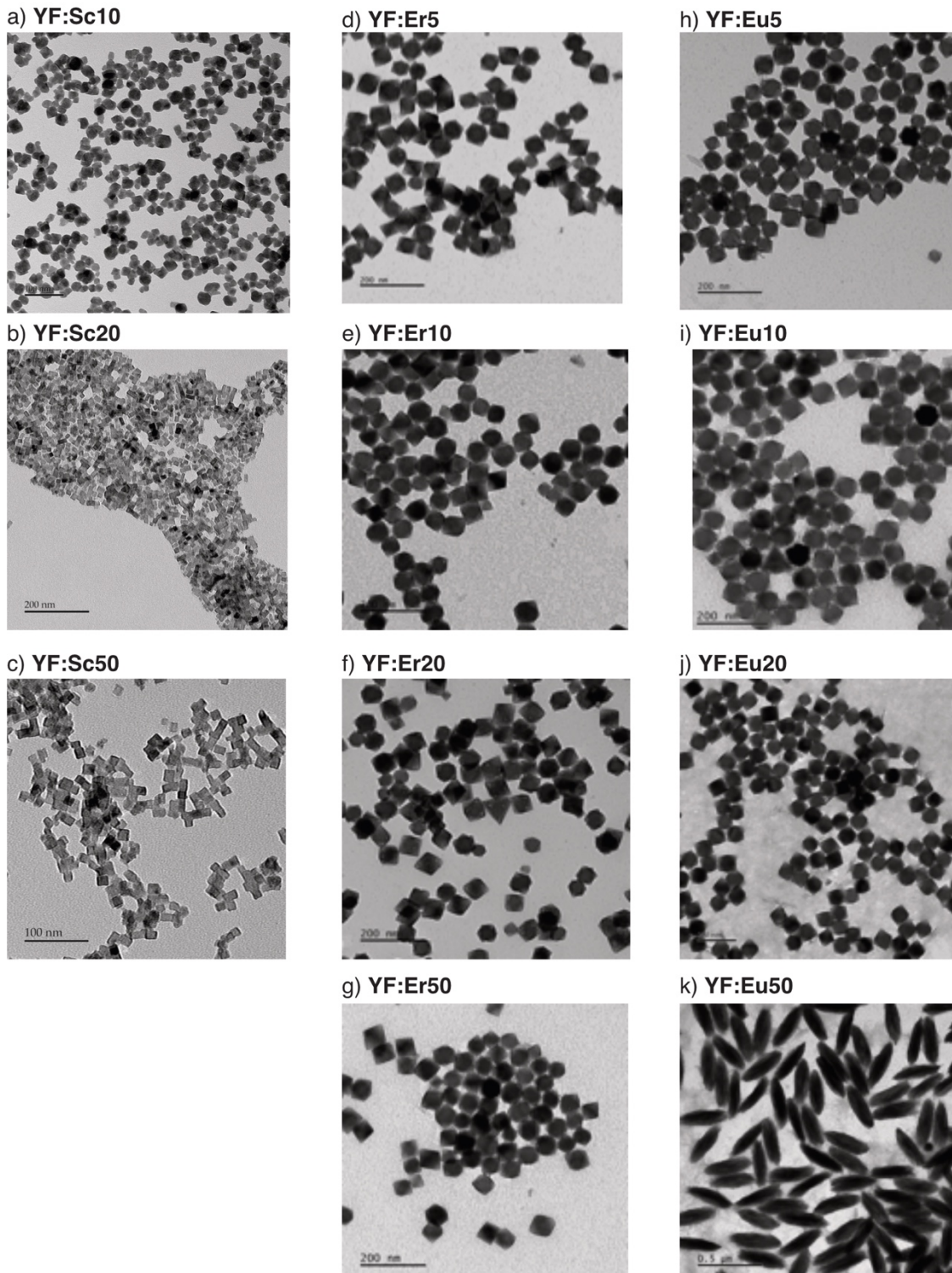


Figure C1. TEM images of the YF samples prepared with RE^{3+} ions, which were used to measure the particle sizes.

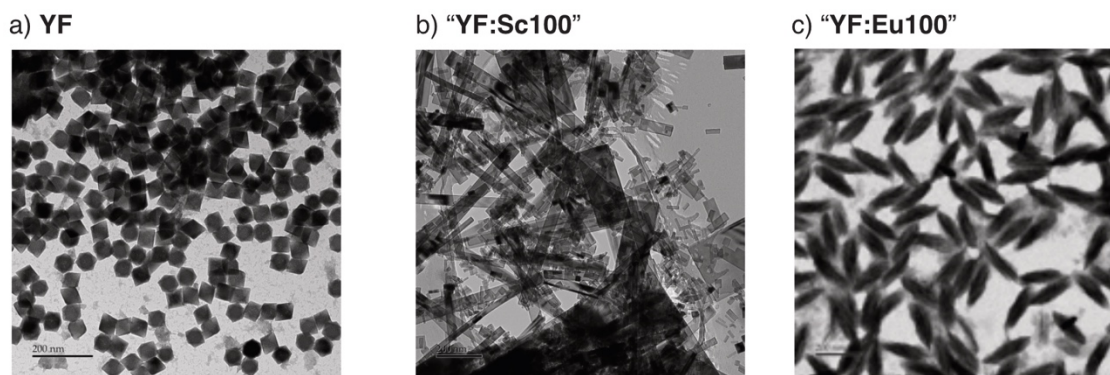


Figure C2. TEM images of NPs prepared with 100% (RE)Cl₃ a) RE = Y (YF NPs), b) RE = Sc c) RE = Eu.

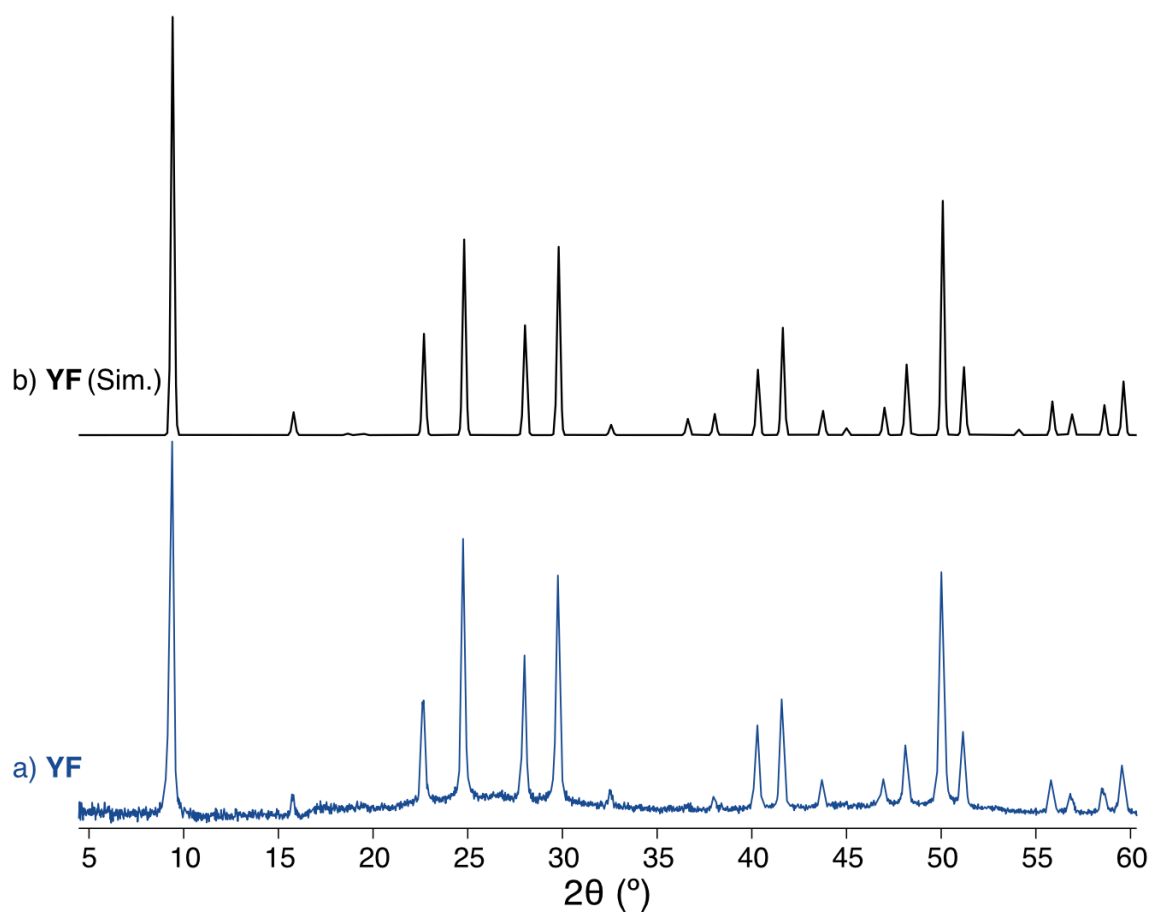


Figure C3. Powder X-ray diffraction patterns of the undoped YF NPs: a) experimental data, and b) a pattern simulated from the previously-reported crystal structure.¹⁹

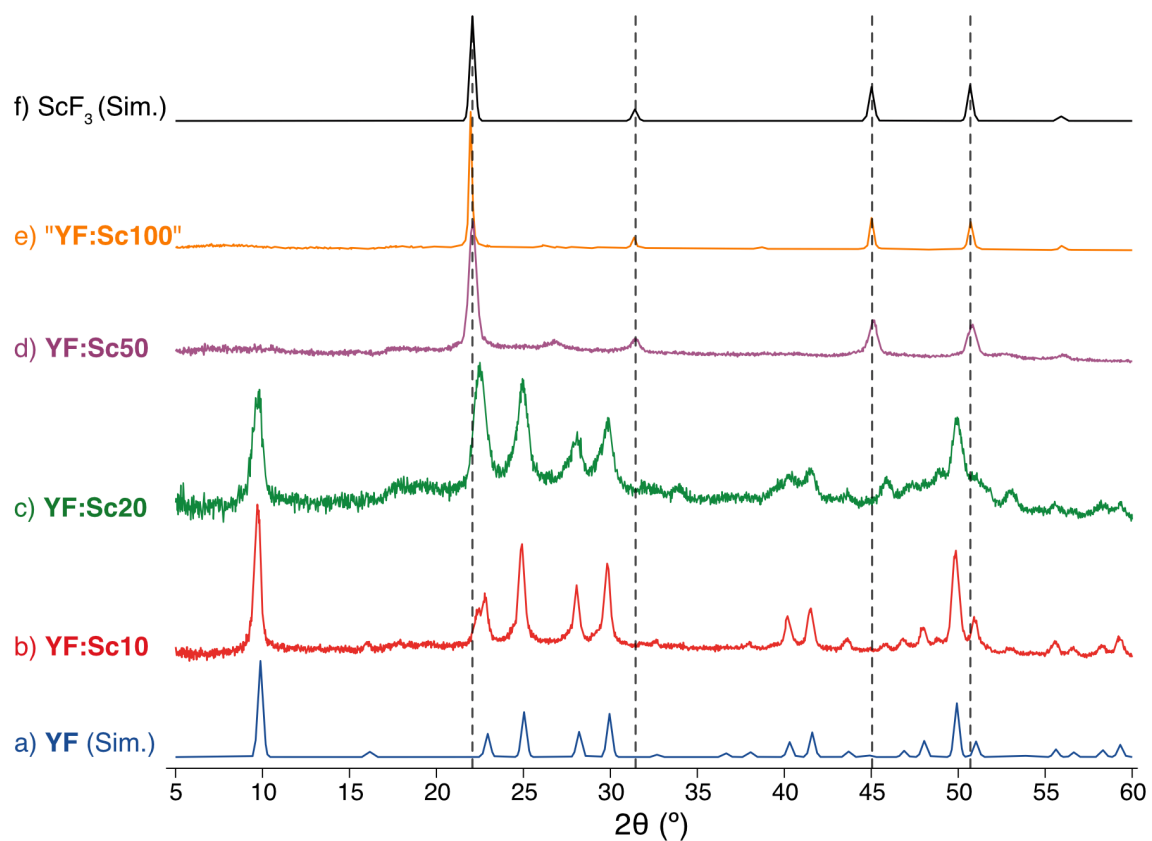


Figure C4. Powder X-ray diffraction patterns of the Sc-containing NP samples and related materials. Patterns simulated from published crystal structures are shown for a) undoped YF NPs and e) bulk ScF_3 , b-e) show experimental data for the Sc-containing samples. Dashed lines indicate features present in the pattern simulated from the crystal structure of bulk ScF_3 .³⁴

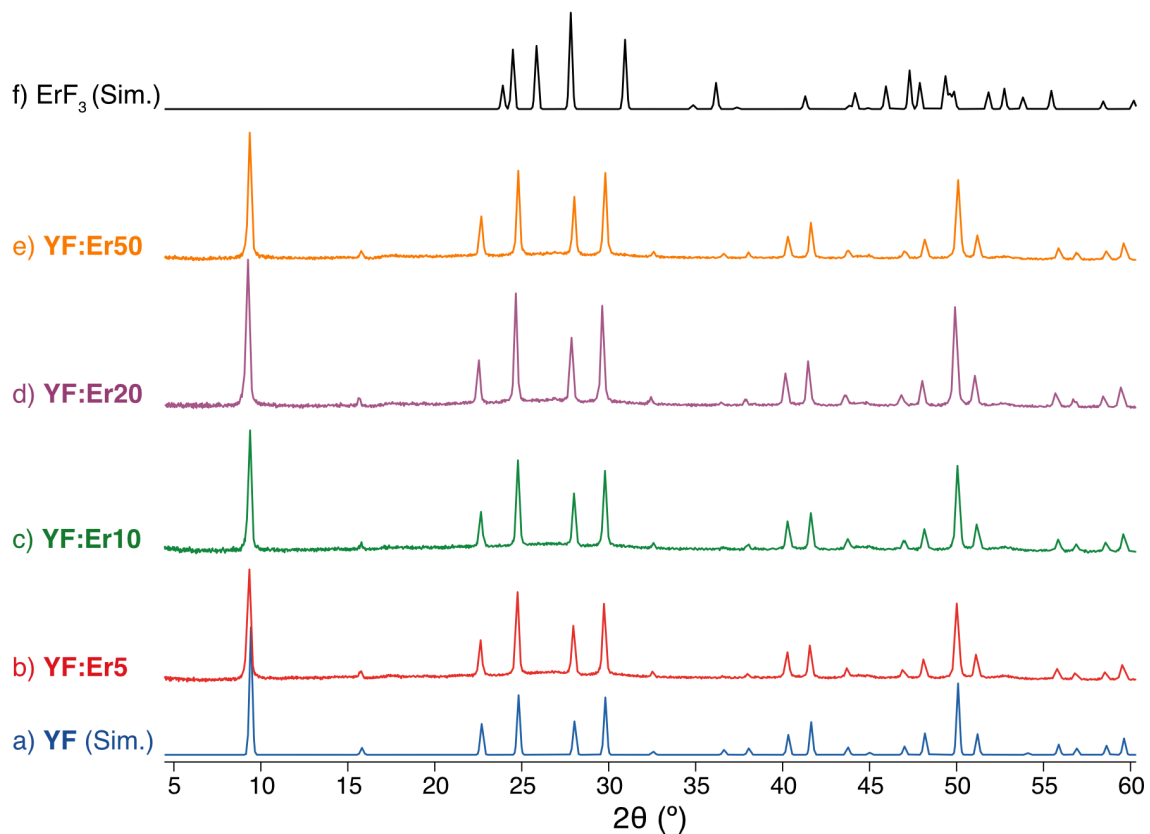


Figure C5. Powder X-ray diffraction patterns of the Er-containing NP samples and related materials. Patterns simulated from published crystal structures are shown for a) undoped **YF** NPs and e) bulk ErF_3 , b-e) show experimental data for the Er-containing samples.

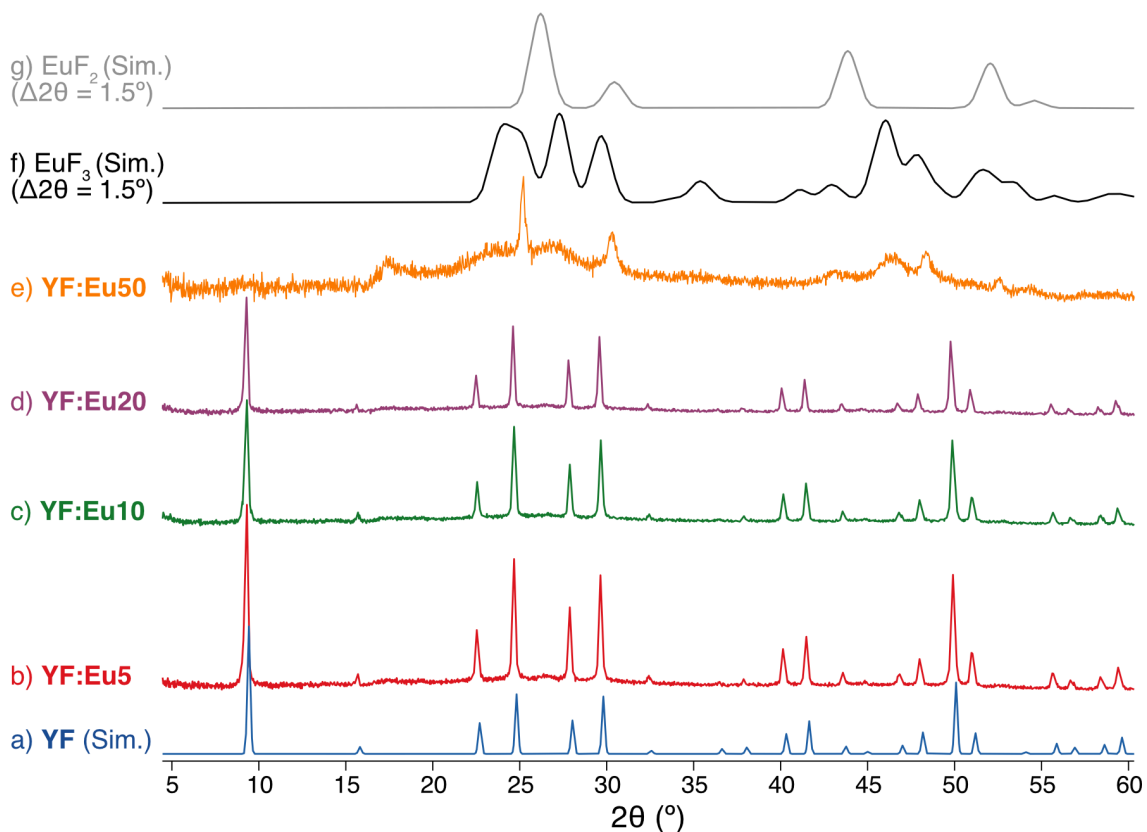


Figure C6. Powder X-ray diffraction patterns of the Eu-containing NP samples and related materials. Patterns simulated from published crystal structures are shown for a) undoped YF NPs,¹⁹ f) bulk EuF_3 ,⁶⁴ and g) bulk EuF_2 .⁶⁵ The latter 2 patterns were simulated with additional line broadening ($\Delta 2\theta = 1.5^\circ$) to simulate the effects of low crystallinity. b-e) show experimental data for the Eu-containing samples.

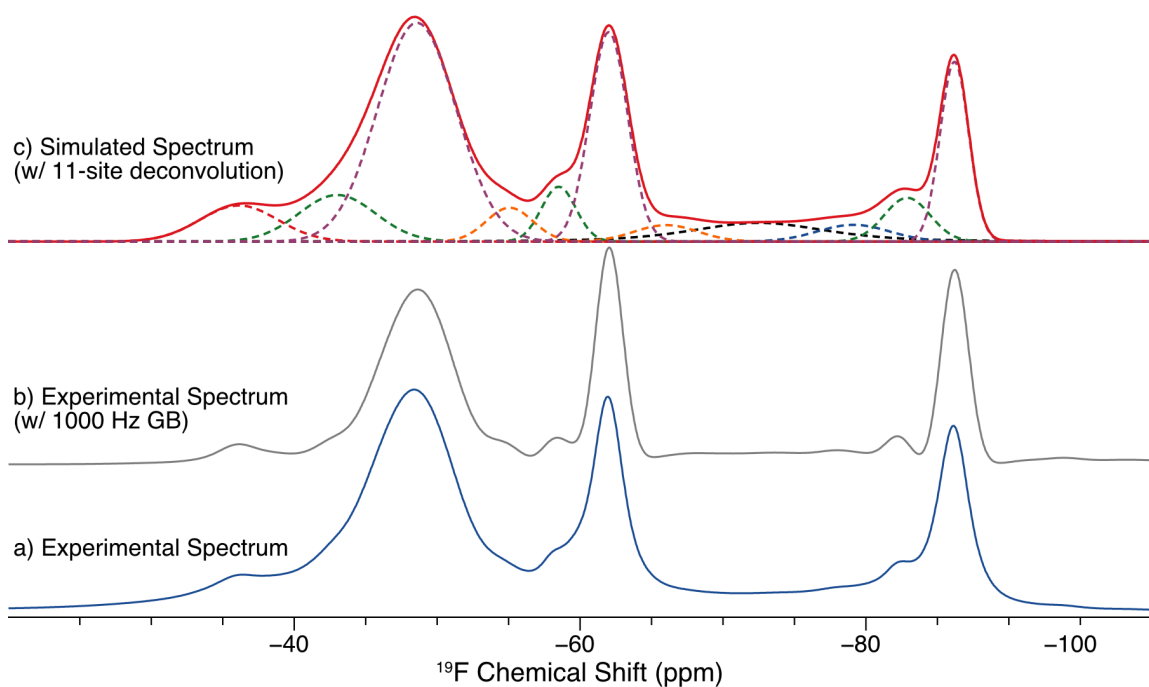


Figure C7. Experimental ^{19}F UFMAS ($\nu_{\text{rot}} = 60$ kHz) NMR spectrum of the undoped **YF** NPs processed a) without line broadening and b) with 1 kHz line broadening applied using a shifted Gaussian shape with a maximum at 1/3 of the FID (this processing enhances the resolution of the ^{19}F signal and reveals at least 11 distinct features). A simulated spectrum is shown in c) with the deconvoluted peaks and combined pattern shown as dashed and solid lines, respectively. The dashed lines in the deconvolution are colored according to their peak assignments, see text for details.

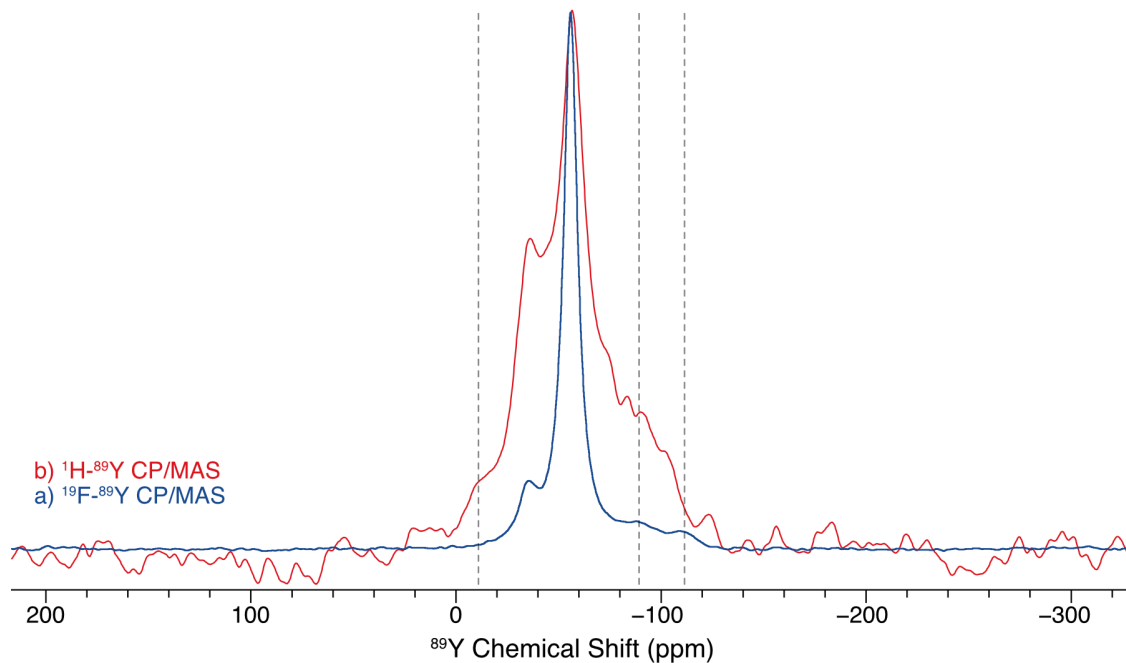


Figure C8. a) ^{19}F - ^{89}Y and b) ^1H - ^{89}Y CP/MAS ($\nu_{\text{rot}} = 5$ kHz) spectra of the undoped **YF** NPs. Dashed lines indicate peaks of interest, see text for details.

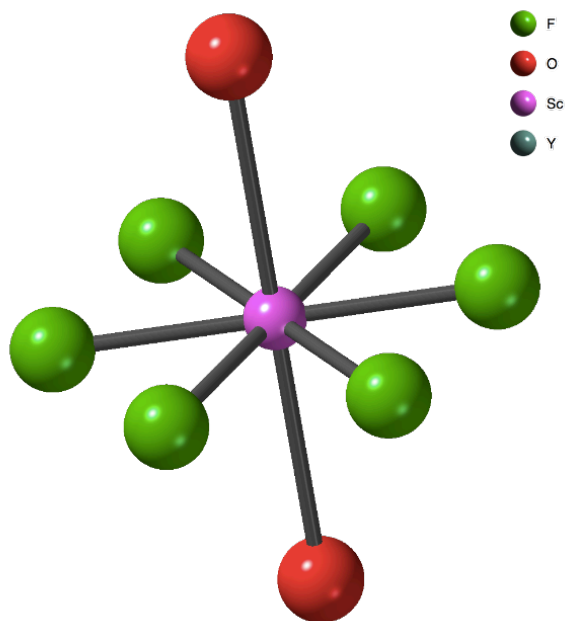


Figure C9. Possible eight-coordinate scandium environment in the Sc-doped **YF** materials. Water molecules are shown without hydrogen atoms.

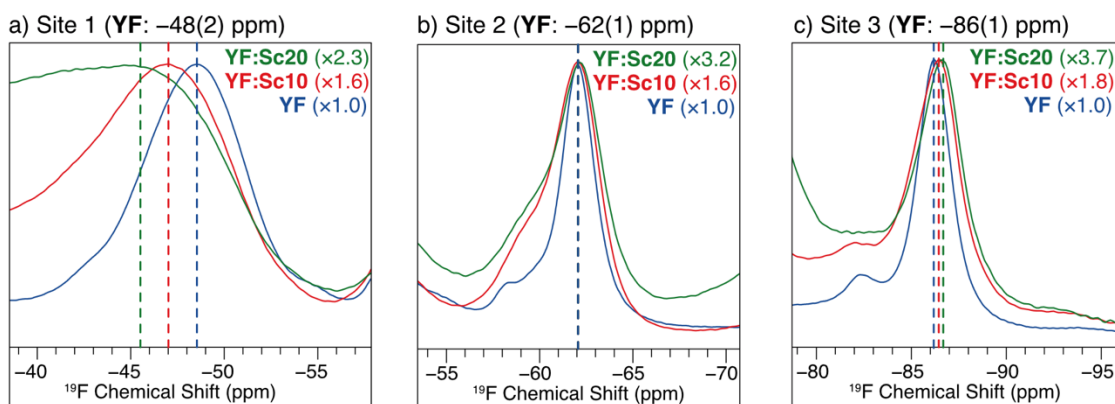


Figure C10. Expansions of the ^{19}F UFMAS ($\nu_{\text{rot}} = 60$ kHz) NMR spectra of the undoped **YF** NPs (blue trace), **YF:Sc10** (red trace), and **YF:Sc20** (green trace), showing the features corresponding to the zeolitic $(\text{H}_3\text{O})\text{Y}_3\text{F}_{10}\cdot x\text{H}_2\text{O}$ structure. Dashed lines indicate the centers of gravity of the peaks. The vertical scalings of the spectra were chosen such that the peaks have the same maximum intensities. The corresponding scaling factors are listed in the figures.

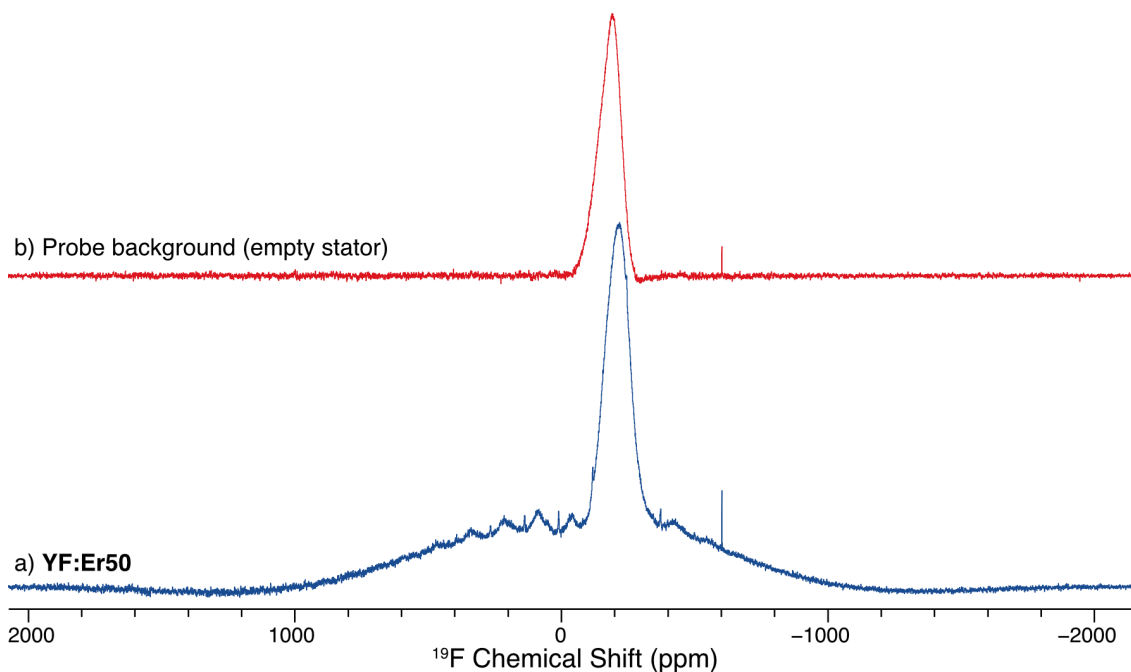


Figure C11. a) ^{19}F UFMAS ($\nu_{\text{rot}} = 60$ kHz) NMR spectrum of **YF:Er50**. The most intense figure, and a sharp figure at lower frequency are probe background signals, as demonstrated by the ^{19}F NMR spectrum acquired with an empty stator (b).

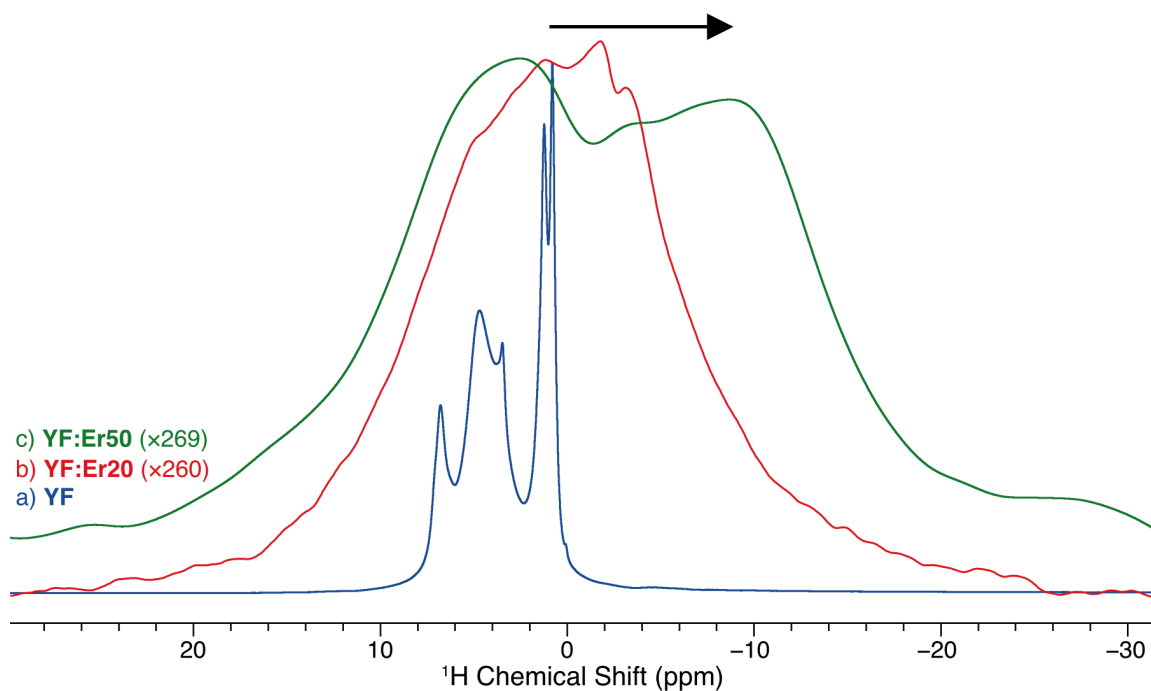


Figure C12. ^1H UFMAS ($v_{\text{rot}} = 60$ kHz) NMR spectra of a) undoped **YF** NPs, b) **YF:Er20** and c) **YF:Er50** vertically scaled to have the same maximum intensity. The arrow denotes the direction of the shift of the low frequency features with increasing dopant, see text for details.

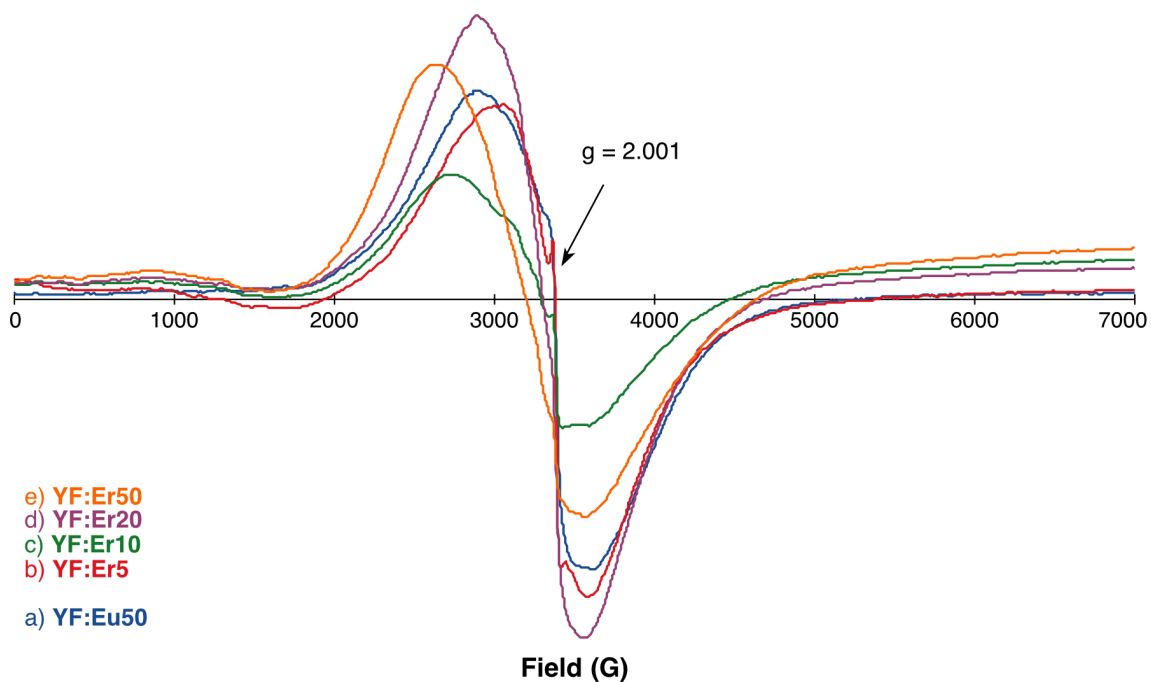


Figure C13. X-band EPR spectra of the paramagnetic samples. The arrow denotes the g -factor, which is approximately 2.001 for each sample.

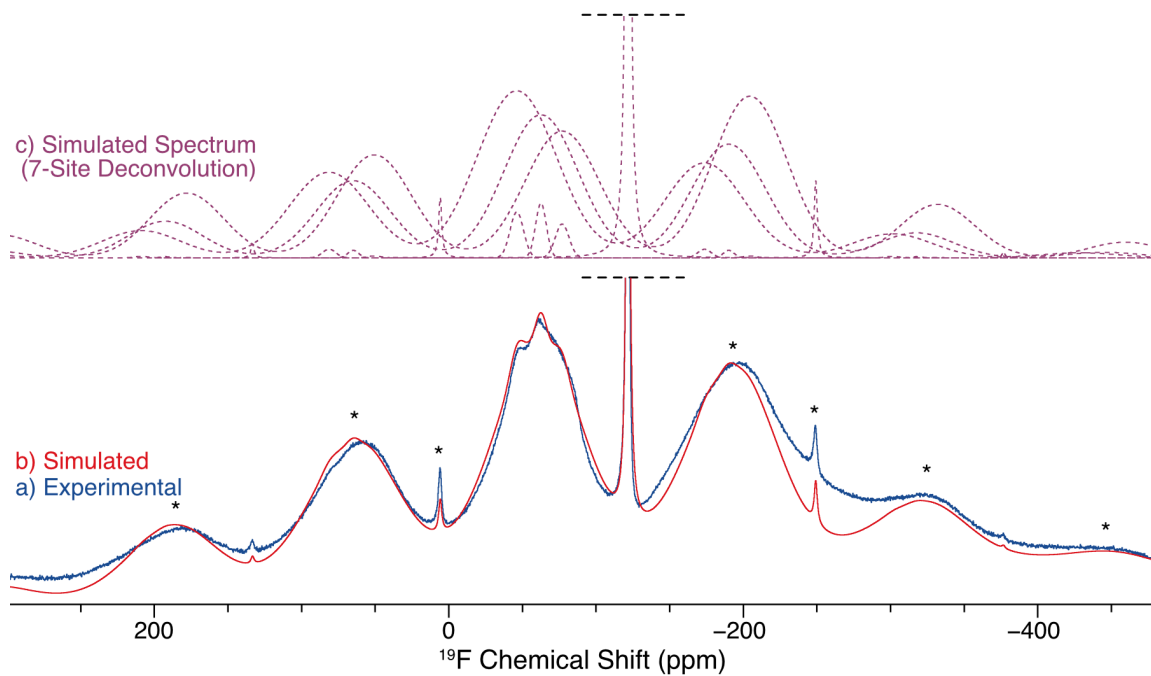


Figure C14. a) Experimental ^{19}F UFMAS ($v_{\text{rot}} = 60$ kHz) NMR spectrum of **YF:Eu50** and b) a simulated spectrum matching the experimental data. The latter was generated using seven sites, as shown in c). The feature at -122 ppm is a F^- impurity. Asterisks denote spinning sidebands.

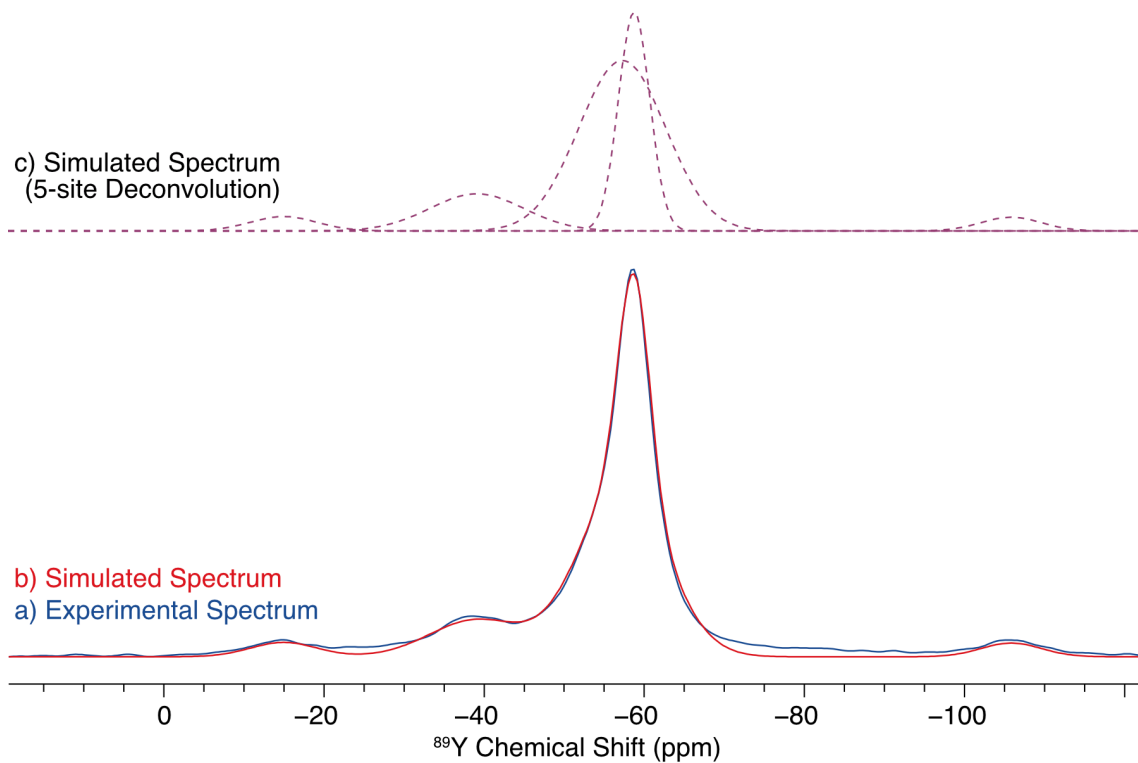


Figure C15. a) Experimental ^{19}F - ^{89}Y CP/MAS ($\nu_{\text{rot}} = 5$ kHz) NMR spectrum of **YF:Eu5** and b) a simulated spectrum matching the experimental data. The latter was generated using five sites, as shown in c).

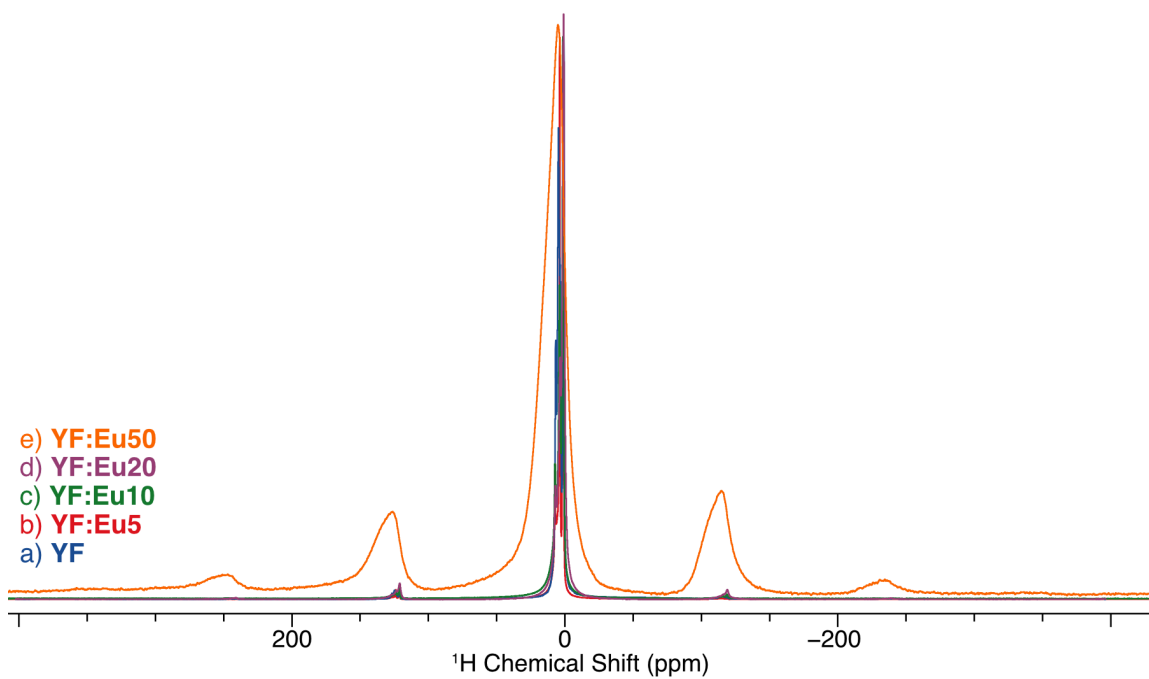


Figure C16. ^1H UFMAS ($\nu_{\text{rot}} = 60$ kHz) NMR spectra of the Eu-containing materials and **YF**. The spectra are scaled to have the same maximum intensity.

Appendix D: Supporting Tables and Figures for Chapter 5

Table D1. Sample characteristics, measured DNP enhancements, and relaxation properties.

Sample name and composition of the impregnating liquid	Brand name/retailer	$\epsilon_{\text{C}}(\text{CP})$	$\epsilon_{\text{Cl}}(\text{CP})$	$T_{\text{DNP}}(^1\text{H})$ /s	^{13}C Sensitivity	Recycle delay /s ^b
Hist (15 mM TEKPol, TCE)	Sigma-Aldrich	260	50	302	22.2	30
Ambr (15 mM TEKPol, TCE)	Sigma-Aldrich	92	15	28	38.0	30
Diph (15 mM TEKPol, 1,3-dibromobutane)	Sigma-Aldrich	25	6	3	0.7	22
Diph Dosage (15 mM TEKPol, 1,3-dibromobutane)	Life Brand (25 mg)	16	— ^a	16.9	0.5	22
Isox (15 mM TEKPol, TCE)	Sigma-Aldrich	86	12	14.7	8.0	20
Isox Dosage (15 mM TEKPol, TCE)	Prevention Labs (10 mg)	12	— ^a	13.8	2.3	20
Ceti (15 mM TEKPol, 1,3-dibromobutane)	Sigma-Aldrich	20	5.8	14.1	8.7	10
Ceti Dosage (15 mM TEKPol, 1,3-dibromobutane)	Reactine (10 mg)	8	2.6	12	8.2	10

^a $\epsilon_{\text{Cl}}(\text{CP})$ is not measurable for these dosage forms as the MW off spectra would require excessive experimental time. ^bThe optimized recycle delay of $1.3 \times T_1(^1\text{H})$ was used for both ^{13}C and ^{35}Cl experiments.

Table D2. Weight percentage of chlorine in the samples, and wt-% of the API in the dosage forms.

sample name	composition of the impregnating liquid	API wt-% ^a	Cl wt-% ^b
Hist	15 mM TEKPol, TCE	98	18.31
Ambr	15 mM TEKPol, TCE	99	8.38
Isox	15 mM TEKPol, TCE	98	10.3
Isox Dosage	15 mM TEKPol, TCE	4.95	0.52
Diph	15 mM TEKPol, 1,3-dibromobutane	98	11.9
Diph Dosage	15 mM TEKPol, 1,3-dibromobutane	6.12	0.74
Ceti	15 mM TEKPol, 1,3-dibromobutane	98	7.52

^aThe percent weight of the active ingredient within the bulk form (*i.e.*, purity) was indicated by Sigma-Aldrich upon purchase. The percent weight of the active ingredient within the dosage form was calculated as follows: % weight of API = $\frac{\text{Dose of active ingredient}}{\text{Tablet weight}} \times 100\%$

^bThe percent weight of Cl within the bulk form was calculated as follows:

$$\% \text{ weight of API} = \frac{\text{moles Cl}}{\text{moles API}} \times \frac{\text{MW of Cl}}{\text{MW of API}} \times \text{purity of sample} \times 100\%$$

The percent weight of the Cl within the dosage form was calculated as follows:

$$\% \text{ weight of Cl} = \left[\frac{\left(\frac{\text{Stoichiometric MW of Cl in API}}{\text{MW of API}} \right) \times \text{Dose of API}}{\text{Tablet Mass}} \right] \times 100\%$$

Table D3. Acquisition parameters for ^1H - ^{13}C CP/MAS SSNMR experiments.

		Hist	Ambr	Isox		Diph		Ceti	
		Bulk	Bulk	Bulk	Dosage	Bulk	Dosage	Bulk	Dosage
Number of Scans	MW on	4	4	8	64	32	4	8	8
	MW off	4	4	8	256	64	16	8	8
Experimental time (min)	MW on	2.0	2.0	2.4	19.2	2.1	1.5	1.3	1.3
	MW off	2.0	2.0	2.4	76.8	4.3	5.9	1.3	1.3
Recycle delay (s)		30	30	18	18	4	22	10	10
Spinning speed (kHz)		8	8	9	9	8	8	8	8
^1H 90° pulse width [$\pi/2$] (μs)		2.8	2.5	2.5	2.5	2.5	2.5	2.5	2.5
Contact time (ms)		2	2	2	2	2	2	2	2
^1H rf field during contact pulse (kHz)		100	100	100	100	100	100	100	100
^{13}C rf field during contact pulse (kHz)		71	71	71	71	71	71	71	71
^1H decoupling field (kHz)		90	90	90	90	90	90	90	90
Spectral width (kHz)		59.5	59.5	59.5	59.5	59.5	59.5	59.5	59.5
Acquisition length (number of points)		3802	3802	3802	2970	2048	3802	3802	3802

Table D4. Acquisition parameters for ^{13}C - ^{35}Cl D-HMQC- R_3 /MAS SSNMR experiments on hist.

	Hist
Spinning frequency (kHz)	8
Number of scans per t1 increment	8
Number of t1 increment	256
Recycle delay (s)	25
t1 increment (μs)	62.5
Spectral width in F2 (kHz)	25
Spectral width in F1 (kHz)	16
Acquisition length (number of points in F2)	1500
^1H 90° pulse width [$\pi/2$] (μs)	2.5
^{13}C 90° pulse width [$\pi/2$] (μs)	3.0
^{35}Cl 90° pulse width [$\pi/2$] (μs)	3.1
^{13}C R3 recoupling power (kHz)	9.6
Contact pulse length (ms)	2
^1H rf field during contact pulse (kHz)	80
^{13}C rf field during contact pulse (kHz)	40
^1H rf field during decoupling (kHz)	100

Table D5. Acquisition parameters for ^1H - ^{35}Cl CP SSNMR experiments on hist.

		CP-CPMG	CP-echo (slow MAS)	CP-echo (MAS)
Number of Scans	MW on	4	4	4
	MW off	8	4	16
Experimental time (min)	MW on	2.5	0.7	4
	MW off	5	0.7	16
Spinning speed (Hz)		0	250	8000
Recycle delay (s)		30	10	60
Spectral Width (kHz)		100	100	50
^1H $\pi/2$ pulse width (μs)		2.5	2.8	2.5
Contact time (ms)		6	6	9
^1H rf field during contact pulse (kHz)		70.7	70.7	50
^{35}Cl rf field during contact pulse (kHz)		51	51	18
^1H decoupling field (kHz)		87	100	50
Acquisition length (number of points)		13400	512	800
Meiboom-Gill loops [N] (i.e. Number of echoes)		30	-	-
Refocusing pulse width (μs)		6.6	-	-

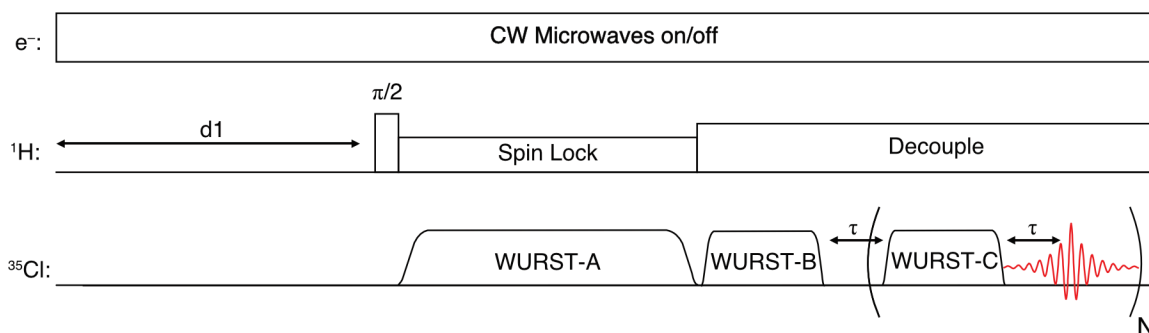
Table D6. Acquisition parameters for ^1H - ^{35}Cl BCP SSNMR experiments.

	Ambr	Isox		Diph		Ceti	
	Bulk	Bulk	Dosage	Bulk	Dosage	Bulk	Dosage
Number of scans	16	16	3200	512	1024	32	2048
Experimental time (h)	0.3	0.1	16.0	3.1	6.3	0.2	10.2
Recycle delay (s)	30	20	18	22	22	18	18
Spectral Width (kHz)	500	500	500	500	500	500	500
^1H $\pi/2$ pulse width (μs)	2.5	2.5	2.5	2.5	2.5	2.5	2.5
Contact time (ms)	15	8	8	8	8	25	25
^1H Hartmann-Hahn matching field (kHz)	75	75	75	75	75	75	75
^{35}Cl Hartmann-Hahn matching field (kHz)	69	69	69	69	69	69	69
^1H decoupling field (kHz)	95	95	95	95	95	95	95
Meiboom-Gill loops [N] (i.e., Number of echoes)	250	250	160	50	50	200	200
Acquisition length (number of points)	75250	75250	48250	15270	15270	60250	60250
Refocusing pulse width (μs)	25	25	25	25	25	25	25
Sweep range of refocusing pulses (kHz)	250	250	250	250	250	250	250
Sweep range of ^{35}Cl contact pulse (μs)	250	200	250	150	150	250	250

Table D7. Experimental ^{35}Cl EFG tensor parameters for the HCl salts.^a

Sample name	C_Q (MHz) ^b	η_Q ^c	δ_{iso} (ppm) ^d	Ω (ppm) ^{e,h}	κ ^{f,h}	α (°) ^{g,h}	β (°) ^{g,h}	γ (°) ^{g,h}
Hist	1.8(1)	0.72(2)	16(5)	—	—	—	—	—
Ambr	5.6(2)	0.82(2)	74(25)	—	—	—	—	—
Diph	4.6(2)	0.16(4)	50(50)	20(50)	0.48(25)	0(90)	0(45)	0(45)
Isox	5.7(2)	0.27(3)	120(50)	50(50)	0.5(3)	0(90)	0(45)	0(45)
Ceti	Site 1	7.3(1)	0.65(5)	120(10)	—	—	—	—
	Site 2	4.0(5)	0.90(5)	50(10)	—	—	—	—

^aThe experimental uncertainty in the last digit(s) for each value is indicated in parentheses. ^b $C_Q = eQV_{33}/h$; ^c $\eta_Q = (V_{11} - V_{22})/V_{33}$; ^d $\delta_{\text{iso}} = (\delta_{11} + \delta_{22} + \delta_{33})/3$; ^e $\Omega = \delta_{11} - \delta_{33}$; ^f $\kappa = 3(\delta_{22} - \delta_{\text{iso}})/\Omega$. ^gThe Euler angles, α , β , and γ , define the relative orientation of the CS and EFG tensors. ^hAccurate determination of the CSA parameters and Euler angles is not possible without spectra acquired at a second field strength. For diph and isox, CSA parameters were used based on those previously reported.²¹

**Figure D1.** ^1H - ^{35}Cl BCP pulse sequence used for the DNP-enhanced ^{35}Cl SSNMR experiments. For experiments with SOSO, the sample was rotated during the recycle delay ($d1$).

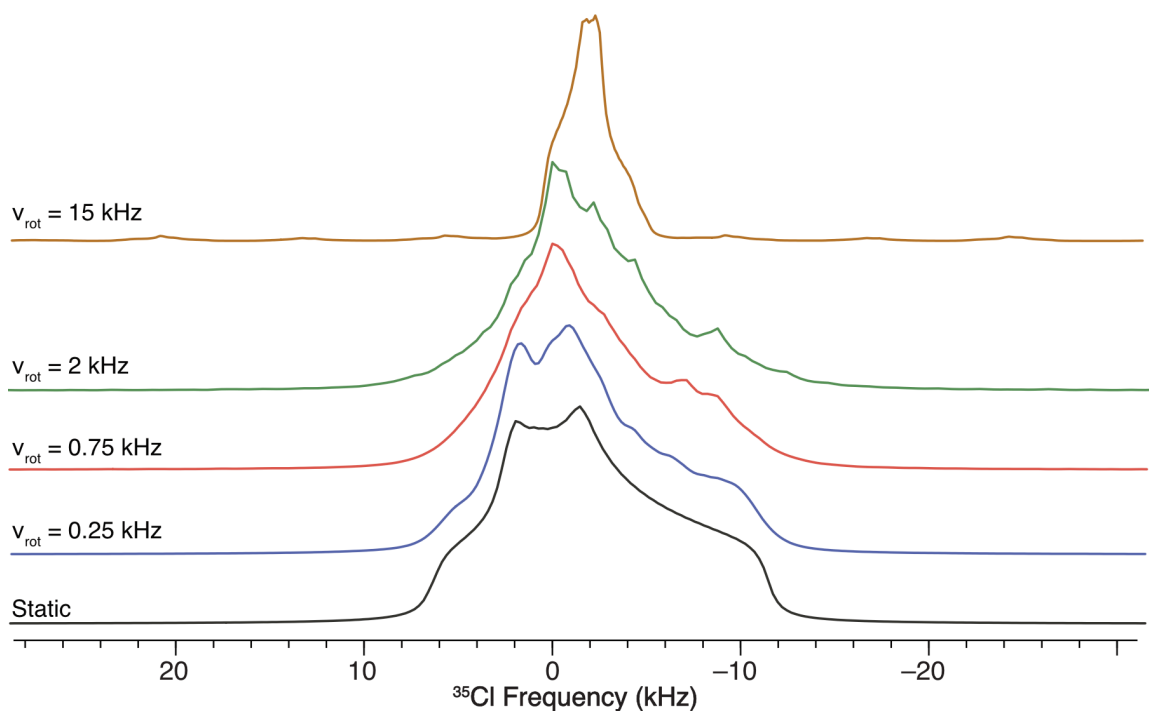


Figure D2. Simulated ^{35}Cl SSNMR spectra of hist under MAS at various spinning speeds.

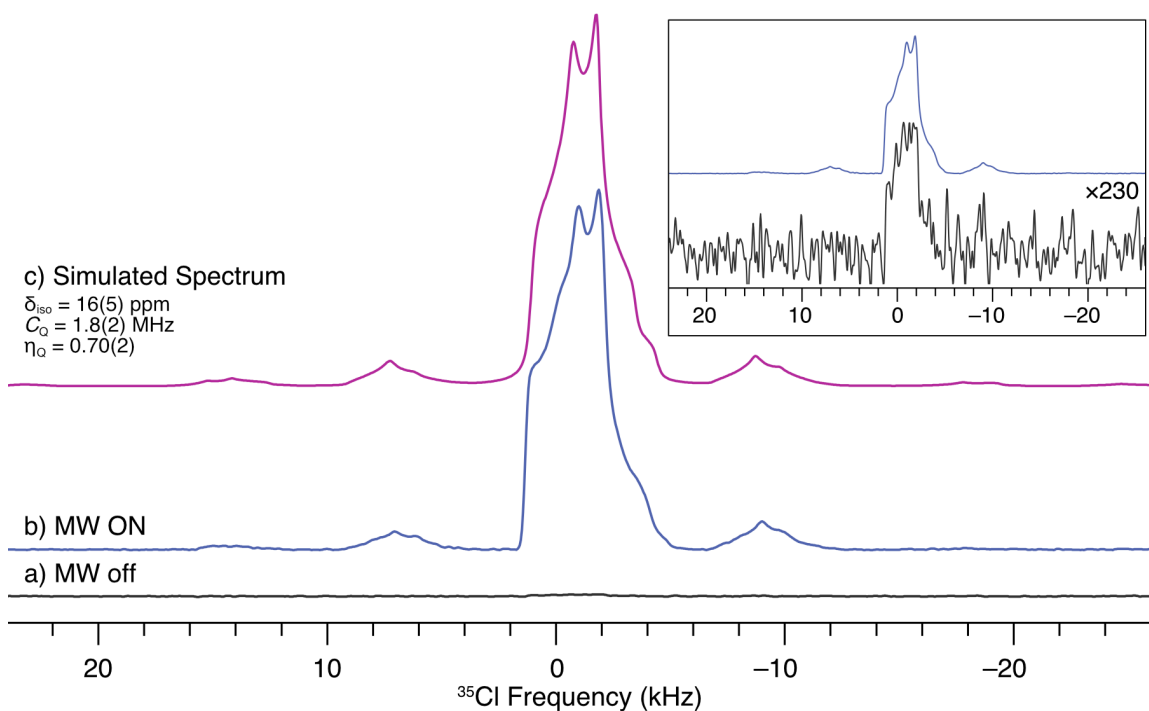


Figure D3. ^1H - ^{35}Cl CP-echo MAS ($v_{\text{rot}} = 8$ kHz) SSNMR spectra of hist acquired with a) microwaves off, and b) microwaves on. c) shows an analytical simulation of the spectra and the parameters used to generate the simulated spectrum. The inset contains the experimental spectra scaled to the same maximum intensity.

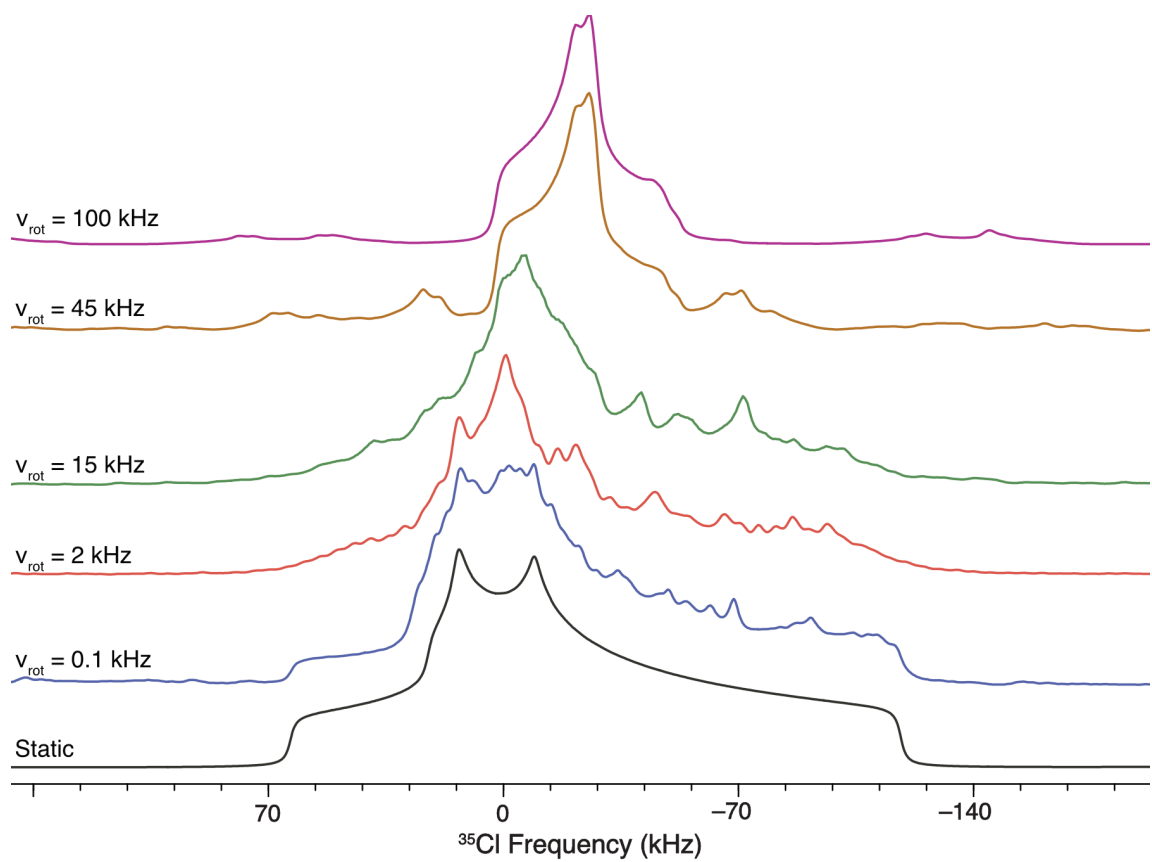


Figure D4. Simulated ^{35}Cl SSNMR spectra of ambr under MAS at various spinning speeds.

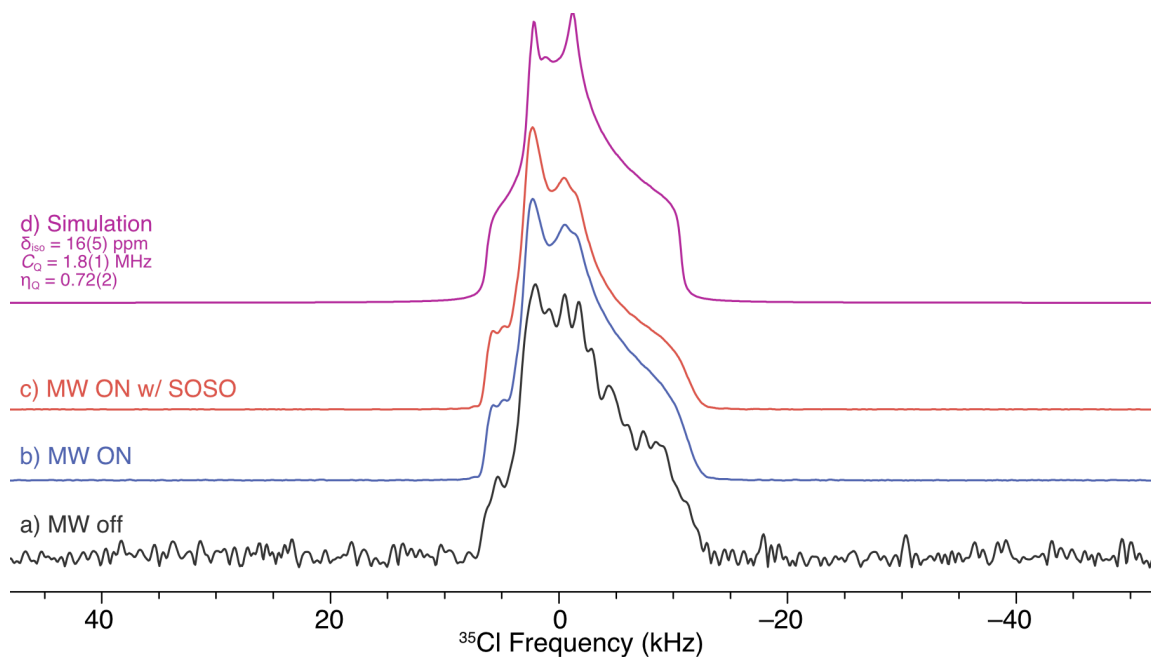


Figure D5. ^1H - ^{35}Cl CP SSNMR spectra of hist (a-c) and the corresponding analytical simulation (d). The parameters used to generate the simulated spectrum are shown in the figure.

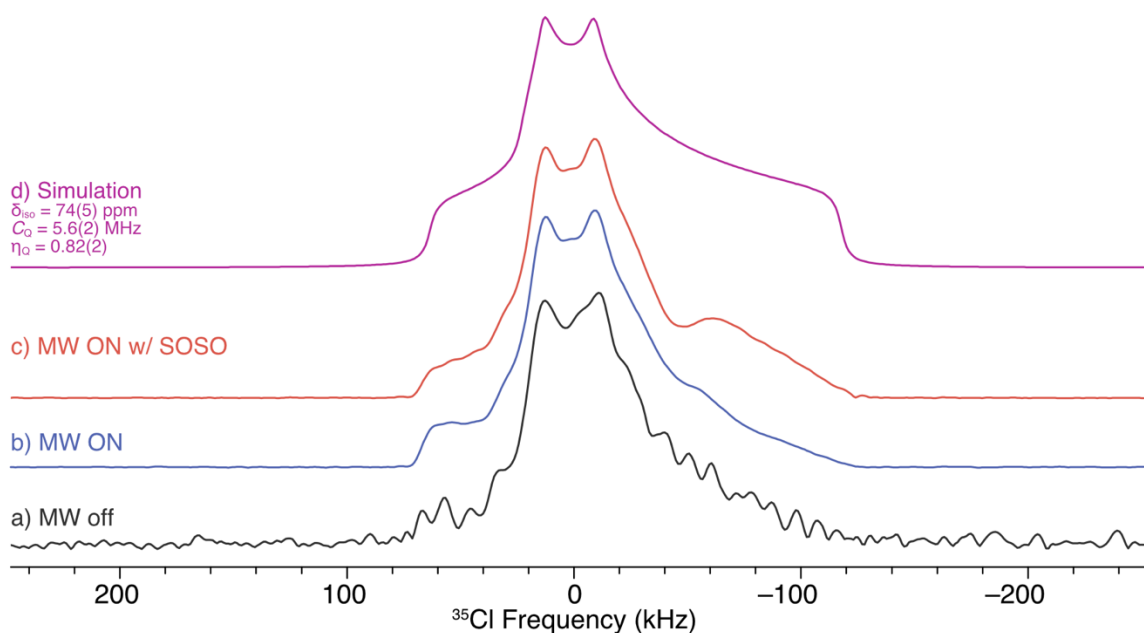


Figure D6. ^1H - ^{35}Cl CP SSNMR spectra of ambr (a-c) and the corresponding analytical simulation (d). The parameters used to generate the simulated spectrum are shown in the figure.

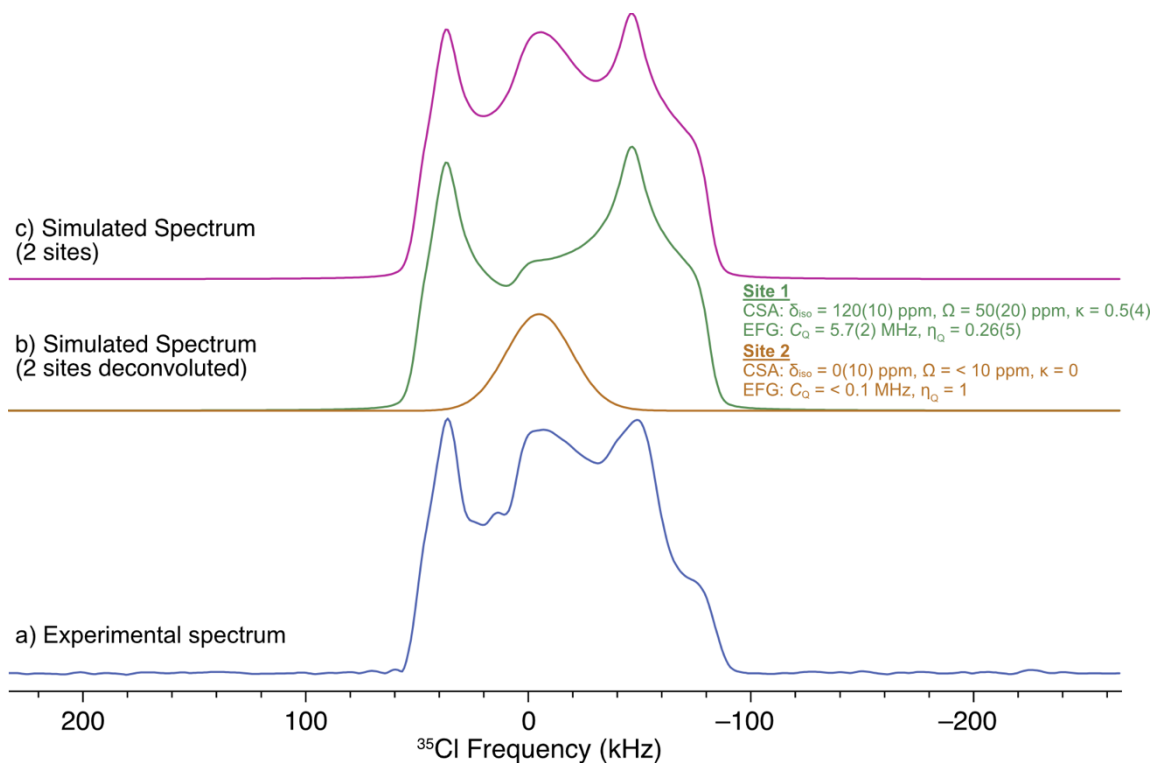


Figure D7. ^1H - ^{35}Cl CP SSNMR spectrum of isox (a) and the corresponding two-site analytical simulation (b-c). Parameters used to generate the simulated spectra are listed in the figure.

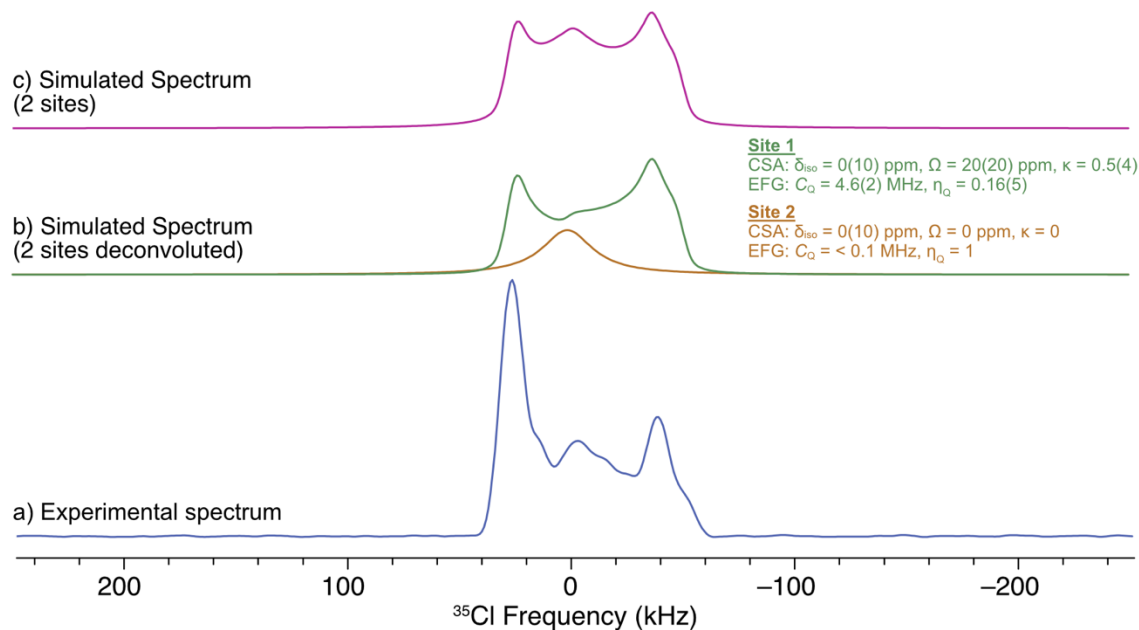


Figure D8. ^1H - ^{35}Cl BCP SSNMR spectrum of diph (a) and the corresponding two-site analytical simulation (b-c). Parameters used to generate the simulated spectra are listed in the figure.

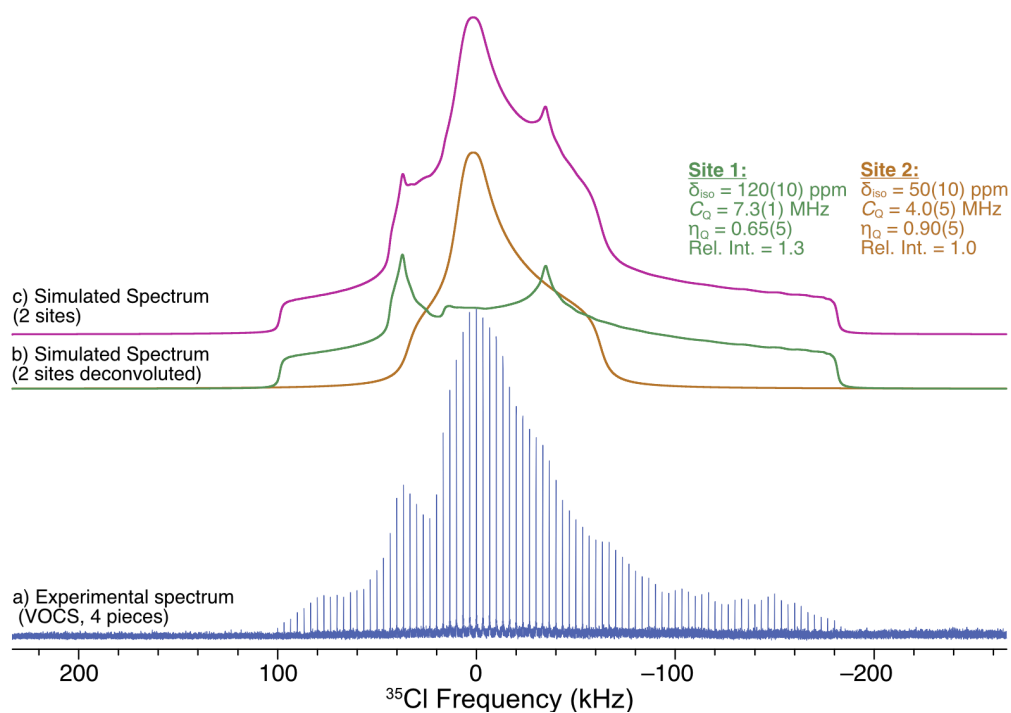


Figure D9. a) Experimental ^1H - ^{35}Cl BCP SSNMR spectrum of ceti acquired with VOCS acquisition. Four sub-spectra were coadded together to produce the final spectrum. b) and c) show the 2-site simulation of the pattern as a deconvolution and combined spectrum, respectively. The quadrupolar parameters associated with this simulation are shown on the right of the figure.

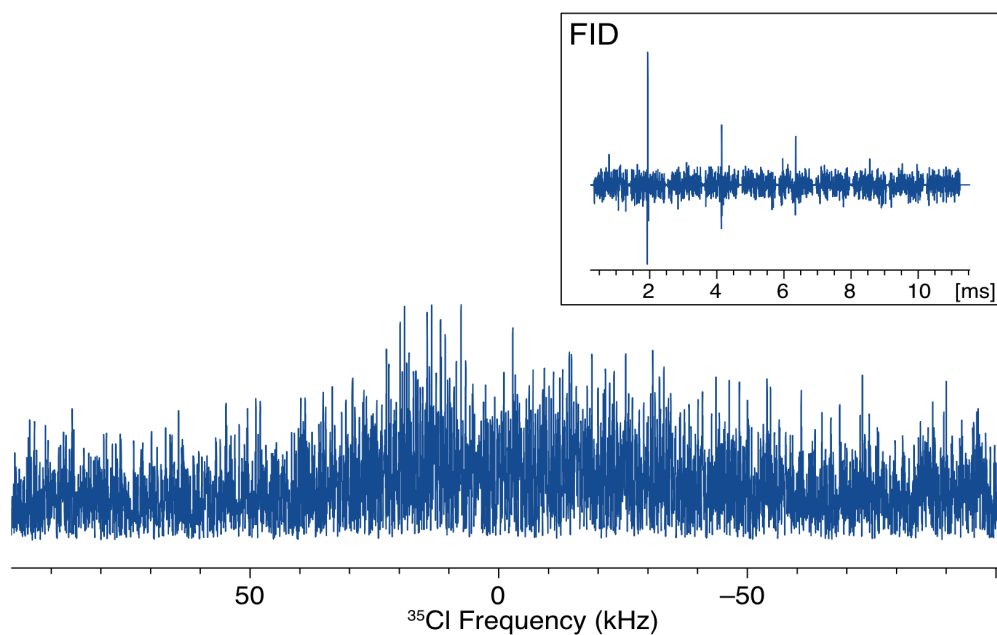


Figure D10. ^1H - ^{35}Cl BCP spectrum of ambr acquired with 700 mb bearing gas flow and no drive gas flow (~ 4 Hz spinning detected). The FID for this spectrum (inset) has several echoes that are not properly refocused due to the spinning.

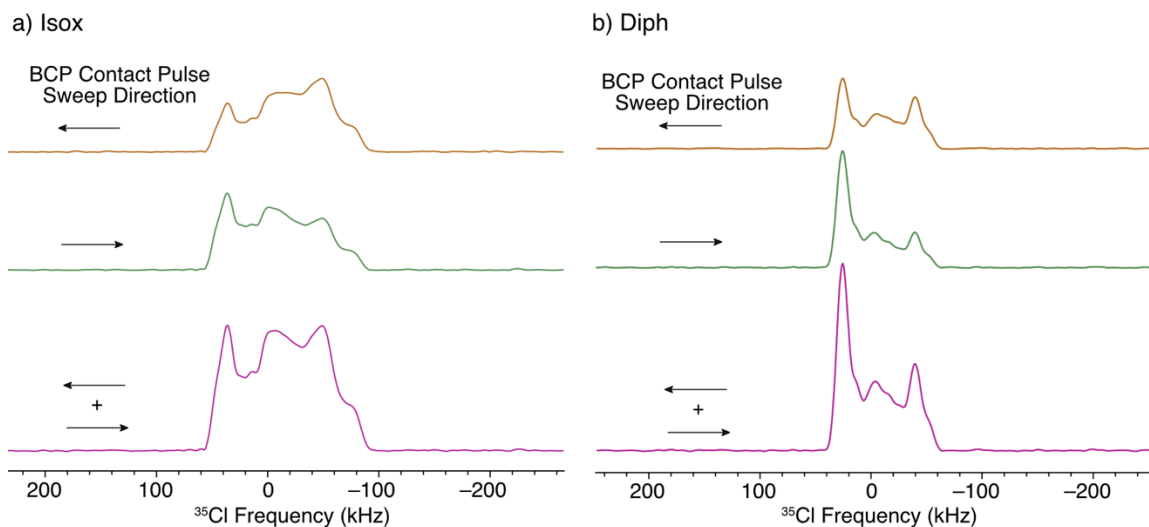


Figure D11. ^1H - ^{35}Cl BCP SSNMR spectra of a) isox and b) diph acquired with MW on. As shown in the figure, the sweep direction of the BCP contact pulse has a large effect on the shape of the pattern. This effect may result from relaxation processes [*i.e.*, $T_{1\rho}(^1\text{H})$] occurring over the course of the swept pulse that cause differences in CP efficiency. The true lineshape is obtained by combining two sub-spectra acquired when sweeping in opposite directions (purple).

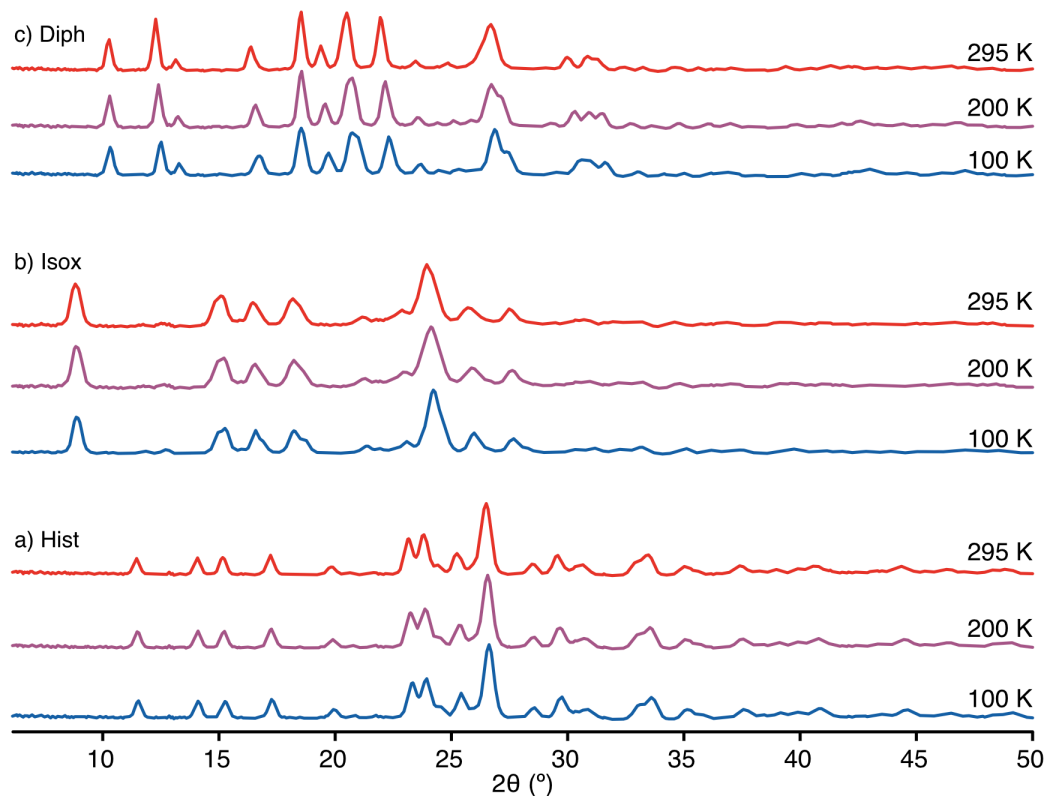


Figure D12. VT-PXRD diffraction patterns of a) hist, b) isox, and c) diph acquired at three temperatures: 295 K, 200 K, and 100 K. The patterns indicate that the crystalline structure of each material remains unchanged with cooling to 100 K.

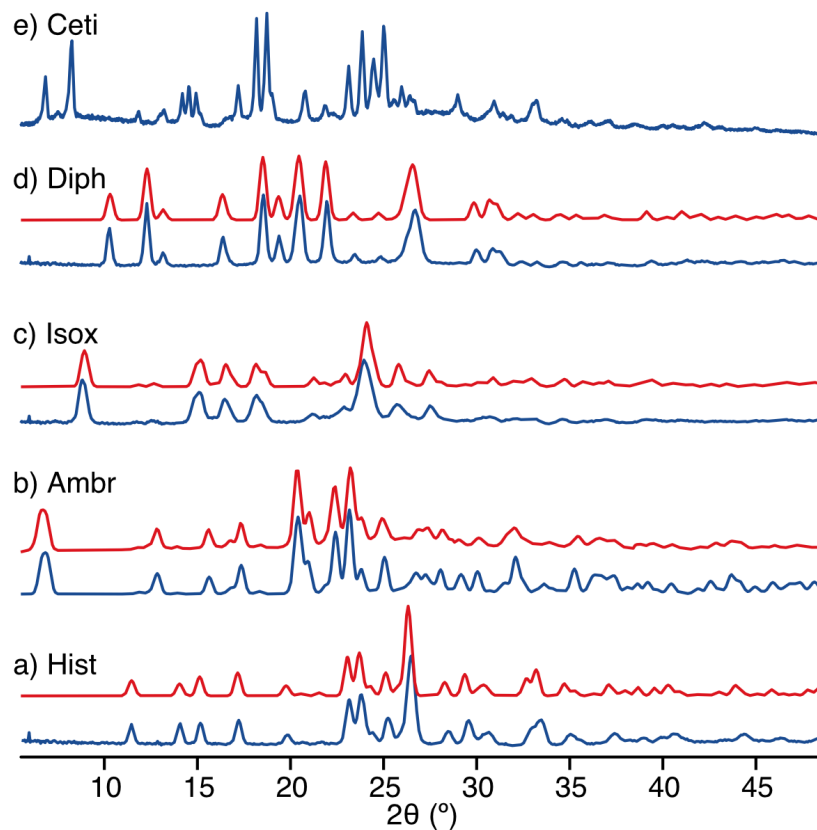


Figure D13. PXRD patterns of as received a) hist, b) ambr, c) isox, d) diph, and e) ceti obtained experimentally at 298 K (blue) or simulated using published crystal structures⁸¹⁻⁸⁴ (red). No simulated pattern is available for ceti due to the lack of a published crystal structure.

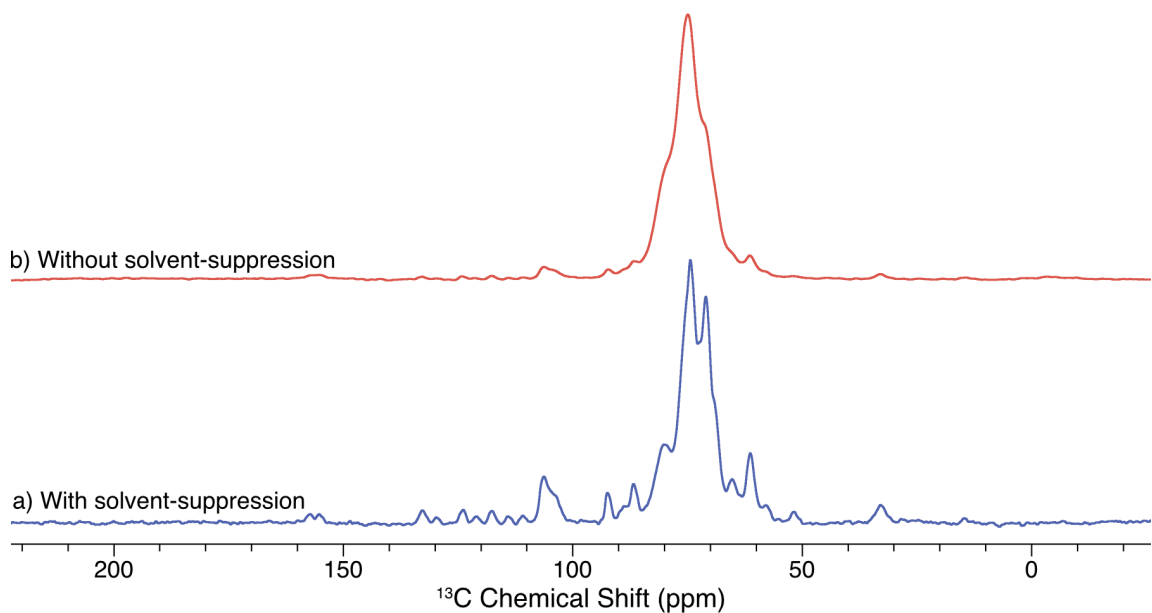


Figure D14. ^1H - ^{13}C CP/MAS ($\nu_{\text{rot}} = 9$ kHz) spectra of the dosage form of isox acquired a) with a 10 ms spin-echo added to the pulse sequence for solvent suppression, and b) without the use of a spin-echo.

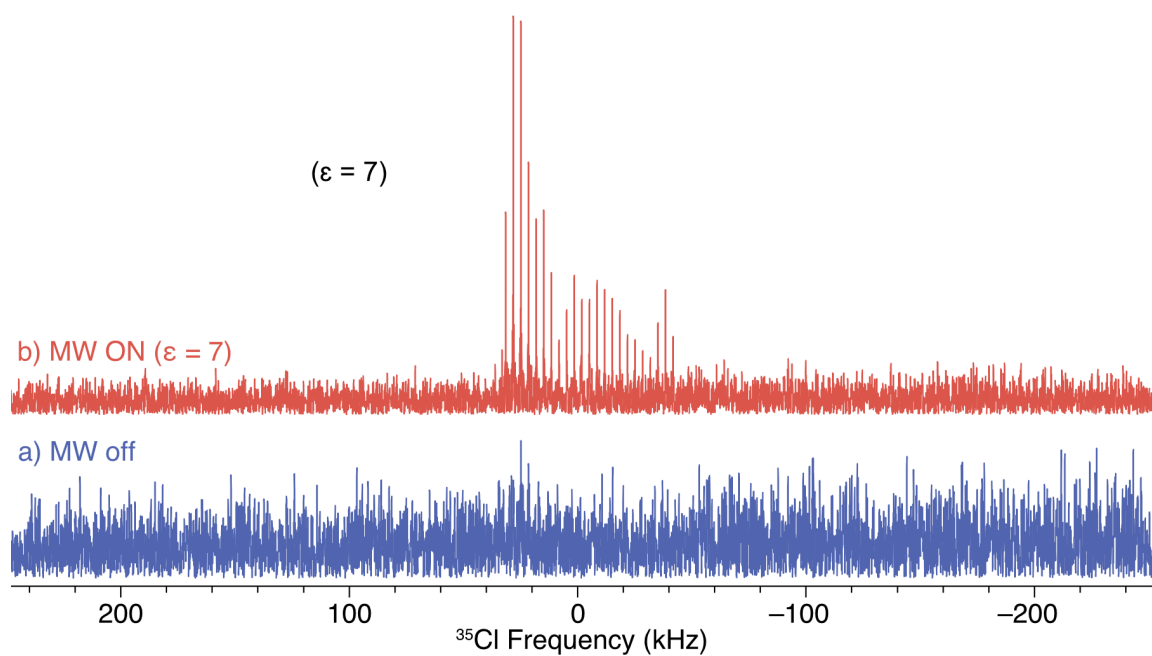


Figure D15. ^1H - ^{35}Cl BCP spectra of diph acquired with a) microwaves off and b) microwaves on used to measure the DNP enhancement. Both spectra were acquired with one BCP sweep direction and a Fourier transform was applied directly to the CPMG echo train (*i.e.*, without coadding the echoes).

Appendix E: Supporting Tables and Figures for Chapter 6

Table E1. Acquisition parameters for $^{35}\text{Cl}\{^1\text{H}\}$ WURST-CPMG experiments on the **PiogHCl** samples under static sample conditions.

	All Samples
Number of scans	14400
Experimental time (h)	4
Recycle delay (s)	1
Spectral Width (MHz)	1
^{35}Cl WURST pulse width (μs)	25
^{35}Cl WURST pulse rf (kHz)	20.3
^1H decoupling field (kHz)	61.5
Sweep range of WURST pulses (kHz)	500
Points in WURST shape [N]	500
Meiboom-Gill loops [N] (i.e., Number of echoes)	122
Length of echoes (μs)	125
Acquisition length (number of points)	53250

Table E2. Acquisition parameters for $^{23}\text{Na}\{^1\text{H}\}$ MAS ($v_{\text{rot}} = 12$ kHz) Hahn echo experiments on the mixed samples containing NaSt.

	All Samples
Number of scans	2048
Experimental time (min)	34.1
Recycle delay (s)	1
^{23}Na 90° (CT-selective) pulse width [$\pi/2$] (μs)	1.25
Inter-pulse delay [τ] (μs)	83.3
^{23}Na 180° (CT-selective) pulse width [π] (μs)	2.5
^{23}Na rf field (kHz)	100
^1H rf decoupling strength (kHz)	67.4
Spectral width (kHz)	50
Acquisition length (# of points)	4096

Table E3. Acquisition parameters for ^1H MAS ($\nu_{\text{rot}} = 12$ kHz) Hahn echo experiments on the PiogHCl and stearate-containing samples.

All Samples	
Number of scans	16
Experimental time (min)	5.3
Recycle delay (s)	20
^1H 90° pulse width [$\pi/2$] (μs)	2.5
Inter-pulse delay [τ] (μs)	83.3
^1H 180° pulse width [π] (μs)	5
^1H rf field (kHz)	100
Spectral width (kHz)	100
Acquisition length (# of points)	4096

Table E4. Acquisition parameters for ^1H - ^{13}C CP/MAS ($\nu_{\text{rot}} = 12$ kHz) experiments on the PiogHCl and stearate-containing samples.

All Samples	
Number of scans	2880
Experimental time (hrs)	4
Recycle delay (s)	5
^1H 90° pulse width [$\pi/2$] (μs)	2.5
Contact time (ms)	2
^1H rf field during contact pulse (kHz)	43
^{13}C rf field during contact pulse (kHz)	48
^1H decoupling field (kHz)	47
Spectral width (kHz)	59.5
Acquisition length (number of points)	4096

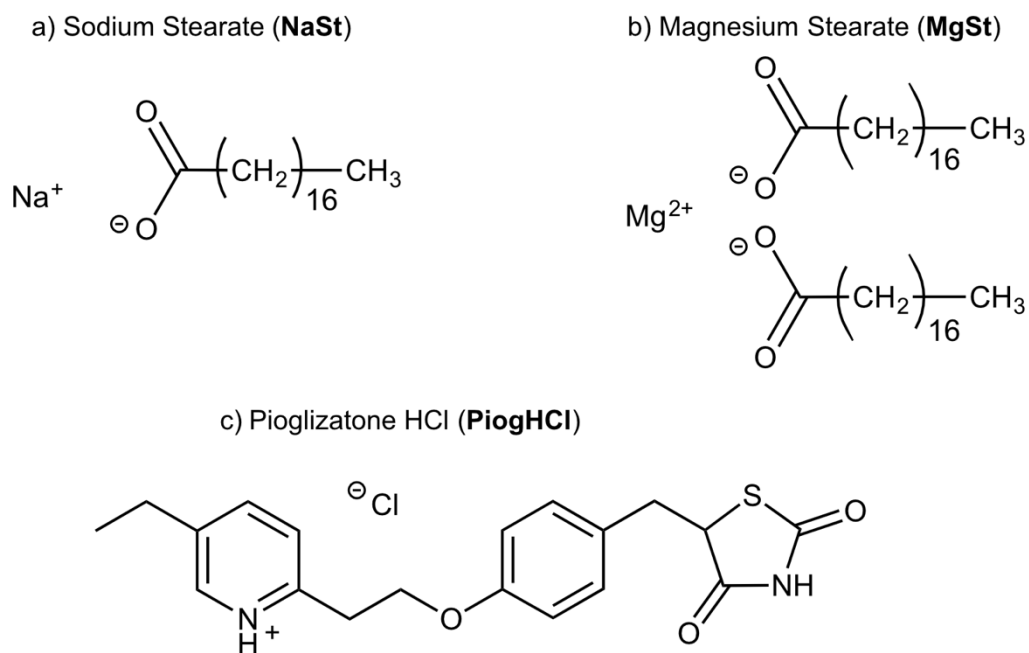


Figure E1. Molecular structures of the compounds used in this study.

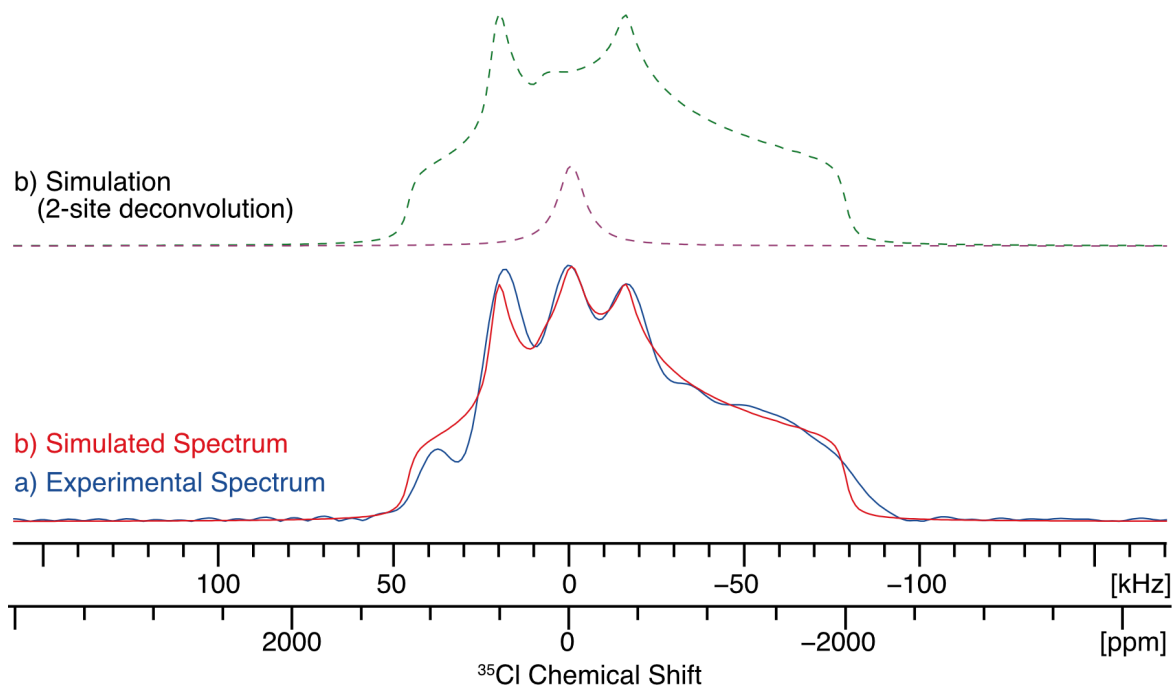


Figure E2. a) Experimental $^{35}\text{Cl}\{^1\text{H}\}$ WURST-CPMG NMR spectrum of **NaSt_X**, and b) the corresponding analytical simulation of the pattern constructed with the 2 subspectra shown in c). The broader site (green dashed line) was created with the parameters from the ^{35}Cl NMR spectrum of pure **PiogHCl**.

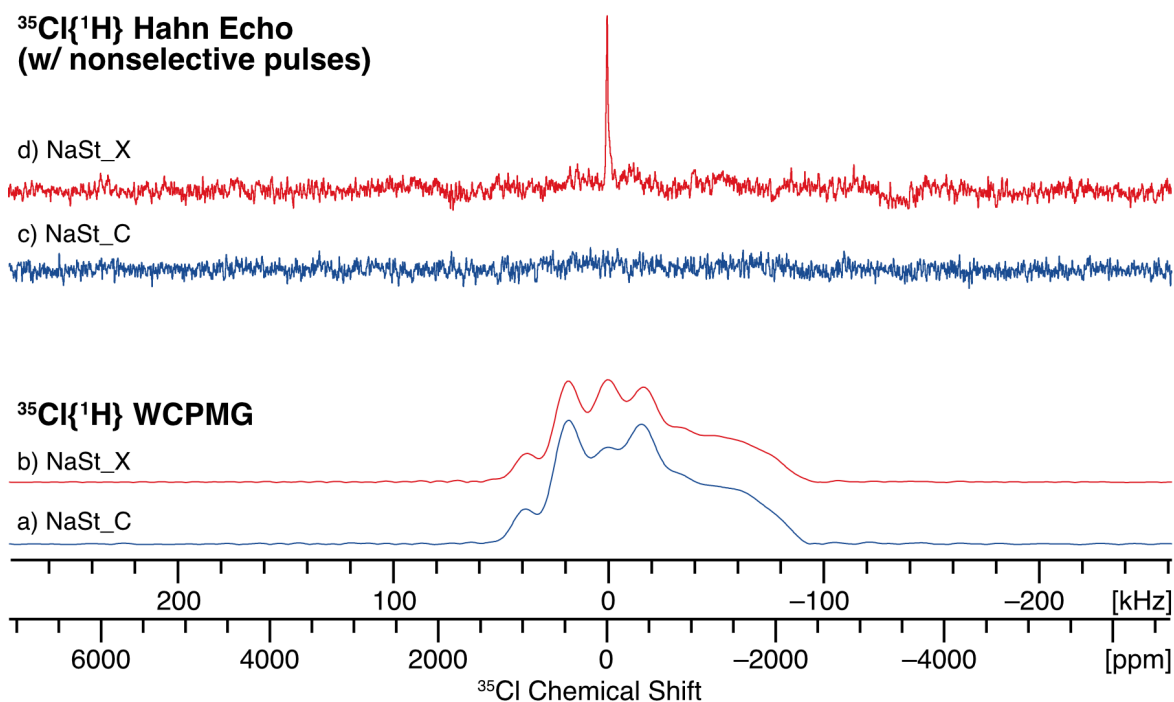


Figure E3. $^{35}\text{Cl}\{^1\text{H}\}$ NMR spectra of the NaSt-containing sample mixtures, a) and c) NaSt_C, b) and d) NaSt_X. The spectra at the bottom were acquired with WURST-CPMG, the spectra at the top were acquired with a Hahn echo sequence using nonselective pulses.

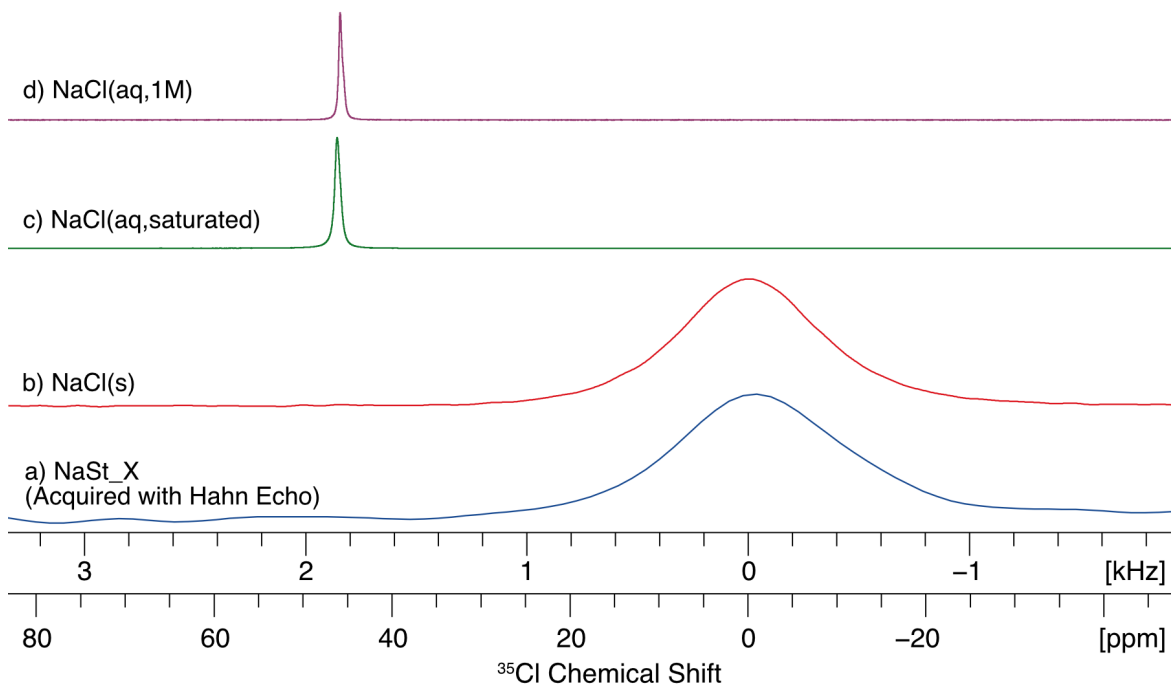


Figure E4. $^{35}\text{Cl}\{^1\text{H}\}$ Hahn echo NMR spectra of a) NaSt_X, b) solid NaCl, c) saturated NaCl solution in H_2O , and d) 1 M NaCl solution in H_2O . The spectrum of NaSt_X is the same as that in **Figure E3**.

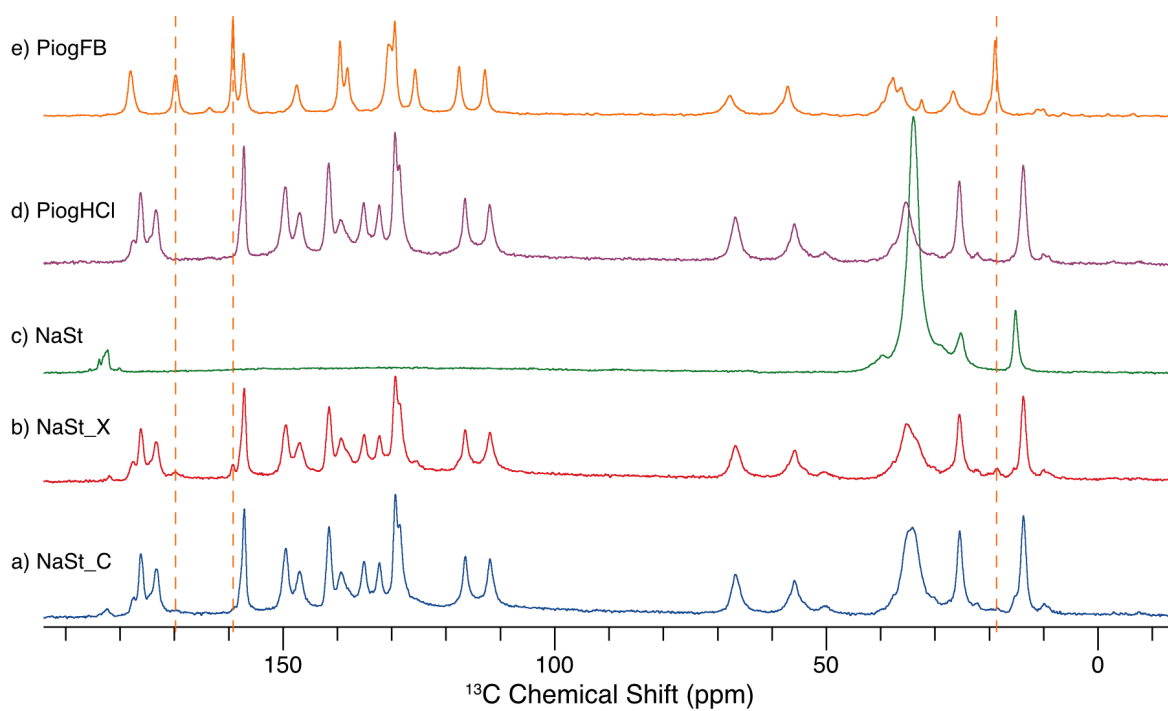


Figure E5. ^1H - ^{13}C CP/MAS ($\nu_{\text{rot}} = 12$ kHz) NMR spectra of **NaSt**-containing mixed samples and related materials. Dashed lines indicate distinct peaks from **PiogFB** that appear in the spectrum of **NaSt_X** (but not **NaSt_C**).

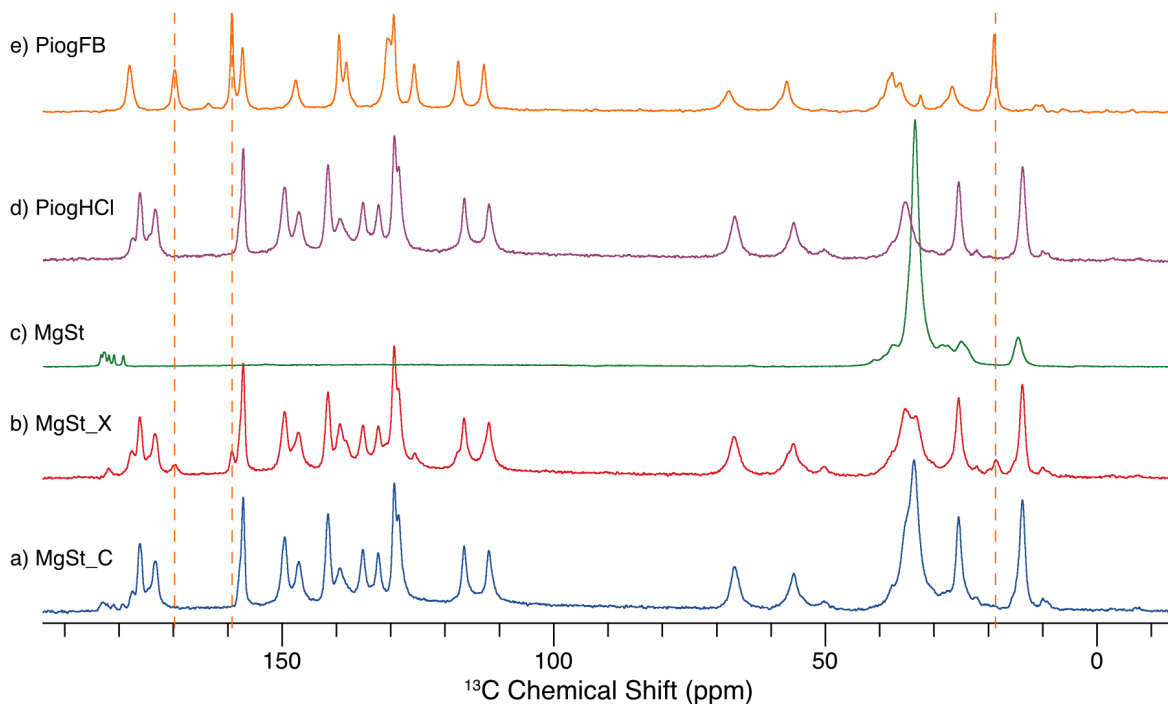


Figure E6. ^1H - ^{13}C CP/MAS ($v_{\text{rot}} = 12$ kHz) NMR spectra of **MgSt**-containing mixed samples and related materials. Dashed lines indicate distinct peaks from **PiogFB** that appear in the spectrum of **MgSt_X** (but not **MgSt_C**).

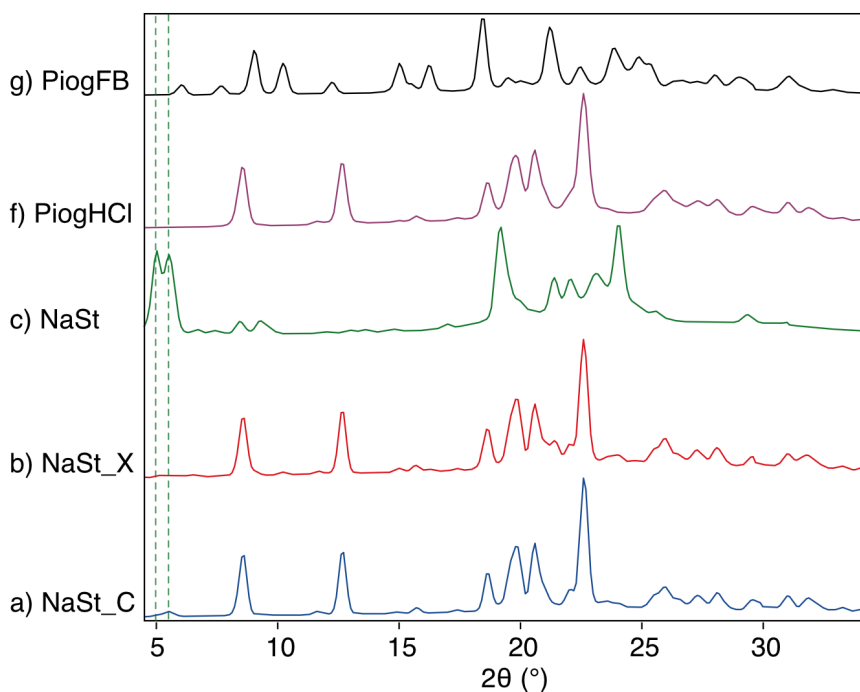


Figure E7. Experimental PXRD patterns of the **NaSt**-containing samples and pure constituents. Dashed lines indicate distinct features from the stearate that are present in the diffraction pattern of **NaSt_C**.

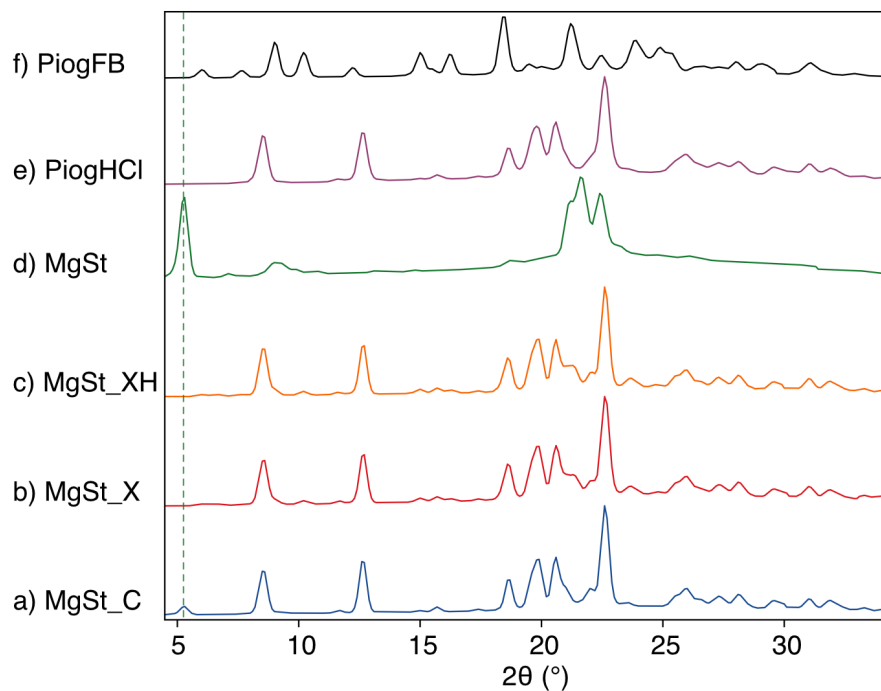


Figure E8. Experimental PXRD patterns of the **MgSt**-containing samples and pure constituents. Dashed lines indicate distinct features from the stearate that are present in the diffraction pattern of **MgSt_C**.

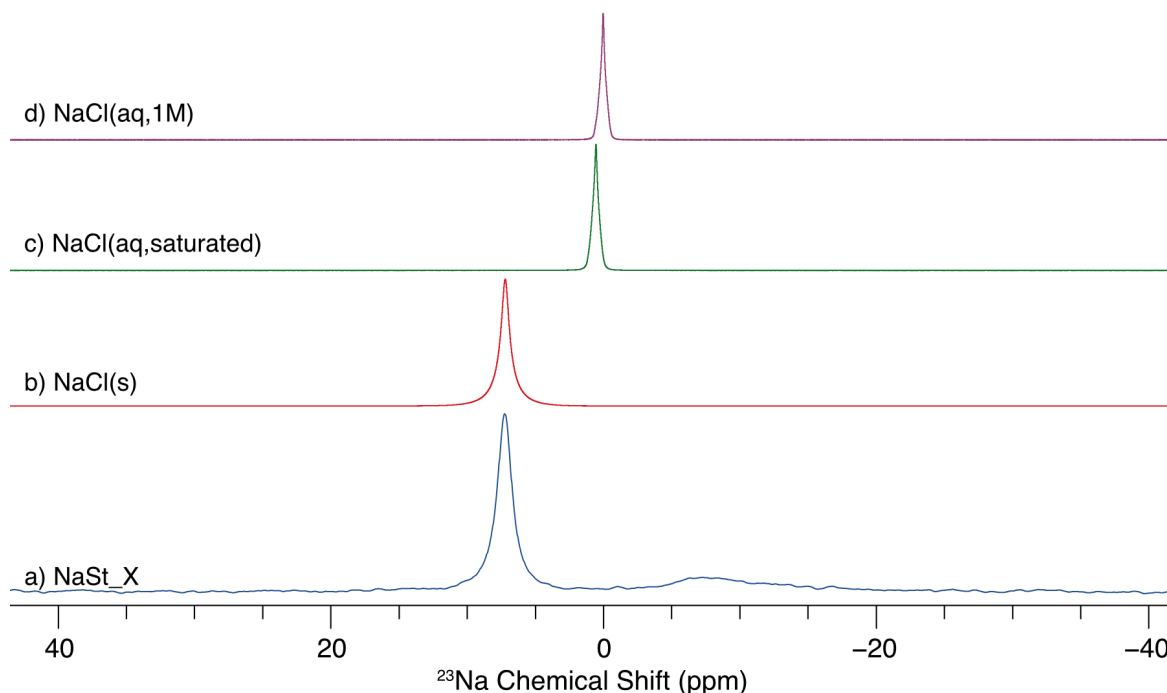


Figure E9. ^{23}Na Hahn echo NMR spectra of a) **NaSt_X**, b) solid NaCl, c) a saturated NaCl solution in H_2O , and d) a 1 M NaCl solution in H_2O . Spectra of the solid samples were acquired with MAS ($v_{\text{rot}} = 12$ kHz). The spectrum of **NaSt_X** is the same as that in **Figure 6.4b**.

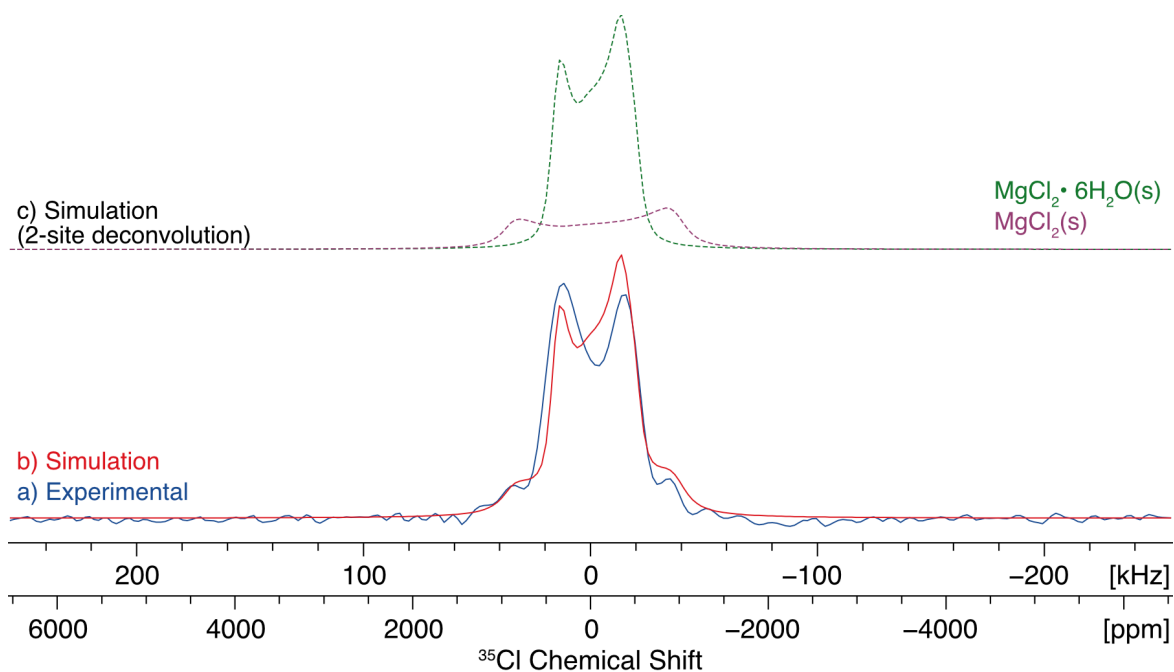


Figure E10. a) Experimental ^{35}Cl WURST-CPMG NMR spectrum of the disproportionation product in the **MgSt_X** sample (obtained by subtracting the signal in the spectrum of **MgSt_C** from that of **MgSt_X**), b) analytical simulation of the pattern constructed with the 2 subspectra shown in c).

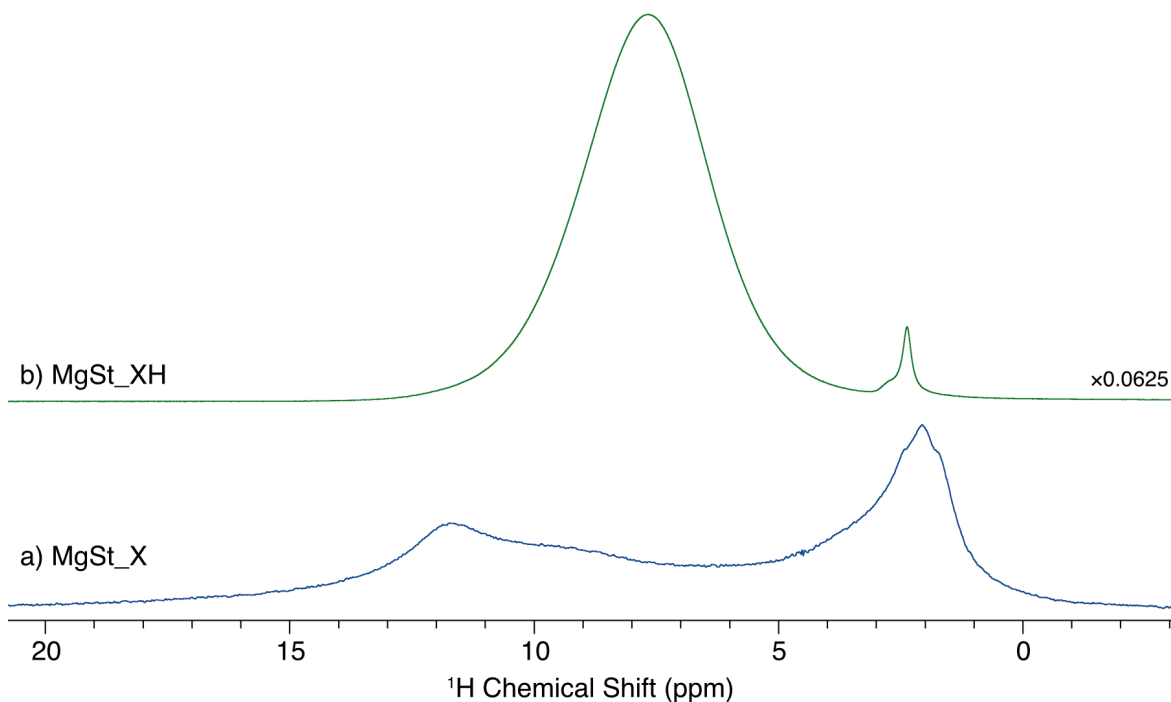


Figure E11. ^1H NMR spectra acquired under static sample conditions of a) **MgSt_X**, and b) **MgSt_XH**, which was prepared by placing 300 mg of **MgSt_X** in a 75% RH chamber for 4 hours.

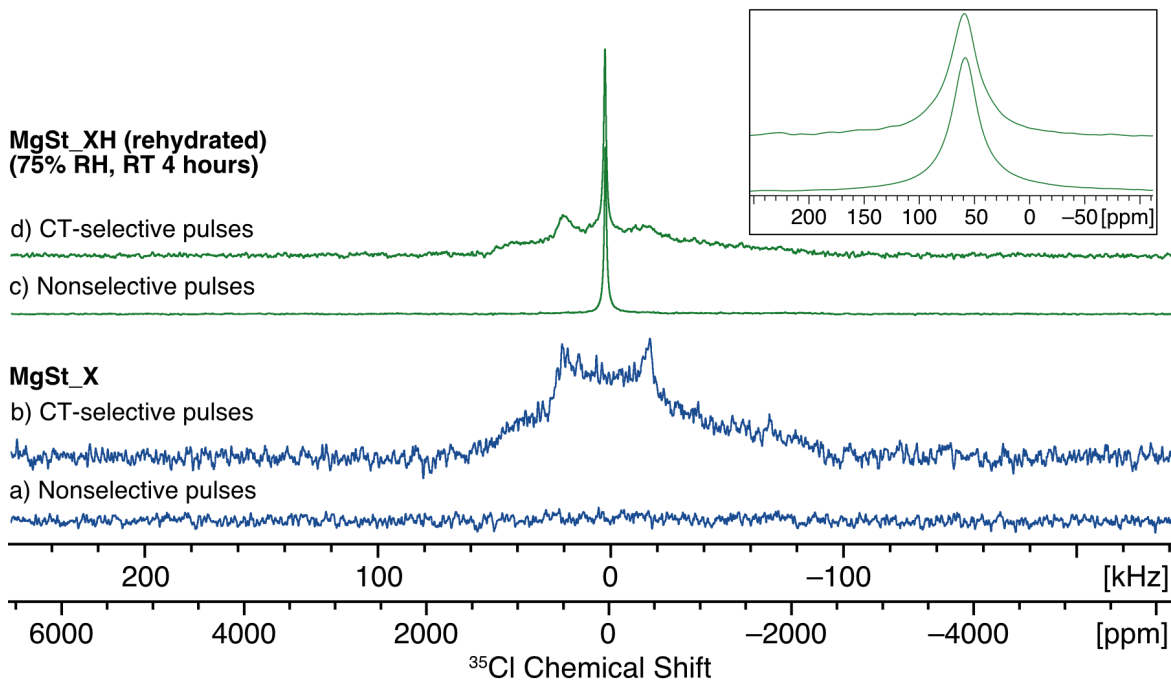


Figure E12. ^{35}Cl Hahn echo NMR spectra of **MgSt_X** (bottom, blue) and **MgSt_XH** (top, green) acquired with nonselective pulses, a) and c), or CT-selective pulses, b) and d). The inset shows an expansion of the region containing the sharp features in the spectra of **MgSt_XH**.

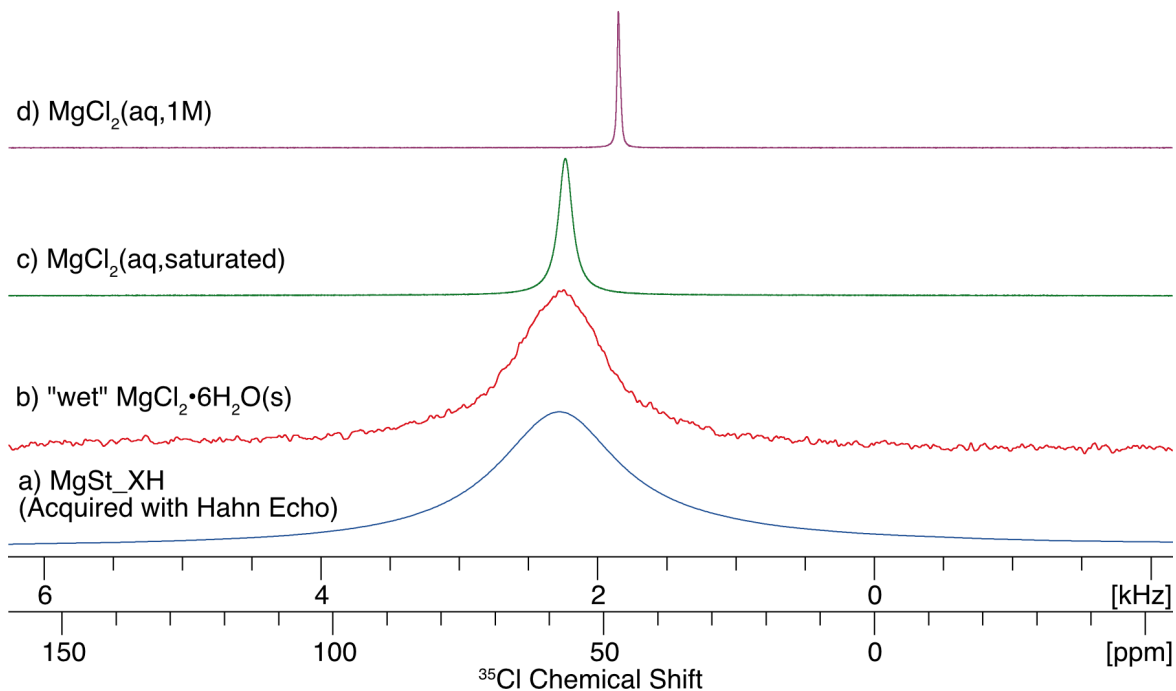


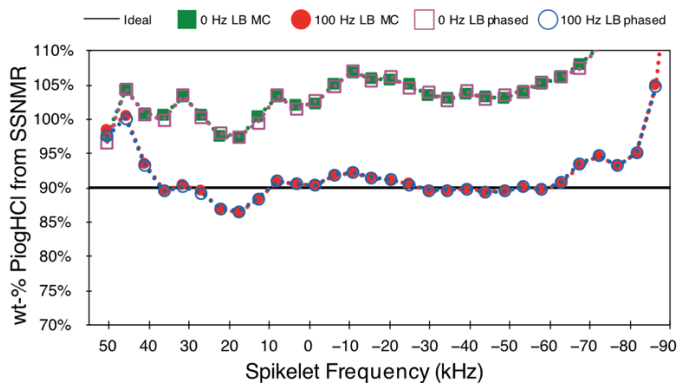
Figure E13. $^{35}\text{Cl}\{^1\text{H}\}$ Hahn echo NMR spectra of a) **MgSt_XH**, b) solid $\text{MgCl}_2 \cdot 6\text{H}_2\text{O}$ that was exposed to moisture in the air, c) saturated MgCl_2 solution in H_2O , and d) 1 M MgCl_2 solution in H_2O . The spectrum of **MgSt_XH** is the same as that in **Figure E12c**.

Effects of Processing Parameters on Quantification of ^{35}Cl SSNMR Spectra

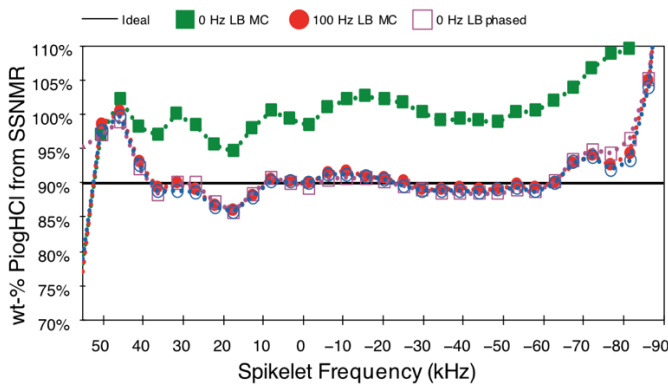
The following discussion pertains to the **PiogHCl 90%** sample, but the results are consistent for all of the standardization samples. **Figure E14a** and **Figure E14b** show the results of the quantification analysis for all of the spikelets in spectra processed using a total of four different processing methods. These four data sets were prepared from the same experimental data, using combinations of 100 Hz of exponential line broadening (or no line broadening), and by taking the absolute magnitude of the spectrum (or phasing). In the plots, a solid horizontal black line indicates the amount of **PiogHCl** that is expected to be in the sample based on the sample's preparation (*i.e.*, sample masses of the constituents). Each point in the colored lines corresponds to a measured value based on the intensity of a given spikelet. As such, the closer a point is to the black line, the higher the accuracy of the measurement.

For measurements using maximum spikelet intensity (**MSI, Figure E14a**), spectra processed without line broadening (solid green and open purple squares) produce nearly identical results, and both have poor accuracy (*i.e.*, all of the values are 10-20 wt-% higher than the expected value). However, with the addition of 100 Hz of line broadening, nearly all of the points move within 5 wt-% of the ideal value, due to increased S/N. Additional line broadening was tested, but produced the same results as 100 Hz and did not lead to improvements in the accuracy. For all of the processing methods, there are a few points at the left and right side of the spectrum that provide inaccurate measurements, regardless of the processing method. Measurements using these points are likely hindered by the low signal at these frequencies due to the inherent shapes of the second-order powder patterns (*cf.* spectrum in **Figure E14c**).

a) Maximum Spikelet Intensity (MSI)



b) Integrated Spikelet Intensity (ISI)



c) Spectrum

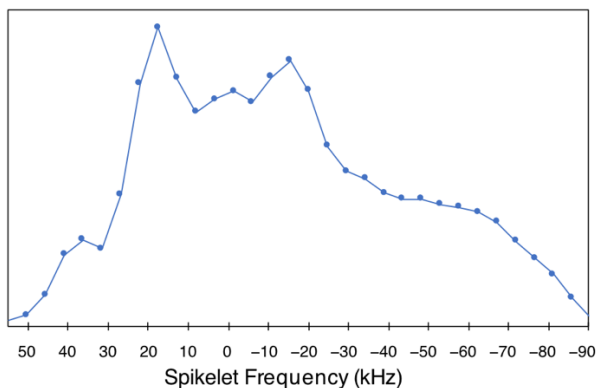


Figure E14. Results of the quantification analysis of the ^{35}Cl NMR spikelet spectrum of **PiogHCl 90%** using different processing parameters. Intensities were measured using a) spikelet intensities and b) integrated intensities of the spectrum, depicted in c). In a) and b), data were obtained from spectra processed by taking the absolute magnitude (closed shapes) or phasing (open shapes), with (squares) and without (circles) the application of 100 Hz of exponential line broadening.

For measurements using the integrated intensities of the spikelets (**ISI, Figure E14b**), the only method with poor accuracy is magnitude processing without line broadening (solid green squares). However, when 100 Hz of exponential line broadening are applied prior to Fourier transformation and magnitude calculation, the results are just as accurate as those obtained when phasing the spectra, and are close to the expected value. Unlike the previous case using peak intensity measurements, if the spectrum is phased, differences in line broadening do not affect the accuracy.

Interestingly, the accuracy of the measurement does not seem to be correlated with the relative intensity of the spikelet as long as the signal is above some minimum threshold. For example, the highest intensity spikelets (known as the "horns") perform about as well as other parts of the pattern. As mentioned above, points at the two ends of the spectrum (where the pattern has lowest signal intensity) do not perform well, regardless of the processing method used.

The origins of these differences in accuracy are unclear at the moment. We speculate that the importance of line broadening stems from a need to ensure that the echo train has decayed by the end of the acquisition period for accurate quantification. **PiogHCl** has a long T_2^{eff} , and it is possible that measurements on samples with shorter T_2^{eff} will not be as influenced by line broadening. Additionally, there may be other processing methods that may affect the measurement accuracy, or other factors of the experimental setup that may play a role (*e.g.*, parameters in the swept WURST pulses). Such issues should be tackled with a theoretical approach that is outside the scope of the current proof-of-concept work.

In conclusion, for the **PiogHCl** system, we observe empirically that 100 Hz line broadening improves the measured values, and that taking the absolute magnitude of the spectra (rather than phasing) is sufficient.

Appendix F: Supporting Tables and Figures for Chapter 7

Table F1. Acquisition parameters for $^{35}\text{Cl}\{^1\text{H}\}$ WURST-CPMG experiments ($B_0 = 9.4$ T).

	All Samples
Number of scans	44056
Experimental time (h)	6.12
Recycle delay (s)	0.5
Spectral Width (MHz)	1
^{35}Cl WURST pulse width (μs)	25
^{35}Cl WURST pulse rf (kHz)	19
^1H decoupling field (kHz)	62
Sweep range of WURST pulses (kHz)	500
Points in WURST shape [N]	500
Meiboom-Gill loops [N] (<i>i.e.</i> , Number of echoes)	44
Length of echoes (μs)	100
Acquisition length (number of points)	16700

Table F2. Acquisition parameters for $^{35}\text{Cl}\{^1\text{H}\}$ quadrupolar-echo experiments ($B_0 = 21.1$ T).

	All Samples
Number of scans	16384
Experimental time (h)	9.1
Recycle delay (s)	2
Spectral Width (kHz)	250
^{35}Cl pulse width (μs)	4
^{35}Cl pulse rf (kHz)	32
Inter-pulse delay [τ] (μs)	50
^1H decoupling field (kHz)	80
Acquisition length (number of points)	1024

Table F3. Acquisition parameters for ^1H - ^{13}C CP/MAS ($\nu_{\text{rot}} = 12$ kHz) experiments.

	As Received	All Other Samples
Number of scans	789	1248
Experimental time (hrs)	1.1	1.73
Recycle delay (s)	5	5
^1H 90° pulse width [$\pi/2$] (μs)	2.5	2.5
Contact time (ms)	1.5	1.5
^1H rf field during contact pulse (kHz)	40	40
^{13}C rf field during contact pulse (kHz)	51	51
^1H decoupling field (kHz)	47	47
Spectral width (kHz)	59.5	59.5
Acquisition length (number of points)	4096	4096

Table F4. Acquisition parameters for $^2\text{H}\{^1\text{H}\}$ quadrupolar-echo experiments.

	All Samples
Number of scans	201-600
Experimental time (min) ^b	120-15
Recycle delay (s) ^c	30-1
^2H 90° pulse width [$\pi/2$] (μs)	2.4
Inter-pulse delay [τ] (us)	24
^2H rf field (kHz)	101
^1H decoupling field (kHz)	50
Spectral width (MHz)	1
Acquisition length (# of points)	2008

^aThe experimental time varied due to differences in the optimal recycle delay and number of scans acquired. ^bThe recycle delay was optimized at each sample temperature. The optimal value progressively decreased as the sample was heated.

Table F5. Acquisition parameters for ^1H MAS Hahn echo experiments.

	All Samples	
Number of scans	16	48
Experimental time (min)	2.7	4
Recycle delay (s)	10	5
^1H 90° pulse width [$\pi/2$] (μs)	2.5	2.083
Inter-pulse delay [τ] (us)	83.3	16.67
^1H 180° pulse width [π] (μs)	5	4.166
^1H rf field (kHz)	100	120
Spectral width (kHz)	150	33.33
Acquisition length (# of points)	1024	1024
MAS Rate (kHz)	12	60

Table F6. Acquisition parameters for ^{19}F UFMAS ($\nu_{\text{rot}} = 60$ kHz) Hahn echo experiments.

	As Received
Number of scans	800
Experimental time (min)	67
Recycle delay (s)	5
^{19}F 90° pulse width [$\pi/2$] (μs)	2.083
Inter-pulse delay [τ] (μs)	16.67
^{19}F 180° pulse width [π] (μs)	4.166
^{19}F rf field (kHz)	120
Spectral width (kHz)	740
Acquisition length (# of points)	4090

Table F7. Additional parameters used in the DFT-D2* calculations conducted with CASTEP.

Parameter	Value
k -point spacing	0.07 \AA^{-1}
Plane-wave cutoff energy	700 eV
Thresholds for structural convergence	
Maximum energy change	$5 \times 10^{-6} \text{ eV/atom}$
Maximum displacement	$5 \times 10^{-4} \text{ \AA/atom}$
Maximum Cartesian force	0.01 eV/\AA
Dispersion correction damping function parameters	
s_6	1.00
d	3.25

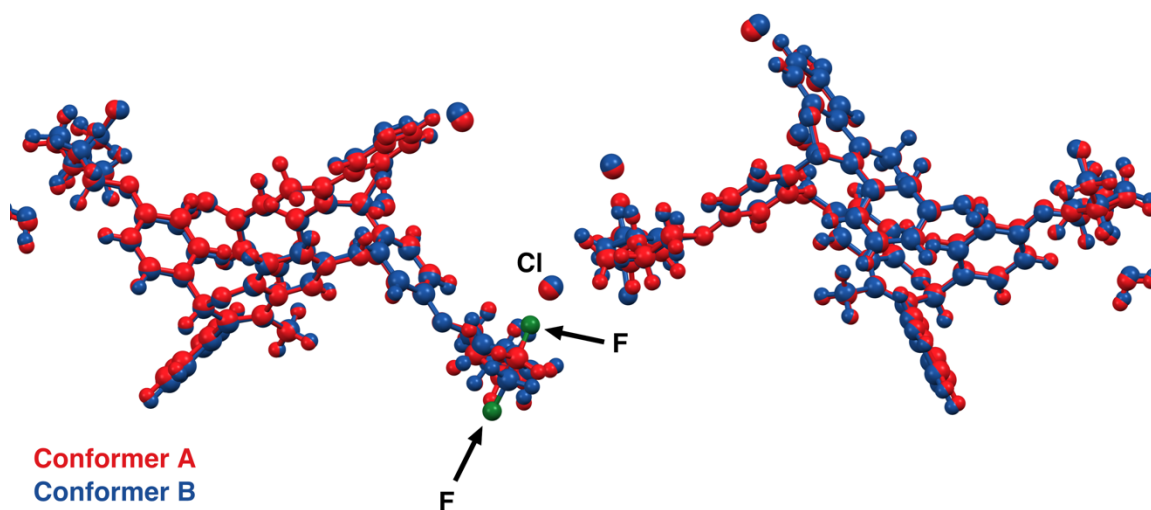


Figure F1. Overlay of the structures of the two GNE-A conformers **Conformer A** (red) and **Conformer B** (blue). The F atom (green) points either toward (**Conformer A**) or away from (**Conformer B**) the labeled Cl atom. See text for details.

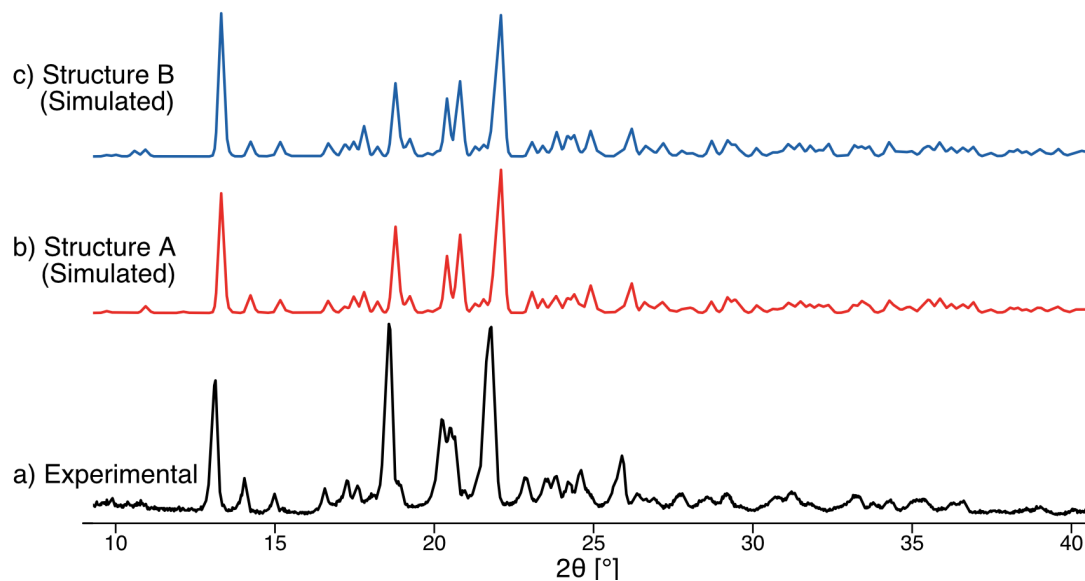


Figure F2. PXRD diffraction patterns of GNE-A a) obtained experimentally at 298 K or simulated from the crystal structures of the two conformers b) **Conformer A**, and c) **Conformer B** obtained at 100 K. Slight discrepancies in the peak positions result from unit cell contraction at the low temperature.

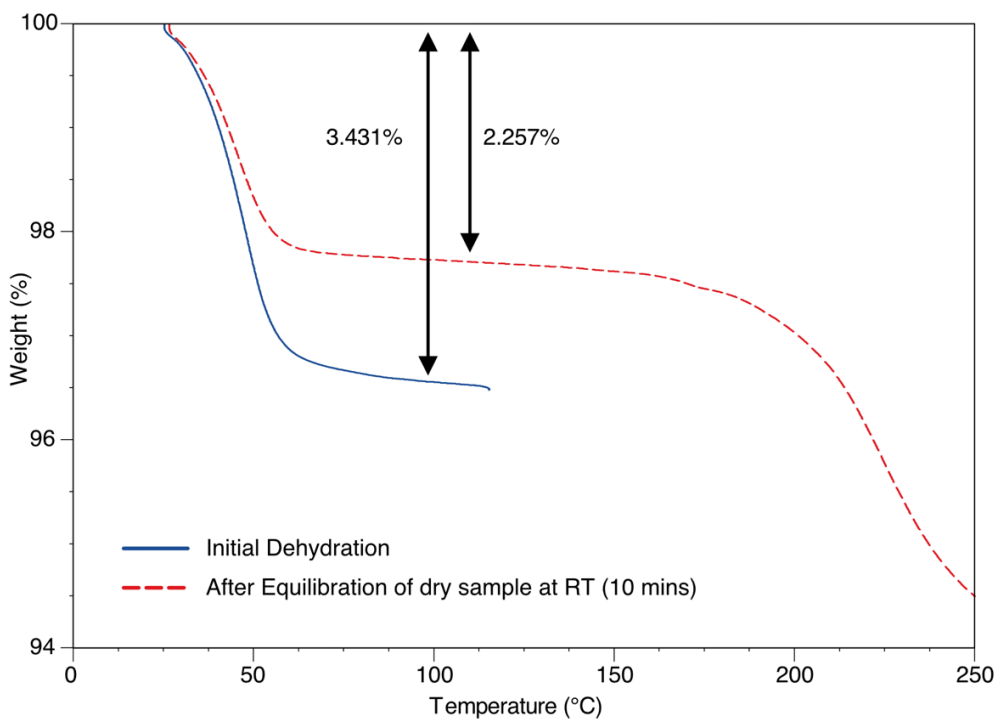


Figure F3. TGA data acquired for the **As Received** GNE-A sample (blue solid line) and the same sample after cooling and re-equilibrating at ambient humidity for 10 minutes (red dashed line).

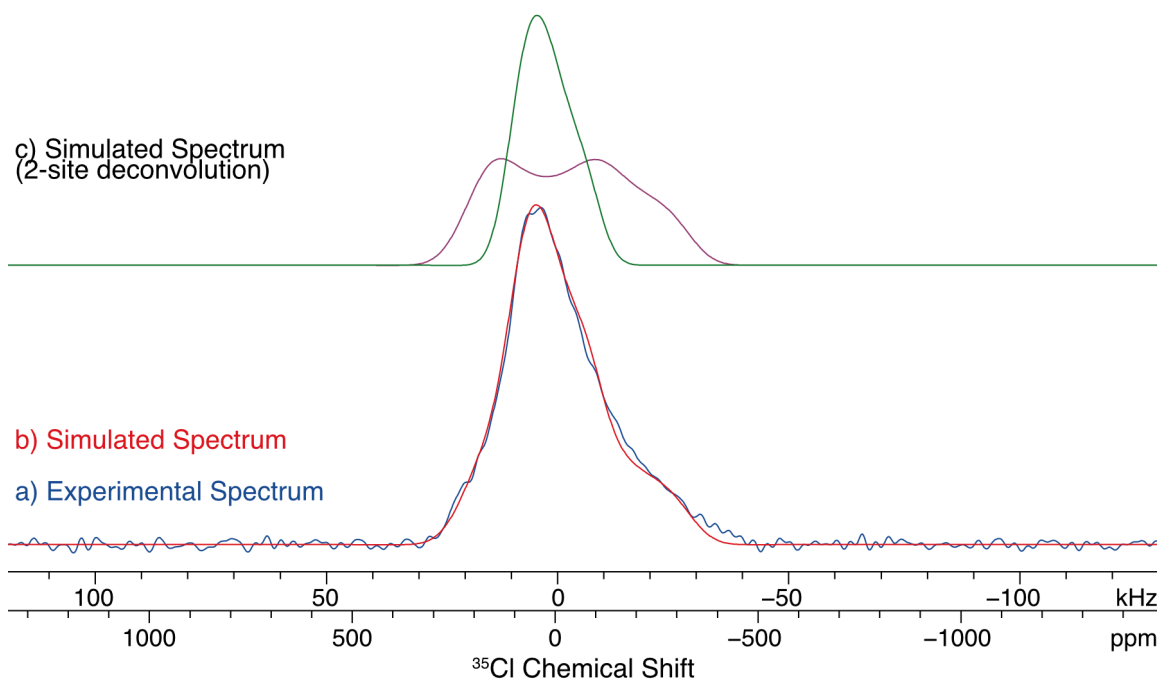


Figure F4. a) Experimental $^{35}\text{Cl}\{^1\text{H}\}$ quadrupolar echo NMR spectrum of GNE-A acquired at $B_0 = 21.1$ T, b) analytical simulation of the pattern constructed with the 2 subspectra shown in c).

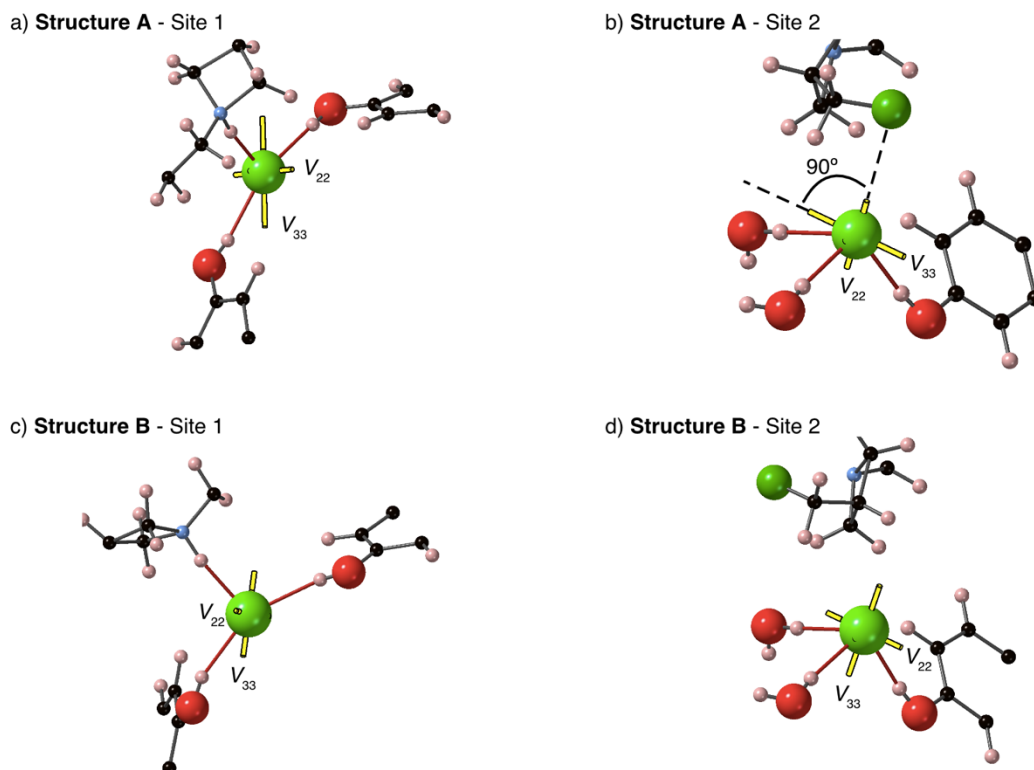


Figure F5. ^{35}Cl EFG tensor orientations in GNE-A calculated using CASTEP. The top row shows the two Cl^- environments in **Conformer A**, the bottom shows the corresponding environments in **Conformer B**. In b), the dashed lines indicate the orientations of V_{33} and the $\text{Cl}\cdots\text{F}$ contact, respectively. See text for details.

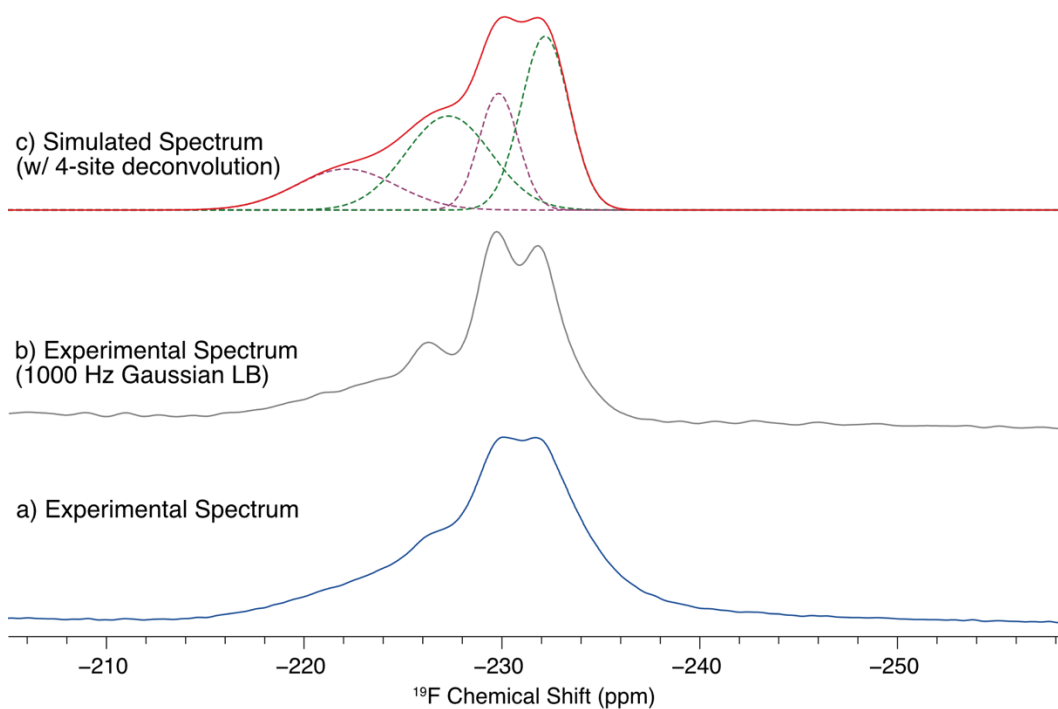


Figure F6. Experimental ^{19}F UFMAS ($\nu_{\text{rot}} = 60$ kHz) spectra of GNE-A processed a) without line broadening and b) with 1 kHz Gaussian line broadening (which enhances the resolution of the ^{19}F signal and reveals at least 4 distinct features). A simulated spectrum is shown in c) with the deconvoluted peaks and combined pattern shown as dashed and solid lines, respectively. The dashed lines in the deconvolution are colored according to possible peak assignments to the two crystallographically-distinct ^{19}F sites in the conformers: **Conformer A** (green), **Conformer B** (purple).

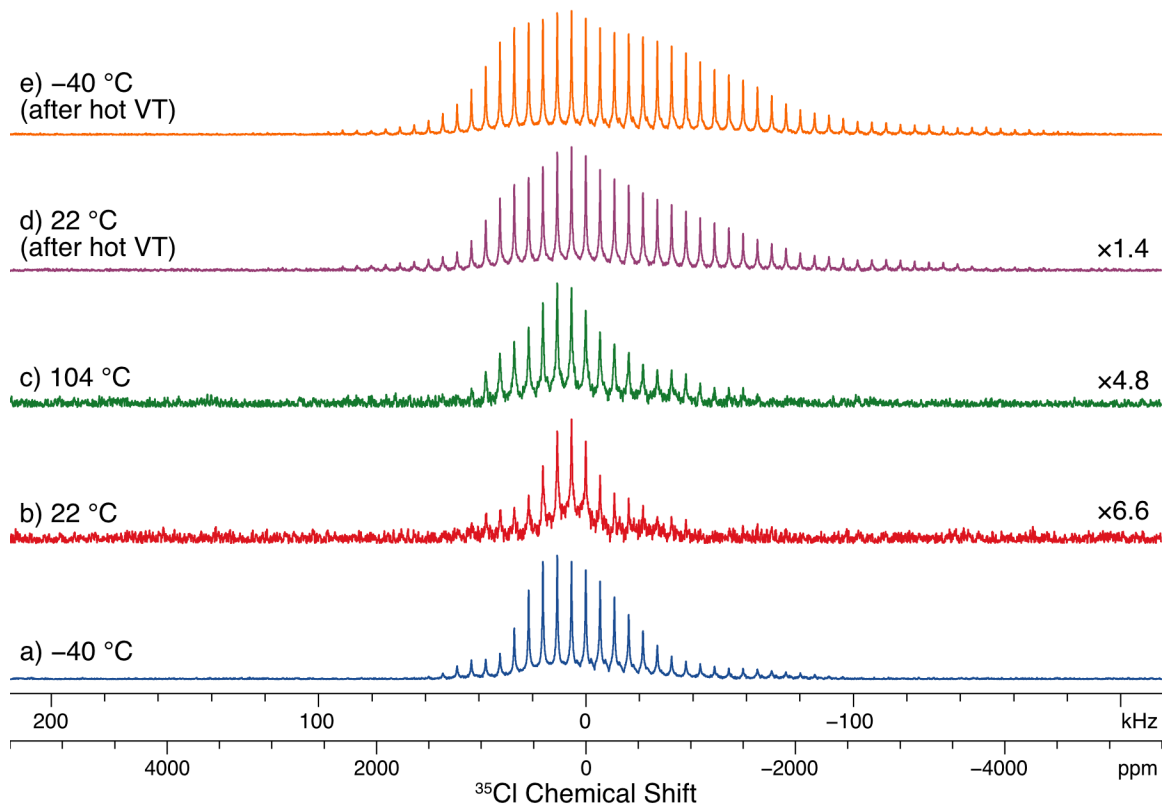


Figure F7. Variable temperature $^{35}\text{Cl}\{^1\text{H}\}$ WURST-CPMG NMR spectra of GNE-A acquired under static sample conditions. The spectra are presented in the order in which they were acquired starting at a) $-40\text{ }^\circ\text{C}$ before heating and ending with e) $-40\text{ }^\circ\text{C}$ after heating. Spectra are vertically scaled to have the same maximum intensity (the scaling factors are shown on the right).

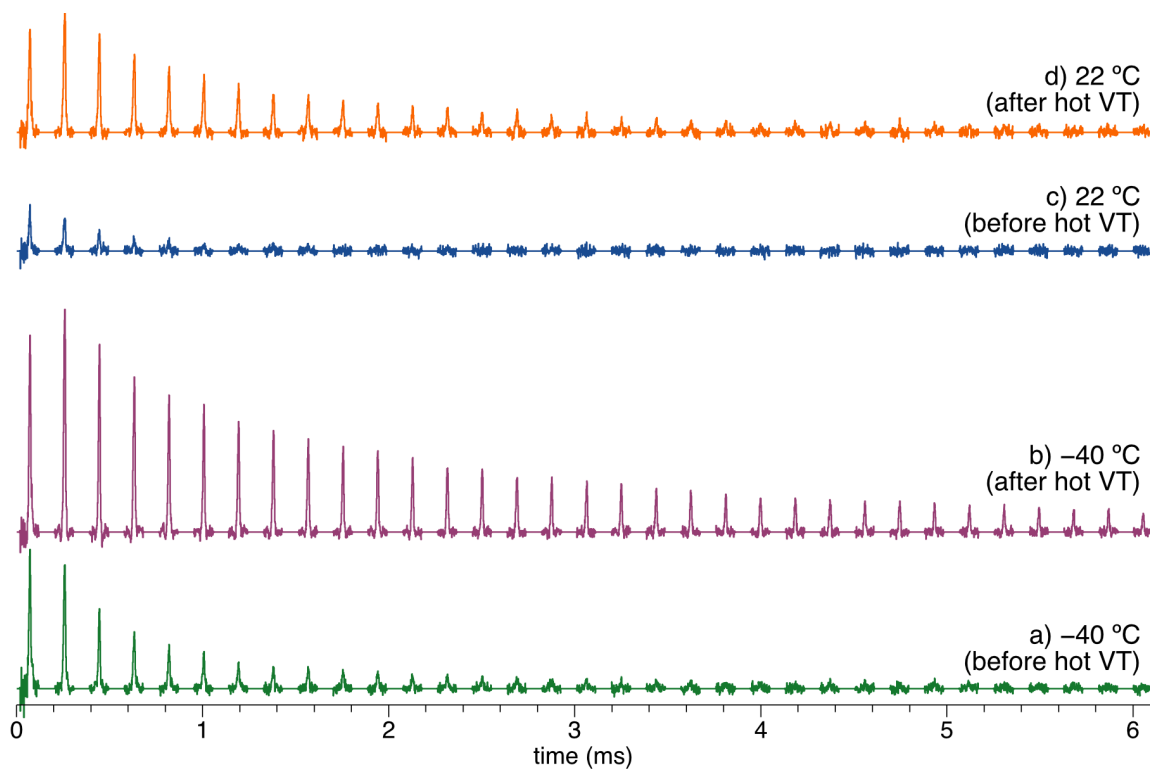


Figure F8. Experimental $^{35}\text{Cl}\{^1\text{H}\}$ WURST-CPMG echo trains of GNE-A acquired at $-40\text{ }^\circ\text{C}$ or $22\text{ }^\circ\text{C}$, before or after the samples were heated in the magnet (as indicated in the figure). $T_2^{\text{eff}}(^{35}\text{Cl})$ values measured from these data are shown in **Table 7.3**.

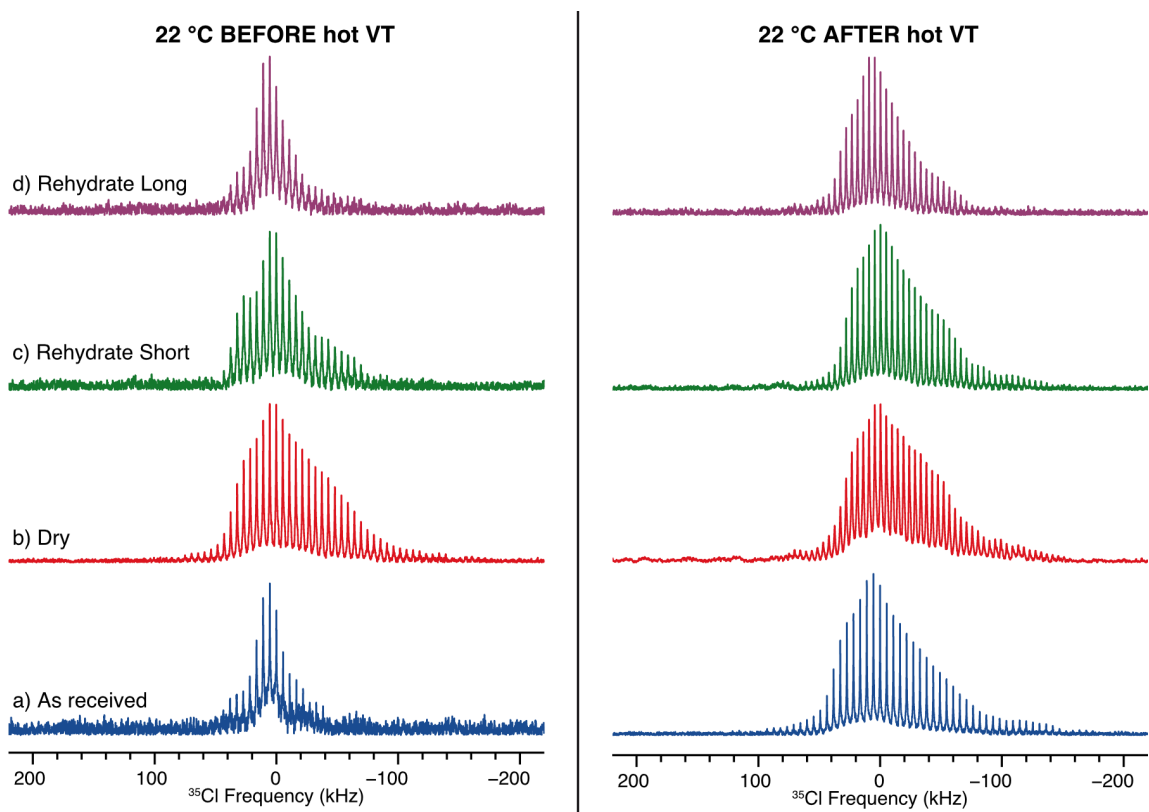


Figure F9. Experimental $^{35}\text{Cl}\{^1\text{H}\}$ WURST-CPMG NMR spectra of the four GNE-A samples acquired at 22 °C before (left column) and after (right column) heating in the magnet.

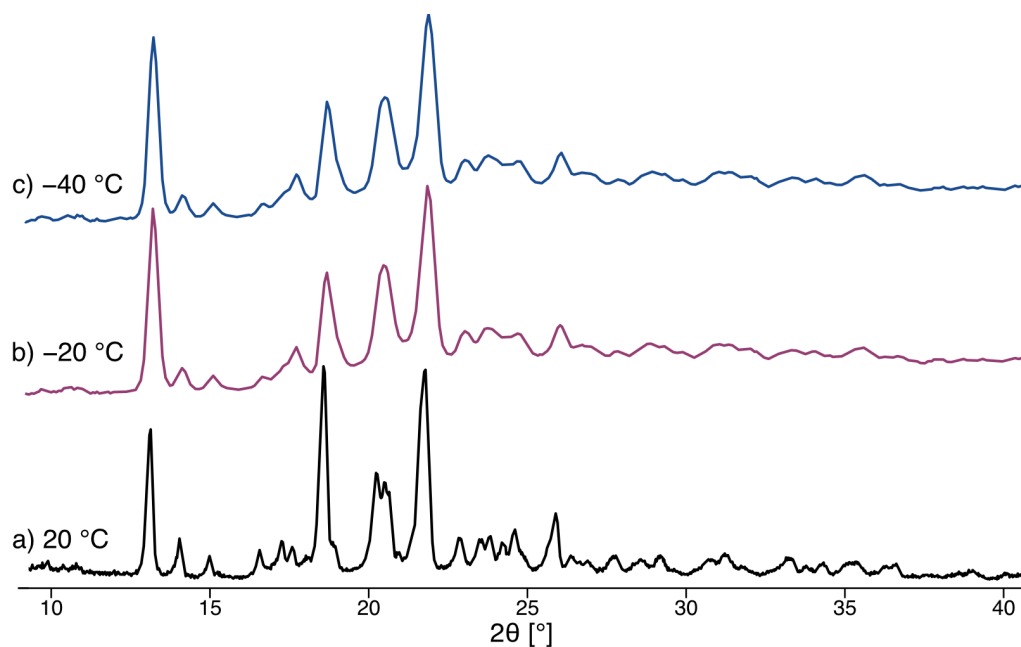


Figure F10. PXRD patterns of GNE-A acquired at a) 20 °C, b) -20 °C, and c) -40 °C. The patterns in b) and c) were acquired using a Bruker Hi-Star area detector, which has inherently lower resolution than the Proto AXRD used to acquire the pattern in a).

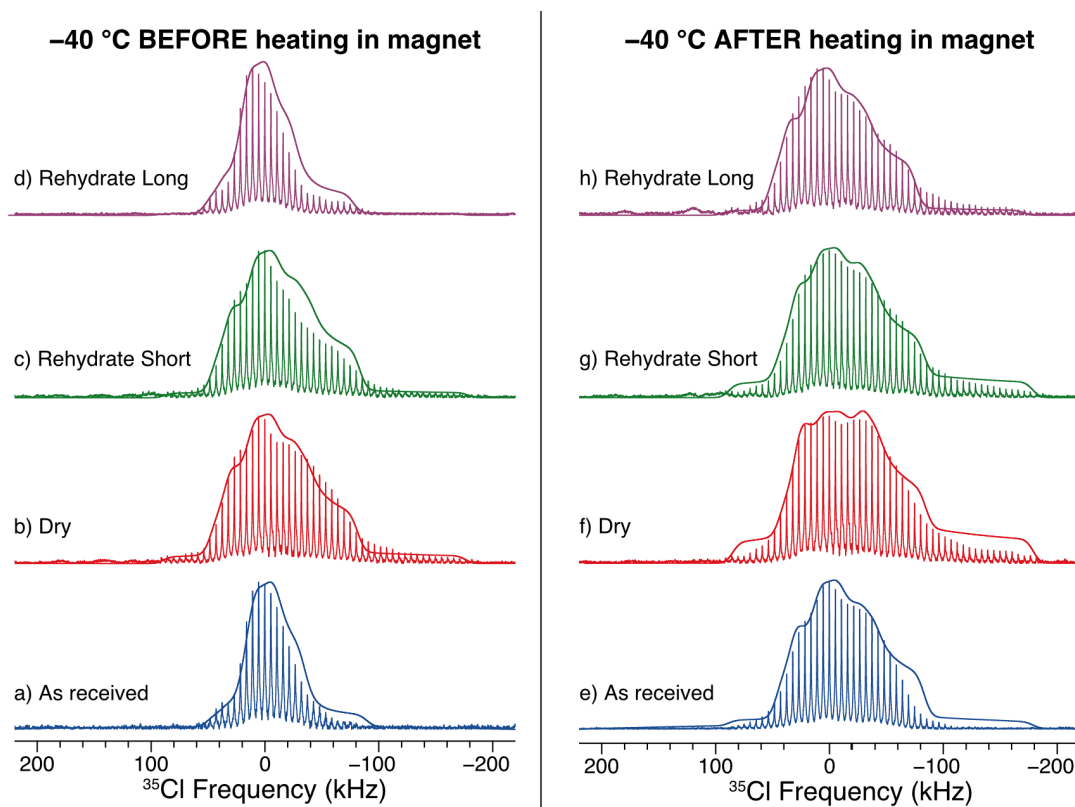


Figure F11. Experimental $^{35}\text{Cl}\{^1\text{H}\}$ WURST-CPMG NMR spectra of the four GNE-A samples acquired at $-40\text{ }^\circ\text{C}$ before (left) and after (right) heating in the magnet. This figure is identical to **Figure 7.5**, but without the deconvoluted spectra.

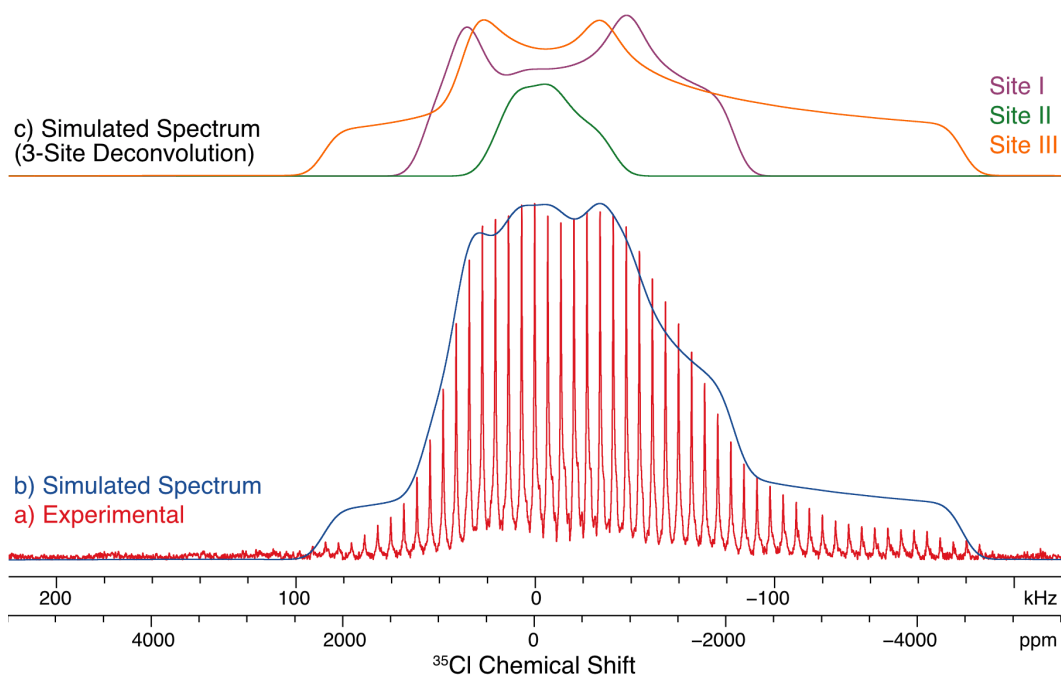


Figure F12. a) Experimental $^{35}\text{Cl}\{^1\text{H}\}$ WURST-CPMG NMR spectrum of the Dry sample, acquired at $-40\text{ }^\circ\text{C}$ after heating in the magnet, b) analytical simulation of the pattern constructed with the 3 subspectra shown in c).

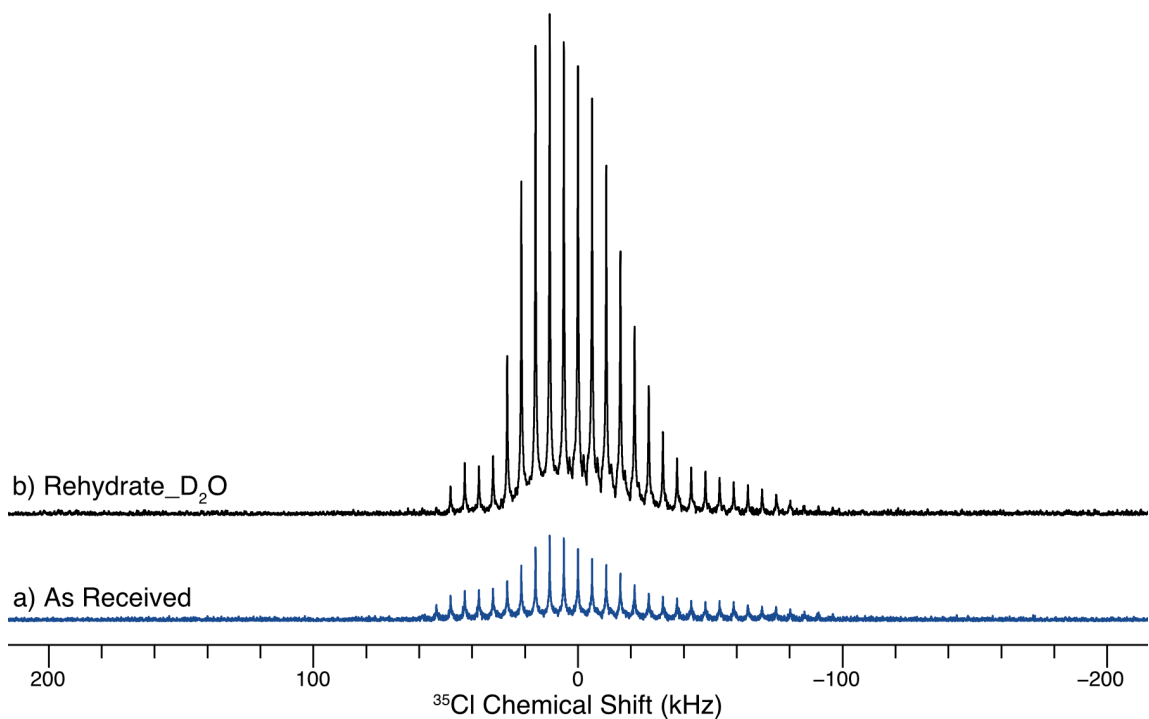


Figure F13. Experimental $^{35}\text{Cl}\{^1\text{H}\}$ WURST-CPMG NMR spectra of GNE-A a) **As Received** and b) after being dried and then rehydrated in a hydration chamber with D_2O (**Rehydrate- D_2O**). Spectra were acquired at $-40\text{ }^\circ\text{C}$.

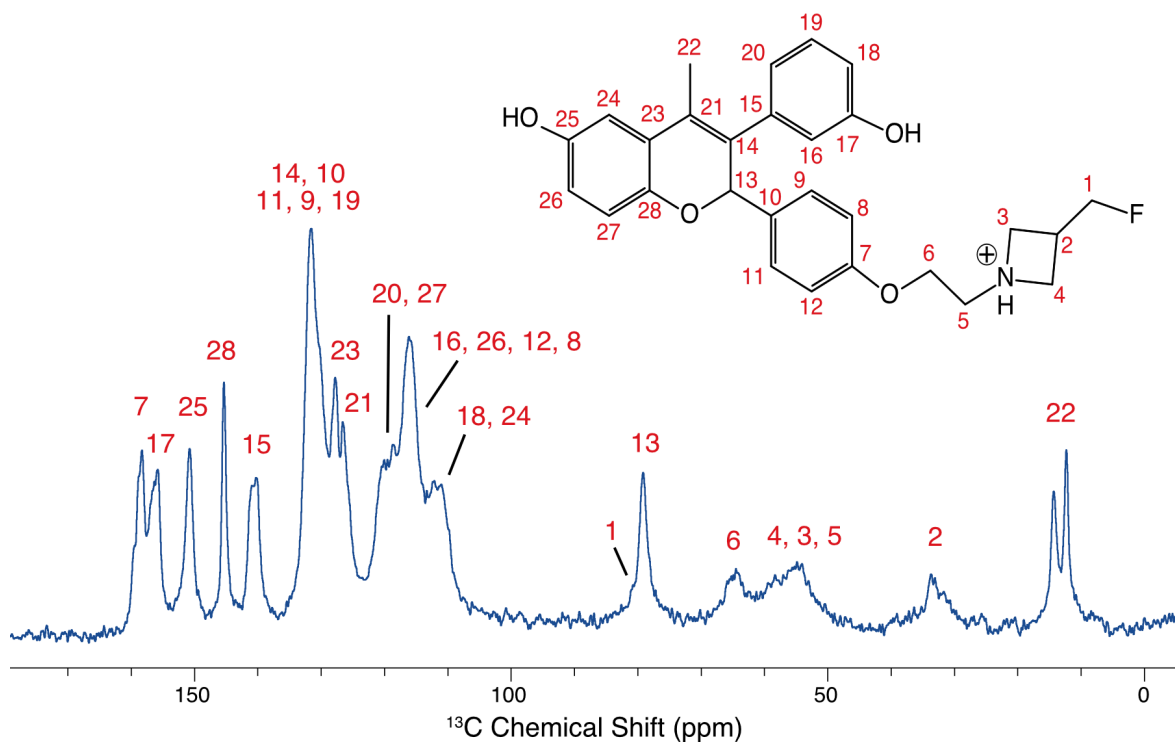


Figure F14. Peak assignments of the ^1H - ^{13}C CP/MAS ($\nu_{\text{rot}} = 12$ kHz) spectrum of the **As Received** sample (the structure of GNE-A is shown in the inset).

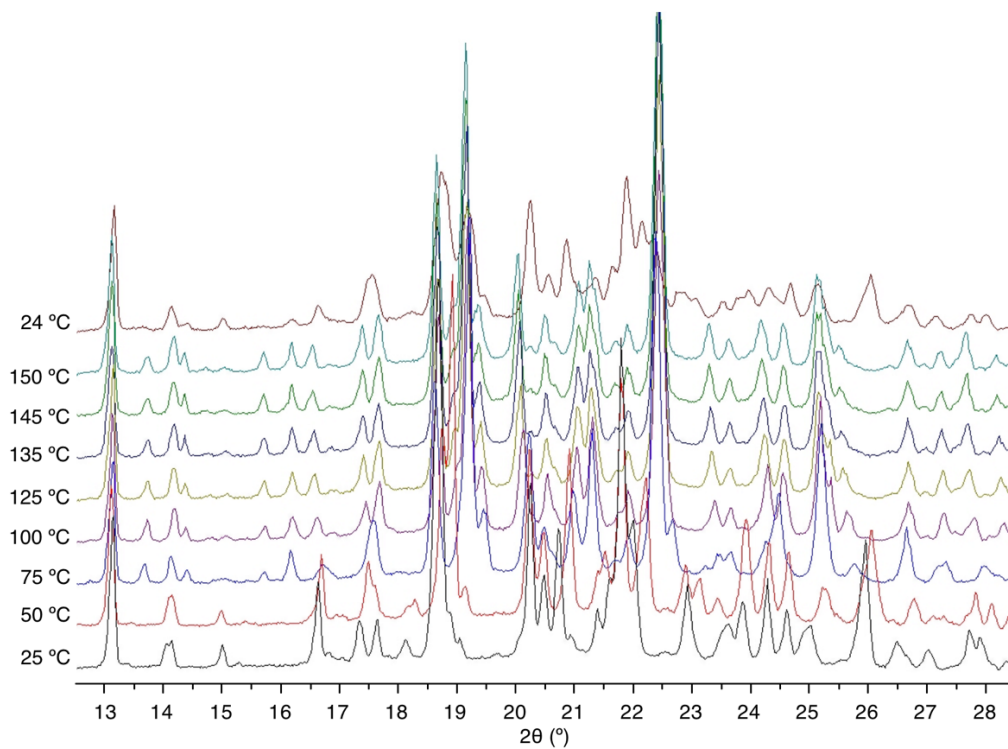


Figure F15. PXRD diffraction patterns of GNE-A obtained at various temperatures. The patterns were acquired in the order shown, from bottom to top.

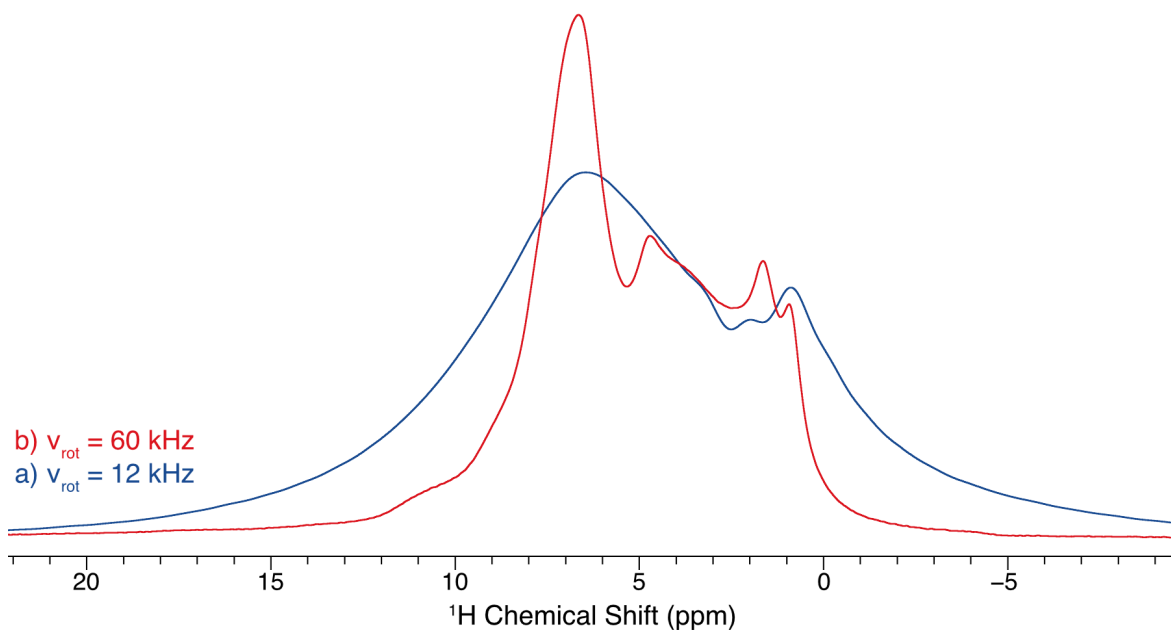


Figure F16. ^1H MAS spectra of GNE-A (As Received) at two different spinning rates a) $v_{\text{rot}} = 12 \text{ kHz}$, b) $v_{\text{rot}} = 60 \text{ kHz}$.

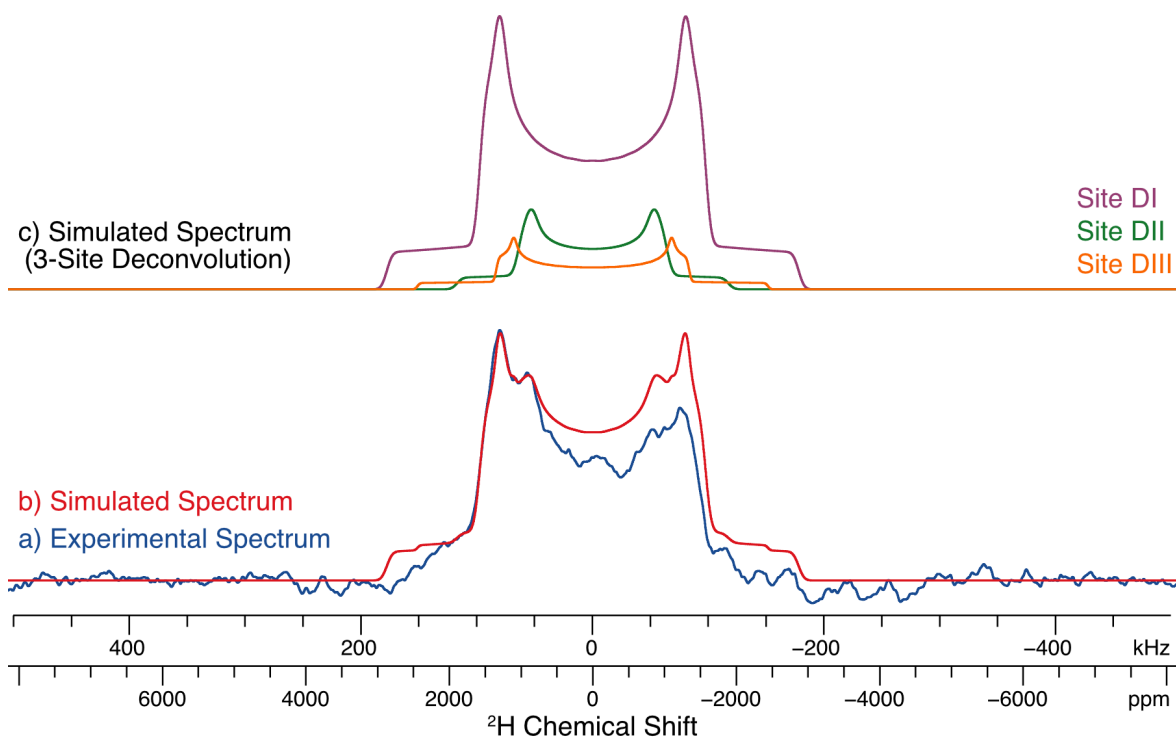


Figure F17. a) Experimental $^2\text{H}\{^1\text{H}\}$ quadrupolar-echo spectrum of **Rehydrate- D_2O** acquired at $-125 \text{ }^\circ\text{C}$, b) analytical simulation without ^2H dynamics (*i.e.*, in the slow-motion limit) of the pattern constructed with the 3 subspectra shown in c).

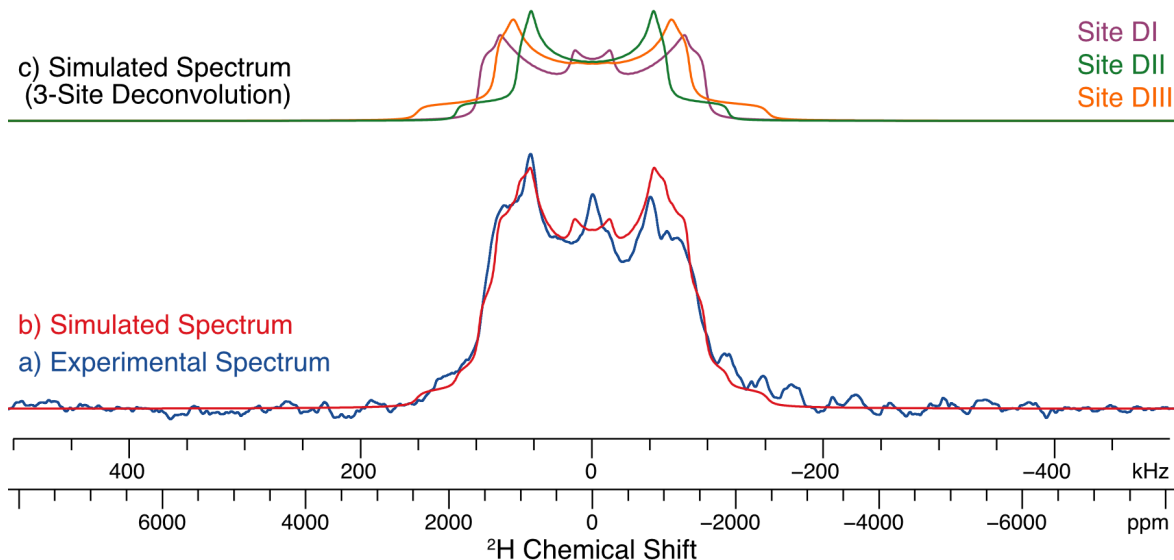


Figure F18. a) Experimental $^2\text{H}\{^1\text{H}\}$ quadrupolar-echo spectrum of **Rehydrate- D_2O** acquired at $-20\text{ }^\circ\text{C}$, b) analytical simulation of the pattern constructed with the 3 subspectra shown in c). The powder patterns were simulated with the effects of deuterium dynamics for **Site DI** (purple) and **Site DIII** (orange). Patterns were generated with the 180° flipping motion of a D_2O molecule about its C_{2v} axis at a rate of 0.75 MHz or 0.04 MHz, respectively. **Site DII** (green) is not affected by motion and was simulated in the slow-motion limit (see text for details).

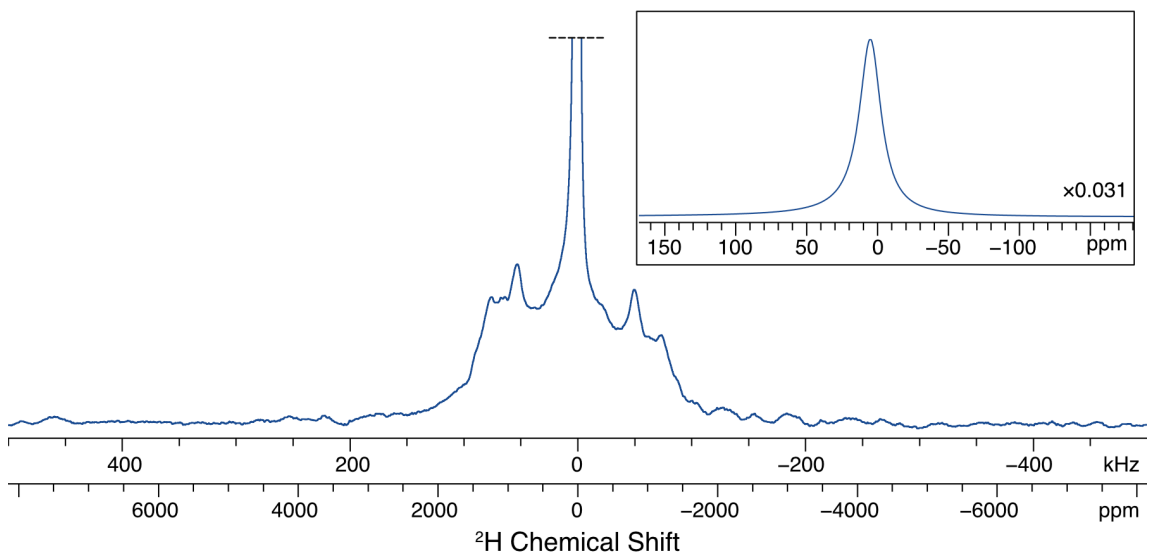


Figure F19. Experimental $^2\text{H}\{^1\text{H}\}$ quadrupolar-echo spectrum acquired at $22\text{ }^\circ\text{C}$ of a sample of **Rehydrate- D_2O** packed immediately after removal from the hydration chamber. This sample was damp, and likely contains liquid D_2O (as seen in the sharp feature at the center of the pattern, and in the inset). Before further experimentation, this sample was allowed to dry under ambient conditions in a vial for 2 weeks, at which point the spectra shown in **Figure 7.8** were acquired. Such storage conditions likely remove some of the bulk D_2O in the sample.

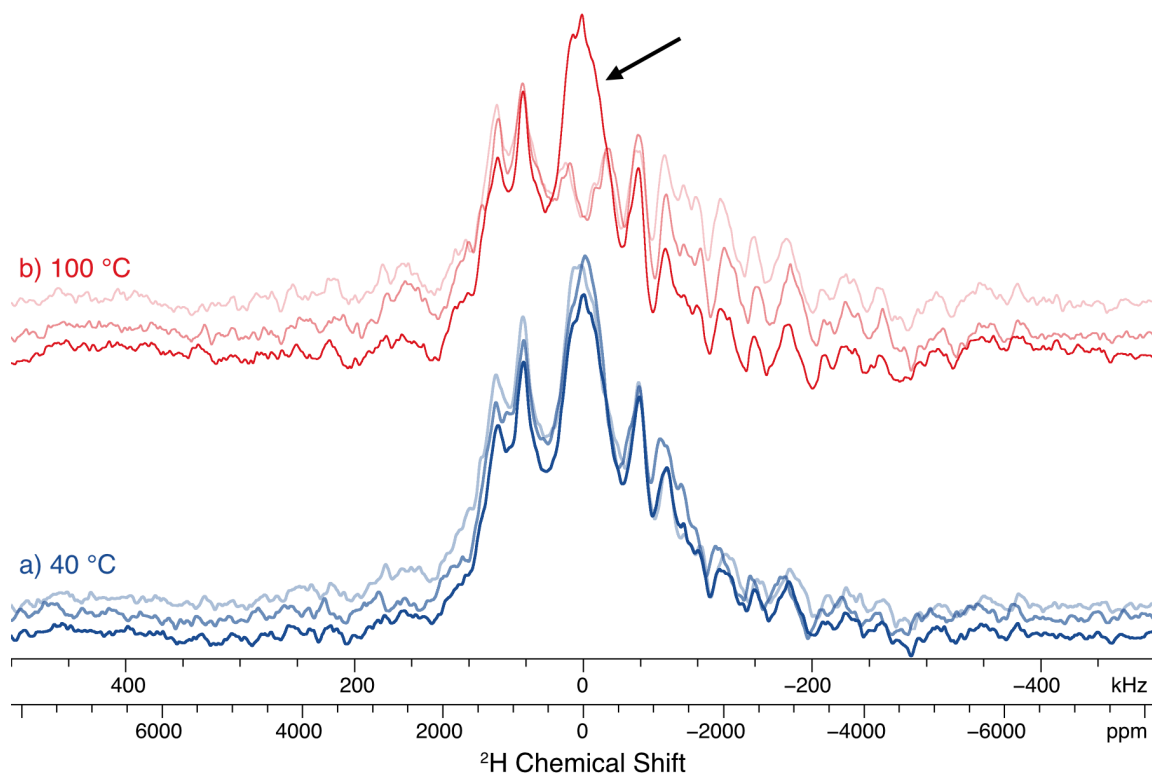


Figure F20. Experimental $^2\text{H}\{^1\text{H}\}$ quadrupolar-echo NMR spectra of **Rehydrate-D₂O** acquired at a) 40 °C (blue) or b) 100 °C (red). Three spectra are shown for each temperature, acquired sequentially in 15 minute increments. The darkest color was acquired first, and the faintest last. The arrow indicates the signal from mobile D₂O species that disappear from the spectrum after the sample is heated at 100 °C for *ca.* 15 minutes.

Vita Auctoris

NAME: David Alexander Hirsh

PLACE OF
BIRTH: Washington, DC

YEAR OF
BIRTH: 1989

EDUCATION: Sidwell Friends School, Washington, DC, 2008

Washington University in St. Louis, B.A., St. Louis, MO, 2010